



T.C.  
ÇANAKKALE ONSEKİZ MART ÜNİVERSİTESİ  
LİSANSÜSTÜ EĞİTİM ENSTİTÜSÜ

***CANAKKALE ONSEKİZ MART UNIVERSITY  
JOURNAL OF ADVANCED  
RESEARCH IN NATURAL AND  
APPLIED SCIENCES***



ISSN 2757-5195

**Journal of Advanced Research in Natural and Applied Sciences** (abbreviated as J. Adv. Res. Nat. Appl. Sci. or JARNAS) is an international, peer-reviewed, and open-access journal.

**J. Adv. Res. Nat. Appl. Sci.** is a science journal focusing on new science theories or their applications.

**JARNAS** was founded in 2015, and its first issue was published on 29 Dec 2015.

**Language:** As of 2024, JARNAS accepts contributions in American English only.

**Frequency:** 4 Issues Per Year

**Publication Dates:** March, June, September, and December

**ISSN:** 2757-5195

**Editor-in-Chief:** [Hüseyin Çavuş](#)

**Email:** jarnas.journal@gmail.com

**Publisher:** Çanakkale Onsekiz Mart University

**APC:** JARNAS incurs no article processing charges.

**Review Process:** Double-Blind Peer Review

**DOI Numbers:** The published papers are assigned DOI numbers.

## Journal Boards

### Editor-in-Chief

[Hüseyin Çavuş](#)

h\_cavus@comu.edu.tr

Çanakkale Onsekiz Mart University, Türkiye

### Editors

[Ali Bilici](#)

alibilici@comu.edu.tr

Çanakkale Onsekiz Mart University, Türkiye

[Fahri Aliçavuş](#)

fahrialicavus@comu.edu.tr

Çanakkale Onsekiz Mart University, Türkiye

[Nurcihan Hacıoğlu Doğru](#)

nhacioglu@comu.edu.tr

Çanakkale Onsekiz Mart University, Türkiye

[Serdar Enginođlu](#)

serdarenginoglu@gmail.com

Çanakkale Onsekiz Mart University, Türkiye

[Aykut Or](#)

aykutor@comu.edu.tr

Çanakkale Onsekiz Mart University, Türkiye

[Burcu Mestav](#)

burcumestav@comu.edu.tr

Çanakkale Onsekiz Mart University, Türkiye

[Alper Sađlık](#)

alpersaglik@gmail.com

Çanakkale Onsekiz Mart University, Türkiye

[Samet Memiş](#)

samettmemis@gmail.com

Bandırma Onyedi Eylül University, Türkiye

[Volkan Eskizeybek](#)

veskizeybek@comu.edu.tr

Çanakkale Onsekiz Mart University, Türkiye

[Ayça Aydođdu](#)

ayca.aydogdu@comu.edu.tr

Çanakkale Onsekiz Mart University, Türkiye

[Özgür Turay Kaymakçı](#)

okaymakci@comu.edu.tr

Çanakkale Onsekiz Mart University, Türkiye

[Mehmet Ali Yücel](#)

aliyucel@comu.edu.tr

Çanakkale Onsekiz Mart University, Türkiye

[Murat Efgan Kibar](#)

efgankibar@kocaeli.edu.tr  
Kocaeli University University, Türkiye

[Mehmet Özgür](#)

mehmetozgur@comu.edu.tr  
Çanakkale Onsekiz Mart University, Türkiye

[Deniz Şanlıyüksel Yücel](#)

denizsyuksel@comu.edu.tr  
Çanakkale Onsekiz Mart University, Türkiye

[Bulut Ozan Ceylan](#)

bceylan@bandirma.edu.tr  
Bandırma Onyedli Eylül University, Türkiye

[Abdulkadir Atalan](#)

abdulkadiratalan@gmail.com  
Çanakkale Onsekiz Mart University, Türkiye

## Section Editors

### Mathematics

[Mehmet Gümüş](#), Çanakkale Onsekiz Mart University, Türkiye

[Tuğçe Aydın](#), Çanakkale Onsekiz Mart University, Türkiye

[Ebu Talib Çelik](#), Çanakkale Onsekiz Mart University, Türkiye

[Gönül Selin Savaşkan](#), Çanakkale Onsekiz Mart University, Türkiye

[Hakan Şahin](#), Bursa Teknik University, Türkiye

[Erdal Ulualan](#), Kütahya Dumlupınar University, Türkiye

[Muhammad Riaz](#), Punjab University, Pakistan

### Physics

[Doğukan Taşer](#), Çanakkale Onsekiz Mart University, Türkiye

[Emrah Sarıca](#), Başkent University, Türkiye

[Hyo-Seob Kim](#), Korea Institute of Industrial Technology, Korea

[Neslihan Alan](#), İstanbul University, Türkiye

## **Biology**

[Çiğdem Gül](#), Çanakkale Onsekiz Mart University, Türkiye

[Nurşen Çördük](#), Çanakkale Onsekiz Mart University, Türkiye

[Ersin Karabacak](#), Çanakkale Onsekiz Mart University, Türkiye

[Sefer Demirbaş](#), Namık Kemal University, Türkiye

[Tuğba Ergül Kalaycı](#), Recep Tayyip Erdoğan University, Türkiye

[Abdelkarim Laatamna](#), University of Djelfa, Algeria

## **Chemistry**

Serkan Karakaya, Çanakkale Onsekiz Mart University, Türkiye

[Gülbin Kurtay](#), Hacettepe University, Türkiye

[Arianit A. Reka](#), University of Tetova, Republic of North Macedonia

## **Information and Computing Sciences**

[Engin Şahin](#), Çanakkale Onsekiz Mart University, Türkiye

[Sait Can Yücebaş](#), Çanakkale Onsekiz Mart University, Türkiye

[Uğur Erkan](#), Karamanoğlu Mehmetbey University, Türkiye

[Serhat Kılıçarslan](#), Bandırma Onyediy Eylül University, Türkiye

[Mehmet Akif Bülbül](#), Kayseri University, Türkiye

[Bharat Garg](#), Thapar Institute of Engineering and Technology, India

## **Chemical Engineering**

[Filiz Uğur Nigiz](#), Çanakkale Onsekiz Mart University, Türkiye

[Hasan Arslanoğlu](#), Çanakkale Onsekiz Mart University, Türkiye

[Derya Ünlü](#), Bursa Teknik University, Türkiye

Meltem Yıldız, Kocaeli Üniversitesi, Türkiye

Özge Kerkez Kuyumcu, Marmara Üniversitesi, Türkiye

## **Environmental Engineering**

[Simgе Taner Çankaya](#), Kocaeli University, Türkiye

Elif Durna Pişkin, Kocaeli University, Türkiye

### **Food Engineering**

Neşe Yılmaz Tuncel, Çanakkale Onsekiz Mart University  
Dilvin İpek, Çanakkale Onsekiz Mart University

### **Maritime Engineering**

[Oğuzhan Der](#), Bandırma Onyedi Eylül University, Türkiye  
[Cağlar Karatug ](#), İstanbul Technical University, Türkiye  
[Tayfun Uyanık](#), İstanbul Technical University, Türkiye  
[Onur Akdaş](#), Dokuz Eylül University, Türkiye  
[Pelin Erdem](#), Tyne Coast College, United Kingdom  
[Mina Tadros](#), Newcastle University, United Kingdom

### **Fluid Mechanics and Thermal Engineering**

[Hatice Sinem Şaş Çaycı](#), Sabancı University, Türkiye

### **Material Engineering, Mechanical Engineering**

[Bircan Haspulat Taymaz](#), Konya Technical University, Türkiye  
[Okan Demir](#), Konya Technical University, Türkiye

### **Manufacturing and Industrial Engineering**

[Murat Koyunbakan](#), Kütahya Dumlupınar University, Türkiye

### **Control Engineering, Mechatronics and Robotics**

[Yusuf Şahin](#), Niğde Ömer Halisdemir University, Türkiye

### **Mechanical Engineering**

[Emine Feyza Şük r](#), Samsun University, Türkiye  
Adem Yar, Bing l Üniversitesi, Türkiye

### **Automotive Engineering**

[Ferhat Yıldırım](#), Çanakkale Onsekiz Mart University, Türkiye

### **Nanotechnology**

[Adem Yar](#), Bing l University, Türkiye

### **Geomatics Engineering**

[Ali Melih Bařaraner](#), Yıldız Teknik Üniversitesi, Türkiye

[Atınc Pirtı](#), Yıldız Teknik Üniversitesi, Türkiye

[İsmail Rakip Karas](#), Karabük University, Türkiye

[Şükran Yalpir](#), Konya Technical University, Türkiye

[Osman Sami Kırtılođlu](#), İzmir Katip Çelebi Üniversitesi, Türkiye

### **Civil Engineering**

[İlknur Dalyan](#), Çanakkale Onsekiz Mart University, Türkiye

[Fevziye Ayça Saraçođlu](#), Çanakkale Onsekiz Mart University, Türkiye

Fatih Yonar, Çanakkale Onsekiz Mart University, Türkiye

[Selen Aktan](#), Çanakkale Onsekiz Mart University, Türkiye

[Muhammet Gökhan Altun](#), Çanakkale Onsekiz Mart University, Türkiye

[Erdiñ Keskin](#), Kırklareli University, Türkiye

[Rasoul Daneshfaraz](#), University of Maragheh, İran

### **Geological and Mining Engineering**

[İsmail Onur Tunc](#), Çanakkale Onsekiz Mart University, Türkiye

[Şebnem Önder](#), Çanakkale Onsekiz Mart University, Türkiye

[Mustafa Çınar](#), Çanakkale Onsekiz Mart University, Türkiye

[Alper Baba](#), İzmir Institute of Technology, Türkiye

### **Built Environment and Design**

[Pelin Fırat ÖRS](#), Çanakkale Onsekiz Mart University, Türkiye

Tutku AK, Çanakkale Onsekiz Mart University, Türkiye

[Elif SAĞLIK](#), Çanakkale Onsekiz Mart University, Türkiye

[Ali Tolga ÖZDEN](#), Çanakkale Onsekiz Mart University, Türkiye

### **Electrical and Electronics Engineering**

[Muzaffer Yücel](#), Çanakkale Onsekiz Mart University, Türkiye

[Muharrem Mercimek](#), Yıldız Technical University, Türkiye

[Muhammed Ali Nur Öz](#), Sakarya University of Applied Sciences, Türkiye

## Statistics

[Berrin GÜLTAY](#), Çanakkale Onsekiz Mart University, Türkiye

[Canan Güneş](#), Çanakkale Onsekiz Mart University, Türkiye

[Hande Konşuk Ünlü](#), Hacettepe University, Türkiye

[Kadir Karakaya](#), Selçuk University, Türkiye

[Aynur Yonar](#), Selçuk University, Türkiye

## Occupational Health and Safety

[Gülçin Özcan Ateş](#), Çanakkale Onsekiz Mart University, Türkiye

### Statistics Editor

[Burcu Mestav](#)

burcumestav@comu.edu.tr

Çanakkale Onsekiz Mart University, Türkiye

### Language Editor

Öznur Cengiz Çeliker

oznurcengiz@comu.edu.tr

Çanakkale Onsekiz Mart University, Türkiye

[Mehmet Yıldız](#)

mehmetyildiz@comu.edu.tr

Çanakkale Onsekiz Mart University, Türkiye

### Layout Editors

[Burak Arslan](#)

tburakarslan@gmail.com

Çanakkale Onsekiz Mart University, Türkiye

Kenan Sapan

kenannsapan@gmail.com

Çanakkale Onsekiz Mart University, Türkiye

Production Editors

[Deniz Fidan](#)

fidanddeniz@gmail.com

Çanakkale Onsekiz Mart University, Türkiye

[Rabia Özpınar](#)

rabiaozpınar@gmail.com

Bandırma Onyedli Eylül University, Türkiye

## CONTENTS

Research Article **Page : 771–785**

1. Classifying Sunn Pest Damaged and Healthy Wheat Grains Across Different Species with YOLOV8 and Vision Transformers

Melike Çolak , Özgü Özkan , Nergis Pervan Akman , Ali Berkol , Murat Olgun , Zekiye Budak Başçiftçi , Nazife Gözde Ayter Arpacioğlu , Okan Sezer , Murat Ardiç

Research Article **Page : 786–802**

2. Theoretical Calculations and Molecular Docking Analysis of 4-(2-(4-Bromophenyl)Hydrazineylidene)-3,5-Diphenyl-4H-Pyrazole Molecule

Kenan Gören , Mehmet Bağlan , Veysel Tahiroğlu , Ümit Yıldık

Research Article **Page : 803–818**

3. Assessing Drainage Performance of Turfgrass Rootzone in Sports Fields

Erdal Kesgin , Kadir Gezici , Remziye İlayda Tan Kesgin , Hayrullah Ağaçoğlu , Mustafa Karaagaçlı , Mehmet Turgut Sağlam

Research Article **Page : 819–832**

4. Machine Learning and Medical Data: Predicting ICU Mortality and Re-admission Risks

Ulya Bayram , Runia Roy

Research Article **Page : 833–844**

5. Effect of Compost Addition on Porosity and Hydraulic Properties of Different Textured Soils

Nurten İşler , Yasemin Kavdır

Research Article **Page : 845–860**

6. Sustainable Self-Healing Coatings: Optimizing Microencapsulation of Biodegradable Linseed and Hemp Seed Oils for Enhanced Corrosion Protection

Merve Mocan , Nazife Bengisu Sarıkaya

Research Article **Page : 861–874**

7. Investigation of Gamma Radiation Shielding in NiMnGa-Doped Multifunctional Smart Polymer Composites Using Geant4 and WinXCOM

Mustafa Kaya , Serpil Yalçın Kuzu , Seçil Niksarlıoğlu , Mustafa Ersin Pekdemir , Mediha Kök

Research Article **Page : 875–898**

8. A Bibliometric Analysis on Federated Learning

Ömer Algorabi , Yusuf Sait Türkan , Mesut Ulu , Ersin Namlı

Research Article **Page : 899–912**

9. A Novel Approach for Detection of Cyber Attacks in MQTT-Based IIoT Systems Using Machine Learning Techniques

Serkan Gönen

Research Article **Page : 913–921**

10. Performance of PMMA/Ta2O5 Composites as Medical Radiation Shielding: WinXCom and MCNP6 Studies

Mustafa Çağlar

Research Article **Page : 922–937**

11. Comparative Forecasting of Some Key Economic Indicators Using Artificial Neural Networks and Ordinary Differential Equations: A Case Study of the Turkish Economy

Bahatdin Daşbaşı , Murat Taşyürek

Research Article **Page : 938–953**

12. Assessment of Dyeing Properties of Hibiscus sabdariffa on Ostrich Leather

Mehmet Mete Mutlu , Deniz Kılıçaslan , Nilay Örk Efendioğlu

Research Article **Page : 954–967**

13. Accuracy of the Photometric Redshifts of Brightest Cluster Galaxies Identified in the CFHTLS-W1

Sinan Aliş

Research Article **Page : 968–980**

14. Real-Time Detection of Milk Adulteration with a Portable Multispectral Analysis Device: A Multispectral Sensor and Optimized Logistic Regression Approach

Mahmut Durgun

Research Article **Page : 981–995**

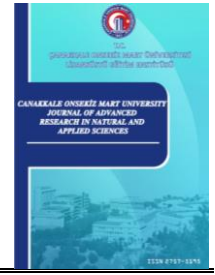
15. Ecological Footprint Awareness of Generation Z: A Case Study of Selçuk University Faculty of Science

Halil Osman Erbek , Yunus Akdoğan , Tenzile Erbayram

Research Article **Page : 996-1006**

16. Classification of Melanoma Cancer Using Deep Convolutional Neural Networks

Ali Güneş , Emrah Dönmez



# Classifying Sunn Pest Damaged and Healthy Wheat Grains Across Different Species with YOLOV8 and Vision Transformers

Melike Çolak<sup>1</sup> , Özgü Özkan<sup>2</sup> , Nergis Pervan-Akman<sup>3</sup> , Ali Berkol<sup>4</sup> , Murat Olgun<sup>5</sup> , Zekiye Budak-Başçiftçi<sup>6</sup> , Nazife Gözde Ayter-Arpacıoğlu<sup>7</sup> , Okan Sezer<sup>8</sup> , Murat Ardiç<sup>9</sup> 

<sup>1,2,3,4</sup>BİTES Defence and Aerospace Technologies, Ankara, Türkiye

<sup>5,6,7</sup>Department of Field Crop, Faculty of Agriculture, Eskişehir Osmangazi University, Eskişehir, Türkiye

<sup>8,9</sup>Department of Biology, Faculty of Science, Eskişehir Osmangazi University, Eskişehir, Türkiye

## Article Info

Received: 08 Jul 2024

Accepted: 27 Oct 2024

Published: 31 Dec 2024

Research Article

**Abstract** – Sunn pest damage is one of the most crucial types of agricultural damage. Authorities and farmers are working together to find a cost-effective solution for separating the damaged crops from the healthy ones. This challenge can be tackled cost-effectively with emerging technology. Over time, the number of researchers focusing on this problem by using various machine learning algorithms and image processing techniques has increased. This paper presents an approach using a recurrent neural networks-based transformer to identify different varieties of wheat grain that have been sunn pest-damaged and healthy. First, wheat grains were separated from each other using YOLOv8. Then, the dataset was enriched with different data augmentation techniques, and data-efficient vision transformers were used to classify sunn pest-damaged and healthy grains. Conversely, a high accuracy score of 98.61% was achieved on the augmented dataset while surpassing the accuracy score of 93.36% in the raw dataset. This paper's contributions to literature can be divided into three categories. In contrast to the previous research, perfectly shaped, broken, and half-wheat grains are used to better fit findings in real-life environments such as factory production lines. Moreover, this study employs a combination of augmentation techniques, implying that two separate augmentation techniques, texture-based and one morphological, were applied to the same image. Finally, no study in the available literature uses a vision transformer to classify healthy and sunned pest-damaged wheat grains. That leads to using a data-efficient vision transformer algorithm and achieving a high accuracy score of 98.61%.

**Keywords** – Sunn pest, sunn pest detection, wheat cultivars, wheat grain segmentation, crop quality

## 1. Introduction

The most traditional and significant grain crop is wheat. About 20% of the world's total nutritional calories and proteins come from this crop [1] due to being the raw material of various foods. Among the most crucial types of wheat are common wheat (*Triticum aestivum*), used for bread production; durum wheat (*Triticum durum*), used for pasta; and club wheat (*Triticum compactum*), a softer variety used for making cakes, crackers, cookies, pastries, and flours. A small amount of wheat is also utilized by industry to make items, including starch, paste, malt, dextrose, gluten, and alcohol [2]. Moreover, wheat is one of the most popular foods consumed worldwide. China leads the world in wheat consumption, with India close behind [3].

Sunn pests are one of the primary insects that harm wheat grains. The sunn pest causes significant qualitative

<sup>1</sup>melike.colak@bites.com.tr (Corresponding Author); <sup>2</sup>ozgu.ozkan@bites.com.tr; <sup>3</sup>nergis.pervan@bites.com.tr; <sup>4</sup>ali.berkol@bites.com.tr; <sup>5</sup>molgun@ogu.edu.tr; <sup>6</sup>zbudak@ogu.edu.tr; <sup>7</sup>gayter@ogu.edu.tr; <sup>8</sup>oksezer@ogu.edu.tr; <sup>9</sup>mardic@ogu.edu.tr

and quantitative damage in the Middle East and numerous other regions. Damage caused by sunn pests is characterized by the yellowing and death of stems and leaves and stunted growth of tips and buds. These pests typically feed on other parts of the plant and do not commonly affect flower formation and coloration. When sunn pests feed on seeds after they have matured, they may become shriveled, discolored (usually white), or hollow. However, if these pests feed on the seeds before they fully develop, it can lead to seed abortion. Both adults and nymphs can also feed on dry grains when moisture is present [4]. It has infested about 15 million hectares of wheat crops across the Middle East. The sunn pest damages wheat grain during various phases of development. The sunn pest sucks out the protein in the wheat grain at this stage, as the grains will lose their germination power. Additionally, they lose their qualities as flour. Economic devastation results from this loss of quality; in Iran alone, damage to wheat and barley crops exceeding 9 million tons has been reported [5].

Integrating advanced technology into the agricultural sector has spurred numerous research endeavors within wheat grain analysis, leveraging Machine Learning (ML) methodologies. Farmers eliminate damaged wheat grains manually because the machines that do this automatically are prohibitively expensive. Thus, the need for cheaper, faster, and more accurate quality control in wheat grains has paved the way for sunn pest damage detection [6-8] and classification [9] studies in wheat grains. In addition, since wheat species are used to produce different foods, they must not mix. In light of this motivation, researchers have conducted classification studies with datasets containing many different wheat species [10-19].

Researchers have tackled classification studies using datasets comprising several wheat varieties. The effective analysis of wheat grains is facilitated through the implementation of segmentation techniques, particularly in intricate tasks such as isolating individual wheat grains from image backgrounds [14, 20] or from each other [9], mainly when presented in bulk as in our dataset [21]. Besides, researchers have used segmentation algorithms to classify different species of wheat grains [22]. In Computer Vision (CV), the variety and abundance of data are one of the main factors affecting model training performance. Therefore, researchers have diligently expanded and enriched their datasets by strategically employing data augmentation techniques [8, 22-24] specifically tailored to address the intricacies of wheat grain analysis. The culmination of these extensive studies has yielded compelling results, demonstrating the model's capacity to distinguish between damaged wheat attributed to sunn pests and healthy wheat with impressive accuracy. Such accomplishments hold profound significance within the agricultural sector, where the reliable classification of wheat grains is pivotal.

In this study, our primary goal was to achieve a highly accurate classification of sunn pest-damaged and healthy grains in various wheat grain species with the Data-efficient Image Transformer (DeiT) algorithm. To conduct our experiments, the wheat grain dataset previously introduced in our research was leveraged [21]. Additionally, the aim to deepen our comprehension of wheat grain features by employing the You Only Look Once version 8 (YOLOv8) model for segmentation on a dataset containing bulk wheat grains was pursued. As part of this segmentation process, each wheat kernel was individually recorded as a separate image, leading to the generation of a novel and enriched dataset through diverse data augmentation techniques. Our study contributes to the literature in various ways by improving the existing studies on wheat grain species and sunn pest-damaged wheat grain classification.

*i.* Our study provides an adaptable model for grains not in the whole wheat form in a production line by including broken and partial wheat grains in the dataset.

*ii.* In addition to the data augmentation techniques applied to the dataset separately in the literature, the model's performance was increased by combining various techniques to create a dataset that can be adapted to many environmental conditions, such as lighting conditions, image contrast, and the presence of shadows. This versatile approach allows our model to perform effectively in various scenarios.

*iii.* Our study is the first in the available literature to examine sunn pest damage to different wheat species.

*iv.* Finally, the approach we presented is a pioneer in applying Transformer-based models in wheat grain analysis, with an accuracy score of 98.61%, and it is the first study of such an approach.

The remainder of this paper is structured as follows: Section 2 presents related works from reviewing the literature in the subsections Augmentation, Segmentation, and Classification. Section 3 describes the dataset used in this study and the YOLOv8 model used for the wheat grain segmentation. Section 4 encompasses a detailed explanation of the data augmentation techniques used. Section 5 presents an exploratory data analysis of the augmented dataset. Section 6 explains the sunn pest damage classification in different wheat species. Section 7 contains the analysis and comparison of the results of the presented experiment in the subsections Segmentation, Augmentation, and Classification. Section 8 encapsulates the conclusions drawn from the study and outlines potential avenues for future research. Last of all, the final section explains the future work.

## **2. Related Work**

Upon reviewing the literature, it became evident that several methods exist for resolving the classification issue between sunn pest-damaged and healthy grain. The authors have used various segmentation models and augmentation techniques to achieve a higher accuracy score. This section focuses on various augmentation techniques, segmentation methods, and classification problems.

### **2.1. Augmentation**

The reviewed literature demonstrates the necessity for more enormous datasets, which led to various augmentation methods. The authors conducted diverse studies about this specific problem.

Shen et al. [22] utilized a dataset of 130 images that included damaged but beneficial wheat grains, such as unsound grains, injured grains, speckled grains, broken grains, germinated grains, and moldy grains. Subsequently, they applied five data augmentation methods to process the images to enhance recognition accuracy and deliberately highlight local characteristics and regions of interest. These methods included brightness reduction, noise addition, random point insertion, translation, and flipping. Bernandes et al. [23] sampled 1200 seeds, with 600 seeds infected by Fusarium Head Blight (FHB) and 600 healthy seeds. In this study, signs of fungal colonization in wheat seeds due to FHB infection were characterized by roughness, a wrinkled appearance, and pink-colored tissues. To avoid overfitting during hyperparameter optimization, they randomly rotated images by up to 30° and applied a 20% variation in height, width, offset, and zoom.

Furthermore, they rotated half of the images horizontally and used the closest strategy to fill in any newly created pixels that might appear after rotation or width/height shifting. Unlarsen et al. [24] applied rotation and zoom operations to wheat grain bulk samples. First, they randomly determined an angle to rotate the image between -30 to +30 degrees. Then, the zoom operation was executed with a randomly determined rate between -10% and +10% on the rotated images. After the data augmentation, they obtained 3200 images, 800 from each wheat variety. In their study, Sabanci et al. [8] rotated and applied Gaussian noise to cropped wheat grain images. They also adjusted the zoom, size, and positioning of the images. This process expanded the dataset, yielding 1200 wheat grain images, 600 of which are healthy samples and 600 of which are sunned pest-damaged samples. Out of these, 1000 images were allocated for training deep learning models, while the remaining 200 were set aside for testing.

### **2.2. Segmentation**

Segmentation is an image processing technique that divides an image into meaningful parts, enabling detailed analysis. In agriculture, this technique helps to identify different wheat species and detect damage from sunn pests or other bugs. This technique outlines grain boundaries to distinguish healthy and damaged grains. While common in corn, beans, and coffee grain analysis, specific studies on wheat are less frequent.

Researchers have studied various segmentation techniques to better examine the characteristics of wheat grains. Gao et al. [25] present a study to detect unsound wheat kernels based on an improved Residual Neural Network (ResNet), six kinds of wheat, including the sound kernel, broken kernel, sprouted kernel, injured

kernel, moldy kernel, and spotted kernel are considered as the samples. The designed two-kernel adhesion wheat segmentation algorithm based on a concave mask exhibits high accuracy, with an error rate of 0.93% for 9988 wheat grains. Sharma and Singh [15] utilized Artificial Neural Networks (ANN), Support Vector Machine (SVM), partial least squares discriminant analysis, Random Forest (RF), and K-Nearest Neighbor (KNN) to classify wheat seed varieties using near-infrared hyperspectral imaging. The ANN model with Savitzky-Golay second derivative preprocessing achieved the highest accuracy of 97.77%.

### 2.3. Classification

There are two different kinds of wheat classification issues: The classification of wheat species and the classification of damaged or healthy grains. This section investigates both approaches.

Considering damage classification problems, the research conducted by Motie et al. [26] utilized SVM with a radial basis function kernel to achieve an accuracy exceeding 90% in differentiating sunn pest-infected wheat clusters from healthy plants using near-infrared images. Abbaspour-Gilandeh et al. [27] achieved 100% accuracy in discriminating healthy wheat grains from grains infected with *Fusarium* using SVM. Fazel-Niari et al. [28] studied various classification algorithms, including linear and quadratic statistical discriminant analysis and SVM, and achieved an average accuracy of 97.6% in classifying wheat grain groups. Shedole et al. [17] developed a Convolutional Neural Networks (CNN) based classification system for wheat grain using 900 images. The Decision Tree and Multilayer Perceptron classifiers achieved 98.7% accuracy, while the Naïve Bayes classifier had a lower precision of 94.22%. Additionally, the validation accuracy of the CNN model showed strong performance, ranging from 94% to 96%. Kaya and Saritas [29] developed a classification system using ANN for classifying type-1252 durum wheat kernels based on their clarity, achieving a maximum classification accuracy of 93.46%. In a study conducted by Erkinbaev et al. [30] achieved overall classification accuracies ranging from 83% to 100% using spectral data and ML techniques with a unified heuristic approach. Zhang and Ji [31] classified wheat grains into different states using hyperspectral imaging, with an SVM model achieving an average recognition accuracy of 98.5%.

Using pre-trained models such as Resnet, Alexnet, or Densely Connected Networks (DenseNet), which are trained with large datasets, is often more advantageous than training a model from scratch. In the literature, authors used a transfer learning approach to achieve higher accuracy scores in wheat grain classification problems. They used pre-trained models directly or combined different pre-trained model architectures with their models [8, 9, 24, 32]. Table 1 summarizes related work, including whether the paper is used as an augmentation, segmentation, or classification reference. Then, there is a studies column, a dataset column that shows a summary of the dataset, a methods column, and a column that explains the essential outcomes.

**Table 1.** Literature summary

Category	Studies	Dataset	Methods Used	Key Outcomes
Augmentation	[22]	130 wheat grain images (damaged and unsound)	Brightness reduction, noise addition, random point insertion, translation, and flipping	Enhanced recognition accuracy by emphasizing local characteristics.
	[23]	1200 wheat grain images (600 FHB infected, 600 healthy)	Random rotation (up to 30°), height/width shifting (20%), horizontal flip, closest pixel strategy	Avoided overfitting, characterized fungal colonization.
	[24]	3200 wheat grain bulk images	Rotation (-30° to 30°) and zoom (-10% to 10%)	Processed 800 images per wheat variety.
	[8]	1200 wheat grain (600 healthy, 600 damaged)	Rotation, Gaussian noise, zoom, resizing, positioning adjustments	Expanded dataset for training deep learning models.

**Table 1.** (Continued) Literature summary

Category	Studies	Dataset	Methods Used	Key Outcomes
Segmentation	[25]	9988 wheat grain images (6 types of kernels)	Improved ResNet, concave mask-based two-kernel adhesion segmentation	Achieved an error rate of 0.93% in segmentation.
	[15]	Near-infrared hyperspectral imaging (15 different wheat varieties; 936 wheat from each variety)	ANN, SVM, Random Forest, KNN with Savitzky-Golay second derivative preprocessing	ANN model achieved the highest accuracy of 97.77%.
Classification	[26]	Near-infrared images of wheat clusters (Sunn-pest damaged and healthy wheat grains)	SVM with radial basis function kernel	Over 90% accuracy in classifying sunn pest-infected wheat clusters.
	[27]	Wheat grains (300 healthy vs. 300 Fusarium infected)	SVM	Achieved 100% accuracy.
	[28]	Wheat grain groups (7 different wheat types, a total of 21000 single wheat grains)	SVM, linear, and quadratic discriminant analysis	Achieved an average accuracy of 97.6%.
	[17]	900 wheat grain images (dataset includes four classes: good grain, damaged grain, broken grain, and foreign particles).	CNN, Decision Tree, Multilayer Perceptron and Naïve Bayes	CNN model accuracy between 94% and 96%, Decision Tree/MLP 98.7%, Naïve Bayes 94.22%.
	[29]	Durum wheat kernels	ANN	Maximum classification accuracy of 93.46%.
	[30]	Spectral data (180 Healthy kernels, 60 Fusarium-damaged kernels, and 60 Ergot-damaged kernels)	ML techniques with a unified heuristic approach	Classification accuracy ranges from 83% to 100%.
	[31]	Hyperspectral imaging of wheat grains (220 healthy wheat grains, 220 germinated wheat grains, 220 mildewed wheat grains, and 220 shriveled wheat grains (wheat grains infected with fusarium head blight))	SVM	Achieved average accuracy of 98.5%.

### 3. Data Collection

The Related Work section explains that the authors handle wheat grain differently. These datasets vary in many aspects, including being created in controlled or uncontrolled environments, camera models and equipment in the shooting environment, camera angle, direction and type of wheat, and the focused problem such as species classification or damaged region detection. The dataset used in this study was prepared for the classification stage after preprocessing and segmenting different types of wheat grains affected by the sunn pest, presented in [21].

#### 3.1. Raw Wheat Grain Dataset

In [21], a new dataset was introduced, which was used to develop an image classification model for classifying wheat grain species as Damaged and Healthy. The dataset includes a wide variety of wheat and covers six species: Bezostaja, Müfitbey, Nacibey, Sönmez-2001, Tosunbey, and Ekiz, the species made in Türkiye. Wheat grains differ in various parameters, such as width, length, color, stain condition, and wrinkled texture.

The dataset comprises 83 images of sunn pest damage and 87 images of healthy wheat grains. Additionally, 2502 healthy and 1063 damaged wheat grains were extracted from 170 bulk wheat grain images. Wheat grains vary in width, length, color, stain status, and wrinkled texture. The distribution of the cultivars is displayed in Table 2.

**Table 2.** Distribution of wheat grains

Cultivar	Healthy	Damaged
Bezostaja	427	107
Müfitbey	311	120
Nacibey	342	203
Sönmez-2001	370	120
Tosunbey	322	183
Ekiz	730	330

Due to the wheat grain dataset being multiclass and may be used for variety classification, it stands out from others due to its diverse species and condition, including broken, sunn pest damaged, and healthy wheat grain. However, the dataset is appropriate for detecting sunn pest damage when the condition of sunn pest damage is considered. Furthermore, the dataset contains grains that come into contact with one another, increasing its applicability to real-world issues. As can be seen, the dataset includes a range of wheat species that are impacted by sunn pests, demonstrating that the promised dataset is appropriate for many ML tasks, including segmentation, detection, and classification.

### 3.2. Wheat Grains Segmentation with YOLOv8

The dataset used in our study is the most crucial contribution that distinguishes the study from other studies in the literature. Although studies conducted with wheat grains in a particular order, facing the same direction, and of the same size give promising accuracy scores, it is not expected that the ML model will be able to solve the problem correctly in the face of wheat grains scattered in the real-life production line. For this reason, some processes were applied to the raw dataset to bring a new perspective to academic studies and to offer realistic solutions that can be adapted to real life in wheat agriculture.

In the segmentation process, the dataset was split into 60%, 20%, and 20% as train, test, and validation, respectively. The split 60%-20%-20% is commonly used to ensure a balanced model training and evaluation approach. The 60% training set provides enough data for the model to learn underlying patterns effectively. The 20% validation set helps tune the model's hyperparameters and avoid overfitting. The 20% test set is reserved to evaluate the model's generalization performance on unseen data, ensuring a reliable assessment of its accuracy. Then, to transfer the data to the model during training, the file paths of the train, test, and validation sets were given to the file data.yaml, and the class name was set as wheat.

The model YOLOv8 was utilized for the training process. YOLOv8, known for its efficiency and accuracy in object detection tasks, is particularly suitable for our problem due to its ability to handle varying object scales and dense environments. The default parameters of YOLOv8 were used, which include an initial learning rate of 0.01, momentum of 0.937, and weight decay of 0.0005.

YOLOv8's architecture consists of a backbone network that extracts essential features from input images and a head network that predicts bounding boxes and class probabilities. The model is pre-trained on the Common Objects in Context (COCO) dataset, allowing it to leverage transfer learning for better initial performance on our wheat grain dataset.

In the training process, YOLOv8's advanced anchor-free detection mechanism plays a significant role in accurately predicting the locations and sizes of wheat grains, which can vary significantly in a production line setting. After each epoch, the model's performance was continuously monitored by evaluating the Mean Average Precision (mAP) on the validation set. Train results, including precision, recall, and mAP scores, will be discussed in the Results section, comprehensively evaluating our model's performance.

## 4. Data Augmentation

After the segmentation process, augmentation techniques were applied to segmented wheat grains to expand our data by a factor of seven. 15 different augmentation methods were applied. Initially, two distinct kinds of augmentation were used: morphological and texture-based.

The morphological augmentation techniques include;

*i.*Affine: Scales images to a value of 40 to 80% of their original size.

*ii.*Fliplr: Reflects photos horizontally.

*iii.*Flipud: Reflects photos vertically.

*iv.*Furthermore, texture-based augmentations contain;

*v.*Add to Brightness: This function adds a constant value to an image's brightness. The range is set from +30 to -30.

*vi.*Linear Contrast: Adjusts the contrast of each image by  $127\alpha(v - 127)$ , where  $v$  represents the pixel value, and alpha is uniformly sampled (once per image) from the interval [0.4, 1.6].

*vii.*Multiply Saturation: The augmenter first converts images to Hue Saturation Value (HSV) colorspace, doubling the pixel values in the H channel before converting back to RGB. The range is determined between 0.5 and 1.5.

In addition to these six techniques, all of them are combined. Firstly, one from morphological and one from texture-based are picked to acquire a combined augmentation technique. The first method is used, followed by the second. For instance, if both Fliplr and Linear Contrast are picked, the image is flipped horizontally first, and then linear contrast is applied. With this process, nine more augmentation techniques are obtained. In Table 3, the combined augmentation techniques are shown.

**Table 3.** Combined augmentation techniques

Morphological	Texture-Based	Combined
Affine (AF)	Add To Brightness (BR)	AFBR
Affine (AF)	Linear Contrast (LC)	AFLR
Affine (AF)	Multiply Saturation (MS)	AFMS
Flipud (FUD)	Add To Brightness (BR)	FUDBR
Flipud (FUD)	Linear Contrast (LC)	FUDLR
Flipud (FUD)	Multiply Saturation (MS)	FUDMS
Fliplr (FLR)	Add To Brightness (BR)	FLRBR
Fliplr (FLR)	Linear Contrast (LC)	FLRLC
Fliplr (FLR)	Multiply Saturation (MS)	FLRMS

Table 3 shows the new combined augmentation techniques and what is used to create them. When augmentation, morphological, and texture-based techniques are combined in Table 3, 15 augmentation techniques are obtained. None of these augmentation techniques were utilized on a single wheat grain image. Initially, six were selected for every image. For each image, 2 out of 3 morphological and texture-based augmentation techniques and 2 out of 9 combined techniques were selected. First, two morphological augmentations are performed, chosen at random, for each image. Subsequently, two texture-based techniques were picked randomly and applied, and finally, two combined techniques were selected randomly and implemented. Ultimately, each image has been featured seven times, including itself. In Figure 1, the rows represent texture-based augmentations, and the columns represent morphological augmentations. Their crossing image illustrates the combination of these two augmentation techniques. As a result, the raw image and 15 images representing the 15 different augmentation techniques were used.

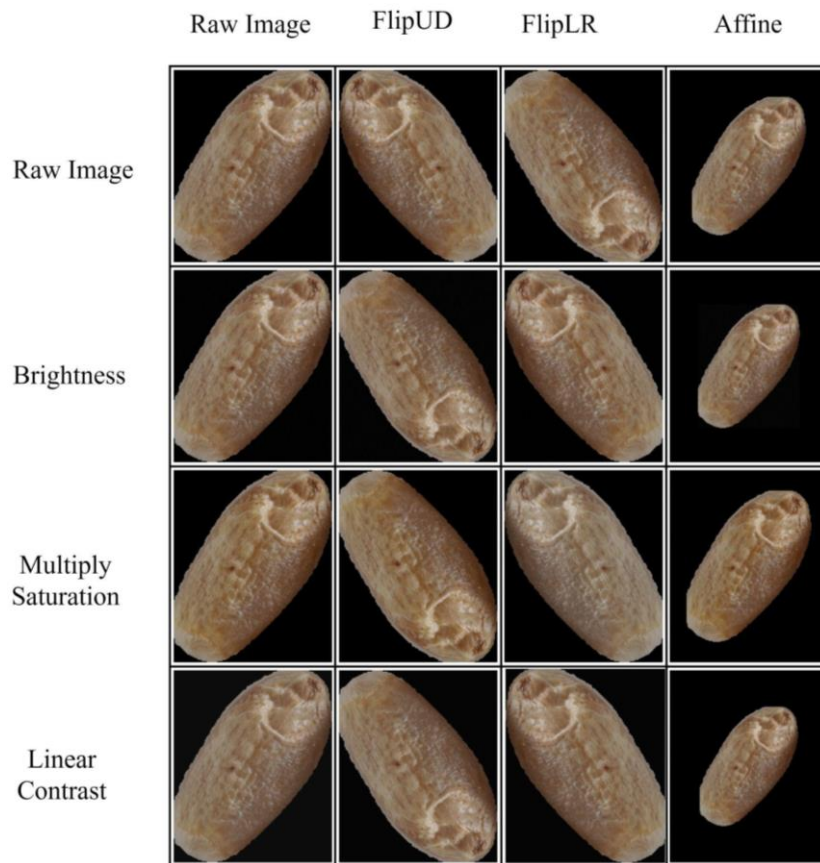


**Figure 1.** Image before and after each augmentation technique

Ultimately, when the data is augmented with the raw images, there are 24759 images. For each of the wheat varieties, the augmented image count without the raw images is as follows:

- i.*Bezostaja: 3144
- ii.*Müfitbey: 2538
- iii.*Tosunbey: 2988
- iv.*Nacibey: 3336
- v.*Ekiz: 6222
- vi.*Sönmez-2001: 2994

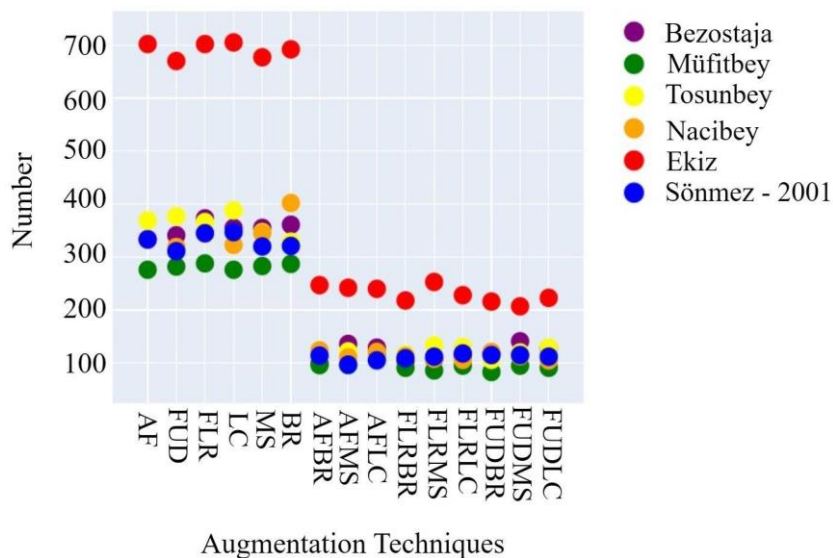


**Figure 2.** Augmented image count according to wheat varieties

In Figure 2 the distribution of all augmented image counts according to their relative wheat varieties has been illustrated. The combined augmentation techniques' counts are lower than the initial augmentation techniques' counts because 4 out of 6 in the initial ones were picked. However, in the combined techniques, 2 out of 15 were picked. So, the probability of choosing the same augmentation technique is less in combined augmentation methods. Conversely, the Ekiz varieties have a far larger count than the others since their raw version likewise has a higher count, and the difference widens when it is increased 6 times.

Wheat grains were segmented from the raw image, then these augmentation methods were applied. Following the augmentation process, zero padding was added based on the segmentation coordinates of the wheat grains. At the end of this process, all of the wheat grains were extracted one by one with a black background, leading to the final dataset.

## 5. Exploratory Data Analysis

In this section, exploratory data analysis is presented in our augmented dataset. In our research, graphs displaying brightness for wheat damaged by sunn pests against healthy wheat were carefully examined. As can be seen in Figure 3, a significant disparity in average brightness values was discovered. The damaged wheat grains had an average brightness of 85.23, compared to 116.40 for the healthy wheat grains. This significant difference shows that brightness may effectively distinguish between the two conditions. Moreover, uncommon brightness levels, or outliers, were examined in damaged and healthy wheat. Despite finding extreme levels, it is seen between the 0-200 range, they distribute similarly. This means that using only brightness might not be enough to separate damaged and healthy wheat, which presents a challenge, for instance, classification in wheat grain condition.

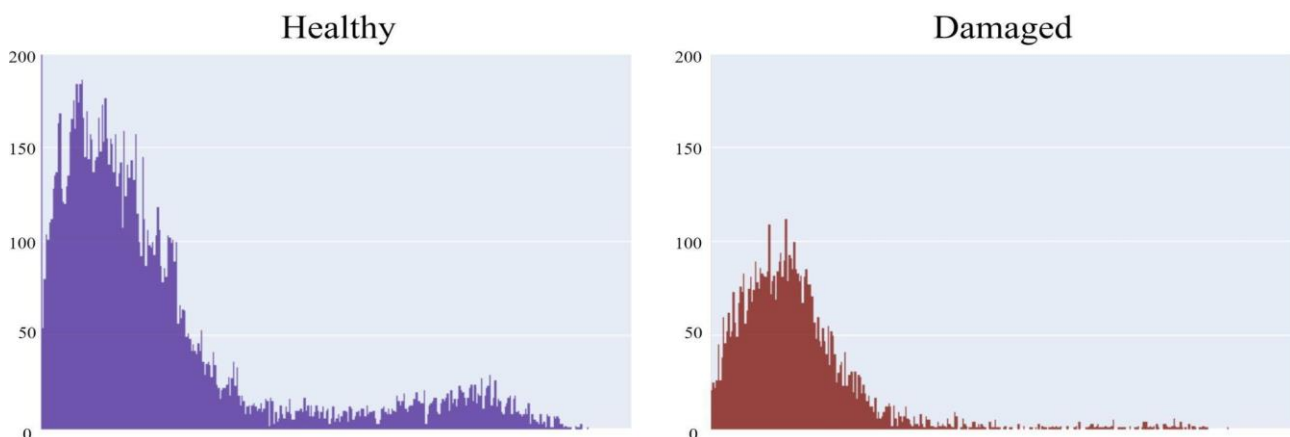
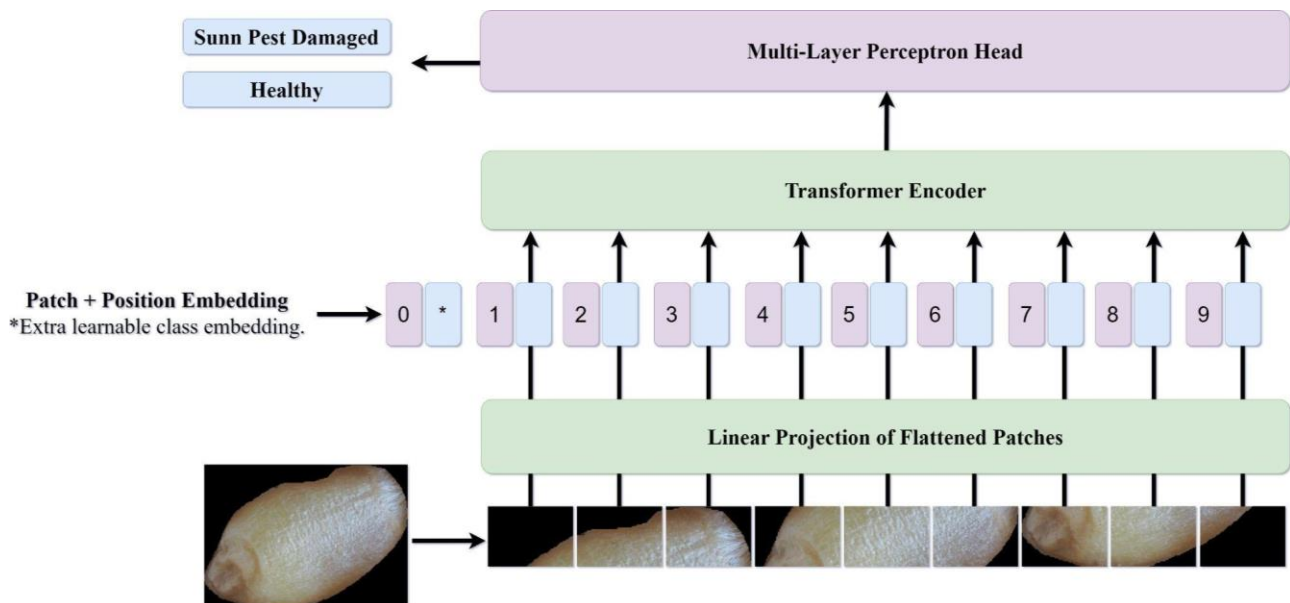


Figure 3. Brightness-frequency histogram

## 6. Sunn Pest Damage Classification in Different Wheat Species

When the literature is examined, it is seen that CNN and state-of-the-art models are preferred in studies that use image data. Since this transformer-based algorithm is not available in the literature, the DeiT model with the transfer learning approach was used in our research. Touvron et al. [33] assert that the DeiT represents a significant advancement in training Transformers to enhance CV performance. Despite CNN being the prevailing method for CV tasks in the past eight years and benefiting from numerous enhancements and adjustments, DeiT's performance is already on par with them. DeiT stands for data-efficient transformer, which focuses on making a convolution-free model trained on less data and can outperform CNN-based algorithms. DeiT model pre-trained and fine-tuned on ImageNet-1k at resolution 384x384. The last layer of the DeiT model was frozen, and seven layers were added with fine-tuning: Linear, Relu, and Dropout. Figure 4 shows the model architecture and classification process.



**Figure 4.** Our model architecture

Our experiments were conducted with two datasets: segmented wheat grains and expanded with augmentation techniques of these data. In both scenarios, the datasets' train, test, and validation sets were split, with proportions of 80%, 20%, and 20%, respectively. The learning rate is 0.00005, the batch size is 128, and the epochs are 200. During the training stage, early stopping was used to prevent the model from memorizing the training data and from overfitting the test data. Early stopping was controlled according to validation loss, with a patience coefficient of 3. The results of both scenarios were discussed comparatively in the Results section.

## 7. Results

### 7.1. Segmentation

In the wheat segmentation process, YOLOv8 was utilized to segment wheat grains from the images. This model was chosen for its advanced object detection and segmentation capabilities, making it well-suited for tasks involving dense and overlapping objects such as wheat grains. YOLOv8 represents a significant advancement in real-time object detection and segmentation, building upon the solid foundation laid by previous versions of the YOLO family. The defining feature of YOLO models is their ability to predict multiple bounding boxes and corresponding class probabilities in a single forward pass through the neural network. This design ensures that the model operates with exceptional speed and efficiency, making it suitable for real-time applications.

The YOLOv8 model incorporates several state-of-the-art enhancements for superior performance. The network architecture is significantly deeper and wider, capturing complex features and finer details. Advanced feature pyramid networks (FPN) combine features from different layers, improving precision and recall by detecting objects at various scales. YOLOv8 also uses an optimized anchor-free detection strategy to directly predict object centers and scales, reduce computational complexity, and enhance accuracy, especially for small, densely packed objects. Cross Stage Partial Network (CSPNet) also improves gradient flow and reduce computational load, leading to more efficient training and inference while maintaining high accuracy.

The high precision and recall values indicate that the YOLOv8 model is highly effective in correctly identifying and segmenting wheat grains within the test images. The precision score reflects the model's accuracy in detecting true positives among the identified grains. In contrast, the recall score indicates the model's ability to identify all actual grains in the images. The mAP values comprehensively measure the model's performance. The mAP50 value, which considers a single Intersection over the Union (IoU) threshold of 50%, shows an impressive score of 99.4%. This high score signifies that the model can accurately detect

and segment wheat grains with a moderate overlap threshold. The mAP50-95 value averages the precision across multiple IoU thresholds from 50% to 95%, slightly lower at 93.3% for bounding boxes and 91.3% for segmentation masks. This indicates that while the model performs exceptionally well at moderate thresholds, there is a slight decrease in performance at higher thresholds. This decrease could be attributed to the challenges in segmenting wheat grains with fine details or densely packed regions.

## 7.2. Augmentation

When the segmentation process was finished, different augmentation techniques were performed. There are morphological augmentation techniques, texture-based augmentation techniques, and combined augmentation techniques consisting of one morphological and one texture-based technique. When the augmentation is considered, it is seen that performing augmentation techniques dramatically increased the accuracy by %5 - from %93.36 to %98.61-. The reason for the increase is not only the higher data number but also the chosen technique. Due to some of the augmentation methods, the grain color gets brighter, as a result, the sunn pest damage point has become more visible, and thus accuracy increased. In contrast, the sunn pest damaged point and the color of the grains both go darker in the Multiply Saturation method; nevertheless, the sunn pest damaged point becomes so much darker that it becomes more noticeable. On the other hand, in Linear Contrast, by enhancing the contrast of the images, the model can better distinguish between damaged and undamaged grains, leading to higher accuracy and more reliable predictions.

## 7.3. Classification

After the augmentation stage, two experiments were performed on the raw and augmented datasets. Determining optimal hyperparameters and layer values added to the end of the DeiT model was a critical step before model training. Parameters in the linear layer input sizes 1024, 512, 256, and 128 were tested to maximize classification accuracy. Additionally, dropout layer coefficients were tested as 0.20, 0.35, and 0.50 for both models. In both cases, the best parameters were specified as an input size 512 and a dropout coefficient of 0.50. The models trained on the raw and augmented datasets utilized a V100 GPU, with training durations of 10359.64 and 1644.41 seconds, respectively. As a result of the binary classification, a test accuracy score of 93.36% and 98.61% were achieved. The precision score was obtained as 99.39%, recall as 98.62%, specificity as 98.56%, F1-Score as 99.00%, and Matthews Correlation Coefficient (MCC) as 96.67%. In the model trained with the raw dataset, these results were 95.93%, 95.01%, 95.47%, 93.60%, and 84.58%, respectively. Comparative results between these models are shown in Figure 5.

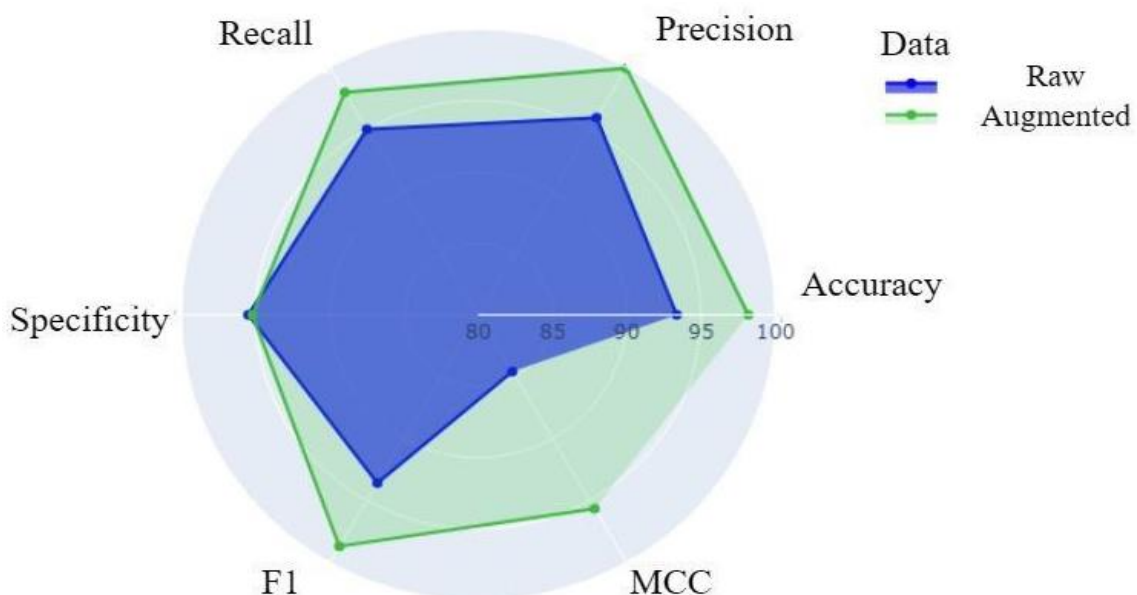


**Figure 5.** Raw and augmented results comparison

As shown in Figure 5, accuracy, precision, recall, specificity, F1 score, and Matthews Correlation Coefficient (MCC) are the six critical metrics used to compare the performance analysis between raw and augmented data. Each axis represents one of these measures, ranging from 80 to 100. The blue polygon shows the performance of the raw data, while the green polygon shows the augmented data. The raw data performs admirably with accuracy at 93.36%, precision at 95.93%, recall at 95.01%, specificity at 95.47%, F1 score at 93.60%, and MCC at 84.58%. The augmented data, however, greatly improves these metrics: MCC increases to 96.67%, accuracy to 98.61%, precision to 99.39%, recall to 98.62%, specificity to 98.52%, and F1 score to 99.00%. The enhanced performance of the augmented data across all measures is evident in this visualization, suggesting that data augmentation is a valuable technique for improving the predictive powers of the model. The green polygon highlights these benefits's more extensive area than that of the blue polygon, which supports the use of data augmentation approaches in ML problems.

The impressive performance of the self-attention mechanism in the Transformer-based Diet model lies behind the high accuracy score. Self-attention has been essential in identifying fine distinctions between sunn pest damage and healthy wheat grains. The self-attention mechanism helps the model handle long-range dependencies. This makes it more effective in understanding the relationships between different parts of wheat, ultimately leading to a more comprehensive classification structure.

## 8. Conclusion

One of the most critical forms of damage in agriculture is caused by sunn pests. Detecting sunn pest damage in wheat grains is a task that is both time-consuming and costly when done manually. Authors have studied this issue to make detecting sunn pest damage easier and classify healthy and damaged wheat grains, which is the purpose of our paper. This paper includes three critical processes: wheat grain segmentation, data augmentation, and classification with DeiT. The wheat grains were identified using YOLOv8 and cropped from the base image in the segmentation part. After that, 15 distinct augmentation methods were applied to these grains. These methods enrich the dataset and make it challenging for the model to understand the difference between healthy and damaged conditions. For this reason, significant success was achieved as results with a high accuracy score of 98.61% on the augmented dataset were yielded by our Transformer-based model, while 93.36% was obtained on the raw dataset.

Our contributions include a combination of augmentation techniques, implying that two separate augmentation techniques, texture-based and morphological, were applied to the same image. Additionally, whole and broken/half grains are included in the dataset, making it more suitable for real-life production bands. Furthermore, -to the best of our knowledge- using a multiclass dataset makes it the first study to work on a multiclass wheat grain dataset for sunn pest damage detection. Lastly, implementing the RNN-based algorithm in the evaluation process is one of the most important contributions of our study.

In future research, expanding the dataset and exploring alternative models and algorithms to enhance the model's accuracy would be beneficial. This exploration could include looking beyond RNN-based algorithms and considering architectures like CNNs or hybrid models that merge CNNs with Transformers. These alternatives might more effectively capture spatial features, complementing the Transformer's strength in handling temporal and sequential data. Additionally, exploring Graph Neural networks might offer a more intricate way to model the relationships between grain structures. Adopting such approaches could lead to new ways to improve the durability and efficiency of systems designed to classify damage caused by sunn pests.

## Author Contributions

The first and second authors performed the data analysis, experiments, and statistical analysis and wrote the paper. The third author reviewed and edited the paper. The sixth, seventh, eighth, and ninth authors collected the data. The fourth and fifth authors supervised the project. All authors read and approved the final version of the paper.

## Conflicts of Interest

All the authors declare no conflict of interest.

## Ethical Review and Approval

No approval from the Board of Ethics is required.

## References

- [1] B. Shiferaw, M. Smale, H.-J. Braun, E. Duveiller, M. Reynolds, G. Muricho, *Crops that feed the world 10. Past successes and future challenges to the role played by wheat in global food security*, Food Security 5 (2013) 291–317.
- [2] Britannica, Wheat (Plant) (2024), <https://www.britannica.com/plant/wheat>, Accessed 30 June 2024.
- [3] Statista, Wheat consumption worldwide in 2023/2024, by country (in 1,000 metric tons)\* (2024), <https://www.statista.com/statistics/1094065/total-global-wheat-consumption-by-country/>, Accessed 30 June 2024.
- [4] Plant Health Australia, Sunn pest (2024), <https://www.planthealthaustralia.com.au/wp-content/uploads/2024/01/Sunn-pest-FS.pdf>, Accessed 30 June 2024.
- [5] M. Alamouti, M. Majdi, R. Talebi, M. Dastranj, A. Bandani, G. H. Salekdeh, M. R. Ghaffari, *Transcriptome wide identification of neuropeptides and G protein-coupled receptors (GPCRs) in Sunn pest, Eurygaster integriceps Puton*, Gene 893 (2024) 147911 14 pages.
- [6] K. Sabanci, *Detection of sunn pest-damaged wheat grains using artificial bee colony optimization-based artificial intelligence techniques*, Journal of the Science of Food and Agriculture 100 (2) (2020) 817–824.
- [7] Z. Basati, B. Jamshidi, M. Rasekh, Y. Abbaspour-Gilandeh, *Detection of sunn pest-damaged wheat samples using visible/near-infrared spectroscopy based on pattern recognition*, Spectrochimica Acta Part A: Molecular and Biomolecular Spectroscopy 203 (2018) 308–314.
- [8] K. Sabanci, M. F. Aslan, E. Ropelewska, M. F. Unleresen, A. Durdu, *A novel convolutional-recurrent hybrid network for sunn pest-damaged wheat grain detection*, Food Analytical Methods 15 (6) (2022) 1748–1760.
- [9] K. Laabassi, M. A. Belarbi, S. Mahmoudi, S. A. Mahmoudi, K. Ferhat, *Wheat varieties identification based on a deep learning approach*, Journal of the Saudi Society of Agricultural Sciences 20 (5) (2021) 281–289.
- [10] M. Olgun, A. O. Onarcan, K. Özkan, Ş. Işık, O. Sezer, K. Özgişi, N. G. Ayter, Z. B. Başçiftçi, M. Ardiç, O. Koyuncu, *Wheat grain classification by using dense SIFT features with SVM classifier*, Computers and Electronics in Agriculture 122 (2016) 185–190.
- [11] K. Sabanci, M. F. Aslan, A. Durdu, *Bread and durum wheat classification using wavelet based image fusion*, Journal of the Science of Food and Agriculture 100 (15) (2020) 5577–5585.
- [12] K. Sabanci, A. Kayabasi, A. Toktas, *Computer vision-based method for classification of wheat grains using artificial neural network*, Journal of the Science of Food and Agriculture 97 (8) (2017) 2588–2593.
- [13] A. Taner, Y. B. Öztekin, A. Tekgüler, H. Sauk, H. Duran, *Classification of varieties of grain species by artificial neural networks*, Agronomy 8 (7) (2018) 123 14 pages.
- [14] D. Agarwal, Sweta, P. Bachan, *Machine learning approach for the classification of wheat grains*, Smart Agricultural Technology 3 (2023) 100136 10 pages.

- [15] A. Sharma, T. Singh, N. Garg, *Combining near-infrared hyperspectral imaging and ANN for varietal classification of wheat seeds*, in: Manu Malek (Ed.), 2022 Third International Conference on Intelligent Computing Instrumentation and Control Technologies (ICICICT), Kannur, 2022, pp. 1103–1108.
- [16] A. Khatri, S. Agrawal, J. M. Chatterjee, *Wheat seed classification: Utilizing ensemble machine learning approach*, *Scientific Programming* 2022 (1) (2022) Article ID 2626868 9 pages.
- [17] S. Shedole, S. B. J, N. A. V. P, *A convolution neural network-based wheat grain classification system*, *Journal of Scientific Research of The Banaras Hindu University* 66 (2) (2022) 204 22–29.
- [18] S. Lingwal, K. Bhatia, M. Tomer, *Image-based wheat grain classification using convolutional neural network*, *Multimedia Tools and Applications* 80 (28) (2021) 35441–35465.
- [19] A. Kayabasi, *An application of ANN trained by ABC algorithm for classification of wheat grains*, *International Journal of Intelligent Systems and Applications in Engineering* 6 (1) (2018) 85–91.
- [20] W. Zhao, S. Liu, X. Li, X. Han, H. Yang, *Fast and accurate wheat grain quality detection based on improved YOLOv5*, *Computers and Electronics in Agriculture* 202 (2022) 107426 10 pages.
- [21] N. Pervan Akman, M. Çolak, Ö. Özkan, T. Tümer Sivri, A. Berkol, M. Olgun, Z. Budak Başçiftçi, G. Ayter, O. Sezer, M. Ardiç, *Wheat dataset for species classification and sunn pest damage detection (2023)*, <https://data.mendeley.com/datasets/gmw48bvxdz/1>, Accessed 30 June 2024.
- [22] R. Shen, T. Zhen, Z. Li, *Segmentation of unsound wheat kernels based on improved mask RCNN*, *Sensors* 23 (7) (2023) 3379 17 pages.
- [23] R. C. Bernardes, A. De Medeiros, L. da Silva, L. Cantoni, G. F. Martins, T. Mastrangelo, A. Novikov, C. B. Mastrangelo, *Deep-learning approach for fusarium head blight detection in wheat seeds using low-cost imaging technology*, *Agriculture* 12 (11) (2022) 1801 14 pages.
- [24] M. F. Unlarsen, M. E. Sonmez, M. F. Aslan, B. Demir, N. Aydin, K. Sabanci, E. Ropelewska, *CNN–SVM hybrid model for varietal classification of wheat based on bulk samples*, *European Food Research and Technology* 248 (8) (2022) 2043–2052.
- [25] H. Gao, T. Zhen, Z. Li, *Detection of wheat unsound kernels based on improved ResNet*, *IEEE Access* 10 (2022) 20092–20101.
- [26] J. B. Motie, M. H. Saedirad, M. Jafarian, *Identification of sunn-pest affected (*eurygaster integriceps put.*) wheat plants and their distribution in wheat fields using aerial imaging*, *Ecological Informatics* 76 (2023) 102146 15 pages.
- [27] Y. Abbaspour-Gilandeh, H. Ghadakchi-Bazaz, M. Davari, *Discriminating healthy wheat grains from grains infected with fusarium graminearum using texture characteristics of image-processing technique, discriminant analysis, and support vector machine methods*, *Journal of Intelligent Systems* 29 (1) (2019) 1576–1586.
- [28] Z. Fazel-Niari, A. H. Afkari-Sayyah, Y. Abbaspour-Gilandeh, I. Herrera-Miranda, J. L. Hernandez Hernandez, M. Hernandez-Hernandez, *Quality assessment of components of wheat seed using different classifications models*, *Applied Sciences* 12 (9) (2022) 4133 12 pages.
- [29] E. Kaya, İ. Saritas, *Towards a real-time sorting system: Identification of vitreous durum wheat kernels using ann based on their morphological, colour, wavelet and gaborlet features*, *Computers and Electronics in Agriculture* 166 (2019) 105016 9 pages.
- [30] C. Erkinbaev, M. Nadimi, J. Paliwal, *A unified heuristic approach to simultaneously detect fusarium and ergot damage in wheat*, *Measurement: Food* 7 (2022) 100043 6 pages.
- [31] L. Zhang, H. Ji, *Identification of wheat grain in different states based on hyperspectral imaging technology*, *Spectroscopy Letters* 52 (6) (2019) 356–366.

- [32] W. Zhang, H. Ma, X. Li, X. Liu, J. Jiao, P. Zhang, L. Gu, Q. Wang, W. Bao, S. Cao, *Imperfect wheat grain recognition combined with an attention mechanism and residual network*, Applied sciences 11 (11) (2021) 5139 12 pages.
- [33] H. Touvron, M. Cord, M. Douze, F. Massa, A. Sablayrolles, H. Jegou, *Training data-efficient image transformers distillation through attention*, in: Marina Meila, Tong Zhang (Eds.), 38th International Conference on Machine Learning, Austria, 2021, pp. 10347–10357.



# Theoretical Calculations and Molecular Docking Analysis of 4-(2-(4-Bromophenyl)Hydrazineylidene)-3,5-Diphenyl-4H-Pyrazole Molecule

Kenan Gören<sup>1</sup> , Mehmet Bağlan<sup>2</sup> , Veysel Tahiroğlu<sup>3</sup> , Ümit Yıldıkı<sup>4</sup> 

<sup>1,2</sup>Department of Chemistry, Faculty of Art and Science, Kafkas University, Kars, Türkiye

<sup>3</sup>Department of Nursing, Faculty of Health Science, Şırnak University, Şırnak, Country

<sup>4</sup>Department of Bioengineering, Engineering of Architecture Faculty, Kafkas University, Kars, Türkiye

## Article Info

Received: 14 Jul 2024

Accepted: 07 Oct 2024

Published: 31 Dec 2024

Research Article

**Abstract** – The molecular structure of 4-(2-(4-bromophenyl)hydrazineylidene)-3,5-diphenyl-4h-pyrazole (BHDH) molecule, which is a pyrazole derivative, was investigated theoretically using the Gaussian 09 program according to the Moller-Plesset (MP2) method. The MP2 method was optimized for these theoretical calculations using DGDZVP and 6-311G(d,p) basis sets. By taking geometric structures, Highest-Energy Molecular Orbital (HOMO) and Lowest-Energy Molecular Orbital (LUMO) analysis, Mulliken Atomic Charges, Molecular Electrostatic Potential (MEPS), Nonlinear Optical (NLO) features, and Natural Bond Orbital (NBO) images of the molecule from this optimized structure were analyzed. In the continuation of the study, Absorbed, Distributed, Metabolized, and Excreted (ADME) analysis was performed to evaluate the BHDH molecule as a drug. Many possible drugs for treating various medical diseases have taken their place in the world market. Drug interactions involve combinations with drugs or other substances that change the effect of a drug on the body. Molecular docking analysis of BHDH molecule on obesity disease was performed with acetylcholinesterase (AChE) and butyrylcholinesterase (BChE) enzymes. The highest binding energies and binding conformations between ligands and enzymes were predicted.

**Keywords** – AChE, BChE, molecular docking, ADME, NBO

## 1. Introduction

The beneficial biological functions of pyrazole compounds, an important family of heterocyclic compounds, include antidepressant, antipyretic, antibacterial, anti-inflammatory, analgesic, herbicidal, and insecticidal effects. These properties make them excellent targets for synthetic chemists [1]. Furthermore, the commercial sale of certain compounds possessing the pyrazole structure has increased interest in pharmaceutical and synthetic organic chemistry for pyrazole compounds' production and the study of their bioactive characteristics. For instance, fipronil is frequently used as an insecticide, zaleplon is used to treat insomnia, crizotinib is used to treat cancer, and penflufen is used because it has an antifungal impact [2]. Pyrazole derivatives are also utilized in pharmaceutical, agricultural, electronics, and other areas. It works well in a variety of contexts. It is employed in many fields, including medication creation and as an insecticide and pesticide in agriculture [3]. It is employed for optical qualities in the technology and pharmaceutical sectors, among other industrial domains. Polymers with pyrazole groups, for instance, are utilized in optoelectronic tools like light-releasing diodes and transistors because of their narrow band gaps. It is beneficial for gadgets [4].

<sup>1</sup>kenangoren49@gmail.com;

(Corresponding Author)

<sup>2</sup>mehmebaglan36@gmail.com;

<sup>3</sup>veysel0793@hotmail.com;

<sup>4</sup>yildiko1@gmail.com

Globally, the frequency of overweight or obesity in children has grown, and this poses a serious public health emergency with financial ramifications and high medical expenses. Additionally, there is a correlation between juvenile obesity and a higher prevalence of comorbidities such as insulin [5]. Increased direct and indirect expenditures result from cardiovascular disease, diabetes, hypertension, resistance, and sleep apnea. The non-communicable diseases (NCD) Risk Factor Collaboration recently combined and examined population-based data on global patterns of childhood obesity [6]. It was shown that while childhood's high rates and teenage obesity continued in several Asian nations, rises in children and adolescents' body mass index stayed steady in high-income countries between 1975 and 2016. Furthermore, these inclinations have nothing to do with adult impulses anymore. Due to these factors, it is imperative that childhood obesity be prevented by detecting obese children at a young age so that successful intervention can start [7]. Children and teenagers with obesity have adipose tissue that secretes a lot of adipocytokines in addition to storing fat. Overproduction of adipocytokines can lead to oxidative stress, elevated blood pressure, insulin resistance, and abnormal lipid metabolism [8].

The term metabolic syndrome (MetS) refers to a set of risk factors that include glucose intolerance, abdominal obesity, hypertension, and problems with lipid metabolism that are linked to cardiovascular disease and type II diabetes. The persistent obesity pandemic in children and adolescents has made MetS a public health issue in this demographic as well. For improved public health, biomarkers that can forecast adolescent or pediatric populations' risk of developing metabolic syndrome are essential [9]. Handling this syndrome Acetylcholine and other choline esters are hydrolyzed by a class of enzymes that includes cholinesterase (ChE). Human tissues contain two distinct forms of ChE enzymes: acetylcholinesterase (AChE) and butyrylcholinesterase (BChE). AChE is located in the erythrocyte membrane of the skeletal muscles and central nervous system, while BChE, sometimes referred to as pseudocholinesterase, is produced in the liver and discharged into plasma [10]. At the cholinergic synapse, AChE's primary job is to hydrolyze acetylcholine. Although BChE's exact job in the body is unknown, it could be related to tissue development or detoxification. The phenylalanine residue in the acyl-binding pocket defines the pocket's structure, which in turn determines ChE enzymes' substrate specificity. The physiological role of BChE, located at the ChE catalyst's valley at the bottom, is still unknown; however, Numerous investigations have demonstrated its involvement in neurogenesis, cellular adhesion, myelin maintenance, and toxin scavenging [11]. Adult patients with hepatobiliary illnesses have been included in current investigations examining the activities of BChE in humans. Studies examining alterations in BChE activity in adult patients or those with MetS are few. Fewer studies have looked at the connection between obesity and plasma BChE concentrations in the general adolescent population, despite numerous researchers having found elevated levels of BChE in the plasma of people with MetS and abdominal obesity. Furthermore, it is yet unknown if raising BChE levels might help adolescents with MetS, although this topic has recently gained greater attention. While elevated BChE levels have been linked to obesity in several populations, the Chinese teenage population has not shown evidence of this connection [12].

An example of an ab-initio approach is the Moller-Plesset (MP) perturbation theory. The average interaction between electrons is the only factor considered by the Hartree-Fock wave function. On the other hand, immediate interactions among electrons must also be considered. Because electrons repel each other [13]. When the instantaneous interactions of the movements of electrons with each other are included in the wave function, it can be said that the instantaneous electron correlation is included in the wave function. This method also adds the electron correlation effect to the Hartree-Fock method. It does this using Rayleigh-Schrödinger perturbation theory. The Moller-Plesset method is generally used for second-, third-, and fourth-order calculations, symbolized by MP2, MP3, and MP4, respectively [14].

In this study, MP2 calculations of the pyrazole derivative BHDH [15] molecule were made with the Gaussian 09 program. In the continuation of this study, the drug properties of the 4-(2-(4-bromophenyl)hydrazineylidene)-3,5-diphenyl-4h-pyrazole (BHDH) molecule on obesity disease were examined by Absorbed, Distributed, Metabolized, and Excreted (ADME) analysis. In addition, molecular docking analysis of the BHDH molecule on obesity disease was performed with BChE and AChE enzymes.

## 2. Materials and Methods

For MP2, the BHDH molecule's theoretical analysis was performed utilizing Gaussian 09 [16] programs. First, the MP2 approach optimized the molecule's gas phase using the DGDZVP and 6-311G(d,p) basis sets. The BHDH compound's ADME analysis was conducted utilizing the online database Admetlab 2.0 (<https://admetmesh.scbdd.com/>). Schrödinger's Maestro Molecular Modeling platform (version 11.8) [17] was used for molecular docking analysis, and the resulting receptor was used to visualize 3D interactions. The Discovery Studio 2016 [18] program was used. The Origin 2019b 64-bit program was used to compare Mulliken loads graphically.

## 3. Results and Discussion

This section should provide/introduce/investigate the findings and discussion/definitions and theorems. Findings/Concepts obtained from the study should be supported in this section by figures, tables/propositions, and examples. For Results and Discussion, the similarities and differences of the obtained results with other studies should be provided, and the possible reasons for these should be discussed based on the literature. For Results and Discussion, the contribution and importance of the results to science should be emphasized. The obtained results should be interpreted, avoiding unnecessary repetitions.

### 3.1. Structure Details and Analysis

In chemical computation, geometry optimization is a crucial procedure. Finding the minimal energy conformers at which all other attributes are acquired for conformationally flexible molecules requires a conformational search. Foresman and Frisch state that geometric parameters like bond length and bond angle may be effectively assessed as long as the experimental value's bond length differs from the expected value by less than 0.01 and the variation in the bond length angle is less than 1-2° [19]. Atomic attributes, including electronegativity, bond energy, and atomic size, are all determined by the length of the bond. Conversely, bond energy and electronegativity are equal to bond distance. With the DGDZVP and 6-311G(d,p) basis sets, the MP2 technique was used to compare BHDH molecule's bond lengths and angles [20].

Table 1 lists the optimized characteristics of the molecule, including the bond length between atoms, dihedral angles, and bond angles. When these two different basis sets are compared, the bond between the C-C atom for the DGDZVP basis set varied between 1.40Å-1.46Å, while the bond between the C-C atom for the 6-311G(d,p) basis set varied between 1.42Å-1.48Å. For both basis sets, the bond between C-C atoms showed close values. Bond angles and all bond lengths in phenyl rings are within the normal range. C-H bond lengths in the aromatic ring varied between 1.08-1.090Å. The distance between C23-Br26, C1-N2, and N2-N3 atoms has changed between 1.9032Å-1.9694Å, 1.3347Å-1.3631Å, and 1.4241Å-1.5222Å, respectively. All C-C-C angles for both basis sets are between 112° and 122°. The bond angle of C1-N2-N3 in the compound is 107.645°-109.018°, C5-N18-N19 is 119.677°-120.440°, and C22-C23-Br26 is 119.534°-119.632°. We observed that the dihedral angles of the molecule are compatible with each other for both basis sets. We saw that the obtained theoretical bond lengths were close to the experimental numerical data in the literature [21, 22].

**Table 1.** BHDH molecules theoretically computed some bond lengths (Å) and bond angles (°)

Bond Lengths	MP2 DGDZVP	MP2 6-311G(d,p)	Bond Lengths	MP2 DGDZVP	MP2 6-311G(d,p)
C1-C5	1.45607	1.48908	C23-Br26	1.90326	1.96941
C4-C7	1.46574	1.48363	C5-N18	1.33650	1.35145
C8-C9	1.40394	1.42236	N2-N3	1.42417	1.52221
C7-C13	1.41334	1.43248	C1-N2	1.33474	1.36311
C15-C16	1.40574	1.42472	N3-C4	1.33227	1.35902
C7-C17	1.41349	1.43205	N19-C20	1.40973	1.43087
C1-C6	1.47190	1.48954	N19-H37	1.03005	1.02721
C20-C25	1.41334	1.42403	C17-H36	1.08954	1.09245
C20-C21	1.40786	1.42593	C12-H31	1.09348	1.09688
C24-C25	1.40226	1.42154	C24-H40	1.08946	1.09246
C1-C5-C4	103.34091	103.97700	N18-N19-C20	120.71695	119.87856
C4-C7-C17	121.27805	121.12912	N18-N19-H37	120.84485	121.06601
C1-N2-N3	109.01830	107.64582	C7-C4-N3	122.40228	121.97692
C5-N18-N19	119.67752	120.44011	C20-C21-C22	119.30439	119.34826
C22-C23-Br26	119.53433	119.63225	C20-N19-H37	118.43199	119.05126
C5-C4-C7-C13	149.85934	148.61603	N18-C5-C4-N3	166.71326	168.21426
N3-C4-C5-N18	166.71326	168.21426	C21-C20-N19-H37	177.21979	175.67830
C21-C22-C23-Br26	179.97135	179.91207	C22-C23-C24-H40	179.80592	179.84972
C5-N18-N19-C20	178.16709	177.98597	C7-C4-N3-N2	178.89941	178.63592

### 3.2. Mulliken Atomic Charges

Mulliken charges are present in the surrounding electron density, or charge density. It is helpful since it is susceptible to probability density and only depends on the base set [23]. Several MP2 approaches are used in Mulliken population studies to quantify the nuclear charges on atoms [24]. The MP2 technique and the basis set for DGDZVP and 6-311G(d,p) were used in its execution. Table 2 lists the Mulliken atomic charges. We observed either positive or negative Mulliken atomic charge values on carbon atoms. Every hydrogen atom had a positive net charge. When we look at the DGDZVP basic set values in Table 2, we observed that the electronegative atoms N2 (-0.234), N3 (-0.291), N18 (-0.121), and N19 (-0.606) had negative values. These atoms serve as acceptor atoms. When we examined both basis sets, we observed close values with negative values of Br26 -0.149 and -0.069. Additionally, graphical representations of the comparison of Mulliken charges of the BHDH molecule using two different base sets have been shown in Figure 1. When the Mulliken loads were compared in the two basic sets, we saw that the values were compatible.

**Table 2.** BHDH molecule's Mulliken atomic charges

ATOMS	MP2 / DGDZVP	MP2 / 6-311G(d,p)	ATOMS	MP2 / DGDZVP	MP2 / 6-311G(d,p)
C1	0.179	0.124	N3	-0.291	-0.244
C4	0.217	0.161	N18	-0.121	0.024
C6	0.051	0.240	N19	-0.606	-0.657
C7	0.120	0.260	Br26	-0.149	-0.069
C9	-0.242	-0.215	H27	0.268	0.246
C11	-0.245	-0.220	H28	0.347	0.218
C13	-0.275	-0.297	H29	0.249	0.221
C15	-0.241	-0.210	H30	0.245	0.217
C17	-0.288	-0.293	H32	0.276	0.251
C20	0.506	0.540	H33	0.239	0.212
C21	-0.338	-0.307	H34	0.240	0.213
C22	-0.216	-0.107	H35	0.233	0.207
C23	0.039	-0.345	H37	0.505	0.426
C24	-0.225	-0.107	H38	0.291	0.270
C25	-0.383	-0.375	H39	0.266	0.237
N2	-0.234	-0.189	H41	0.247	0.224

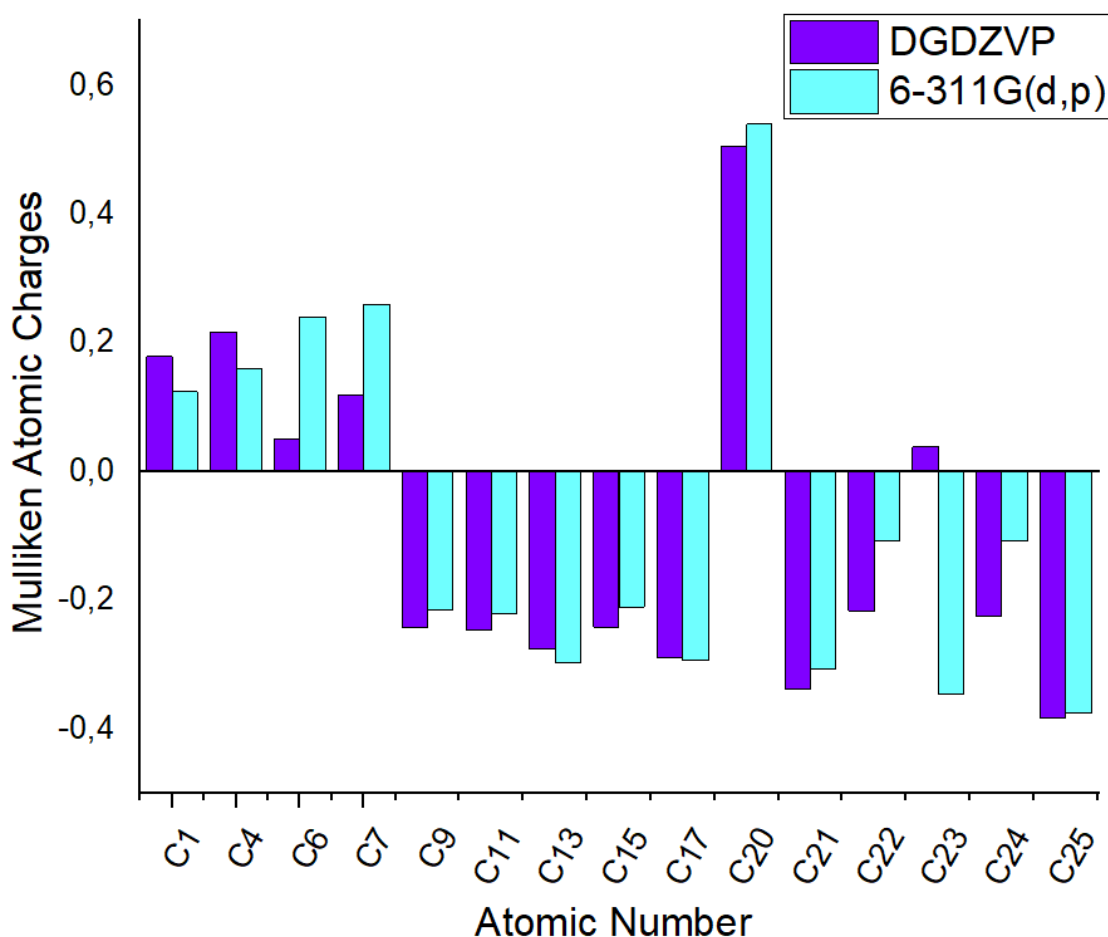


**Figure 1.** Mulliken atomic charge comparison for BHDH molecule

### 3.3. HUMO and LUMO Analysis

Molecules with soft expression, poor kinetic stability, and strong chemical reactivity are typically linked to their frontier orbital space. The molecule's relationships with other molecules are identified by its Highest-Energy Molecular Orbital (HOMO) and Lowest-Energy Molecular Orbital (LUMO) orbitals [25]. Band gap energies are computed, and HOMO-LUMO is predicted utilizing a solvation technique for a range of polar (water, DMSO, and ethanol) and non-polar (benzene) solvents. In advanced molecular orbital computation, the terms lowest unoccupied molecular orbital (LUMO) and highest occupied molecular orbital, HOMO, are recognized as significant FMO (frontier molecular orbital) orbitals [26]. Electrons in HOMO orbitals absorb high-frequency radiation, which causes them to leap into LUMO orbitals. Energies have a role in determining how sensitive Frontier Molecular Orbitals are overall to several descriptors, including electronegativity, global softness, electron affinity, global hardness, and chemical potential, as well as the molecule's global electrophilicity index [27]. The HOMO and LUMO orbital representations' of the densities of the BHDH molecule have been shown in Figures 2 and 3. As seen in Table 3, LUMO and HOMO for the DGD2VP set were calculated as -8.3535 eV and -0.1235 eV, respectively, while for the 311G(d,p) set, HOMO and LUMO were calculated as -8.4155 eV and -0.3671 eV, respectively. For the other orbitals of the DGD2VP set, HOMO<sup>-1</sup> and LUMO<sup>+1</sup> were calculated as -8.5399 eV and 2.2938 eV, respectively, while for the different orbitals of the 311G(d,p) set, LUMO<sup>+1</sup> and HOMO<sup>-1</sup> have been calculated as -8.2289 eV and 2.6313 eV, respectively. When we examine the two essential chemical orbitals for LUMO and HOMO energies in Figures 2 and 3, the HOMO and LUMO electron clouds are completely localized along the compound's ligand, as can be shown.

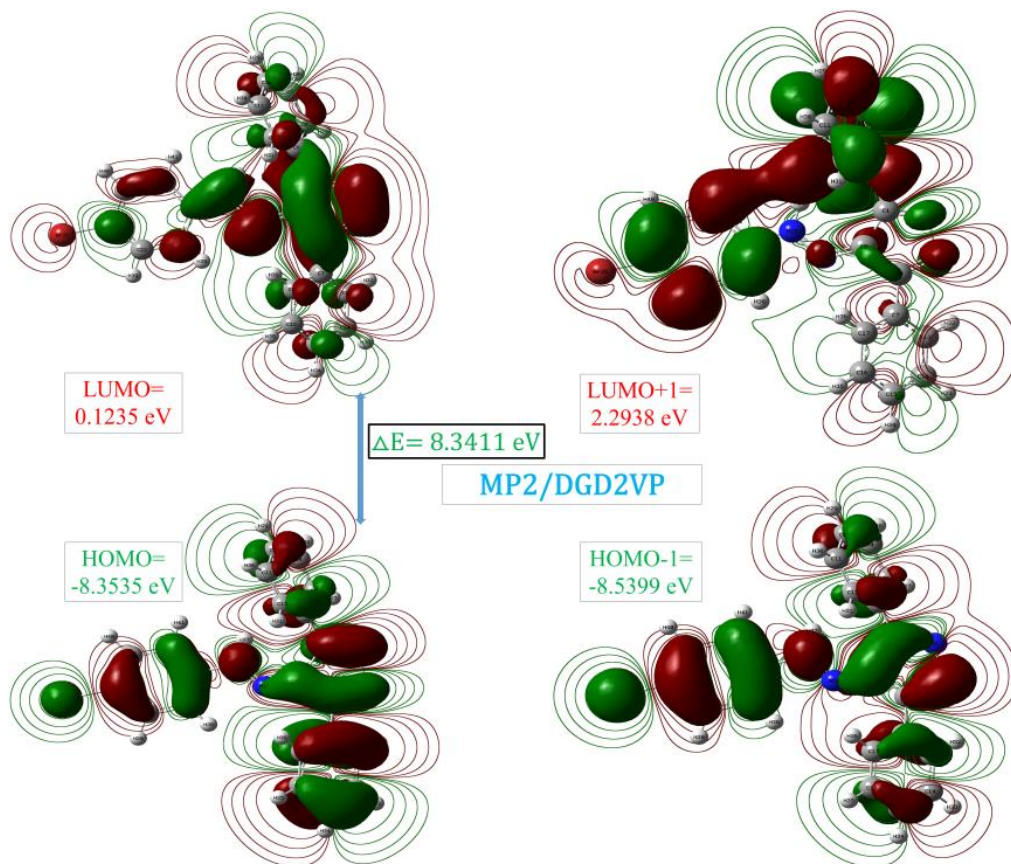


**Figure 2.** BHDH molecule's boundary molecular orbitals computed with the DGD2VP basic set

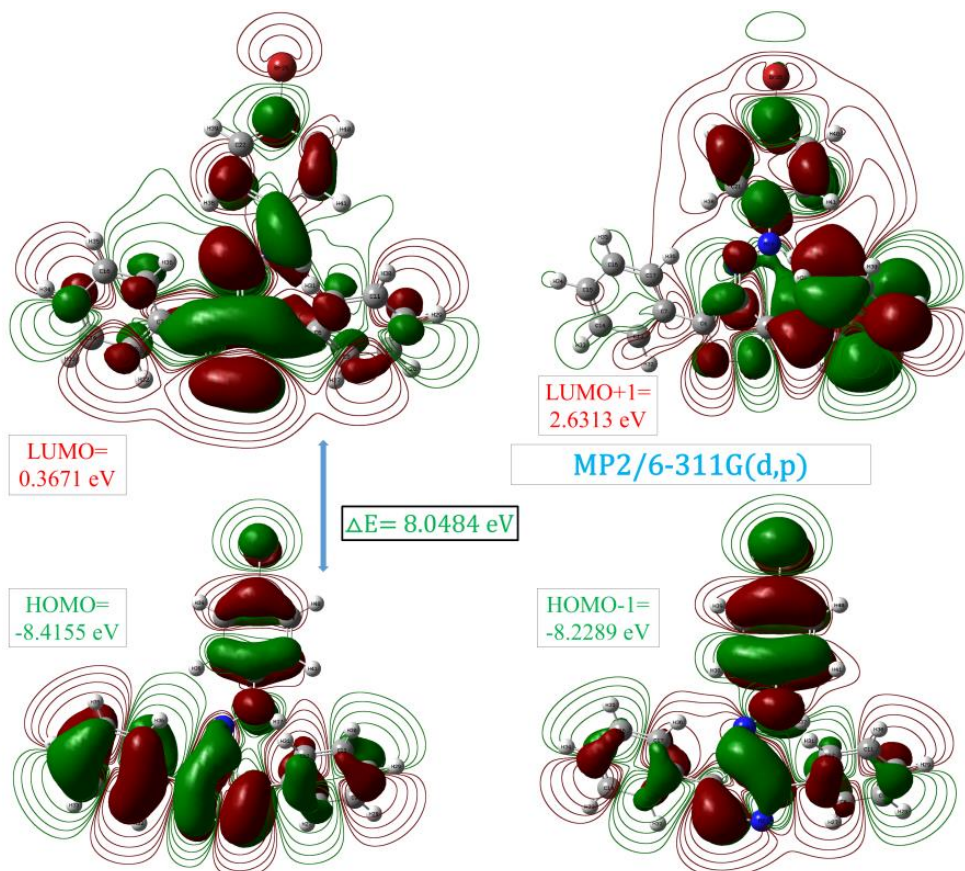


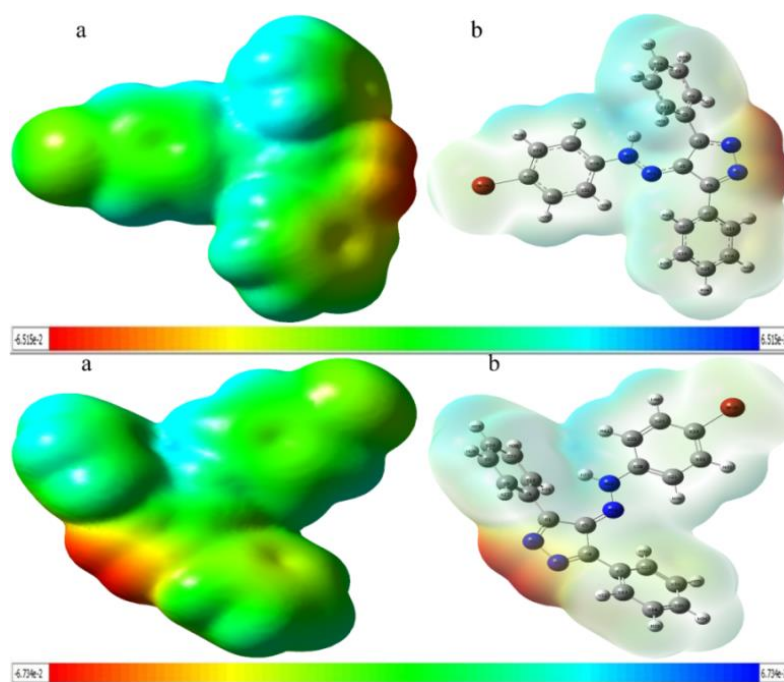
**Figure 3.** BHDH molecule's boundary molecular orbitals computed with the 6-311G (d,p) basic set

**Table 3.** Quantum chemical characteristics of the BHDH molecule computed utilizing the MP2/DGDZVP-MP2/6-311G techniques

Molecules Energy		MP2/DGD2VP	MP2/6-311G(d,p)
$E_{LUMO}$		0.1235	0.3671
$E_{HOMO}$		-8.3535	-8.4155
$E_{LUMO+1}$		2.2938	2.6313
$E_{HOMO-1}$		-8.5399	-8.2289
<b>Energy Gap</b>	$(\Delta E) E_{HOMO}-E_{LUMO} $	-8.477	-8.7826
<b>Ionization Potential</b>	$(I=-E_{HOMO})$	8.3535	8.4155
<b>Electron Affinity</b>	$(A=-E_{LUMO})$	-0.1235	-0.3671
<b>Chemical hardness</b>	$(\eta=(I-A)/2)$	8.477	8.7826
<b>Chemical softness</b>	$(s=1/2\eta)$	4.2385	4.3913
<b>Chemical Potential</b>	$(\mu=-(I+A)/2)$	-4.115	-4.0242
<b>Electronegativity</b>	$(\chi=(I+A)/2)$	8.23	8.0484
<b>Electrophilicity index</b>	$(\omega=\mu^2/2\eta)$	71.7715	71.41135

### 3.4. Molecular Electrostatic Potential (MEP)

The relative reactivity sites to nucleophilic and electrophilic attacks in a species are estimated using the molecular electrostatic potential, or MEP. Understanding nucleophilic (positive) and electrophilic (negative) locations for hydrogen bond interactions and chemical reactions depends on MEP surface analysis [28]. MEP displays the molecule size, shape, and electrostatic potential in point color order [29]. Different MEP values correspond to different hues. Maximum positive electrostatic potential is represented by the blue zone, zero potential by the green region, and maximum negative electrostatic potential by the red region. MEP accelerates the blue>green>red>orange process. Negative MEP seems to hold onto a proton depending on the electron density's evaluation within the molecule, while positive MEP detects protons repelled by their blue color (atomic nuclei) [30]. Figure 4 displays the MEP map of the compound BHDH using the MP2 technique with the basis sets DGDZVP and 6-311G(d,p). The MEP map displays positive and negative potential based on the measured data, clearly indicating the biological activity of BHDH. As expected, the negative sites were localized to the nitrogen in the pyrazole ring.

**Figure 4.** BHDH molecule's MEP surface calculated DGDZVP and 6-311G(d,p) basis sets

### 3.5. Nonlinear Optical Properties

When electromagnetic fields interact in disparate contexts, they produce new fields with distinct points, repetition, proficiency, and other characteristics from the dividing fields. This phenomenon is known as the Nonlinear Optical (NLO) effect [31].  $\pi$ -conjugated particles and polymers are perfect for discovering these applications because of their ultrafast reactions and remarkable nonlinear characteristics. The blends of NLO materials show promise for all-optical interchange, recording, and restraint devices, even though they are not as promising for use in rapid electro-optical modulators and switches [32]. (3.1)-(3.3) demonstrate that the first-order hyperpolarizability of  $\beta$ , the second dipole moment  $\mu$ , is the total first static hyperpolarizability of the x, y, and z components using the DGDZVP and 6-311G(d,p) basis sets with the MP2 technique and Using the restricted field technique, the polarizability  $\alpha$  was found. Table 4 presents the  $\mu$ ,  $\alpha$ , and  $\beta$  recorded for the studied atoms. The total values determined by the MP2 method using DGDZVP and 6-311G(d,p) basis sets to the DHPM compound are  $2.77 \times 10^{-30}$  esu and  $2.70 \times 10^{-30}$  esu, respectively.

$$\mu = (\mu_x^2 + \mu_z^2)^{\frac{1}{2}} \tag{3.1}$$

$$\beta_{Total} = (\beta^2x + \beta^2y + \beta^2z)^{\frac{1}{2}} \tag{3.2}$$

and

$$\beta_{Total} = [(\beta_{xxx} + \beta_{xyy} + \beta_{xzz})^2 + (\beta_{yyy} + \beta_{yxx} + \beta_{yzz})^2 + (\beta_{zzz} + \beta_{zxx} + \beta_{zyy})^2]^{\frac{1}{2}} \tag{3.3}$$

**Table 4.** NLO parameters of BHDH molecule computed using DGDZVP and 6-311G(d,p) basis sets with MP2 method

Parameters	MP2/DGD2VP	MP2/6-311G(d,p)	Parameters	MP2/DGD2VP	MP2/6-311G(d,p)
$\mu_x$	-4.2394	-2.9822	$\beta_{xxx}$	-329.0799	-244.5529
$\mu_y$	1.8038	0.5759	$\beta_{yyy}$	-0.7758	-12.5027
$\mu_z$	0.3618	0.4898	$\beta_{zzz}$	-4.4802	-13.4906
$\mu(D)$	4.6214	3.0765	$\beta_{xyy}$	-52.8030	-6.8949
$\alpha_{xx}$	-206.8374	-183.9689	$\beta_{xxy}$	-41.0396	-35.9322
$\alpha_{yy}$	-136.2896	-137.6760	$\beta_{xxz}$	-35.0058	13.0767
$\alpha_{zz}$	-168.1933	-170.7588	$\beta_{xzz}$	-54.4855	-87.1807
$\alpha_{xy}$	-9.4492	-9.3979	$\beta_{yzz}$	6.9026	-10.8462
$\alpha_{xz}$	-6.5791	-2.6943	$\beta_{yyz}$	-16.2187	4.9378
$\alpha_{yz}$	-1.1804	3.4442	$\beta_{xyz}$	-2.0695	-16.8616
$\alpha$ (au)	-175.172	-169.8441	$\beta$ (esu)	$2.77 \times 10^{-30}$	$2.70 \times 10^{-30}$

### 3.6. NBO Analysis

The Natural Bond Orbital (NBO) study demonstrates increased conjugation, rearrangement, and intramolecular charge transfer of electrons in diverse orbitals. Research on natural bond orbitals sheds light on a compound's intra- and intermolecular hydrogen bonding and conjugative and hyper-conjugative interactions [33, 34]. The donor-acceptor stabilization energy  $E(2)$  related to delocalization  $i \rightarrow j$  is computed as  $E(2) = q_i F(i,j) / (\epsilon_j - \epsilon_i)$  for each donor NBO (i) and acceptor NBO (j).  $F(i,j)$  is the off-diagonal NBO Fock matrix element, and  $q_i$  is the donor orbital occupancy. Because the stabilizing energy ( $E(2)$ ) is larger, the conjugation across the molecular system is more extensive [35]. Table 5 presents the NBO analysis findings from the BHDH molecule utilizing the 6-311G(d,p) basis set and the MP2 technique. When we examine the results in Table 5, in the instance of C20/C25 benzene ring,  $\pi$ C20-C24 with  $\pi^*$ C21-C22 (17.98 kcal/mol),  $\pi$ C21-C22 with  $\pi^*$ C20-C25 (22.66 kcal/mol),  $\pi$ C23-C25 with  $\pi^*$ C21-C22 (20.99 kcal/mol), and  $\sigma$ C24-C25 and  $\sigma^*$ C23-Br26 (22.66 kcal/mol) have high interaction energies. The molecule's intramolecular charge transfer and stability of the benzene rings under study are mostly due to

previously discussed stabilization energies. These energies stabilized the investigated molecule's structure, and an aromatic ring resonance interaction occurred between the heteroatoms. Additionally, the BHDH molecule has  $\pi\text{C8-C9} \rightarrow \pi^*\text{C6-C12}$  (22.04 kcal/mol),  $\pi\text{C15-C16} \rightarrow \pi^*\text{C7-C17}$  (21.27 kcal/mol), and  $\pi\text{C10-C11} \rightarrow \pi^*\text{C6-C12}$  (21.05 kcal/mol). The other highest stabilization energies include  $\pi\text{C6-C12} \rightarrow \pi^*\text{C10-C11}$  (20.74 kcal/mol) and  $\pi\text{C7-C17} \rightarrow \pi^*\text{C13-C14}$  (19.38 kcal/mol). Consequently, the donor-acceptor interaction could be stabilized by electron delocalization between non-Lewis-type natural bond orbitals and unoccupied occupied Lewis. Further delocalization within the molecular system is seen from the electron density of double bonds and the conjugated single in the conjugated system. This leads to intramolecular charge transfer (ICT), stabilizing the system. These interactions weaken the corresponding bonds in the C-C antibonding orbital, manifesting as an increase in electron density (ED). Table 5 shows the significant stabilization energy of 22.66 kJ/mol and provides evidence for intramolecular charge transfer from (C21-C22) to  $^*(\text{C20-C25})$  antibonding orbitals. Also, the charge distribution of all hydrogen atoms is the same.

**Table 5.** Selected NBO results of BHDH molecule computed using DGDZVP and 6-311G(d,p) basis sets

NBO(i)	Type	Occupancies	NBO(j)	Type	Occupancies	E(2) <sup>a</sup> (Kcal/mol)	E (j)-E(i) <sup>b</sup> (a.u.)	F (i, j) <sup>c</sup> (a.u.)
C1-N2	$\sigma$	1.98091	C5-N18	$\sigma^*$	0.01944	4.44	1.25	0.067
C1-N2	$\pi$	1.88422	C5-N18	$\pi^*$	0.32111	16.07	0.27	0.062
C1-C5	$\sigma$	1.97259	C4-C7	$\sigma^*$	0.03186	5.45	1.12	0.070
N3-C4	$\pi$	1.88279	C5-N18	$\pi^*$	0.32111	13.91	0.26	0.057
N2-N3	$\sigma$	1.96621	C4-C7	$\sigma^*$	0.03186	6.04	1.10	0.073
C4-C5	$\sigma$	1.95989	C1-C6	$\sigma^*$	0.03285	5.99	1.08	0.072
C4-C5	$\sigma$	1.95989	N18-N19	$\sigma^*$	0.02382	6.32	0.96	0.070
C5-N18	$\pi$	1.80320	N3-C4	$\pi^*$	0.24950	14.30	0.35	0.064
C6-C12	$\pi$	1.65932	C10-C11	$\pi^*$	0.32831	20.74	0.28	0.068
C7-C17	$\pi$	1.62775	C13-C14	$\pi^*$	0.29730	19.38	0.28	0.067
C8-C9	$\sigma$	1.98000	C1-C6	$\sigma^*$	0.03285	4.53	1.12	0.064
C8-C9	$\pi$	1.64005	C6-C12	$\pi^*$	0.39361	22.04	0.26	0.068
C8-H27	$\sigma$	1.97715	C6-C12	$\sigma^*$	0.02668	5.85	1.00	0.068
C9-H28	$\sigma$	1.97757	C10-C11	$\sigma^*$	0.01544	4.77	1.02	0.063
C10-C11	$\pi$	1.64875	C6-C12	$\pi^*$	0.39361	21.05	0.27	0.067
C10-H29	$\sigma$	1.97848	C11-C12	$\sigma^*$	0.01486	4.86	1.03	0.063
C11-H30	$\sigma$	1.97771	C6-C12	$\sigma^*$	0.02668	5.27	1.03	0.065
C13-C14	$\pi$	1.65560	C7-C17	$\pi^*$	0.37611	20.41	0.27	0.067
C13-H32	$\sigma$	1.97710	C7-C17	$\sigma^*$	0.02402	5.59	1.01	0.067
C14-H33	$\sigma$	1.97777	C15-C16	$\sigma^*$	0.01559	4.69	1.03	0.062
C15-C16	$\pi$	1.65498	C7-C17	$\pi^*$	0.37611	21.27	0.27	0.069
C15-H34	$\sigma$	1.97883	C13-C14	$\sigma^*$	0.01382	4.71	1.04	0.063
C16-C17	$\sigma$	1.97960	C4-C7	$\sigma^*$	0.03186	4.48	1.12	0.064
C16-H35	$\sigma$	1.97787	C7-C17	$\sigma^*$	0.02402	5.17	1.02	0.065
C20-C25	$\pi$	1.64550	C21-C22	$\pi^*$	0.30596	17.98	0.29	0.065
C21-C22	$\pi$	1.67199	C20-C25	$\pi^*$	0.40257	22.66	0.26	0.070
C23-C24	$\pi$	1.68181	C21-C22	$\pi^*$	0.30596	20.99	0.29	0.070
C24-C25	$\sigma$	1.96833	C23-Br26	$\sigma^*$	0.04044	5.21	0.76	0.056

### 3.7. ADME Analysis

One of its shared objectives is predicting Absorbed, Distributed, Metabolized, and Excreted (ADME) boundaries from subatomic structures. Lipinski and colleagues' landmark study looked at complicated combinations supplied orally to categorize physicochemical probes based on how likely they were to become oral drugs (drug-likeness) [36]. This illustrates the connection between pharmacokinetic and physicochemical limitations and is also known as the Rule of Five. The fivefold Lipinski standard meets roughly 91% of the ADME criteria. The standard explicitly addresses drug penetration through mixing-free drug distribution

within cell films. Special instances of this norm include tranquilizers that are effectively transported across cell layers by transporter proteins [37]. In the analysis conducted on ADME, Admetlab 2.0 (<https://admetmesh.scbdd.com/>), a free web tool for assessing drug similarity, was evaluated. This study investigated the drug-likeness of the BHDH molecule and ADME. Table 6 presents the estimated findings and interpretations of the investigated compound's physicochemical and lipophilicity features. Additionally, the medicinal chemistry applicability and comments of the compound are given in Table 7. Table 7 illustrates compliance with  $49.11 < 140$  (Topological Polar Surface Area) requirements for Lipinski's MW 402.05g/mol ( $< 500$ ), lipophilicity coefficient LogP 5.361 ( $\leq 5$ ), H-acceptor 4 ( $\leq 12$ ), H-bond donor 1 ( $< 7$ ). The color zones and physicochemical parameters map of the studied compound are given in Figure 5. The outcomes demonstrated no breach of Lipinski's five rules, indicating how drug-like the molecule is. Because of the compound's promising permeability, lipophilicity, and solubility, it demonstrated excellent absorption. The polar surface region and the quantity of rotatable bonds showed the investigated compound's high bioavailability.

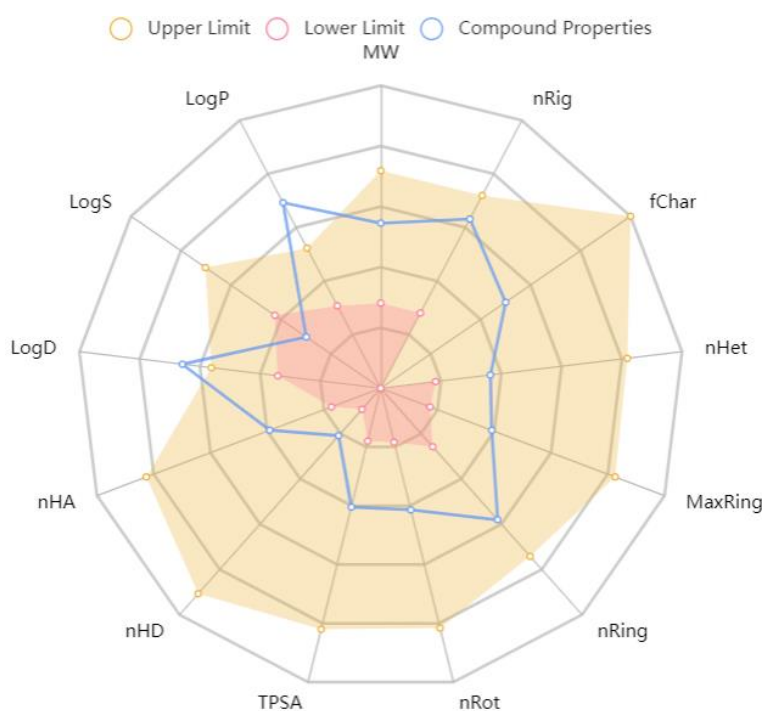


**Figure 5.** Color regions and physicochemical parameters of BHDH molecule

**Table 6.** Physicochemical and lipophilicity of BHDH molecule

Property	Value	Comment
Molecular Weight	402.05	Contain hydrogen atoms. Optimal:100~600
nHA	4	Number of hydrogen bond acceptors. Optimal:0~12
nHD	1	Number of hydrogen bond donors. Optimal:0~7
nRot	4	Number of rotatable bonds. Optimal:0~11
nRing	4	Number of rings. Optimal:0~6
MaxRing	6	Number of atoms in the biggest ring. Optimal:0~18
nHet	5	Number of heteroatoms. Optimal:1~15
nRig	24	Number of rigid bonds. Optimal:0~30
TPSA	49.11	Topological Polar Surface Area. Optimal:0~140
logS	-6.038	Log of the aqueous solubility. Optimal: -4~0.5 log mol/L
logP	5.361	Log of the octanol/water partition coefficient. Optimal: 0~5

**Table 7.** Medicinal chemistry of BHDH molecule

Property	Value	Decision	Comment
QED	0.604	-	A measure of drug-likeness based on the concept of desirability; Attractive: > 0.67; unattractive: 0.49~0.67; toocomplex: < 0.34
Fsp3	0.0	-	Fsp <sup>3</sup> ≥ 0.42 is considered a suitable value.
MCE-18	38.0	-	MCE-18 stands for medicinal chemistry evolution. MCE-18 ≥ 45 is considered a suitable value.
LipinskiRule	Accepted	-	MW ≤ 500; logP ≤ 5; Hacc ≤ 10; Hdon ≤ 5 If two properties are out of range, a poor absorption or permeability is possible; one is acceptable.
Pfizer Rule	Rejected	-	logP > 3; TPSA < 75 Compounds with a high log P (>3) and low TPSA (<75) are likely to be toxic.
Golden Triangle	Accepted	-	200 ≤ MW ≤ 50; -2 ≤ logD ≤ 5 Compounds satisfying the Golden Triangle rule may have a more favorable ADMET profile.
PAINS	0 alerts	-	Pan Assay Interference Compounds, frequent hitters, Alpha-screen artifacts, and reactive compound
ALARMNMR	2 alerts	-	Thiol reactive compounds
BMS	0 alerts	-	Reactive compounds, Undesirable
ChelatorRule	0 alerts	-	Chelating compounds

### 3.8. Molecular Docking Studies

All functions and activities in any living system, human, animal, plant, fungal, or bacterial, can be converted into biological processes at the molecular, cellular, or organ level. Molecular docking is a crucial method in medication design based on a structure that can help expedite and simplify the new medication creation process [38]. Molecular docking estimates any species' binding conformations and affinities to the goal protein, enabling scientists to digitally scan the interaction between the protein and the ligand [39]. By providing predictions for the bound shape of the ligand and a way to energetically rank the protein-ligand interaction, molecular docking techniques aid in the characterization of the protein-ligand interaction [40]. Molecular docking was done using Schrödinger's Maestro Molecular Modeling platform to analyze the ligand-protein interactions of the BHDH molecule with acetylcholinesterase (AChE) and butyrylcholinesterase (BChE) enzymes on obesity disease [17]. Acetylcholinesterase (AChE) (PDB: 1ACJ) and butyrylcholinesterase (BChE) (PDB: 1P0I) enzymes required for docking were searched from the online resource RSCB protein database. Using the Discovery Studio Client 2017 program, good docking poses were chosen for the docking analysis on obesity illness, and the protein-ligand interaction was shown [18]. Protein binding and active sites are often anchored in structured cavities and pockets. In order to prevent steric hindrance, water molecules were eliminated from the crystal packing. Excellent enzyme binding affinity was attained: -9.73 kcal for BChE and -10.00 kcal for AChE. The binding energy value affects the target protein's choice of ligand docking. Each species has a stronger capacity to attach to the target protein, the more negatively its binding energy value is. Given the high binding affinity of the BHDH molecule, we believe that the chemical we studied will be crucial to creating medications based on structure to treat obesity. The docking scores of these enzymes are given in Table 8. Visualized findings of the BHDH molecule and the ligands' interactions and separations have been given in Figures 6 and 7. Additionally, essential interactions, amino acids, and bond length data of our study compound in the docking analysis are given in Tables 9 and 10.

**Table 8.** Docking score of BHDH molecule PDB: 1ACJ and PDB: 1P0I

Compound	Docking Score	
	(PDB: 1ACJ)	(PDB: 1P0I)
<b>BHDH Molecule</b>	-10.00	-9.73

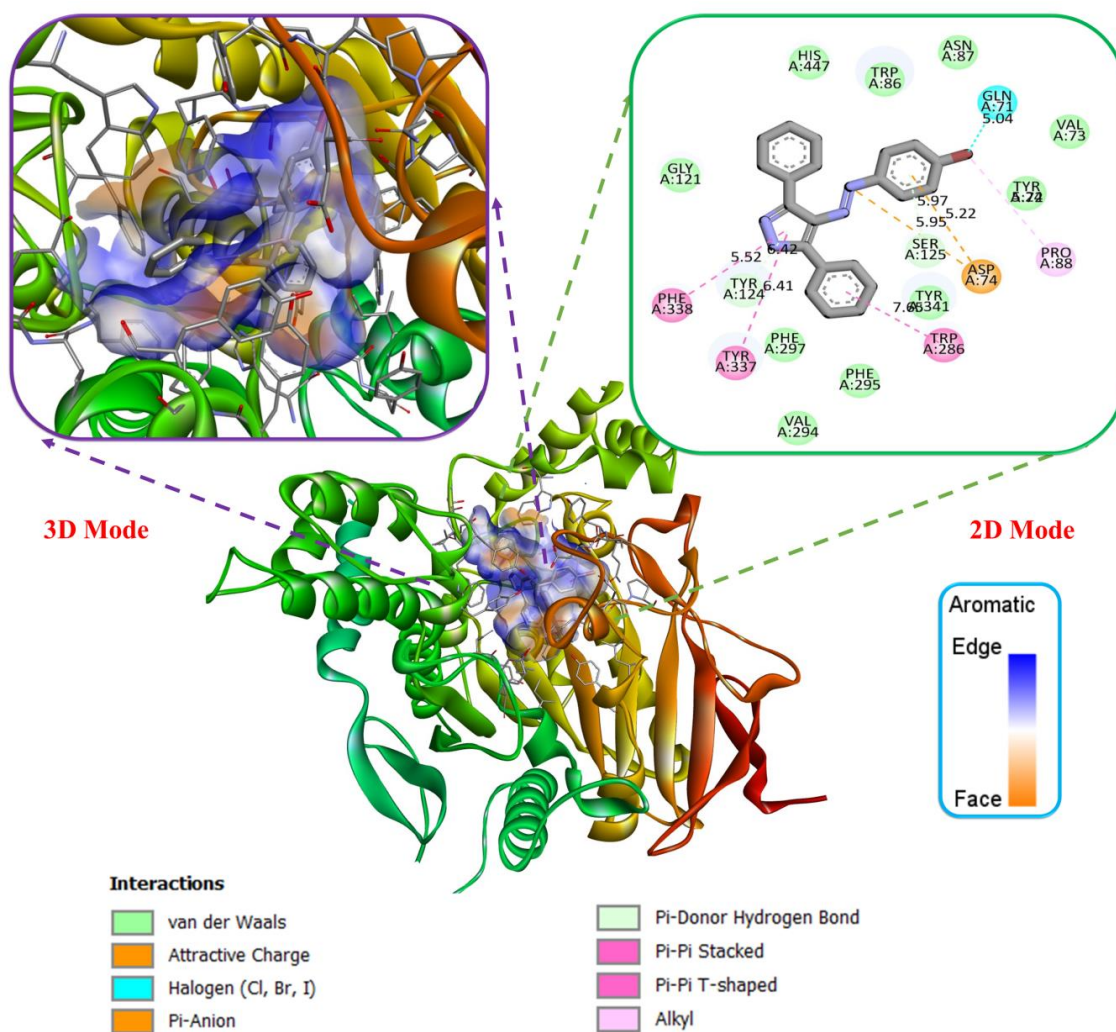


**Figure 6.** 3D and 2D representations of the interaction between BHDH compound of AChE enzyme

**Table 9.** Parameters of the interaction between BHDH compound of AChE enzyme

Important Interactions	Full Name	Type	Bond Length (Å)	Color
Attractive Charge	A:ASP74	AsparticAcid	5.95	Orange
Halojen	A:GLN71	Glutamine	-	Cyan
Pi-Pi Stacked	A:TRP286	Tryptophan	7.65	Pink
Pi-Pi T-shaped	A:TYR337	Tyrosine	6.41	Pink
	A:PHE338	Phenylalanine	5.52	Pink
Alkyl	A:PRO88	Proline	5.74	Light Pink
Pi-Anion	A:ASP74	AsparticAcid	5.22	Orange
Pi-donor Hydrogen Bond	A:SER125	Serine	5.97	Light Green
Van der Waals	A:VAL73	Valine	-	Light Green
	A:ASN87	Asparagine	-	Light Green

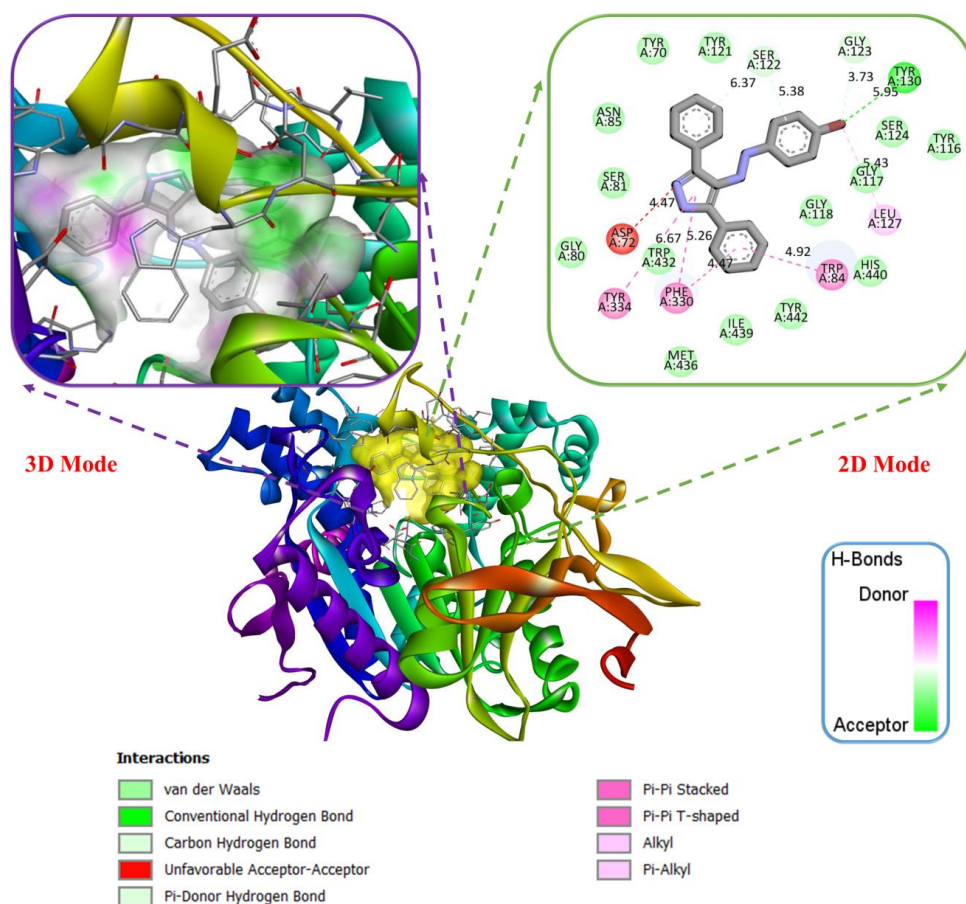


**Figure 7.** 3D and 2D representations of the interaction between BHDH compound of BChE enzyme

**Table 10.** Parameters of the interaction between BHDH compound of BChE enzyme

Important Interactions	Full Name	Type	Bond Length (Å)	Color
Conventional Hydrogen Bond	A:TYR130	Tyrosine	5.95	■
Unfavorable Acceptor-acceptor	A:ASP72	AsparticAcid	4.47	■
Pi-Pi Stacked	A:TRP84	Tryptophan	4.94	■
Pi-Pi T-shaped	A:PHE330	Phenylalanine	5.26, 4.47	■
Pi-Alkyl	A:LEU127	Leucine	5.43	■
Carbon Hydrogen Bond	A:GLY123	Glycine	3.73	■
Pi-donor Hydrogen Bond	A:SER122	Serine	5.38, 6.37	■
Van der Waals	A:SER81 A:MET436	Serine Methionine	- -	■

#### 4. Conclusion

This study, quantum chemical calculations were made for the 4-(2-(4-bromophenyl)hydrazineylidene)-3,5-diphenyl-4h-pyrazole (BHDH) molecule using the MP2 method and DGDZVP and 6-311G(d,p) basis sets. These two basis sets have computed structural parameters (bond lengths, bond angles, and dihedral angles). We found that the structural parameters calculated with these basis sets are compatible. NLO, HOMO-LUMO,

MEP, NBO, and Mulliken loadings were visualized using the same basis sets. The investigated chemical was suitable for use as an NLO material. From the calculations made for the BHDH molecule, polarity ( $\alpha=-175.172$  au and  $\alpha=-169.8441$  au) and static high-order polarity ( $\beta=2.77\times 10^{-30}$  esu and  $\beta=2.70\times 10^{-30}$  esu) parameters were determined. The boundary molecular energy gap between LUMO and HOMO calculations of the examined compound is -8.477 eV for the DGD2VP set and -8.7826 eV for the 6-311G(d,p) set; this indicates greater stability of the molecule. When we examined the MEP of our compound, the negative regions were localized to the nitrogen in the pyrazole ring, as we expected. When we compared the mulliken atomic charges in the two sets used, we observed the compatibility of the mulliken charges in the two sets. In the continuation of the study, ADME analysis was performed to evaluate the BHDH molecule as a drug. We discovered that the molecule had strong ADME qualities and met Lipinski's rule requirements, indicating that it is a viable therapeutic candidate that should be investigated further. Finally, our study analyzed the ligand-protein interactions of the BHDH molecule with AChE and BChE enzymes in obesity disease. Good binding affinity for the enzyme was obtained, with the binding affinity being -10.00 for AChE and -9.73 kcal for BChE. Since the BHDH molecule has good binding affinity, this study compound will be an essential prediction in structure-based drug design on obesity disease.

### Author Contributions

All the authors equally contributed to this work. They all read and approved the final version of the paper.

### Conflicts of Interest

All the authors declare no conflict of interest.

### Ethical Review and Approval

No approval from the Board of Ethics is required.

### References

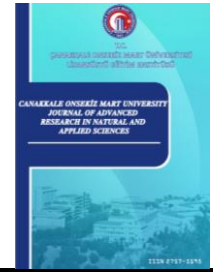
- [1] J. V. Faria, P. F. Vegi, A. G. C. Miguita, M. S. Dos Santos, N. Boechat, A. M. R. Bernardino, *Recently reported biological activities of pyrazole compounds*, *Bioorganic and Medicinal Chemistry* 25 (21) (2017) 5891–5903.
- [2] A. M. Youssef, E. G. Neeland, E. B. Villanueva, M. S. White, I. M. El-Ashmawy, B. Patrick, A. Klegeris, A. S. Abd-El-Aziz, *Synthesis and biological evaluation of novel pyrazole compounds*, *Bioorganic and Medicinal Chemistry* 18 (15) (2010) 5685–5696.
- [3] H. Ma, S. Chen, Z. Liu, Y. Sun, *Theoretical elucidation on the inhibition mechanism of pyridine–pyrazole compound: A Hartree Fock study*, *Journal of Molecular Structure: THEOCHEM* 774 (1-3) (2006) 19–22.
- [4] A. R. Thomas, Y. S. Mary, K. Resmi, B. Narayana, B. Sarojini, G. Vijayakumar, C. Van Alsenoy, *Two neoteric pyrazole compounds as potential anti-cancer agents: Synthesis, electronic structure, physico-chemical properties and docking analysis*, *Journal of Molecular Structure* (1181) (2019) 455–466.
- [5] B. E. Levin, *Factors promoting and ameliorating the development of obesity*, *Physiology and Behavior* 86 (5) (2005) 633–639.
- [6] R. Dent, R. McPherson, M. E. Harper, *Factors affecting weight loss variability in obesity*, *Metabolism* 113 (154388) (2020).
- [7] B. E. Levin, *Developmental gene environment interactions affecting systems regulating energy homeostasis and obesity*, *Frontiers in Neuroendocrinology* 31 (3) (2010) 270–283.

- [8] L. S. Adair, *Child and adolescent obesity: Epidemiology and developmental perspectives*, *Physiology Behavior* 94 (1) (2008) 8–16.
- [9] I. Orhan, B. Şener, M. Choudhary, A. Khalid, *Acetylcholinesterase and butyrylcholinesterase inhibitory activity of some Turkish medicinal plants*, *Journal of Ethnopharmacology* 91 (1) (2004) 57–60.
- [10] G. Chuiko, V. Podgornaya, Y. Zhelnin, *Acetylcholinesterase and butyrylcholinesterase activities in brain and plasma of freshwater teleosts: Cross-species and cross-family differences*, *Comparative Biochemistry and Physiology Part B: Biochemistry and Molecular Biology* 135 (1) (2003) 55–61.
- [11] R. Scacchi, M. Ruggeri, R. M. Corbo, *Variation of the butyrylcholinesterase (BChE) and acetylcholinesterase (AChE) genes in coronary artery disease*, *Clinica Chimica Acta* 412 (15–16) (2011) 1341–1344.
- [12] F-G. Koçanc, B. Aslım, *Structure and functions of acetylcholinesterase and acetylcholinesterase inhibitory activity of plants*, *Manas Journal of Agriculture Veterinary and Life Sciences* 6 (1) (2016) 19–35.
- [13] O. Christiansen, *Møller–Plesset perturbation theory for vibrational wave functions*, *The Journal of Chemical Physics* 119 (12) (2003) 5773–5781.
- [14] T. Takatani, C. D. Sherrill, *Performance of spin-component-scaled Møller–Plesset theory (SCS-MP2) for potential energy curves of noncovalent interactions*, *Physical Chemistry Chemical Physics* 9 (46) (2007) 6106–6114.
- [15] F. Turkan, A. Cetin, P. Taslimi, İ. Gulçin, *Some pyrazoles derivatives: Potent carbonic anhydrase,  $\alpha$ -glycosidase, and cholinesterase enzymes inhibitors*, *Archiv der Pharmazie* 351 (10) (2018) 1800200.
- [16] T. J. Frisch, G. W. Trucks, H. B. Schlegel, G. E. Scuseria, M.A. Robb, J. R. Cheeseman, G. Scalmani, V. P. G. A. Barone, G. A. Petersson, H. J. R. Nakatsuji, *Gaussian 16 Revision C.01*. Gaussian Inc, Wallingford, Connecticut, 2016.
- [17] S. Release, 1: Maestro, Schrodinger, LLC, New York, 2019.
- [18] BIOVIA Discovery Studio D. SYSTÈMES BIOVIA Corporate Europe, BIOVIA 334 Cambridge Science Park Cambridge, 2016. <http://accelrys.com/products/collaborativescience/biovia-discovery-studio>.
- [19] K. Gören, M. Bağlan, İ. Çakmak, *Theoretical investigation of  $^1H$  and  $^{13}C$  NMR spectra of diethanol amine dithiocarbamate RAFT agent*, *Journal of the Institute of Science and Technology* 12 (3) (2022) 1677–1689.
- [20] K. Gören, Ü. Yıldiko, *Aldose reductase evaluation against diabetic complications using ADME and molecular docking studies and DFT calculations of spiroindoline derivative molecule*, *Süleyman Demirel University Journal of Natural and Applied Sciences* 28 (2) (2024) 281–292.
- [21] R. Renjith, Y. S. Mary, C. Y. Panicker, H. T. Varghese, M. Pakosińska-Parys, C. Van Alsenoy, T. Manojkumar, *Spectroscopic (FT-IR, FT-Raman), first order hyperpolarizability, NBO analysis, HOMO and LUMO analysis of 1, 7, 8, 9-tetrachloro-10, 10-dimethoxy-4-[3-(4-phenylpiperazin-1-yl) propyl]-4-azatricyclo [5.2. 1.02, 6] dec-8-ene-3, 5-dione by density functional methods*, *Spectrochimica Acta Part A: Molecular and Biomolecular Spectroscopy* 124 (2014) 500–513.
- [22] K. Gören, M. Bağlan, Ü. Yıldiko, *Melanoma cancer evaluation with ADME and molecular docking analysis, DFT calculations of (E)-methyl 3-(1-(4-methoxybenzyl)-2,3-dioxindolin-5-yl)-acrylate molecule*, *Journal of the Institute of Science and Technology* 14 (3) (2024) 1186–1199.
- [23] K. Gören, M. Bağlan, Ü. Yıldiko, V. Tahiroğlu, *Molecular docking and DFT analysis of thiazolidinone-bis Schiff base for anti-cancer and anti-urease activity*, *Journal of the Institute of Science and Technology* 14 (2) (2024) 822–834.

- [24] M. Arivazhagan, V. Subhasini, R. Kavitha, R. Senthilkumar, *The spectroscopic (FT-IR, FT-Raman), MESP, first order hyperpolarizability, NBO analysis, HOMO and LUMO analysis of 1, 5-dimethyl naphthalene by density functional method*, Spectrochimica Acta Part A: Molecular and Biomolecular Spectroscopy 131 (2014) 636–646.
- [25] M. Suhasini, E. Sailatha, S. Gunasekaran, G. Ramkumaar, *Vibrational and electronic investigations, thermodynamic parameters, HOMO and LUMO analysis on Lornoxicam by density functional theory*, Journal of Molecular Structure 1100 (2015) 116–128.
- [26] M. Bağlan, K. Gören, Ü. Yıldıkıo, *HOMO–LUMO, NBO, NLO, MEP analysis and molecular docking using DFT calculations in DFPA molecule*, International Journal of Chemistry and Technology 7 (1) (2023) 38–47.
- [27] P. Demir, F. Akman, *Molecular structure, spectroscopic characterization, HOMO and LUMO analysis of PU and PCL grafted onto PEMA-co-PHEMA with DFT quantum chemical calculations*, Journal of Molecular Structure 1134 (2017) 404–415.
- [28] M. Bağlan, Ü. Yıldıkıo, K. Gören, *Computational Investigation of 5.5'',7''-trihydroxy-3,7-dimethoxy-4'-4'''-O-biflavone from Flavonoids Using DFT Calculations and Molecular Docking*, Adiyaman University Journal of Science 12 (2) (2022) 283–298.
- [29] M. Bağlan, K. Gören, Ü. Yıldıkıo, *DFT Computations and Molecular Docking Studies of 3-(6-(3-aminophenyl)thiazolo[1,2,4-triazol-2-yl]-2H-chromen-2-one (ATTC) Molecule*, Hittite Journal of Science and Engineering 10 (1) (2023) 11–19.
- [30] M. Arivazhagan, V. Subhasini, R. Kavitha, R. Senthilkumar, *The spectroscopic (FT-IR, FT-Raman), MESP, first order hyperpolarizability, NBO analysis, HOMO and LUMO analysis of 1,5-dimethyl naphthalene by density functional method*, Spectrochimica Acta Part A: Molecular and Biomolecular Spectroscopy 131 (2014) 636–646.
- [31] M. Bağlan, Ü. Yıldıkıo, K. Gören, *Dft Calculations And Molecular Docking Study In 6-(2-Pyrrolidinone-5-yl)-Epicatechin Molecule From Flavonoids*, Eskişehir Technical University Journal of Science and Technology B-Theoretical Sciences 11 (1) (2023) 43–55.
- [32] A. Mahmood, S. U. D. Khan, U. A. Rana, M. R. S. A. Janjua, M. H. Tahir, M. F. Nazar, Y. Song, *Effect of thiophene rings on UV/visible spectra and nonlinear optical (NLO) properties of triphenylamine based dyes: A quantum chemical perspective*, Journal of Physical Organic Chemistry 28 (6) (2015) 418–422.
- [33] E. Çimen, V. Tahiroğlu, *3-[1-(5-Amino-[1,3,4]tiadiazol-2-il)-2-(1H-imidazol-4-il)-etilimino]-2,3-dihidro-indol-2-on Theoretical Study of the Molecule*, Turkish Journal of Nature and Science 13 (2) (2024) 6–13.
- [34] K. Gören, E. Çimen, V. Tahiroğlu, Ü. Yildıkıo, *Molecular Docking and Theoretical Analysis of the (E)-5-((Z)-4-methylbenzylidene)-2-((E)-4-methylbenzylidene)hydrazineylidene)-3-phenylthiazolidin-4-one Molecule*, Bitlis Eren University Journal of Science 13 (3) (2024) 659–672.
- [35] M. Govindarajan, M. Karabacak, *Spectroscopic properties, NLO, HOMO–LUMO and NBO analysis of 2,5-Lutidine*, Spectrochimica Acta Part A: Molecular and Biomolecular Spectroscopy 96 (2012) 421–435.
- [36] N. Lohit, A. K. Singh, A. Kumar, H. Singh, J. P. Yadav, K. Singh, P. Kumar, *Description and in silico ADME studies of US-FDA approved drugs or drugs under clinical trial which violate the Lipinski's rule of 5*, Letters in Drug Design Discovery 21 (8) (2024) 1334–1358.
- [37] M. P. Gleeson, A. Hersey, S. Hannongbua, *In-silico ADME models: A general assessment of their utility in drug discovery applications*, Current Topics in Medicinal Chemistry 11 (4) (2011) 358–381.
- [38] S. Yenigun, Y. Basar, Y. Ipek, L. Behcet, I. Demirtas, T. Özen, *Comprehensive evaluation of Ixoroside:*

*An iridoid glycoside from Nepeta aristata and N. baytopii, assessing antioxidant, antimicrobial, enzyme inhibitory, DNA protective properties, with computational and pharmacokinetic analyses*, Journal of Biologically Active Products from Nature 14 (3) (2024) 286–315.

- [39] R. Riaz, S. Parveen, M. Rashid, N. Shafiq, *Combined experimental and theoretical insights: Spectroscopic and molecular investigation of polyphenols from fagonia indica via DFT, UV-vis, and FT-IR approaches*, ACS Omega 9 (1) (2023) 730–740.
- [40] A. A. Tanrıverdi, K. Altun, Ü. Yıldırım, İ. Çakmak, *Structural and spectral properties of 4-(4-(1-(4-Hydroxyphenyl)-1-phenylethyl)phenoxy)phthalonitrile: Analysis by TD-DFT method, ADME analysis and docking studies*, International Journal of Chemistry and Technology 5 (2) (2021) 147–155.



## Assessing Drainage Performance of Turfgrass Rootzone in Sports Fields

Erdal Kesgin<sup>1</sup> , Kadir Gezici<sup>2</sup> , Remziye İlayda Tan<sup>3</sup> , Hayrullah Ağaçcıoğlu<sup>4</sup> , Mustafa Karaağaçlı<sup>5</sup>   
Mehmet Turgut Sağlam<sup>6</sup> 

<sup>1</sup>Department of Civil Engineering, Faculty of Civil Engineering, Istanbul Technical University, Istanbul, Türkiye

<sup>2</sup>Department of Civil Engineering, Faculty of Engineering, Atatürk University, Erzurum, Türkiye

<sup>3</sup>Department of Civil Engineering, Faculty of Engineering, Fatih Sultan Mehmet Vakıf University, Istanbul, Türkiye

<sup>4</sup>Department of Civil Engineering, Faculty of Civil Engineering, Yıldız Technical University, Istanbul, Türkiye

<sup>5,6</sup>Department of Soil Sciences and Plant Nutrition, Faculty of Agriculture, Namık Kemal University, Tekirdağ, Türkiye

### Article Info

Received: 08 Aug 2024

Accepted: 18 Oct 2024

Published: 31 Dec 2024

Research Article

**Abstract** – Sports fields are used by many national and international organizations worldwide. For this reason, carefully studying the hydraulic and mechanical properties of sports field surfaces is a major engineering concern. This study aimed to increase sports turf's resilience and determine the mixing ratios and fertilizer doses in the rootzone in order to enable effective water drainage. In the field test, the mixture of 3 different soils (100% sand; 10% mixture + 90% sand; 20% mixture + 80% sand) was used for the mix of 70% ryegrass (*Lolium perenne* L.) and 30% bluegrass (*Poa pratensis* L.) in baskets with a size of 1.3 x 0.5 x 0.20 m. Moreover, the turfgrasses were grown through the application of two different doses (2.5 ml (A) and 3.0 ml (B)) of liquid humic acid named Run/Black Jak in addition to basic fertilization of 18-22-0 (slow-release fertilizer) + Nu Film spreader-sticker + 26-05-11 (slow-release fertilizer) + 9-9-9 (slow-release fertilizer containing +9% Fe). It was observed that 2 cm layer was formed under the turfgrass in rootzones with 80% sand + 20% silt+clay mixture by slowing water drainage and negatively affecting infiltration, making it unsuitable for sports fields. Penetration, infiltration, and vane shear tests were performed, and it was determined that the best rootzone in terms of hydraulic and mechanical surface properties was the rootzone treatment formed with 10% silt-clay-organic mixture + 90% sand mixture.

**Keywords** – Sports field, rootzone, turfgrass, fertilizer, drainage

## 1. Introduction

Football is one of the sports branches that interests people of all ages, which is very important in health, economy, and prestige. Contact of the turf with air causes them to be significantly affected by environmental conditions such as precipitation, temperature, and humidity [1]. The surfaces of the pitches must be sufficiently smooth and durable to maintain the enjoyment of the game, prevent injuries to players, and maintain the quality of the game at its highest level. Moreover, the fields meet in the design phase the conditions such as homogeneity and vividness of turfgrass, in addition to technical conditions for the bouncing and rolling the ball [2]. Therefore, lack of clear arrangements in the design of field surfaces, abrasion of turfgrass due to unsuccessful design and building processes, surface imbalance, and drainage problems are frequently encountered.

<sup>1</sup>kesgine@itu.edu.tr; <sup>2</sup>kadirgezici@atauni.edu.tr (Corresponding Author); <sup>3</sup>ritankesgin@fsm.edu.tr; <sup>4</sup>agacci@yildiz.edu.tr; <sup>5</sup>mkaaraagaccli@yahoo.com; <sup>6</sup>turgutsaglam@yahoo.com

There are various layered sections developed for sports fields, such as pipe drains, suspended water table drainage, sand grooving, and sand slit drainage [3]. Despite different designs, these systems generally consist of gravel, sand, rootzone (sand + silt-clay-organic substance), and turfgrass from bottom to top (Figure 1). The evaluation of the turfgrass species and rootzone mixture to be employed, as well as the precipitation characteristics of the relevant region, are essential factors in preventing accumulations on field surfaces and creating continuous playgrounds [4]. In the case of short-term severe precipitation, draining water amount and turfgrass abrasion increase, and surface resistance decreases. On behalf of to prevent this situation, it is aimed to prevent the formation of accumulation on the field surfaces and to protect the mechanical properties of the grass and rootzone by developing sand channeling and sand slit drainage systems. In addition, the use of fast-growing turfgrass resistant to stepping by means of high sand content should be considered in the design phase for the regions characterized by severe precipitation.

Turfgrass covers the soil surface, grows in a thick manner, forms a dense pattern with intense rooting, has a homogeneous appearance, and requires low nutrition and water by being kept short. It is the name given to green field surfaces that do not hinder the movement on them [5]. The turfgrass, which is in direct contact with factors such as precipitation and temperature due to its positioning on top of the field, is critical in meeting the game's requirements and enabling the exhibition of sportspersons' skills at their maximum level. It is necessary to perform optimal turfgrass selection by considering parameters such as climatic conditions, intensity and duration of rainfall in the area where the field will be built, and frequency of field usage [6]. High temperatures slow turfgrass growth and cause downsizing, wear, and curling of leaf blades [7]. Moreover, darkening and a reduction in the development of leaves are observed. It is impossible to eliminate such effects of temperature, but growing species resistant to temperature, keeping the soil moisture at an optimum level, and performing irrigation, especially during midday at high temperatures, are among the preventive measures. Turfgrass obtains the water that it requires to be healthy and to grow via the roots in the rootzone (sand + silt-clay-organic substance) present in the lower layer. Rootzone is the section that is present right under the surface of turfgrass, which generally has a height of 15-30 cm and consists of a mixture of sand (~90%) and a slight silt-clay-organic substance (~10%) [8]. During the preparation of the sand and silt-clay-organic substance mixture, it should be considered to have sufficient water content for both effective and rapid drainage and the wellness of turfgrass. Considering these two parameters, the preparation requirement of 90% sand and 10% silt-clay-organic substance mixture may be stated [9]. The interaction of rootzone and turfgrass and the obtainment of water from the rootzone through root growth for the turfgrass's wellness are essential regarding surface hardness and color, tolerance against abrasion, and slip resistance [10].

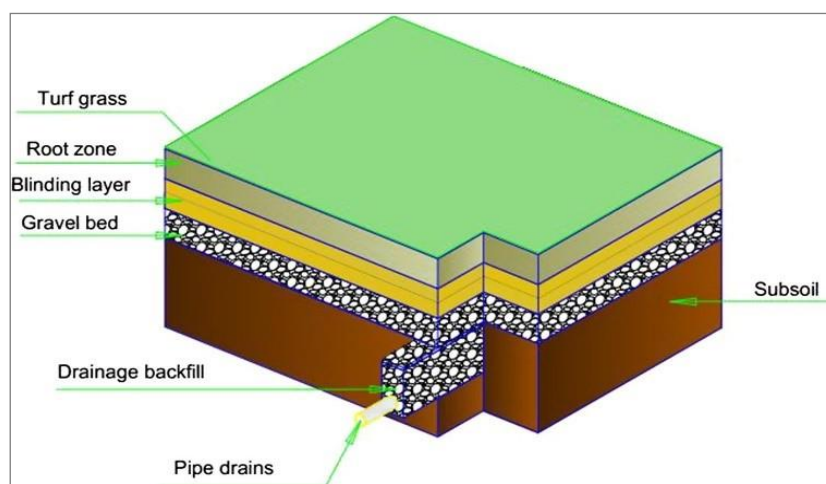


**Figure 1.** General systematic of three-layered drainage systems [6]

Studies are performed in the literature on different turfgrass species used at sports fields and the rootzone, the most significant drainage layer. However, the studies conducted to determine the interaction between these two layers and of optimum design are very limited. In the scope of the study, it was intended to select the turfgrass species to be used at sports fields that attract large audiences and have international economic

importance, and to determine the soil and turfgrass mixture and fertilizer dose that will ensure the optimum conditions. To examine the interaction of turfgrass with rootzone, penetration, infiltration, and Vane shear tests were performed, and the infiltration and hardness conditions of the ground and the resistance of turfgrass were tested. Moreover, it was intended to determine the turfgrass and rootzone mixture and its design, which will decrease the injury risks that arise due to field surface conditions and which will prevent infiltration and drainage problems in terms of maximization of game quality (bouncing and rolling of ball) and exhibition of players' skills (sprint, spin, and shoot).

## 2. Materials and Methods

### 2.1. Turfgrass and Rootzone

The natural turfgrass surfaces of sports fields consist of plants that grow in the soil's rootzone, and they are selected considering their abrasion, resistance, and temperature tolerance [11]. The turfgrass species are frequently used at sports fields and their characteristics are given in Table 1.

**Table 1.** Turfgrass species frequently used at sports fields, and their characteristics [12]

Species	Growth Rate	Fertilizer Requirement	Germination Period (days)
Lolium Perenne	Fast	Medium	4 - 10
Festuca Rubra	Medium	Low	7 - 15
Festuca Arundinacea	Medium	Medium	7-15
Poa Pratensis	Slow	High	12 - 21
Agrostis Tenuis	Medium	High	12 - 18

The height of turfgrass for the quality fields where high-level competitions are performed varies between 18 and 50 mm depending on the maintenance and type of sports [13]. For the growth of natural turfgrass, it is required to adjust to various conditions, such as sunlight, rainwater, and slight wind, in a proper and balanced manner. Negative weather conditions and extreme climates significantly affect the football fields. Therefore, nearly all the companies dealing with this business intend to be able to tackle hard conditions through various methods such as various mixtures of soil types, different fertilizer preferences, and integration of artificial turfgrass and natural turfgrass through new technologies. For this reason, the characteristics of turfgrass to be used on fields, their mixture, and their mutual effects should be analyzed in detail. [14] performed with the use of seven Randall grass (*Festuca arundinacea*) species and one ryegrass (*Lolium perenne* L.) species, emphasized that *Lolium perenne* L. was more successful in terms of growth rate, cold winter conditions, and textural characteristics and that *Festuca arundinacea* species were more effective under high temperature and drought conditions. *Lolium perenne* L. is a plant whose fairly big seeds germinate easily, are erected easily, and which tillers highly [15]. *Lolium perenne* L. (ryegrass) is used at a high level, either in pure form or in mixtures, due to its characteristics of fast growth, plentitude of leaves, and resistance to being stepped on and trampled. But based on the number of seeds, it is required for the seeds of *Lolium perenne* L. not to exceed 20-25% in seed mixture. When it is at a higher rate in the seed mixture, it causes a stressing and suffocating effect on thin turfgrass such as *Festuca*, *Poa*, and *Agrostis* due to its fast germination and growth characteristics [16].

*Poa pratensis* is a plant that forms a dense, fine-textured, dark green, and quality turfgrass cover. Despite its slow germination and growth rate, its rhizomes spread rapidly following erection. Its resistance to cold is very good, but its resistance to drought and shading is weak. It is highly resistant to being stepped on and trampled [17]. *Poa pratensis* is deemed as a species complementing *Lolium perenne* L. especially at football fields [16]. Success in the constitution of turfgrass fields depends on the selection of species conforming to the purpose of constitution and the conditions of growth, on the use of quality seed, and continuous maintenance. A good turfgrass field is assessed in terms of color, fast growth in the initial period and then slow growth, resistance against drought, being stepped on and frequent mowing, longevity, spread on the ground, rooting in the soil and on the soil, strong root development, and resistance against diseases. *Lolium perenne* is frequently

highlighted in the literature for its widespread use, primarily due to its leaf tissue characteristics, resilience to damage from usage, and rapid growth traits [18]. Moreover, several studies have indicated that a mixture of *Lolium perenne* and *Poa pratensis* effectively maintains a high percentage of grass cover [16, 19]. For these reasons, a mixture of 70% perennial ryegrass (*Lolium perenne* L.) and 30% Kentucky bluegrass (*Poa pratensis* L.) was chosen as the turfgrass blend, taking into account the climate data of the study area, Istanbul. These grass species were explicitly selected due to their classification as cool-season plants, making them well-suited for the region's climate.

The rootzone is one of the most significant components due to its functions, such as drainage right under the turfgrass surface, soil resistance, surface hardness, and water supply required by turfgrass [20]. The fields hosting elite-level competitions should have optimum surface hardness, be flexible against impacts, and resist tears. In addition, the formation of water accumulation on the field's surface should be prevented with good drainage [21, 22]. The most significant point in meeting these is the selection of rootzone [9]. Soils with high clay and silt content cause compaction and poor drainage, and it is required to use a high rate of sand in the rootzone to prevent these two negative states. However, soil with 100% sand content will be unable to meet the water required to ensure turfgrass wellness due to its inability to retain water due to extremely high infiltration rates. The rootzone consists of about 90% sand and 10% silt, clay, and organic substances in order to prevent the accumulation of water on the field surface, increase the infiltration rates, prevent the air and water balance, and ensure the stability of the surface [8, 23]. The rootzone determines the mechanical of the field surface's characteristics, such as the surface's hardness, infiltration state, and shear strength [10]. Surface hardness, apart from the interaction of sportspersons and field surface, is critical regarding game quality and sportspersons' health as it closely concerns game characteristics, such as bouncing and rolling the ball.

Quartz sand (0.4-0.7 mm), commonly used in the drainage of football fields, was selected for the experiments. Sieve analysis tests were conducted to determine the characteristics of the material, including its particle size distribution. Additionally, separate tests were performed to assess the sand's bulk density, porosity, field capacity, and water content, summarized in Table 2.

**Table 2.** Characteristic properties of quartz sand used in the experiments

Characteristic feature	Value	Characteristic feature	Value
D <sub>10</sub> (mm)	0.28	Coefficient of Curvature (C <sub>c</sub> )	1.38
D <sub>30</sub> (mm)	0.43	Water content (%)	0.02
D <sub>50</sub> (mm)	0.48	Bulk density (g/cm <sup>3</sup> )	2.65
D <sub>60</sub> (mm)	0.50	Porosity	0.45
Coefficient of Uniformity (C <sub>u</sub> )	1.79	Field capacity (%)	27.95

Clegg hammer test and penetrometers are frequently used in the evaluation of the penetration resistance and hardness of the field. [24], by the use of penetration equipment, found high penetration resistance of the sand-based rootzone compared to different systems such as amended topsoil, undrained section, pipe underdrain, and slit drainage. [25], in his study, he examined the frequency of injuries due to ground hardness, found by the readings with a penetrometer that depths of 3.5 cm and 6 cm were the limit values for hard and soft ground, respectively. [26] emphasized that applying the natural turfgrass surface slip resistance is required for sportspersons wearing crampons, but that high resistance may cause injuries. Both mechanical and biomechanical tests indicated that the sand-based sports fields' grounds have higher dynamic rigidity and slip resistance than clay-based grounds [27]. Materials such as silt and clay cause lower slip resistance and higher plastic deformation due to their high-water retention capacities compared to sand-based grounds [11]. Slip resistance and lower water retention capacities of sand-based grounds have caused their usage at high rates (90%) in the rootzone of sports fields. Some technical properties of the mixtures used in the study are given in Table 3.

**Table 3.** Some technical properties of the experimental materials

Material	pH	Organic content (%)	Silt-Clay (%)	Sand (%)	Class
% 100 sand	7.87	0	0	100	Sandy
%90 sand+%10 silt-clay	7.51	0.21	10	90	Sandy loam
%80 sand+%20 silt-clay	2.43	0.36	20	80	Sandy loam

## 2.2. FIFA Quality Parameters

FIFA (Fédération Internationale de Football Association) has created the FIFA Quality Programme for Football Turf with the goal of creating durable, long-lasting football fields that do not increase the risk of injury to players on both natural and artificial fields. There are three main categories defining the general performance of a surface suitable for football games here are three main categories defining the general performance of a surface suitable for football games. (i) Ground's abrasion resistance and wear (resistance), (ii) Ground's reaction to the game being played on it (ball-surface interaction), (iii) Relationship between the ground and the football player (player-surface interaction).

For a football field to get approval following the determination of its conformity to the above three categories, it is primarily subjected to laboratory tests. The second stage consists of field tests, and the fields successfully passing these two stages get usage approval. FIFA follows the diagram below to obtain usage approval for turfgrass fields to be designed (Figure 2). The fields passing the required standard tests are defined by the FIFA quality (1 star) and FIFA high quality (2 star) marks.

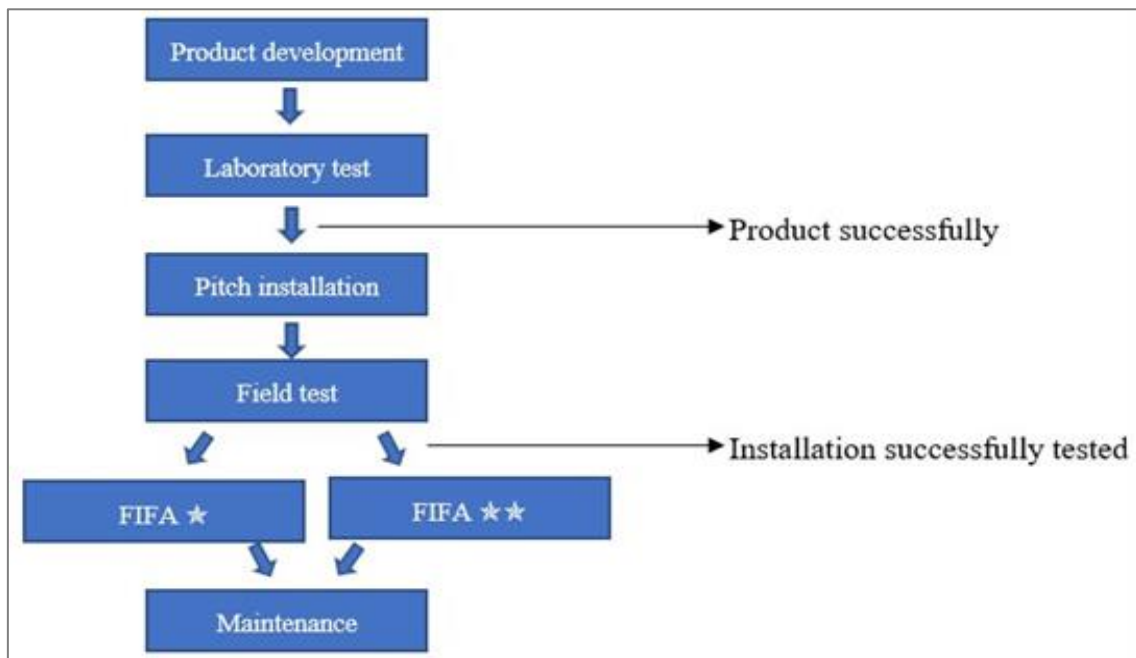


**Figure 2.** The certification process for football turf pitches [28]

All the football turfgrass fields that desire to host international games are obliged to conform to FIFA's official rules. The fields are classified as 2 starred and 1 starred, respectively, depending on the usage requirements of professionals and the public. The characteristics of materials to be used in the field are extensively tested under laboratory conditions, and after succeeding in the tests, the field is built, and field tests are performed. These tests reflect the technical requirements (vertical deformation, spin resistance, bouncing of the ball, etc.) and material characteristics. Football fields receive the status of conforming to FIFA criteria following successful laboratory and field tests, and they provide long-term usage facilities due to regular resistance [28]. Table 4 indicates some test methods, field characteristics, and suitable value ranges regarding the quality class determined by FIFA for football fields.

**Table 4.** FIFA test method and requirements [28]

Characteristics	Test Method	Requirements	
		FIFA PRO Quality (★★)	FIFA Quality (★)
Vertical ball bounce	FIFA 01	60cm-85cm	60cm-100cm
Shock absorption	FIFA04A	60%-70%	55%-70%
Vertical deformation	FIFA05A	4mm-10mm	4mm-11mm
Spin resistance	FIFA 06	30Nm-45Nm	25Nm-50Nm
Game surface's surface regularity	FIFA 12	<10mm	<10mm

### 2.3. Experimental Methodology

Determining a suitable soil and turfgrass mixture and fertilizer dose, which will increase the resistance of turfgrass and enable fast and effective drainage in the rootzone, constitutes the basis of the study. For that reason, initially, sampling was made from the systems formed using different root layer mixtures and fertilizers, and the development and length of roots were examined. Next, penetration and infiltration tests were performed on the layers. Finally, Vane shear tests were performed on the samples, the slip resistance of turfgrasses was calculated, and their resistance characteristics were compared. For the performance of rootzone tests, baskets with a length of 1.3 m, a width of 0.5 m, and a depth of 0.2 m were used. Each mixture was manually mixed until full homogeneity was achieved. After mixing, the mixtures were evenly placed into experimental baskets through leveling and compaction. After placing the rootzones along with the turfgrass, they were regularly maintained daily and fertilized at specific intervals. Six baskets were formed using three rootzones and two fertilization doses (Figure 3). Three different mixtures, 100% sand, 90% sand + 10% silt-clay-organic mixture, and 80% sand + 20% silt-clay-organic mixture were formed for the rootzones. As for fertilizer application, basic fertilization of 18-22-0 (slow-release fertilizer) + 26-05-11 (slow-release fertilizer) + 9-9-9 (slow-release fertilizer containing +9% Fe) was applied to all the baskets, and the turfgrasses were grown through the application of two different doses (2.5 ml (A) and 3.0 ml (B)) of liquid humic acid named Run/Black Jak. In agricultural activities, in order to be able to avoid problems such as low fertilizer retention, high porosity, and excessive irrigation, materials that will be able to absorb large amounts of water and which have the ability to release nutrients for a long period have been developed [29]. The SRF (slow-release fertilizer) used within the scope of the study prevents the nitrification process, thus minimizing the nitrogen loss and increasing the lifetime and success.



**Figure 3.** Basket with a size of 1.3m x 0.5m x 0.2m in which rootzones were placed

After about 30 days, it was considered that the turfgrass had enrooted sufficiently, and the tests were performed on the rootzones. This study used *Lolium perenne* and *Poa pratensis*, with 60% *Lolium perenne* and 40% *Poa pratensis*. Samples were taken from each rootzone using the tool in Figure 4a for sampling. The fertilizer type and rootzone mixture to be used were agreed upon considering the samples' root lengths and densities, and the infiltration tests performed on the rootzones. Then, penetration tests, determining the ground hardness, were performed on different rootzones. Penetration test equipment is provided in Figure 4b. The test was performed

with the help of a thin needle, and the ground hardness was determined according to the penetration of the needle tip into the ground. The permeability of rootzones regarding drainage is also a significant parameter. Therefore, infiltration tests were performed to determine the unsaturated hydraulic conductivities in the rootzones (Figure 4c).

Moreover, saturated hydraulic conductivity coefficients of rootzone mixtures were determined. With the help of a mini disc infiltrometer, unsaturated hydraulic conductivity values were calculated according to the water content in the rootzones. In total, 30 tests, 5 for each rootzone, were performed. The 5 tests, performed on each of the rootzones, were conducted continuously at the same point and consecutively. It was deemed that the water content of the following test would be higher than the previous test, and all the tests were performed accordingly. Finally, Vane shear tests were performed on turfgrasses left for radication in the baskets prepared for rootzones and subjected to fertilizer doses A and B, and the slip resistances of the turfgrasses were calculated. As observed in Figure 4d, the tests were performed with the Vane shear apparatus, and angles of rupture were determined with the help of the goniometer, which is located on the top of the testing equipment and which indicates the angle of rupture and slip resistance values were calculated according to the angles of rupture.

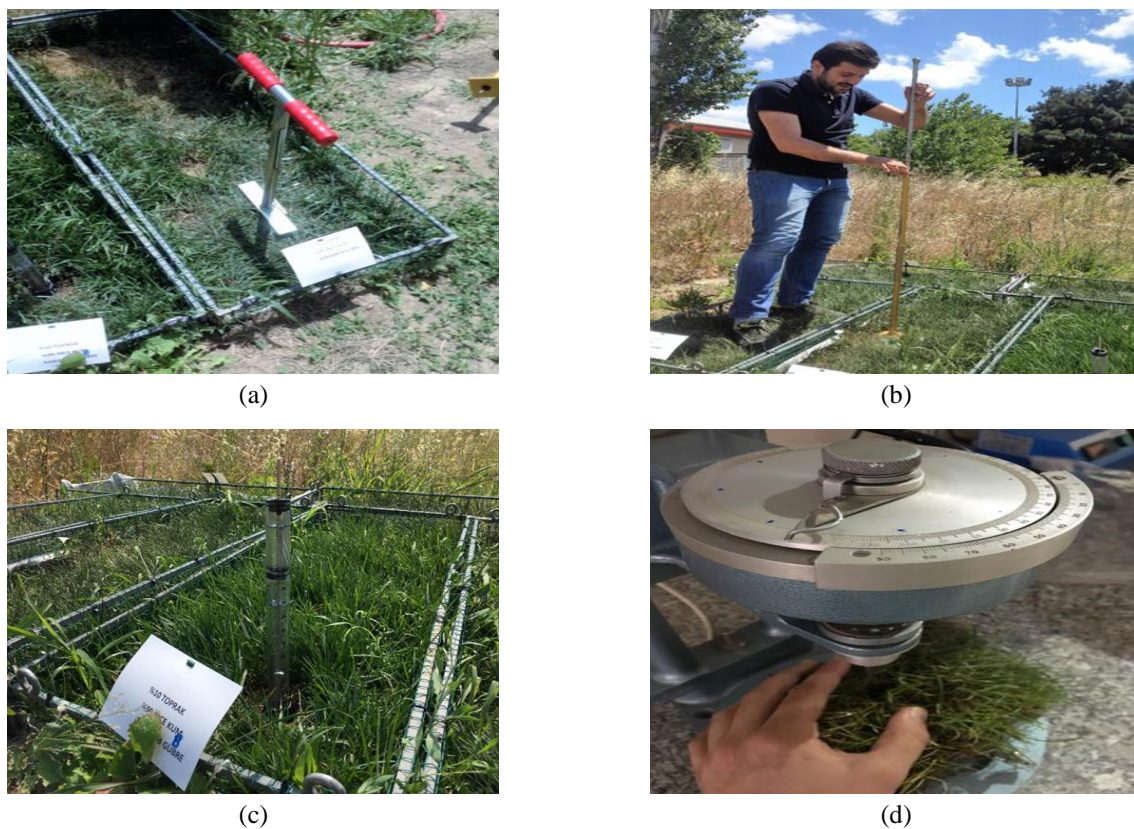


**Figure 4.** Testing apparatuses used within the scope of the study. a) Sampling equipment, b) Penetration test equipment, c) Mini Disc Infiltrrometer, d) Vane shear apparatus

### 3. Results and Discussion

Regarding the turfgrass and rootzone mixtures used at sports fields, the fertilizer type and rootzone mixture to be used were agreed upon considering the samples' root lengths and densities and the infiltration tests performed on the rootzones. Moreover, by the penetration tests and Vane shear tests, the fields' hardness statuses and resistances were compared, and an extensive evaluation of turfgrass and rootzone mixtures was performed. Figure 5a and Figure 5b indicate the samples taken from rootzones formed with 100% sand content and to which fertilizer doses A and B were applied. When these rootzones were examined, it was observed that high turfgrass rooting was not present and that thin roots of 2-3 cm in length were growing. Even if just a bit, more rooting was observed in the 100% sand-based rootzone on which the fertilizer dose B was applied.

Consequently, it was observed that rooting was not much in rootzones completely formed of sand and that the turfgrass didn't completely integrate with the underlying rootzone. As this circumstance directly affects turfgrass's surface stability, quality, and lifetime, using such rootzones at sports fields is considered inappropriate. Figures 5c and 5d show the samples from rootzones formed with a 10% clay-silt-organic material mixture and 90% sand content, on which fertilizer doses A and B were applied. When compared with the 100% sand-based rootzone, it was observed that the roots were longer and denser. Moreover, it can be stated that the sample from the rootzone with 10% clay and silt mixture on which fertilizer dose B was applied had more root density than the sample on which fertilizer dose A was applied. Figure 5e and Figure 5f indicate the samples taken from rootzones formed with a 20% clay and silt mixture to which fertilizer doses A and B were applied. When the rootzones with a 20% clay and silt mixture were compared with other samples, it was observed that they had higher root length and density. However, due to the 20% clay and silt mixture, it was observed that about a 2 cm layer had formed under the turfgrass. As this state causes slower drainage of water to lower layers by negatively affecting the infiltration of the rootzone, opting for it at sports fields is improper. The root growth rates obtained for all the tests are given in Table 5.

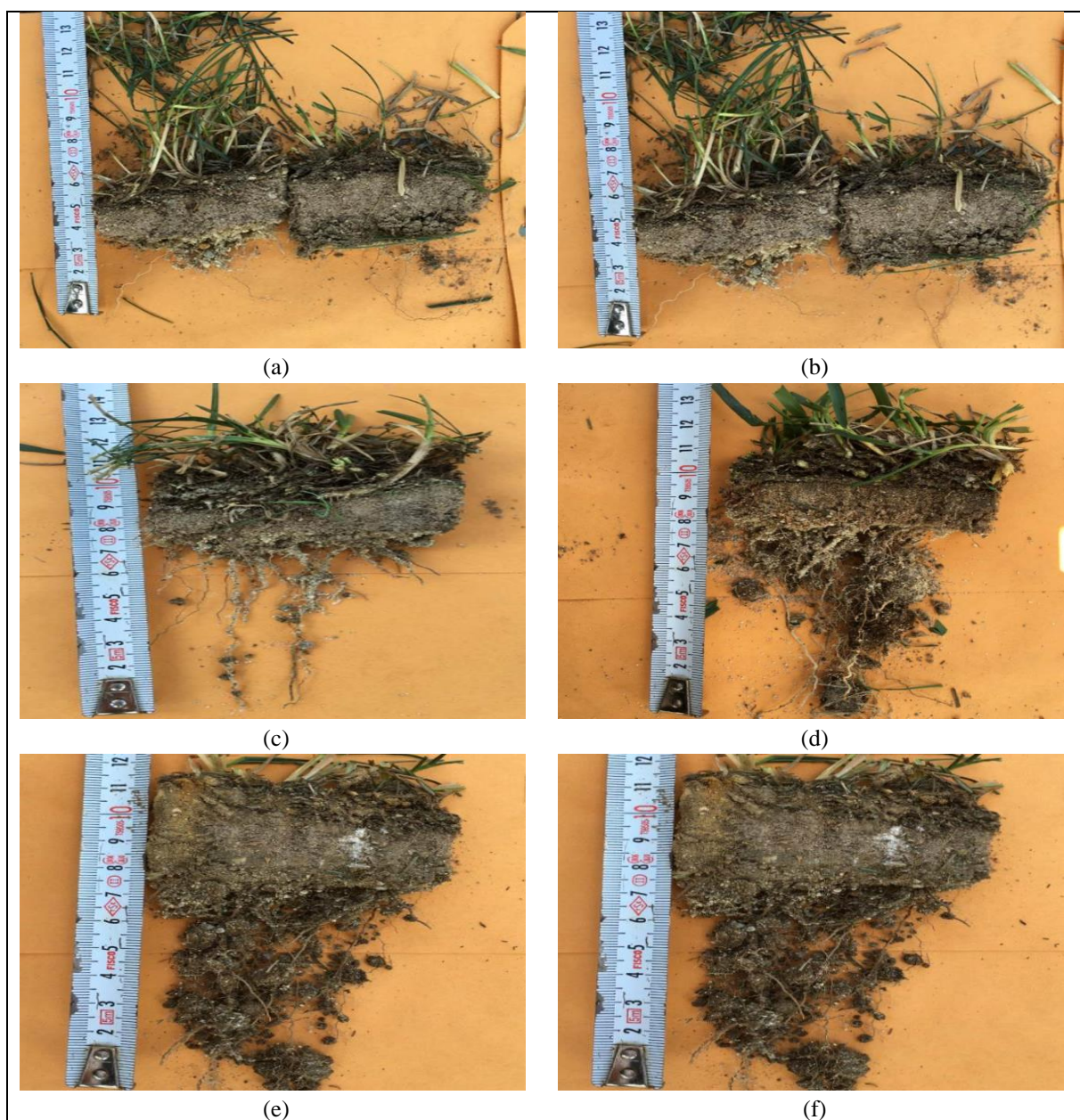


**Figure 5.** Root depths of different rootzone and fertilizer mixtures: a) 100% sand – fertilizer A, b) 100% sand – fertilizer B, c) 10% silt and clay, and 90% sand – fertilizer A, d) 10% silt and clay, and 90% sand – fertilizer B, e) 20% silt and clay, and 80% sand – fertilizer A, f) 20% silt and clay, and 80% sand – fertilizer B.

**Table 5.** Root depths of different rootzones and fertilizer mixtures

Rootzone	Fertilizer Type	Approximate Root Depth (cm)
100% sand	A	3.1
	B	3.3
90% sand+10% silt+clay	A	7.0
	B	7.8
80% sand+20% silt+clay	A	8.3
	B	8.7

[30] has defined quality indicators for natural grass surfaces based on various mechanical and hydraulic characteristics, primarily focusing on ball roll, shock absorption, surface hardness, ground coverage, and root depth. In FIFA's 2022 guidelines [30], a root length of less than 5 cm is unacceptable. In our study, the root depths in the sample with 100% sand content were determined to be 3.1 and 3.3 cm, which falls within the "unacceptable" category. Additionally, the mixture containing 90% sand and 10% silt-clay-organic material was classified under FIFA's "satisfactory quality" category (7-8.49 cm). Finally, the soil with 80% sand and 20% silt-clay-organic material meets FIFA's criteria for "good quality" (8.5-9.99 cm). However, considering the potential drainage and infiltration issues posed by a 2 cm layer formed by the 20% silt-clay-organic material, the most suitable choice would be the soil containing 90% sand and 10% silt-clay-organic material.

Penetration tests, which would determine the ground hardness, were performed on different rootzones. With the test performed with the help of a thin needle, the ground hardness was determined according to the penetration of the needle tip into the ground (Figure 4b). At sports fields, it is required for the penetration needle to penetrate the ground in the range of 5-7 mm. The results of penetration tests are given in Figure 6 as fertilizer A and B at different rootzones. Random measurements were taken from frames representing the top view of the baskets (1.5m x 0.5m), and contour graphs were drawn. Measurements were taken at many points regarding representing real values on the basket. The measurements taken from different points of the baskets were interpolated using the Kriging method through the Surfer program. When the results of penetration tests were compared, it was observed that the values were generally ranging between 5 mm and 8 mm. It was observed that the ground was softer at some points in the rootzones with a 20% clay and silt mixture and that the values generally ranged between 7 mm and 8 mm. [31] conducted field experiments to assess surface characteristics over time and space by evaluating various parameters such as surface hardness, soil moisture content, ground surface grass cover percentage, and normalized difference vegetation index (NDVI). They reported a negative correlation between soil moisture and surface hardness, observing higher soil moisture in areas with softer surfaces.

Additionally, [32] highlighted that root layers with high clay, silt, and organic matter exhibit greater water retention capacity. This study observed the softest surface hardness in samples with the highest silt, clay, and organic matter content (20%), which can be attributed to their water retention capacity and soil moisture levels. When the hardness of all the rootzone samples was examined, it was considered that they didn't constitute a negative circumstance in terms of sports organizations. Ground softening, along with the increase in the percentage of silt and clay mixture, needs to be considered in the design of fields, especially in regions with long-term and severe precipitation.

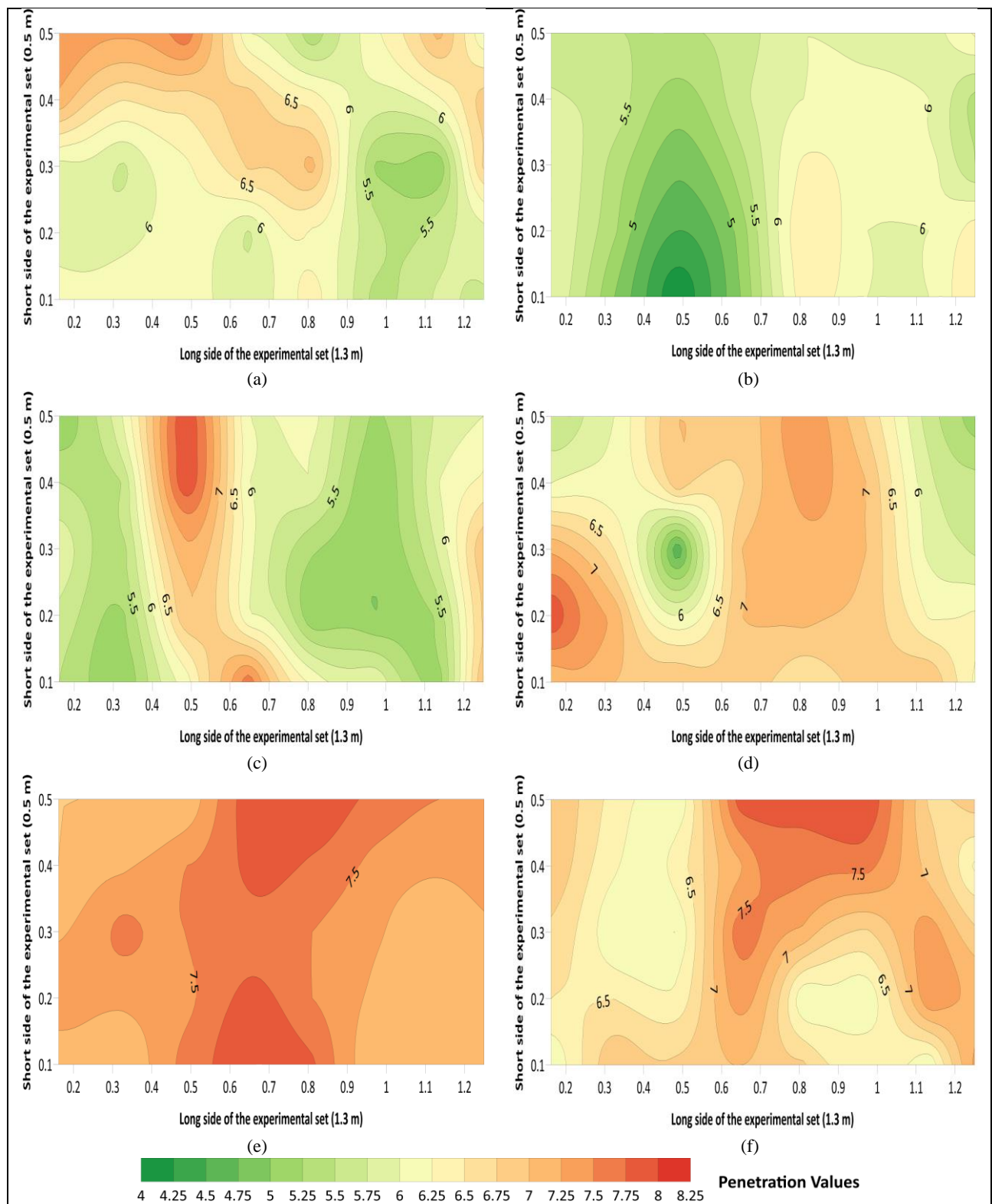


**Figure 6.** Display of results of penetration tests with contour graphs: a) 100% sand – fertilizer A, b) 100% sand – fertilizer B, c) 10% silt and clay, and 90% sand–fertilizer A, d) 10% silt and clay, and 90% sand – fertilizer B, e) 20% silt and clay, and 80% sand – fertilizer A, f) 20% silt and clay, and 80% sand–fertilizer B

The saturated hydraulic conductivity of rootzones regarding drainage is also a significant parameter measured in the study. The infiltration tests for evaluating the unsaturated hydraulic conductivity were also performed on rootzones. As a result, saturated hydraulic conductivity coefficients of rootzone mixtures are given in Table 6. These values were determined under laboratory conditions in the study of [4].

**Table 6.** Saturated hydraulic conductivities of rootzone mixtures

Rootzone	Saturated hydraulic conductivity (K <sub>s</sub> )
100% Sand	0.0285 cm/s
10% Clay-Silt, 90% Sand	0.0053 cm/s
20% Clay-Silt, 80% Sand	0.0046 cm/s

Moreover, with the help of an infiltrometer, unsaturated hydraulic conductivity values were calculated according to the increasing water content in the rootzones (Table 7). In total, 180 tests, being 30 tests for each rootzone, were performed. The tests performed on each rootzone were conducted continuously at the same point and consecutively. It was deemed that the water content of the following test would be higher than the previous test, and all the tests were performed accordingly. According to the relation between hydraulic conductivity and water content, as the water content of the soil increases, the unsaturated hydraulic conductivity value also increases up to the saturated water content. In the presented experiments, even though the measured unsaturated hydraulic conductivity values increased, and 30 experiments were conducted for each set, they did not go up to the saturated hydraulic conductivity. The results obtained from the tests performed were measured in Table 7 for prepared experimental conditions.

When Table 7 was analyzed, it was observed that the unsaturated hydraulic conductivity coefficients were decreasing as 100% sand, 10% clay and silt mixture and 90% sand, and 20% clay and silt mixture and 80% sand in descending order, as expected. The increase of silt-clay-organic mixture in sand material reduced the hydraulic conductivity value. Moreover, regarding the mixtures having similar water content in the same rootzone, the hydraulic conductivity values of rootzones prepared with fertilizer dose B were measured higher than those of grounds prepared with fertilizer dose A. In brief, it is a fact that unsaturated hydraulic conductivities (Table 7) became much closer to saturated hydraulic conductivity (Table 6) with an increasing number of experiments.

**Table 7.** Unsaturated hydraulic conductivities for 30 experiments in this study

Rootzone	Fertilizer Type	Unsaturated Hydraulic Conductivity (cm/s)	
		Minimum	Maximum
100% sand	A	0.002121	0.008258
	B	0.002369	0.009467
90% sand+10% silt-clay- organic mixture	A	0.003732	0.010131
	B	0,004161	0.014522
80% sand+20% silt-clay-organic mixture	A	0.002563	0.009763
	B	0.003476	0.009974

Finally, Vane shear tests were performed on turfgrasses that had been left for radication in the rootzone baskets and had received fertilizer doses A and B, and the slip resistances of the turfgrasses were calculated. As observed in Figure 4d, the tests were performed with the Vane shear apparatus, and angles of rupture were determined with the help of the goniometer, which is located on the top of the testing equipment and indicates the angle of rupture. Slip resistance values were calculated according to the angles of rupture. Slip resistance, being important in abrasion damage, especially at rootzones with high sand content, can cause field surface deformations and player injuries [33]. For the sake of ensuring optimum conditions at turfgrass sports fields, [34] stated that it is required for the slip resistance to change between 10 and 20 kPa. As a result of the tests performed, the slip resistance (cu) was determined as an average of 14.25 kPa for fertilizer dose A and 18.22 kPa for fertilizer dose B (Table 8). Both mechanical and bio-mechanical tests indicated that the sand-based sports fields' grounds have higher dynamic rigidity and slip resistance than clay-based grounds [27]. Materials such as silt and clay cause lower slip resistance and higher plastic deformation due to their high-water retention capacities compared to sand-based grounds [11]. Slip resistance and lower water retention capacities of sand-based grounds have caused their usage at high rates (90%) in the rootzone of sports fields. The values obtained

for both conditions meet the optimum conditions. Still, as the slip resistance calculated for fertilizer dose B (basic fertilization + 3.0ml Run/Black Jak addition) was higher, it was considered that it is required to opt for the rootzone on which this fertilizer dose was applied in terms of resistance.

**Table 8.** Root depths of different rootzones and fertilizer mixtures

Rootzone	Fertilizer Slip Resistance (kPa)	
100% sand	A	16.09
	B	19.53
90% sand+10% silt-clay- organic mixture	A	13.89
	B	18.02
80% sand+20% silt-clay-organic mixture	A	12.77
	B	17.11

This study aimed to improve the durability of sports fields by determining the mix ratios and fertilizer doses in the rootzone to ensure effective water drainage. [19] emphasized that a football field must meet efficient and adequate mechanical properties, such as surface hardness and slip resistance, and hydrological parameters, including infiltration, surface temperature, rootzone soil moisture, and drainage. The numerous and often conflicting parameters and the lack of a standardized specification make achieving optimal conditions for the field surface challenging [22]. Therefore, considering the different requirements of the game, players, and field conditions, it can be stated that the field surface is designed in layers. However, it has been particularly emphasized that the top few centimeters of the surface must consist of sand material to ensure good permeability and effective drainage [6]. In our study, the 2 cm layer formed beneath materials with 20% silt-clay content presents a significant challenge regarding infiltration and drainage conditions. Soils with 100% sand content exhibit high drainage and infiltration capacity and are less prone to compaction. However, they require more frequent irrigation and fertilization to maintain healthy turf growth [35]. Therefore, the mixture of 90% sand and 10% silt-clay-organic matter provides the most optimal conditions for efficient drainage and surface stability while ensuring that grassroots can access the necessary water in the rootzone.

As a result of penetration, infiltration, and vane tests, it was determined that the best rootzone was formed with 10% silt-clay-organic mixture + 90% sand. This finding supported the results of [8, 23, 24]. However, it was observed that the rootzones consisting entirely of sand did not provide sufficient rooting and full integration with the grass. Since this situation has a direct effect on the durability and quality of the surface and the life of the grass, it was considered that it is not suitable for use in sports fields [6]. On the other hand, it was observed that a layer of about 2 cm was formed under the grass in the rootzones with 80% sand + 20% silt-clay-organic mixture. This situation is not suitable for sports fields as it slows down water drainage and negatively affects the infiltration of the rootzone, especially in areas with prolonged and heavy rainfall, this situation can be a significant problem [3].

The importance of the rootzone has been emphasized throughout the study due to its functions such as drainage, soil resistance, surface hardness, and meeting the water requirements of the grass. The correct composition of the rootzone, approximately 90% sand and 10% silt, clay, and organic matter, is vital for preventing water accumulation on the surface, increasing infiltration rates, and stabilizing the surface. Slip resistance, essential regarding abrasion damage and player safety, was within the recommended range of 10-20 kPa for both A and B fertilizer doses [36]. The importance of an effective drainage system to ensure the durability of the pitch surface and minimize water-related problems on the pitch is supported by previous literature [36-38]. Previous studies have also emphasized the need for sports pitches to be constructed with a high sand content for satisfactory infiltration rates and surface aeration.

In conclusion, this study provides valuable information on the composition of the rootzone and appropriate fertilizer doses to improve the durability of sports pitches. Using a rootzone composed of 10% silt-clay-organic material and 90% sand is optimal for effective water drainage and turf health. Furthermore, the research emphasizes the importance of an effective drainage system and highlights the necessity of sports pitches with

high sand content for proper infiltration rates and player functionality. Regarding fertilizer dosage, the B fertilizer dose proves to be more effective across all soil mixtures, promoting healthier turfgrass by enabling sufficient water uptake from the rootzone due to the longer root lengths observed. Additionally, with its higher hydraulic conductivity, the B fertilizer dose allows rainfall and irrigation water to drain more quickly and efficiently from the field surface. Both fertilizer doses exhibit optimal conditions in terms of slip resistance values. Therefore, fertilizer dose B should be preferred for developing grass cover, promoting better root establishment, effective drainage, and overall resilience. Overall, the findings of this study provide essential contributions to sports field management and offer valuable guidance to turf professionals, sports field designers, and companies engaged in sports field development.

#### 4. Conclusion

In the design phase of the sports fields, it is crucial to know the turfgrass species to be used and the fertilizer applications, as well as the drainage, surface hardness, and slip resistance characteristics of the rootzone, which is the most significant part of the drainage layer. The selection of proper species and mixtures will make the exhibition of players' skills possible and fulfill the game requirements. FIFA evaluates the resistance of the field surfaces, the ball-surface interaction, and the player-surface interaction before approving FIFA Pro Quality or FIFA Quality certificates. According to [30] criteria, less than 5 cm root length values are classified as unacceptable quality. This study measured root depths in the 100% sand sample at 3.1 and 3.3 cm, confirming its categorization as unacceptable. Additionally, a soil composition of 90% sand and 10% silt-clay-organic matter falls within the satisfactory quality range (7-8.49 cm) defined by FIFA. Lastly, according to FIFA criteria, soil containing 80% sand and 20% silt-clay-organic matter is classified as relatively good quality (8.5-9.99 cm). However, considering that the 2 cm layer formed by the 20% silt-clay-organic matter will create drainage and infiltration challenges, it can be concluded that the optimal choice would be soil comprising 90% sand and 10% silt-clay-organic matter.

In terms of infiltration, it can be stated that the saturated hydraulic conductivity (0.0046 cm/s) of the root layer with 20% clay and silt mixture and 80% sand content may cause drainage problems according to providing the FIFA minimum infiltration condition (0.005 cm/s). Although slip resistance and penetration values are within acceptable standards for football fields, there may be issues with injuries and drainage in places with frequent severe precipitations due to the increased silt-clay concentration in the root layer.

The tests (examination of root samples, penetration, infiltration, and Vane test) performed on different rootzones developed for being used at sports fields, indicated that the best rootzone formed with 10% clay and silt mixture and 90% sand. The fertilizer dose B (18-22-0 (slow-release fertilizer) + Nu Film spreader-sticker + 26-05-11 (slow-release fertilizer) + 9-9-9 (slow-release fertilizer containing +9% Fe) + 3.0ml Run/Black Jak addition) application should be preferred in terms of the development of turfgrass layer, better radication and resistance. As much as being good in terms of drainage, the quality and healthy radication of the turfgrass used at sports fields are also significant parameters. The rootzone formed of 100% sand may be considered the best drainage due to having a better hydraulic conductivity coefficient. However, in the previous studies and this study, it was observed that it is required to have a specific rate of clay and silt organic substance mixture, which will increase the root quality and density of turfgrass in the rootzone. The literature emphasizes the necessity for the top few centimeters of the surface layer to consist of sandy material to ensure good permeability and effective drainage. Considering the tests of rootzone in which 20% clay and silt mixture was used, the formation of about 2 cm layer under the turfgrass surface through the examination of root lengths would negatively affect the infiltration. It would cause decreases in the transmission rate of water to lower layers. Therefore, a mixture of 90% sand and 10% silt-clay-organic matter provides the optimal conditions for effective drainage, surface stability, and the ability of grassroots to access the necessary water from the rootzone. Moreover, it may be stated that relatively high values observed in penetration tests, along with the increase of clay and silt mixture, would cause players' injuries by causing an increase in field surface abrasions. Therefore, considering the drainage, slip resistance, and sand and rootzone interaction, the use of rootzone

with 10% clay and silt organic substance mixture on which fertilizer dose B (basic fertilization + 3.0ml Run/Black Jak addition) was applied may be considered as the most suitable solution.

In future studies, the hydrological and mechanical characteristics of natural and artificial fields, to be obtained as the result of applying similar methods on artificial turfgrass fields that are increasingly being used in recent years, may be compared and evaluated. Moreover, the study's scope may be extended by applying tests such as bouncing and rolling the ball, spin resistance, and impact absorption.

## Author Contributions

The fourth and sixth authors directed the project and supervised this study's findings. The first, second, and third authors devised the main conceptual ideas and developed the theoretical framework. The first, second, and fifth authors performed the experiment and statistical analyses. The first author wrote the manuscript with support from the second and third authors. The fourth and sixth authors reviewed and edited the paper. All authors read and approved the final version of the paper. This paper is derived from the fifth author's master's thesis, supervised by the sixth author. The authors read and approved the final version of the paper.

## Conflicts of Interest

All the authors declare no conflict of interest.

## Ethical Review and Approval

No approval from the Board of Ethics is required.

## Acknowledgment

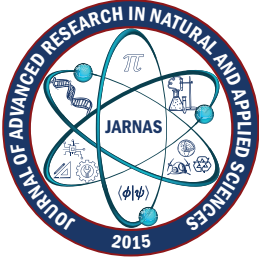
This work was supported by the Turkish Scientific and Technical Research Council (TUBITAK), Grant number: 214M616.

## References

- [1] E. Kesgin, A. Doğan, H. Ağaçcıoğlu, *Experimental and numerical investigation of drainage mechanisms at sports fields under simulated rainfall*, Measurement (125) (2018) 360–370.
- [2] I. T. James, M. J. Hann, R. J. Godwin, *Design and operational considerations for the use of mole ploughing in the drainage of sports pitches*, Biosystems Engineering 97 (1) (2007) 99–107.
- [3] K. Gezici, E. Kesgin, H. Ağaçcıoğlu, *Hydrological assessment of experimental behaviors for different drainage methods in sports fields*, Journal of Irrigation and Drainage Engineering 147 (9) (2021) Article Number 04021034 10 pages.
- [4] E. Kesgin, H. Ağaçcıoğlu, A. Doğan, *Experimental and numerical investigation of drainage mechanisms at sports fields under simulated rainfall*, Journal of Hydrology 580 (2020) Article Number 124251 19 pages.
- [5] M. Karaağaçlı, *Investigation of proper mixture of soil and fertilizer at the rootzone of pitch grass of sport fields to provide durability, fast and efficient drainage conditions*, Master's Thesis Namık Kemal University (2019) Tekirdağ.
- [6] Sport England, Natural turf for sport: Design guidance note, English Sports Council, London, 2011.
- [7] X. Liu, B. Huang, *Root physiological factors involved in cool-season grass response to high soil temperature*, Environmental and Experimental Botany 53 (3) (2005) 233–245.

- [8] D. H. Taylor, G. R. Blake, *Sand content of sand-soil-peat mixtures for turfgrass*, Soil Science Society of America Journal 43 (2) (1979) 394–398.
- [9] J.J. Henderson, J. R. Crum, T. F. Wolff, J. N. Rogers, *Athletic field rootzone mixes: what is the best mix for your field*, In Proceedings of the 71st Annual Michigan Turfgrass Conference, Michigan, 2001, pp. 96–99.
- [10] I. T. James, *Advancing natural turf to meet tomorrow's challenges*, Proceedings of the Institution of Mechanical Engineers Part P: Journal of Sports Engineering and Technology 225 (3) 2011 115–129.
- [11] M. C. J. Caple, I.T. James, M. D. Bartlett, *The effect of grass leaf height on the impact behavior of natural turf sports field surfaces*, Sports Technology 4 (1-2) 2011 29–40.
- [12] A. Doğan, H. Ağaçcıoğlu, L. Basayığıt, *Research on techniques that will provide rapid and effective drainage of sports fields under various hydrological and meteorological conditions.*, Report number: 214M616, Ankara, TUBITAK, 2018.
- [13] S. J. Mooney, S. W. Baker, *The effects of grass cutting height and pre-match rolling and watering on football pitch ground cover and playing quality*, Journal of Turfgrass Science (76) (2000) 70–77.
- [14] T. Eraşık, *Investigations on the turf quality of some new tall fescue (Festuca arundinacea) cultivars in Mediterranean ecology*, Master's Thesis Ege University (2014) İzmir.
- [15] W.A. Bentley, *Studies of Raindrops and Raindrop Phenomena*, Monthly Weather Review 32 (10) 1904 450–456.
- [16] E. Açıkgöz, *Yem Bitkileri*, Uludağ Üniversitesi Ziraat Fakültesi Yayınları, Bursa, 1991.
- [17] J. B. Beard, *Turfgrass: Science and culture*, Prentice-Hall, New Jersey, 1972.
- [18] C. Brito, H. Ferreira, L. T. Dinis, H. Trindade, D. Marques, C. M. Correia, J. Moutinho-Pereira, *Different LED light intensity and quality change perennial ryegrass (Lolium perenne L.) physiological and growth responses and water and energy consumption*, Frontiers in Plant Science 14 (2023) Article ID 1160100 13 pages.
- [19] P. Stachowski, *Retention and water needs of natural grass turf of football fields*, Rocznik Ochrona Środowiska, 25 (2023) 256–264.
- [20] K. Gezici, H. Ağaçcıoğlu, E. Kesgin, *Comparison of natural and synthetic grass football fields in terms of drainage designs*, Uludağ University Journal of the Faculty of Engineering 27 (1) 2022 487–502.
- [21] A. J. Turgeon, *Turfgrass management*. 3rd Edition, Prentice-Hall Inc, New Jersey, 1991.
- [22] E. Kesgin, K. Gezici, H. Ağaçcıoğlu, *An overview of sports field drainage: Creation of an experimental study system*, Journal of the Faculty of Engineering and Architecture of Gazi University 38 (4) 2023 2495–2504.
- [23] S. W. Baker, *Soil physical conditions of the rootzone layer and the performance of winter games' pitches*, Soil Use and Management 5 (3) 1989 116–122.
- [24] S. Magni, M. Volterrani, S. Miele, *Soccer pitches performances as affected by construction method, sand type and turfgrass mixture*, Acta Horticultural (661) 2004 281–285.
- [25] J. Orchard, *The AFL penetrometer study: Work in progress*, Journal of Science and Medicine in Sport 4 (2) 2001 220–232.
- [26] M. Caple, I. James, M. Bartlett, *Mechanical behavior of natural turf sports pitches across a season*, Sports Engineering 15 (3) 2012 129–141.
- [27] V. H. Stiles, I. N. Guissasola, I. T. James, S. J. Dixon, *Biomechanical Response to Changes in Natural Turf during Running and Turning*, Journal of Applied Biomechanics 27 (1) 2011 54–63.

- [28] Fédération Internationale de Football Association (FIFA), FIFA quality programme for football turf, handbook of test methods, Switzerland, 2015.
- [29] R. A. Ramli, *Slow release fertilizer hydrogels: a review*, Polymer Chemistry 10 (45) 2019 6073–6090.
- [30] Fédération Internationale de Football Association (FIFA), *FIFA natural pitch rating system (2022)*, [https://digitalhub.fifa.com/m/58aa765dd3e85f26/original/FIFA-natural-pitch-rating-system\\_EN.pdf](https://digitalhub.fifa.com/m/58aa765dd3e85f26/original/FIFA-natural-pitch-rating-system_EN.pdf), Accessed 9 October 2024.
- [31] C. M. Burbrink, C.M. Straw, *Spatiotemporal variability of a stadium football pitch during a professional tournament*, Sports Engineering 26 (8) 2023 1–9.
- [32] O. E. Alabi, *Impact of Natural Turfgrass Sports Field Characteristics and Management Strategies on Field Quality and Playability*, Master's Thesis Agricultural and Mechanical College of Texas University (2023) Texas.
- [33] S. Hejduk, S. W. Baker, C. A. Spring, *Evaluation of the effects of incorporation rate and depth of water-retentive amendment materials in sports turf constructions*, Acta Agriculturae Scandinavica Section B- Soil and Plant Science 62 (1) 2012 155–164.
- [34] S. W. Baker, C. W. Richards, *The effect of compaction energy and initial moisture content on laboratory determinations of soil physical properties of rootzone mixes for soccer pitches*, International Turfgrass Society Research Journal (7) 1993 430–436.
- [35] C. M. Straw, C. O. Samson, G. M. Henry, C. N. Brown, *A review of turfgrass sports field variability and its implications on athlete–surface interactions*, Agronomy Journal 112 (4) 2020 2401–2417.
- [36] C. F. Cereti, F. Rossini, F. Romoli, *Improvement of the drainage capacity in sports turf*, Acta Horticulturae (661) 2003 315–318.
- [37] M. R. Simpson, P. R. Fleming, M.W. Frost, *Briefing: Sustainable drainage for sports pitch developments*, In Proceedings of the Institution of Civil Engineers Municipal Engineer 166 (4) 2013 211–215.
- [38] P.R. Fleming, M. W. Frost, M. R. Simpson, *Drainage Behavior of Sports Pitches- Findings from a Research Study*, Loughborough University, Loughborough, 2016.



# Machine Learning and Medical Data: Predicting ICU Mortality and Re-admission Risks

Ulya Bayram<sup>1</sup> , Runia Roy<sup>2</sup> 

<sup>1</sup>Department of Electrical and Electronics Engineering, Faculty of Engineering, Çanakkale Onsekiz Mart University, Çanakkale, Türkiye

<sup>2</sup>Neural Stem Cell Institute, New York, USA

## Article Info

Received: 15 Aug 2024

Accepted: 12 Dec 2024

Published: 31 Dec 2024

Research Article

**Abstract** – Intensive care units (ICUs) are divisions where critically ill patients are treated by medical experts. The unmet and vital need for automated clinical decision-making mechanisms is critical to maneuvering the large influx of patients. This became more apparent after the COVID-19 pandemic. Existing studies focus on determining the probability of patients dying in the ICUs and prioritizing patients in dire need. Only a few studies have calculated the patient's probability of returning to the ICUs after discharge. These studies reduce the problem into a binary task of predicting mortality or re-admission only. However, this is unrealistic since both outcomes are highly possible for each patient. In this interdisciplinary study, two main contributions are proposed for the automated clinical decision-making state-of-the-art: (1) using the real-life data collected from thousands of ICU patients by healthcare professionals, three possibilities (recovery, mortality, and returning to the intensive care unit within 30 days) are predicted for patients in intensive care instead of just one possibility. (2) A novel feature extraction approach is proposed by the biomedical expert in our team. Four machine learning algorithms are applied to the finalized feature set to understand the difference between the binary and the multi-class classification problems. Obtained results reach 78% success, proving the possibility of developing better clinical decision-making mechanisms for ICUs.

**Keywords** – Clinical decision making, machine learning, intensive care units, mortality prediction, re-admission prediction

## 1. Introduction

It is well recognized that many of the mortality cases in intensive care units (ICUs) were preventable if and only if the deteriorating decline of the patient could have been noticed at the right time [1,2]. However, there are too few healthcare professionals with ICU expertise in the hospitals. Furthermore, since these professionals work for long hours, it becomes difficult to track the progress of every patient 24/7, non-stop. To overcome this challenge and reduce potentially dire consequences, healthcare professionals developed scoring systems specifically for the ICU. These systems involve healthcare professionals' manually noting the patient's condition obtained through measurements of vital signs and laboratory test results under certain categories, where the professional is required to access the

<sup>1</sup>ulya.bayram@comu.edu.tr (Corresponding Author); <sup>2</sup>rroy7@binghamton.edu

state of the patient and assign the correct score for each category, then obtaining a mathematical score by summing the noted scores from all categories, named the Acute Physiology and Chronic Health Evaluation (APACHE) scoring method. Based on 12 physiological parameters and the Glasgow coma score (GSC), the total score is 71. Any patient with scoring greater than 25 is considered to be at a higher risk for dying [3]. In real ICUs, this scoring is used for clinical decision-making - prioritizing care, intervention needs, monitoring trends over time, and resource and staff allocation [4].

Although still used today, methods like manual APACHE scoring have numerous drawbacks. It is difficult for healthcare employees under an intense workload to frequently visit every ICU patient, assign accurate scores, and repeat this process every 24 hrs or as the patients' conditions alter. Moreover, a statistical study found that scoring methods can make incorrect decisions depending on the patient's ethnicity [5]. Another study reports that these manual methods often calculate the patient's risk scores higher than the actual states [6], which means the patients received higher mortality scores, causing a shift of attention and workload from the actual high-risk patients towards less risky ones. This results in more frequent visits to less critical patients, thus wasting precious time that could have been dedicated to another, more risky patient. Such an error in the ICU can cause preventable deaths. This resource allocation and management issue in the ICUs became especially evident in early 2020 during the COVID-19 pandemic.

The in-hospital mortality rates in the United States published by the Centers for Disease Control and Prevention (CDC) [7] shows that in the United States alone, there was an unprecedented increase in in-hospital mortality rates in 2020, 2021, and 2022, while the rates started lowering in 2023 (Figure 1). Studies indicate that these mortality rate increases are not because of the coronavirus alone but are also due to the overcrowded ICUs, the inadequacy of the number of healthcare professionals, and their inability to allocate attention and time to the excessive number of ICU patients [8]. These rates only highlight the urgent need for the real-life use of automated clinical decision-making systems in this technology-driven century.

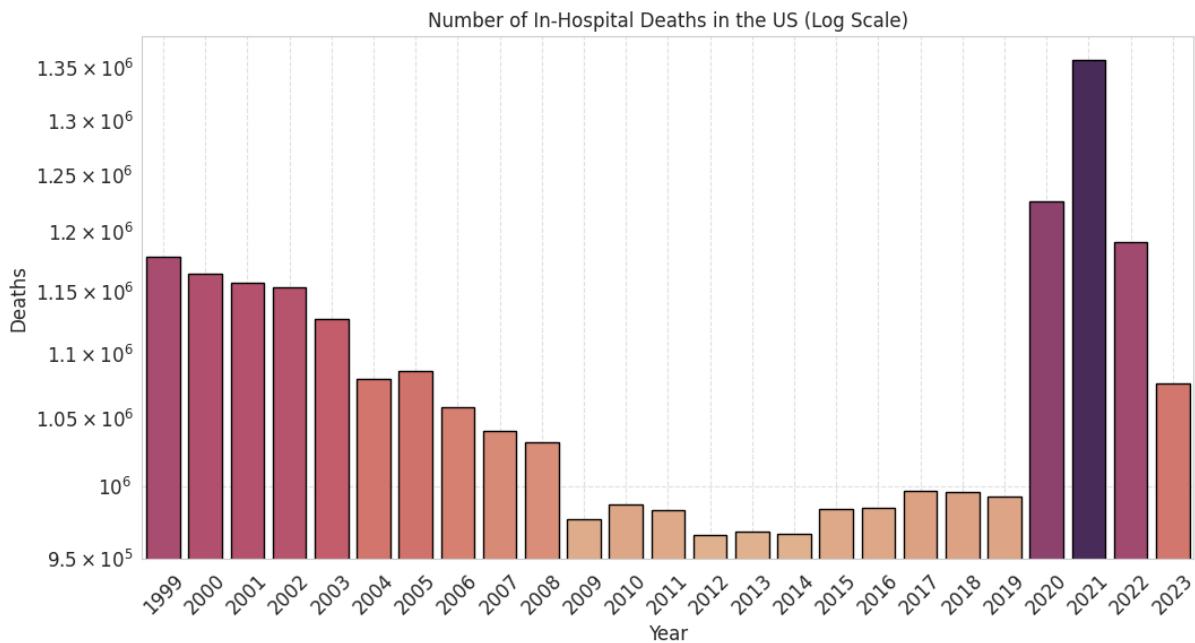


**Figure 1.** Annual hospital mortality rates in the United States of America.

To progress towards developing automated clinical decision-making systems, a team of researchers from interdisciplinary fields conducted various studies focusing on predicting specific pressing problems that can cause critical patients suffering from diseases such as circulatory failure, sepsis (blood poisoning),

or kidney failure [9–12] in ICUs to lose their lives. Meanwhile, some studies showed that even small errors in dosages can be fatal for ICU patients [13, 14]. For example, if the circulatory failure is correctly predicted and intervened immediately, many lives can be saved. The machine learning methods these studies used to span from Logistic Regression (LR) to Support Vector Machines (SVM), LightGBM (LGB), and XGBoost (XGB). In addition to these specific predictive studies, researchers also attempted to model the general risk of ICU patients' mortality. For example, a study modeled the probability of patient deaths within 48 hours of ICU admission using a deep learning model called Long Short-Term Memory (LSTM) on doctor's notes [15]. These studies reached up to 80% success rates in predicting mortality in ICU.

Potential dire outcomes in an ICU environment are not restricted by patient mortality. Another critical problem is discharging ICU patients early. When an ICU patient is discharged early, before completing the treatment, or without following their progress a little longer, the condition of the patient can worsen without the care or attention of professionals, which might cause death to the patient. Alternatively, suppose the patient's condition is not as dire but has worsened after discharge. In that case, the patient will need to be re-admitted to the ICU; certain mandatory and expensive measurements will have to be repeated, and the treatments will need to be restarted in addition to handling the patient's worsened condition. This situation causes high financial losses and excessive use of medical resources [16]. To overcome this predicament and prevent follow-up and subsequent re-admissions, a few studies attempted to predict the likelihood of returning to the ICU within 30 days after getting discharged [17–19]. They used machine learning methods including LR, Naive Bayes, Random Forest (RF), SVM, Convolutional Neural Networks (CNN), and LSTMs and reported up to 75% success rates in predicting re-admission risk.

Thanks to the developments in artificial intelligence (AI) technology and the digitization of healthcare data, developing automated clinical decision-making systems is possible. However, existing studies show that there is still much more to achieve before the real-life use of these systems. First, they mainly rely on a binary classification task. Most studies focus on the easier task of mortality prediction, ignoring the re-admission risk. The same is true for the vice versa; re-admission prediction studies do not consider mortality prediction. Yet, a real-life clinical decision-making system for ICUs should be able to predict both risks at the same time. Second, existing studies do not conduct feature engineering, which is essential for obtaining explainable predictive systems. In this study, both issues are addressed.

The proposed study – to develop an improved and standardized clinical decision-making system for use in the ICU – introduces a novel feature extraction approach informed by biomedical expertise. Following a thorough feature engineering process, the study addresses the challenging multi-class classification problem of predicting mortality, re-admission, and survival risks together. Furthermore, the study accounts for data imbalance, which is how these cases are distributed in real life. Also, rather than deep learning techniques, the study used conventional machine learning methods and a few complex methods for several reasons. Considering the real-life application, lightweight methods such as traditional machine learning are preferable to heavy, data-demanding models. Plus, traditional methods perform as well as more complex methods in some scenarios [20, 21]. By focusing on feature engineering and leveraging domain expertise, the study maximizes the utility of conventional methods, proving them highly effective for this application.

In the next sections, the dataset and the selected methods are explained. Then, experiments and the obtained results are demonstrated, and discussions are conducted on the findings. Finally, conclusions are provided.

## 2. Materials and Methods

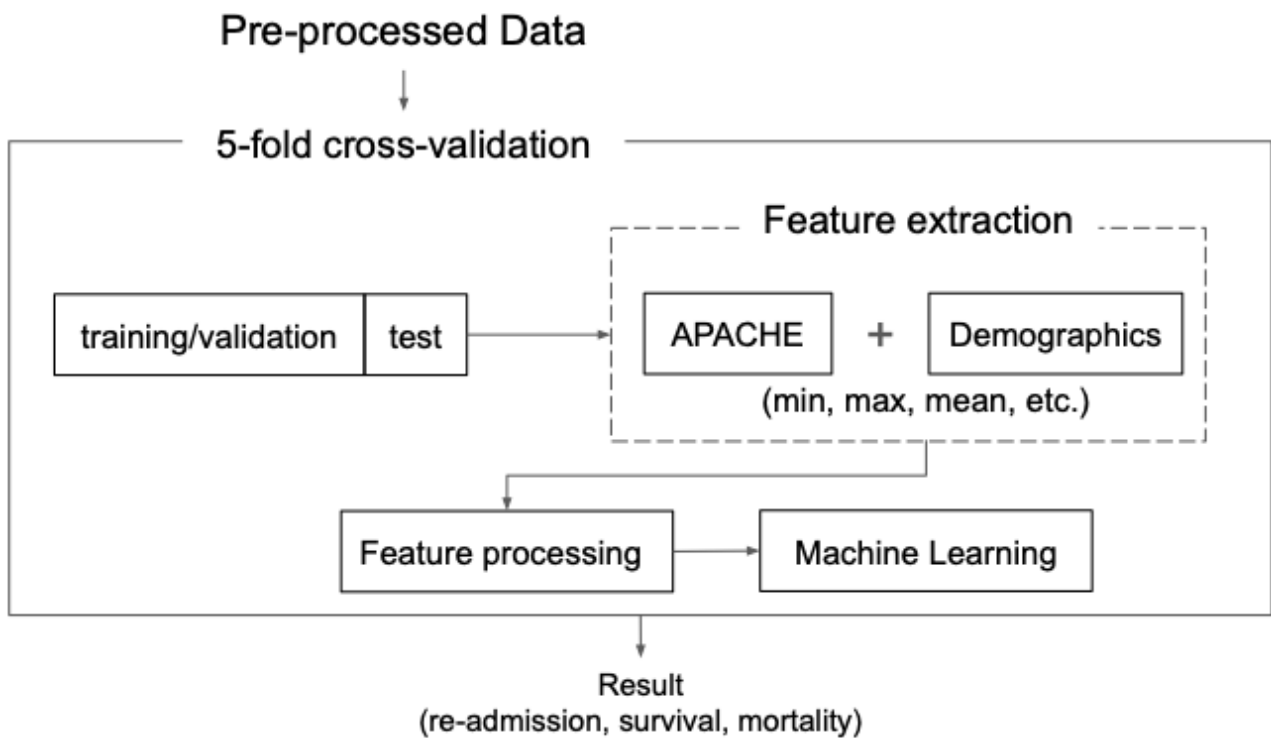


**Figure 2.** Work-flow of the present study.

The main workflow of the current study is present in Figure 2. Details of each step are explained in the following sections.

### 2.1. Data

This study uses the publicly available and popular Medical Information Mart for Intensive Care-III (MIMIC-III) dataset. This dataset contains various types of patient measurements collected from the ICU patients of Beth Israel Deaconess Medical Center in Boston, Massachusetts, between the years of 2001 and 2012 [22–24]. It contains information on each ICU patient, including demographics such as age, gender, and marital status. The entries were de-identified to protect the patients’ identities, and information such as date of admission or date of birth was coded as a dummy number in the dataset.

For this study, patients outside the age range of 18 and 75 are excluded to develop a model for adults. After selecting only the adult patients, the number decreased from 47805 to 34969. This choice is made considering the possibility that older and younger age groups might need different clinical decision-making systems [25, 26]. There were also many erroneous data within the dataset. The most important problem among the whole dataset is the number of missing data. Some patients lack demographic information such as gender, some measurements were never obtained for some patients such as height or weight. Another critical issue is the lack of mortality and discharge dates for some patients altogether. After removing all these errors, the dataset contains 4253 ICU mortality, 2806 ICU re-admissions, and 30057 survivors who were discharged and did not get re-admitted to the ICU within 30 days after the discharge. Then, the complete dataset is divided into training and test sets following the common 80-20% division rate within a 5-fold cross-validation framework. Within each fold, to fine-tune the parameters of the complex machine learning methods, the training set of each fold is split into training and validation sets with the 80-20% division.

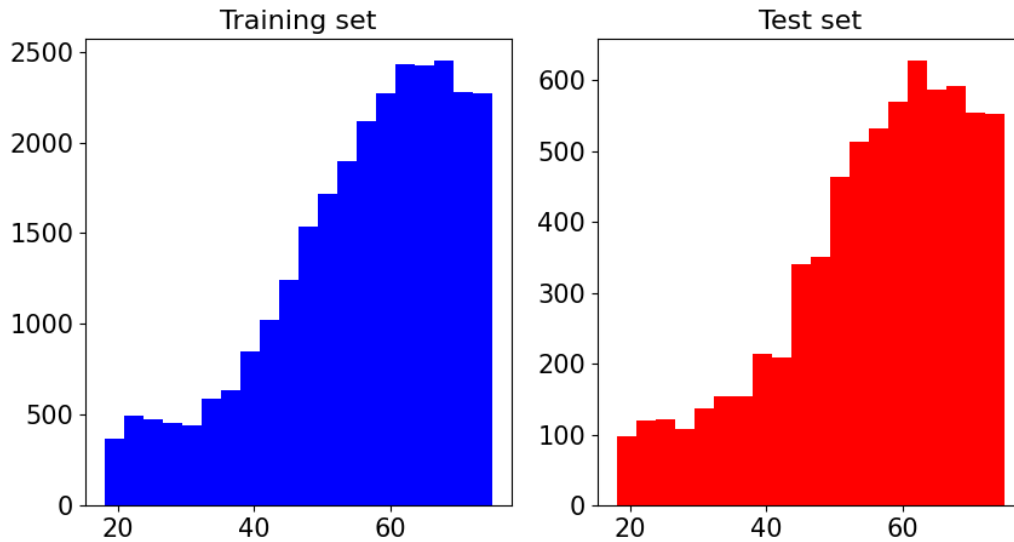


**Figure 3.** Age distributions in the training and test sets.

The age distributions of the remaining adult patients in the training and test sets are present in Figure 3. Distributions are similar between training and test sets, which shows the success of random sampling when dividing the dataset into these sets. Another visual finding from the age distributions is the higher number of elderly patients in the dataset compared to fewer young adults. Therefore, the number of deaths and re-admissions will be determined more heavily based on the conditions most older adults have in the ICUs.

**Table 1.** Sample size of the MIMIC-III dataset used in the experiments. (0: re-admission, 1: survival, 2: mortality)

	Re-admission (0)	Survival (1)	Mortality (2)
<b>Training</b>	2311	24006	3375
<b>Test</b>	495	6051	878

Another distribution obtained from the data is in Table 1. The table shows the high imbalance present in the training and test sets. Label 1 represents the dominant class, which is the recovery class. The remaining classes, 0 and 2, represent the re-admission and mortality classes, respectively. The number of patients in these two classes is similar. Therefore, the machine learning experiments will need to focus on not letting the dominant class (survival) overpower the decision-making process so that the system will predict the two rare classes: mortality and re-admission.

The distributions of the remaining demographics from the dataset are not shown in this study due to the large number of NULL values. For the rest of the study, to handle the NULL values, they are filled with the averages of the columns as was done in the previous literature that used the MIMIC-III dataset [27, 28].

## 2.2. Feature Extraction

The MIMIC-III dataset has 26 tables full of different data that can be used as features for training machine learning models. However, selecting the correct set of features is key to achieving good performance from machine learning [29, 30]. The biomedical collaborator brought knowledge and hard work

to accomplish this good performance to the feature engineering task. Influenced by the aforementioned scoring method actively used in the ICUs in the United States, which requires healthcare professionals to manually score various conditions of the patients and develop a final mortality risk score, known as APACHE scoring, is selected as a valid basis. Leveraging this manual scoring approach, the following measurements are selected as the initial set of features:

- i.* Age (years) computed from the dataset after subtracting the date of birth from the date of admission, both de-identified.
- ii.* Temperature (C) of the patient.
- iii.* Mean arterial pressure (mmHg) of the patient.
- iv.* pH measurement.
- v.* Heart rate (beats per min).
- vi.* Respiratory rate (breaths per minute).
- vii.* Serum sodium (mEq/L), potassium (mEq/L), creatinine (mg/dL) measurements.
- viii.* Hematocrit.
- ix.* WBC (cells/ul).
- x.* Glasgow-coma-scale points.
- xi.* A - a gradient (if  $\text{FiO}_2 \geq 0.5$ ) (mmHg)
- xii.*  $\text{PaO}_2$  (if  $\text{FiO}_2 < 0.5$ ) (mmHg)
- xiii.* History of organ insufficiency.
- xiv.* History of immunocompromise.

In addition to the above APACHE features, available demographics are included in the features such as gender, marital status, height, weight, etc. It is necessary to note that except for the constant features such as age or gender, the other measurement values are prone to change over the patient's progress during the ICU stay. Thus, for each patient, there are many measurements for most of the above features. To best express the range of measurements per patient, this study uses the range information, including minimum, maximum, and mean. Hence, in total, 165 features per patient are obtained.

### 2.3. Machine Learning Methods

Reducing the numerical difference between real-life patient feature values is essential before applying machine learning methods.

To overcome this problem, scaling the feature values in the data collection has become a standard approach. Scaling is achieved through the following:

$$x_i = \frac{x_i - \nu}{\rho}$$

where  $x_i$  represents the feature's value  $i$ ,  $\nu$  is the mean value of the feature column in the training set, and  $\rho$  shows the standard deviation of the same column. Through this operation, feature values present in the dataset are scaled to a smaller version of itself. Within the same features, their mathematical relations are preserved, meanwhile between the features, high differences are scaled down.

Machine learning methods have been popular in the biomedical research domain for many years [31]. To achieve comparability with the ICU mortality and re-admission prediction studies summarized

in the introduction section, the same machine learning methods commonly used in interdisciplinary ICU-related research are selected: LR, XGB, and LGBM. In addition, RF is also selected.

LR is considered the baseline approach since it has the simplest methodology within its algorithmic structure. LR returns the correct classification result by combining selected attributes with a linear mathematical formula [20]. This method focuses on separating data from one class at a time in the most successful way. L2 was used as the loss function. This simple approach becomes the baseline.

The other approach, RF, is an ensemble method that constructs multiple decision trees and averages their decisions into one decision. As a more complex variant of an RF method, another approach used in the experiments is XGB. It is perhaps the most popular method among the ensemble methods in recent years. It is an optimized distributed gradient boosting method designed to be highly efficient, flexible, and portable. It applies machine learning algorithms under the Gradient Boosting framework. XGB provides a parallel tree-boosting solution that solves many data science problems quickly and accurately [32]. Unfortunately, its disadvantage is that it is highly parametric, meaning that it becomes difficult to achieve a good performance if the correct parameters are not selected.

Next, the LGBM method is included in the experiments. It combines multiple decision trees, each focusing on improving the predictions of the previous ones within a gradient-boosting framework, just like the XGB method. However, unlike XGB, this method creates histograms for each feature and uses them to approximate the best-split point [33]. LGBM has other algorithmic differences, such as allowing leaf-wise growth rather than depth-wise growth in the trees.

## 2.4. Optimization

Despite their success in performing accurate predictions, one disadvantage shared by most machine learning methods is the number of parameters they need to be tuned. It is unrealistic to expect to find the perfect parameters for each model. However, with the help of methods such as a grid or a random search, it is possible to search over a set of possible parameters and find an optimal combination. In the present study, a library named Optuna is used to find optimal parameters for each method [34].

For each method, ten trials are conducted within every fold of the 5-fold cross-validation framework, where each trial tried a different parameter subset. The Optuna library moves towards the parameters that returned high performance in the previous trials, thus ensuring an optimal parameter set. The highest average macro F1 scores are selected and used in the tests as the performance criteria. Also, since all classification tasks have high-class imbalance problems, the class weights are provided inside all machine learning methods, considering the class imbalance.

## 3. Results and Discussion

As stated earlier, studies in the literature mainly focus on the binary classification task of detecting mortality risk among ICU patients. A few studies follow the same binary classification task for detecting the re-admission risk. However, no studies have conducted a multi-class classification task and provided a deep comparison with the binary tasks. To complete this lack of comparative information, this study performs three distinct experiments:

- i.* Conducting a binary classification task for mortality risk detection.
- ii.* Conducting a binary classification task for re-admission detection.
- iii.* Conducting a multi-class classification task to identify the likelihood of an ICU patient dying, recovering during the current ICU stay, or getting re-admitted after discharge.

For comparability, the same four machine learning methods and the same set of 165 features (APACHE and demographics) are used in the above experiments. Considering the data imbalance in the test set, among the possible performance scoring methods, Area under the curve (AUC) is selected for its ability to provide fair scoring [35], and its popularity as a scoring method in the mortality and re-admission prediction tasks as seen in Table 3. Meanwhile, macro F1 and recall (sensitivity) scores are also utilized to overcome possible overestimations AUC may return. Thanks to the macro setting of the F1 and recall metrics, class imbalance in the test set is handled fairly.

**Table 2.** AUC, macro F1, and macro recall scores of the proposed novel feature space used with four machine learning methods.

Goal	Metric	LR	RF	LGBM	XGB
Mortality	AUC	89.40	91.51	<b>92.43</b>	91.51
	F1	70.13	80.39	79.17	<b>82.65</b>
	Recall	80.75	78.78	<b>83.63</b>	79.36
Re-admission (30 days)	AUC	<b>65.03</b>	64.67	61.77	58.31
	F1	48.81	53.12	<b>53.15</b>	49.11
	Recall	<b>60.52</b>	52.75	54.71	50.58
Multiclass	AUC	75.54	<b>77.94</b>	76.98	76.50
	F1	48.92	53.49	<b>54.19</b>	54.03
	Recall	57.33	52.68	<b>58.26</b>	51.77

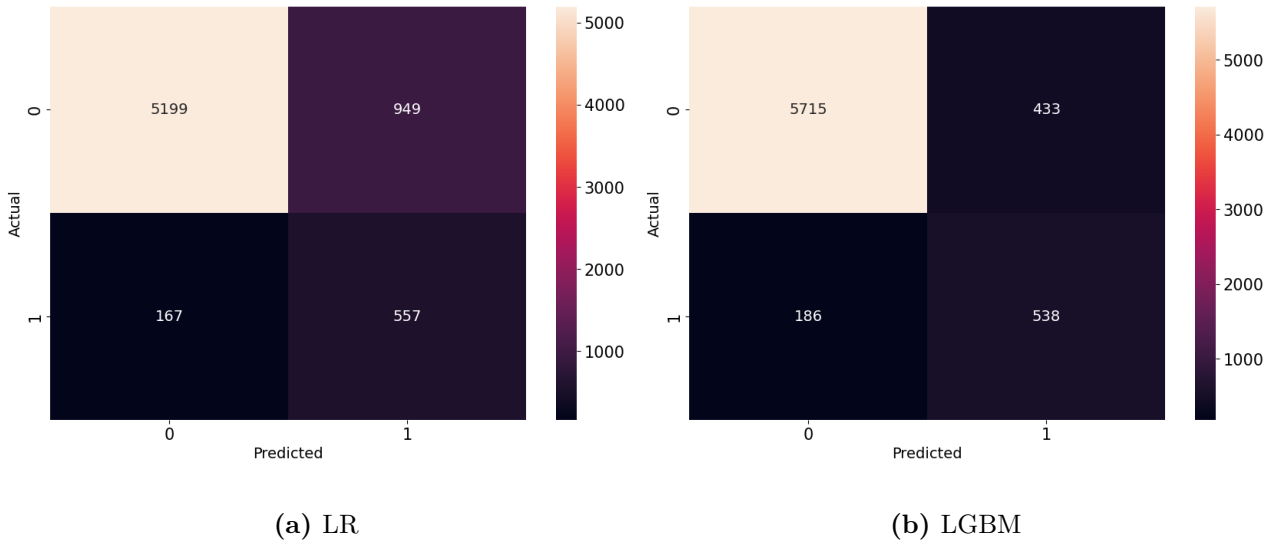


**Figure 4.** Confusion matrices of the mortality prediction task obtained from the baseline and the best-performing methods.

According to the results presented in Table 2, the mortality prediction task returned AUC scores around 90% with each method. Meanwhile, the highest F1 score is from the XGB method, and the highest sensitivity belongs to the LGBM. Compared to the mortality prediction results in the literature in Table 3, mortality prediction performance in the current study outperformed the past. Because the studies in the literature focused on specific disease mortality, which is more straightforward than a general mortality prediction, the current results are significant. This finding shows that including all the APACHE metrics as features, computing their statistical changes over the ICU stay of the patients

through min, max, mean, and median operations, among others, provide more robust outcomes for mortality prediction. Also, by including the demographics in the feature set, mortality prediction can be achieved with better performance. This is particularly interesting as it points to the genetic variability and risk factors of the patients and shows the importance of considering demographics for clinical decision-making. Another finding is regarding the choice of methods. Figure 4 highlights that the choice of machine learning method does not affect the mortality prediction task thanks to the novel feature space introduced in the current study.

**Table 3.** Some prediction objectives and scores from the literature that used the MIMIC-III dataset, excluding the clinical notes. Each re-admission study performs a 30-day prediction.

Objective	Features	Method	Score	Study
Mortality (heart failure)	Patient measures (overlap with APACHE), demographics	LR, XGB	84.16 AUC	[28]
Mortality (ventilated)	Patient measures (overlap with APACHE), demographics, history	KNN, LR, DT, RF, XGB, ANN	82.1 AUC	[27]
Mortality (pancreatitis)	Patient measures (overlap with APACHE), demographics	LR, Random, ANN	76.9 AUC	[36]
Re-admission	17 APACHE measures, demographics, ICD-9 embeddings	LSTM	74.2 recall, 79.1 AUC	[17]
Re-admission	Patient measures (overlap with APACHE), demographics, ICD-9 embeddings	LR, RF, SVM, ANN	65 accuracy, 60 AUC	[19]
Re-admission	Patient measures (overlap with APACHE), demographics, ICD-9 code	LR, RF, XGB	37 F1, 75 AUC	[37]

Re-admission prediction within the 30 days after discharge proves to be more complex than the mortality prediction according to the results in Table 2, which is validated by the scores in the literature Table 3. F1 score of 37% obtained in the literature [37] proves the difficulty of re-admission prediction even in a binary classification setting. In the current study, LR returned the highest AUC score of 65% for re-admission. Compared to the readmission AUC scores in Table 3, this score falls in the middle of the range in the literature. The F1 rate of 53% reported in the current study is higher than that of the literature. In Figure 5, two confusion matrices show that the LR method misclassified the survived patients as re-admission, and the XGB method did the opposite and misclassified the re-admissions as survived. One must decide based on the trade-off between high false positives and false negatives. Creating a model that returns high false positives would cause too much money and attention to be given to patients who are well, and high false negatives would cause patients who will be re-admitted within 30 days to be released early, which also causes a waste of money and resources. One conclusion from these findings is that, although APACHE features and demographics are successful at identifying mortality, they are not enough to predict ICU re-admission. Therefore, the current feature space needs to be enriched further for a higher re-admission prediction performance.

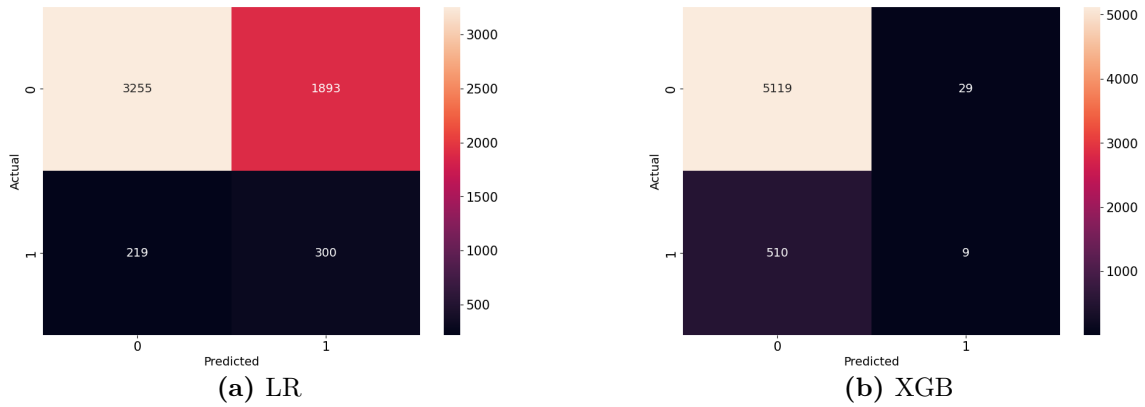


**Figure 5.** Confusion matrices of the 30 days re-admission prediction task obtained from the baseline and the worst performing methods

The last experiment tackles the challenge of performing multi-class classification to determine if a patient in the ICU will die, recover, or get re-admitted 30 days after getting discharged from the ICU. Table 2 shows that each method returned around 77% AUC for multi-class classification. Meanwhile, the F1 and recall scores show a distinction between the results. The confusion matrices in Figure 6 display the similarities and differences between the selected methods. The matrices of the RF and XGB methods appear too similar. For example, both methods failed to capture re-admissions, which is explainable considering the similarities between their algorithms - using decision trees within. The remaining two methods, LR and LGBM, returned more acceptable confusion matrices by successfully capturing re-admission cases. Among the two, LGBM has the best performance. For a 3-class classification problem, an F1 score of 54% is acceptably good compared to the random chance of 33%. LGBM’s capability to capture complex non-linear relationships between a mix of numerical and categorical variables proves it to be better than the remaining models in the current context.

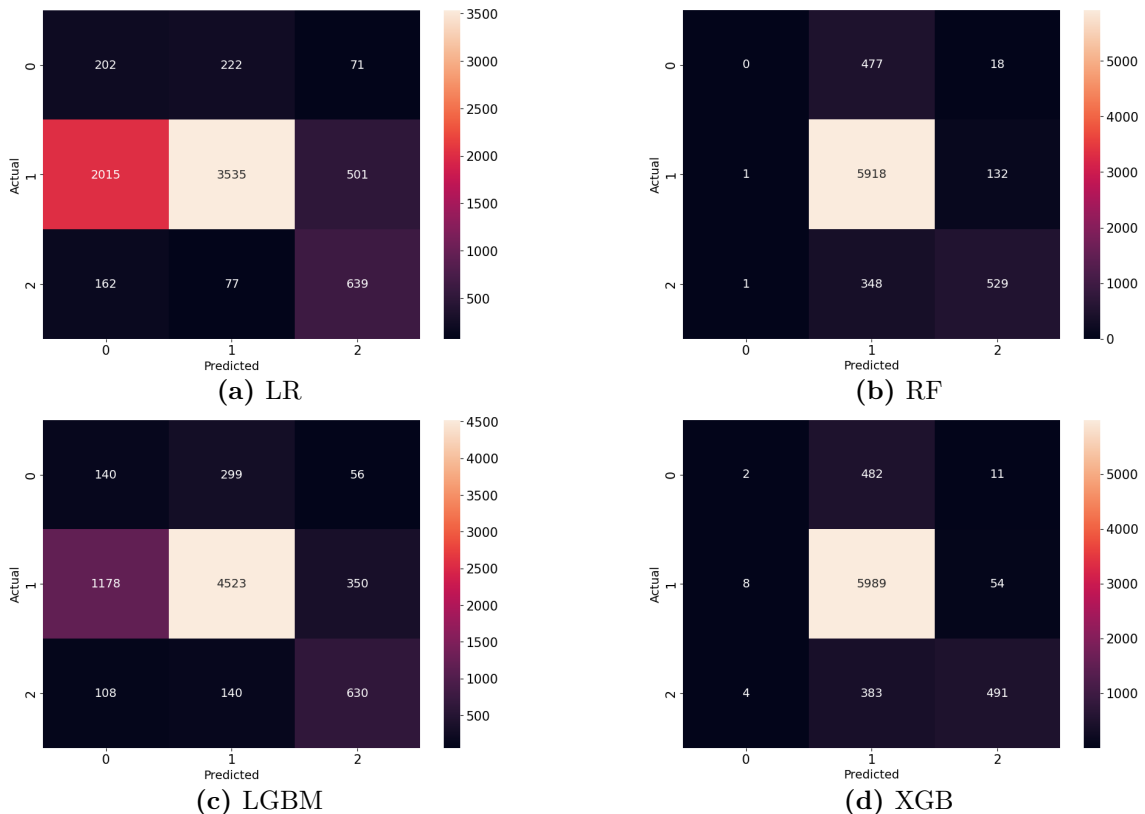


**Figure 6.** Confusion matrices of the three-class classification framework obtained from the baseline and the best-performing methods (Re-admission=0, survival=1, mortality=2)

## 4. Conclusion

The study carried out in this paper showed the simplicity of mortality prediction tasks in the ICU setting, using the APACHE measures together with the demographics, which explains the reasoning behind the vast number of available studies that focus only on mortality prediction. In parallel, the study showed the difficulty of the 30-day re-admission prediction task. The state-of-the-art machine learning methods that win various imbalanced data classification competitions failed the re-admission prediction task, while the simple baseline method outperformed the rest. This finding shows the difficulty of the re-admission prediction task and the failure of the APACHE and demographics data in providing predictive power. Because real-life expert healthcare providers signed off on the discharge forms of these patients during the data collection process, it is possible to conclude that machine learning methods still performed better than the actual human experts, with a 65% success rate. Yet, there is still room for improvement. Furthermore, the multi-class classification performance showed 77% success at differentiating recovery, mortality, and returning to the intensive care unit in 30 days, which are highly acceptable results to be used in real-life automated clinical decision-making systems. The proposed system with a simple baseline approach can help healthcare professionals save more lives and reduce the risk of early discharges without adding features - since APACHE features and demographics are mandatory to collect already. Finally, our dataset was limited to MIMIC III, which contains the medical history and data of all patients admitted to Beth Israel Deaconess Medical Center in Boston, Massachusetts, between 2001 and 2012. Thus, while predicting re-admission, our study could not consider the possibility of the patients being re-admitted to another hospital.

The overloaded ICUs during the COVID-19 pandemic before vaccines were available showed the unmet need for automated clinical decision-making systems. While the proposed system has demonstrated acceptable performance, in the rework, more features that are also mandatory to collect in an ICU setting will be included in the experiments to increase the re-admission prediction performance. Future work will also consist of evaluating different real-life ICU data collections.

## Author Contributions

The first author performed coding, running the experiments, and wrote the manuscript. The second author analyzed the raw data, guided the data science, and wrote the manuscript. All authors read and approved the final version of the paper.

## Conflicts of Interest

All the authors declare no conflict of interest.

## Ethical Review and Approval

No approval from the Board of Ethics is required.

## Acknowledgment

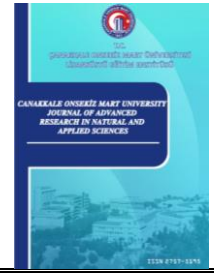
This work was supported by the Office of Scientific Research Projects Coordination at Çanakkale Onsekiz Mart University, Grant number: FHD-2021-3737. Neural Stem Cell Institute is not responsible for the statements and results of the paper.

## References

- [1] K. Cooley-Rieders, K. Zheng, *Physician documentation matters. Using natural language processing to predict mortality in sepsis*, *Intelligence-Based Medicine* 5 (2021) 100028 7 pages.
- [2] Y.-W. Lin, Y. Zhou, F. Faghri, M. J. Shaw, R. H. Campbell, *Analysis and prediction of unplanned intensive care unit readmission using recurrent neural networks with long short-term memory*, *Plos One* 14 (7) (2019) e0218942 22 pages.
- [3] T.C. Sağlık Bakanlığı, Yoğun Bakım Skorlama, <https://shgmkalitedb.saglik.gov.tr/TR,9024/yogun-bakim-skorlama.html>, Accessed: 2024-07-28.
- [4] H. Mumtaz, M. K. Ejaz, M. Tayyab, L. I. Vohra, S. Sapkota, M. Hasan, M. Saqib, *APACHE scoring as an indicator of mortality rate in ICU patients: A cohort study*, *Annals of Medicine and Surgery* 85 (3) (2023) 416–421.
- [5] R. Sarkar, C. Martin, H. Mattie, J. W. Gichoya, D. J. Stone, L. A. Celi, *Performance of intensive care unit severity scoring systems across different ethnicities in the USA: A retrospective observational study*, *The Lancet Digital Health* 3 (4) (2021) e241–e249.
- [6] H. Yang, L. Kuang, F. Xia, *Multimodal temporal-clinical note network for mortality prediction*, *Journal of Biomedical Semantics* 12 (2021) 1–14.
- [7] Centers for Disease Control and Prevention, National Center for Health Statistics, National Vital Statistics System, Provisional Mortality on CDC WONDER Online Database, <http://wonder.cdc.gov/mcd-icd10-provisional.html>, Accessed: 2024-07-24.
- [8] B. G. Pijls, S. Jolani, A. Atherley, R. T. Derckx, J. I. Dijkstra, G. H. Franssen, S. Hendriks, A. Richters, A. Venemans-Jellema, S. Zalpuri, M. P. Zeegers, *Demographic risk factors for COVID-19 infection, severity, ICU admission and death: A meta-analysis of 59 studies*, *BMJ Open* 11 (1) (2021) e044640 10 pages.
- [9] S. L. Hyland, M. Faltys, M. Hüser, X. Lyu, T. Gumbsch, C. Esteban, C. Bock, M. Horn, M. Moor, B. Rieck, M. Zimmerman, D. Bodenham, K. Borgwardt, G. Rätsch, T. M. Merz, *Early prediction of circulatory failure in the intensive care unit using machine learning*, *Nature Medicine* 26 (3) (2020) 364–373.
- [10] A. Mohammed, F. Van Wyk, L. K. Chinthala, A. Khojandi, R. L. Davis, C. M. Coopersmith, R. Kamaleswaran, *Temporal differential expression of physiomarkers predicts sepsis in critically ill adults*, *Shock* 56 (1) (2021) 58–64.
- [11] J. Liu, J. Wu, S. Liu, M. Li, K. Hu, K. Li, *Predicting mortality of patients with acute kidney injury in the ICU using XGBoost model*, *Plos One* 16 (2) (2021) e0246306 11 pages.
- [12] J. Wang, L. Zhou, Y. Zhang, H. Zhang, Y. Xie, Z. Chen, B. Huang, K. Zeng, J. Lei, J. Mai, J. Pan, Y. Chen, J. Wang, Q. Guo, *Minimum heart rate and mortality in critically ill myocardial infarction patients: An analysis of the MIMIC-III database*, *Annals of Translational Medicine* 9 (6) (2021) 496 9 pages.
- [13] Y. Chen, Y. Du, C. Sun, W. Tan, *Lactate is associated with increased 30-day mortality in critically ill patients with alcohol use disorder*, *International Journal of General Medicine* 14 (2021) 2741–2749.
- [14] Y. Ji, L. Li, *Lower serum chloride concentrations are associated with increased risk of mortality in critically ill cirrhotic patients: An analysis of the MIMIC-III database*, *BMC Gastroenterology* 21 (1) (2021) 200–208.

- [15] H. Yang, L. Kuang, F. Xia, *Multimodal temporal-clinical note network for mortality prediction*, Journal of Biomedical Semantics 12 (2021) 1–14.
- [16] S. Upadhyay, A. L. Stephenson, D. G. Smith, *Readmission rates and their impact on hospital financial performance: A study of Washington hospitals*, INQUIRY: The Journal of Health Care Organization, Provision, and Financing 56 (2019) 1–10.
- [17] Y.-W. Lin, Y. Zhou, F. Faghri, M. J. Shaw, R. H. Campbell, *Analysis and prediction of unplanned intensive care unit readmission using recurrent neural networks with long short-term memory*, Plos One 14 (7) (2019) e0218942 22 pages.
- [18] M. Jamei, A. Nisnevich, E. Wetchler, S. Sudat, E. Liu, *Predicting all-cause risk of 30-day hospital readmission using artificial neural networks*, Plos One 12 (7) (2017) e0181173 14 pages.
- [19] R. Assaf, R. Jayousi, *30-day hospital readmission prediction using MIMIC data*, in: 2020 IEEE 14th International Conference on Application of Information and Communication Technologies (AICT), IEEE, 2020, pp. 1–6.
- [20] U. Bayram, L. Benhiba, *Determining a person’s suicide risk by voting on the short-term history of tweets for the clpsych 2021 shared task*, in: Proceedings of the Seventh Workshop on Computational Linguistics and Clinical Psychology: Improving Access, 2021, pp. 81–86.
- [21] U. Bayram, J. Pestian, D. Santel, A. A. Minai, *What’s in a word? Detecting partisan affiliation from word use in congressional speeches*, in: 2019 International Joint Conference on Neural Networks (IJCNN), IEEE, 2019, pp. 1–8.
- [22] A. L. Goldberger, L. A. Amaral, L. Glass, J. M. Hausdorff, P. C. Ivanov, R. G. Mark, J. E. Mietus, G. B. Moody, C.-K. Peng, H. E. Stanley, *PhysioBank, PhysioToolkit, and PhysioNet: Components of a new research resource for complex physiologic signals*, Circulation 101 (23) (2000) e215–e220.
- [23] A. Johnson, T. Pollard, R. Mark, *MIMIC-III clinical database (version 1.4)*, PhysioNet 10 (2016) 1–2.
- [24] A. E. Johnson, T. J. Pollard, L. Shen, L.-W. H. Lehman, M. Feng, M. Ghassemi, B. Moody, P. Szolovits, L. Anthony Celi, R. G. Mark, *MIMIC-III, a freely accessible critical care database*, Scientific Data 3 (1) (2016) 1–9.
- [25] S. Lesser, S. Zakharkin, C. Louie, M. R. Escobedo, J. Whyte, T. Fulmer, *Clinician knowledge and behaviors related to the 4Ms framework of age-friendly health systems*, Journal of the American Geriatrics Society 70 (3) (2022) 789–800.
- [26] F. Zakirov, A. Krasilnikov, *Age-related differences in decision-making process in the context of healthy aging*, in: BIO Web of Conferences, Vol. 22, EDP Sciences, 2020, pp. 1–6.
- [27] Y. Zhu, J. Zhang, G. Wang, R. Yao, C. Ren, G. Chen, X. Jin, J. Guo, S. Liu, H. Zheng, Y. Chen, Q. Guo, L. Li, B. Du, X. Xi, W. Li, H. Huang, Y. Li, Q. Yu, *Machine learning prediction models for mechanically ventilated patients: Analyses of the MIMIC-III database*, Frontiers in medicine 8 (2021) 662340 9 pages.
- [28] F. Li, H. Xin, J. Zhang, M. Fu, J. Zhou, Z. Lian, *Prediction model of in-hospital mortality in intensive care unit patients with heart failure: Machine learning-based, retrospective analysis of the MIMIC-III database*, BMJ Open 11 (7) (2021) e044779 17 pages.
- [29] P. Domingos, *A few useful things to know about machine learning*, Communications of the ACM 55 (10) (2012) 78–87.

- [30] U. Bayram, *Applying machine learning to online data?: Beware! computational social science requires care*, in: Opportunities and Challenges for Computational Social Science Methods, IGI Global, 2022, pp. 100–125.
- [31] J. Pestian, D. Santel, M. Sorter, U. Bayram, B. Connolly, T. Glauser, M. DelBello, S. Tamang, K. Cohen, *A machine learning approach to identifying changes in suicidal language*, Suicide and Life-Threatening Behavior 50 (5) (2020) 939–947.
- [32] T. Chen, C. Guestrin, *Xgboost: A scalable tree boosting system*, in: Proceedings of the 22nd ACM Sigkdd International Conference on Knowledge Discovery and Data Mining, 2016, pp. 785–794.
- [33] G. Ke, Q. Meng, T. Finley, T. Wang, W. Chen, W. Ma, Q. Ye, T.-Y. Liu, *Lightgbm: A highly efficient gradient boosting decision tree*, Advances in Neural Information Processing Systems 30 (2017) 3149–3157.
- [34] T. Akiba, S. Sano, T. Yanase, T. Ohta, M. Koyama, *Optuna: A next-generation hyperparameter optimization framework*, in: Proceedings of the 25th ACM Sigkdd International Conference on Knowledge Discovery and Data Mining, 2019, pp. 2623–2631.
- [35] T. Yang, Y. Ying, *AUC maximization in the era of big data and AI: A survey*, ACM Computing Surveys 55 (8) (2022) 1–37.
- [36] N. Ding, C. Guo, C. Li, Y. Zhou, X. Chai, *An artificial neural networks model for early predicting in-hospital mortality in acute pancreatitis in MIMIC-III*, BioMed Research International 2021 (1) (2021) Article ID 6638919 8 pages.
- [37] A. Pakbin, P. Rafi, N. Hurley, W. Schulz, M. H. Krumholz, J. B. Mortazavi, *Prediction of ICU readmissions using data at patient discharge*, in: 2018 40th annual international conference of the IEEE engineering in medicine and biology society (EMBC), IEEE, 2018, pp. 4932–4935.



# Effect of Compost Addition on Porosity and Hydraulic Properties of Different Textured Soils

Nurten İşler<sup>1</sup> , Yasemin Kavdır<sup>2</sup> 

<sup>1,2</sup>Department of Soil Science and Plant Nutrition, Faculty of Agriculture, Çanakkale Onsekiz Mart University, Çanakkale, Türkiye

## Article Info

Received: 08 Aug 2024

Accepted: 18 Oct 2024

Published: 31 Dec 2024

Research Article

**Abstract** – This research aimed to investigate the temporal variations in soils of three distinct textures that were amended with composts derived from olive pomace (OPC) and vineyard pruning waste (VPC). The compost was prepared in reactors with automatic temperature and aeration control. This research encompasses three distinct soil textures, five varying compost applications, and ten separate sampling intervals following the compost application and replicated four times. After 210 days of incubation, 6% VPC application increased the field capacity value by 27.7% compared to the control, especially in sandy loam soil. At the same treatment and time, total porosity increased by 14.29% in clay soil. The highest increase in hydraulic conductivity was observed in clay and loam soil with 6% VPC and in sandy loam soil with 6% OPC. Compost applications increased field capacity the most in sandy loam soil. The impact of compost on field capacity and porosity of soils varied according to soil texture, compost material, application amount, and time elapsed after compost application. The high BJH surface area of clay soil decreased from 15.830 m<sup>2</sup>/g to 12.977 m<sup>2</sup>/g with the addition of OPC.

**Keywords** – *Vineyard pruning waste, olive pomace, compost, hydraulic conductivity, soil physics*

## 1. Introduction

Soil is a critical component in maintaining terrestrial ecosystems by providing essential ecosystem services such as maintaining nutrient cycling for all living organisms' lives, filtering and transforming substances, and providing the physical environment to support plant growth. Soil quality can be classified into three primary categories: physical, chemical, and biological [1]. The physical characteristics of soil play a crucial role in ensuring agricultural land's sustainability and environmental quality protection [2]. Soil physics is primarily concerned with the interactions between soil and water. Consequently, the physical, chemical, and biological processes within the soil are influenced by the quantity and composition of water present [3]. The water-holding capacity of soils is also related to the soil's total porosity and specific surface area and soil texture directly affecting the water-holding capacity. Sandy soils have less total pore volume than clay soils and low water-holding capacities [4]. Pore size distribution is an essential physical property of soil that provides the ability of soil to store water and air [5]. Soil porosity and pore size distribution affect water retention, gases, and root growth [6].

The gradual reduction of organic matter in the soil, attributable to intensive agricultural practices, results in the deterioration of soil structure and contributes to soil degradation. Therefore, enhancing and stabilizing the amount of soil organic matter [7-8]. Concerns about global warming resulting from the increase in atmospheric

<sup>1</sup>nurtenisler83@gmail.com; <sup>2</sup>kavdirya@comu.edu.tr (Corresponding Author)

carbon dioxide (CO<sub>2</sub>) and methane (CH<sub>4</sub>) emissions in recent years have led to increased research on the carbon stock potential of soils. Incorporating organic materials, such as compost, into soil decomposes a portion of the organic carbon, subsequently releasing CO<sub>2</sub>, while the rest remains in the soil [9]. Therefore, it has been stated [10] that when an organic carbon source is added to the soil, it should be considered for its positive effects on the soil while simultaneously causing an increase in CO<sub>2</sub> concentration in the atmosphere. Small soil pores retain water strongly, while large pores drain easily. Applying compost can modify soil's hydrological characteristics by altering its texture, thereby increasing the size and quantity of soil pores. [5]. Many studies [11-13] have reported that soil organic carbon enhances hydraulic conductivity by stabilizing soil aggregates [14] and increasing porosity. The influence of organic materials on soils with varying textures may differ significantly. It has been reported in many studies [15-17] that the beneficial effects of compost addition are significant, especially in sand and clay soils. It can improve plant water and nutrient availability in sandy soils with low water holding capacity [18] and improve aeration and structural stability in clay soils with low aeration [19]. Given the diverse microbial properties inherent in different organic materials, their impacts on soil characteristics can vary considerably [20]. Among composts with other properties, the ones with higher carbon content may have a greater effect on soil organic matter content [21]. This study aimed to assess the impact of various compost types, specifically olive pomace (OPC) and vineyard pruning waste (VPC), on the physical properties and hydrological characteristics of soils with three distinct textures: clay (C), loam (L), and sandy loam (SL). To achieve this objective, a 210-day soil incubation experiment was conducted. Temporal variations in total porosity (TP) and field capacity (FC) within the soil-compost mixtures were monitored through sampling at ten different intervals. Following a 210-day incubation period, measurements of saturated hydraulic conductivity (K<sub>sat</sub>) and Brunauer-Emmett-Teller (BET) results were obtained for soils characterized by three different textures.

## 2. Materials and Methods

### 2.1. Properties of Compost

Olive pomace and vineyard composts were produced at ÇOMU-TETAM. The olive pomace (OP) was obtained from an olive oil factory, while the vineyard pruning waste (VP) was collected from a local orchard in Çanakkale. The compost used in the research was produced in specially constructed stainless steel compost reactors, each with a capacity of 100 liters. To monitor the compost temperature hourly, three K-type thermocouples were strategically positioned at each reactor's bottom, center, and top. Aeration fans were employed to facilitate proper aeration within the reactors. The fans are activated if the compost temperature is higher than the set temperature (above 60 °C). The temperature and aeration parameters of the composting processes were carefully controlled, and data was systematically recorded utilizing a programmable logic controller. The water content of compost was assessed three times per week by subjecting a compost sample to drying in an oven at 70 °C for 48 hours.

The moisture levels of the compost were regulated to remain within the range of 45-60% through the addition of water. The ratios of compost feedstock mixtures were established through calculations to guarantee that the resultant compost would achieve the desired carbon-to-nitrogen (C:N) ratio. The olive pomace compost comprised an equal proportion of pomace and farmyard manure (FM). In contrast, the VPC was formulated with 20% FM and 80% VPW. The pH and EC values of OPC and VPC were 6.82 and 4.81 mS/cm and 8.04 and 5.95 mS/cm, respectively. The total phenolic content of OPC and VPC were 3.09 and 1.99 mg GAE /g. The C:N values of OPC and VPC were 11.7 and 20.7, and the CEC values were 51.7 and 35.1 cmol/kg, respectively [22].

### 2.2. Soil Properties

Soil with clay texture was taken from 40°15'04.2 "N, 26°34'52.3" E in Çanakkale and classified in the Chromic Haploxererts sub-group of the Vertisol order according to Soil Taxonomy. The soil with a sandy loam texture

was obtained from Çanakkale (40°15'58.8 "N, 26°35'40.2" E), and it was included in the Entisol order Xerofluvents large group [23]. The soil with loam texture was sampled from the Lapseki, Çanakkale (40°18'51.8 "N, 26°38'36.4" E). According to soil taxonomy, it was included in the Haploxerolls large group of the Mollisol order [24].

### 2.3. Incubation Study

After air-drying, the soil was sieved through a 6 mm sieve and used in the incubation study. Some physical and chemical analyses of the soils were performed after sieving the soil through a 2 mm sieve, and the results are presented in Table 1. The prepared compost [22] was dried in an oven at 65 °C, then ground and sieved through a 2 mm sieve. For the incubation study, plastic rectangular storage containers with a capacity of two liters were utilized. To maintain aerobic conditions, ventilation holes were drilled near the top of the containers. A mixture of 3% and 6% VPC and OPC was prepared separately for soils of all three textures. The control treatment consisted of soils without compost. The experiment was conducted using a randomized design that included five distinct treatments, three varying textures, four replications, and ten incubation periods. The treatments comprised a control group at 0%, 3%, and 6% of olive pomace and vineyard pruning waste composts. According to our previous studies, a positive effect of 2% OPC treatment on selected soil properties was observed, and it was concluded that OPC treatment above 6% was not economical [25,26]. The study utilized 600 samples subjected to controlled atmospheric conditions at a temperature of  $26 \pm 2$  °C during the incubation period. To ensure appropriate moisture levels, the containers were periodically weighed, and water was added as needed to maintain a moisture level of 60% of field capacity. Soil analyses were performed at 15-day intervals during the initial phase of the experiment, and then soil analyses were carried out every 30 days for the following 210-day period.

**Table 1.** Some physical and chemical properties of soils [22]

Texture	Clay (%)	Silt (%)	Sand (%)	Field Capacity (%)	CaCO <sub>3</sub> (%)	pH	EC (µS/cm)	TC (%)	CEC (cmol/kg)
Clay	46.92	34.22	18.86	35.13	11.72	8.33	391	3.32	37.64
Loam	23.65	44.86	31.49	33.87	13.09	8.31	365	2.81	34.40
Sandy loam	12.22	22.62	65.16	27.02	1.58	8.07	147	0.86	21.16

FC; Field Capacity, TC; Total Carbon, OM; Organic Matter, TN; Total Nitrogen. CEC; Cation Exchange Capacity

### 2.4. Methods for Analyzing Soil and Compost

Soil and compost pH and electrical conductivity (EC) values were assessed by preparing solutions with ratios of 1:2.5 for soil:water and 1:10 for compost:water. [27]. Total C and N content of materials were determined by dry digestion method using LECO Truspec 2000 C.N elemental analyzer [28], and cation exchange capacity (CEC) was measured by sodium acetate method [29]. The phenol content was quantified using the colorimetric method based on the Folin Ciocalteu [30]. The ammonium and nitrate content of the compost was determined by the Kjeldahl method using 2M KCl [31]. Soil texture was assessed using the standard hydrometer method outlined by Gee and Bauder [32], and CaCO<sub>3</sub> content was determined using the Scheibler method [33]. Field capacity and total porosity were determined by saturating a certain volume of soil and determining on a weight basis [34]. After the undisturbed soil samples were saturated with 0.1 M calcium chloride (CaCl<sub>2</sub>) solution, the hydraulic conductivity ( $K_{sat}$ ) value was determined in accordance with Darcy's law [35] by measuring the amount of water passing through the soil column at specified times under constant water load. BET analyses of three different textured soils and control soils mixed with the highest dose of 6% OPC and 6% VPC compost and incubated for 210 days were carried out at ÇOMÜ-ÇOBİLTUM using the Brunauer, Emmet and Teller (BET) methodology [36] with BET surface area measuring device (Quantachrome Quadrasorb SI) in liquid nitrogen environment at 77K based on nitrogen (N<sub>2</sub>) gas adsorption technique.

## 2.5. Method of Statistical Analysis

In order to examine the effect of texture, treatment, and time (X, Y, Z, ...) on the traits, the analysis of variance technique was used in a factorial arrangement of randomized plots experimental design. Tukey's multiple comparison test was subsequently applied to identify the specific groups or subgroups responsible for observed differences. The data collected during the study were analyzed using STATISTICA 12 software (StatSoft Inc.).

## 3. Results and Discussion

### 3.1. Changes in Soil Field Capacity Value After Incubation

The results of field capacity (FC) analysis of different doses of OPC and VPC applied to soils of three different textures at various times are presented in Figure 1. The difference between compost treatments on clay, loam, and sandy loam soil was statistically significant at all sampling times. In C, L, and SL soils, the highest value was found in 6% VPC application, whereas the control soil consistently exhibited the lowest values across all measurement intervals. In clay soil, the application of 6% VPC had a statistically significant effect on FC up to the 45th day after application, compared to other treatments. In loam soil, the FC began to increase from the 45th day onward, while in sandy loam soil, the FC value increased significantly until 90 days after application. It was [37] reported that although soil texture is the primary factor influencing water-holding capacity, an increase in organic carbon content also plays a crucial role in enhancing water-holding capacity. Furthermore, compost had a more pronounced effect on water-holding capacity in coarse-textured soils.

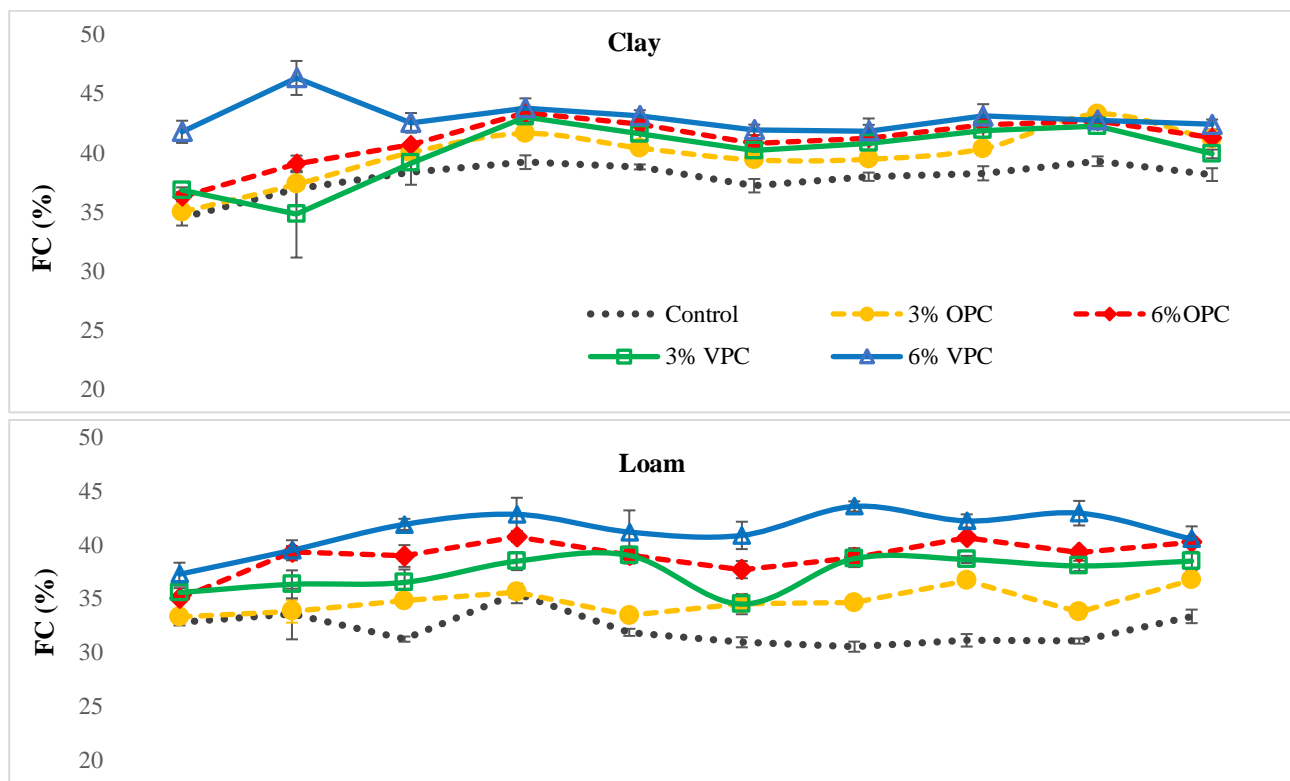


**Figure 1.** The impact of varying VPC and OPC application rates on field capacity over a 210-day incubation period. Error bars represent the standard errors of the means ( $n = 4$ )

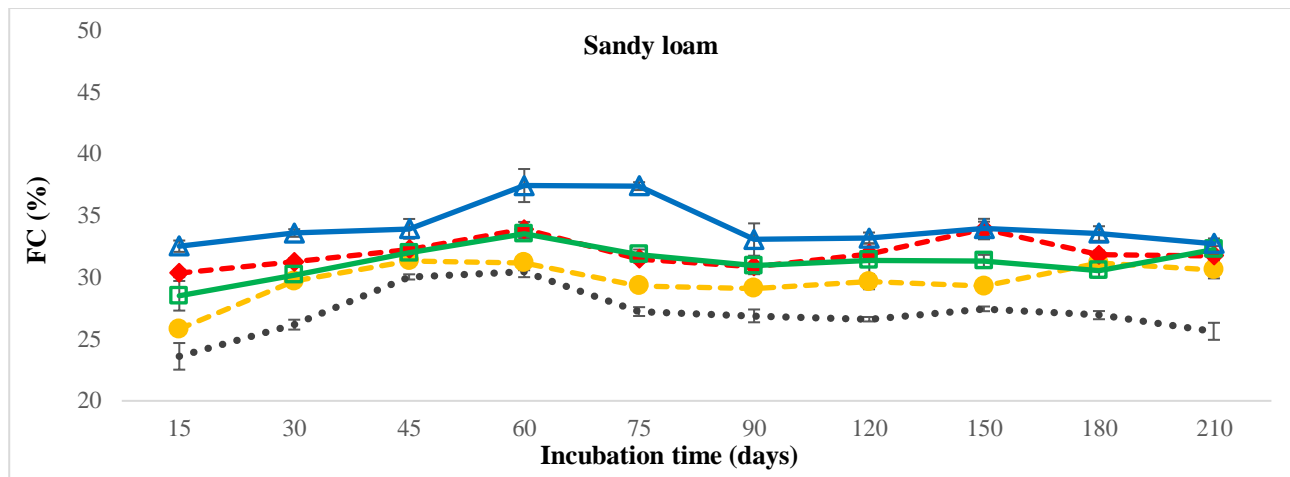


**Figure 1.** (Continued) The impact of varying VPC and OPC application rates on field capacity over a 210-day incubation period. Error bars represent the standard errors of the means ( $n = 4$ )

When analyzing the variation between sampling times for the same soil texture and treatment, the difference in sampling times following 3% OPC application was statistically significant ( $p \leq 0.05$ ) in clay and sandy loam soils. However, this significance is not observed in loam soil.

In clay soil treated with pomace compost, the maximum value of FC was recorded on day 180 (43.30%), while the minimum value was observed on day 15 (35.02%). In sandy loam soil, the highest field capacity value was found on the 45th day (31.34%), and the lowest FC value was determined on the 15th day (25.83%). The difference between the 6% OPC application time averages was significant in all three textures. The 3% and 6% VPC applications were significant across all three textures. The highest FC value in C, L, and SL soils in 3% VPC treatment was 43.41%, 38.49%, and 33.55% on day 60, respectively. The highest FC value in clay, loam, and sandy loam textures in 6% VPC treatment was found on day 30 (46.36%), day 120 (43.57%), and day 60 (37.46%), respectively (Figure 1).

When the differences in soil texture averages were compared at the identical sampling times and treatments, each treatment showed statistically significant differences at each time point. The highest FC value of 6% VPC treatment was observed in loam soil on the 120th day and in clay soil at all other sampling times. The lowest FC value was found in sandy loam soil across all treatments and sampling times. The highest FC value for the control group and the treatments involving 3% and 6% OPC and 3% VPC was consistently recorded in clay soil across all measurement intervals. In contrast, the lowest value was recorded in sandy loam soil. Soil texture and organic matter content significantly affect soil water-holding capacity. Pore content distribution, pore size distribution, and surface area of soils are essential parameters that determine the soil's water-holding capacity [4]. Tension force in soil depends on pore diameter; therefore, water retention is stronger in small pores [38]. Furthermore, sandy soils have a reduced surface area and fewer micropores than clay soils, resulting in a lower capacity for water retention. It has been reported by many authors [39-43] that organic materials incorporation into the soil positively affects the water-holding capacity.

A positive correlation ( $r^2=0.79$ ) between organic matter content and water-holding capacity in sandy soils was also reported by [40]. In this study, compost application increased the field capacity most in sandy loam soil. After 210 days of incubation, all treatments increased field capacity between 4.6% and 11.1% in clay soil, 10.1% and 21.5% in loam soil, and 19.4% and 27.7% in sandy loam soil.

### 3.2. Total Porosity Change After Incubation

According to the total porosity (TP) analysis of samples collected at various times from soils with different textures and varying doses of OPC and VPC, the differences between treatments in clay soil were statistically significant on days 15, 45, 60, 120, and 210 ( $p \leq 0.05$ ). The maximum total porosity was observed in the 6%

VPC treatment on days 15, 45, and 120, the 3% VPC treatment on day 60, and the 3% OPC treatment on day 210 for clay soils.

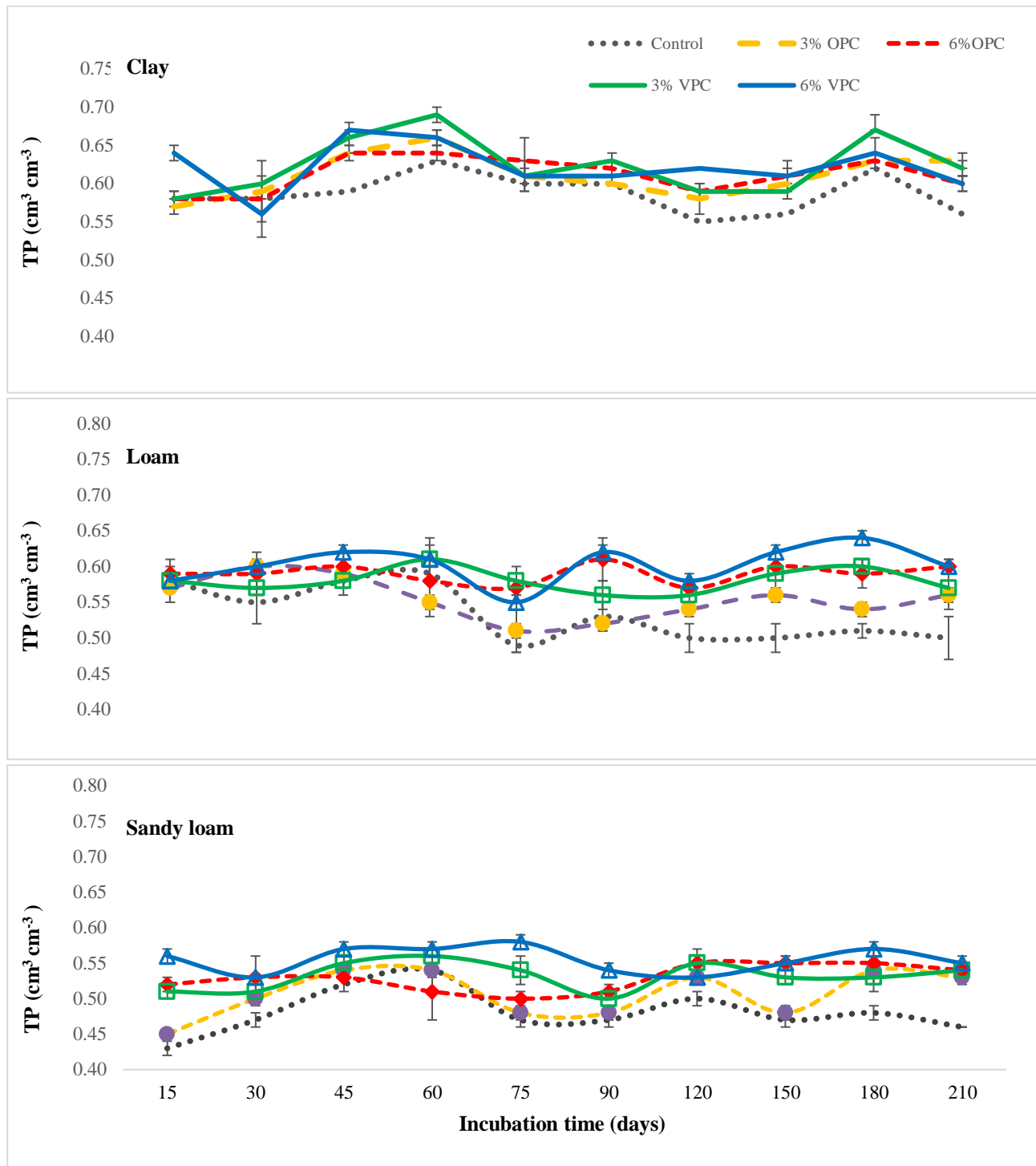


**Figure 2.** The impact of varying VPC and OPC application rates on soil total porosity over a 210-day incubation period. Error bars represent the standard errors of the means ( $n = 4$ )

In loam soil, the differences between the treatments were not statistically significant during the first four sampling periods; however, they became significant in the later periods. The highest total porosity (TP) value was obtained in the 6% VPC treatment between days 90 and 210.

There was no difference between the treatments on sandy loam soil on days 45, 60, and 120. The highest TP value was found in 6% of VPC applications on days 15, 30, 75, 90, 90, 150, 180, and 210 (Figure 2). Compost increases soil stability and, thus, macropores through various organisms [44]. [45] reported that the porosity of different composts varied between 60.7% and 72.4%.

According to the total porosity analysis results (Figure 2), the differences in incubation periods following the application of 3% OPC on C, L, and SL soils were found to be statistically significant ( $p \leq 0.05$ ). The highest TP value was observed on day 60 in clay soil and on day 30 in loam soil treated with 3% OPC. Conversely, the lowest TP value was recorded on day 15 in sandy loam soil and on day 75 in loam soil. In contrast, the differences in the average TP values resulting from applying 6% OPC across all three soil textures were not statistically significant (Figure 2).

The difference in time averages for the 3% VPC application was significant in clay soil but not other soil textures. The highest TP value ( $0.69 \text{ cm}^3/\text{cm}^3$ ) was found on day 60, while the lowest TP value ( $0.58 \text{ cm}^3/\text{cm}^3$ ) was found on day 15 in clay soil. Additionally, the difference between the time averages of the 6% VPC application was significant in both C and L soils. In clay soil, the highest TP value ( $0.67 \text{ cm}^3/\text{cm}^3$ ) was found on day 45, and the lowest TP value ( $0.56 \text{ cm}^3/\text{cm}^3$ ) was found on day 30. The highest TP value was found in loam soil on day 180 and the lowest on day 75.

When TP values of soils of different textures were compared at the same time and in the same application, 3% OPC application showed a difference according to texture at all times. The highest TP value was always found in C soil, and the lowest TP value was found in SL soil. In 6% VPC treatment, the difference was significant at all times except day 210. Loam soil had the highest TP value on days 15 and 30, while clay soil had the highest TP value at all other times. Sandy loam soil consistently had the lowest TP value. The difference was statistically significant throughout the 3% VPC treatment, except day 120. TP value was high in clay soil on days 15, 45, 60, 75, and 120 and loam soil on days 30, 90, 150, and 180. On day 75, loam soil had the lowest TP value; at other times, sandy loam soil had the lowest value (Figure 2). [46] reported that TP value varied between  $0.59\text{-}0.64 \text{ cm}^3/\text{cm}^3$  in clay soil and  $0.42\text{-}0.56 \text{ cm}^3/\text{cm}^3$  in loam soil after adding compost to the soil at different doses ( $0\text{-}75\text{-}150\text{-}300 \text{ m}^3/\text{ha}$ ). In this study, since the organic matter added to the soil increased with both compost treatments, it can be said that total porosity increased in all textures. The application that increased the most was 6% VPC. It was also reported by [47] that pruning waste compost increased soil porosity.

### 3.3. Saturated Hydraulic Conductivity Change After Incubation

The results of the  $K_{\text{sat}}$  analysis of soils after 210 days of incubation in which different doses of composts were applied to soils with different textures are presented in Table 2. According to the statistical analysis results, the effect of compost application on  $K_{\text{sat}}$  was found to be significant in C and L soil, while it was not statistically significant in L soil. In clay soil, the highest  $K_{\text{sat}}$  value ( $0.039 \text{ cm/s}$ ) was in 6% VPC application, and the lowest  $K_{\text{sat}}$  value ( $0.016 \text{ cm/s}$ ) was in control soil. In sandy loam soil, the highest  $K_{\text{sat}}$  value ( $0.033 \text{ cm/s}$ ) was in the 6% OPC treatment, and the lowest  $K_{\text{sat}}$  value ( $0.006 \text{ cm/s}$ ) was in the control soil.

**Table 2.** Impact of varying application rates of OPC and VPC on hydraulic conductivity (cm/s) of soils with different textures after 210 days of incubation

	Clay	Loam	Sandy loam
<b>Control</b>	$0.006 \pm 0.001 \text{ Cb}$	$0.007 \pm 0.001 \text{ Aab}$	$0.016 \pm 0.001 \text{ Ca}$
<b>3% OPC</b>	$0.028 \pm 0.004 \text{ Ba}$	$0.013 \pm 0.002 \text{ Ab}$	$0.024 \pm 0.003 \text{ ABa}$
<b>6% OPC</b>	$0.029 \pm 0.003 \text{ ABa}$	$0.014 \pm 0.001 \text{ Ab}$	$0.033 \pm 0.004 \text{ Aa}$
<b>3% VPC</b>	$0.028 \pm 0.001 \text{ ABa}$	$0.015 \pm 0.001 \text{ Ab}$	$0.020 \pm 0.005 \text{ Bab}$
<b>6% VPC</b>	$0.039 \pm 0.001 \text{ Aa}$	$0.016 \pm 0.001 \text{ Ab}$	$0.022 \pm 0.003 \text{ Bb}$

In the same column, the differences between the treatment mean shown with different capital letters are statistically significant ( $p \leq 0.05$ ).

In the same row, the differences between the texture mean shown with different lower-case letters t are statistically significant ( $p \leq 0.05$ ).

In the same compost application, the variations in the  $K_{\text{sat}}$  values of soils exhibiting varying textures were determined to be statistically significant ( $p < 0.05$ ). In the control soil without compost application, the highest and lowest  $K_{\text{sat}}$  values were measured in sandy loam and clay-textured soil, respectively. In the applications involving 3% OPC, 3%, and 6% VPC, the maximum  $K_{\text{sat}}$  value was observed in clay, whereas the minimum

$K_{sat}$  value was recorded in loam soil. In the 6% OPC application, the highest  $K_{sat}$  value was in sandy loam soil, and the lowest  $K_{sat}$  value was in loam soil (Table 2). Water infiltration rate in the soil is primarily influenced by various soil characteristics, including water content, soil texture, porosity,  $K_{sat}$ , swelling properties, and organic matter content [48,49]. In addition, properties such as aggregate size and distribution and the amount of carbon in the soil play an important role in controlling hydraulic conductivity [50]. Increasing organic carbon in the soil increases aggregate stability and porosity, thus increasing hydraulic conductivity [51,12]. This study obtained the highest  $K_{sat}$  values with 6% VPC application in clay soil and 6% OPC application in SL soil. Therefore, the hydraulic conductivity of clay soils increased in about 7 months after compost application.

### 3.4. Surface Area Results of Soils

According to the Barrett-Joyner-Halenda (BJH) method, the pore radius was 1.54 nm, 1.54 nm, and 2.18 nm for control, 6% OPC, and 6% VPC treatments in clay soil, respectively. In loam soil, it is 1.54, 1.55, and 1.72 nm; in sandy loam soil, it is 1.55 nm, 2.18 nm and 2.18 nm, respectively. The average pore radius of BJH of VPC was 2.47 nm, while that of OPC was 1.73 nm (Table 3). These results correlate with the results of the previous hydraulic conductivity analyses. The average pore radius increased in both compost treatments, and the hydraulic conductivity values (Table 2) also increased.

Specific surface area is an essential property in evaluating the physical interaction of soils with chemical stabilizers. The BJH surface area of clay soil was found to be 15.830 m<sup>2</sup>/g. The high BJH surface area of the clay soil decreased significantly from 15.830 m<sup>2</sup>/g to 12.977 m<sup>2</sup>/g due to the addition of OPC (0.449 m<sup>2</sup>/g) (Table 3). A similar result was observed for the BET surface area. Clay soil (62.470 m<sup>2</sup>/g) had a much higher BET surface area than sandy loam soil (11.868 m<sup>2</sup>/g) (Table 3). The BET surface area values of the different soil textures were found to be in the following order: clay > loam > sandy loam. According to the International Union of Fundamental and Applied Chemistry (IUPAC), solids with an average pore diameter <2 nm are called microporous, and those with 2-50 nm belong to mesoporous solids. Therefore, OPC and soils other than VPC can be classified as microporous. Microporous materials usually have a larger specific surface area than mesoporous materials, which may contribute to a higher biosorption capacity. The BET-specific surface area of OPC and VPC are 0.518 m<sup>2</sup>/g and 0.555 m<sup>2</sup>/g, respectively. These values are smaller than those of composted cow manure (2.085 m<sup>2</sup>/g) and composted mushroom residues (1.16 m<sup>2</sup>/g). The average pore radius increased with the application of VPC in all three soil textures. It is thought that the organic materials released by the decomposition of the compost during the incubation period clogged the surface pores of the clay and, therefore, blocked the nitrogen gas entry during BET surface area measurement, leading to a lower surface area value. The surface area results determined by [52] with the same method in clay soils with different properties are similar.

**Table 3.** BJH and BET values after 210 days of incubation in soils treated with 6% compost

		OPC	VPC	Clay			Loam			Sandy Loam		
				Control	OPC	VPC	Control	OPC	VPC	Control	OPC	VPC
<b>BJH adsorption</b>	Surface area (m <sup>2</sup> /g)	0.449	2.815	15.830	12.977	14.526	10.540	14.249	16.331	5.530	3.952	4.228
	Pore volume (cm <sup>3</sup> /g)	0.001	0.007	0.029	0.025	0.028	0.020	0.027	0.030	0.016	0.013	0.013
	Pore radius (nm)	1.73	2.47	1.54	1.54	2.18	1.54	1.55	1.72	1.55	2.18	2.18
<b>Multi-Point BET</b>	Surface area (m <sup>2</sup> /g)	0.518	0.555	62.470	51.674	55.722	48.031	61.185	52.107	11.868	8.269	9.393
<b>Total pore volume</b>	Total pore volume smaller than the radius of interest (cm <sup>3</sup> /g)	6.87.10 <sup>-2</sup>	6.87.10 <sup>-2</sup>	5.28.10 <sup>-2</sup>	4.43.10 <sup>-2</sup>	4.89.10 <sup>-2</sup>	3.90.10 <sup>-2</sup>	5.04.10 <sup>-2</sup>	4.79.10 <sup>-2</sup>	1.95.10 <sup>-2</sup>	1.48.10 <sup>-2</sup>	1.56.10 <sup>-2</sup>
	Pores smaller than <math>\text{\AA}</math> (Radius)	196.0	210.2	199.1	207.6	213.0	209.3	218.7	232.6	217.3	209.6	221.5

## 4. Conclusion

Incorporating compost into the soils enhanced their total porosity (TP) and field capacity (FC) across C, L, and SL soils. The compost application improved field capacity compared to the control group, with increases observed in clay soil from 4% to 11%, loam soil from 10% to 21%, and sandy loam soil from 19% to 27%. After 210 days of incubation, applying 6% VPC and 6% OPC increased overall porosity by 7.1% and 20.0%, respectively, with notable effects observed in clay and loam soils. In all three textures, the pore radius increased with 6% OPC and 6% VPC treatments. As a result of 6% OPC and VPC application, the hydraulic conductivity value of clay soil increased by 4.8 and 6.5 times, respectively, while it increased by 2.0 and 2.3 times in loam soil and 2.1 and 1.4 times in sandy loam soil, respectively, compared to the control.

Compost application increased the hydraulic conductivity value of clay textured soils and the field capacity value of sandy loam soils. Therefore, some negative physical properties of the soil due to its texture can be improved by compost application. Adding composts with high organic carbon content to the soil increased soil stability concerning the increase in total carbon content [22]. Since the obstacles that cause clogging of soil pores are eliminated, it can facilitate water movement in the soil by increasing porosity and, therefore, hydraulic conductivity in heavy textured soils with high clay content. A new study in which applying VPC and OPC at a rate of 6% will also be tested on plants under field conditions will benefit the widespread use of compost.

## Author Contributions

All the authors equally contributed to this work. This paper is derived from the first author's doctoral dissertation supervised by the second author. They all read and approved the final version of the paper.

## Conflicts of Interest

All the authors declare no conflict of interest.

## Ethical Review and Approval

No approval from the Board of Ethics is required.

## Acknowledgment

This study was supported by the Office of Scientific Research Projects Coordination at Çanakkale Onsekiz Mart University, Grant number: FDK-2018-1366, and the BET analyses were supported by the ÇOMÜ BAP FHD-2020-3405. We would also like to thank TUBITAK for supporting the BIDEB-2211-C PhD scholarship. The author would like to thank Dr Soner YİĞİT for his help with the statistical analysis.

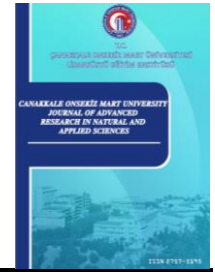
## References

- [1] M. Gavrilesco, *Water, soil and plants interactions in a threatened environment*, Water 13 (19) (2021) Article Number 2746 25 pages.
- [2] J. P. Van Leeuwen, T. Lehtinen, G. J. Lair, J. Bloem, L. Hemerik, K. V. Ragnarsdóttir, G. Gísladóttir, J. S. Newton, P. C. De Ruiter, *An ecosystem approach to assess soil quality in organically and conventionally managed farms in Iceland and Austria*, Soil 1 (1) (2015) 83–101.
- [3] E. C. Brevik, A. Cerdà, J. Mataix-Solera, L. Pereg, J. N. Quinton, J. Six, K. Van Oost, *The interdisciplinary nature of soil*, Soil, 1 (1) (2015) 117–129.
- [4] A. Vengadaramana, P. T. J Jashothan, *Effect of organic fertilizers on the water holding capacity of soil*

- in different terrains of Jaffna peninsula in Sri Lanka*, Journal of Natural Product and Plant Resources 2 (4) (2012) 500–503.
- [5] W. D. Reynolds, C. F. Drury, C. S. Tan, C. A. Fox, X. M. Yang, *Use of indicators and pore volume-function characteristics to quantify soil physical quality*, Geoderma 152 (3-4) (2009) 252–263.
- [6] M. Pagliai, N. Vignozzi, *The soil pore system as an indicator of soil quality*, Annals of arid zone 45 (3-4) (2006) 69–80.
- [7] P. Smith, J. I. House, M. Bustamante, J. Sobocká, R. Harper, G. Pan, T.A. Pugh, *Global change pressures on soils from land use and management*, Global Change Biology 22 (3) (2016) 1008–1028.
- [8] M. Castellini, M. Diacono, A. Preite, F. Montemurro, *Short-and medium-term effects of on-farm compost addition on the physical and hydraulic properties of a clay soil*, Agronomy 12 (6) (2022) Article Number 1446 16 pages.
- [9] M. Diacono, F. Montemurro, *Long-term effects of organic amendments on soil fertility*, Sustainable Agriculture (2) (2011) 761–786.
- [10] C. Mondini, P. Sequi, *Implication of soil C sequestration on sustainable agriculture and environment*, Waste Management 28 (4) 2008 678–684.
- [11] G. Adugna, *A review on impact of compost on soil properties, water use and crop productivity*, Academic Research Journal of Agricultural Science and Research 4 (3) (2016) 93–104.
- [12] M. Mahmoodabadi, B. Ahmadbeigi, *Dry and water-stable aggregates in different cultivation systems of arid region soils*, Arabian Journal of Geosciences 6 (8) (2013) 2997–3002.
- [13] Y. Le Bissonnais, D. Blavet, G. De Noni, J. Y. Laurent, J. Asseline, C. Chenu, *Erodibility of Mediterranean vineyard soils: Rardelevant aggregate stability methods and significant soil variables*, European Journal of Soil Science 58 (1) (2007) 188–195
- [14] D. Killi, Y. Kavdır, *Effects of olive solid waste and olive solid waste compost application on soil properties and growth of solanum lycopersicum*, International Biodeterioration and Biodegradation (82) (2013) 157–165.
- [15] F. Tambone, P. Genevini, F. Adani, *The effects of short-term compost application on soil chemical properties and on nutritional status of maize plant*, Compost Science and Utilization 15 (3) (2007) 176–183.
- [16] J. K. Whalen, H. Benslim, Y. Jiao, B. K. Sey, *Soil organic carbon and nitrogen pools as affected by compost applications to a sandy-loam soil in Québec*, Canadian Journal of Soil Science 88 (4) (2008) 443–450.
- [17] R. S. Mylavarapu, G. M. Zinati, *Improvement of soil properties using compost for optimum parsley production in sandy soils*, Scientia Horticulturae 120 (3) (2009) 426–430
- [18] M. J. Curtis, V. P. Claassen, *Compost incorporation increases plant available water in a drastically disturbed serpentine soil*, Soil Science 170 (12) (2005) 939–953.
- [19] T. T. Duong, C. Penfold, P. Marschner, *Differential effects of composts on properties of soils with different textures*, Biology and Fertility of Soils 48 (6) (2012) 699–707.
- [20] R. Sonnleitner, E. Lorbeer, F. Schinner, *Effects of straw, vegetable oil and whey on physical and microbiological properties of a chernozem*, Applied Soil Ecology 22 (3) (2003) 195–204.
- [21] M. Annabi, Y. Le Bissonnais, M. Le Villio-Poitrenaud, S. Houot, *Improvement of soil aggregate stability by repeated applications of organic amendments to a cultivated silty loam soil*, Agriculture, Ecosystems and Environment 144 (1) (2011) 382–389.

- [22] N. İşler, R. İlay, Y. Kavdir, *Temporal variations in soil aggregation following olive pomace and vineyard pruning waste compost applications on clay, loam, and sandy loam soils*, Environmental Monitoring and Assessment 194 (6) (2022) Article Number 418 17 pages.
- [23] Y. Yiğini, *Detailed soil survey, mapping and land evaluation of Çanakkale-Umurbey soils*, Master's Thesis Çanakkale Onsekiz Mart University (2006) Çanakkale.
- [24] N. Ünal, *Temporal effects of olive pomace and vineyard waste composts on the physical properties in soils of different texture*, Doctoral dissertation Çanakkale Onsekiz Mart University Graduate School (2020) Çanakkale.
- [25] Y. Kavdir, D. Killi, *Influence of olive oil solid waste applications on soil pH, electrical conductivity, soil nitrogen transformations, carbon content and aggregate stability*, Bioresource Technology 99 (7) (2008) 2326–2332.
- [26] Y. Kavdir, R. İlay, A.J. Smucker, İ. Kavdır, *Soil structure stabilization of olive oil solid waste and compost applied soils*, In International Soil Tillage Research Organization 18th Triennial Conference, İzmir, 2009.
- [27] L. A. Richards, (1954). *Diagnosis and Improvement of Saline and Alkali Soils*. US Department of Agriculture Handbook, US, 1954, pp. 60–94.
- [28] W. Kirsten, *Organic elemental analysis: Ultramicro, micro, and trace methods*, Elsevier, 1983.
- [29] H. D. Chapman, *Cation-exchange capacity*, Methods of Soil Analysis: Part 2 Chemical and Microbiological Properties 9 (1965) 891–901.
- [30] V. L. Singleton, J. A. Rossi, *Colorimetry of total phenolics with phosphomolybdic-phosphotungstic acid reagents*, American Journal of Enology and Viticulture 16 (3) (1965) 144–158.
- [31] J. T. Bremner, *Inorganic forms of nitrogen*, Methods of Soil Analysis: Part 2 Chemical and Microbiological Properties 9 (1965) 1179–1237.
- [32] G.W. Gee, J. W. Bauder, *Particle-size analysis*, 2nd Edition, American Society of Agronomy, Madison, 1986, pp. 383–411.
- [33] H. P. Blume, K. Stahr, P. Leinweber, *Bodenkundliches praktikum; Eine einfuhrung in pedologisches arbeiten fur ökologen, land-und forstwirte,geo-und umweltwissenschaftler*, Springer, Verlag 2011.
- [34] G. R. Blake, K. H. Hartge, *Bulk density*, Methods of soil analysis: Part 1 Physical and mineralogical methods 5 (1986) 363–375.
- [35] A. Klute, C. Dirksen, *Hydraulic conductivity and diffusivity*, Laboratory methods Methods of Soil Analysis: Part 1 Physical and Mineralogical Methods 5 (1986) 687–734.
- [36] P. H. Emmett, S. Brunauer, *The use of low temperature van der Waals adsorption isotherms in determining the surface area of iron synthetic ammonia catalysts*, Journal of the American Chemical Society 59 (8) (1937) 1553–1564.
- [37] S. Brown, M. Cotton, *Changes in soil properties and carbon content following compost application: Results of on-farm sampling*, Compost Science and Utilization 19 (2) (2011) 87–96.
- [38] V. V. Volk, C. H. Ullery, Department of Soil Science, Oregon State University, Corvallis, 1993, pp. 50.
- [39] M. Pagliai, N. Vignozzi, S. Pellegrini, *Soil structure and the effect of management practices*, Soil and Tillage Research 79 (2) (2004) 131–143.
- [40] B. D. Hudson, *Soil organic matter and available water capacity*, Journal of Soil and Water Conservation 49 (2) (1994) 189–194.
- [41] B. L. Leroy, M. S. K. Herath, S. De Neve, D. Gabriels, L. Bommele, D. Reheul, M. Moens, *Effect of*

- vegetable, fruit and garden (VFG) waste compost on soil physical properties, *Compost Science and Utilization* 16 (1) (2008) 43–51.
- [42] R. F. Gonzalez, L. R. Cooperband, *Compost effects on soil physical properties and field nursery production*, *Compost Science and Utilization* 10 (3) (2002) 226–237.
- [43] E. Arthur, W. M. Cornelis, J. Vermang, E. De Rucker, *Amending a loamy sand with three compost types: Impact on soil quality*, *Soil Use and Management* 27 (1) (2011) 116–123.
- [44] B. Liu, M. L. Gumpertz, S. Hu, J. B. Ristaino, *Long-term effects of organic and synthetic soil fertility amendments on soil microbial communities and the development of southern blight*, *Soil Biology and Biochemistry* 39 (9) (2007) 2302–2316.
- [45] E. S. G. Khater, *Some physical and chemical properties of compost*, *International Journal of Waste Resources* 5 (1) (2015) 1–5.
- [46] S. M. Aggelides, P. A. Londra, *Effects of compost produced from town wastes and sewage sludge on the physical properties of a loamy and a clay soil*, *Bioresource Technology* 71 (3) (2000) 253–259.
- [47] N. Teutscherova, E. Vazquez, D. Santana, M. Navas, A. Masaguer, M. Benito, *Influence of pruning waste compost maturity and biochar on carbon dynamics in acid soil: Incubation study*, *European Journal of Soil Biology* 78 (2017) 66–74.
- [48] V. Bagarello, M. Iovino, D. Elrick, *A simplified falling-head technique for rapid determination of field-saturated hydraulic conductivity*, *Soil Science Society of America Journal* 68 (1) (2004) 66–73.
- [49] V. M. Chowdary, M. D. Rao, C. S. Jaiswal, *Study of infiltration process under different experimental conditions*, *Agricultural Water Management* 83 (1–2) (2006) 69–78.
- [50] N. Yazdanpanah, M. Mahmoodabadi, A. Cerdà, *The impact of organic amendments on soil hydrology, structure and microbial respiration in semiarid lands*, *Geoderma* 266 (2016) 58–65.
- [51] N. Eibisch, W. Durner, M. Bechtold, R. Fuß, R. Mikutta, S. K. Woche, M. Helfrich, *Does water repellency of pyrochars and hydrochars counter their positive effects on soil hydraulic properties?*, *Geoderma* 245 (2015) 31–39.
- [52] A. U. Dogan, M. Dogan, M. Onal, Y. Sarikaya, A. Aburub, D. E. Wurster, *Baseline studies of the clay minerals society source clays: specific surface area by the Brunauer Emmett Teller (BET) method*, *Clays and Clay Minerals* 54 (1) (2006) 62–66.



# Sustainable Self-Healing Coatings: Optimizing Microencapsulation of Biodegradable Linseed and Hemp Seed Oils for Enhanced Corrosion Protection

Merve Mocan<sup>1</sup> , Nazife Bengisu Sarıkaya<sup>2</sup> 

<sup>1</sup>Department of Materials Science and Engineering, Faculty of Engineering, Gebze Technical University, Kocaeli, Türkiye

<sup>2</sup>Department of Bioengineering, Faculty of Engineering, Gebze Technical University, Kocaeli, Türkiye

## Article Info

Received: 06 Sep 202x

Accepted: 09 Dec 2024

Published: 31 Dec 2024

Research Article

**Abstract** – Corrosion is one of the biggest challenges in metal surfaces, especially when scratches and impacts damage the coating. Self-healing agents in the coating ensure long-term protection, effectively shielding the metal from corrosion. However, these materials are not environmentally friendly in general. To improve sustainability, we propose encapsulating renewable and biodegradable natural drying oils (linseed and hemp seed oils) to enhance the self-healing properties of the coatings. In-situ polymerization of these urea-formaldehyde microcapsules was performed at 60 °C using different stirring rates (200, 300, and 400 rpm). The structural, morphological, and thermal analyses were carried out by using Fourier Transform Infrared Spectrometer (FTIR), Scanning Electron Microscope (SEM), and Thermogravimetric Analysis (TGA). The particle size and oil content measurements were also performed. It was observed that a 300-rpm stirring rate resulted in optimum morphology, particle size, and oil content. 10 wt% microcapsules containing pure epoxy coatings were successfully applied to metal surfaces. It was observed that coatings with microcapsules provided better surface protection compared to pure coatings, and linseed oil-loaded microcapsules outperformed hemp seed oil-loaded microcapsules. These materials hold promise for future self-healing applications that are both effective and environmentally friendly.

**Keywords** – Corrosion protection, self-healing, encapsulation, urea-formaldehyde microcapsules, drying oils

## 1. Introduction

Metals are used in many fields, such as chemistry, industry, transportation, construction, paint, electronics, and medical implants. The main problem for metals is surface wear or corrosion, which destroys the surface [1]. In 2013, the global cost of corrosion was estimated at US\$2.5 trillion, representing 3.4% of the worldwide gross domestic product, the total value of goods and services produced worldwide within a year [2]. This situation creates a major economic problem and leads to environmental destruction. Corrosion contaminates nature, water, and air, accumulates in nature, and threatens the health of living beings [3]. Coating, painting, and lubrication have been used to reduce the effects of damage caused by corrosion on the material corrosion [4]. However, if the surface is damaged in any way, the exposed metal will inevitably corrode. In recent years, self-healing polymer coating systems, inspired by living organisms' self-healing mechanisms, have been used to prevent corrosion and extend the life of metal surfaces. Self-healing agents, encapsulated in micron-sized capsules, are protected from degradation and uniformly distributed across the surface. Promising results have

<sup>1</sup>mmocan@gtu.edu.tr (Corresponding Author); <sup>2</sup>bengisusarikaya@gmail.com

been achieved with self-healing polymers in preventing surface corrosion caused by wear over time [5], mainly through methods that involve breaking the bonds of an encapsulated polymer and filling them with the help of a crosslinker [6], frequently used to develop technologies aimed at extending material longevity. Self-healing coating using various polymers is used in many sectors, such as agriculture, food, packaging, biomedical, metal, and electronics [7]. Product examples include cell phones, varnishes, boat hulls, and adhesives [8].

Using bio-based and biodegradable materials tackles waste management challenges at the end of their lifecycle and significantly lowers the carbon footprint by maintaining a closed carbon cycle. With this objective, catalyst-free, natural drying oils, and non-toxic polymers are offered to achieve a successful self-healing system. Urea-formaldehyde (UF) microcapsules, with self-healing properties to prevent corrosion of metal surfaces, were synthesized that contain natural oils, linseed oil, and hemp seed oil, produced from linseeds and hemp seeds (Figure 1), can be oxidized at room temperature. The reasons for using urea-formaldehyde as a capsule shell include impermeability, flexibility, good penetration resistance, and durability [9]. Epoxy is widely used to coat metal surfaces. Linseed oil, a frequently used drying oil, has a high molecular weight and high fatty acid content and was selected as a curing agent by completing cross-linked polymerization in a short time [10]. Hemp seed oil, extracted from hemp seeds, is reported as a successful material to prevent corrosion [11].



**Figure 1.** (a) Linseed and (b) hemp seed, whose oils serve as natural self-healing agents in the study

The microcapsules were synthesized via in-situ polymerization using stirring rates of 200, 300, and 400 rpm, and their particle size, oil content, and structural, morphological, and thermal properties were analyzed. Based on these evaluations, an optimal stirring rate of 300 rpm was determined. The self-healing properties of the oil-filled microcapsules were assessed using a salt spray test, demonstrating that the epoxy coating with microcapsules effectively prevented corrosion compared to the pure epoxy coating. As the materials used were easily accessible and inexpensive, it has high potential for rapid realization in industrial applications. These materials can be used in many applications, such as metals, electronics, artificial tissue, and implants.

## 2. Materials and Methods

Polyvinyl alcohol (PVA) (partially hydrolyzed, %85-89) was kindly provided from Beta Kimya AŞ. Sodium dodecyl sulfate (SDS) (%90) was purchased from Sigma-Aldrich, USA. Urea (99%), ammonium chloride (99%), and formaldehyde (37 wt% aq) were purchased from ISOLAB, Germany. Resorcinol (98%), NaOH and HCl (37%) were purchased from Merck, Germany. Slim as epoxy resin and its hardener (used a 2:1 (v/v) ratio) were purchased from Resinin, Mersin, Türkiye. Linseed oil and hemp seed oil were purchased from Mecitefendi, İzmir, Türkiye. All chemicals were used without any purification.

### 2.1. Synthesis of the Urea-Formaldehyde Microcapsules

Based on the study of Abdipour et al. [12], UF-based microcapsules were synthesized by in-situ polymerization in an oil-in-water emulsion. First, 0.5 g of PVA was dissolved in 300 mL of water in a 500 ml round flask with

two necks at 60 °C. Heating was stopped. 0.15 g of SDS was added. PVA particles were mixed at a certain mixing rate for 2 hours -three alternative mixing rates (200, 300, and 400 rpm). Then, the solution received 5 g urea, 0.5 g resorcinol, and 0.5 g of ammonium chloride. By using aqueous solutions of 0.1 N NaOH and 0.1 N HCl, the pH was adjusted to 3.5. 15 mL of linseed oil or 15 mL of hemp seed oil were introduced with a micropipette at a 1 ml/min rate to create an emulsion, which was then allowed to stabilize for 15 minutes. To keep the molar ratio of formaldehyde to urea to 1.9:1, 11.8 mL of formaldehyde solution was added to the emulsion [13]. The reaction medium was slowly heated to 55 °C and kept at this temperature for 4 h [14]. The suspension was then cooled to room temperature. After phase separation, vacuum filtration isolated the capsules from the suspension. They were then rinsed with distilled water and xylene to eliminate residual impurities. The microcapsules were stored in an xylene and distilled water (1:2 by volume) emulsion to prevent agglomeration.

## 2.2. Determination of Oil Content in the Microcapsules

The amount of core material (healing agent) in the microcapsules was measured using the extraction method [15]. For this purpose, 1 g of microcapsules ( $m_1$ ) were mixed with 10 mL acetone and sonicated for 1 min. The suspension was passed through ultrafine filter paper to remove the remaining shell materials. The filtrate was then rinsed several times with acetone and dried in a vacuum oven at 40 °C until steady mass ( $m_2$ ). (2.1) was used to calculate oil content.

$$\text{Oil content (\%)} = \frac{m_1 - m_2}{m_1} 100 \quad (2.1)$$

## 2.3. Preparation of Epoxy Resin Coating and Salt Spray Test

At ambient temperature, microcapsules (10 wt%) were transferred into the uncured epoxy resin and stirred using a glass stirrer for 5 min slowly to prevent the formation of bubbles until the microcapsules were homogeneously distributed. Before the coatings were applied, the metals were cleaned using a metallography sample-sanding and polishing device. The microcapsule in epoxy was spread on the metal specimens slowly without causing air bubbles. The specimens were maintained at room temperature for 6 h, then cured for 1 h at 80 °C. A pure epoxy resin coating was prepared as a control sample. Three repeated incisions at three different depths were made on a metal sheet with a scalpel to observe the self-healing mechanism. A salt spray test was then performed. A 5 wt% saline solution was sprayed on the metal sheet at regular intervals as to be 4 times a day for 4 days to assess the corrosion resistance of the coated sheets, which was a rather high salt percentage (sea water salt percentage: 3.5%) to simulate harsh conditions and accelerate the rusting. As the desired level of corrosion had not been achieved, the experiment was repeated with deeper cuts after 4 days to further accelerate the rusting process.

## 2.4. Characterization

A Phillips XL30 SFEG scanning electron microscope determined the surface morphology of the samples. A gold layer was coated onto all samples to minimize charging effects and then analyzed at an accelerating voltage of 15 kV. To ensure comprehensive imaging, at least three separate areas were assessed. Linseed and hemp seed oil-loaded UF capsules' thermal stability was characterized using Mettler Toledo TGA/SDTA851e. The heating rate was 10 °C/min in the 20 – 720 °C temperature range. Particle size was determined using a Malvern particle-size analyzer. Structural analyses of the oils and oil-loaded microcapsules were carried out using a Perkin Elmer 100 FTIR spectrometer. An optical microscope was used to determine the distribution of the microcapsules in the epoxy coating, releasing the oil after forming the scratch on the coating.

### 3. Results and Discussion

#### 3.1. Microcapsules at Different Phases

The text linseed oil and hemp seed oil containing microcapsules can be denoted as KT and KV, respectively. The numbers beside them express the rpm value at which the microcapsules were synthesized. First, the microcapsules were characterized at the top and bottom phases in a 1:2 emulsion of xylene and water (Figure 2) (Top phase: xylene, bottom phase: water). Particle sizes at the phases were investigated at the stirring rate of 300 rpm. The following characterizations will further discuss the reason for selecting this stirring rate.

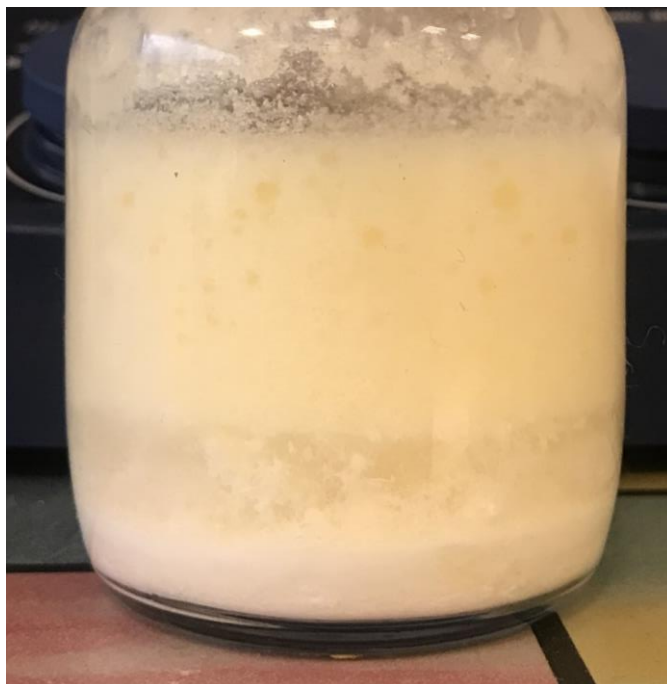


**Figure 2.** The general appearance of hemp-containing microcapsules in xylene-water emulsion.

Based on the general appearance of the microcapsules (Figure 1), regardless of the oil type used, the xylene phase contained a greater quantity of microcapsules, which appeared more yellowish, likely due to the oil content. In contrast, the lower phase (water) had fewer microcapsules, and they exhibited a whiter color.

Particle size analysis of the phases, as shown in Table 1, revealed some significant differences. The top phase of linseed oil and hemp seed oil microcapsules had average particle sizes of 80.73  $\mu\text{m}$  and 120.18  $\mu\text{m}$ , respectively, while the lower phase of microcapsules measured 39.14  $\mu\text{m}$  and 14.46  $\mu\text{m}$ . SEM images (Figure 3) also revealed the size and shape differences of the microcapsules at the top and bottom phases. It was observed that the capsules at the top had larger particle sizes, which can enable more oil storage, which is crucial for enhancing their crack-sealing capability in the study. In contrast, smaller particles at the bottom of the solution may be less effective in storing oil. Therefore, the microcapsules at the xylene phase were chosen for further characterization.

**Table 1.** Particle size of synthesized capsules at different positions in the solution

Capsule Location	Particle Size ( $\mu\text{m}$ )
Linseed top oil phase	80.62 $\pm$ 4.17
Linseed oil bottom phase	39.14 $\pm$ 4.05
Hemp seed oil top phase	120.18 $\pm$ 18.71
Hemp seed oil bottom phase	14.46 $\pm$ 6.94

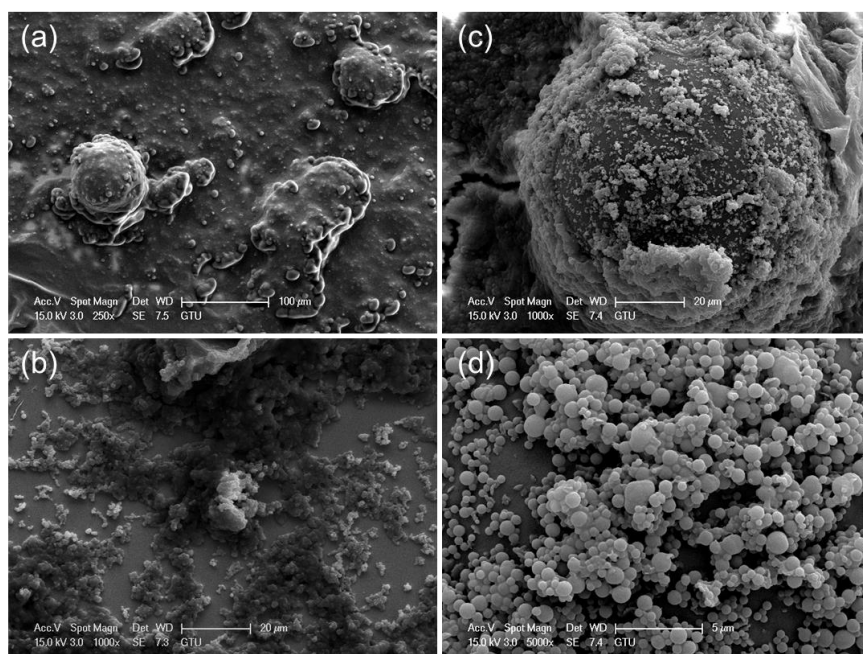


**Figure 3.** SEM images of (a, b) linseed oil and (c, d) hemp oil-loaded microcapsules at the (a, c) top phase and (b, d) bottom phase, respectively

### 3.2. Chemical Structure of the Microcapsules and Oils

The FTIR spectrophotometer performed the structural analysis of the microcapsule materials. Here, FTIR peaks of microcapsules filled with linseed oil and hemp seed oil prepared at 300 rpm were obtained as precisely overlapping each other (Figure 4). The peaks of the microcapsules matched well with urea-formaldehyde resin where the peak at  $3300\text{ cm}^{-1}$  is the N-H stretching, the peaks between  $2850\text{--}2972\text{ cm}^{-1}$  correspond to CH stretching of  $\text{CH}_2$ ,  $\text{CH}_2\text{OH}$ , and  $\text{N-CH}_2$ , the peak at  $1741\text{ cm}^{-1}$  occurs due to  $\text{C=O}$  stretching of formaldehyde (also that of linseed oil), the peaks at  $1616$  and  $1535\text{ cm}^{-1}$  are results of  $\text{C=O}$  stretching of amide I and  $\text{C-N}$  and  $\text{N-H}$  deformation of amide II,  $1372$  and  $1240\text{ cm}^{-1}$  peaks belong to  $\text{C-H}$  stretching and  $\text{OH}$  deformation of  $\text{CH}_2\text{OH}$  group.  $1158\text{ cm}^{-1}$  is due to asymmetric stretching of  $\text{N-CH}_2$  (and also probably the  $\text{C-O}$ -group of oil [16]), and  $1016\text{ cm}^{-1}$  occurs because of  $\text{C-O}$  stretching in the methyl group [17]. Plus, as the microcapsules were crashed during FTIR analysis, the peaks belonging to oils were also visible, such as  $731$ ,  $1108$ , and  $1450\text{ cm}^{-1}$  (shown in red) as being the corresponding peaks of  $\text{cis CH=CH}$  (of linseed oil),  $\text{C-O}$  and  $\text{CH}_3$  groups of the oils [16].

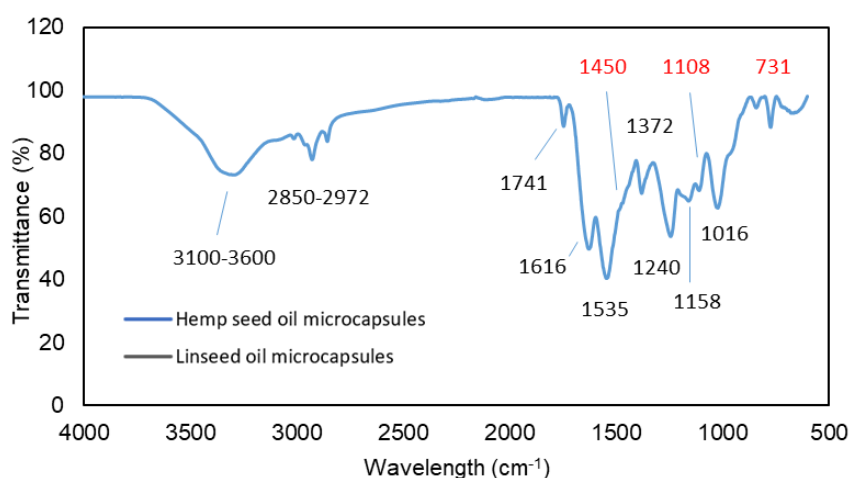


**Figure 4.** FTIR spectrum of UF microcapsules filled with hemp seed oil and linseed oil prepared at 300 rpm. peaks shown in red belong to oils only

Linseed and hemp seed oil were also structurally characterized (Figure 5). The oils contained the same characteristic peaks on the spectrum where  $2971\text{ cm}^{-1}$ ,  $2918$ , and  $2850\text{ cm}^{-1}$  peaks correspond to the vibrations of  $=\text{C-H}$ ,  $-\text{CH}_3$ , and  $-\text{CH}_2-$  bonds, respectively.  $1746\text{ cm}^{-1}$  peak is the  $\text{C=O}$  stretching,  $1640\text{ cm}^{-1}$  peak occurs because of the unsaturated  $\text{C=C}$  bonds,  $1366$  and  $1451\text{ cm}^{-1}$  peaks belong to  $-\text{CH}_3$  groups,  $1161\text{ cm}^{-1}$  peak belong to  $\text{C-O-}$  group,  $722\text{ cm}^{-1}$  is the vibration of *cis*  $\text{CH=CH}$  double bonds [16] which was shifted to  $731\text{ cm}^{-1}$  in the UF capsule.

The slight difference between linseed oil and hemp seed oil is the peak at  $722$  and a bump on the  $755$  peak as the vibration of *cis*  $\text{CH=CH}$  bonds [16] and  $=\text{CH}$  bending [18] occurring due to the double bonds that exist in the fatty acid structure. This difference is probably because of the difference in the fatty acid type and content of the oils. Linseed oil contains more linolenic acid with three double bonds. In contrast, hemp seed contains more linoleic acid that has two double bonds (Linseed oil: 53.21% linolenic acid, 17.25% linoleic acid, 18.51% oleic acid, etc. [19]. Hemp seed oil: 58.71% linoleic acid, 16.81% linolenic acid, 13.05% oleic acid, etc. [20]) linseed oil had slightly showed higher intensity of those mentioned peaks.

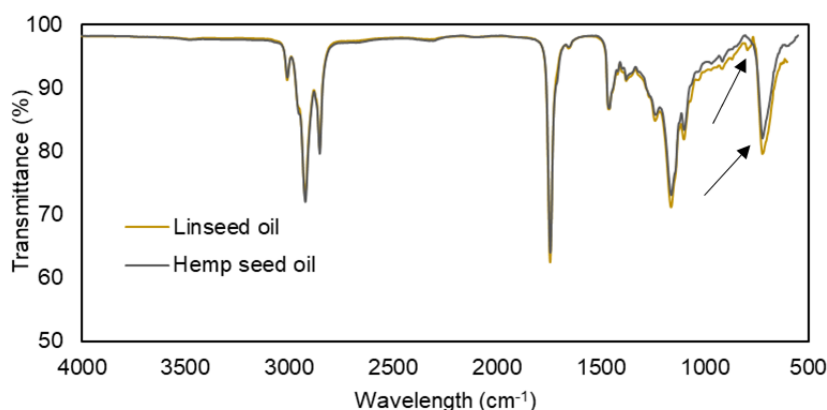


**Figure 5.** FTIR spectra of linseed oil and hemp seed oil

### 3.3. Effect of Stirring Rate

#### 3.3.1. Structural Properties

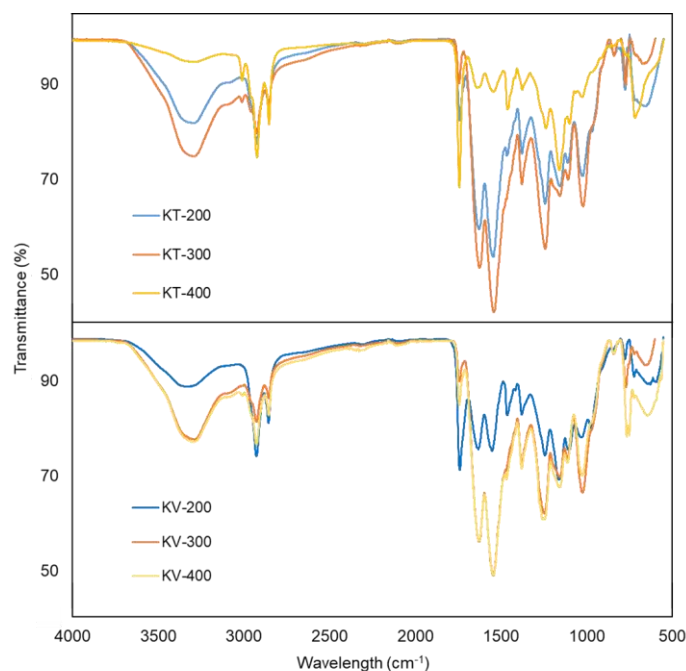


**Figure 6.** FTIR spectra of linseed oil (up) and hemp seed oil (down) containing microcapsules prepared at different stirring rates

The effect of stirring rate on the structural properties of the microcapsules is given in Figure 6. For this, we focus on the peaks  $3000\text{--}3500\text{ cm}^{-1}$  and  $1740\text{ cm}^{-1}$  belonging to the N-H group of UF resin and C=O oil group stated earlier. For linseed oil containing microcapsules, more oil was observed for microcapsules prepared at 400 rpm than other stirring rates. The least amount of oil and the highest amount of UF was observed for KT-300, which may indicate strong cross-linking of UF microcapsule. (The analysis of oil percentage will be further discussed.) For hemp seed oil containing microcapsules, while similar results were obtained for 300 and 400 rpm, the highest amount of oil was observed for 200 rpm samples.

### 3.3.2. Morphology and Particle Size Distribution

On the self-healing ability, microcapsules should have a spherical morphology with an oil-containing core and a stable particle size. The effect of stirring rates on the morphology of the linseed and hempseed-containing microcapsules is shown in Figure 7. At 200 rpm, the linseed oil microcapsules appeared as rather large chunks, and upon magnification, some bumps were visible, which may indicate combined microcapsules. At 400 rpm, instead of chunks, large and combined spheres were observed, and close magnification revealed a broad oily surface with no distinct microcapsules, indicating that no microcapsules were formed to store the oil, which is consistent with the high oil content observed in the FTIR analysis for this sample. However, at 300 rpm, the desired spherical microcapsules were achieved with sizes that were consistent with each other. For hemp seed oil containing microcapsule preparation, large spheres were formed for both 200 and 400 rpm stirring rates, a close magnification showed no small microcapsule formations on these spheres. Whereas, like linseed microcapsules, the 300 rpm stirring rate also resulted in spherical microcapsule formations. However, hemp seed oil microcapsules exhibited some size variation and appeared stickier than those in the linseed oil system. SEM findings revealed that the microcapsules produced at a stirring rate of 300 rpm were more homogeneously distributed and spherical. This successful microcapsule formation enables efficient release of the agents thereby enhancing the self-healing performance of the coating.

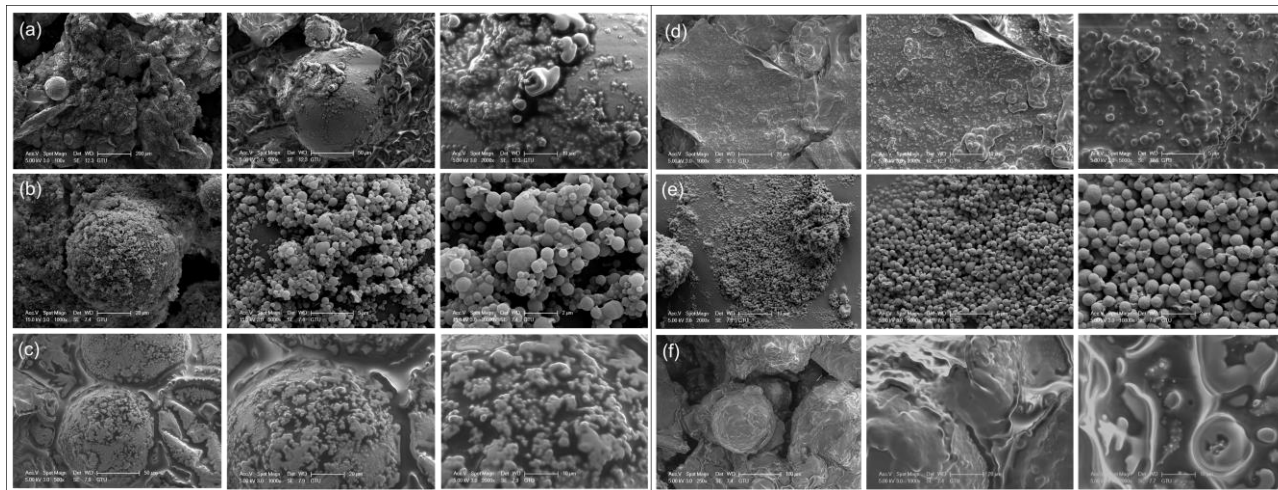


**Figure 7.** SEM images of linseed oil-loaded capsules at (a) 200, (b) 300, (c) 400 rpm and hemp seed oil-loaded capsules at (d) 200, (e) 300, (f) 400 rpm

The particle size analysis of the microcapsules prepared at different stirring rates is given in Figure 8. For both oil systems, 200 and 400 rpm produced larger microcapsules (or urea-formaldehyde resins in various forms) with greater size variability, as confirmed by SEM images where larger chunks were predominantly observed and at 300 rpm linseed and hemp seed oil containing microcapsules resulted in sizes of  $77.25\text{ }\mu\text{m}$  and  $116.30\text{ }\mu\text{m}$ , respectively, where hemp seed oil microcapsules showed a larger deviation which was also detected in SEM images. These size differences are also supported by the optical microscope images of KT-300 and KV-300, distributed in an epoxy matrix, in Figure 9, where linseed oil microcapsules are smaller than hemp seed oil microcapsules. Here, the oil in the microcapsules also appears clearly as a light hue.

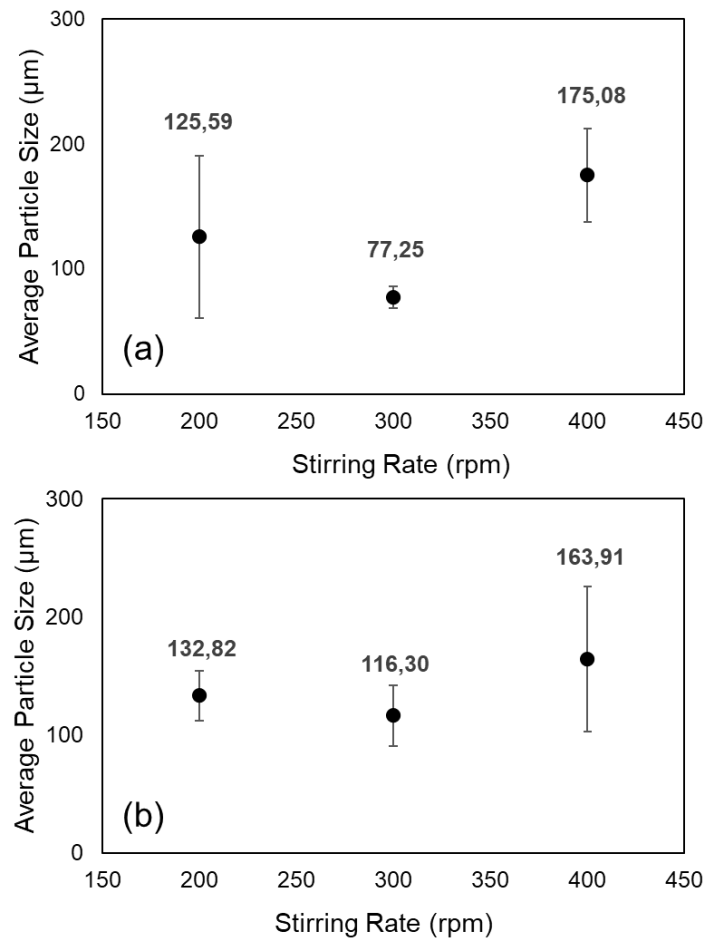


**Figure 8.** Average particle sizes of the (a) linseed oil and (b) hemp seed oil-loaded microcapsules prepared at 200, 300, and 400 rpm

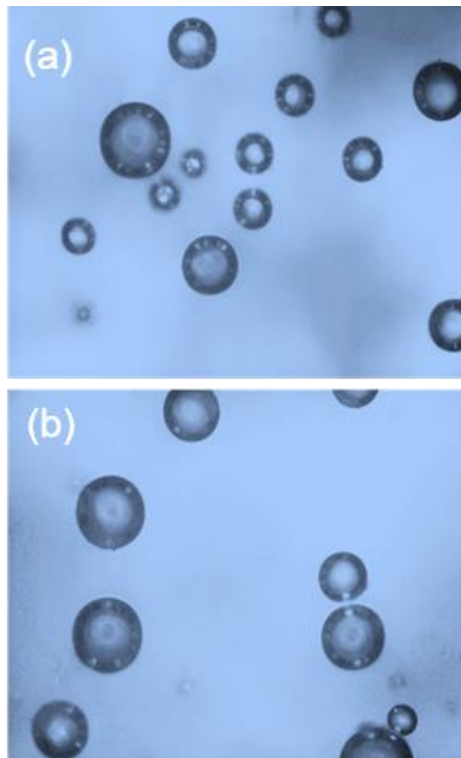


**Figure 9.** Optical microscope images of (a) linseed oil and (b) hemp seed oil-filled microcapsules prepared at 300 rpm distributed in epoxy ( $\times 50$  magnification)

In the study of Behzadnasab and colleagues, synthesis was performed at 500-1500 rpm, and microcapsules of 16-181  $\mu\text{m}$  sizes were obtained [21]. Abdipour and colleagues report stirring rate from 300 to 900 rpm decreased particle sizes from 74 to 62  $\mu\text{m}$  [12]. Hatami Boura and colleagues show that 400 rpm and 600 rpm stirring rates resulted in 75 and 50  $\mu\text{m}$ . However, only two stirring rates were tested [22]. While the particle size decrease between 200 and 300 rpm aligns with previous studies, an increase in microcapsule size was observed at 400 rpm. These findings suggest an optimal stirring rate beyond which particle size begins to increase. SEM images of the synthesis at 400 rpm indicate that deformation and probably agglomeration occurred in the microcapsules, increasing particle size. Icduygu and colleagues indicate that at high stirring rates, the frequency and intensity of collisions between microcapsules increase during encapsulation, leading to agglomeration [23]. As a result, to prevent agglomeration and ensure successful microcapsule formation, it was found that an optimal stirring rate is essential.

### 3.3.3. Oil Content of the Microcapsules

**Table 2.** The oil content of microparticles, both linseed oil (KT) and hemp seed oil (KV)-loaded microcapsules at 200, 300, and 400 rpm

Capsule Type	Oil (%)
KT-200	7.56
KT-300	65.00
KT-400	63.52
KV-200	9.46
KV-300	68.15
KV-400	52.05

The oil content of microcapsules is crucial for effective self-healing performance and should be maximized in well-formed, cross-linked spherical microcapsules. According to the results in Table 2, for both oil systems, the lowest oil content belonged to the 200-rpm stirring rate, which is less than 10%. This low oil content was also confirmed in the FTIR spectrum of hemp seed oil containing microcapsules prepared at 200 rpm. However, when the stirring rate was increased to 300 rpm, the oil content significantly rose to 65% and 68.15%, representing significant increases of 740% and 620% for linseed and hemp seed oil-loaded microcapsules compared to those prepared at 200 rpm. This is expected, as a properly cross-linked microcapsule structure was achieved (SEM images) at the stirring rate of 300 rpm, allowing maximum oil storage. The oil content difference between linseed oil and hemp seed oil-loaded microcapsules at 300 rpm may be due to their particle size reported earlier (77.25 and 116.30  $\mu\text{m}$ , respectively), as larger particles can capture more oil inside. KT-400 and KV-400 also contain rather high amounts of oil. However, according to SEM images, this oil is probably not properly trapped in microcapsules, as the obtained microstructures were more likely disordered. Abdipour and colleagues achieved oil contents ranging from 60% to 90% at stirring speeds of 300 to 900 rpm [12]. Behzadnasab and colleagues reported oil contents between 63% and 77% for stirring rates of 500 to 1500 rpm in linseed oil-urea formaldehyde microcapsules [21]. Both studies demonstrated that oil content was inversely proportional to the stirring rates used during encapsulation. Here, similar to the microcapsule size situation, an optimum stirring rate (300 rpm) was found for maximum oil content (65% and 68% for linseed and hemp seed oil-loaded microcapsules, respectively) in the microcapsules.

### 3.3.4. Thermal Properties

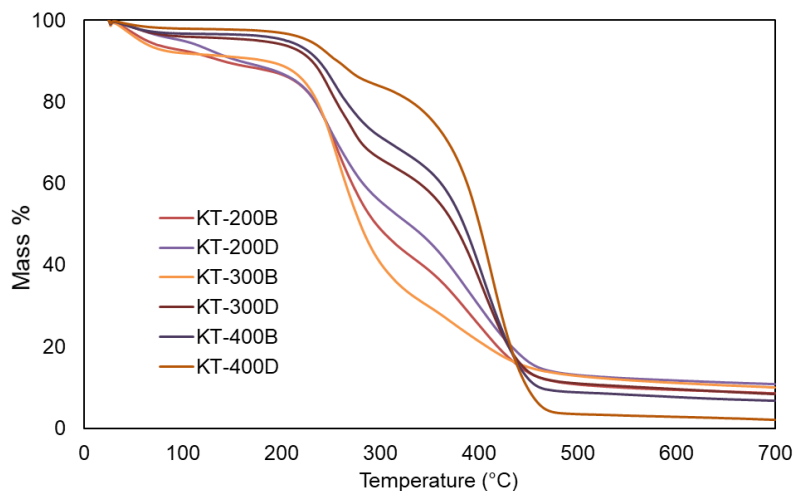


**Figure 10.** TGA thermograms of linseed oil containing microcapsules prepared at different stirring rates (extracted shells: B and non-extracted microcapsules: D)

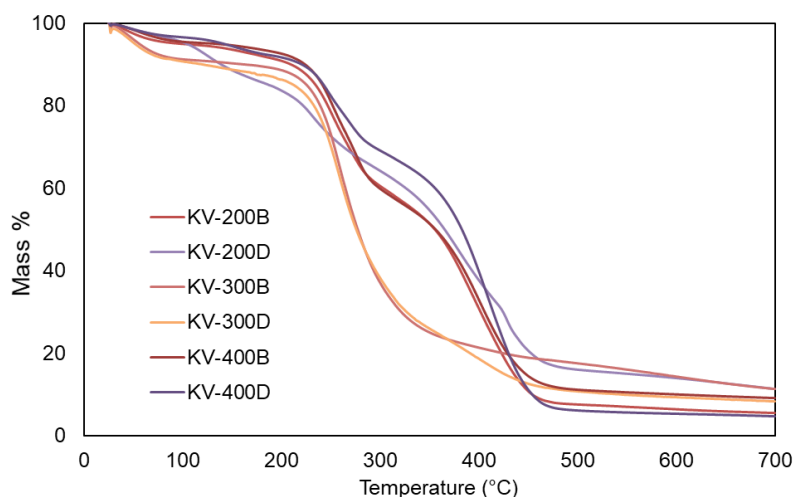


**Figure 11.** TGA thermograms of hemp seed oil containing microcapsules prepared at different stirring rates (extracted shells: B and non-extracted microcapsules: D)

Thermal degradation results of UF microcapsules (D), extracted UF shells (B) prepared with linseed oil (KT), and hemp seed oil (KV) as a function of stirring are given in Figures 10 and 11. The degradation of microcapsules consists of three steps—mass loss around 100 °C results from evaporation of water and unreacted formaldehyde. The mass loss between 200–300 °C is because of the evaporation of formaldehyde in the microcapsules. The degradation between 300 and 400 °C is probably due to the evaporation of hemp seed and linseed oils, as their boiling points are around 316 °C. The following mass loss after 400 °C is because of the oxidative removal of nitrogen, oxygen, hydrogen, and other elements, leading to the carbonization of the cross-linked UF shell. [24]

Although Yang et al., who reported the microencapsulation of isophorone diisocyanate, found similar thermal properties for all microcapsules prepared at different stirring rates, we observed apparent changes in the thermal stability as a function of stirring rates. [25] For microcapsules containing linseed oil, a noticeable difference was observed for each stirring rate between the oil-containing and extracted microcapsules, with the oil-containing microcapsules exhibiting higher thermal stability at 300–400 °C. When we investigate thermal stability as the shift of the initial degradation temperatures, except the extracted shell of KT-300, there is an increasing thermal stability trend with the increasing rpm values. For hemp seed oil containing

microcapsules, similarly, microcapsules prepared at 400 rpm had higher initial degradation temperatures (so higher thermal stability) than those prepared at 300 rpm. However, the results for microcapsules prepared at 200 rpm were less stable than those for linseed oil microcapsules. This instability is likely due to the improper formation of spherical microcapsules and the significantly lower oil content than those prepared at 300 and 400 rpm. A suitable amount of oil in the microcapsules with proper spherical structure guarantees a sufficient healing agent to discharge and repair cracks.

Both for microcapsules prepared with linseed and hemp seed oils at 300 rpm, the mass loss characteristic of oils at 300–400 °C was less observable compared to microcapsules prepared at other stirring rates, probably because the optimum cross-linking degree and higher thickness resulted in the strong entrapment of oil inside the UF microcapsules. For both oil systems, the stirring rate of 400 rpm resulted in the lowest mass loss at the same degradation temperature region. This is likely due to the failure to achieve a properly spherical microcapsule structure at this specific stirring rate and high oil content, leading to the easy release (or already exposed) of oil on the UF surface.

### 3.4. Evaluation of Self-Healing Process

Based on the previous findings, microcapsules prepared at 300 rpm were chosen for self-healing studies. 10 wt% of capsules were mixed into the epoxy coating, and optical microscopy was used to examine their distribution (Figure 12). After mixing with epoxy, the microcapsules retained their spherical shape and oil core within the coating. Additionally, linseed oil-loaded microcapsules (Figure 12a) demonstrated better distribution in the epoxy matrix than hemp seed oil-loaded microcapsules (Figure 12b).

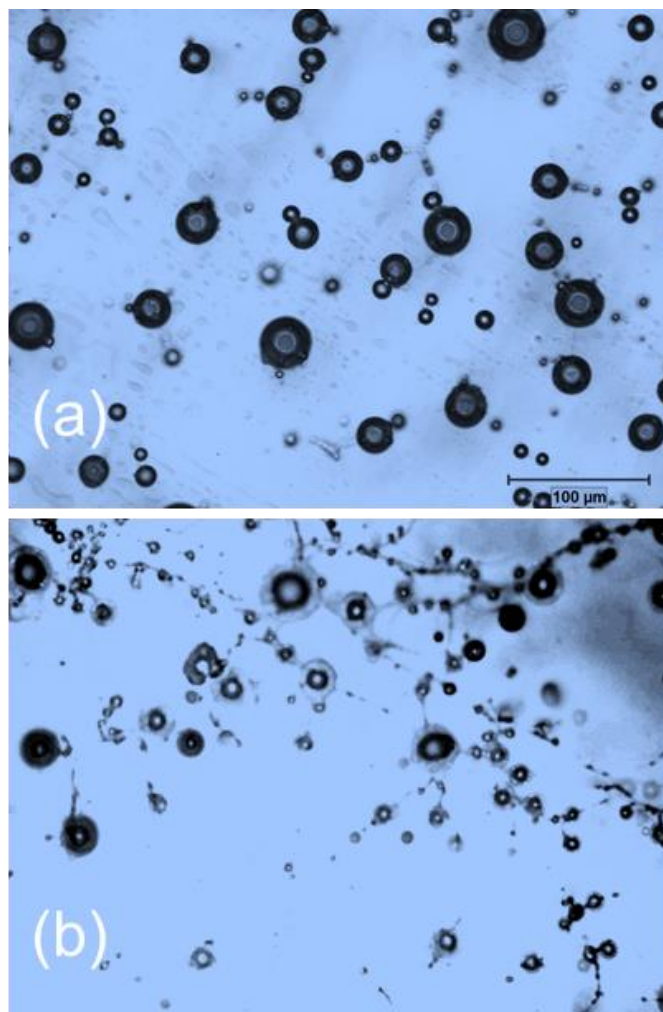


**Figure 12.** Optical microscope images of 10% (a) KT-300 and (b) KV-300 capsules in epoxy coatings, respectively

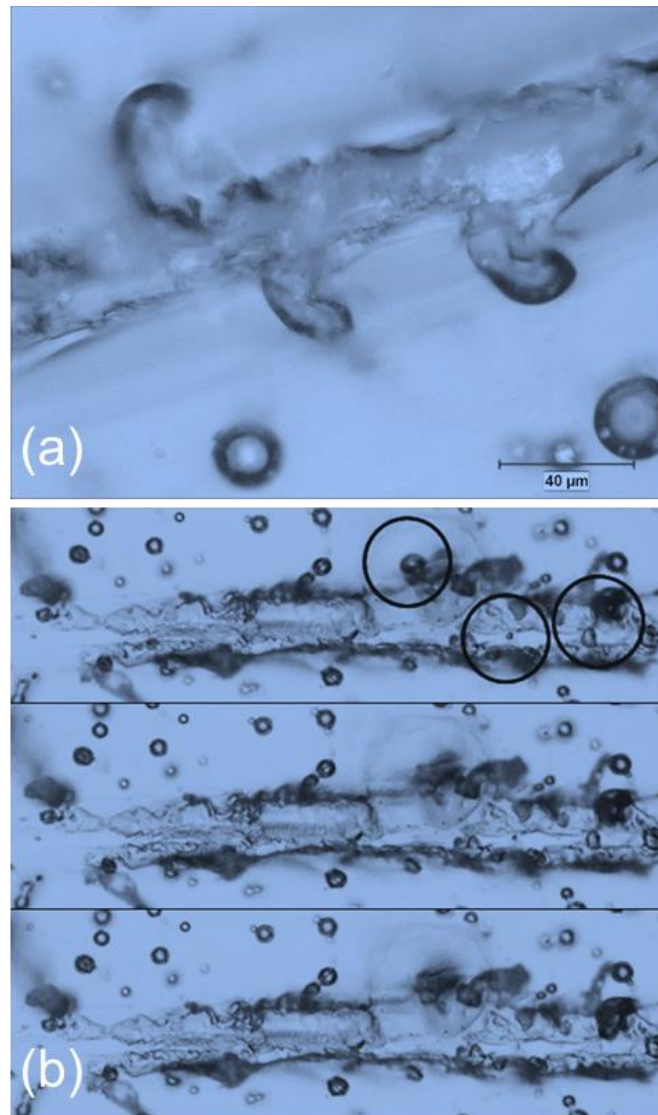


**Figure 13.** (a) The moment at which oil is released after scratching the epoxy surface containing linseed oil-loaded microcapsules. (b) Optical microscope images of coating filled with hemp oil-loaded microcapsules were taken during 20 minutes of observation after the scratch

Under optical microscopy, the incision in the coatings was observed in (Figure 13a). After the scratch, the oil was released as some microcapsules burst and disrupted their shell structure, causing the oil to escape gradually due to internal pressure (Figure 13b). Once the capsules are broken, oils are released and fill the scratch. After that, oil oxidation occurs. Since hemp seed and linseed oils are drying oils, the oil oxidizes in the air to form a protective layer in the scratch. The self-healing properties of the coating are achieved through the function of these natural oils. However, not all regions contained microcapsules. Proper distribution and quantity of capsules in self-healing coatings are crucial, as uneven dispersion can result in areas that lack self-healing capability [26].

### 3.4.1. Salt Spray Test

A salt spray test was conducted to visually assess the self-healing performance to induce corrosion on the coatings. For this, manual scratches were applied to coatings prepared with either only epoxy coating as a control epoxy coating containing 10% linseed and hemp seed oil microcapsules, separately (Figure 14). On the second day of the test, rust started to appear on areas without epoxy coating, while only small rust spots were observed on the inner parts of the pure epoxy coating. In contrast, the coatings with microcapsules did not show such rust formation. On the fourth day of the salt test, rust began to appear at the scratches on the

pure epoxy coating, while no rust was observed on the coatings prepared with both linseed oil and hemp seed oil loaded microcapsules. All microcapsule-containing coatings effectively prevented corrosion in the salt-spray test compared to epoxy coatings without capsules.

After the first four days, the corrosion experiment was continued by applying deeper cuts to the existing ones to accelerate the rusting process. As previously mentioned, this salt concentration exceeds seawater's, effectively simulating harsh conditions. On day eight, rust was severe across all samples, with noticeable rust around the scratches on the pure epoxy coating. It was also observed that linseed oil-containing microcapsules performed better, as one of the samples showed no rust on the scratches except at the edges where there was no coating. In contrast, rust was more extensive around the scratches on the hemp seed oil-containing microcapsules.

In the study conducted by Behzadnasab and colleagues, where linseed oil microcapsules were incorporated into an epoxy coating, it was observed that after 6 days of salt spray testing, rust formation was significantly reduced in samples containing 10% microcapsules compared to those without microcapsules or with 5% microcapsule content [21]. In the study by Hamed Abdipour and colleagues, corrosion began within 3 days [12]. Similarly, in the Hatami Boura and colleagues' study, visible degradation was observed after 5 days [22]. This study observed no rusting in the scratches for up to 4 days, except in the epoxy coating without microcapsules. However, the 5th day of the test was not monitored, and deeper cuts were applied after the 4th day. These results indicate that the encapsulated coatings were more effective at preventing rust than coatings without microcapsules. The layer of dried oil isolates the metal substrate from direct contact with the environment, thereby protecting it from corrosion.

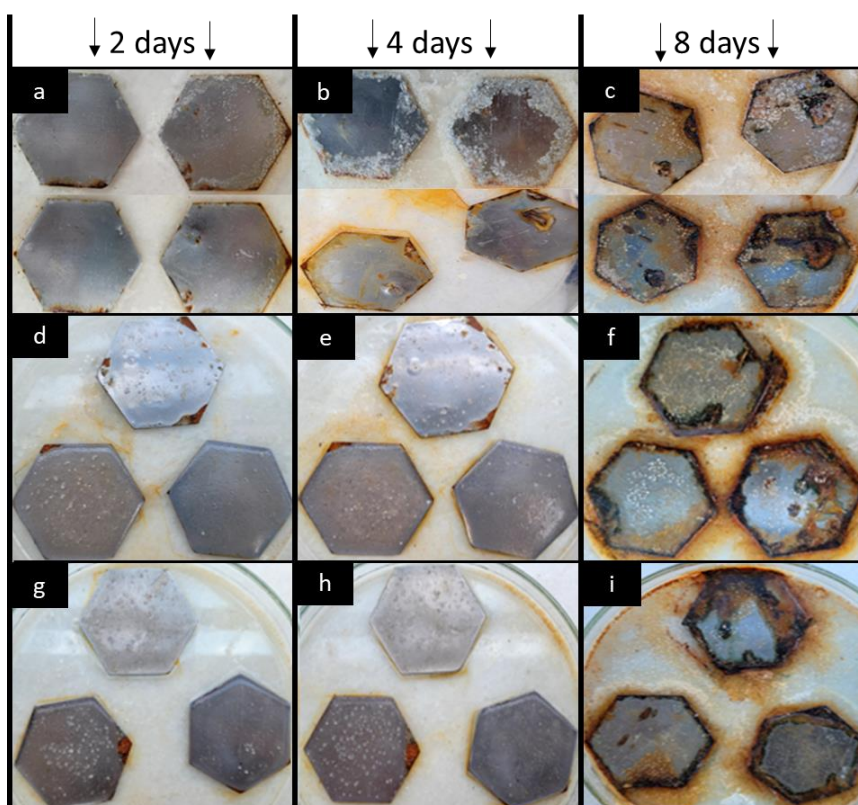


**Figure 14.** Salt test of (a) pure epoxy, (b) linseed oil, (c) hemp seed oil-loaded microcapsules monitored for 8 days

#### 4. Conclusion

In this study, to prevent metal surfaces from oxidation, natural oils such as linseed and hemp seed oils were encapsulated in UF microcapsules and incorporated into an epoxy matrix as self-healing agents, providing a more sustainable approach for coated metal surfaces. The effect of stirring rate during microcapsule synthesis

is investigated by structural, morphological, thermal, particle size, and oil content analyses. Optimum morphology, particle size, and oil content were achieved at 300 rpm. The prepared microcapsules effectively slowed the oxidation of metal surfaces under harsh conditions through their self-healing mechanism, consistent with findings from previous literature. Additionally, linseed oil-containing microcapsules outperformed those containing hemp seed oil compared to the pure coating.

For further improvements, the microcapsule content in the epoxy coating can be increased (up to 30%) to enhance self-healing performance without compromising the mechanical properties of the coating. While being more sustainable, as these materials are low in cost, readily accessible, abundant, and highly effective, they will be well-suited for industrial applications.

## Author Contributions

The first author conceptualized the study and supervised the findings. The second author performed the experiments. The first and second authors wrote and visualized the manuscript. The first author reviewed and edited the paper. All authors read and approved the final version of the paper.

## Conflicts of Interest

All the authors declare no conflict of interest.

## Ethical Review and Approval

No approval from the Board of Ethics is required.

## Acknowledgment

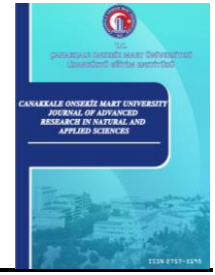
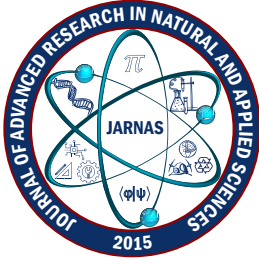
This work was supported by The Scientific and Technological Research Council of Türkiye by TÜBİTAK 2209A Project, Application number 1919B012208897. The authors thank Adem Şen for particle size, İpek Ömeroğlu for FTIR, Ahmet Nazım for SEM, and Ahmet Şenocak for TGA analyses.

## References

- [1] S. An, M. W. Lee, A. L. Yarin, S. S. Yoon, *A review on corrosion-protective extrinsic self-healing: Comparison of microcapsule-based systems and those based on core-shell vascular networks*, Chemical Engineering Journal 344 (2018) 206–220.
- [2] J. Varney, N. Thompson, O. Moghissi, M. Gould, J. Payer, *International measures of prevention, application, and economics of corrosion technologies study* NACE International: Dublin, Ohio and APQC, Houston, Texas, 2016.
- [3] C. Yerli, T. Çakmakçı, U. Sahin, Ş. Tüfenkçi, *The effects of heavy metals on soil, plant, water and human health*, Turkish Journal of Nature and Science 9 (Special Issue) (2020) 103–114.
- [4] Z. Tang, *A review of corrosion inhibitors for rust preventative fluids*, Current Opinion in Solid State and Materials Science 23 (4) (2019) 100759 16 pages.
- [5] C. I. Idumah, C. M. Obele, E. O. Emmanuel, A. Hassan, *Recently emerging nanotechnological advancements in polymer nanocomposite coatings for anti-corrosion, anti-fouling and self-healing*, Surfaces and Interfaces 21 (2020) 100734 23 pages.
- [6] D. Fortman, J. Brutman, G. Hoe, R. Snyder, W. Dichtel, M. Hillmyer, *Approaches to sustainable and continually recyclable cross-linked polymers*, ACS Sustainable Chemistry and Engineering 6 (9) (2018) 11145–11159.

- [7] Z. Yang, P.-F. Sun, X. Li, B. Gan, L. Wang, X. Song, H.-D. Park, C. Tang, *A critical review on thin-film nanocomposite membranes with interlayered structure: Mechanisms, recent developments, and environmental applications*, Environmental Science and Technology 54 (24) (2020) 15563–15583.
- [8] S. Umoren, M. Solomon, *Protective polymeric films for industrial substrates: A critical review on past and recent applications with conducting polymers and polymer composites/nanocomposites*, Progress in Materials Science 104 (2019) 380–450.
- [9] R. Qin, G. Xu, L. Guo, Y. Jiang, R. Ding, *Preparation and characterization of a novel poly(urea-formaldehyde) microcapsules with similar reflectance spectrum to leaves in the uv-vis-nir region of 300–2500 nm*. Materials Chemistry and Physics, 136 (2012) 737–743.
- [10] K. Liu, H. Y. T. Ng, S. Zhang, H. Liu, *Effects of temperature on a mixotrophic dinoflagellate (lepidodinium sp.) under different nutritional strategies*, Marine Ecology Progress Series 678 (2021) 37–49.
- [11] M. Damej, Z. Meryem, M. Doubi, M. Chellouli, B. Hayat, H. Erramli, *Study of the protective effect of green inhibitor extracted from seeds oil of cannabis sativa l. Against corrosion of brass 60cu–40zn in seawater medium*, International Journal of Corrosion and Scale Inhibition 9 (2020) 1564–1579.
- [12] H. Abdipour, M. Rezaei, F. Abbasi, *Synthesis and characterization of high durable linseed oil-urea formaldehyde micro/nanocapsules and their self-healing behaviour in epoxy coating*, Progress in Organic Coatings 124 (2018) 200–212.
- [13] E. Brown, M. Kessler, N. Sottos, *In situ poly(urea-formaldehyde) microencapsulation of dicyclopentadiene*, Journal of Microencapsulation 20 (2003) 719–730.
- [14] B. R. Nair, D. J. Francis, *Kinetics and mechanism of urea-formaldehyde reaction*, Polymer 24 (5) (1983) 626–630.
- [15] H. Es-Haghi, M. Mirabedini, M. Imani, R. Farnood, *Preparation and characterization of pre-silane modified ethyl cellulose-based microcapsules containing linseed oil*, Colloids and Surfaces A: Physicochemical and Engineering Aspects 447 (2014) 71–80.
- [16] G. L. Téllez, E. Viguera-Santiago, S. Hernández-López, *Characterization of linseed oil epoxidized at different percentages*, Superficies y Vacío 22 (1) (2009) 5–10.
- [17] A. G. Aizat, B. Paiman, S. H. Lee, A. Zaidon, *Physico-mechanical properties and formaldehyde emission of rubberwood particleboard made with uf resin admixed with ammonium and aluminum-based hardeners*, Pertanika Journal of Science and Technology 27 (1) (2019) 473-488.
- [18] M. Trivedi, A. Branton, D. Trivedi, H. Shettigar, K. Bairwa, S. Jana, *Fourier transform infrared and ultraviolet-visible spectroscopic characterization of biofield treated salicylic acid and sparfloxacin*, Natural Products Chemistry and Research 3 (5) (2015) 1000186 6 pages.
- [19] P. Viorica-Mirela, A. Lukinich-Gruia, D. Raba, D.-G. Dumbravă, C. Moldovan, D.-M. Bordean, C. Mateescu, *Fatty acids composition and oil characteristics of linseed (Linum usitatissimum l.) from Romania*, Journal of Agroalimentary Processes and Technologies 18 (2) (2012) 136–140
- [20] G. Xin, J. Yang, R. Li, Q. Gao, R. Li, J. Wang, J. Zhang, J. Wang, *Dietary supplementation of hemp oil in teddy dogs: Effect on apparent nutrient digestibility, blood biochemistry and metabolomics*, Bioengineered 13 (3) (2022) 6173–6187.
- [21] M. Behzadnasab, M. Esfandeh, S. M. Mirabedini, M. J. Zohuriaan-Mehr, R. R. Farnood, *Preparation and characterization of linseed oil-filled urea-formaldehyde microcapsules and their effect on mechanical properties of an epoxy-based coating*, Colloids and Surfaces A: Physicochemical and Engineering Aspects 457 (2014) 16–26.

- [22] S. Hatami Boura, M. P. Peikari, A. Ashrafi, M. Samadzadeh, *Self-healing ability and adhesion strength of capsule embedded coatings—micro and nano-sized capsules containing linseed oil*, *Progress in Organic Coatings* 75 (4) (2012) 292–300.
- [23] M. G. Icduygu, M. Asilturk, M. C. Altan, *Microcapsules of poly(methyl methacrylate) containing epoxy resin and multi-walled carbon nanotubes*, *AIP Conference Proceedings* 1914 (1) (2017) 030017 6 pages.
- [24] E. Katoueizadeh, S. M. Zebarjad, K. Janghorban, *Investigating the effect of synthesis conditions on the formation of urea-formaldehyde microcapsules*, *Journal of Materials Research and Technology* 8 (1) (2019) 541–552.
- [25] J. Yang, M. W. Keller, J. S. Moore, S. R. White, N. R. Sottos, *Microencapsulation of isocyanates for self-healing polymers*, *Macromolecules* 41 (24) (2008) 9650–9655.
- [26] A. Kanellopoulos, P. Giannaros, A. Al-Tabbaa, *The effect of varying volume fraction of microcapsules on fresh, mechanical and self-healing properties of mortars*, *Construction and Building Materials* 122 (2016) 577–593.



# Investigation of Gamma Radiation Shielding in NiMnGa-Doped Multifunctional Smart Polymer Composites Using Geant4 and WinXCOM

Mustafa Kaya<sup>1</sup> , Serpil Yalçın Kuzu<sup>2</sup> , Seçil Niksarlıoğlu<sup>3</sup> , Mustafa Ersin Pekdemir<sup>4</sup> ,

Mediha Kök<sup>5</sup> 

<sup>1,2,3,5</sup> Department of Physics, Faculty of Science, Fırat University, Elazığ, Türkiye

<sup>4</sup> Polymer and Biomaterials Research Laboratory, Department of Chemistry, Faculty of Science, Fırat University, Elazığ, Türkiye

## Article Info

Received: 23 Sep 2024

Accepted: 18 Dec 2024

Published: 31 Dec 2024

Research Article

**Abstract** – This study assesses the gamma radiation shielding efficiency of polymer composites doped with varying amounts of alloy, using software to demonstrate the potential application of innovative materials in radiation protection. Specifically, Poly Lactic Acid (PLA) and Poly Ethylene Glycol (PEG) composites doped with NiMnGa at concentrations of 2, 6, 10, and 15% were analyzed across an energy range of 0.0595 to 1.41 MeV using Geant4 and WinXCOM software. The radiation protection ability of the composites and the pure alloy were assessed by calculating key parameters, including the mass attenuation coefficient ( $\mu_m$ ), linear attenuation coefficient ( $\mu$ ), half value layer (HVL), tenth value layer (TVL), and mean free path (MFP). The analyses indicated strong agreement between the results obtained from Geant4 and WinXCOM, demonstrating the performance of the software in investigating the radiation shielding characteristics of polymer-based materials. It was investigated that increasing the amount of NiMnGa in the composite structure significantly enhanced its radiation shielding capabilities. Notably, composites with 15% NiMnGa exhibited superior performance, comparable to traditional heavy metals, while maintaining the lightweight and flexible nature of polymer-based materials. The strong agreement between Geant4 and WinXCOM results further validates the computational approach. These findings highlight the potential of NiMnGa-doped polymer composites as eco-friendly, cost-effective alternatives to lead-based shields for medical and industrial applications, offering enhanced protection with reduced toxicity and environmental impact.

**Keywords** – Alloy, composites, polyethylene glycol (PEG), polylactic acid (PLA), gamma rays

## 1. Introduction

Radiation is an energy form in matter and space classified into ionizing and non-ionizing types. Ionizing radiation, such as high-energy X-rays, alpha, beta, and gamma rays, are biologically hazardous, necessitating effective shielding to minimize exposure [1]. Ionizing radiation, such as gamma and high-energy ultraviolet rays, can cause significant biological damage to tissues by damaging DNA. This damage can lead to mutations in the genetic code and cause cancer. Moreover, other tissues and organs can be harmed, resulting in burns and erythema[2]. Non-ionizing radiation, conversely, has lower energy and poses minimal biological risk. Developing protective materials with specific shielding properties is essential to mitigate the effects of radiation from various sources. The radiation shielding capability of the materials varies according to the

<sup>1</sup>mustafakaya23100@gmail.com (Corresponding

Author);

<sup>2</sup>skuzu@firat.edu.tr;

<sup>3</sup>sniksarlioglu@firat.edu.tr;

<sup>4</sup>ersinpkdmr58@gmail.com; <sup>5</sup>msoglu@firat.edu.tr

radiation types [3]. In radiation protection, photon energy diminishes as photons interact with the atoms in the material, which strongly depends on its density and atomic number [4]. The preferred materials for radiation protection are alloys, glasses, ceramics, high-density building materials, and composites [5]. Moreover, due to their intelligent properties, research focused on improving radiation shielding materials based on shape-memory alloys (SMAs) and shape-memory polymers (SMPs).

Shape Memory Alloys (SMAs) are an innovative class of materials with the remarkable ability to recover their original shape when exposed to specific stimuli, such as heat or magnetic fields. This shape memory effect, driven by reversible phase transformations between austenite and martensite phases, allows SMAs to combine high strength, flexibility, and adaptability. SMAs like NiMnGa have gained attention for their magnetic shape memory properties, enabling actuation without direct thermal input. Their excellent fatigue resistance, energy-damping capacity, and ability to sustain large strains make them ideal for dynamic and high-performance environments, including aerospace, robotics, and biomedical applications.

Shape Memory Polymers (SMPs), on the other hand, are exceptional materials offering lightweight, flexible, and durable solutions for various industrial applications compared to metal, glass, and concrete. Unlike SMAs, SMPs are primarily valued for returning to a predetermined shape upon exposure to stimuli like heat, light, or electricity [6]. This property simplifies design and reduces the need for complex mechanical systems. SMPs also exhibit superior chemical resistance, durability against UV radiation, and adaptability to extreme environmental conditions. Their moldability and energy efficiency further enhance their appeal, making them an ideal choice for medical, construction, and aerospace applications [7].

NiMnGa is one of the SMAs becoming prominent in healthcare, dental implants, energy generation, smart batteries, sensors, and actuators due to its magnetic shape memory feature [8]. Polylactic acid (PLA) and polyethylene glycol (PEG) are commonly used SMPs that are preferred for their rigid physical structure and biocompatibility, respectively [9]. Using PLA/PEG blends with NiMnGa enhances the implementation of the alloy in various fields with its shaping capability through heat transfer and low cost [10]. Radiation oncologists, nuclear power plant workers, and military personnel widely utilize lead-containing protective gears to protect against radiation. However, lead aprons have significant drawbacks, including environmental pollution, soil degradation, and potential harm to human tissues due to toxic waste release [11]. These disadvantages necessitate the development of alternative radiation-shielding materials [12]. Polymers alone can be insufficient for radiation protection due to their atomic numbers [13], which can be improved by adding alloys with high atomic numbers [14,15]. Recent studies have demonstrated that blending PLA/PEG films with alloys at varying ratios significantly improves radiation protection [16]. Despite the high cost of producing NiMnGa alloy, combining it with PLA/PEG smart polymers in different proportions has shown promising results in cost-effectiveness and material performance [9, 17, 18]. Due to the great importance of the uniform distribution of metallic alloy fillers for the stability and reliability of shielding materials, a composite shielding material can be formed by mixing NiMnGa alloy with a polymer. This process ensures that the internal structure of the polymer is not damaged and the alloy filler is uniformly dispersed. Additionally, for the alloy's uniform compatibility, the material's performance can be improved by increasing the interface compatibility with polymers.

The field of radiation shielding has advanced by focusing on developing effective materials such as dense substances, glass systems, and innovative compositions. The selection of suitable radiation shielding materials has required careful consideration of various factors, including the weight, space requirements, and cost of these materials. Considering these factors, polymers have been widely adopted as gamma radiation shielding materials due to their advantages, such as ease of formability, convenient handling, affordability, and lower maintenance requirements. These polymer composites offer numerous advantages over traditional shielding materials like lead, especially in applications where the shield's weight is critical. At the same time, conventional lead shields provide adequate protection due to their high density but pose significant challenges during transportation and usage. Heavy shields can be cumbersome for users and equipment, particularly in applications requiring portability and flexibility. In contrast, polymer composites are lightweight due to their

low density and are easier to shape. For this purpose, this study investigated the radiation shielding properties of PLA/PEG polymers doped with NiMnGa alloy at various concentrations. The radiation protection capabilities of these composites were analyzed over a wide energy range (59.5 to 1400 keV) using the Monte Carlo simulation toolkit Geant4 [19] and the WinXCOM software [20]. The selection of Geant4 and WinXCOM for this study is motivated by their well-documented accuracy, reliability, and widespread use in radiation physics research. Geant4, a Monte Carlo simulation toolkit, is extensively used in high-energy physics, medical physics, and radiation protection due to its ability to simulate complex particle interactions with matter, including gamma radiation shielding, with high precision [20]. Its flexibility in defining material properties and geometry makes it suitable for modeling composites with varying compositions, such as the PLA/PEG-NiMnGa systems studied in this work.

Furthermore, Geant4 has demonstrated excellent agreement with experimental data, showing deviations within acceptable limits for mass attenuation coefficients [21]. On the other hand, WinXCOM is a widely used tool for calculating photon cross-sections and attenuation coefficients of elements, compounds, and mixtures. Its simplicity, computational efficiency, and ability to provide accurate theoretical results make it a reliable reference for benchmarking simulation data [20]. Studies consistently report strong agreement between WinXCOM calculations and experimental results, further supporting its reliability [3]. While other tools like FLUKA and Phy-X/PSD are also used in gamma shielding studies, FLUKA requires more computational resources, which is not necessary for the corresponding research, and Phy-X/PSD, though effective, is less extensively validated compared to Geant4 and WinXCOM [22]. The complementary nature of Geant4 for detailed simulations and WinXCOM for theoretical benchmarking ensures a comprehensive and reliable analysis of the shielding properties of NiMnGa-doped polymer composites. The simulations effectively calculate the radiation interaction parameters of different composites, providing valuable insights into their shielding effectiveness for gamma radiation.

## 2. Materials and Methods

### 2.1. Materials

In the study, the PLA and PEG polymer films were supplied by ABG Filament Company and Sigma Aldrich. The Ni<sub>49.5</sub>Mn<sub>29</sub>Ga<sub>21</sub> alloy was produced using a vacuum arc melting method, employing high-purity Nickel (99.8%), Manganese (99.9%), and Gallium (99.9%) in a water-cooled copper crucible [7]. The NiMnGa alloy ingot was ground in a high-speed grinding machine to obtain nano-sized NiMnGa alloy powder [7]. After grounding it to nano size, NiMnGa was added to the PLA/PEG films in varying proportions. For this purpose, NiMnGa was powdered to 0.01 g and mixed with 0.25 g of PLA and 0.25 g of PEG. The resulting mixture containing 2% NiMnGa was poured into a petri dish using the solvent casting [7] and dried in an oven. The same procedure was followed for the preparation of composites, including 6% (0.03 g), 10% (0.05 g), and 15% (0.075 g) concentrations of NiMnGa [7]. The gamma attenuation coefficients were calculated based on the chemical compositions of the polymer composites summarized in Table 1 with corresponding elemental explanations and theoretical densities. The table presents the progressive incorporation of NiMnGa into the PLA/PEG matrix, demonstrating modification of the elemental compositions and theoretical densities with increasing amounts of NiMnGa.

**Table 1.** Elemental compositions and densities for composites containing PLA/PEG and NiMnGa

Sample	Ni	Mn	Ga	H	C	O	Theoretical density ( $\text{g cm}^{-3}$ )
NiMnGa	49.5	29.5	21	-	-	-	8.35
NiMnGaPLAPEG2	0.9702	0.5782	0.4116	7.2265	51.2407	39.5680	0.6884
NiMnGaPLAPEG6	2.8017	1.6697	1.1186	6.9538	49.3069	38.0751	0.7132
NiMnGaPLAPEG10	4.5040	2.6815	1.9089	6.7001	47.5089	36.6886	0.7378
NiMnGaPLAPEG15	6.4554	3.8468	2.7390	6.4097	45.4497	35.0966	0.7681

## 2.2. Materials

The attenuation coefficient is critical in determining the materials' radiation shielding properties. The photon mass attenuation coefficients of the samples were calculated using Beer-Lambert's law [23].

$$I = I_0 e^{-\mu x}$$

Where  $x$  (cm),  $\mu$ ,  $I_0$ , and  $I$  represent the sample thickness, the linear attenuation coefficient (LAC), the initial intensity of photons passing through a sample of thickness  $xx$ , and the attenuated intensity, respectively.

The mass attenuation coefficient (MAC) ( $\mu_m$ ) defines radiation absorption of the material per unit mass that is computed as:

$$\mu_m (cm^2 g^{-1}) = \frac{\mu}{\rho}$$

Where  $\rho$  is the density of the sample, the mass attenuation coefficient, described as  $\mu/\rho$ , is influenced by the atomic numbers of the constituent elements and the photon energy [23]. For a chemical compound or an alloy mixture,  $\mu_m$  is calculated using the mixture rule:

$$\mu_m = \sum_i w_i (\mu_m)$$

where  $w_i$  represents the weight fraction of each element. The thickness per unit mass affects the material's attenuation properties, investigated using the LAC, Half Value Layer (HVL), and Tenth Value Layer (TVL) parameters. The LAC value represents the material's photon absorption ability calculated as:

$$\mu = \mu_m \rho$$

Depending on its thickness, the radiation shielding property of a material can be defined using the HVL that quantifies the required thickness of the material to absorb half of the incident radiation. The following equation calculates the HVL:

$$HVL = \frac{\ln 2}{\mu}$$

Similarly, the TVL represents the thickness that reduces radiation to 10% of its initial value, which is expressed as:

$$TVL = \frac{\ln 10}{\mu}$$

The mean free path (MFP) indicates the average distance that photons travel through the material before interacting, which is defined as:

$$MFP = \frac{1}{\mu}$$

## 2.3. Computational Methods

The radiation shielding parameters of the alloy and NiMnGa added composites were computed using Geant4 and WinXCOM software for the energy range from 0.0595 to 1.41 MeV. WinXCOM is a widely used software

program for calculating various materials' photon cross-sections and attenuation coefficients, such as compounds and mixtures [21]. It is preferred because of its accuracy and reliability in calculating radiation shielding parameters by utilizing input data containing the elemental compositions of the corresponding materials [24].

Geant4 is a Monte Carlo simulation toolkit used for the modeling penetration of particles through matter [25]. It has been extensively applied in high-energy physics, medical physics, and radiation protection studies since it provides detailed information about interactions between photons and materials, enabling researchers to evaluate the radiation absorption performance of the materials under different conditions[13].

The main aim of the present study is to assess the composite materials' radiation shielding capacity, including different portions of the alloy compared to pure NiMnGa. To investigate the radiation protection ability of the composites and pure NiMnGa, the MAC, LAC, HVL, TVL, and MFP parameters were computed from Geant4 and WinXCOM separately for different photon energies. Moreover, the consistency of the simulation results was examined, using the deviation percentage for the mass attenuation coefficient between WinXCOM and Genat4 [3] defined as follows:

$$\Delta \% = \frac{(\mu_m)_{\text{WinXCOM}} - (\mu_m)_{\text{Geant4}}}{(\mu_m)_{\text{WinXCOM}}} 100$$

### 3. Results and Discussion

#### 3.1. The Mass Attenuation Coefficient (MAC)

The mass attenuation coefficients of NiMnGa and the composites calculated by Geant4 and WinXCOM within the photon energy range of 0.0595 MeV to 1.41 MeV are represented in Figure 1 and summarized in Table 2. The deviations between the MAC values computed from Geant4 and WinXCOM are listed in Table 3. Considering deviations, it is concluded that MAC values computed from Geant4 and WinXCOM are consistent for all materials.

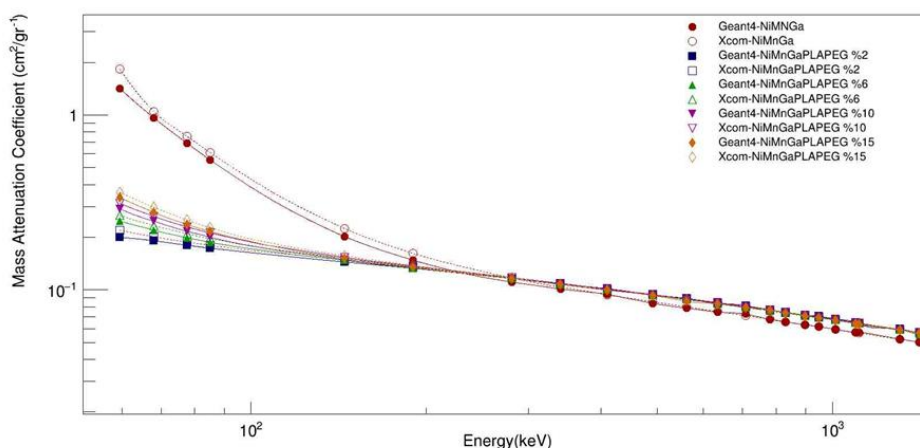


**Figure 1.** MAC of NiMnGa and the composites computed by Geant4 and WinXCOM

The difference between the MAC values derived from the programs was less than 10%. The results indicate that the mass attenuation coefficients of NiMnGa and the composites decreased exponentially with the increase in photon energy. These changes can result from the increase in the percentage of NiMnGa in the composites. While the mass attenuation coefficients of NiMnGa show a sharp decrease in the low energy region demonstrated in Figure 1, the reduction is more gradual in the composite materials.

The decrease in the mass attenuation coefficients of the alloy and composite materials is lower in the medium and high energy regions, which may result in photon-matter interaction in the energy range [26].

**Table 2.** List of the MAC values calculated by Geant4 and WinXCOM for the materials

Energy (keV)	Mass Attenuation Coefficients ( $\mu_m$ ) ( $\text{cm}^2/\text{g}$ )									
	NiMnGa		NiMnGaPLAPEG2		NiMnGaPLAPEG6		NiMnGaPLAPEG10		NiMnGaPLAPEG15	
	WinXcom	Geant4	WinXcom	Geant4	WinXcom	Geant4	WinXcom	Geant4	WinXcom	Geant4
59.5	1.4851	1.4215	0.2186	0.2005	0.2661	0.2480	0.3121	0.2904	0.3618	0.3373
68	1.0501	0.9666	0.2011	0.1909	0.2331	0.2193	0.2637	0.2466	0.2970	0.2779
72.6	0.7566	0.6881	0.1877	0.1798	0.2092	0.1981	0.2297	0.2166	0.2520	0.2365
85	0.6105	0.5526	0.1801	0.1731	0.1963	0.1869	0.2119	0.2007	0.2287	0.2165
145	0.2241	0.2019	0.1479	0.1442	0.1508	0.1473	0.1535	0.1486	0.1565	0.1507
190	0.1614	0.1475	0.1349	0.1327	0.1359	0.1330	0.1368	0.1335	0.1379	0.1343
280.8	0.1171	0.1106	0.1173	0.1159	0.1173	0.1161	0.1177	0.1157	0.1173	0.1156
340	0.1038	0.0961	0.1091	0.1083	0.1089	0.1076	0.1087	0.1076	0.1085	0.1071
410	0.0936	0.0944	0.1013	0.1010	0.1010	0.1004	0.1007	0.1006	0.1004	0.0998
491.3	0.0852	0.0836	0.0940	0.0939	0.0937	0.0936	0.0934	0.0933	0.0930	0.0930
560.7	0.0798	0.0788	0.0888	0.0891	0.0885	0.0887	0.0882	0.0881	0.0878	0.0877
635	0.0750	0.0743	0.0841	0.0843	0.0838	0.0838	0.0834	0.0848	0.0831	0.0833
710	0.0710	0.0705	0.0800	0.0813	0.0797	0.0801	0.0793	0.0796	0.0790	0.0790
780	0.0678	0.0675	0.0766	0.0769	0.0763	0.0766	0.0760	0.0762	0.0756	0.0759
830.3	0.0657	0.0656	0.0744	0.0747	0.0741	0.0743	0.0738	0.0741	0.0734	0.0738
897	0.0632	0.0631	0.0717	0.0720	0.0714	0.0716	0.0711	0.0713	0.0709	0.0709
946.6	0.0615	0.0616	0.0699	0.0705	0.0696	0.0700	0.0693	0.0696	0.0689	0.0692
1012.2	0.0595	0.0594	0.0677	0.0682	0.0674	0.0674	0.0677	0.0676	0.0668	0.0671
1096.2	0.0571	0.0579	0.0651	0.0651	0.0648	0.0650	0.0645	0.0647	0.0642	0.0640
1111.2	0.0567	0.0570	0.0646	0.0646	0.0643	0.0640	0.0640	0.0640	0.0637	0.0636
1305	0.0522	0.0523	0.0595	0.0596	0.0593	0.0592	0.0590	0.0589	0.0587	0.0599
1410	0.0502	0.0502	0.0572	0.0567	0.0569	0.0568	0.0567	0.0568	0.0564	0.0566

**Table 3.** Deviations of the MAC values between Geant4 and WinXCOM for the materials

Energy (keV)	The Deviations of the MAC Values (% $\Delta$ )				
	NiMnGa	NiMnGaPLAPEG2	NiMnGaPLAPEG6	NiMnGaPLAPEG10	NiMnGaPLAPEG15
59.5	4.2825	8.2799	6.8019	6.9528	6.7716
68	7.9516	5.0721	5.9202	6.4846	6.4288
72.6	9.0536	4.2088	5.3059	5.7030	6.1507
85	9.4840	3.8867	4.7885	5.2855	5.3344
145	9.9062	2.5016	2.3209	3.1921	3.7060
190	8.6121	1.6308	2.1339	2.4122	2.6105
280.8	5.5508	1.1935	1.0230	1.6992	1.4492
340	7.4181	0.7332	1.1937	0.0993	1.2903
410	-0.8547	0.2961	0.5940	0.0993	0.5976
491.3	1.8779	0.1063	0.1067	0.1070	0
560.7	1.2531	-0.3378	-0.2259	0.1133	0.1138
635	0.9333	-0.2378	-0.1193	-1.1678	-0.2406
710	0.7042	-1.625	-0.5018	-0.4065	0
780	0.4225	-0.3916	-0.3931	-0.2812	-0.3968
830.3	0.1522	-0.4032	-0.2699	-0.4329	-0.5449
897	0.1582	-0.4184	-0.2801	0.1477	0
946.6	-0.1626	-0.8583	-0.5747	-0.3100	-0.4354
1012.2	0.1680	-0.7385	4.1543	0.1477	-0.4491
1096.2	-1.4010	-0.15366	-0.3086	-0.3100	0.3152
1111.2	-0.5291	1.2383	0.4665	0	0.1569
1305	-0.1915	-0.1680	0.1686	0.1694	-2.0442
1410	0	0.8741	0.1757	-0.1763	-0.3546

A high mass attenuation coefficient in the low energy region indicates higher radiation protection efficiency (RPE). According to the results obtained from the software, the deviation percentages between the programs were derived as follows: NiMnGa alloy (10%), NiMnGaPLAPEG2 (9%), NiMnGaPLAPEG6 (7%), NiMnGaPLAPEG10 (7%), and NiMnGaPLAPEG15 (7%). The relatively higher deviations observed in the photon energy range of 59.5 to 340 keV (Table 3) can be attributed to several factors. In this range, the photoelectric effect is the dominant interaction mechanism, and its cross-section is highly sensitive to the material's composition, density, and atomic number. Slight discrepancies in these input parameters between Geant4 and WinXCOM can amplify errors in calculated mass attenuation coefficients, leading to more significant deviations [20].

Furthermore, this energy range marks a transition where the photoelectric effect diminishes, and Compton scattering becomes more significant, introducing complexities in accurately modeling these overlapping interaction mechanisms. Similar discrepancies during this transition have been reported in previous studies comparing Monte Carlo simulations and theoretical methods [3]. Additionally, the NiMnGa-doped composites analyzed here involve complex compositions with varying atomic numbers, which may lead to differences in how Geant4 and WinXCOM handle material heterogeneity [20]. Deviations may also stem from input data limitations, such as assumptions in density or photon cross-sections, which are critical at lower photon energies. Moreover, geometric and boundary conditions in Monte Carlo simulations may introduce minor errors at lower energies that do not affect WinXCOM's analytical calculations, with such discrepancies decreasing at higher energies due to reduced sensitivity to material interfaces [24]. Despite these higher deviations, the overall agreement between Geant4 and WinXCOM remains strong, with deviations within acceptable limits for computational studies of radiation shielding.

### 3.2. The Linear Attenuation Coefficient (LAC)

The linear attenuation coefficient (LAC) is a gamma radiation shielding parameter defined by the density of the material and the relative mass attenuation coefficient. The LAC of composites with NiMnGa is presented in Figure 2, and the values are listed in Table 4. The polymer composites have lower LAC values due to the elements with low atomic numbers, such as C, H, and O, in the polymer structure. It is concluded that the difference between the  $\mu$  values of the polymer composite material decreases as the photon energy of the alloy and polymer composite material increases. It explains the photon and matter interaction depending on the increasing percentage of alloy amounts in the polymer composite. There is a significant improvement in the linear attenuation coefficients depending on the amount of gamma energies. NiMnGa alloy shows high gamma radiation at low energy.

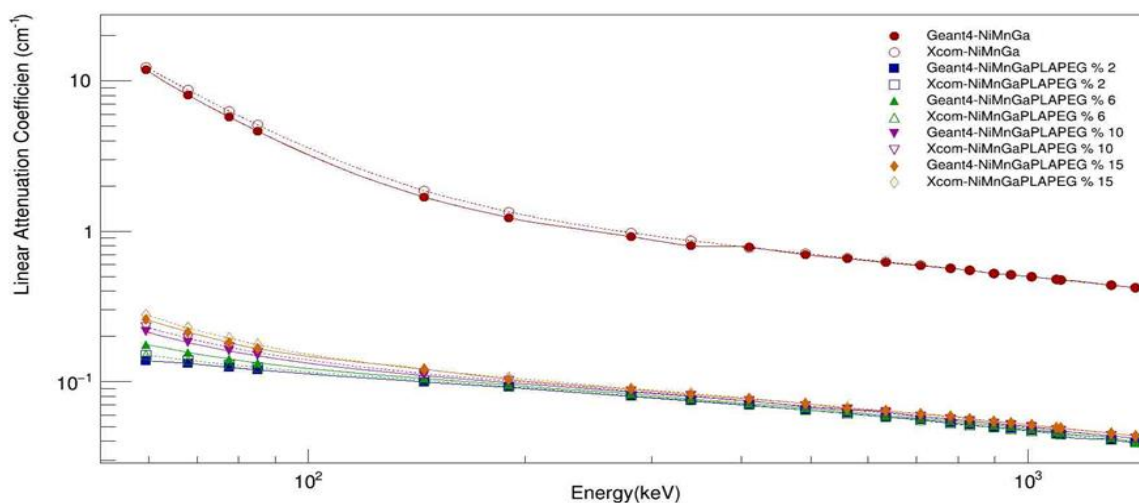


**Figure 2.** LAC of NiMnGa and the composites computed by Geant4 and WinXCOM

Moreover, PLA/PEG/NiMnGa composite materials provide sound gamma radiation in low-energy regions. It protects against gamma radiation depending on the amount of alloy added to the polymer. The linear attenuation coefficient at low energies shows more significant radiation shielding than higher energies. The fact that the photoelectric cross section is at a low energy level affects its exponential decrease with photon energy [27]. It has been observed that in exponential decay, the absorption ability of photons increases at low energies and decreases with increasing energy. It was concluded that the Compton scattering cross section and absorbing properties are related to the atomic number and energy gaps. An increase in the armoring effect was detected by increasing the alloy contribution. As photon energy increases, pair formation increases. A similar trend is observed between the linear and mass attenuation coefficients.

**Table 4.** LAC values of NiMnGa and composites computed by Geant4 and WinXCOM

Energy (keV)	Linear Attenuation Coefficient ( $\mu$ ) (cm <sup>2</sup> /g)									
	NiMnGa		NiMnGaPLAPEG2		NiMnGaPLAPEG6		NiMnGaPLAPEG10		NiMnGaPLAPEG15	
	WinXcom	Geant4	WinXcom	Geant4	WinXcom	Geant4	WinXcom	Geant4	WinXcom	Geant4
59.5	12.3957	11.8692	0.1505	0.1380	0.1897	0.1768	0.2302	0.2142	0.2778	0.2590
68	8.7675	8.0713	0.1384	0.1314	0.1662	0.1564	0.1945	0.1820	0.2281	0.2135
72.6	6.3176	5.7466	0.1292	0.1238	0.1492	0.1413	0.1694	0.1598	0.1935	0.1816
85	5.0976	4.6171	0.1239	0.1192	0.1400	0.1333	0.1563	0.1481	0.1756	0.1662
145	1.8704	1.6858	0.1018	0.0993	0.1075	0.1050	0.1132	0.1096	0.1202	0.1157
190	1.3404	1.2321	0.0928	0.0913	0.0969	0.0948	0.1009	0.0985	0.1059	0.1032
280.8	0.9769	0.9241	0.0807	0.0798	0.0836	0.0828	0.0865	0.0853	0.0900	0.0888
340	0.8667	0.8024	0.0751	0.0745	0.0776	0.0768	0.0802	0.0794	0.0833	0.0822
410	0.7817	0.7887	0.0697	0.0695	0.0720	0.0716	0.0742	0.0742	0.0771	0.0766
491.3	0.7120	0.6985	0.0647	0.0646	0.0668	0.0668	0.0689	0.0688	0.0714	0.0714
560.7	0.6665	0.6570	0.0611	0.0613	0.0631	0.0633	0.0650	0.0650	0.0674	0.0673
635	0.6268	0.6211	0.0579	0.0580	0.0597	0.0597	0.0615	0.0626	0.0638	0.0640
710	0.5932	0.5890	0.0551	0.0559	0.0568	0.0571	0.0585	0.0587	0.0607	0.0607
780	0.5662	0.5641	0.0527	0.0529	0.0544	0.0546	0.0560	0.0564	0.0581	0.0583
830.3	0.5490	0.5479	0.0512	0.0514	0.0528	0.0530	0.0544	0.0547	0.0564	0.0566
897	0.5281	0.5272	0.0493	0.0495	0.0509	0.0510	0.0524	0.0526	0.0543	0.0544
946.6	0.5141	0.5143	0.0481	0.0485	0.0496	0.0499	0.0511	0.0513	0.0529	0.0531
1012.2	0.4969	0.4963	0.0466	0.0469	0.0480	0.0480	0.0499	0.0499	0.0513	0.0515
1096.2	0.4767	0.4767	0.0448	0.0448	0.0462	0.0464	0.0476	0.0477	0.0493	0.0491
1111.2	0.4735	0.4760	0.0445	0.0444	0.0459	0.0457	0.0472	0.0472	0.0489	0.0488
1305	0.4362	0.4370	0.0410	0.0410	0.0422	0.0422	0.0435	0.0435	0.0451	0.0453
1410	0.4196	0.4198	0.0393	0.0390	0.0406	0.0405	0.0418	0.0419	0.0433	0.0435

### 3.3. The Half Value Layer (HVL)

TVL has an absorbing effect that reduces the radiation effect by one-tenth, providing information about protecting the material against gamma radiation [29]. The TVL values of the alloy and composites calculated from Geant4 and WinXCOM are represented in Figure 3 and Table 5. The results revealed that adding NiMnGa decreased the TVL of composites, as expected from the HVL calculations. Figures 3 and 4 illustrate that the HVL and TVL results are consistent. In addition, from the figures, it is comprehended that increasing the doping amount of NiMnGa to the polymer-based composites enhances the usability of the materials for gamma radiation protection at low energies. The values from the computation of Geant4 and WinXCOM confirm each other.

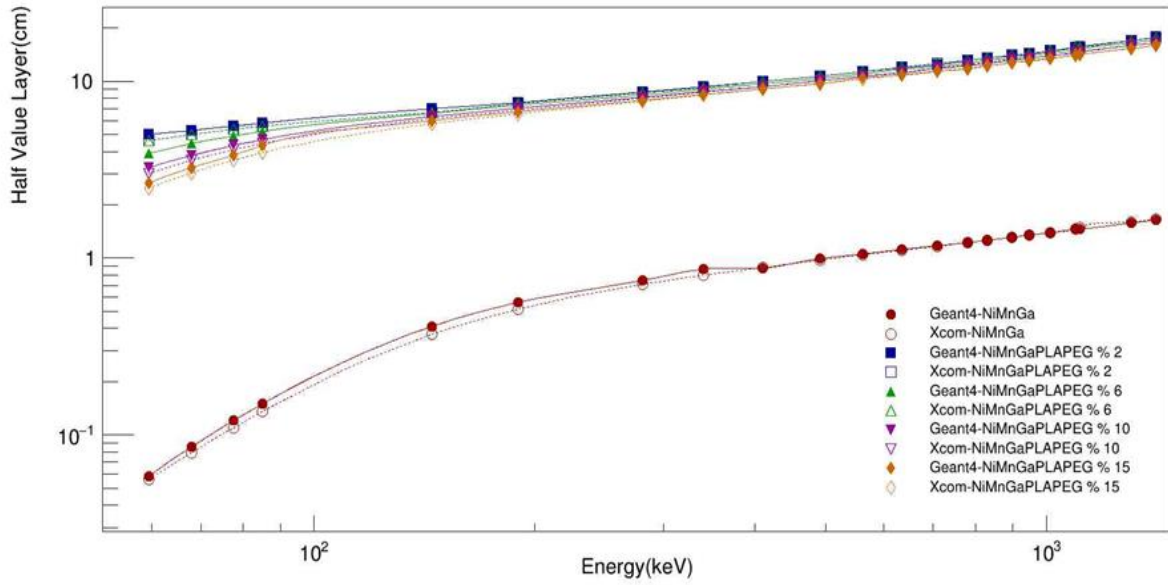
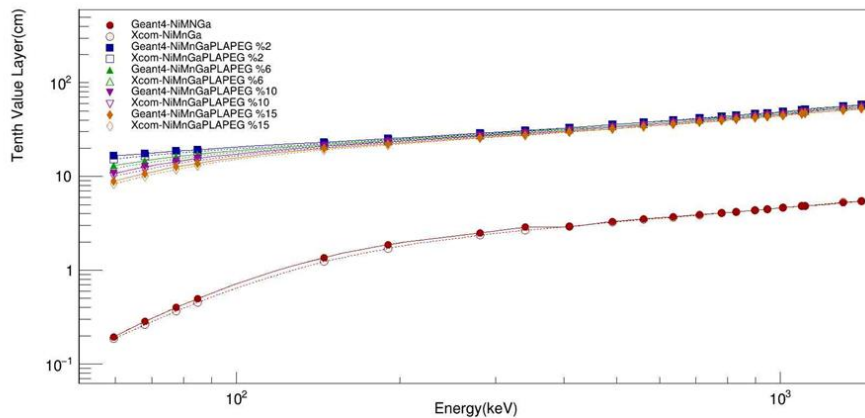


Figure 3. The HVL of NiMnGa and the composites computed by Geant4 and WinXCOM

Table 5. HVL values of NiMnGa and composites computed by Geant4 and WinXCOM

Energy (keV)	Half Value Layer									
	NiMnGa		NiMnGaPLAPEG2		NiMnGaPLAPEG6		NiMnGaPLAPEG10		NiMnGaPLAPEG15	
	WinXcom	Geant4	WinXcom	Geant4	WinXcom	Geant4	WinXcom	Geant4	WinXcom	Geant4
59.5	0.0559	0.0583	4.6056	5.0213	3.6535	3.9185	3.0101	3.2359	2.4951	2.6751
68	0.0790	0.0858	5.0064	5.2718	4.1690	4.4299	3.5626	3.8085	3.0387	3.2461
72.6	0.1097	0.1206	5.3640	5.5984	4.6451	4.9043	4.0900	4.3375	3.5810	3.8154
85	0.1359	0.1501	5.5900	5.8145	4.9506	5.1999	4.4335	4.6834	3.9473	4.3391
145	0.3705	0.4111	6.6807	6.9803	6.4442	6.5957	6.1205	6.3202	5.7666	5.9891
190	0.5143	0.5625	7.4636	7.5869	7.1510	7.3070	6.8676	7.0302	6.5452	6.7151
280.8	0.7095	0.7500	8.5838	8.6806	8.2852	8.3703	8.0095	8.1174	7.6939	7.8051
340	0.7997	0.8637	9.2284	9.2965	8.9242	9.0241	6.6427	8.7254	8.3210	8.4271
410	0.8866	0.8788	9.9390	9.9661	9.6216	9.6754	9.3302	9.3390	8.9902	9.0430
491.3	0.9735	0.9922	10.7010	10.7215	10.3702	10.3764	10.0581	10.0748	9.6984	9.7021
560.7	1.0398	1.0549	11.3376	11.2927	10.9762	10.9450	10.6523	10.6539	10.2718	10.2993
635	1.1057	1.1159	11.9714	11.9301	11.5949	11.6105	11.2651	11.0729	10.8643	10.8211
710	1.1683	1.1766	12.5775	12.3997	12.1925	12.1200	11.8486	11.8082	11.4192	11.4117
780	1.2240	1.2286	13.1352	13.0920	12.7323	12.6787	12.3599	12.2854	11.9302	11.8893
830.3	1.2625	1.2650	13.5248	13.4670	13.1128	13.0659	12.7311	12.6509	12.2898	12.2317
897	1.3124	1.3147	14.0341	13.9831	13.6017	13.5687	13.2103	13.1729	12.7651	12.7206
946.6	1.3482	1.3475	14.3955	14.2680	13.9578	13.8768	13.5531	13.4984	13.0955	13.0339
1012.2	1.3947	1.3965	15.8712	14.7540	14.4165	14.4405	13.8741	13.8795	13.5063	13.4510
1096.2	1.4538	1.4540	15.4627	15.4720	14.9934	14.9385	14.5581	14.5100	14.0569	14.0912
1111.2	1.4638	1.4561	15.5627	15.6111	15.0946	15.1673	14.6601	14.6791	14.1516	14.1776
1305	1.5887	1.5860	16.9006	16.9060	16.3903	16.4252	15.9341	15.9270	15.3623	15.2741
1410	1.6516	1.6509	17.6015	17.7730	17.0549	17.1147	16.5468	16.5192	15.9891	15.9192

### 3.4. The Tenth Value Layer (TVL)



**Figure 4.** The TVL of NiMnGa and the composites computed by Geant4 and WinXCOM

TVL has an absorbing effect that reduces the radiation effect by one-tenth, providing information about protecting the material against gamma radiation [29]. The TVL values of the alloy and composites calculated from Geant4 and WinXCOM are represented in Figure 4 and Table 6. The results revealed that adding NiMnGa decreased the TVL of composites, as expected from the HVL calculations. Figures 3 and 4 illustrate that the HVL and TVL results are consistent. In addition, from the figures, it is comprehended that increasing the doping amount of NiMnGa to the polymer-based composites enhances the usability of the materials for gamma radiation protection at low energies. The values from the computation of Geant4 and WinXCOM confirm each other.

**Table 6.** The TVL values of NiMnGa and composites computed by Geant4 and WinXCOM

Energy (keV)	Tenth Value Layer (TVL)									
	NiMnGa		NiMnGaPLAPEG2		NiMnGaPLAPEG6		NiMnGaPLAPEG10		NiMnGaPLAPEG15	
	WinXcom	Geant4	WinXcom	Geant4	WinXcom	Geant4	WinXcom	Geant4	WinXcom	Geant4
59.5	0.1857	0.1939	15.2995	16.6805	12.1367	13.0170	9.9991	10.7496	8.2886	8.8875
68	0.2626	0.2852	16.6316	17.5128	13.8493	14.7158	11.8341	12.6515	10.0946	10.7839
72.6	0.3644	0.4006	17.8190	18.5977	15.4308	16.2917	13.5861	14.4091	11.8959	12.6741
85	0.4516	0.4986	18.5696	19.3153	16.4458	17.2737	14.7281	15.5475	13.1126	13.8543
145	1.2310	1.3657	22.6142	23.1881	21.4072	21.9106	20.3318	20.9955	19.1562	19.8841
190	1.7085	1.8687	24.7936	25.2034	23.7551	24.2735	22.8136	23.3646	21.7430	22.3091
280.8	2.3569	2.4915	28.5149	28.8219	27.5231	27.8056	26.6071	26.9655	25.5581	25.9301
340	2.6566	2.8687	30.6561	30.8823	29.6457	29.9776	28.7105	28.9852	27.6421	27.9911
410	2.9455	2.9193	33.0167	33.1069	31.9625	32.1410	30.9941	31.0237	29.8641	30.0401
491.3	3.2339	3.2961	35.5666	35.6161	34.4492	34.4698	33.4143	33.8525	32.2175	32.3670
560.7	3.4543	3.5043	37.6855	37.5136	36.4621	36.3585	35.3861	35.4243	34.1224	34.2137
635	3.6733	3.7069	39.7683	39.6997	38.5176	38.5692	37.4221	36.7641	36.0906	35.9491
710	3.8812	3.9088	41.7811	41.1911	40.5028	42.2620	39.3601	39.1729	37.9938	37.9081
780	4.0660	4.0814	43.6343	43.4909	42.2958	42.1178	41.0581	40.8115	39.6314	39.4954
830.3	4.1940	4.2024	44.9284	44.7364	43.5600	43.4040	42.2881	42.0256	40.8259	40.6338
897	4.3598	4.3674	46.6204	46.4511	45.1842	45.0744	43.8831	43.7595	42.4048	42.2570
946.6	4.4788	4.4766	47.8210	47.3977	46.3669	46.0977	45.0251	44.8409	43.5024	43.2979
1012.2	4.6332	4.6393	49.4010	49.0120	47.8907	47.9705	46.0881	46.1070	44.8672	44.6841
1096.2	4.8294	4.8302	51.3660	51.3969	49.8071	49.7318	48.3631	48.2014	46.6961	46.8100
1111.2	4.8626	4.8373	51.7155	51.8600	50.1434	50.4952	48.7011	48.6804	47.0107	47.0972
1305	5.2777	5.2687	56.1428	56.1606	54.4475	54.5636	52.9321	52.9086	51.0324	50.7401
1410	5.4866	5.4844	58.4709	58.2932	56.6553	56.8539	54.9674	54.8757	53.1161	52.8841

### 3.5. The Mean Free Path (MFP)

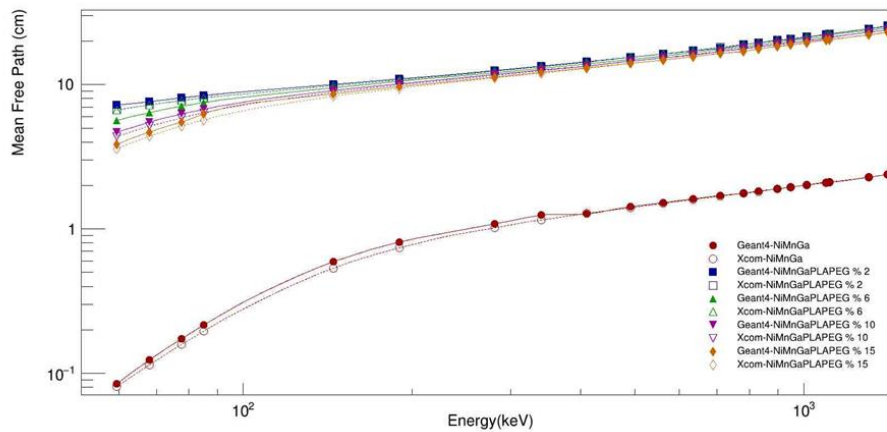


**Figure 5.** MFP of NiMnGa and the composites computed by Geant4 and WinXCOM

The Mean free path (MFP) values of the alloy and composites calculated by Geant4 and WinXCOM are represented in Figure 5 and Table 7. From the figure, it is concluded that the MFP increases from lower to higher energy regions for all materials. We increase the photon energy depending on the amount of the alloy in the values. Since the PLA and PEG polymers have low density, the MFP values change concerning the amount of the doped alloy in the composites [22]. An increase in the alloy amount in the composites decreases the MFP, consistent with the HVL and TVL results. Both computations exhibited similar results for each material.

**Table 7.** MFP values of NiMnGa and composites computed by Geant4 and WinXCOM

Energy (keV)	Mean Free Path (MFP)									
	NiMnGa		NiMnGaPLAPEG2		NiMnGaPLAPEG6		NiMnGaPLAPEG10		NiMnGaPLAPEG15	
	WinXcom	Geant4	WinXcom	Geant4	WinXcom	Geant4	WinXcom	Geant4	WinXcom	Geant4
59.5	0.0806	0.0842	6.6445	7.2463	5.2714	5.6561	4.3440	4.6685	3.5997	3.8610
68	0.1140	0.1238	7.2254	7.6103	6.0168	6.3938	5.1413	5.4945	4.3840	4.6838
72.6	0.1582	0.1740	7.7399	8.0775	6.7024	7.0771	5.9031	6.2578	5.1679	5.5066
85	0.1961	0.2165	8.0710	8.3892	7.1428	7.5018	6.3979	6.7521	5.6947	6.2617
145	0.5346	0.5931	9.8231	10.0704	9.3023	9.5238	8.8339	9.1240	8.3194	8.6430
190	0.7420	0.8116	10.7758	10.9529	10.3199	10.5485	9.9108	10.1522	9.4428	9.6899
280.8	1.0236	1.0821	12.3915	12.5313	11.9617	12.0772	11.5606	11.7233	11.1111	11.2612
340	1.1538	1.2462	13.3155	13.4228	12.8865	13.0208	12.4688	12.5944	12.0048	12.1654
410	1.2792	1.2679	14.3472	14.3884	13.8888	13.9664	13.4770	13.4770	12.9701	13.0548
491.3	1.4044	1.4316	15.4559	15.4798	14.9700	14.9700	14.5137	14.5348	14.0056	14.0056
560.7	1.5003	1.5220	16.3666	16.3132	15.8478	15.7977	15.3846	15.3846	14.8367	14.8588
635	1.5954	1.6100	17.2711	17.2117	16.7504	16.7504	16.2601	15.9744	15.6739	15.6250
710	1.6857	1.6977	18.1488	17.8890	17.6056	17.5131	17.0940	17.0357	16.4744	16.4744
780	1.7661	1.7727	18.9753	18.9035	18.3823	18.3150	17.8571	17.7304	17.2117	17.1526
830.3	1.8214	1.8251	19.5312	19.4552	18.9393	18.8679	18.3823	18.2815	17.7304	17.6678
897	1.8935	1.8968	20.2839	20.2020	19.6463	19.6078	19.0839	19.0114	18.4162	18.3823
946.6	1.9451	1.9443	20.7900	20.6185	20.1612	20.0400	19.5694	19.4931	18.9035	18.8323
1012.2	2.0124	2.0149	21.4592	21.3219	20.8333	20.8333	20.0400	20.0400	19.4931	19.4174
1096.2	2.0977	2.0977	22.3214	22.3214	21.6450	21.5517	21.0084	20.9643	20.2839	20.3665
1111.2	2.1119	2.1008	22.4719	22.5225	21.7864	21.8818	21.1864	21.1864	20.4498	20.4918
1305	2.2925	2.2883	24.3902	24.3902	23.6966	23.6966	22.9885	22.9885	22.1729	22.0750
1410	2.3832	2.3820	25.4452	25.6410	24.6305	24.6913	23.9234	23.8663	23.0946	22.9885

## 4. Conclusion

Alloys containing high atomic number (Z) elements, such as lead or tungsten, exhibit exceptional gamma radiation shielding properties compared to polymers. However, polymers, primarily composed of low-Z elements like carbon, oxygen, and hydrogen, are inherently less effective in attenuating gamma rays. Incorporating high Z elements into polymers, such as composite materials, significantly enhances their radiation shielding capabilities. This study evaluates the gamma radiation protection efficiency of NiMnGa doped PLA/PEG-based composites, demonstrating the potential of smart materials in radiation shielding applications. By varying the concentration of NiMnGa in these composites, the research highlights how tailored, smart materials can meet specific shielding requirements, offering a flexible, lightweight, and efficient solution for radiation protection. The study calculated critical shielding parameters MAC, LAC, HVL, TVL, and MFP for pure NiMnGa alloy and composites containing 2, 6, 10, and 15% NiMnGa, across an energy range of 0.0595 to 1.41 MeV. The results indicate that increasing the alloy concentration significantly enhances the gamma radiation protection of the composites at low photon energy levels. For instance, the MAC of the 15% NiMnGa composite at 59.5 keV reached 0.3618 cm<sup>2</sup>/g, outperforming the 2% composite (0.2186 cm<sup>2</sup>/g) and approaching the performance of pure NiMnGa alloy. Comparisons with existing literature confirm that these composites provide comparable or superior shielding efficiency to materials like Pb-doped PLA/PEG or tungsten trioxide (WO<sub>3</sub>) composites while maintaining the advantages of reduced toxicity, lower weight, and higher flexibility.

Furthermore, NiMnGa-doped composites exhibited decreasing radiation protection efficiency at higher photon energies due to the transition from photoelectric dominance at low energies to Compton scattering and pair production at higher energies. This behavior aligns with previously reported trends in NiMnGa-based and other SMA composites, further validating the computational methodologies employed in this study using Geant4 and WinXCOM. The computational results from both tools demonstrated consistency, reinforcing their reliability for assessing gamma radiation shielding properties. The findings underscore the potential of NiMnGa-doped polymers as a lightweight, non-toxic alternative to traditional shielding materials like lead, making them ideal for wearable and portable applications. Future work should focus on experimental validation of the findings, particularly to resolve discrepancies observed in the intermediate energy range (59.5–340 keV). Optimizing material compositions for targeted applications and conducting detailed cost analyses will further establish commercial feasibility. Exploring the incorporation of other high-Z elements or nanoparticles could enhance shielding performance at higher photon energies, broadening the applicability of these materials.

## Author Contributions

All the authors equally contributed to this work.

## Conflicts of Interest

All the authors declare no conflict of interest.

## Ethical Review and Approval

This work was supported by the Management Unit of the Scientific Research Projects of Fırat University (FUBAP), Grant number: FF.24.23.

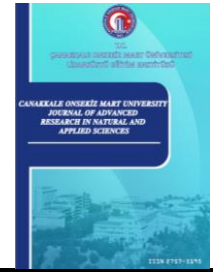
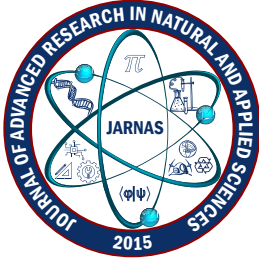
## Acknowledgment

We thank Dr. Kamuran Dilsiz and Dr. Sibel Selçuk Pekdemir for all their support.

## References

- [1] M. E. Mahmoud, A. M. El-Khatib, M. S. Badawi, A. R. Rashad, R. M. El-Sharkawy, A. A. Thabet, *Fabrication, characterization and gamma rays shielding properties of nano and micro lead oxide-dispersed-high density polyethylene composites*, Radiation Physics and Chemistry 145 (2018) 160–173.
- [2] R. K. Chaurasia, B. K. Sapra, D. K. Aswal, *Interplay of immune modulation, adaptive response and hormesis: Suggestive of threshold for clinical manifestation of effects of ionizing radiation at low doses?*, Science of the Total Environment 917 (2024) 170178 18 pages.
- [3] A. H. Taqi, A. M. Ghalib, H. N. Mohammed, *Shielding properties of Cu-Sn-Pb alloy by Geant4, XCOM and experimental data*, Materials Today Communications 26 (2021) 101996 12 pages.
- [4] T. A. A. Junior, M.S. Nogueira, V. Vivolo, M. P. A. Potiens, L.L. Campos, *Mass attenuation coefficients of X-rays in different barite concrete used in radiation protection as shielding against ionizing radiation*, Radiation Physics and Chemistry, 140 (2017) 349–354.
- [5] H. O. Tekin, T. T. Erguzel, M. I. Sayyed, V. P. Singh, T. Manici, E. E. A. Guclu, O. Agar, *An investigation on shielding properties of different granite samples using MCNPX code*. Digest Journal of Nanomaterials and Biostructures, 13 (2) (2018) 381–389.
- [6] O. Agar, Z. Y. Khattari, M. I. Sayyed, H. O. Tekin, S. Al-Omari, M. Maghrabi, M. H. M. Zaid, I.V. Kityk, *Evaluation of the shielding parameters of alkaline earth based phosphate glasses using MCNPX code*, Results in Physics, 12 (2019) 101–106.
- [7] M. E. Pekdemir, M. Kaya, M. Coşkun, Y. Aydoğdu, M. Kök, S. Yalcin Kuzu, *Physicochemical properties of magnetically enhanced shape memory polymer composites doped with NiMnGa*, Journal of Polymer Research, 30 (8) (2023) 293 10 pages.
- [8] T. Defize, R. Riva, J. M. Raquez, P. Dubois, C. Jérôme, M. Alexandre, *Thermoreversibly Crosslinked Poly( $\epsilon$ -caprolactone) as Recyclable Shape-Memory Polymer Network*, Macromolecular Rapid Communications, 32(16) (2011) 1264–1269.
- [9] H. Akhdar, M. Alshehri, *Geant4 Simulation of Photon- and Neutron-Shielding Capabilities of Biopolymer Blends of Poly(lactic acid) and Poly(hydroxybutyrate)*, Polymers, 15(21) (2023) 4257 16 pages.
- [10] M. Kök, Y. Aydoğdu, *Electron Concentration Dependence of Phase Transition and Magnetic Properties in NiMnGa Alloys*, Journal of Superconductivity and Novel Magnetism, 26 (2013) 1691–1696.
- [11] M. Yilmaz, M. E. Pekdemir, E. Ö. Öner, *Evaluation of Pb doped Poly(lactic acid) (PLA) / Poly(ethylene glycol) (PEG) blend composites regarding physicochemical and radiation shielding properties*, Radiation Physics and Chemistry, 202 (2023) 110509 9 pages.
- [12] H. Alavian, H. T. Anbaran, *Comparative study of mass attenuation coefficients for LDPE/metal oxide composites by Monte Carlo simulations*, The European Physical Journal Plus, 135(82) (2020) 9 pages.
- [13] K. Dilsiz, H. Ogul, F. Akman, O. Agar, M. R. Kacal, H. Polat, İ. Dursun, *Evaluation of CdS doped polyester composites regarding gamma and neutron shielding properties*, Progress in Nuclear Energy, 139 (2021) 103865 11 pages.
- [14] F. Kazemi, S. Malekie, M. A. Hosseini, *A Monte Carlo Study on the Shielding Properties of a Novel Polyvinyl Alcohol (PVA)/WO<sub>3</sub> Composite, Against Gamma Rays, Using the MCNPX Code*, Journal of Biomedical Physics and Engineering 9 (4) (2019) 465–472.
- [15] Z. M. Cinan, B. Erol, T. Baskan, S. Mutlu, S. S. Yilmaz, A. H. Yılmaz, *Gamma irradiation and the radiation shielding characteristics: For the lead oxide doped the crosslinked polystyrene-b-polyethyleneglycol block copolymers and the polystyrene-b-polyethyleneglycol-boron nitride*

- nanocomposites*, *Polymers* 13 (19) (2021) 3246–30 pages.
- [16] S. Nambiar, J. T. W. Yeow, *Polymer-composite materials for radiation protection*, *ACS Applied Materials and Interfaces* 4 (11) (2012) 5717–5726.
- [17] H. Shin, S. Thanakkasaranee, K. Sadeghi, *Preparation and characterization of ductile PLA/PEG blend films for eco-friendly flexible packaging application*, *Food Packaging and Shelf Life* 34 (2022) 100966 10 pages.
- [18] K. I. Matumba, M. P. Motloug, V. Ojjo, S. S. Ray, E. R. Sadiku, *Investigation of the effects of chain extender on material properties of PLA/PCL and PLA/PEG blends: Comparative study between polycaprolactone and polyethylene glycol*, *Polymers* 15 (9) (2023) 2230 16 pages.
- [19] S. Agostinelli, J. Allison, K. Amako, J. Apostolakis, H. Araujo, P. Arce, M. Asai, D. Axen, S. Banerjee, G. Barrand, F. Behner, L. Bellagamba, J. Boudreau, L. Broglia, A. Brunengo, H. Burkhardt, S. Chauvie, J. Chuma, R. Chytrcek, G. Cooperman, G. Cosmo, P. Degtyarenko, A. Dell'Acqua, G. Depaola, D. Dietrich, R. Enami, A. Feliciello, C. Ferguson, H. Fesefeldt, G. Folger, F. Foppiano, A. Forti, S. Garelli, S. Giani, R. Giannitrapani, D. Gibin, J. J. Gómez Cadenas, I. González, G. Gracia Abril, G. Greeniaus, W. Greiner, V. Grichine, A. Grossheim, S. Guatelli, P. Gumplinger, R. Hamatsu, K. Hashimoto, H. Hasui, A. Heikkinen, A. Howard, ..., D. Zschesche, *GEANT4 a simulation toolkit*, *Nuclear Instruments and Methods in Physics Research Section A: Accelerators, Spectrometers, Detectors and Associated Equipment* 506 (3) (2003) 250–303.
- [20] L. Gerward, N. Guilbert, K. B. Jensen, H. Levring, *WinXCom a program for calculating X-ray attenuation coefficients*, *Radiation Physics and Chemistry* 71 (3-4) (2004) 653–654.
- [21] S. Niksarlioğlu, F. Akman, M. E. Pekdemir, S. Yalcin Kuzu, M. R. Kaçal, M. Yılmaz, *An extensive investigation on gamma shielding properties of PLA/Gd<sub>2</sub>O<sub>3</sub> nanocomposites*, *Radiation Physics and Chemistry* 140 (2023) 110936 9 pages.
- [22] F. Rouihem, M. M. Albarqi, R. A. Alsulami, F. Hosni, *Lead-free Gamma-ray shielding: Comparative analysis of elastomeric and fluoro-rubber materials using FLUKA and EGSnrc simulations*, *Journal of Radiation Research and Applied Sciences* 17 (1) (2024) 100834 10 pages.
- [23] C. M. Davisson, *Gamma-ray attenuation coefficients*, in: K. Siegbahn (Ed.), *Alpha-, Beta-, and Gamma-Ray Spectroscopy*, Vol. 1, Elsevier, New York, 1965, App. 1, pp.827–843.
- [24] K. I. Hussein, M. S. Alqahtani, H. Algarni, H. Zahran, I. S. Yaha, I. Grelowska, M. Reben, E. S. Yousef, *MIKE: A new computational tool for investigating radiation, optical and physical properties of prototyped shielding materials*, *Journal of Instrumentation* 16 (07) (2021) T07004 23 pages.
- [25] A. Sharma, B. Singh, B. S. Sandhu, *Investigation of photon interaction parameters of polymeric materials using Monte Carlo simulation*, *Chinese Journal of Physics* 60 (2019) 709–719.
- [26] M. M. El-Toony, G. Eid, H. M. Algarni, T. F. Alhuwaymel, E. E. Abel-hady, *Synthesis and characterisation of smart poly vinyl ester / Pb<sub>2</sub>O<sub>3</sub> nanocomposite for gamma radiation shielding*, *Radiation Physics and Chemistry* 168 (2020) 108536 8 pages.
- [27] R. Gutzler, M. Garg, A. R. Christian, K. Kuhnke, K. Kern, *Light-matter interaction at atomic scales*, *Nature Reviews Physics* 3 (6) (2021) 441–453.
- [28] Q. Chang, S. Guo, X. Zhang, *Radiation shielding polymer composites: Ray-interaction mechanism, structural design, manufacture and biomedical applications*, *Materials and Design* 233 (2023) 112253 21 pages.
- [29] S. Sharifi, R. Bagheri, S. P. Shirmardi, *Comparison of shielding properties for ordinary, barite, serpentine and steel–magnetite concretes using MCNP-4C code and available experimental results*, *Annals of Nuclear Energy* 53 (2019) 529–534.



## A Bibliometric Analysis on Federated Learning

Ömer Algorabi<sup>1</sup> , Yusuf Sait Türkan<sup>2</sup> , Mesut Ulu<sup>3</sup> , Ersin Namli<sup>4</sup> 

<sup>1,2,4</sup>Department of Industrial Engineering, Istanbul University, Cerrahpaşa, İstanbul, Türkiye

<sup>3</sup>Department of Occupational Health and Safety, Bandırma Onyedi Eylül University, Balıkesir, Türkiye

### Article Info

Received: 24 Sep 2024

Accepted: 22 Dec 2024

Published: 31 Dec 2024

Research Article

**Abstract** – With the rapid advancement of technology and growing concerns about data privacy, federated learning (FL) has attracted considerable attention from the scientific community. The emergence of FL as a novel machine-learning approach and the volume of relevant papers and studies now call for a thorough investigation of FL. In the present research, an analysis was conducted on 3107 articles about federated learning exported from the Web of Science (WoS). The paper performs a bibliometric analysis to examine the productivity, citations, and bibliographic matching of significant authors, universities/institutions, and countries. The evolution of research material on federated learning over time was analyzed in the research. The study also provides comprehensive analysis by examining the most frequently used terms in the articles and attempting to identify trending areas of study with federated learning. This paper offers primary information on FL for readers worldwide and a comprehensive and accurate analysis of potential contributors.

**Keywords** – Federated learning, bibliometric analysis, network analysis

## 1. Introduction

Federated Learning (FL) is an emerging machine learning approach that addresses the problem of data aggregation and, at the same time, ensures data privacy. This approach integrates the server and clients (organizations, mobile devices, etc.) to develop a decentralized machine-learning operation. This technology was first introduced by Google in 2016. In the first study, the prediction of data input on devices was developed in the case where data is stored on mobile devices [1]. After the first study on FL, the number of studies in this field in literature is rapidly increasing, and its application areas are expanding. In this context, it has become essential to examine the course of the different studies in this field and the conceptual dimensions and applications of FL. Federated learning is, in a sense, a cryptic distributed machine learning scheme. In the system, users' data is not disclosed. The binding of data is achieved by combining local parameter information. Thus, data privacy is ensured, and a common machine-learning model can be developed between clients [2]. Considering the General Data Protection Regulation (GDPR), the federated learning framework has evolved rapidly in recent years. With the rapid increase in the use of artificial intelligence, the federated learning approach has been used in many applications, such as smartphones [3], IoT [4-6], healthcare [7-9], advertising [10], autonomous vehicles [11-12], energy forecasting [13-15], fraud detection [16], and insurance [17].

FL can be classified into Horizontal Federated Learning (HFL), Vertical Federated Learning (VFL), and Transfer Federated Learning (TFL) based on data partitioning. In HFL, the clients' data have the same features, but the sample space is different. In VFL, the IDs of the data come from the same sample, but the features are

<sup>1</sup>omer.algorabi@iuc.edu.tr; <sup>2</sup>ysturkan@istanbul.edu.tr; <sup>3</sup>mesutulu@beykent.edu.tr (Corresponding Author); <sup>4</sup>enamli@iuc.edu.tr

distinct. In the FTL scenario, the sample and attributes of the data differ mainly, while only a small part is similar [18]. There have been remarkable literature studies of these three types in recent years. Li et al. [19] developed a horizontal federated learning model for demand forecasting of e-commerce enterprises. Another study presents a system based on horizontal federated learning for automatically detecting IoT devices [20]. Wang et al. [21] proposed a retail supply chain demand forecasting model with a vertical federated learning framework. A data privacy-based system was developed using social media, e-commerce platforms, and Retailers' data. In a study conducted in 2023, vertical federated learning was used in energy load forecasting. A smart model is presented by incorporating three data sets in electricity demand, electricity generation, and energy price forecasting studies [22]. A federated transfer learning technique study presented a predictive model for cross-domain applications in smart manufacturing systems. They used two datasets of multiple images of pedestrians walking [23]. Chen et al. [24] proposed a federated transfer learning framework for Parkinson's disease diagnosis with smart wearable healthcare.

The privacy mechanism differs in the studies depending on the federated learning framework. The privacy mechanism is related to the aggregation of client data. Ye et al. [25] developed a model aggregation method for federated learning-based image processing. In this method, the clients' parameters in local learning are aggregated on the server. In a 2021 study for the communication of federated learning-based 6G-enabled vehicular networks, the parameter information in different layers of neural networks is aggregated by weighted averaging [26]. Another privacy mechanism used in studies is homomorphic encryption. Ou et al. [27] presented a vertical federated learning model with homomorphic encryption for risk management. Encryption is used to exchange model information. In the study conducted in 2022, a federated learning approach was used to classify medical images in an IoT-based healthcare system, and data privacy was ensured by homomorphic encryption [28]. Zhao et al. [29] presented a federated learning framework for intelligent traffic management using differential privacy. The differential privacy technique adds random noise to the aggregated data and prevents attacks on vulnerable data. Another study analyzed histopathological medical images using federated learning and differential privacy. A method was proposed that interrupts gradient updates and inserts noise in histopathology [30]. Jia et al. [31] presented a blockchain-enabled federated learning approach in the IIoT. Data protection is achieved through homomorphic encryption and differential privacy-based k-means clustering. Another privacy mechanism that is rarely encountered in studies is zero-knowledge systems. In these systems, clients only learn about the output. While these systems provide suitable security, their computational and communication costs are expensive [32]. Chen et al. [33] proposed a zero-knowledge clustering approach with federated learning against attacks on IoT data.

Researchers have developed several methods for data training of federated learning systems. In the literature, these methods can be categorized into three groups: statistical methods, methods based on decision trees, and methods based on neural networks. Gogineni et al. [34] developed a kernel regression model based on Fourier features for training local models. Wei et al. [35] presented a two-part logistic regression method in the learning process of a vertical federated learning system. In another vertical federated learning architecture, a method based on ridge regression is proposed for bi- and multi-party scenarios [36]. When the studies in which decision trees are preferred are examined, Yamamoto et al. [37] presented a gradient-boosting decision tree model based on federated learning for the privacy-based learning process using publicly available datasets. Studies such as financial risk prediction [38], intrusion detection [39], cancer disease prediction [40], etc., have been performed using the random forest method in federated learning applications. In a study predicting hospitalizations due to cardiac events, a support vector machine methodology was developed within the framework of federate learning [41]. Due to the nature of federated learning, neural network methods have been widely used by researchers to address privacy concerns. Vaid et al. [42] used the multilayer perceptron method for local training in a federated learning framework to predict mortality in hospitalized COVID-19 patients. A study using MR images performed local training with deep learning models [43]. LSTM, one of the deep learning methods, is another method used in the federated learning system [44–45]. Metaheuristic algorithms have been widely used for parameter optimization. Genetic algorithms [46], simulated annealing [47], particle swarm optimization [48], etc., have been used for parameter optimization of local training in federated learning

systems. Cui et al. [49] utilized federated learning technology and proposed an adaptive neuro-fuzzy inference system (ANFIS) optimized with gray wolf optimization to predict the reliability of groundwater levels. The literature also includes fuzzy models in the federated learning system [50–52].

In the short history of federated learning, there have been several reviews of the approach. KhoKhar et al. [53] reviewed image processing using federated learning. Reviews have been examined on the application of Federated Learning intrusion detection [54], resource optimization [55], healthcare [56], cyberspace security [57], electric vehicle transportation [58], 6G [59], etc. Javed et al. [60] surveyed vehicle networks and intelligent transportation systems using integrated federated learning and blockchain technologies. A study in 2023 presented a comprehensive survey of attacks and defenses against federated learning [61].

Our study aims to provide a comprehensive bibliometric analysis of federated learning publications. Our study was conducted to fill a research gap in the field of FL. In 2018, there were only two studies on FL, and if we look at the years 2022 and 2023, the fact that more than a thousand studies are proposed annually has led to the need for a comprehensive literature review in this field. As there is no bibliometric study on FL from a holistic perspective, this comprehensive study on FL from a broad perspective is expected to significantly contribute to the literature. The publications discussed in this study were obtained from the WoS database, and then a comprehensive bibliometric analysis was carried out. The content of the study includes (1) publication types, number of publications, citations, and timeline analysis; (2) analysis of prolific authors, countries, organizations, document sources, and funding agencies; (3) collaborative networks using R; (4) keyword identification.

Bibliometric analysis is a popular and meticulous approach for surveying and analyzing large volumes of scientific information [62–63]. This method allows us to statistically analyze the developments in a given field and make predictions in this area. In recent years, bibliometric analysis has gained significant attention. Li et al. [64] analyzed deep learning studies between 2007 and 2019 using VOS Viewer and Cite Space. The study analyzed annual publications, citations, most productive authors, institutions, countries, journals, and publications. In another study where the same analyses were carried out, operations research and management science publications in the Web of Science database were examined [65]. Ezugwu et al. [66] presented an extensive study by performing taxonomic classification and bibliometric analysis of metaheuristic algorithms. Shukla et al. [67] analyzed engineering applications in artificial intelligence from 1998 to 2018, indexed in the Web of Science and Scopus. Big data analytics and machine learning studies were analyzed in another bibliometric analysis of artificial intelligence research, 2006-2020. The articles from Scopus were analyzed by grouping them into clusters according to their fields of study [68]. Yu et al. [69] examined the studies published in the Fuzzy Optimization and Decision-Making journal between 2002 and 2017. In addition to analyzing the most productive publications, authors, countries, and organizations, the co-citation networks of cited authors, sources, and references were also revealed. Zhang et al. [70] conducted a topic change analysis of the Knowledge-Based Systems journal using bibliometric analysis. The study aims to predict future trends.

In this paper, after the introduction and the extensive literature review, Section 2 describes the data and methodology of the bibliometric analysis. Section 3 presents a comprehensive bibliometric analysis of FL. The bibliometric analysis examined the most productive authors, countries, organizations, and journals. Collaborative studies were revealed through network diagrams, and analyses were conducted on frequently used terms. Finally, Section 4 discusses future research directions and concludes the study.

## **2. Bibliometric Analysis**

### **2.1. Data Source and Methodology**

Web of Science is a database that lists the impact of scientific journals published in various disciplines, the number of citations received by published articles, authors' articles, and bibliographies of articles. WoS, also one of the most widely used databases for bibliometric analyses, indexes high-quality publications [69]. Most

review studies on publication, author, time, and other titles are done with the WoS database. The Web of Science Core Collection includes the Science Citation Index Expanded (SCIE), Social Sciences Citation Index (SSCI), Arts & Humanities Citation Index (AHCI), Emerging Sources Citation Index (ESCI), Conference Proceedings Citation Index – Science, Conference Proceedings Citation Index – Social Sciences & Humanities, Book Citation Index – Science, Book Citation Index – Social Sciences & Humanities citation indexes and covers titles from 1900 to the present day [71].

In our study, after reviewing planning, data collection, data analysis, and data visualization steps were carried out. As shown in Figure 1, opinions and suggestions for future research on federated learning were presented after all the steps. Before the data collection phase, the search topic was federated learning. Then, 5,740 publications were searched in the WoS repository. The earliest study in this field was published in 2017. The bibliometric analysis filtered the document type to articles only, and 3,107 searched publications were considered. Since our research aims to examine the studies on federated learning from a broad perspective, no special restrictions have been set for the data to be utilized. On 15 August 2023, all information on the articles included in the bibliometric analysis was transferred from WoS. The bibliometric analysis was initiated in August 2023. Accordingly, publications from 2024 could not be incorporated into the study. Further studies are planned, including an analysis of the current literature.

The exported data contains many attributes such as author, country, author institution, date, title, abstract, keywords, etc. In the bibliometric analysis, tables and figures are presented using total publications (TP), total citations (TC), citations per year, citations per publication (TC/TP), and h index performance indicators. Cooperation networks depict collaborations in the studies. Topics and concepts were analyzed with time graphs, thematic maps, and structure maps.

## 2.2. Data Source and Methodology

Using the WoS database, 5740 publications were found when the subject title was searched as federated learning. The publication types of these studies are given in Figure 2. Most studies were articles (3,107 publications) and proceeding papers (2460 publications). These two document types account for 97% of total publications. In early access and review article types, 204 and 129 studies were reported, respectively. It has been determined that there are insufficient studies on the publication types of correction, book chapters, letters, and book reviews. The number of publications in these document types is reported to be less than 10.

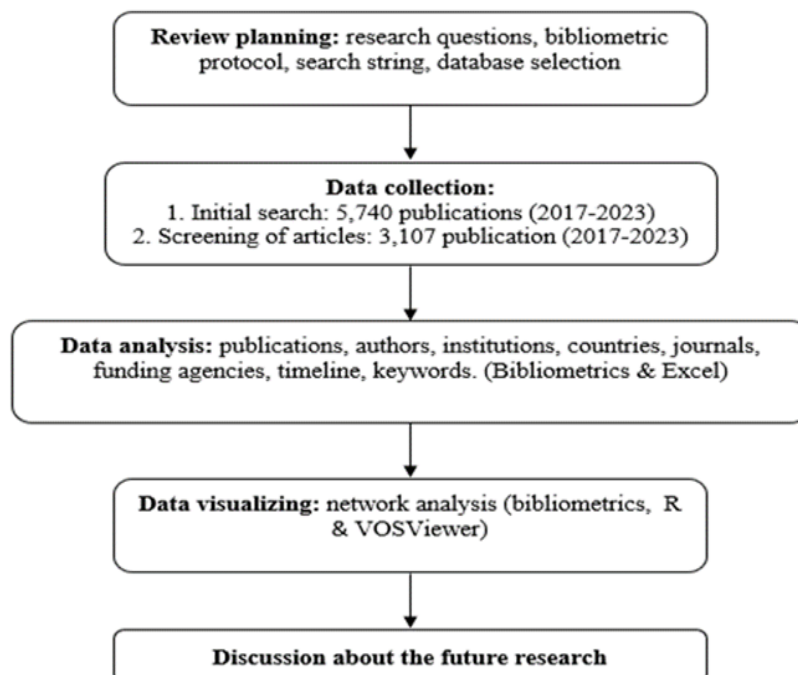
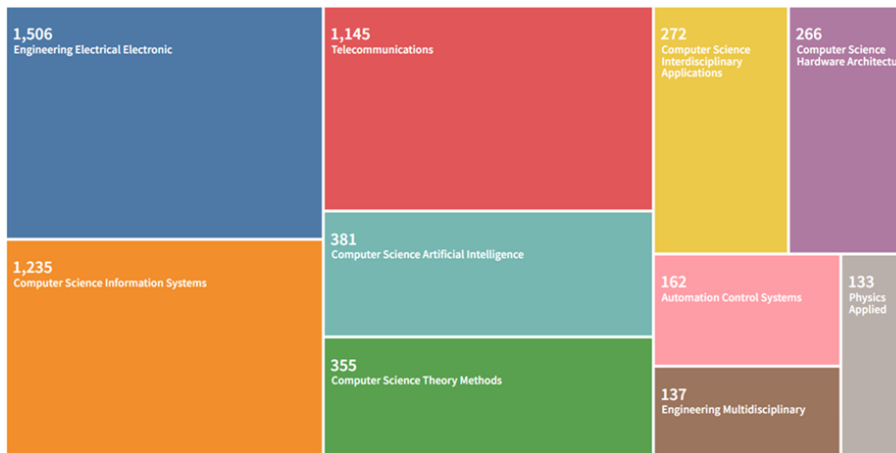


Figure 1. Research design



**Figure 2.** Document types of the publications

The categorization of article studies according to WoS is shown in Figure 3. It was found that article publications were primarily included in the study categories of engineering, electrical engineering, computer science, information systems, and telecommunications. The number of federated learning publications in these categories was more than 1000. After these categories, the fields with the highest number of articles are Computer Science Artificial Intelligence (381 articles) and Computer Science Theoretical Methods (355 articles). In particular, federated learning is known to be highly relevant to the disciplines of electrical and electronic engineering and computer science. The classification of federated learning studies according to research areas is given in Figure 4. Computer science and engineering fields account for 70% of the studies. Mathematics, physics, chemistry, materials science, and other disciplines contributed less than 10% to federated learning studies.



**Figure 3.** Top 10 WOS categories of the publications

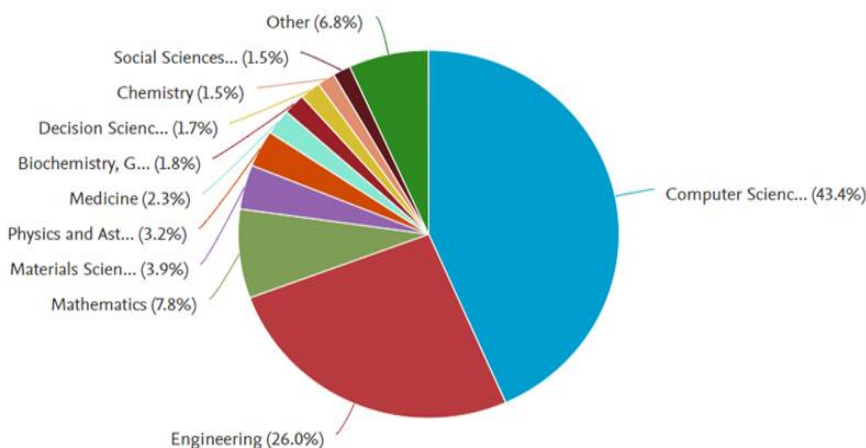


**Figure 4.** Research areas of the publications

According to the data obtained from the WoS database, the annual number of federated learning studies is illustrated in Figure 5. According to the graph, the first publication belongs to 2017. In 2019, studies in this field were limited to 12 articles. In 2020 and beyond, federated learning studies gained momentum, and the number of publications gradually increased. In 2020, the number of articles exceeded 100 for the first time, and in 2022, the number of articles exceeded 1,000. The number of publications in 2022 increased 2.13 times compared to 2021. The number of publications realized in 2023 (until August) is 1,080.

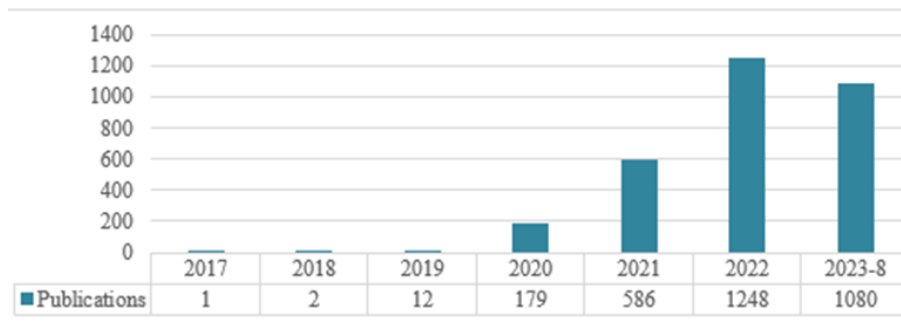


**Figure 5.** Annual publications

Figure 6 shows the annual number of citations and annual citations per publication. According to article studies conducted between 2017 and 2023-8, it was stated that there was an average of 8.83 citations per publication. It has been determined that 2020 publications received the most citations. This year's studies were cited 11276 times, and the average number of citations per article was 63. The highest TC/TP ratio was in 2019, with 482 citations per article. According to these results, it has been determined that the studies conducted in 2019 and 2020 are valuable, worth citing, and essential sources of current studies.

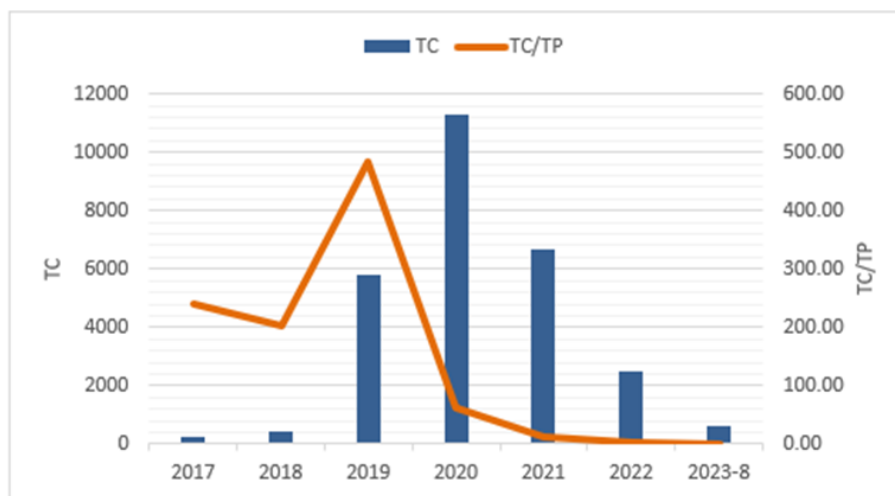


**Figure 6.** Citation trend analysis

The top 10 most influential publications, according to the highest number of citations, are given in Table 1. Yang et al. [72] is the most influential article with 3991 citations. All 10 articles have been cited more than 400 times, while the top 3 have been cited more than 800 times. On average, nine articles in the top 10 are cited 100 or more times per year. When the articles are analyzed, it is seen that all of them have three or more authors. Institutions in China conducted a Yang et al. [72] study. Li et al. [64] article was found to be prepared by USA institutions. Except for the 8th-ranked publication, it was determined that the articles ranked 3-10 were realized with the countries' cooperation.

### 2.2.1. Authorship and Institution Analysis

Since 2019, the authors have carried out many studies with federated learning. The most prolific authors in this field are given in Table 2. Twelve authors have published more than 20 articles. According to the total number of articles, Niyato (46 publications), Poor (38 publications), Han (32 publications), and Guizani (30

publications) are the most contributing authors. Yang and Liu stand out in the number of citations. Especially the article they published in 2019 received 3991 citations. These authors' TC/TP ratios are 210.74 and 191.88, respectively. Another critical performance measure is the h index. Niyato and Poor are the authors with the highest index. When the number of publications and the h index are analyzed together, the h index performance of Xiong, Zheng, and Bennis is also quite impressive.

Institutions' contributions to federated learning publications are given in Figure 7. Especially universities in China have significantly contributed to the FL area. Chinese Academy of Sciences ranks first in this field with 115 publications, followed by Beijing University of Posts Telecommunications with 94 publications. After China, the most productive organizations were found to be from Singapore. Nanyang Technological University has 91 articles in the field of FL. It was determined that the number of articles from the institutions in the top 10 is over 60.

**Table 1.** Most influential articles

Rank	Authors	Year	Title	Journal	Total Citation	TC/Year
1	Yang Q; Liu Y; Chen TJ; Tong YX	2019	Federated Machine Learning: Concept and Applications	ACM Transactions on Intelligent Systems and Technology	3991	798.2
2	Li T; Sahu AK; Talwalkar A; Smith V	2020	Federated Learning: Challenges, Methods, and Future Directions	IEEE Signal Processing Magazine	1233	308.25
3	Wang SQ; Tuor T; Salonidis T; Leung KK; Makaya C; He T; Chan K	2019	Adaptive Federated Learning in Resource Constrained Edge Computing Systems	IEEE Journal on Selected Areas in Communications	815	163
4	Lim WYB; Luong NC; Hoang DT; Jiao YT; Liang YC; Yang Q; Niyato D; Miao CY	2020	Federated Learning in Mobile Edge Networks: A Comprehensive Survey	IEEE Communications Surveys & Tutorials	686	171.5
5	Kairouz P; McMahan HB; Avent B; Bellet A; Bennis M; Bhagoji AN; ...; Than S.	2021	Advances and Open Problems in Federated Learning	Foundations and Trends in Machine Learning	583	194.33
6	Sattler F; Wiedemann S; Muller KR; Samek W	2020	Robust and Communication-Efficient Federated Learning From Non-i.i. Data	IEEE Transactions on Neural Networks and Learning Systems	512	128
7	Wang XF; Han YW; Wang CY; Zhao QY; Chen X; Chen M	2019	In-Edge AI: Intelligentizing Mobile Edge Computing, Caching, and Communication by Federated Learning	IEEE Network	465	93
8	Chen MZ; Yang ZH; Saad W; Yin CC; Poor HV; Cui SG	2021	A Joint Learning and Communications Framework for Federated Learning Over Wireless Networks	IEEE Transactions on Wireless Communications	447	149
9	Reke N; Hancox J; Li W; Milletari F; Roth HR; Albarqouni S; ...; Cardoso MJ.	2020	The Future of Digital Health with Federated Learning	NPJ Digital Medicine	425	106.25
10	Lu YL; Huang XH; Dai YY; Maharjan S; Zhang Y	2020	Blockchain and Federated Learning for Privacy-Preserved Data Sharing in Industrial IoT	IEEE Transactions on Industrial Informatics	419	104.75

**Table 2.** Most productive authors

Rank	Author	ORCID/DBLP	TP	TC	TC/TP	h_index
1	Niyato		46	2624	57.04	20
2	Poor		38	2339	61.55	19
3	Han		32	803	25.09	11
4	Guizani		30	649	21.63	12
5	Yang		27	5690	210.74	11
6	Liu		25	4797	191.88	8
7	Xiong		25	1261	50.44	14
8	Hong		23	1057	45.96	11
9	Li		23	946	41.13	9
10	Bennis		22	1469	66.77	12
11	Zheng		21	1385	65.95	13
12	Quek		21	1030	49.05	10

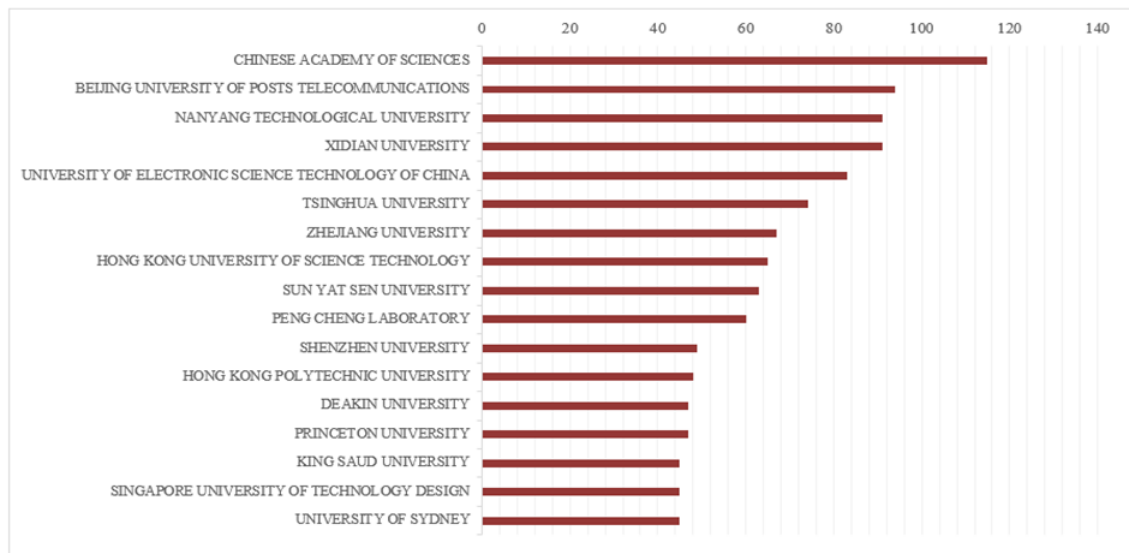


**Figure 7.** Most productive institutions

All scientific data must use the SI system (Système International d'Unités). There should be no space between the % sign and the number. The percent sign (%) is used after the number, e.g., 18%. A decimal point must be used in decimal numbers, e.g., 2.5 instead of 2,5.

### 2.2.2. Country / Region Analysis

Within the framework of bibliometric analysis, the 10 most productive countries were analyzed, and the total number of publications by year is shown in Figure 8. In terms of total articles, China (1715 articles) and the USA (477 articles) were reported to be the most significant contributors to federated learning, followed by Australia (266 articles), Canada (252 articles), England (251 articles), and South Korea (231 articles). India (176 articles), Singapore (147 articles), Saudi Arabia (126 articles), and Japan (1712 articles) countries were found to be less efficient. There has been a rapid increase in the number of publications in China over the years. In 2023 (up to August), they published 597 publications. China contributed 56% of the articles. The USA significantly contributed to federated learning with 233 publications in 2022. The publications in the USA represent 16% of the total number of articles.

The USA conducted its first article on federated learning in 2018. It is the only study in this field this year. Most of the countries in the top 10 appeared to have started work on articles on federated learning in 2019. Studies in India, which is among the top 10 most productive countries, were found to have started in 2021.

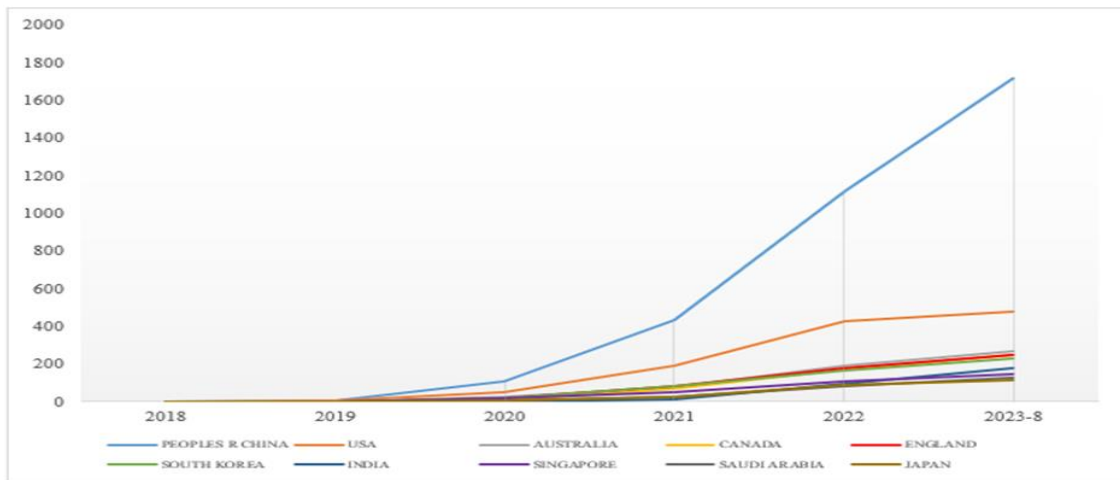


Figure 8. Most productive countries

### 2.2.3. Document Sources and Funding Agencies Analysis

The list of the top 10 publication titles is shown in Figure 9. It was determined that the most published journal of federated learning studies was the IEEE Internet of Things Journal, with 232 articles. IEEE Access follows this journal with 163 articles and IEEE Transactions on Industrial Informatics with 110. The number of publications in the other 10 journals in the top 10 is below 70. These 10 journals, which contribute the most to the field of FL, have 31% of the total articles.

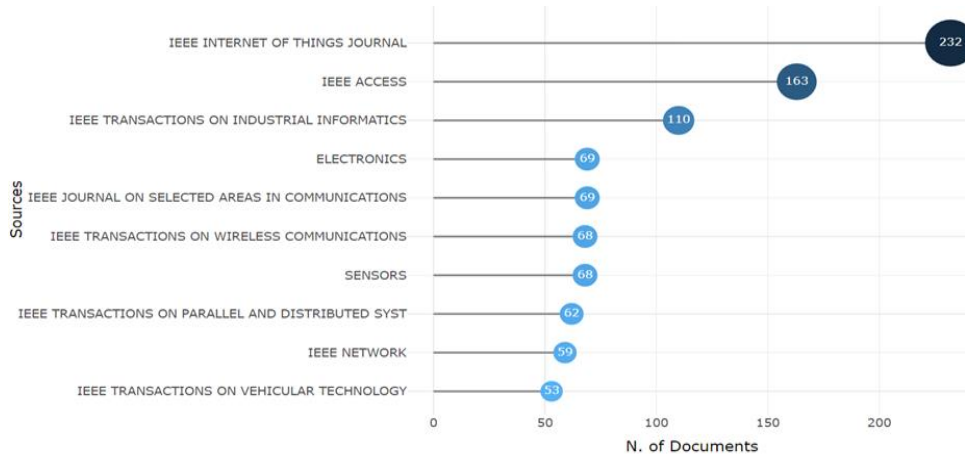


Figure 9. List of the top 10 contributing journals

The list of the top contributing financial agencies is shown in Figure 10. In particular, the National Natural Science Foundation of China (NSFC) ranks at the top in this field, contributing to 1112 articles. NSFC contributed more to the number of publications than the other funding agencies in the top 8. The NSFC organization was found to have funded 36% of the articles analyzed. The National Key Research and Development Program of China and Fundamental Research Funds for the Central Universities are other influential organizations in China with financial support for 242 and 161 articles, respectively. The National Science Foundation NSF (211 publications) from the USA, the National Research Foundation of Korea (126 publications), and the Ministry of Science Ict Msit Republic of Korea (96 publications) from South Korea are other prominent organizations. The European Union Eu is another organization among the top 10 funding agencies, contributing 87 articles.

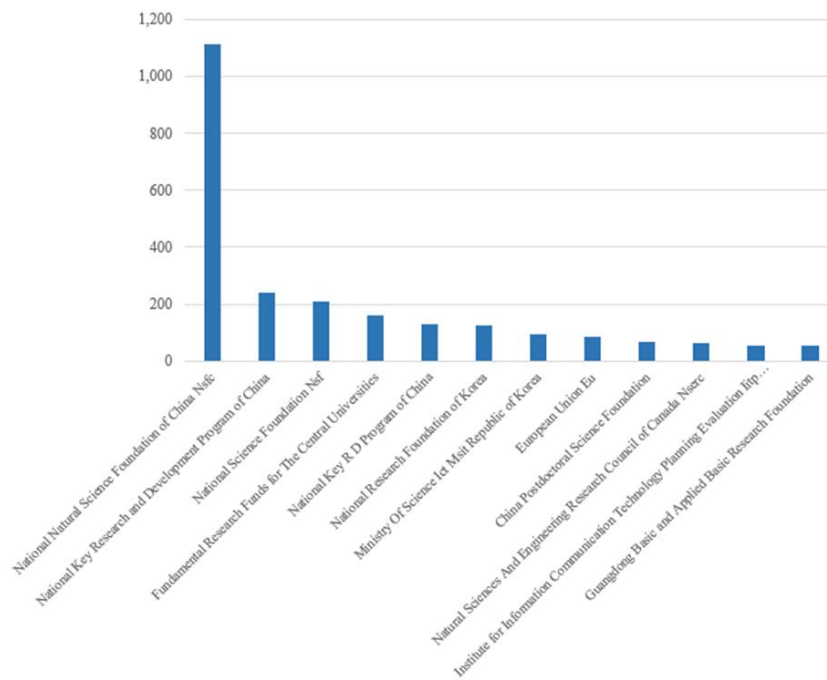


Figure 10. List of top contributing funding agencies

### 2.2.4. Timeline Analysis

The bibliometric analysis investigated the evolution of federated learning research content over time and produced timelines. The timeline illustrating the most commonly used terms in the titles of articles on federated learning is presented in Figure 11. In 2021-2023, it was determined that the most widely used bigrams in article titles other than federated learning were edge computing, learning framework, learning approach, machine learning, and deep learning. In 2023, the use frequency of these terms in titles was 39, 41, 27, 16, and 24. In particular, it was determined that the terms in the top 10 were used 60 or more times in article titles for three years. Upon analysis of the 8 months in 2023, it was found that the usage of the phrases reinforcement learning, intrusion detection, deep reinforcement, and mobile edge increased by 55%, 61%, 100%, and 55%, respectively, compared to 2022.

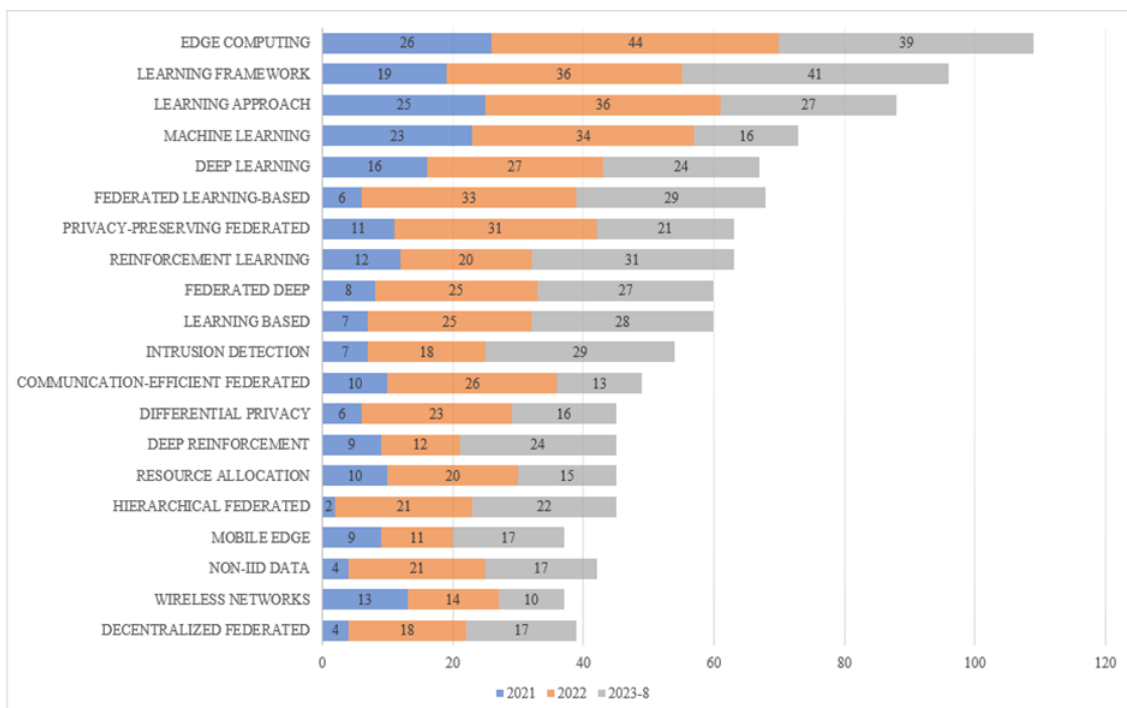
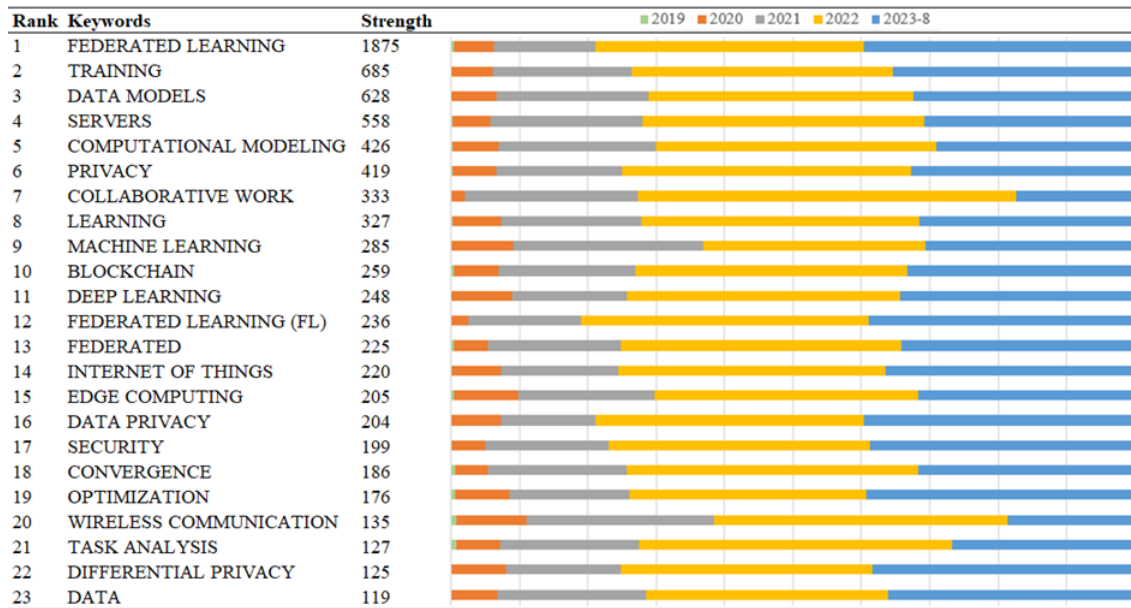


Figure 11. The most common bigrams in article titles



**Figure 12.** The most frequently used keywords in articles

The timeline of the most frequently used keywords in articles between 2019 and 2023 is shown in Figure 12. It was determined that the most commonly used keywords in the articles were Federated Learning, Training, Data Models, and Servers. It is seen that all 23 terms in the list are used as keywords in more than 100 articles. In 2022, the usage rates of Federated Learning and Training keywords in articles were 59% and 21%, respectively. However, in 2023, there was an increase in these rates, with Federated Learning rising to 69% and Training reaching 22%. In 2023, the frequency of server, computational modeling, privacy, and collaborative work in publications declined from 18%, 14%, 14%, and 14%, respectively, to 16%, 11%, 12%, and 5%.

Academic studies must contribute towards sustainable development goals and address environmental, social, and economic challenges. The analysis of the articles within the scope of Sustainable Development Goals is shown in Figure 13. Most of the studies are within the scope of Good Health and Well-Being and Sustainable Cities and Communities. In 2022, 55% of federated learning publications were within the scope of the Good Health and Well-Being sustainable target, while in 2023, this rate decreased to 37%. Federated learning applications for Industry Innovation and Infrastructure, Affordable and Clean Energy, Climate Action, Quality Education, and Responsible Consumption and Production are insufficient.

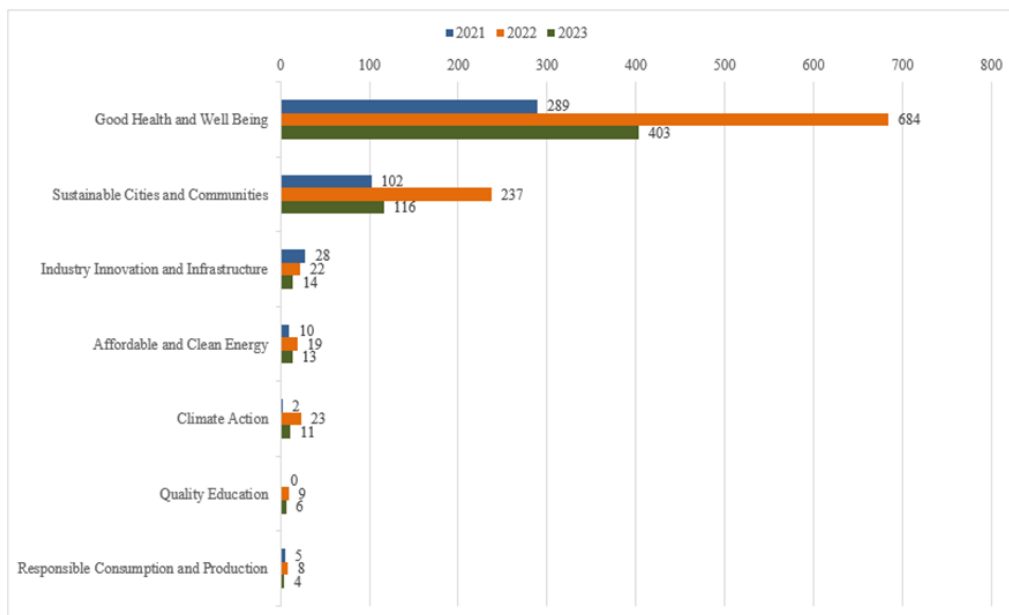


**Figure 13.** Sustainable Development Goals analysis

### 2.2.5. Social Network Analysis

The cooperation relationships of authors, organizations, and countries in federated learning article studies are given in Figures 14-16. The figures were generated using the R programming language's bibliometric library and the Shiny package framework. A link between two nodes signifies a connection between authors, countries, or organizations, where the width of the link represents the frequency of collaboration. The size of the node indicates the total link strength (TLS). Authors and institutions were categorized into six clusters, while countries were classified into two clusters differentiated by color.

In addition to examining clusters, collaborations were assessed based on betweenness and closeness values. Betweenness centrality quantifies the frequency at which a node appears on the quickest path between other nodes. In contrast, closeness centrality evaluates each node based on its proximity to all other nodes within the network.

According to the cooperation of the authors in Figure 14, Niyato's TLS was superior to the other authors. The most substantial collaboration relationship between Niyato was found to be with Xiong (18 articles), Kang (15 articles), and Wei (11 articles). Betweenness and closeness scores of Niyato were calculated to be 241.25 and 0.0145, respectively. Another author with high link strength was found to be Poor. The author frequently collaborated with Li (13 articles) and Chen (10 articles). Betweenness and closeness scores of the Poor are 97.52 and 0.013, respectively. In the analysis of author collaboration, it was observed that Han, Liu, and Bennis exhibited significant TLS values.

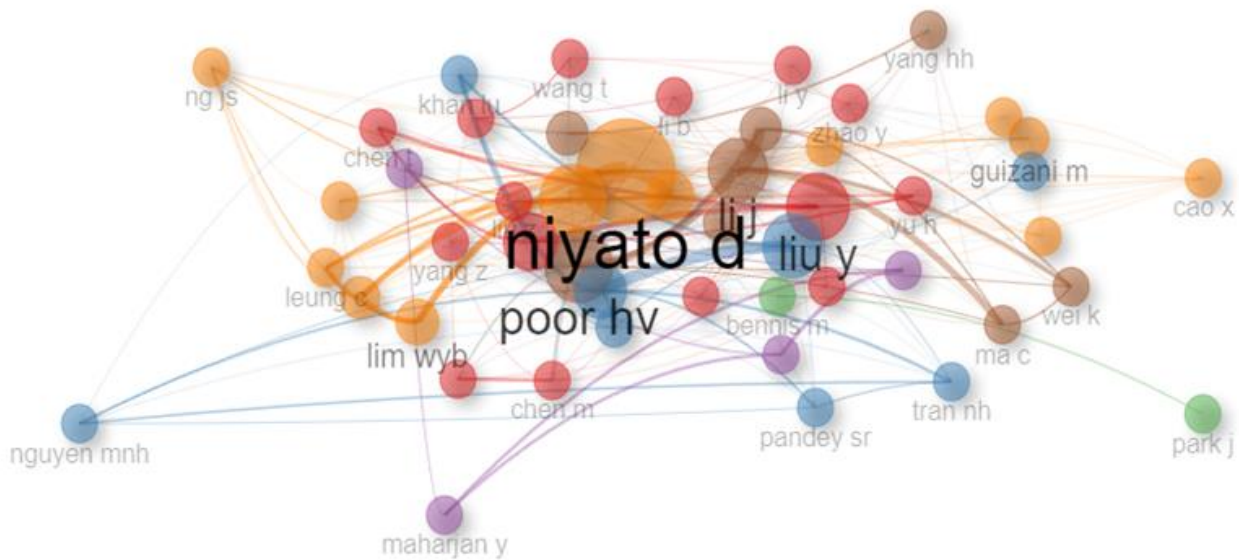


**Figure 14.** The collaboration network of authors

According to the collaborative network of institutions shown in Figure 15, the institutions with the highest betweenness scores are Nanyang Technological University, Tsinghua University, and Xidian University. The betweenness scores of these organizations are 88.22, 62.84, and 46.80, respectively. When looking at the organizations with the most collaborations, the Chinese Academy of Sciences (503 links), Nanyang Technological University (364 links), Tsinghua University (275 links), Xidian University (269 links), and Beijing University of Posts Telecommunications (202 links) stand out. The Chinese Academy of Sciences and the University of Science Technology of China Cas co-authored 39 articles, the highest collaboration.

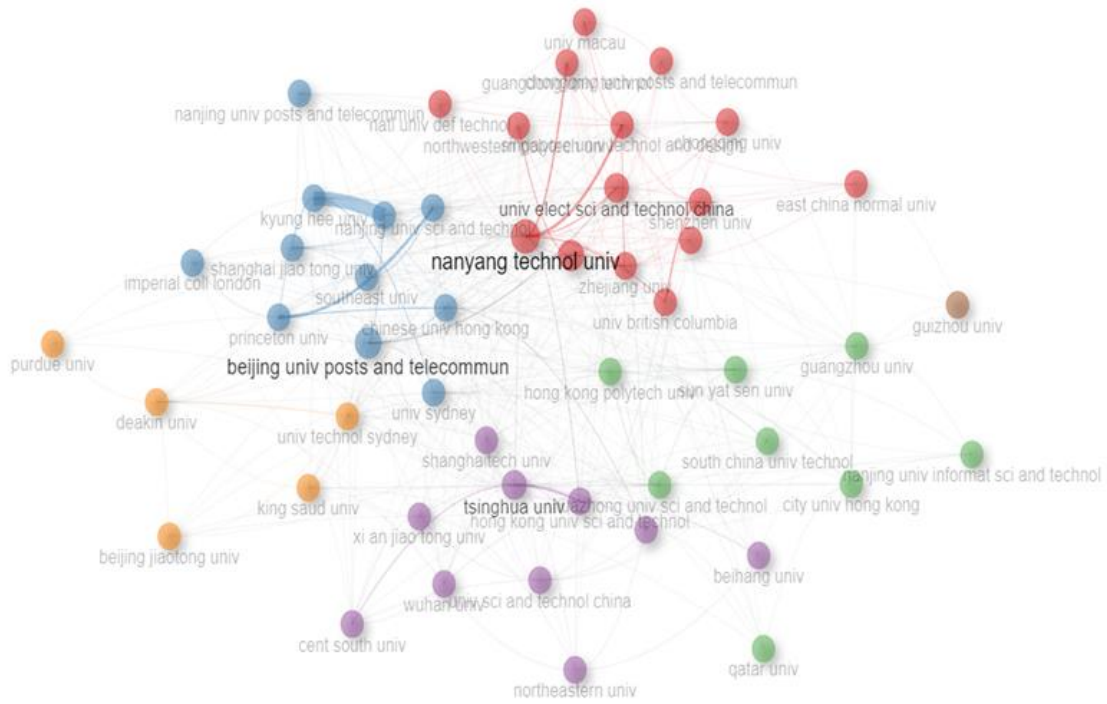


**Figure 15.** The collaboration network of institutions

The analysis reveals that in collaborations among the countries presented in Figure 16, China (1351 links), the USA (741 links), the United Kingdom (478 links), Canada (421 links), Australia (406 links), and South Korea (333 links) stand out in terms of the number of their joint publications. It was determined that China and the USA cooperated in 279 articles on federated learning. This represents 16% and 58% of the total published by China and the USA, respectively. China also has more than 100 collaborative publications with each of the following countries: the United Kingdom, Australia, Canada, and Singapore. Cooperation between the USA and Australia resulted in 56 articles, while cooperation between the USA and South Korea resulted in 55 articles.

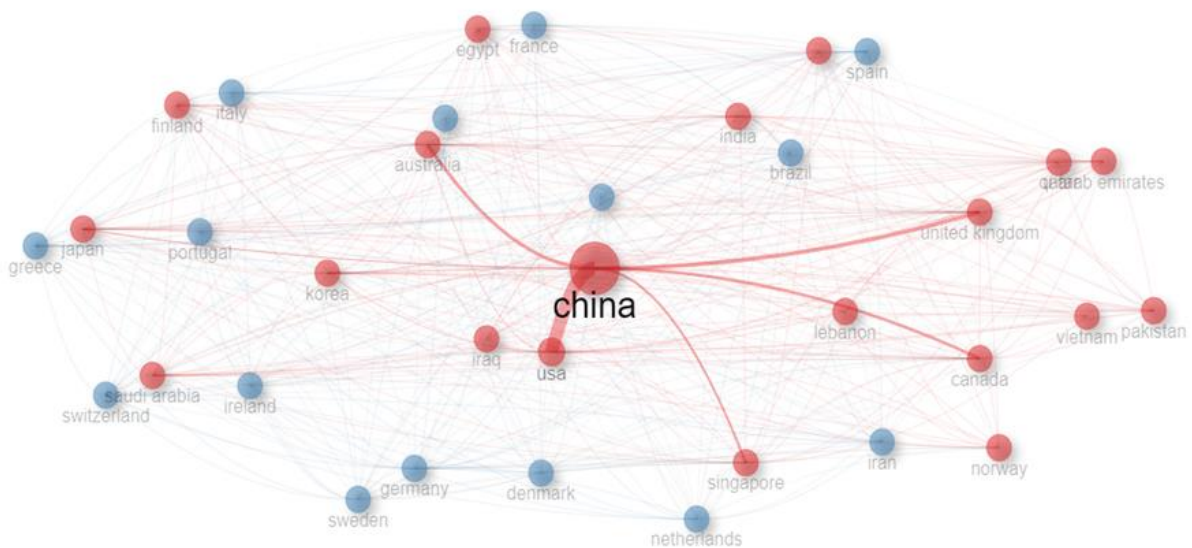


**Figure 16.** The collaboration network of countries



### 2.2.7. Conceptual Structure

This study section presents conceptual structure analyses of studies on federated learning. Thematic maps are intuitive plots that provide insight into the field's current and future sustainability. Themes are derived from the words in the publications. In thematic analysis, themes are derived by using words from publications. In thematic maps, these themes are characterized according to their intensity and centrality. Density is plotted on the y-axis, and centrality on the x-axis. Centrality gives the degree of relationship between topics; density measures the connectedness between nodes. These two characteristics measure whether specific topics are essential or not and the ability of the topic to develop and sustain itself. Themes in thematic maps can be analyzed according to the quadrant in which they are placed: (1) high density-high centrality: motor themes; (2) low density-high centrality: basic themes; (3) low density-low centrality: emerging or disappearing themes; (4) high density-low centrality: very specialized/niche themes.

Figure 19 illustrates the thematic map obtained using the keywords within the federated learning articles. The thematic map's basic themes include convergence, classification, deep, and costs. The basic themes have undergone extensive research and are challenging to anticipate their future direction. Motor themes representing advanced topics include channel estimation, signal processing, forecasting, smart grid, data privacy, optimization, and wireless communication. Distributed data, attention, security, privacy, and intelligence have been recognized as specialized/niche themes, indicating thoroughly researched but disconnected areas. Secret sharing, fault diagnosis, active learning, vertical federated learning, and poisoning attacks are low-density and centrality topics. These themes represent emerging topics or will disappear from the field of study. The federated learning theme is both a basic and motor theme.

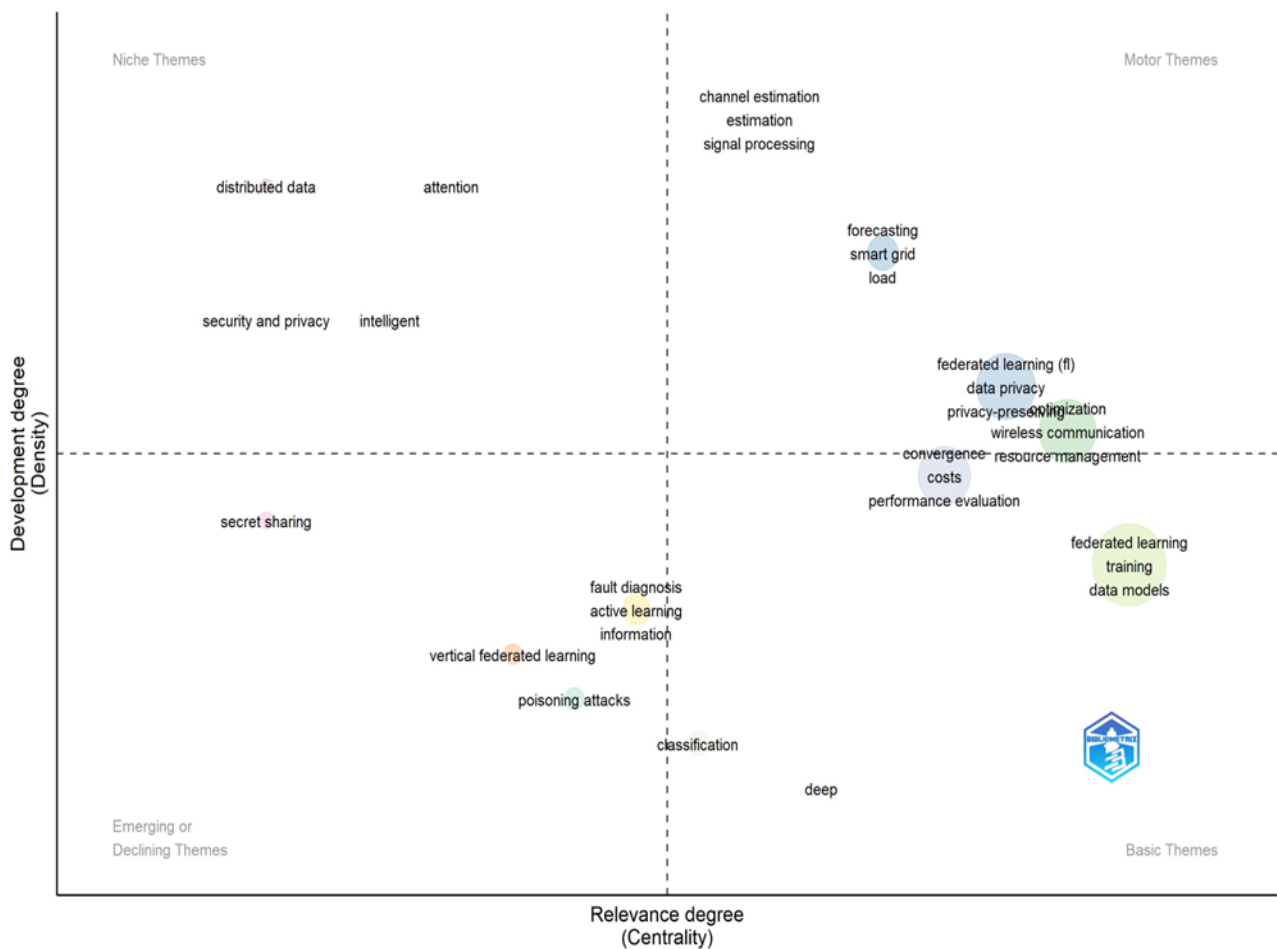


Figure 19. Keywords thematic map

Based on the analysis of an article titled Bigrams, the thematic map is illustrated in Figure 20. The basic themes are federated learning, deep learning, transfer learning, fault diagnosis, detection system, detection system, multiple access, and transportation systems. At the same time, generative adversarial and adversarial networks are motor themes. While gradient descent, activity recognition, image classification, and access networks are among the niche themes open to development, medical data is identified on the map as a topic that may evolve or disappear.

Factorial analysis was performed to reduce the dimensionality of the data and represent it in a low-dimensional space. Multiple correspondence analysis (MCA) is a popular approach for reducing dimensions to analyze the relationship pattern of various categorical dependent variables. The conceptual structure map generated by applying the MCA method is shown in Figure 21. The topics were clustered by determining the number of clusters as five. Cluster 1 (yellow) contains topics mostly about privacy methods, whereas Cluster 2 (blue) is about learning approaches. Cluster 3 (red) includes model-related issues like cloud computing, IoT, servers, and predictive models. Cluster 4 (green) is relevant to application areas such as resource allocation, wireless communication, energy consumption, and scheduling. A single cluster until they reach the topic in use. Height measures the distance between terms or clusters; distant terms describe different concepts.

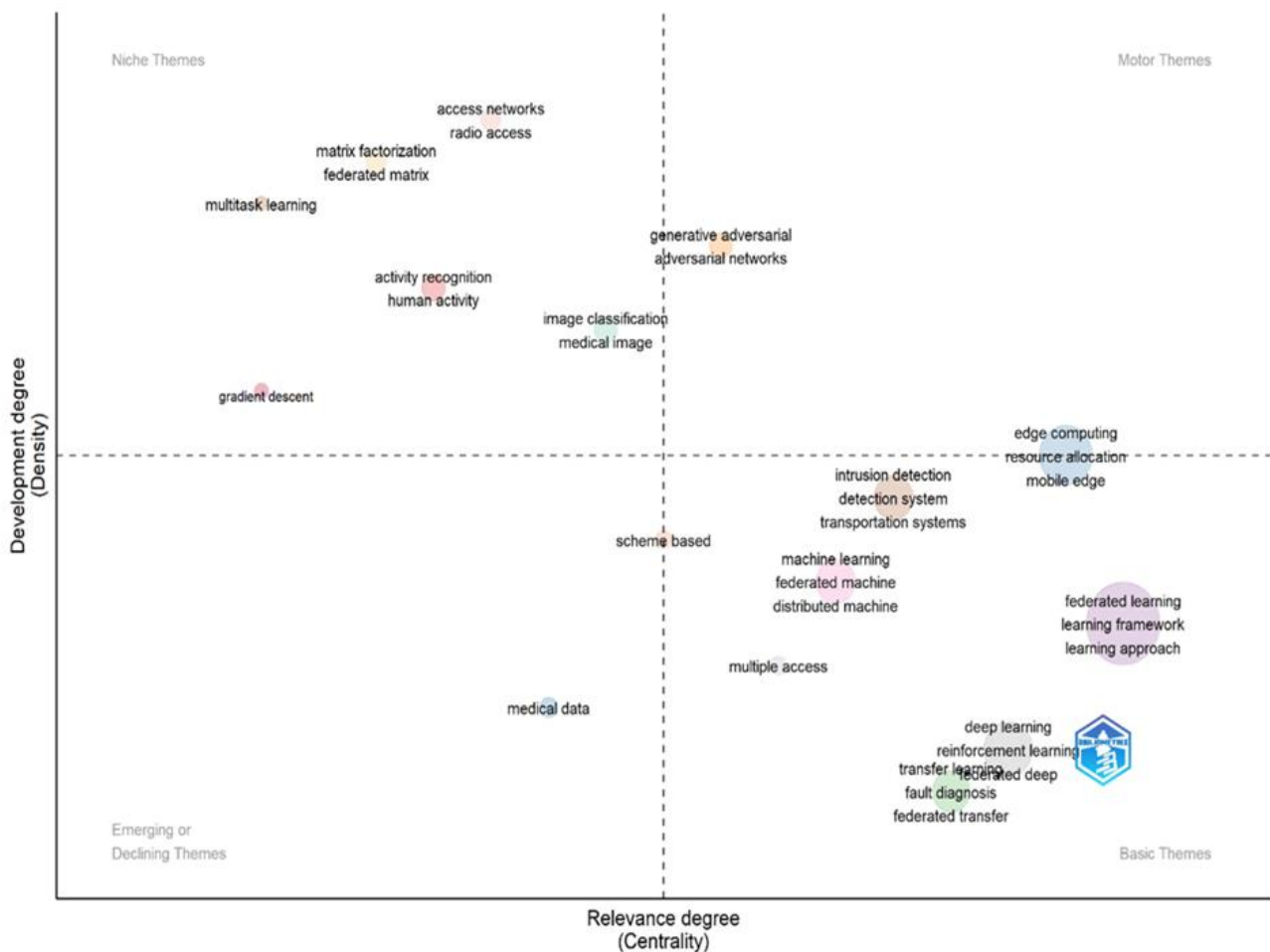


Figure 20. Article title bigrams thematic map

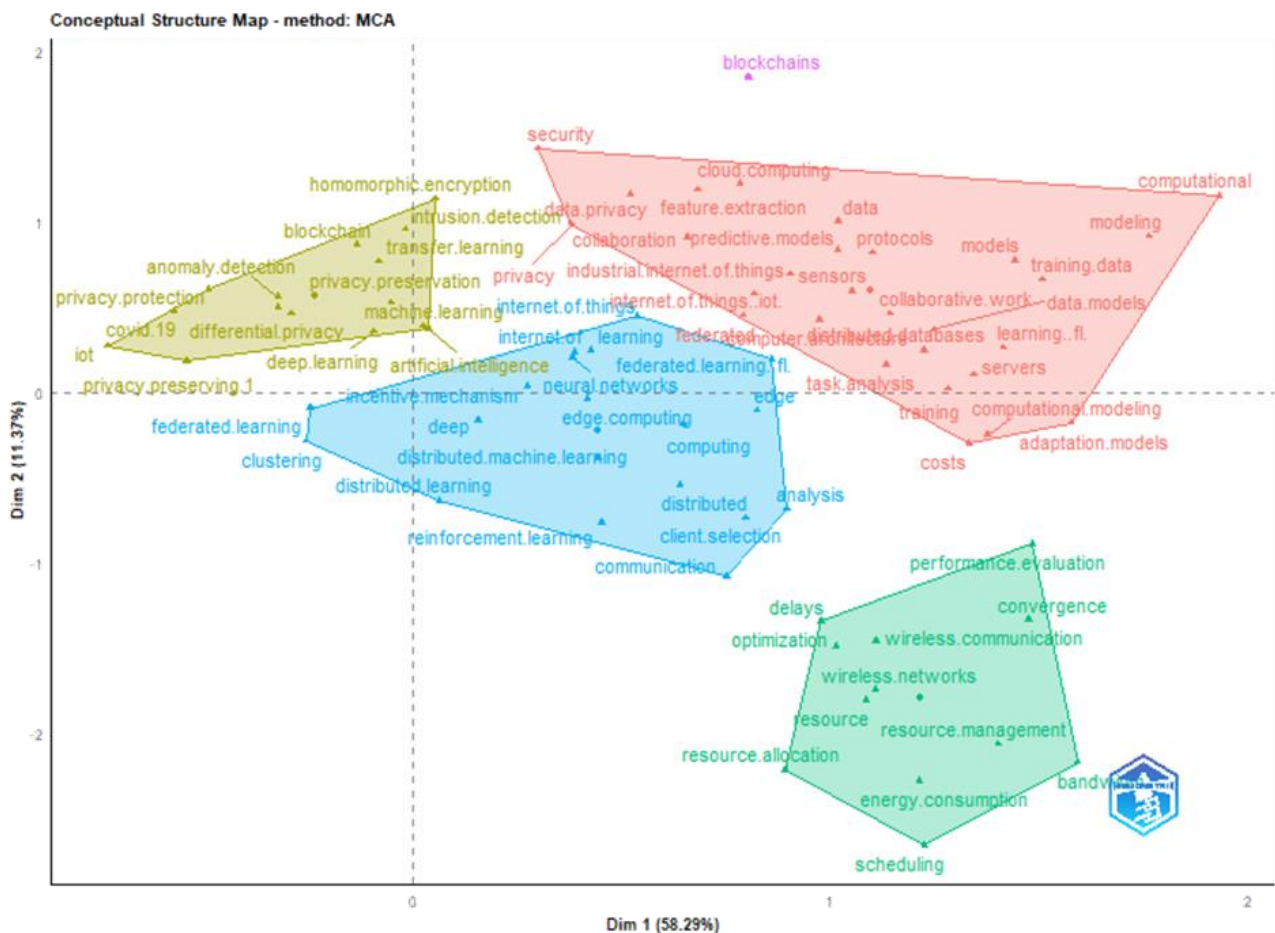


Figure 21. Keywords conceptual structure map

### 3. Results and Discussion

The present study analyzed articles on federated learning from the first publication until now. Publications exported from the WoS database underwent analysis, incorporating various statistical and bibliometric methods. These articles represent 54% of the total publications in different documents. Since federated learning is a new technology, the annual number of articles in this field is not very high. Still, the increase in the number of articles each year is remarkable. Our study has shown that federated learning studies are concentrated in some areas and applications, particularly in the health and energy sectors.

Analyzing publications, citations, and keywords provides insights into the trends and characteristics of articles. Between 2017 and 2023-8, six articles with 500 or more citations out of 3107 publications were retrieved from the WoS database. Niyato, Poor, Han, and Guizani are the most influential authors in the article studies of federated learning. The most commonly occurring terms as Keywords Plus were identified as Internet, Networks, and Privacy. Publications regarding a novel machine learning approach to federated learning technology are anticipated to experience exponential growth soon. In the future, it aims to carry out a study on bibliometric analysis of federated learning publications in health or energy.

The countries with the most extensive articles include China, the USA, Australia, Canada, and England. China was found to have more than 100 articles in collaboration with the following countries: the USA, United Kingdom, Australia, Canada, and Singapore. In other countries, this technology has not yet attracted much interest. Chinese Academy of Sciences (China), Beijing University of Posts Telecommunications (China), and Nanyang Technological University (Singapore) were determined as the most productive institutions.

An analysis of the topic distributions and clusters of studies in the federated learning literature shows that all studies can be grouped into four or five clusters. In particular, when interpreting the results of the conceptual

structure map and the topic dendrogram, it can be seen that the study topics related to establishing data security and privacy methods, one of the main objectives of federated learning, form a cluster. Algorithms and approaches related to machine learning, deep learning, reinforcement, and distributed machine learning, which can be categorized under learning algorithms, form another cluster. As in all machine learning studies, the raw material of federated learning power is data. As a result of bibliometric analysis, a cluster of topics such as IoT, cloud computing, training data, and predictive models have been created to collect, transfer, and process data. In federated learning studies, hardware and software resources and Internet and energy-related resources are extremely important. At this point, research on planning, managing, and evaluating software, hardware, the internet, and energy resources also attracts attention as studies that form another cluster.

The initial studies on federated learning surfaced in 2017, and since then, the number of studies in this field has rapidly increased. Figures 19 and 20 provide thematic maps, and Figure 12 shows the most frequently used keywords in articles, offering insight into the course of these studies. Upon analyzing the usage rates of keywords between 2017 and 2022, it is evident that there has been an increase in the usage of specific keywords in the last two years. After analyzing the positions and potentials of keywords in thematic maps created based on keywords and headings, five main concepts emerge: security and privacy, distributed data, data privacy, data models, and optimization. Although the number of new studies and recent growth potential is increasing, specific areas of interest may decrease. These areas include data poisoning attacks, fault diagnosis, active learning information, and collaborative work on data.

Data reliability is crucial for success in machine learning applications. Traditional approaches are vulnerable to data poisoning, negatively affecting success by compromising data integrity and causing bias in training results. FL, originally conceived to establish a private and secure environment for distributed machine learning model training, currently grapples with notable privacy and security challenges. Aggregating clients' updated models on the global server is susceptible to security lapses, facilitating potential attacks such as poison attacks. Unauthorized access to updates could allow a malicious user to reverse weights, compromising client data.

Consequently, there is a burgeoning interest in researching secure and privacy-preserving FL involving homomorphic encryption, differentiable privacy, and blockchain integrated with client selection models. Preventing malicious attacks from inserting faulty data is necessary to maintain data integrity. Poisoning attack modes, such as model distortion and feedback weaponization, are a topic of study with potential implications for federated learning.

Optimization is one of the most common areas for future work in FL. The optimal selection of customers is crucial in FL because model updates enable global model convergence. Existing customer selection models prioritize how to select customers rather than determining the required number. Currently, a fixed number of customers without standardized criteria is widely used. Although increasing the number of clients may improve convergence, practical limitations such as resource constraints prevent this approach. Therefore, research is needed to determine the optimal number of clients. Additionally, further research is required to develop mechanisms that can dynamically determine client selection in each FL round.

The development of technology and the decrease in sensitivity towards data privacy have caused major problems. Federated learning technology addresses customers' concerns in this regard. Not only is learning a promising technology federated, but it is also a new artificial intelligence business model. Especially considering its advantages of privacy and security, scalability, low power requirements, improved accuracy of results, reduced data training costs, and data minimization, this approach is likely to become increasingly common in machine learning research. On the other hand, the current federated learning technology has many problems related to communication and security breaches. Improvements in the methodology are significant to solve these problems. Therefore, the number of publications on topics such as local training, merging models, communication of clients, communication costs, and attacks on the system will increase.

Once federated learning methodologies are developed, collaborative work on data analysis using FL technology by companies in the same country or different countries will increase rapidly. In particular,

companies with varying service areas can overcome the lack of customer information with this approach and achieve higher percentage accuracy rates in classification, clustering, and prediction studies. Federated learning will become a major requirement in healthcare, energy, retail, smart transport, insurance, banking, manufacturing, etc.

## 4. Conclusion

This study provides an extensive and detailed bibliometric analysis of FL publications, offering valuable insights into the evolution of research in this field. The results show that China and the USA dominate publications, while FL applications in health and energy sectors are emerging as significant focus areas. The thematic analysis also reveals strong research clusters around data privacy, machine learning approaches, and optimization techniques. These findings demonstrate FL's rapid growth and diverse applications, particularly in addressing privacy concerns.

Future studies should address the security and communication challenges associated with FL. As privacy-preserving methods such as homomorphic encryption and differential privacy gain traction, further research is needed to improve scalability and reduce communication costs. Additionally, developing dynamic client selection mechanisms and more efficient optimization techniques will be essential to enhance FL's effectiveness in real-world applications across various industries.

## Author Contributions

The first author: Conceptualization, software, formal, analysis writing—review and editing, visualization. The second author: Data curation, visualization, supervision, project administration. The third author: Methodology, validation, investigation, writing—original draft preparation, supervision. The fourth author: Resources data curation, project administration. All authors read and approved the final version of the paper.

## Conflicts of Interest

All the authors declare no conflict of interest.

## Ethical Review and Approval

No approval from the Board of Ethics is required.

## References

- [1] L. Li, Y. Fan, M. Tse, K. Y. Lin, *A review of applications in federated learning*, Computers and Industrial Engineering 149 (2020) 106854 15 pages.
- [2] C. Zhang, Y. Xie, H. Bai, B. Yu, W. Li, Y. Gao, *A survey on federated learning*, Knowledge-Based Systems 216 (2021) 106775 11 pages.
- [3] C. Yang, Q. Wang, M. Xu, Z. Chen, K. Bian, Y. Liu, X. Liu, *Characterizing impacts of heterogeneity in federated learning upon large-scale smartphone data*, in: J. Leskovec, M. Grobelnik, M. Najork, J. Tang, L. Zia (Eds.), Proceedings of the Web Conference 2021, Ljubljana, 2021, pp. 935-946.
- [4] A. Imteaj, U. Thakker, S. Wang, J. Li, M. H. Amini, *A survey on federated learning for resource-constrained IoT devices*, IEEE Internet of Things Journal 9 (1) (2021) 1-24.
- [5] S. Savazzi, M. Nicoli, V. Rampa, *Federated learning with cooperating devices: A consensus approach for massive IoT networks*, IEEE Internet of Things Journal 7 (5) (2020) 4641-4654.
- [6] J. Pang, Y. Huang, Z. Xie, Q. Han, Z. Cai, *Realizing the heterogeneity: A self-organized federated*

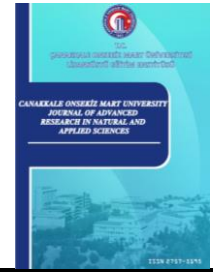
- learning framework for IoT*, IEEE Internet of Things Journal 8 (5) (2020) 3088-3098.
- [7] A. Qayyum, K. Ahmad, M. A. Ahsan, A. Al-Fuqaha, J. Qadir, *Collaborative federated learning for healthcare: Multi-modal COVID-19 diagnosis at the edge*, IEEE Open Journal of the Computer Society 3 (2022) 172–184.
- [8] L. Sun, J. Wu, *A scalable and transferable federated learning system for classifying healthcare sensor data*, IEEE Journal of Biomedical and Health Informatics 27 (2) (2022) 866–877.
- [9] A. Jiménez-Sánchez, M. Tardy, M. A. G. Ballester, D. Mateus, G. Piella, *Memory-aware curriculum federated learning for breast cancer classification*, Computer Methods and Programs in Biomedicine 229 (2023) 107318 10 pages.
- [10] J. Bian, J. Huang, S. Ji, Y. Liao, X. Li, Q. Wang, J. Zhou, D. Dou, Y. Wang, H. Xiong, *Feynman: Federated learning-based advertising for ecosystems-oriented mobile apps recommendation*, IEEE Transactions on Services Computing 16 (5) (2023) 3361–3372.
- [11] S. R. Pokhrel, J. A. Choi, *Decentralized federated learning approach for connected autonomous vehicles*, in: S. Bahk, Y. Kim, S. C. Bang, S. L. Kim, Y. J. Choi (Eds.), IEEE Wireless Communications and Networking Conference Workshops, Seoul, 2020, pp. 1–6
- [12] T. Zeng, O. Semiari, M. Chen, W. Saad, M. Bennis, *Federated learning on the road autonomous controller design for connected and autonomous vehicles*, IEEE Transactions on Wireless Communications 21 (12) (2022) 10407–10423.
- [13] Y. M. Saptura, D. T. Hoang, D. N. Nguyen, E. Dutkiewicz, M. D. Mueck, S. Srikanteswara, *Energy demand prediction with federated learning for electric vehicle networks*, in: V. Cerf, D. Zuckerman, T. Mooren, J. Hong (Eds.), IEEE Global Communications Conference, Waikoloa, 2019, pp. 1–6
- [14] M. Savi, F. Olivadese, *Short-term energy consumption forecasting at the edge: A federated learning approach*, IEEE Access 9 (2021) 95949–95969.
- [15] Y. Wang, I. L. Bennani, X. Liu, M. Sun, Y. Zhou, *Electricity consumer characteristics identification: A federated learning approach*, IEEE Transactions on Smart Grid 12 (4) (2021) 3637–3647.
- [16] Q. Yang, Y. Liu, T. Chen, Y. Tong, *Federated machine learning: Concept and applications*, ACM Transactions on Intelligent Systems and Technology 10 (2) (2019) 1–19.
- [17] H. Gupta, D. Patel, A. Makade, K. Gupta, O. P. Vyas, A. Puliafito, *Risk prediction in the life insurance industry using federated learning approach*, IEEE 21st Mediterranean Electrotechnical Conference, Palermo, 2022, pp. 948–953.
- [18] D. Jatain, V. Singh, N. Dahiya, *A contemplative perspective on federated machine learning: Taxonomy, threats and vulnerability assessment and challenges*, Journal of King Saud University-Computer and Information Sciences 34 (9) (2022) 6681–6698.
- [19] J. Li, T. Cui, K. Yang, R. Yuan, L. He, M. Li, *Demand forecasting of e-commerce enterprises based on horizontal federated learning from the perspective of sustainable development*, Sustainability 13 (23) (2021) 13050 29 pages.
- [20] M. V. Shenoy, *HFedDI: A novel privacy preserving horizontal federated learning-based scheme for IoT device identification*, Journal of Network and Computer Applications 214 (2023) 103616 12 pages.
- [21] H. Wang, F. Xie, Q. Duan, J. Li, *Federated learning for supply chain demand forecasting*, Mathematical Problems in Engineering 2022 (1) (2022) Article ID 4109070 8 pages.
- [22] Z. Mao, H. Li, Z. Huang, Y. Tian, P. Zhao, Y. Li, *Full data-processing power load forecasting based on vertical federated learning*, Journal of Electrical and Computer Engineering 2023 (1) (2023) Article ID 9914169 9 pages.

- [23] I. Kevin, K. Wang, X. Zhou, W. Liang, Z. Yan, J. She, *Federated transfer learning based cross-domain prediction for smart manufacturing*, IEEE Transactions on Industrial Informatics 18 (6) (2021) 4088–4096.
- [24] Y. Chen, X. Qin, J. Wang, C. Yu, W. Gao, *Fedhealth: A federated transfer learning framework for wearable healthcare*, IEEE Intelligent Systems 35 (4) (2020) 83–93.
- [25] D. Ye, R. Yu, M. Pan, Z. Han, *Federated learning in vehicular edge computing: A selective model aggregation approach*, IEEE Access 8 (2020) 23920–23935.
- [26] X. Zhou, W. Liang, J. She, Z. Yan, I. Kevin, K. Wang, *Two-layer federated learning with heterogeneous model aggregation for 6g supported internet of vehicles*, IEEE Transactions on Vehicular Technology 70 (6) (2021) 5308–5317.
- [27] W. Ou, J. Zeng, Z. Guo, W. Yan, D. Liu, S. Fuentes, *A homomorphic-encryption-based vertical federated learning scheme for risk management*, Computer Science and Information Systems 17 (3) (2020) 819–834.
- [28] L. Zhang, J. Xu, P. Vijayakumar, P. K. Sharma, U. Ghosh, *Homomorphic encryption-based privacy-preserving federated learning in IoT-enabled healthcare system*, IEEE Transactions on Network Science and Engineering 10 (5) (2022) 2864–2880.
- [29] Y. Zhao, J. Zhao, M. Yang, T. Wang, N. Wang, L. Lyu, D. Niyato, K. Y. Lam, *Local differential privacy-based federated learning for the Internet of things*, IEEE Internet of Things Journal 8 (11) (2021) 8836–8853.
- [30] M. Adnan, S. Kalra, J. C. Cresswell, G. W. Taylor, H. R. Tizhoosh, *Federated learning and differential privacy for medical image analysis*, Scientific Reports 12 (1) (2022) Article Number 1953 10 pages.
- [31] D. Jatain, V. Singh, N. Dahiya, *A contemplative perspective on federated machine learning: Taxonomy, threats and vulnerability assessment and challenges*, Journal of King Saud University-Computer and Information Sciences 34 (9) (2022) 6681–6698.
- [32] B. Jia, X. Zhang, J. Liu, Y. Zhang, K. Huang, Y. Liang, *Blockchain-enabled federated learning data protection aggregation scheme with differential privacy and homomorphic encryption in IIoT*, IEEE Transactions on Industrial Informatics 18 (6) (2021) 4049–4058.
- [33] Z. Chen, P. Tian, W. Liao, W. Yu, *Zero-knowledge clustering based adversarial mitigation in heterogeneous federated learning*, IEEE Transactions on Network Science and Engineering 8 (2) (2020) 1070–1083.
- [34] V. C. Gogineni, S. Werner, Y. F. Huang, A. Kuh, *Communication-efficient online federated learning framework for nonlinear regression*, in: H. Li, S. Furui, T. Chen (Eds.), IEEE International Conference on Acoustics, Speech and Signal Processing, Singapore, 2022, pp. 5228–5232.
- [35] Q. Wei, Q. Li, Z. Zhou, Z. Q. Ge, Y. Zhang, *Privacy-preserving two-parties logistic regression on vertically partitioned data using asynchronous gradient sharing*, Peer-to-Peer Networking and Applications 14 (2021) 1379–1387.
- [36] J. Cai, X. Liu, Z. Yu, K. Guo, J. Li, *Efficient vertical federated learning method for ridge regression of large-scale samples*, IEEE Transactions on Emerging Topics in Computing 11 (2) (2022) 511–526.
- [37] F. Yamamoto, S. Ozawa, L. Wang, *eFL-Boost: Efficient federated learning for gradient boosting decision trees*, IEEE Access 10 (2022) 43954–43963.
- [38] X. Chen, S. Zhou, B. Guan, K. Yang, H. Fao, H. Wang, Y. Wang, *Fed-eini: An efficient and interpretable inference framework for decision tree ensembles in vertical federated learning*, in: U. Fayyad, X. Zhu (Eds.), IEEE International Conference on Big Data, Virtual Event, 2021, pp. 1242–1248

- [39] T. Markovic, M. Leon, D. Buffoni, S. Punnekkat, *Random forest based on federated learning for intrusion detection*, in: I. Maglogiannis, J. Macintyre (Eds.), *International Conference on Artificial Intelligence Applications and Innovations*, Springer, Cham, 2022, pp. 132–144.
- [40] T. U. Islam, R. Ghasemi, N. Mohammed, *Privacy-preserving federated learning model for healthcare data*, in: S. Vuong (Ed.), *IEEE 12th Annual Computing and Communication Workshop and Conference*, Las Vegas, 2022, pp. 0281–0287.
- [41] T. S. Brisimi, R. Chen, T. Mela, A. Olshevsky, I. C. Paschalidis, W. Shi, *Federated learning of predictive models from federated electronic health records*, *International Journal of Medical Informatics* 112 (2018) 59–67.
- [42] A. Vaid, S. K. Jaladanki, J. Xu, S. Teng, A. Kumar, S. Lee, S. Somani, I. Paranjpe, J. K. De Freitas, T. Wanyan, K. W. Johnson, M. Bıçak, E. Klang, Y. J. Kwon, A. Costa, S. Zhao, R. Miotto, A. W. Charney, E. Böttinger, Z. A. Fayad, G. N. Nadkarni, F. Wang, B. S. Glicksberg, *Federated learning of electronic health records to improve mortality prediction in hospitalized patients with COVID-19: Machine learning approach*, *JMIR Medical Informatics* 9 (1) (2021) e24207 11 pages.
- [43] P. Guo, P. Wang, J. Zhou, S. Jiang, V. M. Patel, *Multi-institutional collaborations for improving deep learning-based magnetic resonance image reconstruction using federated learning*, in: M. S. Brown, R. Sukthankar, T. Tan, L. Zelnik (Eds.), *Proceedings of the IEEE/CVF Conference on Computer Vision and Pattern Recognition*, Nashville, 2021 pp. 2423–2432.
- [44] I. Khan, A. Guerrieri, G. Spezzano, A. Vinci, *Occupancy prediction in buildings: An approach leveraging LSTM and Federated Learning*, *IEEE Intl Conf on Dependable, Autonomic and Secure Computing, Intl Conf on Pervasive Intelligence and Computing, Intl Conf on Cloud and Big Data Computing, Intl Conf on Cyber Science and Technology Congress*, Calabria, 2022 pp. 1–7.
- [45] G. Zhang, S. Zhu, X. Bai, *Federated learning-based multi-energy load forecasting method using CNN-Attention-LSTM model*, *Sustainability* 14 (19) (2022) 12843 14 pages.
- [46] S. Agrawal, S. Sarkar, M. Alazab, P. K. R. Maddikunta, T. R. Gadekallu, Q. V. Pham, *Genetic CFL: Hyperparameter optimization in clustered federated learning*, *Computational Intelligence and Neuroscience* 2021 (1) (2021) Article ID 7156420 10 pages.
- [47] H. N. C. Neto, I. Dusparic, D. M. F. Mattos, N. C. Fernandes, *FedSA: Accelerating intrusion detection in collaborative environments with federated simulated annealing*, in: A. Clemm, G. Maier (Eds.), *IEEE 8th International Conference on Network Softwarization*, Milan, 2022, pp. 420–428.
- [48] S. Park, Y. Suh, J. Lee, *FedPSO: Federated learning using particle swarm optimization to reduce communication costs*, *Sensors* 21 (2) (2021) 600 13 pages.
- [49] F. Cui, Z. A. Al-Sudani, G. S. Hassan, H. A. Afan, S. J. Ahammed, Z. M. Yaseen, *Boosted artificial intelligence model using improved alpha-guided grey wolf optimizer for groundwater level prediction: Comparative study and insight for federated learning technology*, *Journal of Hydrology* 606 (2022) 127384 16 pages.
- [50] X. Zhu, D. Wang, W. Pedrycz, Z. Li, *Horizontal federated learning of Takagi–Sugeno fuzzy rule-based models*, *IEEE Transactions on Fuzzy Systems* 30 (9) (2021) 3537–3547.
- [51] N. Cha, Z. Du, C. Wu, T. Yoshinaga, L. Zhong, J. Ma, F. Liu, Y. Ji, *Fuzzy logic-based client selection for federated learning in vehicular networks*, *IEEE Open Journal of the Computer Society* 3 (2022) 39–50.
- [52] E. Yoo, H. Ko, S. Pack, *Fuzzy clustered federated learning algorithm for solar power generation forecasting*, *IEEE Transactions on Emerging Topics in Computing* 10 (4) (2022) 2092–2098.
- [53] F. A. KhoKhar, J. H. Shah, M. A. Khan, M. Sharif, U. Tariq, S. Kadry, *A review on federated learning*

- towards image processing, *Computers and Electrical Engineering* 99 (2022) 107818 19 pages.
- [54] E. M. Campos, P. F. Saura, A. González-Vidal, J. L. Hernández-Ramos, J. B. Bernabé, G. Baldini, A. Skarmeta, *Evaluating federated learning for intrusion detection in internet of things: Review and challenges*, *Computer Networks* 203 (2022) 108661 16 pages.
- [55] L. G. F. da Silva, D. F. H. Sadok, P. T. Endo, *Resource optimizing federated learning for use with IoT: A systematic review*, *Journal of Parallel and Distributed Computing* 175 (2023) 92–108.
- [56] H. Li, C. Li, J. Wang, A. Yang, Z. Ma, Z. Zhang, D. Hua, *Review on security of federated learning and its application in healthcare*, *Future Generation Computer Systems* 7144 (2023) 271–290.
- [57] F. Liu, M. Li, X. Liu, T. Xue, J. Ren, C. Zhang, *A review of federated meta-learning and its application in cyberspace security*, *Electronics* 12 (15) (2023) 3295 35 pages.
- [58] Z. Teimoori, A. Yassine, *A review on intelligent energy management systems for future electric vehicle transportation*, *Sustainability* 14 (21) (2022) 14100 23 pages.
- [59] Z. Yang, M. Chen, K. K. Wong, H. V. Poor, S. Cui, *Federated learning for 6G: Applications, challenges, and opportunities*, *Engineering* 8 (2022) 33–41.
- [60] A. R. Javed, M. A. Hassan, F. Shahzad, W. Ahmed, S. Singh, T. Baker, T. R. Gadekallu, *Integration of blockchain technology and federated learning in vehicular (IoT) networks: A comprehensive survey*, *Sensors* 22 (12) (2022) 4394 24 pages.
- [61] H. S. Sikandar, H. Waheed, S. Tahir, S. U. R. Malik, W. Rafique, *A detailed survey on federated learning attacks and defenses*, *Electronics* 12 (2) (2023) 260 18 pages.
- [62] N. Donthu, S. Kumar, D. Mukherjee, N. Pandey, W. M. Lim, *How to conduct a bibliometric analysis: An overview and guidelines*, *Journal of Business Research* 133 (2021) 285–296.
- [63] M. Ulu, Y. S. Türkan, *Bibliometric analysis of traffic accident prediction studies from 2003 to 2023: Trends, patterns, and future directions*, *Promet-Traffic and Transportation* 36 (5) (2024) 1–21.
- [64] Y. Li, Z. Xu, X. Wang, X. Wang, *A bibliometric analysis on deep learning during 2007–2019*, *International Journal of Machine Learning and Cybernetics* 11 (2020) 2807–2826.
- [65] J. M. Merigó, J. B. Yang, *A bibliometric analysis of operations research and management science*, *Omega* 73 (2017) 37–48.
- [66] A. E. Ezugwu, A. K. Shukla, R. Nath, A. A. Akinyelu, J. O. Agushaka, H. Chiroma, P. K. Muhuri, *Metaheuristics: A comprehensive overview and classification along with bibliometric analysis*, *Artificial Intelligence Review* 54 (2021) 4237–4316.
- [67] A. K. Shukla, M. Janmajaya, A. Abraham, P. K. Muhuri, *Engineering applications of artificial intelligence: A bibliometric analysis of 30 years (1988–2018)*, *Engineering Applications of Artificial Intelligence* 85 (2019) 517–532
- [68] J. Z. Zhang, P. R. Srivastava, D. Sharma, P. Eachempati, *Big data analytics and machine learning: A retrospective overview and bibliometric analysis*, *Expert Systems with Applications* 184 (2021) 115561 18 pages.
- [69] D. Yu, Z. Xu, W. Wang, *A bibliometric analysis of Fuzzy Optimization and Decision Making (2002–2017)*, *Fuzzy Optimization and Decision Making* 18 (2019) 371–397.
- [70] Y. Zhang, H. Chen, J. Lu, G. Zhang, *Detecting and predicting the topic change of knowledge-based systems: A topic-based bibliometric analysis from 1991 to 2016*, *Knowledge-Based Systems* 133 (2017) 255–268.
- [71] Clarivate, (2023), <https://clarivate.libguides.com/librarianresources/coverage>, Accessed 15 Nov 2023.

- [72] W. Yang, Y. Zhang, K. Ye, L. Li, C. Z. Xu, *Ffd: A federated learning based method for credit card fraud detection*, in: K. Chen, S. Seshadri, L. J. Zhang (Eds.), *Big Data–BigData 2019: 8th International Congress, Held as Part of the Services Conference Federation, San Diego, 2019*, Springer, Proceedings 8, pp. 18–32.



# A Novel Approach for Detection of Cyber Attacks in MQTT-Based IIoT Systems Using Machine Learning Techniques

Serkan Gönen<sup>1</sup> 

<sup>1</sup>Department of Software Engineering, Faculty of Engineering and Architecture, İstanbul Gelişim University, İstanbul, Türkiye

## Article Info

Received: 01 Oct 2024

Accepted: 28 Nov 2024

Published: 31 Dec 2024

Research Article

**Abstract** – The Internet of Things (IoT) and the Industrial Internet of Things (IIoT) have grown significantly in the last decade, underlining the increasing need for effective, secure, and reliable data communication protocols. The widely accepted Message Queuing Telemetry Transport (MQTT) protocol, with its structure that meets the needs of welding-oriented devices in IoT and IIoT applications, is a prime example. However, its user-friendly simplicity also makes it susceptible to threats such as Dispersed Services Rejection (DDoS), Brete-Force, and incorrectly shaped package attacks. This article introduces a robust and reliable framework for preventing and defending against such attacks in MQTT-based IIoT systems based on the theory of merging attacks. The expert system incorporates the Adaboost model and can detect anomalies by processing network traffic in a closed setting and identifying impending threats. With its robust design, the system was subjected to various attack scenarios during testing, and it consistently detected interventions with an average accuracy of 92.7%, demonstrating its potential for use in intervention detection systems. The research findings not only contribute to the theoretical and practical concerns about the effective protection of IIoT systems but also offer hope for the future of cybersecurity in these systems.

**Keywords** – *IoT, IIoT, MQTT, cyber security, machine learning*

## 1. Introduction

In the past few years, systems of the Internet of Things (IoT) and the so-called Industrial Internet of Things (IIoT) have rapidly developed technological paradigms. On the one hand, IoT is more like a network structure where all physical devices are connected to the internet and can share data. At the same time, IIoT firmly takes that technology one step further in automating and enhancing industrial activities in smaller terraces. Fast and better protocols for data exchange between the devices are indispensable if one is to succeed in such systems. In this regard, the telemetry transmission protocol, the MQTT, has replaced the most popular data exchange protocol in IoT and IIoT systems. The MQTT protocol is a variation that provides an interesting solution mainly for low-end devices due to its low resource profiles and bandwidth consumption. This is important, especially in terms of energy efficiency and transmission of data over a network with minimum overhead. However, many cyber security risks exist because of the protocol's simplicity and lightweight. Particularly, crimes of this sort include brute-force attacks, Distributed Denial of Service (DDoS) attacks whereby the target system is flooded with incoming packets from uncontrolled users and malformed packets that attack the application layer of the systems using the MQTT protocol. In this regard, several security measures and intrusion detection systems are being developed to better secure systems based on the MQTT protocol.

<sup>1</sup>sgonen@gelisim.edu.tr (Corresponding Author)

Numerous works of literature aim to prevent the ambiguity of the security issues related to the MQTT protocol. Al-Fayoumi and Al-Haija [1] achieved approximately a 99.5% success rate in detecting low-rate DDoS attacks in MQTT-based IoT environments using various machine learning models, primarily decision trees. Due to the results presented in this paper, it is evident how helpful machine learning algorithms are during attempts to perform an active defense. Simultaneously, Fikriansyah et al. achieved a 95% accuracy rate against DDoS attacks in IIoT environments, which leveraged the Random Forest algorithm to identify the attacks. Considering these findings, it can be reasoned that such attacks against the MQTT protocol employing machine learning devices are easily identifiable [2]. Nevertheless, most of this study has mainly focused on classes of attacks, and it is necessary to broaden the scope of studies. There is a greater demand for real-time detection systems, especially in IIoT. Some IIoT threats involve the latency of threats and detection effectiveness. In inter-industrial IoT connections, potential threats must always be detected and attended to with speed and precision since either dawning or loss of data could halt production or any other proceedings.

This research seeks to create an expert system based on MQTT capable of identifying and guarding against cyber-attacks in IIoT systems. This expert system processes the network traffic in near real-time using machine learning techniques and identifies possible risks. The primary goal of the research is to find a security solution that maintains the performance of IIoT systems while raising their security level. Within this framework, experiments were performed on different kinds of attacks, including brute-force, DDoS, and malicious packet attacks, and machine-learning algorithms were built on the obtained data. In this phase, attacks were performed to gather data to be used in the expert system, and such data was used to monitor network traffic. This system could perform IDS attacks after the learning processes on this data had been completed and all relevant results were analyzed. This study provides many types of attack examples that can be performed, and it provides real-time interaction and reaction. Moreover, in light of the area for improvement, the expert system is expected to be able to meet threats within its scope later on. In such a case, the present study's findings benefit academic and industrial uses and implications.

The present study concerns the cyber security risks in such an MQTT-based IIoT system, draws attention to issues of this kind, and offers new solutions. More precisely, the expert system constructed using the AdaBoost algorithm has high accuracy and less resource utilization, which is an essential advancement in developing real-time detection and preventing intrusions in IIoT systems. This research serves as a critical illustration of the application of technologies such as machine learning and expert systems and, at the same time, offers practical approaches to the problem of security in an industrial context. For this reason, it impacts both the academic and industrial settings and is worth viewing as a valuable addition to the existing body of knowledge on securing IIoT systems.

Incorporating cryptographic models in machine learning has emerged as a pivotal strategy for enhancing data security in IoT and IIoT systems. Techniques such as homomorphic encryption allow machine learning algorithms to operate on encrypted data without decryption, safeguarding data confidentiality throughout training and inference. Integrating these cryptographic models can fortify IIoT systems against data exfiltration and unauthorized access while maintaining operational efficiency.

Within the article, we present how security silos of the systems integrating MQTT protocol are built starting MMA, from generalization and application of Security areas to a review of literature on existing Security solutions targeted at this emerging Security area. Then, it concentrates on the expert system design process with the help of machine learning, the performance analysis, the description of the benefits and the limitations of the system, and the suggestion for further work.

## 2. Literature Research

Due to its lightweight, practical nature, the MQTT protocol is gaining popularity in the transmission of data on the Internet of Things (IoT) and Industrial Internet of Things (IIoT) systems. Nevertheless, this protocol has been a target for cyber security research because of its risks. Al-Fayoumi and Al-Haija [1] utilized decision

trees and machine learning models. They achieved high outcomes in detecting low-rate distributed denial of service attacks (LR-DDoS) within MQTT IoT environments. Likewise, Fikriansyah et al. [2] used a Random Forest algorithm to detect DDoS attacks and reported encouraging results in IIoT environments. At the same time, Shahri et al. [3] proposed and implemented an SDN-based MQTT framework for enhanced real-time performance and scalability within industrial scenarios. Mahajan et al. [4] elevated communication security through symmetric encryption algorithms such as AES and HMAC over the MQTT protocol, from ensuring data integrity to data confidentiality. Moreover, Kombate et al. [5] addressed the weaknesses in the MQTT protocol and provided cyber-range technologies for mitigating cyber threats, including replay attacks, MITM, and DDoS. Buccafurri et al. [6] also presented the OTP verification over blockchain technology to reduce energy consumption and improve security during MQTT communication. It should be noted that, as much as the MQTT protocol facilitates data transfer in IoT and IIoT systems, such systems may be rendered susceptible because of security loopholes.

More specifically, applying algorithms like the AES and HMAC solves problems like data eavesdropping and data tampering, as this guarantees the confidentiality and integrity of the data in question. This study shifts the existing paradigm of MQTT, which relies on security over the resources it hosts, and aims to maintain secure MQTT communication with optimal security resources on devices. Liu et al. [7] further developed that and suggested the adoption of more SM2 and SM4 Cryptographic algorithms along with the MQTT protocol, extending the functionalities of user validation and access control. This scheme fills the conventional emptiness in the protocol's security vulnerabilities, mainly in data security and mutual authentication. These results emphasize that these algorithms do improve security and do not interfere with the efficiency of the systems to a significant extent. Saqib and Moon [8] have also provided lightweight solutions in the form of multi-factor authentication systems for edge computing. A new security architecture was presented for IoT applications based on the MQTT protocol, which allowed the authors to use ECC and fuzzy extractors. This system protects IoT devices from cryptographic attacks by enhancing session essential consent and reciprocated security arrangements. It is more suitable for low-powered people who work with less computation.

As another approach, Koprov et al. [9] proposed a framework for machine authentication for the MQTT 5.0 standard, with the support of functional data analysis (FDA), among others. Through deeper machine data analysis, this technique aims to raise the bar for better machine authentication within IIoT and Smart Manufacturing. This methodology raises confidence in the authentication processes, especially in the digital twins and predictive maintenance domains. Lohachab and Karambir [10] presented one lightweight authentication and authorization method for IoT device Communications using ECC, intended for resource-limited regional IoT devices. This development helps improve IoT device authentication mechanisms by allowing cross-device safe content sharing. In particular, the study attempts to provide such optimal security deployments and focuses on deployment challenges posed by resource-constrained devices. IoT and IIoT systems have created various frameworks and methodologies to solve safety problems caused by these interdependent devices, mainly as they are used more widely in critical infrastructures. Vaccari et al. [11] in MQTTSET suggested that the data set be designed to form a basis for machine learning models to protect MQTT-based IoT networks from possible cyber-attacks. In light of this, Mishra and Kertesz [12] have reviewed the existing literature on using MQTT in IoT systems. Investigation emphasized the aspects in which rapid growth areas and safety measures grow as fast as protocol use. Francis et al. [13] have a genetic algorithm and random forest-based attack detection system (GA\_RF), which obtains almost perfect accuracy in detecting threats in MQTT-enabled IIoT systems. To expand their research, Patel and Doshi [14] developed a new MQTT protocol safety standard that increases user authentication and data safety on IoT networks. Deng [15] proposes spectrogram analysis and an attack detection system that integrates spectrogram analysis and evolving neural networks to better detect interventions in the context of IoT. Prajisha and Vasudevan [16] proposed a better performance of the Intruder detection system using a slight Gradient reinforcement machine through chaos salp herd optimization. Likewise, investigations were conducted on which defense measures could be applied to protect IIoT devices from attacks.

According to Karacaymaz and Artuner [17], the expert system based on AI should be unique. Selamnia et al. [18] aimed to develop a comprehensive cybersecurity training program, including course content development, recruitment, and system setup, utilizing instructors and mentors to deliver practical and theoretical cybersecurity skills over ten months. Zuhari et al. [19] MQTT networks were improved in property engineering for a real-time pseudonym for a relief-based routing protocol. They presented the usefulness of some tree models in perception performance. Sharma and Bhushan propose a hybrid framework incorporating PUFs and machine learning to defend against distributed denial of service (DDoS) attacks in MQTT-based IoT systems. The system improves upon existing credential-based authentication by augmenting the PUF-enabled mechanism to create real-time, in-depth optimization. It combines it with a machine learning-based Intrusion Detection System (IDS), which aims to eliminate malevolent attacks against the system assets at the time of their occurrence. Their findings are not only secure but also efficient in terms of resource utilization, which makes them a better vendor for usage on lightweight IoT devices [20].

This study provides valuable insights into new tendencies toward creating security systems, especially those dedicated to addressing the issue of energy use in IoT devices. In general, the gaps covered by collaboration and some available studies included approaches that raised the level of security on the IIoT systems built on MQTT, including machine learning and encryption technologies. However, to address the issues of real-time detection and flexibility concerning the different aspects of the attacks, the following section describes the expert system developed to enhance security within these environments.

### 3. Methodology

This work focused on creating and applying an expert system based on the MQTT protocol for determining and preventing cyber threats to IIoT systems. This methodology combined classical network defense approaches with contemporary machine learning approaches to solve the security problem of IIoT architectures.

#### 3.1. Overview of the Methodology

The methodology can be broken down into several phases illustrated in Figure 1. This method can be further shown in its three main stages: selecting a machine learning model, including attack simulation and data collection, expert system design, and evolution of the expert system. The first stage included a simulated attack of various attacks against the previously described test bed. At this stage, brute force, DDoS, and poorly formatted package attacks were carried out on the MQTT broker. During these attacks, data on network traffic were then caught to provide a database useful for training machine learning models. Roller was appointed and synthesized by expert systems. This was the background of the methodology for creating an expert system to analyze real-time network traffic and detect potential attacks. Therefore, this expert system was created using machine learning methods to classify network traffic into normal and attack. The system was well planned, aiming at high efficiency and accuracy in detecting attacks to achieve a minimum delay in the network.

The machine learning model selection process was integral to the expert system's critical development. The expert system can try simple machine-learning approaches: decision trees, random forests, and the AdaBoost algorithm. After considering the algorithms' performance, the expert system concluded that the AdaBoost model best determines cyber-attacks in MQTT-based IIoT systems.

**Training and Verification:** After selecting the Adaboost model, training was done against the data set collected from the test bed. The data set was prepared at 70% and 30% for training and verification. This division helped make the model more useful for practical use by enabling the model to apply what it has learned to 'new' and 'invisible' data. The model was taught to identify the different attack classes in network traffic, for example, the traffic models of the explosive DDoS and the misshaped package corresponding to the packaged package structures.

Assessment Metrics: To determine the results of the expert system, performance, accuracy, sensitivity, remembering, and F-score, but not limited to them, were evaluated with various evaluation indices. It was possible to provide an unmistakable appearance on the healing side of the system about systematic attacks and false positives. The Adaboost model was extraordinary in successfully identifying cyber-attacks with 92.7 % accuracy in these tests.

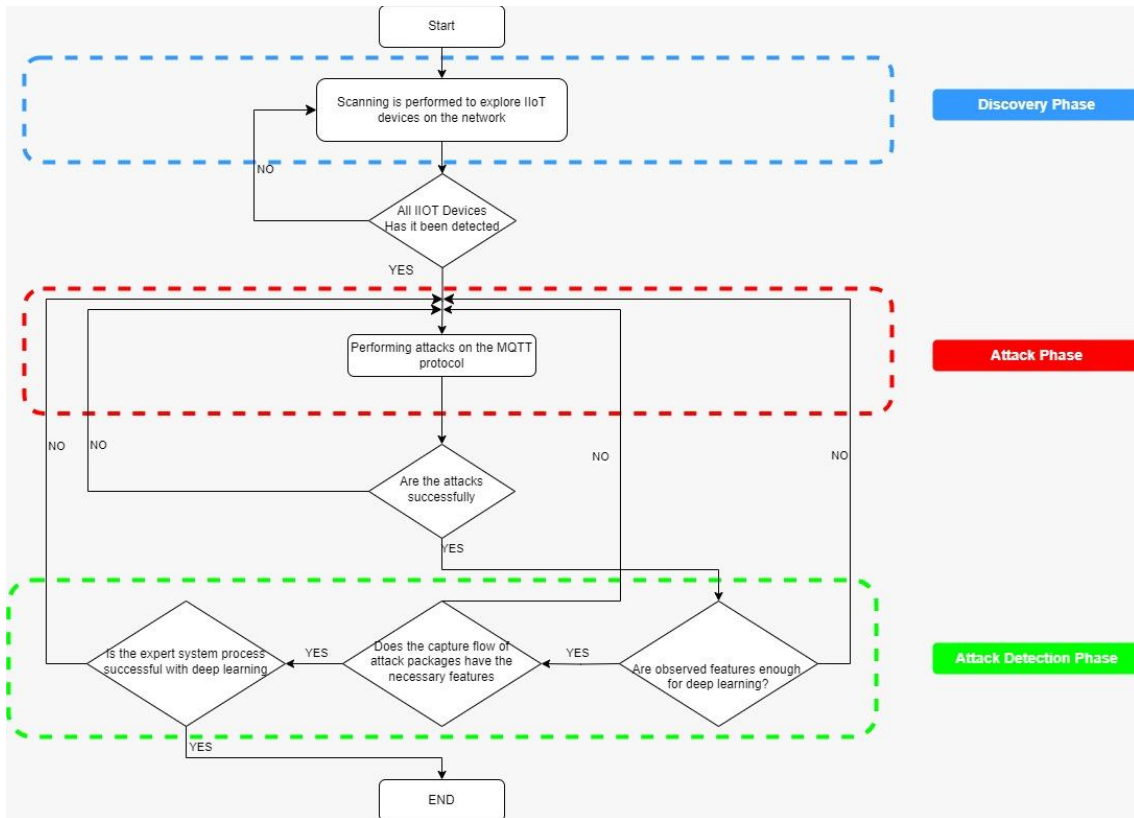


Figure 1. Workflow diagram

### 3.2. Algorithm Comparison and Selection

The approach also included a comprehensive comparison of some machine learning approaches. Decision trees and random forest approaches were among those who were considered promising. However, regarding capturing additional forms such as Bute Force attacks, Adaboost uses many weak classes, making them a single robust classification, thus increasing the overall determination accuracy. Expert system.

### 3.3. Real-time Detection and Visualization

One element of the expert system was to fulfill the analysis purpose and explain that the attack sets would be fast during attacks while answers would be obtained. The system's ability to provide real-time detection was more evaluated during test bed assessments. Even in high-level stress tests interacting with many devices simultaneously, the expert system can detect attacks without much delay against the network. A visualization tool was created as part of the methodology to improve the analysis and understanding of system outputs. The tool reported the output of expert system analysis: what kind of attacks were defined and how the system reacted over time. Graphics were made to demonstrate the number of attacks, the conditions in which the system's perception works effectively, and how the change in the attack affects the system's perception rate.

### 3.4. Increased Learning and Evolution of the Expert System

Finally, the methodology has been provided with a certain flexibility so that the expert system can learn and improve its performance over time. More data are obtained and processed, and machine learning models can

be better re-trained for accuracy and flexibility in new attack styles. Since it is a dynamic environment with a changing threat view, continuous learning ability is necessary for IIOT.

## 4. Testbed

In this study, an advanced test bed was developed instead of just simulating the environment (IIOT) to concentrate on evaluating the safety of the telemetry message transmission protocol, referred to as the MQTT protocol in this work. Another protocol often utilized in piggybacked IoT systems is the MQTT protocol. It is famous for its lightweight and efficiency, whereas other protocols may not function well, and it is increasingly used in IIOT applications. Such simplicity can also be a weakness, as cyber criminals can utilize it through brute attacks, DODS, and malformed packet attacks.

The test environment was meticulously constructed to replicate a realistic MQTT-based IIoT system, encapsulating essential components such as the MQTT broker, simulated IoT devices, and network monitoring tools. The MQTT broker acted as the central communication hub, facilitating data exchange between publishers (data-generating devices) and subscribers (data-receiving applications). The broker's susceptibility to attacks, including brute force, DDoS, and malformed packet injections, was tested to analyze the system's resilience and behavior under controlled conditions.

### 4.1. Components of the Testbed

The testbed was meticulously designed to incorporate all the critical elements in a typical IIoT system that uses the MQTT protocol. It simulates a networked environment where various devices communicate through an MQTT broker, which facilitates the exchange of messages between publishers (devices generating data) and subscribers (applications or devices that consume the data).

**MQTT Broker:** The broker is the backbone of the testbed, acting as the intermediary between IIoT devices. It ensures data integrity and delivery between the publishers and subscribers. In this setup, the broker was exposed to various types of cyberattacks, simulating a real-world scenario where attackers target a central communication hub to disrupt the operation of IIoT systems.

**IoT Devices:** The testbed simulated various IoT devices, representing IIoT sensors and actuators typically found in industrial applications. These devices generate data that is communicated through the broker. The devices were not compromised in this scenario, but the focus was on how the broker and the communication infrastructure handled the data under attack conditions.

**Attack Simulation:** Various tools were used to simulate attacks on the testbed. These included brute-force tools for testing the broker's authentication robustness and DDoS tools that generated flood attacks aimed at overwhelming the broker's capacity. In addition, malformed packets were injected into the communication stream to evaluate how the broker handles corrupted data.

**Network Traffic Monitoring and Data Collection:** The network traffic generated during these attacks was collected and mirrored to a separate analysis system. This data collection was critical for training machine learning models and building an expert system capable of identifying patterns in the network traffic that correspond to different types of attacks. Packet data was collected from legitimate traffic and simulated attacks, ensuring that the machine learning system had a comprehensive dataset for analysis.

### 4.2. Attack Scenarios

The testbed was designed to accommodate several types of attacks that are commonly encountered in MQTT-based IIoT systems:

**Brute-force Attacks:** These attacks target the MQTT broker's authentication system, attempting to gain unauthorized access by systematically trying different username and password combinations. The testbed used

a brute-force attack as a starting point, simulating an attacker's initial attempt to penetrate the system by accessing the broker without authorization.

**DDoS Attacks:** DDoS attacks were simulated by generating a flood of traffic aimed at the MQTT broker, overloading its capacity to handle requests. These attacks are particularly damaging in IIoT environments, where downtime or data loss could severely impact critical industrial operations.

**Malformed Packet Attacks:** In addition to flooding the broker with legitimate traffic, attackers can send malformed or corrupted packets that may cause the broker to crash or behave unpredictably. These attacks were simulated by deliberately corrupting the packet data sent to the broker, testing how well the broker can handle abnormal inputs without failing.

### **4.3. Testbed Performance and Scalability**

The testbed was one of many areas tested for the ability to ensure scalability, which was the primary task of mirroring IIoT systems' behavior in more extensive industrial settings. Every IIoT device still connects and communicates over the network using the MQTT protocol, even as the network grows into thousands of devices. The MQTT broker must cope with this immense network traffic without compromising security. This testbed was created with a view of this reality with an increasing number of devices communicating through the broker even as various attack scenarios were being launched.

Scalability could also be evaluated by gradually increasing the volume of legitimate traffic and introducing malicious packets to see how the broker performed under varied loads. This method helped understand the extent to which the volume could be increased from the basic observation made when the system was not busy with network junk traffic attacking the broker and how effective the experts would be in system attack detection as data volume escalates.

### **4.4. Data Collection for Machine Learning**

The data obtained from the testbed was fundamental for training machine learning models, which would later be utilized within the expert system. This dataset acquired included standard traffic patterns and traffic generated during brute force attacks, DDoS, and malformed packet attacks. The variety of the data was critical to encourage sufficient various types of machine learning algorithms to allow all typical trojan systems to operate even in heavy loads. Data collected during the test phase included a comprehensive mix of legitimate and attack-specific traffic patterns. Network packets captured during brute-force, DDoS, and malformed packet scenarios were mirrored to a dedicated analysis system for further processing. The dataset incorporated diverse traffic instances to train machine learning models effectively. The dataset was divided into two parts so that the system's accuracy could be further assured: 70% was allocated for training the machine learning models, and the other 30% was kept for testing and validation. This approach helped the system extend its learning to new data it had never encountered before, making it more efficient and dependable in practical contexts.

Despite the robust data collection approach, the dataset had limitations that should be acknowledged. The primary constraint was the variety of simulated attack types. Real-world scenarios often exhibit more complex, multi-layered threats beyond the testbed's scope. The dataset size, although sufficient for this study's objectives, may not encompass the full breadth of potential cyber-attacks encountered in expansive IIoT ecosystems. Addressing these gaps by expanding the dataset to include broader attack types and higher volumes would enhance the system's robustness and real-world applicability. In summary, the testbed ensured realism and scalability for the security assessment of the IIoT system based on MQTT. Various attacks were simulated, a reasonable amount of network traffic was collected, and machine learning models were built that were destined to become part of the expert system later on. Testbeds were important as they could create real-

world environments, which helped analyze how effective various ML algorithms would be in combating cyberattacks within IIoT system setups.

### 5. Understanding and Mitigating Attacks on MQTT in IIoT with Expert Systems

Analysis of Attacks on MQTT in IIoT the above section covers the detection of brute force attacks, DDoS (DoS, Flood, Slowite), and malformed packet attacks on the MQTT Protocol developed for use in IIoT Supported by a core expert system. Towards this end, a brute force attack was conducted to gain unauthorized access to the MQTT Broker, which was legal user access, followed by addressing DoS and malformed attacks on the said system. Packets for the said attacks would be acquired through mirroring techniques and fed into machine learning algorithms.

Together with the section above, the results pages of the data mining software concerning the analysis are displayed in the second section. Figure 2 illustrates that each time an attack log compiled for the MQTT protocol analysis under the scope of attack analysis is uploaded to the application, the intention is to execute the expert system as the primary thing to determine the distribution of data and the presence or absence of attack, and in case of presence of attack, to that of what kind throw the packet. Of these 'attack' packets created in the dataset, 30% of the data were used as input for verification, and 70% were used for training the various algorithms shown in Figure 2. After the expert system was used for attack detection, the output was compared Against the figure in Figure 2. The analysis results were made available to users in the last and third phases of the project using these various tools.

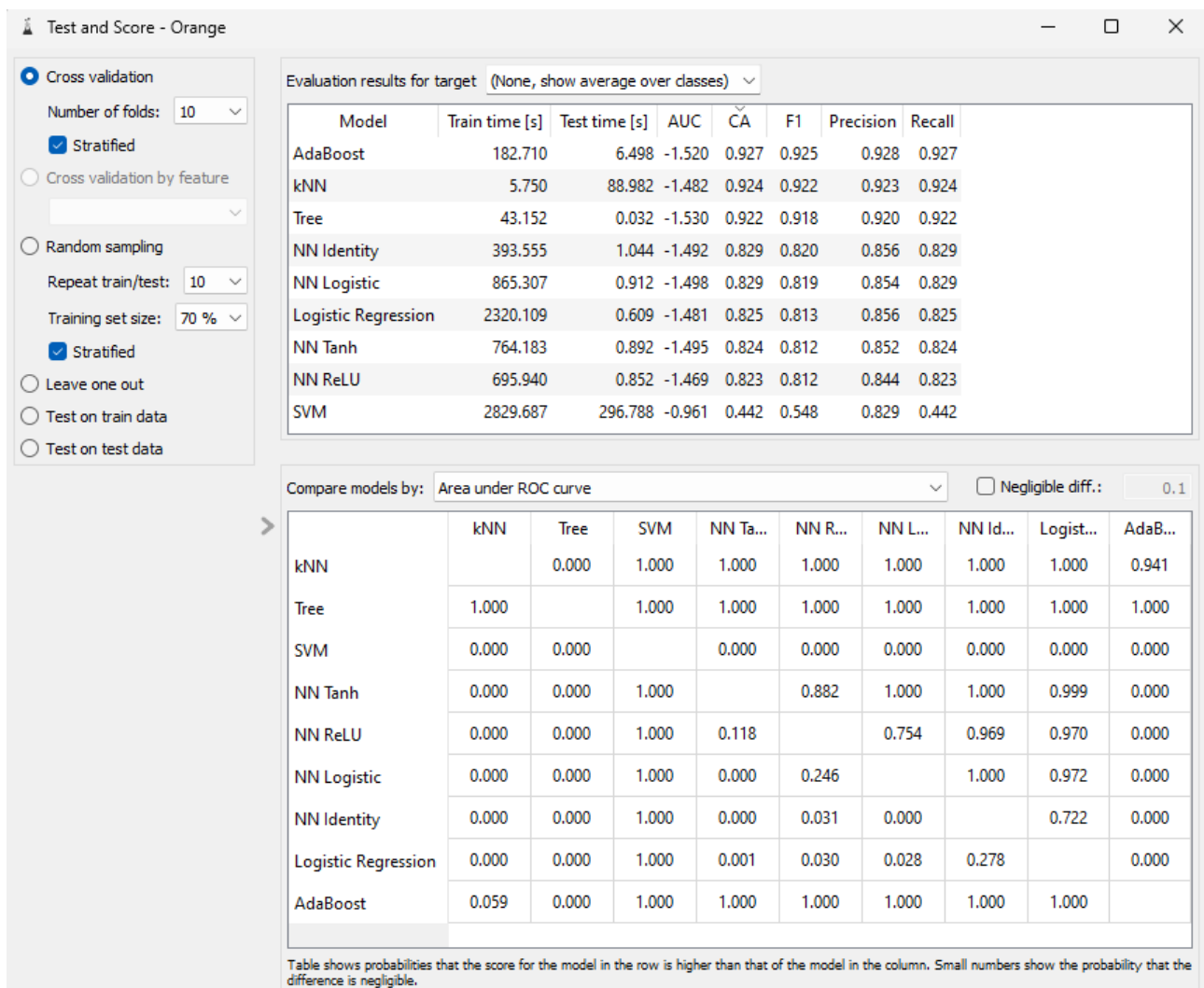


Figure 2. Model comparison table

The results in Figure 2 compare the essential values of different algorithms, such as accuracy, precision, recall, and F-score. The AdaBoost algorithm, which has the highest accuracy value of 92.7% among the compared results, was selected as the expert system, considering other essential values such as f-score, precision, and recursive precision.

In this way, using the AdaBoost algorithm in the expert system model provided higher accuracy and precision in intrusion detection and prevention.

### 5.1. Building and Training the Model

In the second phase of the intrusion detection analysis for IIoT, the AdaBoost algorithm was continued with the AdaBoost algorithm in the expert system since the AdaBoost model is the most successful in detecting attacks on the MQTT protocol used in IIoT through the expert system. The data was collected using natural systems and converted into a whitelist dataset. The created dataset was divided into 70% for training and 30% for validation. The Confusion Matrix of the Adaboost expert system model is shown in Figure 3. When the matrix in Figure 3 is analyzed, it is seen that the attack classification can be detected with high accuracy; in other words, there is no false-positive value.

		Predicted						Σ
		bruteforce	dos	flood	legitimate	malformed	slowite	
Actual	bruteforce	5810	763	1	8	547	41	7170
	dos	477	58687	1	4493	99	163	63920
	flood	1	41	148	106	1	2	299
	legitimate	0	1055	1	79977	4	0	81037
	malformed	1575	518	0	49	3034	91	5267
	slowite	677	375	0	618	95	2695	4460
Σ		8540	61439	151	85251	3780	2992	162153

Figure 3. Confusion matrix

Figure 4 shows the results of the Adaboost model. When Figure 4 is analyzed, it is seen that attacks on the MQTT protocol by the attacker at the same time as legitimate packets can be detected with 92.7% accuracy. This demonstrates the importance of continuous monitoring of network traffic in intrusion detection. This result is significant in ensuring the security and continuity of IIoT systems, which play an essential role in the communication control of critical infrastructures.

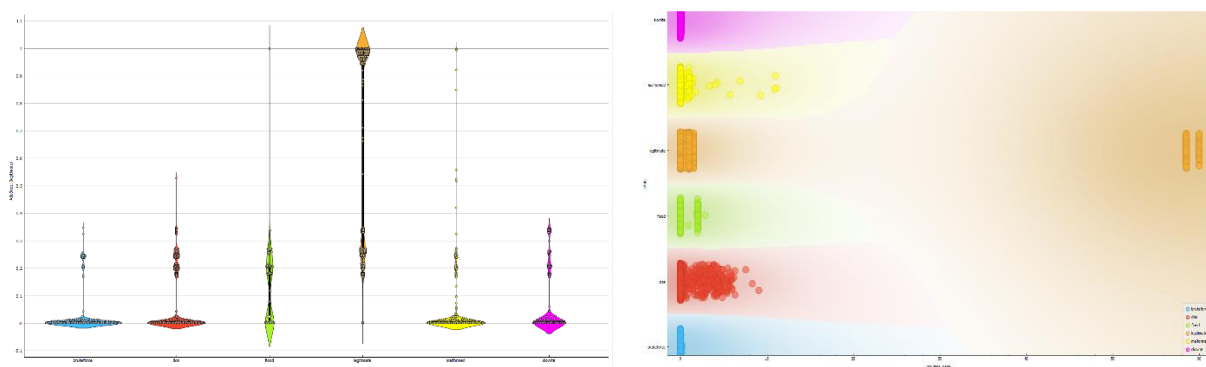


Figure 4. Adaboost expert system model results

The first graph shows the modeled results of various attacks against the MQTT protocol. The X-axis shows the different types of attacks, while the Y-axis shows the model's responses to the attacks. Each color represents a different type of attack:

**Brute Force Attack (Blue):** Brute force attacks usually result in a low response by the model. This indicates that the model has no difficulty detecting the attack as it is continuous and in a specific pattern.

**DoS Attack (Red):** DoS attacks cause a significant response in the model. The model must be able to detect this attack, as it generates heavy network traffic and consumes system resources.

**Flood Attack (Orange):** Flood attacks cause high and variable responses on the model. These attacks aim to degrade system performance by sending many requests to the network, and the model's ability to detect this attack is relatively high.

**Legal Packages (Yellow):** Legal packets represent the system's normal functioning and indicate that the model classifies these packets as usual.

**Deconstructed Packets (Purple):** Corrupted packets result in a high response in the model. This indicates that corrupted data is recognized as an anomaly in the system, and the model can detect these packets.

**Slowite Attacks (Green):** Slowite attacks cause a significant and wide range of responses in the model. This demonstrates the model's flexibility in detecting the attack in different ways.

The second graph shows the time delta (X-axis) and the model's responses (Y-axis) according to the attack types. This graph shows how the different types of attacks are distributed over time and the model's responses to these attacks.

**Brute Force Attack (Blue):** Brute force attacks are regularly distributed over time, and the model detected them. Attacks do not vary over time.

**DoS Attack (Red):** DoS attacks are concentrated at certain intervals along the time delta. The model consistently responds highly to these attacks over time.

**Flood Attack (Orange):** Flood attacks are widely distributed across the time delta, and the model reacts to them consistently well.

**Legal Packets (Yellow):** Legal packets are homogeneously distributed throughout the time delta, and the model reacts poorly. This represents the system's normal functioning.

**Deconstructed Packets (Purple):** Deconstructed packets are concentrated at certain intervals along the time delta, and the model responds highly to them.

**Slowite Attacks (Green):** Slowite attacks are widely distributed across the time delta, and the model reacts differently. This shows the dynamic nature of the attack and the model's resilience to it.

These graphs evaluated the model's ability to detect attacks and respond to attack types. They show the modeled results of various attacks against the MQTT protocol and how they are distributed over time.

## 6. Discussion

This study showed the capability of the expert system created to detect cyber attacks targeting MQTT-based IIoT systems. The Adaboost algorithm implemented in the study gave a high rate of accuracy, around 92.7%, thus improving on other algorithms. This is why Adaboost becomes very effective since it can aggregate weak classifiers into strong ones, hence detecting more advanced and complex types of attacks.

This study illustrated the application of comparison of specific elementary machine learning algorithms. For example, the results of decision trees or random trees were quite encouraging. Nevertheless, the fact that Adaboost is effective because it can obtain more accuracy with fewer resources was an essential consideration

in adopting this model. In particular, this model performed all-around even in infrequently focused attacks such as brute force attacks and malformed packet attacks, which caused high success rates for this model.

One of the striking features of the system is the ability to function in real-time. In IIoT scenarios, managing real-time attacks without detection is critical since industrial activities will likely be disrupted. The expert system developed was able to identify the attacks even with high network usage and still do the work without any degradation in performance. This presents an advantage, especially regarding scaling and suitability for the industries.

Moreover, it is also pertinent that the system's structure allows it to learn continuously to meet any new threats that are likely to come in the future. This is because industrial Internet of Things IIoT systems work in a threat landscape that is always altering, and a static security approach may not be adequate in such cases. However, the expert system constructed within this investigation can adapt and learn new information and discover new attacks that have not been exhibited before. This enhances the system's security in the long run and is a better way of providing security in IIoT applications.

This work has, however, some limitations. First, the testbed would reproduce a small number of attack types. Actual attacks tend to be more complicated and varied, so applying the system to a more extensive dataset would be beneficial. Further, incorporating the system with other protocols could fill the remaining security holes within the IIoT system. In particular, integrating cryptographic measures with machine learning technologies will enhance protection.

Testing this expert system on other IoT and IIoT protocols will also be essential to ascertain its expected security level performance in future works. In addition, implementing and testing a wider range of attacks on the system and measuring how well the system manages these attacks will be invaluable research in the future. This research has successfully provided an efficient strategy for securing MQTT-based IIoT systems against various attacks. It has improved the existing body of knowledge in this area.

## 6.1. Comparison with a Wider Range of Attacks and Their Analysis

To effectively evaluate the robustness of the expert system developed for securing MQTT-based IIoT environments, it is essential to consider a comparative analysis encompassing a wider range of cyber-attacks beyond those initially tested, such as brute-force, DDoS, and malformed packet attacks. This section integrates insights from the literature to outline how the system could be benchmarked against more diverse and sophisticated threats and highlights the implications of such comparisons.

**Advanced Persistent Threats (APTs):** APTs represent prolonged and targeted cyber-attacks often orchestrated by well-resourced threat actors. Unlike the more immediate and high-visibility nature of DDoS or brute-force attacks, APTs are characterized by their stealth and persistence. They infiltrate networks, establish long-term footholds, and exfiltrate sensitive data over extended periods. Literature by Sharma and Bhushan [20] outlines a hybrid framework using Physically Unclonable Functions (PUFs) and machine learning to defend against such attacks in MQTT-based IoT systems. By extending the analysis to APTs, the expert system could be assessed for its capability to detect nuanced patterns associated with prolonged and low-frequency attacks, which are crucial in protecting industrial environments.

**Reflection-Based Attacks (DRDoS):** Distributed Reflection Denial of Service (DRDoS) attacks, as examined in studies like those by Kombate et al. [5], amplify malicious traffic by leveraging legitimate third-party servers. These attacks are challenging to identify due to their indirect nature. Integrating the detection of DRDoS within the expert system would require adaptive algorithms capable of recognizing subtle discrepancies in traffic flows and response patterns. Comparative analysis against such attacks would demonstrate the system's ability to maintain high accuracy in detecting traffic anomalies resulting from amplified, reflected sources.

**Zero-Day Exploits:** Zero-day vulnerabilities, highlighted in works by Deng [15] and Prajisha and Vasudevan [16], are previously unknown security flaws that attackers exploit before patches become available. These exploits pose significant risks to IIoT environments due to their unpredictability and potential to bypass conventional security measures. Incorporating detection models trained on evolving signatures and anomaly-based learning could enhance the expert system's resilience. Evaluating the system against simulated zero-day scenarios would showcase its potential to identify and mitigate unknown threats.

**Multi-Vector Attacks:** Complex, multi-vector attacks combine different techniques—e.g., combining DDoS with data exfiltration—to maximize disruption. Literature such as the study by Francis et al. [13] emphasizes how multi-layered detection systems, leveraging genetic algorithms and ensemble learning, can effectively counter such threats. The expert system's performance could be measured against these multi-faceted threats by implementing layered defensive strategies, including correlation-based detection and cross-protocol monitoring. This would illustrate its ability to adapt and respond to hybrid attack profiles.

**Cryptographic and MITM Attacks:** Research by Mahajan et al. [4] and Saqib and Moon [8] points to vulnerabilities in the MQTT protocol that can be exploited through cryptographic weaknesses or Man-in-the-Middle (MITM) attacks. Integrating encryption algorithms like AES and multi-factor authentication systems into the expert system could enhance its defensive capabilities. A comparative analysis of these attack types would provide valuable insights into the system's efficiency in maintaining data integrity and preventing unauthorized interception of communications.

## 6.2. Implications for Real-World Application

A comparative analysis involving a broader spectrum of attacks would underscore the expert system's comprehensive defensive capabilities and areas for improvement. The system could better withstand a dynamic threat landscape by incorporating multi-class machine learning models and cryptographic methods, as suggested by Liu et al. [7]. Additionally, continuous learning models that adapt to novel attack patterns—as discussed in the studies by Koprov et al. [9] and Zuhairi et al. [19]—would further enhance its long-term efficacy. This extended evaluation would validate the system's existing strengths and refine its ability to detect and respond to emerging threats, solidifying its utility in safeguarding MQTT-based IIoT infrastructures against a comprehensive range of cyber-attacks.

## 7. Conclusion

This study shows how efficient an expert system developed to secure IIoT systems is. The developed system protects against several cyber-attacks and can identify attacks such as brute force, DDoS, or corrupted packet attacks. It was noted that the expert system utilizing the AdaBoost algorithm managed attacks with precision as high as 92.7%. This high success rate was achieved due to Adaboost's ability to build more robust models by integrating several weak classifiers. This shows that the system is crucial in securing IIoT systems as it can identify even sophisticated types of attacks.

Even though the other machine learning algorithms employed in this work, Decision Trees and Random Forest, gave acceptable results, the high accuracy and low amount of resources used to implement the Adaboost algorithm were decisive in selecting this algorithm. Besides, the system's ability to function in real-time is a huge advantage for industrial processes such as IIOT, which highly depends on continuous and uninterrupted operations. The ability of the system to remain functional amid high levels of network traffic and still detect attacks is also of great importance in scaling and applying the system in industries.

The ability of the system to learn constantly means that it will always be ready for any new threat that may be experienced in the future. Since IIoT systems are being utilized in a dynamic threat landscape, more than static security mechanisms may be required. This paper highlights that the expert system engineered in this study can assimilate new information and discern unencountered types of attacks for the first time. Taking the time

to consider the duration enhances the system's sustainability in that the system provides long-term security measures for IIoT applications. There are also some limitations in this study. First, only a limited number of attack types could be reproduced using the testbed. Real-life attacks can be more complex and diverse; thus, testing the system using a large dataset would be ideal. It would also be helpful to integrate the system with other protocols in resource-constrained IIoT to cover other security gaps. In particular, it can enhance security by combining machine learning approaches and cryptographic methods.

Assessing this expert system with other IoT and IIoT protocols will be crucial to determining its security efficacy in future work. In addition, attempting more sophisticated attack scenarios and studying the system's behavior in the face of these attacks may prove valuable in guiding future research. To sum up, this research has offered the appropriate security mechanism for attack detection of MQTT-based IIoT systems and added great value to the body of knowledge in that area.

## Author Contributions

The author read and approved the final version of the paper.

## Conflicts of Interest

The author declares no conflict of interest.

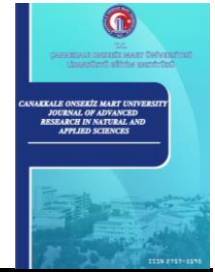
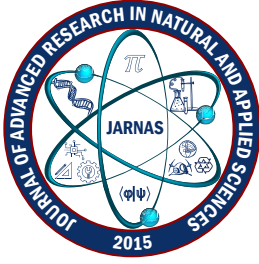
## Ethical Review and Approval

No approval from the Board of Ethics is required.

## References

- [1] M. Al-Fayoumi, Q. A. Al-Haija, *Capturing low-rate DDoS attack based on MQTT protocol in software defined-IoT environment*, *Array* 19 (2023) 100316 10 pages.
- [2] M. I. Fikriansyah, S. A. Karimah, F. Setiadi, *Detection of DDOS attacks in IIoT case using machine learning algorithms*, *International Conference on Data Science and Its Applications (ICoDSA)*, 2024 IEEE, pp. 117–121.
- [3] E. Shahri, P. Pedreiras, L. Almeida, *A scalable real-time SDN-based MQTT framework for industrial applications*, *IEEE Open Journal of the Industrial Electronics Society* 5 (2024) (2024) 215–235.
- [4] R. A. Mahajan, R. G. Mahajan, M. Tatiya, U. H. Mandekar, M. Shahakar, Y. Patil, *Enhancing MQTT security in the internet of things with an enhanced symmetric algorithm*, *Journal of Electrical Systems* 20 (1s) (2024) 126–137.
- [5] Y. Kombate, P. Hougue, O. Samuel, *Securing MQTT: unveiling vulnerabilities and innovating cyber range solutions*, *Procedia Computer Science* 241 (2024) 69–76.
- [6] F. Buccafurri, V. De Angelis, R. Nardone, *Securing mqtt by blockchain-based otp authentication*, *Sensor* 20 (7) (2020) 2002 14 pages.
- [7] Z. Liu, T. Liang, J. Lyu, D. Lang, *A security-enhanced scheme for MQTT protocol based on domestic cryptographic algorithm*, *Computer Communications* 221 (2024) (2024) 1–9.
- [8] M. Saqib, A. H. Moon, *A novel lightweight multi-factor authentication scheme for MQTT-based IoT applications*, *Microprocessors and Microsystems* 110 (2024) (2024) 105088 20 pages.
- [9] P. Koprov, X. Fang, B. Starly, *Machine identity authentication via unobservable fingerprinting signature: A functional data analysis approach for MQTT 5.0 protocol*, *Journal of Manufacturing Systems* 76 (2024) (2024) 59–74.

- [10] A. Lohachab, *ECC-based inter-device authentication and authorization scheme using MQTT for IoT networks*, Journal of Information Security and Applications 46 (C) (2019) 1–12.
- [11] I. Vaccari, G. Chiola, M. Aiello, M. Mongelli, E. Cambiaso, *MQTTset, a new dataset for machine learning techniques on MQTT*, Sensors 20 (22) (2020) Article Number 6578 17 pages.
- [12] B. Mishra, A. Kertesz, *The use of MQTT in M2M and IoT systems: A survey*, IEEE Access 8 (2020) 201071–201086.
- [13] G. T. Francis, A. Souri, N. İnanç, *A hybrid intrusion detection approach based on message queuing telemetry transport (MQTT) protocol in industrial internet of things*, Transactions on Emerging Telecommunications Technologies 35 (9) (2024) 5030 15 pages.
- [14] C. Patel, N. Doshi, *A novel MQTT security framework in generic IoT model*, Procedia Computer Science 171 (2020) 1399–1408.
- [15] X. Deng, *Internet of things (IoT) intrusion detection system (IDS) for home networks*, Doctoral Dissertation The George Washington University (2024) Washington.
- [16] C. Prajisha, A. Vasudevan, *An efficient intrusion detection system for MQTT-IoT using enhanced chaotic salp swarm algorithm and LightGBM*, International Journal of Information Security 21 (6) (2022) 1263–1282.
- [17] G. Karacayılmaz, H. Artuner, *A novel approach detection for IIoT attacks via artificial intelligence*, Cluster Computing 27 (2024) (2024) 10467–10485.
- [18] S. Aymene, K. Lyes, A. Mondher, B. Ahmed, *Securing IIoT Against DDoS attacks: A stochastic approach*, Global Information Infrastructure and Networking Symposium (GIIS) (2024) 1–6.
- [19] M. F. Zuhairi, S. M. Ali, Z. Shahid, M. M. Alam, M. M. Su'ud, *Real-time feature engineering for anomaly detection in IoT-based MQTT networks*, IEEE Access 12 (2024) (2024) 25700–25718.
- [20] A. Sharma, K. Bhushan, *A hybrid approach based on PUF and ML to protect MQTT based IoT system from DDoS attacks*, Cluster Computing 27 (2024) (2024) 13809–13834.



# Performance of PMMA/Ta<sub>2</sub>O<sub>5</sub> Composites as Medical Radiation Shielding: WinXCom and MCNP6 Studies

Mustafa Çağlar<sup>1</sup>

<sup>1</sup>Department of Health Physics, Graduate School of Health Sciences, İstanbul Medipol University, İstanbul, Türkiye

## Article Info

Received: 02 Oct 2024

Accepted: 10 Dec 2024

Published: 31 Dec 2024

Research Article

**Abstract** – The growing reliance on radiation in contemporary applications underscores the imperative to safeguard individuals and the environment from harmful consequences. To mitigate the adverse effects of radiation, polymer composites have begun to garner interest from researchers as potential lead-free shielding materials, largely due to their distinctive attributes, including flexibility, lightness, and environmental benignity. In this study, the gamma radiation shielding capacity of polymethyl methacrylate (PMMA) composites reinforced with varying proportions of Ta<sub>2</sub>O<sub>5</sub> (5%, 10%, and 20% wt) was investigated through the utilization of Windows version of photon cross sections on a personal computer (WinXCom) software and the Monte Carlo N-Particle 6 (MCNP6) code. The alignment of the WinXCom and MCNP6 results, despite their different methodologies, provides a robust and reliable understanding of the radiation shielding performance of these composites. The present study investigated the radiation attenuation properties of PMMA/Ta<sub>2</sub>O<sub>5</sub> composites about shielding coefficients, including mass attenuation coefficients (MAC), half-value layer (HVL), and effective atomic number ( $Z_{\text{eff}}$ ). The findings indicated that all composites demonstrated enhanced shielding performance compared to pure PMMA. The PMMA/20% Ta<sub>2</sub>O<sub>5</sub> composite exhibited MAC values of 1.22-, 1.29-, and 1.28-fold greater than those observed in the silicon-based composites. The MAC increase was observed in the PMMA/20% Ta<sub>2</sub>O<sub>5</sub> composite at an energy of 81 keV. The PMMA/20% Ta<sub>2</sub>O<sub>5</sub> composite demonstrated the most effective radiation shielding properties. In light of these findings, the PMMA/20% Ta<sub>2</sub>O<sub>5</sub> composite can be regarded as a flexible, lightweight, and environmentally friendly shielding material, reassuring these composites' reliability in practical applications.

**Keywords** – Monte Carlo simulation, radiation shielding, tantalum pentoxide, MCNP6

## 1. Introduction

The utilization of ionizing radiation with a high energy level is progressively increasing across various fields, including medical diagnostics, nuclear reactors, food irradiation, research laboratories, particle accelerators, etc. In light of the detrimental impact of radiation on human health, one of the most crucial strategies to safeguard individuals from exposure to high-energy radiation is the deployment of a suitable shielding material. As the conventional shielding material, lead, with its high atomic number and density, is widely used to attenuate high-energy radiation. However, it is also toxic, inflexible, heavy, and has low mechanical strength [1]. The aforesaid disadvantages restrict the utilization of lead, particularly for those engaged in occupations within sectors such as medical diagnosis, research laboratories, and nuclear power plants, who are required to wear lead shields, such as aprons, for extended periods. This can result in significant health issues, including physical fatigue and back pain [2].

<sup>1</sup>drmustafacaglar@gmail.com (Corresponding Author)

In this context, the researchers have concentrated on producing low-weight, environmentally friendly, and flexible alternative materials that can replace lead. A substantial body of research has been conducted on the radiation attenuation performance of polymer composites that exhibit the desired properties. In these studies, polymers have been doped with high Z elements to enhance their shielding capabilities in their pure form, which cannot effectively attenuate high-energy radiation. To illustrate, the radiation-shielding performance of polyvinyl alcohol/tungsten oxide [3], high-density polyethylene/lead oxide [4], poly ether ketone/gadolinium oxide [5], poly (methyl methacrylate)/ MWCNT/Bi<sub>2</sub>O<sub>3</sub> [6], and other similar composites have been the subject of extensive study. The results demonstrated that the shielding efficacy of these composites enhanced with the additive concentration. PMMA has been evaluated as a shielding material in numerous studies—for instance, Bel et al. [7] quantified the neutron and gamma radiation attenuation properties of PMMA/colemanite composites using a Cs-137 radioactive source and a Windows version of photon cross sections on a personal computer (WinXCom) software. The outcomes revealed that the shielding capability of PMMA/colemanite composites increased by 11.1% for gamma radiation and 38.56% for neutrons. Cao et al. [8] investigated the gamma radiation shielding capacity of PMMA/Bi<sub>2</sub>O<sub>3</sub> composites. The gamma-ray attenuation coefficients, including MAC and (HVL), were conducted using five gamma point sources (<sup>57</sup>Co, <sup>60</sup>Co, <sup>109</sup>Cd, <sup>133</sup>Ba, and <sup>137</sup>Cs). The incorporation of Bi<sub>2</sub>O<sub>3</sub> particles into the PMMA matrix was observed to enhance the shielding ability of pure PMMA. It was put forth that these composites are viable candidates for use as radiation shielding materials. In a separate study, Shareef et al. [9] investigated the radiation attenuation performance of PMMA/Gd<sub>2</sub>O<sub>5</sub> composites using <sup>60</sup>Co and <sup>137</sup>Cs point sources. The findings indicated that the shielding capacity of the composites exhibited a gradual increase with an increase in Gd<sub>2</sub>O<sub>5</sub> concentration. Among the additives incorporated into the polymers to enhance their shielding capabilities, tantalum pentoxide (Ta<sub>2</sub>O<sub>5</sub>) is particularly noteworthy due to its high atomic number (Z=73) and K absorption edge value of 67.4 keV, which renders it an efficient X-ray shielding material [10].

Therefore, Ta<sub>2</sub>O<sub>5</sub> can be deemed an appropriate compound for investigation as a radiation shielding agent, and its shielding efficacy has been evaluated in numerous studies. In a previous study, Prabhu and colleagues [11] investigated the gamma-ray attenuation potency of epoxy micro and nano Ta<sub>2</sub>O<sub>5</sub> composites using <sup>22</sup>Na, <sup>60</sup>Co, <sup>133</sup>Ba, and <sup>137</sup>Cs radioactive point sources. The MAC for the epoxy composites with the highest micro and nano dopant content (30% by weight) were found to be 0.136 cm<sup>2</sup>/g and 0.154 cm<sup>2</sup>/g, respectively, at an energy of 0.356 MeV. In a separate investigation, Adliene and colleagues examined the X-ray shielding characteristics of polydimethylsiloxane (PDMS) silicone rubber and universal silicone rubber (UNSI)/Ta and Ta<sub>2</sub>O<sub>5</sub> composites at energies range 50 to 150 keV. The researchers investigated lead equivalent values for composites. It estimated that the UNSI composite with the maximum concentration of Ta and Ta<sub>2</sub>O<sub>5</sub> (50 wt%) exhibited higher values than the recommended 0.25 mmPb value. The composite with Ta exhibited a value of 0.364 mmPb, while the composite with Ta<sub>2</sub>O<sub>5</sub> exhibited a value of 0.313 mmPb [10].

This study aimed to ascertain the gamma radiation shielding properties of poly (methyl methacrylate) (PMMA)/Ta<sub>2</sub>O<sub>5</sub> composites to identify a lightweight, flexible, and chemically stable alternative to lead-based shielding materials. The fundamental radiation shielding coefficients, including the MAC, HVL, and Z<sub>eff</sub>, were investigated using WinXCom software and MCNP6 simulation code.

## 2. Materials and Methods

### 2.1. Shielding Parameters

By the Beer-Lambert equation, the intensity of a gamma ray beam traversing a shield is observed to decrease exponentially in proportion to the chemical composition of the shield in (2.1).

$$I = I_0 e^{-\mu x} \quad (2.1)$$

In this context, the terms  $I$  and  $I_0$  represent the intensity of the incident and transmitted gamma rays, respectively. In this context, the terms  $\mu$  and  $x$  indicate the linear attenuation coefficient and the thickness of

the shield material, respectively [11]. As the linear attenuation coefficient does not account for the density of the shield, the MAC ( $\mu_m$ ) is defined as the linear attenuation coefficient per volume ( $\rho$ ).

$$\mu_m = \frac{\mu}{\rho} (\text{cm}^2\text{g}^{-1}) \quad (2.2)$$

The HVL is another shielding coefficient, defined as the length that reduces the incoming radiation to its half-value. This is expressed in (2.3) [12].

$$\text{HVL} = \frac{\ln 2}{\mu} (\text{cm}) \quad (2.3)$$

On the other hand, since the atomic number of the materials is essential for radiation shielding, the  $Z_{\text{eff}}$  is described as the atomic number of multi-element materials such as mixtures or compounds.  $Z_{\text{eff}}$  can be calculated by interpolation method according to (2.4).

Conversely, given the crucial role of atomic number in radiation shielding,  $Z_{\text{eff}}$  is defined as the atomic number of multi-element materials, including mixtures and compounds. The  $Z_{\text{eff}}$  can be calculated using an interpolation method using the specifications in (2.4).

$$Z_{\text{eff}} = \frac{Z_1(\log \sigma_2 - \log \sigma_{\text{eff}}) + Z_2(\log \sigma_{\text{eff}} - \log \sigma_1)}{\log \sigma_2 - \log \sigma_1} \quad (2.4)$$

In this context,  $\sigma_{\text{eff}}$  represents the effective cross-section of the shield material with  $\sigma_1$  and  $\sigma_2$  denoting the minimum and maximum cross-section values in the vicinity of  $\sigma_{\text{eff}}$ , respectively. Additionally,  $\sigma_{\text{eff}}$  can be defined by (2.5), contingent on the MAC [1].

$$\sigma_{\text{eff}} = \frac{\left(\frac{\mu}{\rho}\right)_{\text{material}}}{N_A \sum \frac{f_i}{A_i}} \quad (2.5)$$

where  $A_i$  is the atomic mass and  $f_i$  is the molar fraction of  $i^{\text{th}}$  element. The quantity  $N_A$  is defined as the Avogadro constant.

## 2.2. WinXCom and MCNP6

WinXCom represents the Windows operating system version of the XCom software developed by Berger and Hubbell [13]. The software can calculate the MAC values and the cross-sections of the shielding materials between 1 keV and 100 GeV per the Mixture Rule, as outlined in (2.6). By this rule, the MAC values of a given material, which may comprise various elements, are calculated as the sum of the weight ratio of each atom present [14].

$$(\text{MAC})_{\text{sample}} = \sum_i^n w_i (\text{MAC})_i \quad (2.6)$$

where  $(\text{MAC})_i$  is MAC value and  $w_i$  is the weight of the  $i^{\text{th}}$  element. The MAC values of the studied composites were calculated by WinXCom software.

Monte Carlo N-Particle (MCNP), a computer code designed by researchers at the Los Alamos National Laboratory, is a widely utilized tool for simulating the transport of particles, including neutrons, photons, and electrons, through a material. A narrow beam geometry consisting of a detector was designed by MCNP and is illustrated in Figure 1. The MCNP6 calculations were performed using the Evaluated Nuclear Data Files (ENDF)/B-VI-Released 8 and the photatomic library MCPLIB04. The sample was situated between the

detector and the radioactive source, as illustrated in Figure 1. The simulation was conducted at five discrete energy values: 81, 356, 662, 1173, and 1332 keV. The initial run was conducted without a sample to ascertain the total flux entering the detector. As shown in Table 1, a simulation was performed for the corresponding composites with varying chemical compositions.

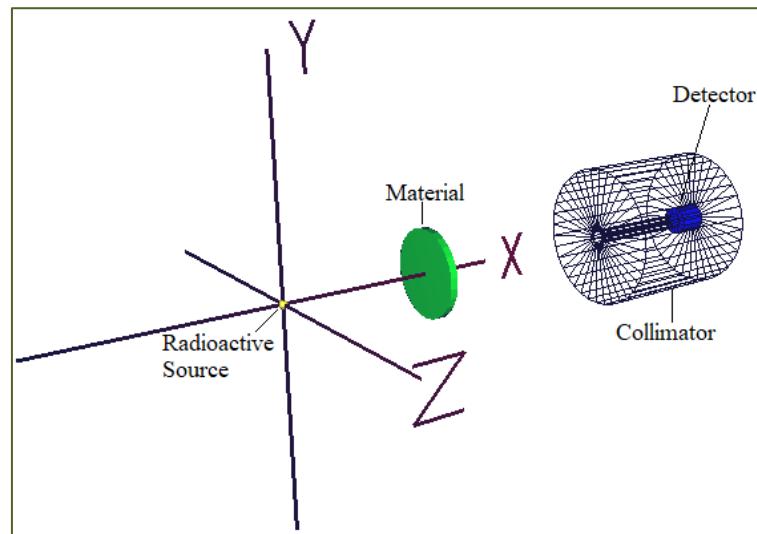


**Figure 1.** The geometry of the detector, source, and shielding material, as well as their placement on axes in a three-dimensional coordinate system, have been simulated using the MCNP6 software

### 2.3. Calculation of Radiation Shielding Parameters

To investigate the radiation shielding performance of PMMA/Ta<sub>2</sub>O<sub>5</sub> composites, MAC values were calculated at energies ranging from 1 keV to 100 GeV using the WinXCom program. Furthermore, MAC values at specific energies, including 81, 356, 662, 1173, and 1332 keV, were also calculated using the MCNP6 simulation package. Other gamma ray shielding coefficients, such as HVL and Z<sub>eff</sub>, were determined by (2.3)-(2.5), respectively. The elemental fractions and densities of pure PMMA and PMMA/Ta<sub>2</sub>O<sub>5</sub> composites utilized in WinXCom and MCNP6 calculations are presented in Table 1.

**Table 1.** The fraction of elements of PMMA and PMMA/Ta<sub>2</sub>O<sub>5</sub> composites

Sample	Element (wt%)				Density (g/cm <sup>3</sup> )
	H	C	O	Ta	
PMMA	0.08054	0.59985	0.31961	--	1.180
PMMA/5% Ta <sub>2</sub> O <sub>5</sub>	0.07651	0.56986	0.31268	0.04095	1.531
PMMA/10% Ta <sub>2</sub> O <sub>5</sub>	0.07249	0.53986	0.30575	0.08190	1.882
PMMA/20% Ta <sub>2</sub> O <sub>5</sub>	0.06443	0.47988	0.29190	0.16379	2.584

## 3. Results and Discussion

### 3.1. MAC Values of PMMA and PMMA/Ta<sub>2</sub>O<sub>5</sub> Composites

The MAC is one of the most significant parameters for evaluating the radiation attenuation properties of various materials. It characterizes the capacity of a shielding material to absorb radiation, which is contingent upon the density of the sample and the energy of the incident photons. A higher MAC value indicates an enhanced shielding capability. Figure 2 illustrates the variations in the MAC of pure PMMA and PMMA/Ta<sub>2</sub>O<sub>5</sub> composites as a function of increasing photon energy.

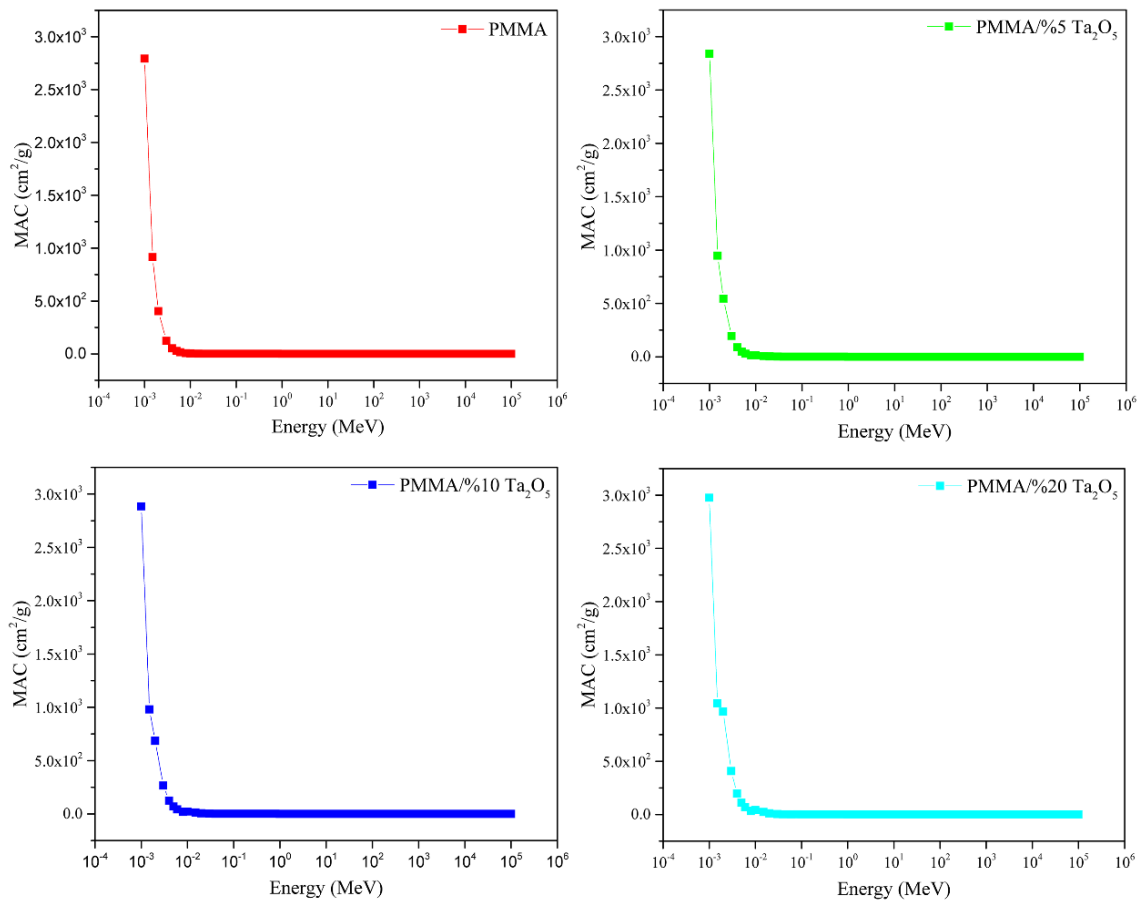


**Figure 2.** MAC values of PMMA and PMMA/Ta<sub>2</sub>O<sub>5</sub> composites as a function of the photon energy

As illustrated in Figure 2, the measured MAC values exhibit a general decrease with increasing photon energies. This phenomenon is contingent upon the interaction mechanism between photons and matter. At low energies, the cross-section for the photoelectric interaction is sufficiently high such that the absorbing medium absorbs nearly all incident photons. This is evidenced by the elevated values observed on the MAC-Energy graph. As the incident photon energy increases, Compton scattering becomes the dominant interaction mechanism, leading to a decline in photon interaction possibilities. At high energy levels, the graph exhibits an exponential decline due to the prevalence of pair production as the dominant interaction mechanism with energy dependence [15]. The MAC values, calculated using the WinXCom software and the MCNP6 code at various energies, are presented in Table 2.

**Table 2.** The following chart presents the MAC values of PMMA/Ta<sub>2</sub>O<sub>5</sub> composites for various energies

Sample	MAC (cm <sup>2</sup> /g)				
	WinXCom/MCNP6	WinXCom/MCNP6	WinXCom/MCNP6	WinXCom/MCNP6	WinXCom/MCNP6
	81 keV	356 keV	662 keV	1173 keV	1332 keV
PMMA	0.174/0.192	0.108/0.111	0.083/0.083	0.063/0.083	0.059/0.083
PMMA/%5 Ta <sub>2</sub> O <sub>5</sub>	0.468/0.492	0.113/0.115	0.083/0.083	0.063/0.083	0.059/0.083
PMMA/% 10 Ta <sub>2</sub> O <sub>5</sub>	0.762/0.785	0.117/0.120	0.084/0.083	0.063/0.083	0.059/0.083
PMMA/% 20 Ta <sub>2</sub> O <sub>5</sub>	1.349/1.360	0.127/0.130	0.085/0.085	0.062/0.085	0.058/0.085

As illustrated in Table 2, the results produced by WinXCom are closely aligned with those obtained by MCNP6. The MAC values of the composites demonstrate a gradual increase with the addition of Ta<sub>2</sub>O<sub>5</sub> at a constant energy value for low-energy particles (81, 356, and 662 keV). The minimum MAC levels are observed in the case of pure PMMA, which contains low Z element components such as C, H, and O. The gradual increase in MAC values with the incorporation of Ta<sub>2</sub>O<sub>5</sub> is attributed to adding high Z elements into the PMMA

matrix. The maximum increase in MAC has been determined to occur in the PMMA/20% Ta<sub>2</sub>O<sub>5</sub> composite at 81 keV. The MAC value of this composite is 7.75 times greater than that of pure PMMA at this energy value. Furthermore, all composites exhibit larger MAC values than pure PMMA, indicating that the addition of Ta<sub>2</sub>O<sub>5</sub> enhances the radiation shielding capacity of PMMA.

The increase in MAC values for composite materials is observed as 2.69-7.75 times greater than that of pure PMMA at an energy of 81 keV. Conversely, MAC values remain relatively constant at high energies above 662 keV, suggesting that the shielding material is inadequate for attenuating high-energy radiation. In contrast, the MAC values of the composites were compared with those of other shielding materials that had been the subject of scientific study. As an instance, the mass attenuation coefficient of the 304 L stainless steel sample was calculated as 0.100 cm<sup>2</sup>/g at 356 keV energy by Buyukyildiz et al. The PMMA/20%Ta<sub>2</sub>O<sub>5</sub> composite prepared in this study exhibited a MAC value of 0.127 cm<sup>2</sup>/g at 356 keV, indicating that this composite exhibited a 1.27 times greater attenuation capacity than the steel sample [16]. In a separate study, Verdipoor et al. employed MCNP simulation to calculate the MAC values of silicon resin composites loaded with tungsten trioxide (WO<sub>3</sub>), lead oxide (PbO), and bismuth oxide (Bi<sub>2</sub>O<sub>3</sub>). The maximum MAC values in the maximum additive-doped composites were determined to be 0.1039, 0.0980, and 0.0989 cm<sup>2</sup>/g for the 0.5 wt% WO<sub>3</sub>-0.5 wt% silicon resin, 0.5 wt% PbO-0.5 wt% silicon resin, and 0.5 wt% Bi<sub>2</sub>O<sub>3</sub>-0.5 wt% silicon resin composite, respectively, at 356 keV energy [17]. PMMA/20%Ta<sub>2</sub>O<sub>5</sub> composite showed 1.22-, 1.29- and 1.28-times bigger MAC values than these silicon-based composites.

In addition, the HVL parameters of the samples were examined to ascertain their shielding efficacy. The term HVL is defined as the length required to reduce the intensity of incident radiation to a level that is half of its original value. Lower HVL values indicate that the radiation can traverse a shorter distance through the absorbing medium, which enhances radiation attenuation ability. Figure 3 compares the HVL values of PMMA/Ta<sub>2</sub>O<sub>5</sub> composites for a range of gamma energies.

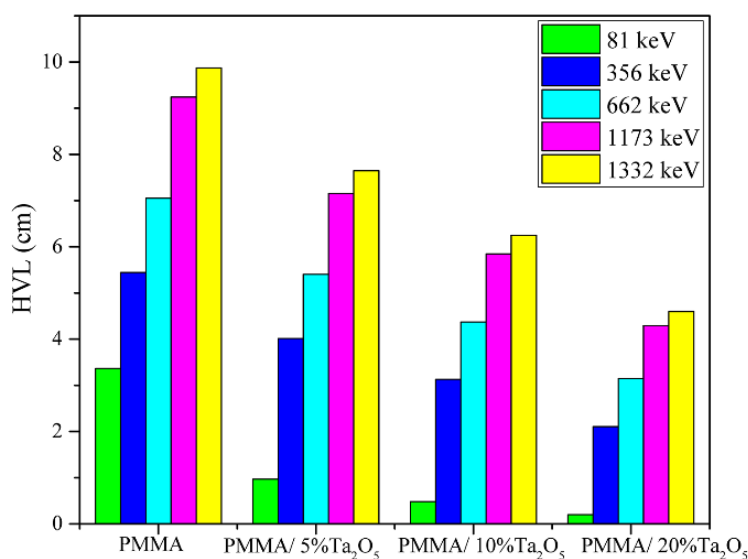


**Figure 3.** HVL values of PMMA/Ta<sub>2</sub>O<sub>5</sub> composites at various photon energies

As illustrated in Figure 3, the HVL values demonstrate an increase in photon energies and a decline with increasing Ta<sub>2</sub>O<sub>5</sub> doping concentration. The elevated HVL values at higher energies suggest that radiation penetration increases with photon energy. Consequently, a greater length is necessary to achieve the desired reduction in radiation. It can thus be concluded that the samples exhibit superior shielding performance at low energies. By the MAC values of the composites, the lowest HVL value, indicative of the optimal shielding performance, is observed in the PMMA/20% Ta<sub>2</sub>O<sub>5</sub> composite at all energy values. Furthermore, all of the composites exhibit lower HVL values than pure PMMA. The HVL value of the PMMA/20% Ta<sub>2</sub>O<sub>5</sub> composite is 16.9 times smaller than that of pure PMMA, indicating that this composite exhibits the best shielding performance.

$Z_{\text{eff}}$ , defined as the average atomic number of multi-element materials, is another crucial parameter for evaluating the gamma-ray shielding capability of PMMA/ Ta<sub>2</sub>O<sub>5</sub> composites. The variation of  $Z_{\text{eff}}$  of pure PMMA and PMMA/ Ta<sub>2</sub>O<sub>5</sub> composites with increasing energy is illustrated in Figure 4.

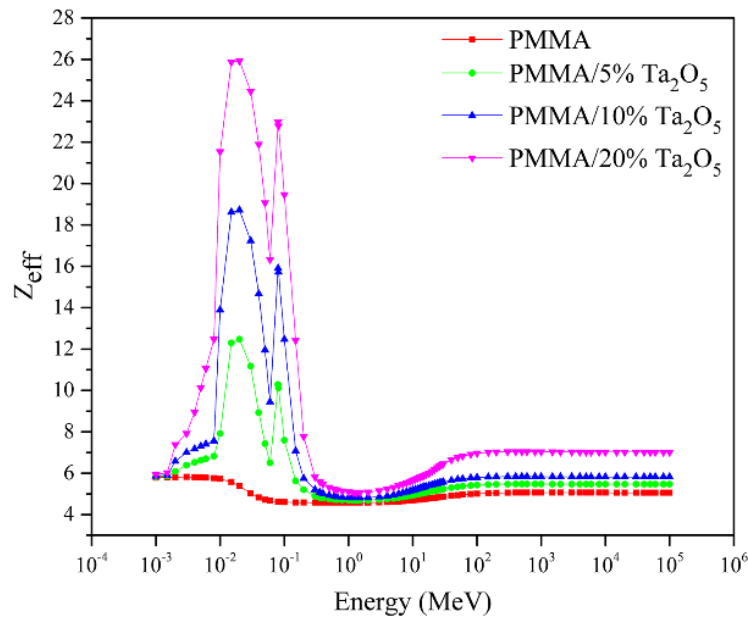


**Figure 4.** The variation of  $Z_{\text{eff}}$  of PMMA and PMMA/Ta<sub>2</sub>O<sub>5</sub> composites with gamma energies

As illustrated in Figure 4, all composites and pure PMMA display  $Z_{\text{eff}}$ -energy plots consistent with those observed in other studies in the literature [1,18,19]. This characteristic of  $Z_{\text{eff}}$ 's behavior about photon energy is associated with the interaction between radiation and matter. In these graphs,  $Z_{\text{eff}}$  tends to have maximum values at the low-energy region due to the dominance of the photoelectric event as the interaction mechanism, which depends on the atomic number  $Z$ . As the energy of the gamma photon increases, Compton scattering becomes the dominant interaction, whose cross-section is independent of  $Z$ , which manifests as a decrease in the graph. Nevertheless, there is a sudden rise in the  $Z_{\text{eff}}$  graphs of the composites in this area at approximately 67 keV. This phenomenon is attributed to the K absorption edge of Ta<sub>2</sub>O<sub>5</sub>. Furthermore, at elevated energies, the  $Z_{\text{eff}}$  values demonstrate an increase due to the dominance of pair generation over Compton scattering [20]. As illustrated in Figure 4, the  $Z_{\text{eff}}$  values of the composites exhibit a discernible increase with the addition of Ta<sub>2</sub>O<sub>5</sub>. This increase in  $Z_{\text{eff}}$  values with Ta<sub>2</sub>O<sub>5</sub> addition can be attributed to the rise in the concentration of high  $Z$  elements in the composites. The lowest  $Z_{\text{eff}}$  value is observed for the pure PMMA, while the highest is for the PMMA/20%Ta<sub>2</sub>O<sub>5</sub> composite. Thus, the PMMA/20%Ta<sub>2</sub>O<sub>5</sub> composite exhibits  $Z_{\text{eff}}$ 's most effective gamma ray attenuation performance.

#### 4. Conclusion

Lead has been employed for decades to protect high-energy radiation, yet it presents several drawbacks, including toxicity, high weight, and low processability. In light of these limitations, researchers have directed their attention toward developing alternative materials to address the shortcomings associated with lead. It is anticipated that these alternative materials will be light in weight, environmentally friendly, and sufficiently flexible to meet the requirements of the intended application. Polymer composites represent a class of materials that provide the aforementioned desired properties. This study investigated the gamma-ray shielding capacity of PMMA/ Ta<sub>2</sub>O<sub>5</sub> composites as a potential lead-free shielding material. The radiation shielding capacity of the composites was determined using WinXCom software and the MCNP6 code. The findings indicated that the incorporation of Ta<sub>2</sub>O<sub>5</sub> into PMMA led to an enhancement in radiation shielding parameters. The MAC values increased with incorporating Ta<sub>2</sub>O<sub>5</sub>, exhibiting a 7.75-fold enhancement compared to pure PMMA for the PMMA/20% Ta<sub>2</sub>O<sub>5</sub> composite at 81 keV gamma energy. Furthermore, the PMMA/20% Ta<sub>2</sub>O<sub>5</sub> composite exhibited the lowest HVL and the highest  $Z_{\text{eff}}$  value among the composites. From this perspective, the

PMMA/20% Ta<sub>2</sub>O<sub>5</sub> composite can be considered a flexible, lightweight, and environmentally friendly shielding material. Nevertheless, further studies could be conducted on additional properties of this material, such as its mechanical and thermal resistance. Furthermore, investigating its efficacy for various radiation energies and types would facilitate the multi-purpose utilization of the material.

## Author Contributions

The author read and approved the final version of the paper.

## Conflicts of Interest

The author declares no conflict of interest.

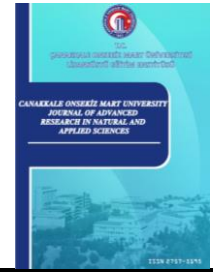
## Ethical Review and Approval

No approval from the Board of Ethics is required.

## References

- [1] M. Çağlar, H. Kayacık, Y. Karabul, M. Kılıç, Z. G. Özdemir, O. İçelli, *Na<sub>2</sub>Si<sub>3</sub>O<sub>7</sub>/BaO composites for the gamma-ray shielding in medical applications: Experimental, MCNP5, and WinXCom studies*, Progress in Nuclear Energy 117 (2019) 103119 11 pages.
- [2] T. Özdemir, A. Güngör, I. K. Akbay, H. Uzun, Y. Babuçuoğlu, *Nano lead oxide and EPDM composite for development of polymer-based radiation shielding material: Gamma irradiation and attenuation tests*, Radiation Physics and Chemistry 144 (2018) 248–255.
- [3] M. A. Hosseini, S. Malekie, F. Kazemi, *Experimental evaluation of gamma radiation shielding characteristics of polyvinyl alcohol/tungsten oxide composite: A comparison study of micro and nano sizes of the fillers*, Nuclear Instruments and Methods in Physics Research Section A 1026 (2022) 166214 6 pages.
- [4] M. E. Mahmoud, A. M. El-Khatib, M. S. Badawi, A. R. Rashad, R. M. El-Sharkawy, A. A. Thabet, *Fabrication, characterization and gamma rays shielding properties of nano and micro lead oxide-dispersed-high density polyethylene composites*, Radiation Physics and Chemistry 145 (2018) 160–173.
- [5] H. Wang, H. Zhang, Y. Su, T. Liu, H. Yu, Y. Yang, X. Li, B. Guo, *Preparation and radiation shielding properties of Gd<sub>2</sub>O<sub>3</sub>/PEEK composites*, Polymer Composites 36 (2015) 651–659.
- [6] S. Chen, S. Nambiar, Z. Li, E. Osei, J. Darko, W. Zheng, Z. Sun, P. Liu, J. T. W. Yeow, *Bismuth oxide-based nanocomposite for high-energy electron radiation shielding*, Journal of Material Science 54 (2019) 3023–3034.
- [7] T. Bel, C. Arslan, N. Baydogan, *Radiation shielding properties of poly (methyl methacrylate)/colemanite composite for the use in mixed irradiation fields of neutrons and gamma rays*, Materials Chemistry and Physics 221 (2019) 58–67.
- [8] D. Cao, Y. Ge, M. Bourham, D. Moneghan, *Gamma radiation shielding properties of poly (methyl methacrylate)/Bi<sub>2</sub>O<sub>3</sub> composites*, Nuclear Engineering and Technology 52 (11) (2020) 2613–2619.
- [9] A. M. Shareef, N. A. Abdulzahara, *Manufacture of shielding for attenuation ionization ray by the preparation of nano gadolinium oxide with PMMA*, NeuroQuantology 19 (8) (2021) 66–69.
- [10] D. Adlienė, L. Gilys, E. Griškonis, *Development and characterization of new tungsten and tantalum-containing composites for radiation shielding in medicine*, Nuclear Instruments and Methods in Physics Research B 467 (2020) 21–26.

- [11] S. Prabhu, S. G. Bubbly, S. B. Gudennavar, *Thermal, mechanical and  $\gamma$ -ray shielding properties of micro and nano-Ta<sub>2</sub>O<sub>5</sub> loaded DGEBA epoxy resin composites*, Journal of Applied Polymer Science 138 (2021) 246–266.
- [12] M. Kamislioglu, *Research on the effects of bismuth borate glass system on nuclear radiation shielding parameters*, Results in Physics 22 (2021) 103844 10 pages.
- [13] M. S. Eid, I. I. Bondouk, H. M. Saleh, K. M. Omar, M. I. Sayyed, A. M. El-Khatib, M. Elsafi, *Implementation of waste silicate glass into composition of ordinary cement for radiation shielding applications*, Nuclear Engineering and Technology 54 (2022) 1456–1463.
- [14] L. Gerward, N. Guilbert, K. B. Jensen, H. Levring, *WinXCom-a program for calculating X-ray attenuation coefficients*, Radiation Physics and Chemistry 71 (2004) 653–654.
- [15] T. A. A. Junior, M. S. Nogueira, V. Vivolo, M. P. A. Potiens, L. L. Campos, *Mass attenuation coefficients of X-rays in different barite concrete used in radiation protection as shielding against ionizing radiation*, Radiation Physics and Chemistry 140 (2017) 349–354.
- [16] M. E. Mahmoud, A. M. El-Khatib, M. S. Badawi, A. R. Rashad, R. M. El-Sharkawy, A. A. Thabet, *Recycled high-density polyethylene plastics added with lead oxide nanoparticles as sustainable radiation shielding materials*, Journal of Cleaner Production 176 (2018) 276–287.
- [17] M. Büyükyıldız, M. Kurudirek, M. Ekici, O. İçelli, Y. Karabul, *Determination of radiation shielding parameters of 304L stainless steel specimens from welding area for photons of various gamma-ray sources*, Progress in Nuclear Energy 100 (2017) 245–254.
- [18] K. Verdipoor, A. Alemi, A. Mesbahi, *Photon mass attenuation coefficients of a silicon resin loaded with WO<sub>3</sub>, PbO, and Bi<sub>2</sub>O<sub>3</sub> micro and nano-particles for radiation shielding*, Radiation Physics and Chemistry 147 (2018) 85–90.
- [19] S. Prabhu, S. G. Bubbly, S. B. Gudennavar, *Thermal, mechanical and  $\gamma$ -ray shielding properties of micro and nano-Ta<sub>2</sub>O<sub>5</sub> loaded DGEBA epoxy resin composites*, Journal of Applied Polymer Science 138 (44) (2021) 51289 16 pages.
- [20] M. S. Al-Buriah, C. Eke, S. Alomairy, A. Yildirim, H. I. Alsaedy, C. Sriwunkum, *Radiation attenuation properties of some commercial polymers for advanced shielding applications at low energies*, Polymers for Advanced Technologies 32 (2021) 2386–2396.
- [21] R. El-Mallawany, M. I. Sayyed, M. G. Dong, Y. S. Rammah, *Simulation of radiation shielding properties of glasses contain PbO*, Radiation Physics and Chemistry 151 (2018) 239–252.



# Comparative Forecasting of Some Key Economic Indicators Using Artificial Neural Networks and Ordinary Differential Equations: A Case Study of the Turkish Economy

Bahatdin Daşbaşı<sup>1</sup> , Murat Taşyürek<sup>2</sup> 

<sup>1</sup>Department of Environmental Basic Sciences, Faculty of Engineering, Architecture and Design, Kayseri University, Kayseri, Türkiye

<sup>2</sup>Department of Computer Engineering, Faculty of Engineering, Architecture and Design, Kayseri University, Kayseri, Türkiye

## Article Info

Received: 02 Oct 2024

Accepted: 08 Dec 2024

Published: 31 Dec 2024

Research Article

**Abstract** – This study explores the relationships between the USD opening exchange rate, the annual change rate of the Consumer Price Index (CPI), the housing loan interest rate in Turkish lira, and the residential construction cost index from January 2015 to May 2024 using data from the Turkish Statistical Institute (TUIK). Artificial Neural Networks (ANN) and Ordinary Differential Equations (ODE) methods were employed to model the interactions among these four variables. In the ANN approach, each variable was modeled as the dependent variable in turn, with the remaining three serving as independent variables, resulting in four distinct analyses. The ODE model, on the other hand, provided a holistic analysis by capturing the time-dependent relationships among all four variables simultaneously. The ANN model predictions achieved accuracy rates of 87.2% for the USD opening exchange rate, 91.4% for the CPI annual change rate, 85.9% for the housing loan interest rate, and 93.1% for the construction cost index. Meanwhile, the ODE model demonstrated its strength by offering a more comprehensive framework with an overall accuracy of 94.6%, effectively capturing the complex interdependencies among the variables. These findings highlight the strengths of both approaches: while the ANN model excels in analyzing individual variables, the ODE model offers a broader perspective by integrating all variables into a unified framework. This study contributes to developing economic forecasting models and provides valuable insights for decision-makers, particularly in times of economic uncertainty.

**Keywords** – Turkish economy, artificial neural networks, ordinary differential equations, comparative forecasting

## 1. Introduction

Economic indicators are critical in understanding a country's economic performance and predicting future trends [1]. In developing countries like Türkiye, variables like exchange, inflation, interest, and construction costs are crucial to economic growth and sustainability. Correctly modeling the relationships between these indicators enables economists and policymakers to make the right decisions [2].

The Turkish economy has faced significant challenges, especially between 2015 and 2024, due to fluctuations in global markets, volatility in exchange rates, and structural changes in domestic markets. The country's economic stability is affected by key financial indicators such as the USD opening rate, Consumer Price Index (CPI), mortgage interest rates, and construction cost index. These indicators are affected by both local and global market dynamics and have a complex relationship with each other. The exchange rate, especially the USD/TL rate, has become an important determinant of economic activity in Turkey [3]. The exchange rate,

<sup>1</sup>bdasbasi@kayseri.edu.tr; <sup>2</sup> murattasyurek@kayseri.edu.tr (Corresponding Author)

which has a major impact on foreign trade, borrowing, and investment decisions, is also closely related to inflation and interest rates. Inflation (CPI), in particular, affects consumer spending and investment decisions, putting pressure on interest rates and construction costs. Mortgage interest rates serve as an indicator of financial conditions for both individual and institutional investors. On the other hand, the construction cost index determines investment costs and growth potential in the sector, especially in countries like Turkey, where the construction sector has a significant share in growth.

Recent advancements in artificial intelligence (AI) and blockchain technologies have significantly impacted various fields, including healthcare and smart community applications. For instance, smart contract-enabled systems have demonstrated secure data-sharing capabilities in mobile cloud-based healthcare environments, ensuring data integrity and confidentiality [4]. Additionally, deep learning techniques, such as facial emotion recognition using principal component analysis (PCA) and neural networks (ANNs), have shown the robustness of AI in handling complex, data-intensive tasks [5]. Moreover, AI and machine learning have been integrated into smart community frameworks to enhance scalability, security, and accessibility in managing critical information systems [6]. These advancements underline the essential role of AI, particularly ANNs, in addressing challenges across dynamic and sensitive domains. Building on these innovations, our study applies ANN-based methodologies to the comparative forecasting of key economic indicators, aiming to leverage their data-driven precision for improved predictive accuracy.

In this study, Artificial Neural Networks (ANN) [7] and Ordinary Differential Equations (ODE) [8] models were applied to estimate the relationships between the USD opening exchange rate, CPI, housing loan interest rates, and construction cost index using Turkish Statistical Institute (TUIK) data. ANN was run as four separate estimation models with different data set combinations; each variable was treated as a dependent variable, respectively. The ODE model provided a holistic approach that evaluated the interactions of all variables in a single model [9].

This study seeks to evaluate the performance of two distinct modeling approaches and identify the scenarios in which each model proves more effective. The findings reveal that both ANN and ODE models successfully estimate economic indicators for Turkey, yet the nature of the relationships between variables varies based on the chosen modeling approach. This research enhances economic forecasting methodologies for the Turkish economy and offers valuable insights to policymakers, aiding them in making informed economic decisions in the future.

## 2. Related Works

Using methods such as ANN and ODE to model complex economic systems has become an increasingly popular area of research today. The accuracy and reliability of economic indicators play a major role in shaping public policies and making financial decisions. Alshawarbeh et al. [10] have estimated volatile stock market indices using the hybrid ARIMA-ANN model in this context. Their research shows that when combined with time series models, ANN significantly increases forecast accuracy, especially in complex and chaotic financial data. This hybrid approach is critical for forecasting highly volatile economic data, especially inflation and exchange rates. In a similar study, Mohamed et al. [11] discussed how ANN can be used in estimating macroeconomic performance indicators. Their analysis showed that ANN outperformed linear regression models and revealed important results encouraging using neural networks in economic forecasting. In this direction, the effectiveness of ANN-based forecasting models was emphasized to increase the accuracy of economic indicators such as inflation and exchange rate fluctuations. However, Wijesinghe et al. [12] also compared ARIMA and ANN models and showed that ANN performs better in stock prices and better captures the stock market's volatility. It was demonstrated that ARIMA handles linear trends well in short-term forecasts, but ANN is superior in adapting to complex and dynamic data models. The findings of this study show how effective ANN can be for long-term forecasts in economic forecasts.

There is a wide range of use of AI-based forecasting models, and significant successes have been achieved in adapting these methods to economic indicators. The systematic literature review conducted by Ramírez et al. [13] highlights the widespread use of AI methods such as artificial neural networks (ANN), fuzzy logic systems (ANFIS), genetic programming (GP), and support vector regression (SVR). This review revealed that these methods can predict economic indicators such as CPI, interest rates, and GDP. The studies show the potential of AI-based methods to increase the accuracy of economic forecasts. The study by Fani et al. [14] focused on using ANN in forecasting gasoline demand in the Tehran metropolis. The study analyzed seven social and economic indicators affecting gasoline demand using a multilayer perceptron artificial neural network (MLP) model. The findings of this study show how successful ANN can be in modeling economic data sets and its sensitivity to different social and economic variables.

ODE-based models are also of great importance in economic analysis. Guerrini et al. [15] studied the economic growth model with a time-lagged investment function. Their work transformed the lagged differential equations into ordinary differential equations (ODE) systems and analyzed the economic growth and investment dynamics over three- and four-dimensional systems. Such studies emphasize the power of ODE models in understanding the long-term dynamics of economic systems and how investments change over time. Similarly, Wu et al. [16] developed a model for parameter estimation and variable selection of linear ODEs. They presented an approach based on similarity transformation and separable least squares (SLS) methods to improve the performance of ODE models in ultra-high dimensional economic systems. This method allows linear ODE systems to provide more accurate and successful results on large data sets. These findings increase the importance of ODE-based approaches in modeling economic systems. Finally, the study of Georgiev et al. [17] on asset price estimation in financial markets using ODE-based methods provides a solution to increase the accuracy of financial models. The ODE-based model developed using polynomials and periodic functions successfully handles the complexity of financial data sets and provides a workable method for investors that can work with a wide set of parameters.

These studies clearly show how powerful the tools ANN and ODE are in estimating economic indicators. In the following sections, the methods used in these studies will be analyzed in depth, and how the current study applies these methods and what innovations it offers in economic estimations will be detailed.

### 3. Materials and Methods

This section first mentions the used data set and presents the ANN and ODE methods.

#### 3.1. Dataset

The dataset used in this study includes economic indicators for different years related to the Turkish economy. The dataset covers a period starting from Jan 2015 to May 2024. Each observation presents important economic indicators, such as monthly Opening (USD), CPI (Annual % Change), Bank Housing Loan TL Interest Rate, and Construction Cost Index. The dataset reflects Turkey's exchange rate changes, inflation rates, housing loan interest rate fluctuations, and how costs change in the construction sector. It allows the application of time series analysis and econometric models. Within the scope of the research, the relationships between economic indicators were examined, and forecasting models were created using methods, such as ANN and ODE. The long-term coverage of the dataset allows for better training of the model, to increase the accuracy of economic forecasts. The data obtained from TÜİK is presented in Table 1.

The observation in Table 1 details the changes that have occurred among the economic indicators over time, and these data provide an essential basis for the economic forecast models that form the main focus of the study. The data in Table 1 were normalized with the Euclidean norm and denormalization was done during the simulation phase. Data normalization is used in machine learning to make model training less sensitive to the scale of the features. This allows our model to converge to better weights, which leads to a more accurate model. Normalization makes the features more consistent, allowing the model to predict the output more

accurately. In mathematics, normalizing a vector means dividing each element by a value  $V$ , so that the resulting vector has a length/norm 1. It turns out that the required  $V$  is equal to the length (length of the vector). The Euclidean norm is obtained as  $\|\text{month}\| = 20667.3656$ ,  $\|\text{USD}\| = 131.765362$ ,  $\|\text{CPI}\| = 373.149781$ ,  $\|\text{interest rate}\| = 211.818758$ , and  $\|\text{Construction cost index}\| = 5455.99528$  using the formula  $\|x\|_2 = (\sum_{i=1}^n |x_i|^2)^{\frac{1}{2}} = \sqrt{x_1^2 + x_2^2 + \dots + x_n^2}$ . Then, each variable was divided into its norms, and normalization was achieved.

**Table 1.** Dataset

Order Number	Date	Month	USD	CPI	Real TL	Interest rate	Construction cost index	total for residential purposes
1	1.01.2015	0	2,3367	7,24		10,97		97,68
2	1.02.2015	30	2,4434	7,55		10,85		97,71
3	1.03.2015	60	2,5117	7,61		10,76		98,12
4	1.04.2015	90	2,598	7,91		10,96		98,91
5	1.05.2015	120	2,6718	8,09		11,18		99,63
6	1.06.2015	150	2,6606	7,2		11,63		99,48
7	1.07.2015	180	2,6817	6,81		12,18		100,61
8	1.08.2015	210	2,7689	7,14		12,42		101,45
9	1.09.2015	240	2,9144	7,95		13,3		102,23
10	1.10.2015	270	3,0254	7,58		14,08		101,57
11	1.11.2015	300	2,9154	8,1		14,29		101,4
12	1.12.2015	330	2,9136	8,81		13,98		101,23
13	1.01.2016	360	2,9177	9,58		14,08		109,67
14	1.02.2016	390	2,9561	8,78		14,47		109,67
15	1.03.2016	420	2,964	7,46		14,46		110,87
16	1.04.2016	450	2,8165	6,57		14,44		111,68
17	1.05.2016	480	2,7954	6,58		14,04		113,15
18	1.06.2016	510	2,9489	7,64		13,93		112,39
19	1.07.2016	540	2,8766	8,79		13,74		112,21
:	:	:	:	:		:		:
113	1.05.2024	3360	32,4178	75,45		44,02		1499,99

### 3.2. Artificial Neural Networks (ANN)

This study used Artificial Neural Networks (ANN) to predict economic indicators. ANN creates a multi-layered model by imitating the information processing structure of the human brain and is particularly successful in modeling complex and non-linear data relationships. The layers used in the model include input, hidden, and output layers. Neural network nodes represent each layer and process data by connecting with nodes in other layers. The training of the ANN is carried out by updating the weights in each iteration, and in this process, the error function is minimized, and the accuracy of the model is increased. In the ANN used in this study, one of the economic indicators is selected as the output (dependent variable). In contrast, the other three indicators are used as model inputs. The model was run four times, and each economic indicator was determined as the output in order. The model's success in predicting future economic indicators was measured by minimizing the error rate during training. The model's accuracy was evaluated with the average error rates in the training and test data sets. The structure of the ANN model used in this study is presented in Figure 1.

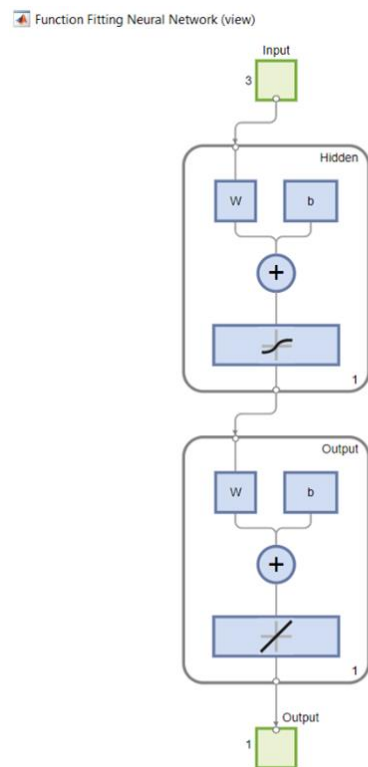


**Figure 1.** Structure of the used ANN model

The ANN model in Figure 1 consists of 3 input layers, a hidden layer, and an output layer. In the input layer, three economic indicators the model will predict are taken as inputs. These inputs are processed with a specific weight and activation function and transferred to the hidden layer. The hidden layers have nodes that increase the learning capacity of the model and enable the neural network to model non-linear relationships. Activation functions are usually non-linear ReLU (Rectified Linear Unit) or sigmoid functions so that the model can obtain more accurate results in complex data. The output layer contains the economic indicator the model will predict (e.g., exchange rate, CPI, or interest rate). The ANN model is trained with the backpropagation algorithm, and the error function is minimized in each iteration. This process increases the model's performance, and the trained network can predict future data.

### 3.3. Ordinary Differential Equations (ODE)

This study used the Ordinary Differential Equations (ODE) approach to model the relationships between economic indicators. ODE is a mathematical modeling method used to analyze the dynamic behavior of systems that change over time. This method defines the rates of change of dependent variables over time and their relationships. Therefore, differential equations and their mathematical models are widely used in many fields of science, such as biomathematics [18,19], physics [20,21], medicine [22,23], chemistry [24-26], engineering [26-28], economics [29,30], etc.

The linear ODE model examined four economic indicators simultaneously and modeled their interactions and how they evolved. ODE models are especially effective in long-term predictions of complex economic processes because these models can capture transitions and dynamic processes in time series. The ODE approach aims to increase the model's accuracy by optimizing the system's parameters and initial conditions. In this study, the model parameters were estimated using numerical methods and used to accurately predict the long-term trends of economic indicators. The linear ODE model presented within the scope of this study was designed to model the dynamic relationships between economic indicators. ODE models are based on differential equations to understand how variables in the system change over time. In such models, the interactions between economic indicators are considered a process that develops over time.

## 4. Results and Discussion

This section delves into a comprehensive analysis of the estimation processes conducted using ANN and ODE models. The study focuses on the predictability of four critical economic variables: the USD Opening Exchange Rate, the Consumer Price Index Annual Percentage Change, the Bank Housing Loan TL Interest Rate, and the Residential Construction Cost Index. These variables, chosen for their significance in understanding economic dynamics, were derived from the dataset summarized in Table 1.

To ensure the reliability and validity of the modeling process, the dataset was meticulously partitioned into three subsets: 70% for training to build the models, 15% for validation to fine-tune and prevent overfitting, and 15% for testing to evaluate the models' predictive performance. This structured approach enhances the robustness of the analysis. It provides a solid foundation for comparing the estimation capabilities of ANN and ODE in capturing the intricate relationships between the selected variables.

By integrating these models with a carefully prepared dataset, this section aims to provide valuable insights into their practical applicability and effectiveness in modeling complex economic interactions.

### 4.1. Metrics and Equations

Experimental evaluations were evaluated using MAD, MSE, RMSE, MAPE, and  $R^2$  metrics [31-34]. As shown in Equation 4.1, MAD calculates the average of the absolute differences between the estimated and actual values. On the other hand, MSE is used to measure the model's error rate and gives the average of the square of the errors. A high MSE indicates that the model makes large errors in its predictions. RMSE is calculated by taking the square root of MSE and expressing the magnitude of the prediction errors more clearly. MAPE expresses the error rate as a percentage and allows the model's performance to be evaluated on a percentage basis.  $R^2$  is a coefficient that measures how well the model makes a prediction. An  $R^2$  value of 1 indicates that the model makes a high-accuracy prediction, as shown in (4.1).

$$\begin{aligned}
 MAD &= \frac{1}{n} \sum_{i=1}^n |y_i - \hat{y}_i| \\
 MSE &= \frac{1}{n} \sum_{i=1}^n (y_i - \hat{y}_i)^2 \\
 RMSE &= \sqrt{\frac{1}{n} \sum_{i=1}^n (y_i - \hat{y}_i)^2} \\
 MAPE &= \frac{100\%}{n} \sum_{i=1}^n \left| \frac{y_i - \hat{y}_i}{y_i} \right| \\
 R^2 &= 1 - \frac{\sum_{i=1}^n (y_i - \hat{y}_i)^2}{\sum_{i=1}^n (y_i - \bar{y}_i)^2}
 \end{aligned} \tag{4.1}$$

In Eqs. (4.1),  $y_i$  is real data,  $\hat{y}_i$  is predicted data, and  $\bar{y}_i$  is the mean value.

The resulting model with ANN's activation function (tanh) has been written as in (4.2).

$$y = b_2 + LW \tanh(b_1 + IWx) \tag{4.2}$$

The general linear ODE mathematical model is shown in (4.3), as  $t$  is the time parameter and the independent variable.

$$\begin{aligned} \frac{dx}{dt} &= \theta_1 x + \theta_2 k + \theta_3 z + \theta_4 h + \theta_5 \\ \frac{dk}{dt} &= \theta_6 x + \theta_7 k + \theta_8 z + \theta_9 h + \theta_{10} \\ \frac{dz}{dt} &= \theta_{11} x + \theta_{12} k + \theta_{13} z + \theta_{14} h + \theta_{15} \\ \frac{dh}{dt} &= \theta_{16} x + \theta_{17} k + \theta_{18} z + \theta_{19} h + \theta_{20} \end{aligned} \tag{4.3}$$

where variables  $x, k, z,$  and  $h$  represent the USD opening exchange rate, CPI annual change rate, housing loan interest rate in Turkish lira, and residential construction cost index values at time  $t$ , respectively.

### 4.2. Analysis of ANN and ODE Models

The ANN model was employed to predict four different variables individually, with the other three as inputs in each case. Specifically, the variables are USD, CPI, Real TL Interest rate, and Construction cost index total for residential purposes. A separate ANN model was trained for each output, and each model's best validation performance was recorded at different epochs. The results for the four trainings are shown in Figures 2-5.

Training Progress				
Unit	Initial Value	Stopped Value	Target Value	
Epoch	0	10000	10000	▲
Elapsed Time	-	00:00:09	-	
Performance	0.979	3.32e-05	1e-10	
Gradient	2.48	4.61e-08	0	
Mu	0.001	1e-16	1e+10	
Validation Checks	0	9.88e+03	1.11e+04	▼

**Figure 2.** Best validation performance is 2.2541e-05 at epoch 116 (USD)

As shown in Figure 2, the model achieved its best validation performance with a minimal error of 2.2541e-05 at epoch 116. This exceptionally low error indicates that the model performs well in predicting USD opening values. The relatively large number of epochs required to reach this performance suggests that the model required extensive training to minimize the error effectively.

Training Progress				
Unit	Initial Value	Stopped Value	Target Value	
Epoch	0	111	10000	▲
Elapsed Time	-	00:00:02	-	
Performance	0.0756	0.000352	1e-16	
Gradient	0.564	6.29e-12	0	
Mu	0.001	1e+10	1e+10	
Validation Checks	0	107	1.11e+06	▼

**Figure 3.** Best validation performance is 0.00011765 at epoch 4 (CPI)

As shown in Figure 3, the best validation performance for the CPI variable was achieved early, with an error of 0.00011765 at epoch 4. The model's ability to converge to an optimal solution in such a short number of epochs indicates that predicting this variable required less complexity, and the model quickly adapted to the underlying patterns within the data.

Unit	Initial Value	Stopped Value	Target Value
Epoch	0	2877	10000
Elapsed Time	-	00:00:04	-
Performance	0.421	0.00034	1e-16
Gradient	1.43	2.95e-09	0
Mu	0.001	1e+10	1e+10
Validation Checks	0	2.81e+03	1.11e+06

Figure 4. Best validation performance is 0.00011765 at epoch 4 (Real TL interest rate)

As shown in Figure 4, the model's best validation performance for the real TL Interest rate was recorded at epoch 67, with an error of 0.0003889. Although this error is slightly higher than the other variables, the model still demonstrated reasonable predictive capability. The comparatively higher error suggests that this variable might exhibit more complexity or variability, making it somewhat more challenging to predict accurately.

Unit	Initial Value	Stopped Value	Target Value
Epoch	0	32	10000
Elapsed Time	-	00:00:01	-
Performance	0.0867	4e-05	1e-16
Gradient	0.234	1.25e-13	0
Mu	0.001	1e+10	1e+10
Validation Checks	0	2	1.11e+06

Figure 5. Best validation performance is 4.1379e-05 at epoch 30 (Construction cost index total for residential purposes)

As shown in Figure 5, The model achieved its best validation performance at epoch 30, with a low error of 4.1379e-05. This result reflects a strong performance in predicting the construction cost index. The moderate number of required epochs indicates that the model efficiently learned the relationships within the data without extensive training. In this context, the activation functions in (4.2) obtained in the estimation process ( $y = b_2 + LW \tanh(b_1 + IWx)$ ) are given in Table 2.

Table 2. Parameters of ANN

	For the USD opening exchange rate ( $x$ )	For the Consumer Price Index (CPI) annual change rate ( $k$ )	For housing loan interest rates in Turkish lira ( $z$ )	For residential construction cost index ( $h$ )
<b>b1</b>	-0,8464	-2,1941	2,9691	0,8936
<b>b2</b>	-1,0069	0,0940	0,7691	0,1714
<b>IW</b>	$\begin{pmatrix} -0,0846 \\ -0,0916 \\ -1,5066 \end{pmatrix}^T$	$\begin{pmatrix} 16,6979 \\ 8,8024 \\ 0,6858 \end{pmatrix}^T$	$\begin{pmatrix} -12,4050 \\ 0,1422 \\ 4,0140 \end{pmatrix}^T$	$\begin{pmatrix} -5,6276 \\ 0,1945 \\ 0,2734 \end{pmatrix}^T$
<b>LW</b>	-1,4558	0,0839	-0,7070	-0,2306

The ANN model's performance across the four variables highlights differences in the complexity and predictability of each target. USD and Real TL Interest rates exhibited low error rates, indicating that the model captured the relationships between the input features and these outputs well. On the other hand, CPI reached optimal performance quickly, suggesting less complexity in the data structure for this variable. In contrast, the

Real TL Interest rate prediction was comparatively more challenging, as evidenced by the higher error and the greater number of epochs required to achieve the best performance. These results demonstrate that the ANN model can handle varying complexity across economic variables. Early stopping ensured that each model's training was halted once the optimal performance was reached, thus preventing overfitting and ensuring robust generalization. Therefore, the activation equations obtained with the coefficients given in Table 2 for each variable are in the form of

$$x = (-1,0069)_{1 \times 1} + (-1,4558)_{1 \times 1} \tanh \left( (-0,8464)_{1 \times 1} + \begin{pmatrix} -0,0846 \\ -0,0916 \\ -1,5066 \end{pmatrix}^T \begin{pmatrix} k \\ z \\ h \end{pmatrix} \right)$$

$$k = (0,0940)_{1 \times 1} + (0,0839)_{1 \times 1} \tanh \left( (-2,1941)_{1 \times 1} + \begin{pmatrix} 16,6979 \\ 8,8024 \\ 0,6858 \end{pmatrix}^T \begin{pmatrix} x \\ z \\ h \end{pmatrix} \right)$$

$$z = (0,7691)_{1 \times 1} + (-0,7070)_{1 \times 1} \tanh \left( (2,9691)_{1 \times 1} + \begin{pmatrix} -12,4050 \\ 0,1422 \\ 4,0140 \end{pmatrix}^T \begin{pmatrix} x \\ k \\ h \end{pmatrix} \right)$$

$$h = (0,1714)_{1 \times 1} + (-0,2306)_{1 \times 1} \tanh \left( (0,8936)_{1 \times 1} + \begin{pmatrix} -5,6276 \\ 0,1945 \\ 0,2734 \end{pmatrix}^T \begin{pmatrix} x \\ k \\ z \end{pmatrix} \right)$$

This study uses the linear ODE model to predict the values of key economic indicators, namely USD, CPI, Real TL Interest rate, and Construction Cost Index (Residential). The aim is to evaluate the ability of the model to predict these economic time series based on historical data. Therefore, the parameters  $\theta_i$  for  $i \in \{1, 2, \dots, n\}$  used in (4.3) are calculated by the least squares method. For this, the approach used in [35] is considered. In this sense, these parameters obtained with the lsqcurvefit function (options.MaxFunctionEvaluations = 2.700000e+03) by solving with the Matlab R2023b program RungeKutta45 are given as  $\theta_1 = -0,43409$ ,  $\theta_2 = 25,35903$ ,  $\theta_3 = 2,88139$ ,  $\theta_4 = -0,22453$ ,  $\theta_5 = 0,13318$ ,  $\theta_6 = 0,00496$ ,  $\theta_7 = 53,26714$ ,  $\theta_8 = 46,52477$ ,  $\theta_9 = -0,23567$ ,  $\theta_{10} = -89,32466$ ,  $\theta_{11} = 1,84924$ ,  $\theta_{12} = -14,07299$ ,  $\theta_{13} = -21,62068$ ,  $\theta_{14} = -39,76487$ ,  $\theta_{15} = 74,41487$ ,  $\theta_{16} = 0,58824$ ,  $\theta_{17} = -17,67795$ ,  $\theta_{18} = 42,26980$ ,  $\theta_{19} = -25,89622$  and  $\theta_{20} = 19,47007$ . A comprehensive discussion of the performance of the linear ODE model for each variable is visualized in Figures 6-9.

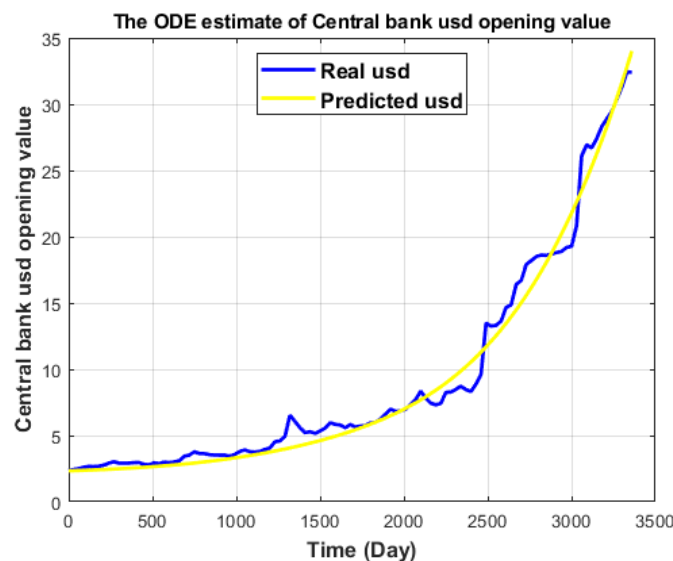
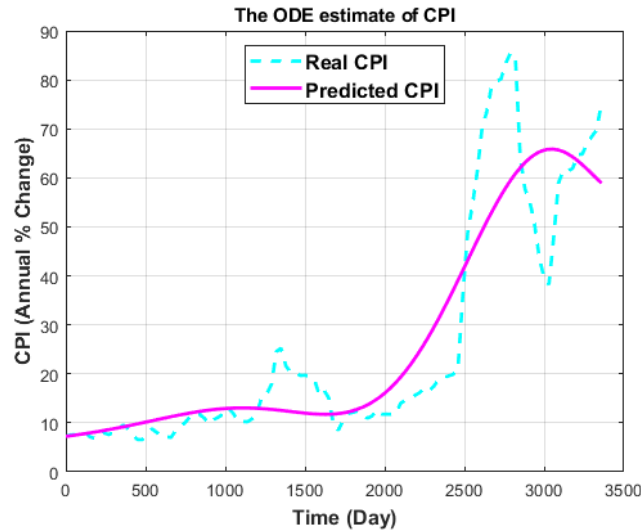


Figure 6. ODE estimate for USD

As shown in Figure 6, USD values exhibit a consistent upward trajectory with intermittent spikes, especially in the later stages. The predicted USD values follow this upward trend closely, with a smooth curve that largely tracks the real data but overlooks the smaller fluctuations. The results highlight the model's robustness in handling the long-term dynamics of the USD exchange rate. Nevertheless, more responsive models, such as those incorporating stochastic components, might be required for short-term financial planning or hedging purposes.



**Figure 7.** ODE estimate for CPI

As shown in Figure 7, CPI exhibits significant volatility throughout the period, with sharp rises and falls in certain intervals. In contrast, the predicted CPI (solid magenta line) shows a much smoother trajectory, capturing the long-term upward trend while attenuating short-term fluctuations. The smoothing effect observed in the predicted CPI is typical in ODE models, which focus on continuous, gradual changes. The model's limitation in capturing volatility may indicate the need for additional components to account for external shocks or seasonal patterns affecting inflation.

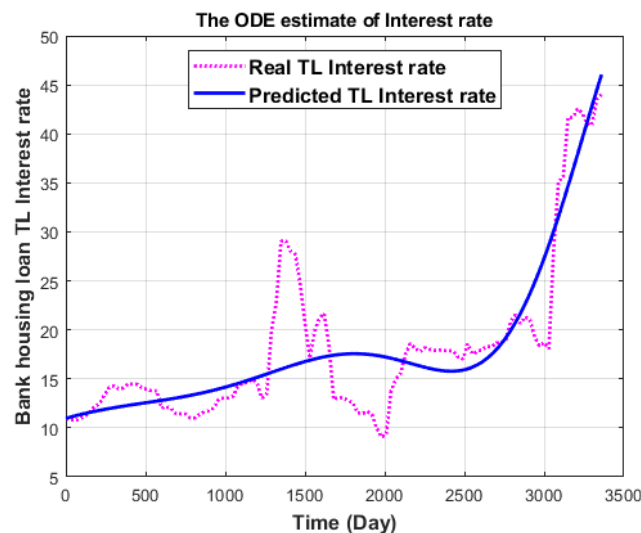


**Figure 8.** ODE estimate for interest rate

As shown in Figure 8, Real interest rates exhibit high volatility, with significant swings throughout the time series, especially in the mid-period (between day 1000 and 2000). In contrast, the predicted interest rates present a much smoother, steadily increasing curve. The divergence between predicted and real values, particularly in periods of volatility, suggests that the ODE model may require adjustments, such as introducing exogenous factors or coupling with stochastic models, to better capture market reactions to economic or political events.

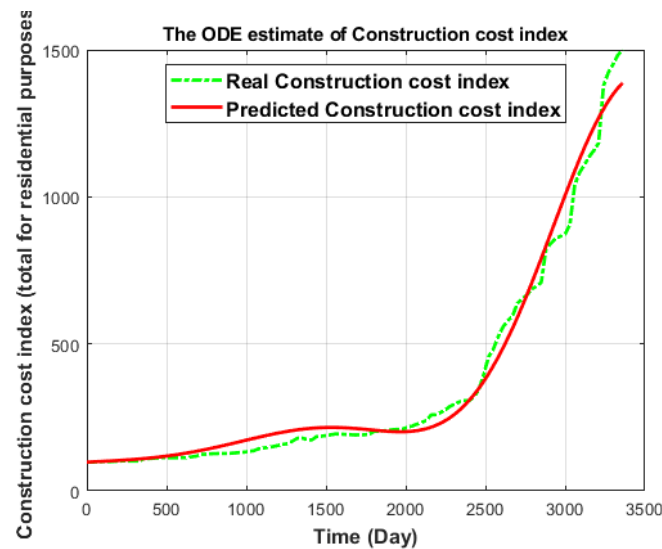


**Figure 9.** ODE estimate for the construction cost index

As shown in Figure 9, the construction cost index (dashed green line) follows an exponential growth pattern with moderate fluctuations. The predicted cost index (solid red line) closely follows the actual data, with only minor deviations throughout the time series. The model's success in predicting the construction cost index suggests that the index's relatively stable growth is well-suited for ODE modeling. This makes the ODE model a reliable tool for forecasting construction-related costs over time, where market conditions are less prone to abrupt changes than other economic variables.

The ODE model's performance across the four economic indicators reveals its strengths and limitations. The model excels in predicting long-term trends, such as the general upward trajectories of USD opening values, construction cost indices, and, to a lesser extent, the CPI and interest rates. However, it struggles with capturing the real CPI and interest rate data volatility, where rapid changes and external shocks significantly influence the time series. This indicates that while ODE models are useful for trend analysis and forecasting stable, long-term economic behaviors, they may require augmentation with other techniques—such as stochastic differential equations or machine learning models—when attempting to model highly volatile or shock-prone variables.

### 4.3. Analysis of ANN and ODE Models

To comprehensively evaluate the predictive capabilities of the ANN and ODE models, several performance metrics were calculated for each model about the four target variables: USD, CPI, Interest Rate, and Construction Cost Index. The metrics used include MAD, MSE, RMSE, MAPE, and R<sup>2</sup>, as presented in Table 3.

**Table 3.** Result of ANN and ODE models

Metric	ANN prediction results for USD	ANN prediction results for CPI	ANN prediction results for Interest Rate	ANN prediction results for Cost Index	ODE prediction results for USD	ODE prediction results for CPI	ODE prediction results for Interest Rate	ODE prediction results for Cost Index
MAD	0,51	5,14	2,71	22,49	0,68	6,99	2,83	262,32
MSE	0,53	69,65	15,05	1275,94	0,92	105,25	15,710	145722,6
RMSE	0,73	8,35	3,88	35,72	0,96	10,25	3,96	381,73
MAPE	7,08	19,21	16,00	5,88	12,95	17,15	10,92	69,64
R <sup>2</sup>	0,99	0,88	0,78	0,998	0,98	0,81	0,77	0,99

The ANN model performs well regarding MAD, with particularly low values for USD (0,51) and Interest Rate (2,71). However, it shows higher deviations in CPI (5,14) and Construction Cost Index (22,49), suggesting that the model struggles more with predicting these two variables. On the other hand, The ODE model exhibits slightly higher MAD values for USD (0,68) and CPI (6,99) but remains comparable to the ANN model for these variables. However, the ODE model's MAD for Construction Cost Index (262,32) is significantly higher than the ANN model's, indicating substantial deviation in predicting this variable.

The ANN model achieves very low MSE for USD (0,53), indicating strong predictive performance. Conversely, CPI (69,66) and Interest Rate (15,05) show much higher MSE, indicating larger squared errors and potential issues predicting these variables. Moreover, The ODE model shows higher MSE values across most variables, particularly for CPI (105,25) and Construction Cost Index (145722,65), suggesting that the ODE model struggles to minimize the squared differences between predicted and actual values, especially for variables with higher volatility or complexity.

Similar to MSE, RMSE values for USD (0,73) and Interest Rate (3,88) are relatively low for the ANN model, while higher errors are observed for CPI (8,35) and Construction Cost Index (35,72). The RMSE metric highlights the difficulties the model encounters in capturing the variability of these latter variables. On the other hand, The ODE model exhibits slightly higher RMSE for USD (0,9604) and substantially higher for Construction Cost Index (381,73), again highlighting the challenge of accurately predicting the construction index using this model.

The ANN model delivers competitive MAPE values for USD (7,08) and Construction Cost Index (5,88), suggesting it performs well in predicting these variables regarding relative error. However, the model has higher MAPE for CPI (19,21) and Interest Rate (16,00), indicating that it struggles to effectively capture these variables' dynamics. Moreover, The ODE model shows a generally higher MAPE for most variables, particularly for USD (12,96), CPI (17,16), and Construction Cost Index (69,64), indicating that its predictions deviate significantly in percentage terms, especially for the Construction Cost Index, where large relative errors occur.

The  $R^2$  values for the ANN model demonstrate strong performance for USD (0,9921) and Construction Cost Index (0,9907), indicating that the model explains over 99% of the variance in these variables. However,  $R^2$  values are lower for CPI (0,8774) and Interest Rate (0,7816), suggesting a reduced ability to explain the variance in these more complex and volatile variables. On the other hand, The ODE model also demonstrates high  $R^2$  values for USD (0,9866) and Construction Cost Index (0,9930) but performs less effectively for CPI (0,8121) and Interest Rate (0,7723), which indicates a somewhat reduced predictive capability in capturing the full variability of these economic indicators.

The results suggest that while the ANN model generally provides superior predictive performance across the board, the ODE model remains a competitive alternative for variables with more stable, long-term trends, such as the USD opening value and Construction Cost Index. However, for highly volatile economic indicators, such as CPI and Interest Rate, the ANN model is better equipped to handle the complexities and non-linear relationships present in the data.

ANN analysis showed better performance for USD and cost index. However, with the ANN model, the output variable can be calculated with the current value of the input variables. On the other hand, the system is an initial value problem throughout the ODE model. In this context, forward-looking estimates can be made with the ODE model. Thus, the scenario envisaged for the USD exchange rate and cost index in the long term is shown in Figure 10.

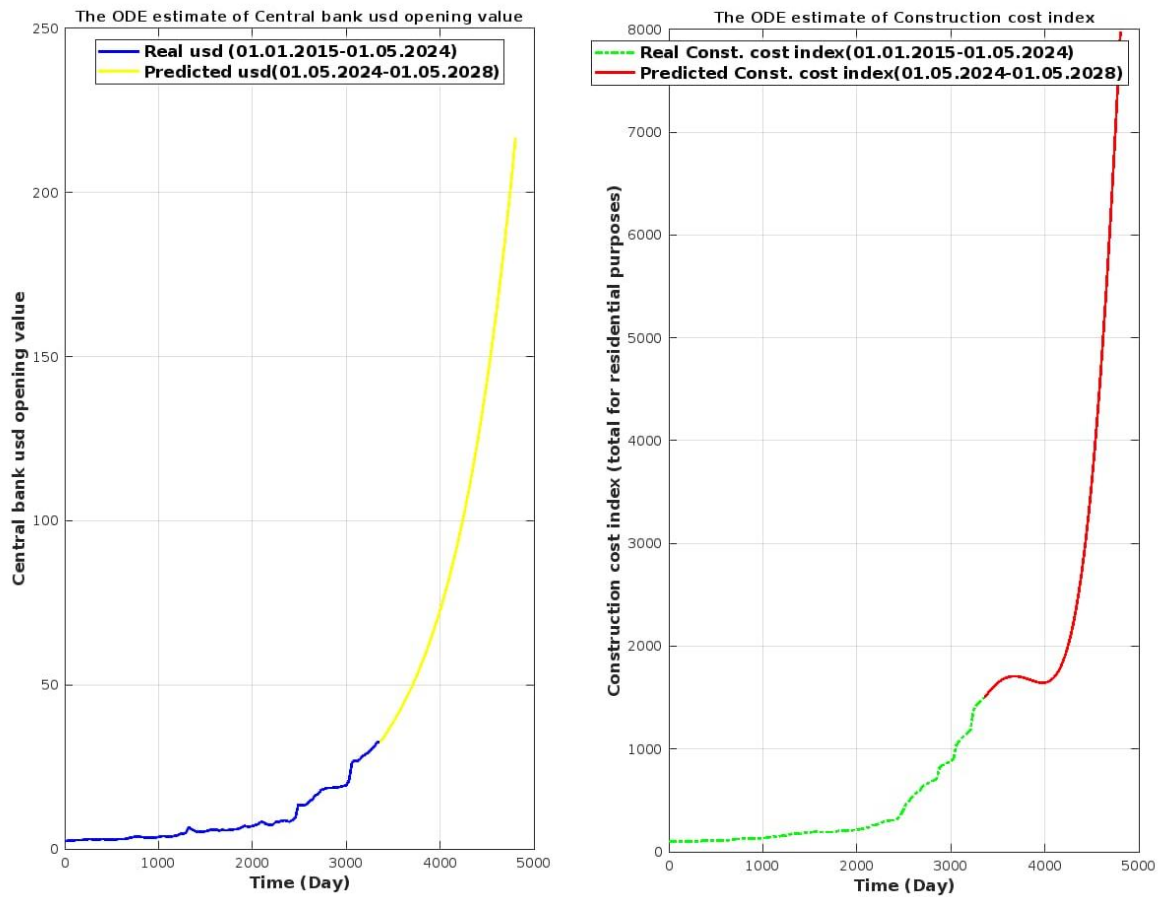


**Figure 10.** ODE estimate for the USD exchange rate and construction cost index (01.05.2024-01.05.2028)

## 5. Conclusion

In this study, we explored the predictive performance of ANN and ODE models for key economic indicators, including USD opening value, Consumer Price Index (CPI), TL housing loan interest rate, and residential construction cost index, using Turkish Statistical Institute (TUIK) data from 2015 to 2024. The aim was to evaluate and compare the accuracy of both models in forecasting economic trends and fluctuations in the Turkish economy.

The results indicate that both models have strong predictive capabilities, but their effectiveness varies depending on the complexity and volatility of the economic indicator. The ANN model demonstrated superior performance in handling variables with complex, non-linear relationships, such as the USD opening value and housing loan interest rates, as evidenced by lower error metrics and higher R-squared values. The ODE model, on the other hand, was particularly effective in capturing the long-term trends of more stable indicators, such as the construction cost index.

The comparison of the models revealed that the ANN model is better equipped to manage volatility and sudden market changes, particularly in variables like CPI and interest rates, which exhibit significant fluctuations. Meanwhile, the ODE model excels in long-term trend analysis, offering a more holistic understanding of the system's dynamic behavior over time.

These findings underscore the importance of selecting the appropriate model based on the specific economic indicator and the analysis context. ANN models are recommended for short- to medium-term forecasts where volatility is expected, while ODE models are more suitable for long-term trend predictions in stable markets. Policymakers and economists can leverage the strengths of both models to enhance the accuracy of economic forecasts, especially during periods of uncertainty or economic instability.

Ultimately, this study contributes to the growing body of literature on economic forecasting by demonstrating the complementary nature of ANN and ODE models. Future research could explore hybrid approaches that combine the strengths of both models to provide more robust predictions across a wider range of economic variables.

## Author Contributions

All the authors equally contributed to this work.

## Conflicts of Interest

All the authors declare no conflict of interest.

## Ethical Review and Approval

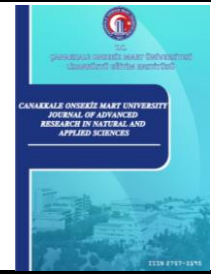
No approval from the Board of Ethics is required.

## References

- [1] N. Frumkin, Guide to economic indicators, 4th Edition, New York, 2015.
- [2] M. K. Heun, J. Santos, P. E. Brockway, R. Pruijm, T. Domingos, M. Sakai, *From theory to econometrics to energy policy: Cautionary tales for policymaking using aggregate production functions*, *Energies* 10 (2) (2017) Article Number 203 44 pages.
- [3] D. Güneş, İ. Özkan, L. Erden, *Economic sentiment and foreign portfolio flows: Evidence from Türkiye*, *Central Bank Review* 24 (1) (2024) 100147 9 pages.
- [4] P. Chinnasamy, A. Albakri, M. Khan, A. A. Raja, A. Kiran, J. C. Babu, *Smart contract-enabled secure sharing of health data for a mobile cloud-based e-health system*, *Applied Sciences* 13 (6) (2023) 3970 19 pages.
- [5] M. Khan, S. Hariharasitaraman, S. Joshi, V. Jain, M. Ramanan, A. SampathKumar, A. A. Elngar, *A deep learning approach for facial emotions recognition using principal component analysis and neural network techniques*, *The Photogrammetric Record* 37 (180) (2022) 435–452.
- [6] T. V. Ramana, G. S. Ghantasala, R. Sathiyaraj, M. Khan, *Artificial intelligence and machine learning for smart community; concepts and applications*, CRC Press, Florida, 2024.
- [7] J. Zou, Y. Han, S. S. So, *Overview of artificial neural networks*, *Artificial Neural Networks: Methods and Applications* 458 (2009) 14–22.
- [8] P. Hartman, *Ordinary differential equations*, Society for Industrial and Applied Mathematics, Philadelphia, 2002.
- [9] B. Zheng, *Ordinary Differential equation and its application*, *Highlights in Science, Engineering and Technology* 72 (2023) 645–651.
- [10] E. Alshawarbeh, A. T. Abdulrahman, E. Hussam, *Statistical modeling of high frequency datasets using the ARIMA-ANN hybrid*, *Mathematics* 11 (22) (2023) 4594 17 pages.
- [11] A. R. Mohamed, *Artificial neural network for modeling the economic performance: A new perspective*, *Journal of Quantitative Economics* 20 (3) (2022) 555–575.
- [12] G. W. R. I. Wijesinghe, R. M. K. T. Rathnayaka, *Stock market price forecasting using ARIMA vs ANN: A case study from CSE*, In 2020 2nd International Conference on Advancements in Computing (ICAC), IEEE, 2020, Vol. 1, pp. 269–274.

- [13] K. M. Ramírez, J. M. Hormaza, S. V. Soto, *Artificial intelligence and its impact on the prediction of economic indicators*, In Proceedings of the 6th International Conference on Engineering and MIS, 2020, pp. 1–8.
- [14] M. Fani, N. Norouzi, *Using social and economic indicators for modeling, sensitivity analysis and forecasting the gasoline demand in the transportation sector: an ANN Approach in case study for Tehran metropolis*, Iranian Journal of Energy 23 (2) (2020) 71–91.
- [15] L. Guerrini, A. Krawiec, M. Szydłowski, *Bifurcations in an economic growth model with a distributed time delay transformed to ODE*, Non-Linear Dynamics 101 (2) (2020) 1263–1279.
- [16] L. Wu, X. Qiu, Y. X. Yuan, H. Wu, *Parameter estimation and variable selection for big systems of linear ordinary differential equations: A matrix-based approach*, Journal of the American Statistical Association 114 (526) (2019) 657–667.
- [17] I. Georgiev, V. Centeno, V. Mihova, V. Pavlov, *A modified ordinary differential equation approach in price forecasting*, in AIP conference proceedings, AIP Publishing 2459 (1) (2022) 030008 7 pages.
- [18] B. Daşbaşı, İ. Öztürk, *The dynamics between pathogen and host with Holling type 2 response of immune system*, Journal Of Graduate School of Natural and Applied Sciences 32 (1) (2016) 1–10.
- [19] S. Paul, A. Mahata, S. Mukherjee, M. Das, P. C. Mali, B. Roy, P. Bharati, *Study of fractional order SIR model with MH type treatment rate and its stability analysis*, Bulletin of Biomathematics 2 (1) (2024) 85–113.
- [20] R. B. Guenther, J. W. Lee, *Partial differential equations of mathematical physics and integral equations*, Courier Corporation, New Jersey, 1996.
- [21] K. Sobczyk, *Stochastic differential equations: with applications to physics and engineering*, Springer Science and Business Media, Dordrecht, 2013.
- [22] B. Daşbaşı, *Fractional order bacterial infection model with effects of anti-virulence drug and antibiotic*, Chaos, Solitons and Fractals 170 (2023) 113331 17 pages.
- [23] H. Niu, Y. Zhou, X. Yan, J. Wu, Y. Shen, Z. Yi, J. Hu, *On the applications of neural ordinary differential equations in medical image analysis*, Artificial Intelligence Review 57 (9) (2024) 236 32 pages.
- [24] B. Daşbaşı, T. Daşbaşı, *Mathematical analysis of Lengyel-Epstein chemical reaction model by fractional-order differential equations system with multi-orders*, International Journal of Science and Engineering Investigations 6 (11) (2017) 78–83.
- [25] N. Manhas, *Mathematical model for IP33 dependent calcium oscillations and mitochondrial associate membranes in non-excitable cells*, Mathematical Modelling and Numerical Simulation with Applications 4 (3) (2024) 280–295.
- [26] E. Sönmez, B. Daşbaşı, T. Daşbaşı, *Some applications on stability analysis of incommensurate and commensurate fractional-order differential equation systems: Brusselator chemical reaction model and bacterial infection model*, Academic Studies in Physics and Mathematics from Theory to Application II, Chapter 10, IKSAD Publishing House, 2022.
- [27] B. Goodwine, *Engineering differential equations: theory and applications*, Springer Science and Business Media, 2010.
- [28] K. S. Miller, *Partial differential equations in engineering problems*, Courier Dover Publications, New Jersey, 2020.
- [29] B. Ersoy, B. Daşbaşı, E. Aslan, *Mathematical modelling of fiber optic cable with an electro-optical cladding by incommensurate fractional-order differential equations*, An International Journal of Optimization and Control: Theories and Applications 14 (1) (2024) 50–61.

- [30] R. Boucekkine, G. Fabbri, P. Pintus, *On the optimal control of a linear neutral differential equation arising in economics*, *Optimal Control Applications and Methods* 33 (5) (2012) 511–530.
- [31] M. D. Johansyah, A. K. Supriatna, E. Rusyaman, J. Saputra, *Application of fractional differential equation in economic growth model: A systematic review approach*, *AIMS Mathematics* 6 (9) (2021) 10266–10280.
- [32] Z. Hosseini-Nodeh, R. Khanjani-Shiraz, P. M. Pardalos, *Portfolio optimization using robust mean absolute deviation model: Wasserstein metric approach*, *Finance Research Letters* 54 (2023) 103735 13 pages.
- [33] Z. Wang, A. C. Bovik, *Mean squared error: Love it or leave it? A new look at signal fidelity measures*, *IEEE Signal Processing Magazine* 26 (1) (2009) 98–117.
- [34] T. O. Hodson, *Root means square error (RMSE) or mean absolute error (MAE): When to use them or not*, *Geoscientific Model Development Discussions*, 15 (2022) 5481–5487.
- [35] E. Işık, B. Daşbaşı, *A compartmental fractional-order mobbing model and the determination of its parameters*, *Bulletin of Biomathematics* 1 (2) (2023) 153–176.



# Assessment of Dyeing Properties of *Hibiscus sabdariffa* on Ostrich Leather

Mehmet Mete Mutlu<sup>1</sup> , Deniz Kılıçaslan<sup>2</sup> , Nilay Ork Efendioglu<sup>3</sup> 

<sup>1,2,3</sup>Department of Leather Engineering, Faculty of Engineering, Ege University, İzmir, Türkiye

## Article Info

Received: 03 Oct 2024

Accepted: 10 Dec 2024

Published: 31 Dec 2024

Research Article

**Abstract** – Natural dyestuffs derived from various plants can be used for dyeing processes in the textile and leather industries. *Hibiscus sabdariffa*, one of these natural dyestuffs, is known to be used in textiles and produces a red color with good dyeing properties. This study aimed to investigate the dyeing effect of *Hibiscus sabdariffa* flower on leather materials and to determine its dyeing properties. To achieve this, a dye was extracted from *Hibiscus sabdariffa*, and all wet processes of ostrich skins—an exotic type of leather—were carried out, incorporating the dye extract by adding a mordant during the dyeing process. Both chrome and vegetable tannins were utilized to examine the effects of the tanning process. Extraction yield, pH measurement, color measurement, to-and-fro rubbing fastness tests, and dyestuff exhaustion measurements were conducted. The results indicated that, particularly when the post-mordant process was applied, the extracted dyestuff yielded superior dyeing properties and color results compared to the non-mordant process. The extract from *Hibiscus sabdariffa* was determined to effectively dye the skins, producing beautiful and satisfying colors, especially when using iron sulfate mordant in vegetable-tanned leathers.

**Keywords** – *Hibiscus sabdariffa*, dyeing, leather, natural dyestuff, ostrich skin

## 1. Introduction

With its distinctive and special skin appearance, Ostrich leather is considered one of the most exotic leathers available. The unique skin texture is characterized by the rounded formations of hair follicles on the skin surface. This type of leather is widely utilized in the leather industry's production of bags, wallets, shoes, and clothing [1]. Due to its softness, flexibility, and durability, ostrich leather is regarded as a luxury material. Further, interest in this product, which can be easily shaped, has grown and rapidly expanded its market [2].

Ostrich skins possess distinct differences from other leathers in shape and grain pattern, which are crucial for marketing purposes and necessitate specialized removal, conservation, and processing technologies [3]. Dyeing is paramount among the various processes that impact leather's visual appeal. A wide range of dyestuffs is employed in the fashion industry to accommodate the ever-evolving fashion preferences and technological advancements, reflecting aesthetic values, luxury, and customer demands. Consequently, the color of finished leather plays a significant role in decision-making and customer satisfaction. In contemporary times, growing environmental awareness and legal regulations have heightened the demand for natural products within the leather industry, mirroring trends in other sectors. Research into natural dyes as alternatives to the chemical products that were prevalent in the past has gained importance. Natural dyestuffs do not contribute to environmental pollution and allow for good fastness properties and various color combinations when combined with mordants [4].

<sup>1</sup>mete.mutlu@ege.edu.tr; <sup>2</sup>denizkilicaslan29@gmail.com; <sup>3</sup>nilay.ork@ege.edu.tr (Corresponding Author)

As implied by their name, natural dyes are derived from renewable resources such as plants, animals, and minerals [5]. It is well established that vegetable dyes can impart color to materials derived from nature through specific processes. Some plants have their entire parts utilized for dyeing, while others employ particular organs (e.g., flowers, leaves, seeds, bark, and roots). For instance, flowers are harvested at their peak maturity, seeds post-ripening, and leaves during the plant's blooming phase. The shells are utilized after the plant has shed its leaves. Vegetable dyes are integral to natural dyeing due to their abundance and diverse color palette. The dyeing process using natural vegetable dyes involves several steps, including harvesting, drying, and preparation, leading to a ready-to-use dyestuff [6].

One notable natural dye is the extract from *Hibiscus sabdariffa*, which has numerous industrial and medicinal applications [7]. It is widely used in various fields, particularly textile dyeing [8-10]. *Hibiscus sabdariffa* (common name: Roselle) belongs to the Malvaceae family and contains anthocyanin, a water-soluble pigment whose color is influenced by pH levels. After undergoing specific natural processes, the pigment from *Hibiscus sabdariffa* (Figure 1) can be utilized as an alternative to synthetic dyes, potentially mitigating environmental damage. The color is generated by grinding and soaking the plant in water, where pH variations impact color intensity [11-12].

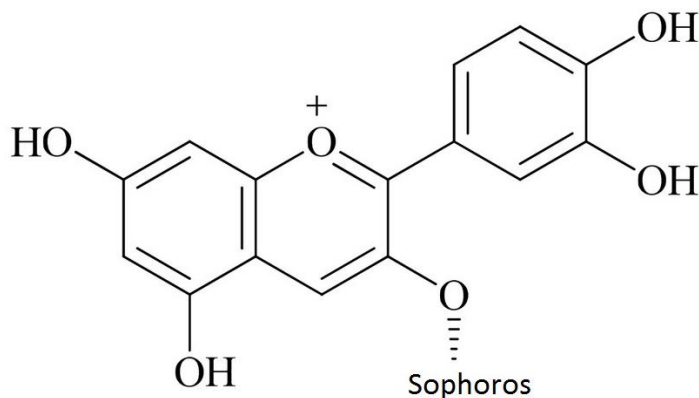


**Figure 1.** Main colorant in *Hibiscus sabdariffa* flower—cyanidin-3-sophoroside [13]

Several methods exist to extract dye from *Hibiscus sabdariffa*, particularly from the calyces, which can be ground or fully soaked in water. Due to their water-soluble pigment nature, they can yield dye without additives, although color intensity may vary [12]. The dyeing material and the plant parts used for dye extraction can be combined directly or through the addition of a mordant, a process referred to as "mordanting." Mordants can be either chemical or natural [14]. Typically, mordants consist of metallic salts (e.g., aluminum, chromium, iron, copper, and tin) and tanning agents [15]. These substances are essential for fixing dyes to fibers, improving dye uptake, and enhancing color and light fastness [15]. Various dyeing techniques also allow for a broader spectrum of colors [16]. The primary purpose of using a mordant is to ensure dye fixation and to achieve diverse color tones [17-18].

To the best of the authors' knowledge, no studies in literature address the dyeing of ostrich skins with natural dyes derived from the *Hibiscus sabdariffa* flower. This study aims to investigate the dyeing of ostrich skins using the natural dye extracted from dried *Hibiscus sabdariffa* flowers, examining its dyeing properties and considerations during the process. For this purpose, two ostrich skins were tanned using chrome and vegetable tannins and then divided into four parts, resulting in eight samples. The leathers tanned with chrome and vegetable tannins were split into four pieces, with one piece of each remaining undyed as a control. This approach allowed for the evaluation of the dyeing processes using the extract from dried *Hibiscus sabdariffa* flowers, with and without the assistance of mordants (copper sulfate and iron sulfate). The dyeing efficacy of *Hibiscus sabdariffa* and the fastness properties of the ostrich leathers were investigated, yielding satisfactory dyeing results.

## 2. Experimental

### 2.1. Materials

This study obtained two raw ostrich skins from Hasmera Ostrich Farm, Çanakkale (Figure 2). Dried flowers of *Hibiscus sabdariffa* (Figure 3), a natural dyestuff sourced from Koç Kardeşler Baharat (Bornova, İzmir), were used for dyeing the ostrich skins. Copper sulfate [ $\text{CuSO}_4 \cdot 5\text{H}_2\text{O}$ ] and iron sulfate [ $\text{FeSO}_4 \cdot 7\text{H}_2\text{O}$ ], obtained in technical grade from BOR-KİM Chemicals, were utilized as mordants. The configuration of the ostrich skins prior to processing is detailed in Table 1. A calibrated Metrohm 848 Titrino plus potentiometer was used to adjust the pH levels. The CIE  $L^*$ ,  $a^*$ ,  $b^*$  color measurements were performed using a Konica Minolta CM-3600d spectrophotometer, ensuring precise and reproducible results. The fastness tests were conducted using a Bally Finish Tester 9029.



**Figure 2.** Raw ostrich skins



**Figure 3.** Dried *Hibiscus sabdariffa* flower

**Table 1.** The layout of the ostrich skins

Code	Definition
C0	Chromium-tanned, non-dyed
C1	Chromium-tanned + dyed with mordant (Copper Sulfate)
C2	Chromium-tanned + dyed with mordant (Iron Sulfate)
C3	Chromium-tanned + dyed with non-mordant
V0	Vegetable-tanned, non-dyed
V1	Vegetable-tanned + dyed with mordant (Copper Sulfate)
V2	Vegetable-tanned + dyed with mordant (Iron Sulfate)
V3	Vegetable-tanned + dyed with non-mordant

## 2.2. Materials

### 2.2.1. Extraction Process, Extraction Yield, and pH Measurement

Dried *Hibiscus sabdariffa* flowers (40 g) were weighed and steeped in 1 liter of water at room temperature for 24 hours to prepare an infusion (Figure 4). The infused solution was then subjected to extraction at 75°C for 3 hours, and the resulting extracts were combined to form a stock solution (Figure 5). This stock solution was concentrated to a constant weight by transferring it into a glass dish and drying it in a hot-air oven at  $100 \pm 2^\circ\text{C}$  until complete evaporation of water. The total solids were determined by weighing the residue left in the dish. The extraction yield was calculated using the following formula:

$$\text{Evaporation Residue (mg/L)} = (A-B) \times 1000/V$$

A= Total weight of the evaporation dish and solid material (mg)

B= Weight of the empty evaporation dish (mg)

V= Volume of sample (mL)



**Figure 4.** The state of *Hibiscus sabdariffa* flowers after infusing in hot water



**Figure 5.** Extracted *Hibiscus sabdariffa* flower

The pH measurement of the dye extract was conducted using a Metrohm 848 Titrino plus potentiometer. After adjusting the extract temperature to  $20 \pm 1^\circ\text{C}$ , pH values were measured with a precision of 0.05 pH units. The pH readings were taken at 30 and 60 seconds after immersing the electrodes in the extract.

### 2.2.2. Leather Processing

The weights of the two salted dry ostrich skins were recorded before processing. The main recipe applied to the raw ostrich skins is presented in Table 2. After the pickle process, two different tanning methods—chrome and vegetable tanning—were employed, following the recipes outlined in Tables 3 and 4.

In studies on mordant use, both pre-mordanting and post-mordanting have been highlighted in the literature [19-22]. While pre-mordanting is commonly applied in textile dyeing processes, some research also indicates its importance in leather processing [23-24]. However, other studies suggest that post-mordanting is more suitable for leather materials [25]. In pre-mordanting, the textile material is treated with the mordant prior to dyeing, facilitating better dye binding. Nevertheless, in some cases, pre-mordanting may cause the mordant to adhere primarily to the surface of the leather, thereby hindering sufficient dye absorption.

Post-mordanting tends to yield better results because the mordant helps bind loosely bound dyes that have penetrated the leather during the dyeing process. After applying the mordant, these dyes more effectively bond to the leather, resulting in a more uniform and stable coloration. The mordant acts as a chemical agent that strengthens the bond between the dye and the leather fibers. Initially, the dyes may form a temporary bond with the surface, but the mordant application allows these bonds to become more permanent. This interaction enables the dye to penetrate deeper into the material, ensuring more consistent and intense coloration.

Based on these considerations, this study employed post-mordanting. In this method, the mordanting process is performed after the material has been dyed. Post-mordanting typically involves treating the dyed material with a solution of the selected mordant. The duration of treatment and the concentration of the mordant solution can significantly influence the final color and properties of the material. The final phase of the process focuses on developing the desired color shade. The effectiveness of post-mordanting depends on various factors, such as the type of material, the dye used, and the desired color outcome [26-29].

The dyestuff was first applied to the dye bath (drum), which penetrated and partially bonded with the leather. Afterward, the mordant was introduced to ensure the residual dyestuff fully bonded to the leather, facilitating a more stable and uniform coloration. This sequence ensures that the mordant works effectively in conjunction with the dye, enhancing the overall depth and permanence of the color.

**Table 2.** Main recipe up to pickle process for ostrich leathers

Process	Amount (%)	Chemicals	Temp. (°C)	Time (min)	Remarks
Pre-Soaking	400	Water	20	45	
	0.5	Wetting agent			
	0.5	Bactericide			
	0.5	Alkaline stabilizer		60	Kept in pre-soaking in mixer for two nights.
Soaking	300	Water	25		
	0.5	Wetting agent			
	0.2	Bactericide			
	0.2	NaHCO <sub>3</sub>		60	
					Drain
	300	Water			
	0.5	Wetting agent			
	0.3	NaHCO <sub>3</sub>		60	pH:4
	0.5	HCOONa	26		Speed 5.4 rpm
	0.6	Ecological degreaser agent			
				After standing overnight, pH control: 7.5	
				Drain	
Liming	500	Water	25		
	0.5	Amine-free liming agent			
	1	Na <sub>2</sub> S			
	6	Ca(OH) <sub>2</sub>		1 night	pH:11
Washing	300	Water	25		
					The fleshing of the skins was made by hand.
2 <sup>nd</sup> Liming	400	Water	25		
	5	Ca(OH) <sub>2</sub>			
	1	Na <sub>2</sub> S			
	0.1	Degreasing Agent		60	
Deliming	300	Water	25		
	2	Deliming agent			
	1	Deliming auxiliaries agent			
	1.5	Polyphosphate			
	0.1	Bating Agent			
	0.3	HCOOH			pH:8.2
Bating	1	Alkaline bating enzyme	32	25	
	5	Degreasing agent		60	Degreasing was done without water. It was kept for one night. The drum was automatic; 5min move/60min stop.
Washing	200	Water	25	45	

**Table 3.** Chrome tanning process for ostrich leather

Process	Amount (%)	Chemicals	Temp. (°C)	Time (min)	Remarks
Pickle	100	Water (7°Be)	25	15	
	2	HCOOH		30	
	2	H <sub>2</sub> SO <sub>4</sub>		20	pH:3-3.2
Tanning	0.5	Fungicide		20	
	5	%33 Basic chromium sulfate	30	60	
	0.4	MgO		90	
	3	%33 Basic chromium sulfate		120	One night in tanning
	1	HCOONa		30	
	1	NaHCO <sub>3</sub>		90	pH:4.1
	1				
Washing	200	Water	40	30	2x15 min
		Horse for two days			
Degreasing	100	Water		30	
	2	Ecological degreaser agent		45	
Retanning	200	Water			
	3	Naphthalene syntan		60	After 1 hour, the temperature was increased.
	3	Phenolic syntan	43	45	
	4	Chromium syntan		90	
Fatliquoring	200	Water	55		
	1	Fatliquor containing lecithin			
	5	Polymeric - synthetic and natural fatliquor			
	2	Synthetic-softy fatliquor (Lightfastness)		90	
	2	Synthetic fatliquor (electrolyte stable)		45	
	1.5	HCOOH		45 (15*3)	pH:3.5-4
Washing	100	Water	30	15	
		After one night on hung to dry, the skins were taken off the hanger before completely drying.			
Rewetting	100	Water	50		
	0.5	Wetting agent		60	
Washing	100	Water	40	45	
Dyeing	60	Water	45		
	2	Dye auxiliary material			
	5	Dye		60	
	1	Mordant (Copper Sulfate / Iron Sulfate)		45	
	3	Fatliquor agent		40	
	2	HCOOH		30 (10*3)	
	2				
Washing	100	Water	30	45	3*15 min
		Horse, hung to dry, dry milling.			

**Table 4.** Vegetable tanning process for ostrich leather

Process	Amount (%)	Chemicals	Temp. (°C)	Time (min)	Remarks
Pickle	100	Water (4°Be)	25	30	
	1.5	HCOOH		30	
	1	H <sub>2</sub> SO <sub>4</sub>		20	pH 4.1
Tanning	0.2	Fungicide		20	
	5	Mimosa (Acacia)	30	60	
	1	Tara		45	
	1	Synthetic fatliquor (electrolyte stable)	32	30	
	1	Dispersant		15	The temperature was raised to 37°C. 11.6 rpm.
	0.2	HCOOH		30	pH:4-4.2
	100	Water	40	15	2x15 min
		Horse for two days			
Degreasing	100	Water		30	
	2	Ecological degreaser agent		45	
Retanning	200	Water			
	4	Tara		60	After 1 hour, the temperature was increased.
	5	Synthetic-vegetable tannin	45	25	
	3	Naphthalene syntan		90	
Fatliquoring	200	Water	55		
	1	Fatliquor containing lecithin			
	5	Polymeric - synthetic and natural fatliquor			
	2	Synthetic-softy fatliquor (Lightfastness)		90	
	2	Synthetic fatliquor (electrolyte stable)		45	
	1	HCOOH		30 (15*2)	pH:3.5-3.8
Washing	100	Water	30	15	
		After one night of hanging to dry, the skins were taken off the hanger before completely drying.			
Rewetting	100	Water	50		
	0.5	Wetting agent		60	
Washing	100	Water	40	45	
Dyeing	50	Water	45		
	2	Dye auxiliary material		20	
	5	Dye		60	
	1	Mordant (Copper Sulfate / Iron Sulfate)		45	
	2.5	Fatliquor agent		40	
	2	Naphthalene syntan		30	
	2	HCOOH		45 (15*3)	
	100	Water	30	30	3*10 min
		Horse, hung to dry, dry milling.			

### 2.2.3. Determination of Color Measurement

A Konica Minolta CM-3600d Spectrophotometer was used to numerically determine the color differences of leathers tanned with different tanning agents and dyed using various mordants. The color measurements were performed according to the CIE L\*, a\*, b\* color system. In this system, the L\* value represents the lightness of the color on a scale from 0 to 100 (with 100 indicating white and 0 indicating black). The a\* value represents the color's position on the red-green axis, where negative values indicate green and positive values indicate red. Similarly, the b\* value represents the blue-yellow axis, where negative values indicate blue and positive values indicate yellow. Color measurements were taken from five distinct points on the leather surface using the device's standard reading area, and the average of these measurements was calculated. The color difference ( $\Delta E$ ) was determined using the following formula:

$$\Delta E = \sqrt{(L_{sample} - L_{target})^2 + (a_{sample} - a_{target})^2 + (b_{sample} - b_{target})^2} \quad (2.1)$$

The color strength values (K/S) were calculated (at  $\lambda_{max} = 400$  nm) according to the Kubelka–Munk formula (2.2), which is written as. K is the scattering coefficient, S is the absorption coefficient, and R is the reflectance. R is the decimal fraction of the reflectance of dyed leather, R = 1.0 at 100% reflectance.

$$K/S = (1 - R)^2 / 2R \quad (2.2)$$

### 2.2.4. Determination of Color Fastness to Cycles of-to-and-fro Rubbing

To assess the color fastness of the leathers, a rubbing test was performed in accordance with ISO 11640, using both dry and wet felts. Samples were cut from the leather using a 15 x 8 cm, with the assistance of a pressing machine. The samples were then subjected to 50 to-and-fro rubbing cycles on a Bally Finish Tester 9029 for the dry rubbing test. For the wet rubbing test, felts soaked in pure water were wrung to remove excess water, and the leathers were rubbed 25 times back and forth. The color transfer and intensity of coloring were evaluated after the tests.

### 2.2.5. Calculation of Dyestuff Exhaustion

To determine the dyestuff exhaustion from the *Hibiscus sabdariffa* extract used for dyeing, bath samples were collected and analyzed with a UV-VIS spectrophotometer at the end of the dyeing process. Initially, the dyestuff was scanned within the 350-750 nm wavelength range to determine the wavelength with maximum absorbance.

Next, solutions of known concentrations were prepared by diluting the 40 g/2410 mL stock solution to 2, 4, 6.25, 10, and 20 times its concentration. Calibration curves were drawn based on the absorbance values at the determined wavelength. After the dyeing process, samples from the dye baths were analyzed using the UV-VIS spectrophotometer to calculate the dyestuff exhaustion.

## 3. Results and Discussion

### 3.1. Extraction Yield and pH Measurement Findings

A total of 2410 mL of *Hibiscus sabdariffa* extract was obtained through the extraction process, and the extraction yield was calculated as 10.6% based on solid matter determination. The pH of the extract was measured at 2.8, indicating an acidic nature suitable for dyeing applications.

### 3.2. Color Measurement Findings

Images of the finished and dyed ostrich leathers processed according to the designed recipes are shown in Figure 6. The images show that the *Hibiscus sabdariffa* extract produced greenish-blue tones on chrome-tanned leathers and reddish-brown tones on vegetable-tanned leathers. This variation is primarily attributed to the intrinsic color characteristics of the tanning agents. Additionally, ostrich leathers dyed with iron sulfate mordant exhibited darker shades.



**Figure 6.** Dyed ostrich leathers (Top row: Chrome-tanned; bottom row: vegetable-tanned, in order from left to right according to the codes)

The color measurement results for the leathers are provided in Table 5, and the color difference ( $\Delta E$ ) values are presented in Table 6. According to the CIE Lab color system, it was observed that leathers dyed using iron sulfate mordant had lower  $L^*$  values, indicating darker colors. This finding is consistent with previous studies in leather and textile dyeing research [30-32]. Moreover, the  $a^*$  values for chrome-tanned leathers were negative, indicating a shift towards green, while for vegetable-tanned leathers, the  $a^*$  values were positive, indicating a shift towards red. This observation further supports the color trends mentioned earlier.

The K/S values, representing color strength, highlight the impact of mordant treatments on dye uptake. Non-dyed samples (C0 and V0) exhibit the lowest K/S values (2.241 and 1.717), reflecting minimal color strength. Mordant-treated samples show significantly higher values, with iron sulfate (C2 and V2) producing the highest K/S (4.126 and 3.983), indicating its superior ability to enhance dye absorption by forming stronger dye-fiber complexes. Copper sulfate (C1 and V1) also improves color strength (2.641 and 3.373), though less effectively than iron sulfate. Non-mordant dyed samples (C3 and V3) show moderate K/S values (2.616 and 2.209), suggesting limited dye uptake without mordants. These results demonstrate the pivotal role of mordants, particularly iron sulfate, in intensifying color strength.

When evaluating the color difference values ( $\Delta E$ ), a significant difference of 13.8 was observed between C0 and C2, calculated using the  $\Delta E$  formula. In contrast, a minimal color difference of 2.2 was found between C1 and C3. A substantial color difference of 18.6 was noted between V0 and V2 for vegetable-tanned leathers.

These findings indicate a considerable color difference between leathers dyed with iron sulfate mordant and those not dyed, particularly for vegetable-tanned leathers. It can also be concluded that copper sulfate as a mordant does not significantly affect the dyeing process, particularly for chrome-tanned leathers. Similar results were reported by Bouagga et al. (2020) [33], who also found that iron sulfate was a more effective mordant than copper sulfate in their studies on wool.

**Table 5.** The color measurement results

Data Name	L*(D65)	a*(D65)	b*(D65)	K/S	Pseudo Color
C0 (non-dyed)	60.866	-1.036	11.536	2.241	
C1 (Copper Sulfate)	54.090	-3.416	5.418	2.641	
C2 (Iron Sulfate)	48.250	-3.072	6.254	4.126	
C3 (non-mordant)	54.094	-5.162	4.090	2.616	
V0 (non-dyed)	66.320	9.988	17.106	1.717	
V1 (Copper Sulfate)	53.654	10.770	15.864	3.373	
V2 (Iron Sulfate)	50.036	7.478	8.528	3.983	
V3 (non-mordant)	60.372	13.336	13.472	2.209	

**Table 6.** The color difference ( $\Delta E$ ) measurement

Type	Data Name	$\Delta E$
Cr	C0-C1	9.4
	C0-C2	13.8
	C0-C3	10.9
	C1-C3	2.2
	C2-C3	6.6
Veg	V0-V1	12.8
	V0-V2	18.6
	V0-V3	7.7
	V1-V3	7.6
	V2-V3	12.9

### 3.3. Color Fastness to Cycles of To-And-Fro Rubbing Findings

In the to-and-fro rubbing fastness test results of leathers tanned with both chromium and vegetable tannins, it was observed that the dry felt did not leave any significant marks on the leather surface, and no color transfer occurred from the leathers to the felts (Figure 7).

When Table 7 is examined, it can be seen that the rubbing fastness of chrome-tanned leathers (5-4/5) is higher than that of vegetable-tanned leathers (4/5-4). This observation is consistent with findings from a review by Mandal and Venkatramani (2023) [34]. However, the wet rubbing fastness test results indicate a slight color transfer from the leather surfaces to the felts. Specifically, the wet rubbing fastness values for chrome-tanned leathers decreased to 3 or 4, while for vegetable-tanned leathers, both undyed and dyed samples showed values as low as 2. This decrease in wet rubbing fastness may be attributed to the hydrophilic properties imparted to the leathers by vegetable tannins. Previous studies have also reported that leathers dyed with other natural dyes exhibit lower wet rubbing fastness than dry rubbing fastness [31, 34-36].



**Figure 7.** Images of leathers after rubbing fastness test (Top row: chrome-tanned; Bottom row: vegetable-tanned, in order from left to right according to the codes)

**Table 7.** Rubbing fastness test results

	Wet		Dry	
	Leather	Felt	Leather	Felt
C0 (non-dyed)	5	4	5	5
C1 (Copper Sulfate)	4	4	4/5	5
C2 (Iron Sulfate)	3	4/5	4/5	5
C3 (non-mordant)	3	4/5	4/5	5
V0 (non-dyed)	2	4/5	4	5
V1 (Copper Sulfate)	2	4	4/5	4/5
V2 (Iron Sulfate)	2	4	4/5	4/5
V3 (non-mordant)	2	4	4	4/5

### 3.4. Dyestuff Exhaustion Findings

For *Hibiscus sabdariffa* extraction, the maximum absorption wavelength was measured at 519.0 nm. The calibration curve and equation for the stock solution of *Hibiscus sabdariffa* extract are shown in Figure 8, and the absorbance values corresponding to different concentrations are presented in Table 8.

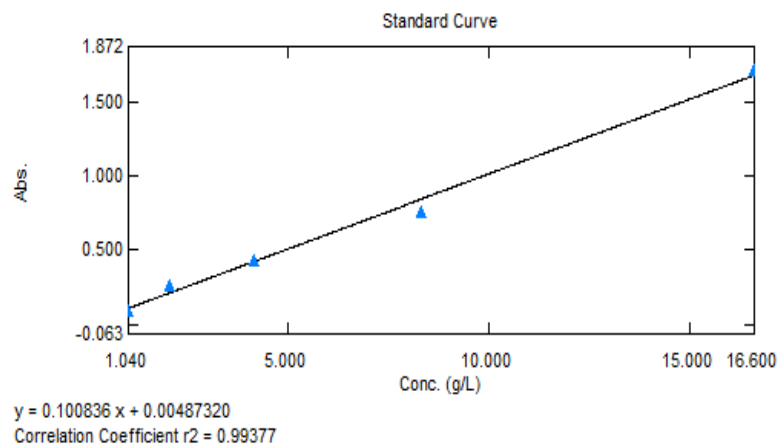


**Figure 8.** Calibration curve and curve equation of *Hibiscus sabdariffa* extract stock solution

**Table 8.** Absorbance values of the *Hibiscus sabdariffa* extract stock solution

Concentration (g/L)	Absorbance
16.600	1.711
8.300	0.763
4.150	0.430
2.080	0.266
1.040	0.098

5% dye solution (50 g of dye in 1000 mL of water) was used during the dyeing process. Based on the calibration curve results, it was determined that approximately 23 g of the 50 g of dye was absorbed by the chrome-tanned ostrich leather, leaving about 27 g of dye remaining in the bath. In contrast, for the ostrich leather tanned with vegetable tannins, around 43 g of dye was absorbed, with approximately 7 g remaining in the bath. The dyestuff exhaustion analysis was based on the stock solution and dye baths used for leather samples dyed without mordants. Samples dyed with mordants were excluded from this analysis due to the impact of mordants on the bath's color, which could affect the accuracy of the dye exhaustion measurements.

#### 4. Conclusion

This study evaluated the dyeing properties of ostrich leathers using *Hibiscus sabdariffa* extract, a natural dye. Based on the analyses and tests conducted, several key findings were identified:

The *Hibiscus sabdariffa* extract produced distinct color variations on chrome-tanned and vegetable-tanned leathers.

The dye exhaustion analysis revealed that the chrome-tanned ostrich leather exhibited lower dye uptake than the vegetable-tanned leather (*Mimosa*), demonstrating a higher affinity for the dye. This suggests that the type of tanning process significantly influences the effectiveness of dye absorption, highlighting the potential of vegetable tanning in enhancing the coloration of ostrich leather.

Although the dye produced visible color variations on chrome-tanned ostrich leathers, it did not yield the expected red tones. Color measurement tests revealed that leathers mordanted with iron sulfate exhibited superior color intensity than undyed leathers. In contrast, those mordanted with copper sulfate displayed colors nearly identical to those of leathers without mordants. The findings suggest that post-mordanting yielded the best color results, improving the dye's effectiveness on ostrich leathers.

In conclusion, *Hibiscus sabdariffa* extract can successfully dye ostrich leathers, producing appealing shades, especially when iron sulfate is used as a mordant. These results pave the way for further investigations into using natural dyes in the leather industry, emphasizing the need for eco-friendly practices. Future studies could focus on the long-term durability of colors produced by *Hibiscus sabdariffa* extract and the exploration of additional natural dye sources.

#### Author Contributions

The first author identified the topic, directed the project, and supervised this study's findings. The first and third authors developed the theoretical and practical framework. The second author performed the experiments and obtained/ interpreted the findings. The second and third authors wrote the manuscript with support from the first author. The first authors reviewed and edited the paper. All authors read and approved the final version of the paper. This paper is derived from the second author's bachelor thesis supervised by the first author.

#### Conflicts of Interest

All the authors declare no conflict of interest.

## Ethical Review and Approval

No approval from the Board of Ethics is required.

## Acknowledgment

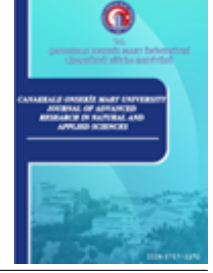
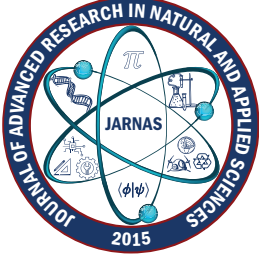
The authors would like to thank Hasmera Ostrich Farm (Çanakkale) for providing the ostrich skins and Koç Kardeşler Baharat (Bornova, İzmir) for supplying the *Hibiscus sabdariffa* flowers. They are also grateful to Dr. Deniz Kalender and Mete Sağlam for their invaluable contributions and to the Leather Engineering Department at Ege University for facilitating this study.

## References

- [1] A. Afsar, G. Gulumser, H. Ozgunay, F. Akyuz, *A study on processing of ostrich leathers and determination of their properties*, Journal of Agriculture Faculty of Ege University 39 (3) (2002) 137–144.
- [2] J. O. Horbanczuk, *The value and utilization for ostrich products*, World Ostrich Congress, Warsaw, 2002, pp. 25–34.
- [3] B.O. Bitlisli, B. Basaran, O. Sari, A. Aslan, G. Zengin, *Some physical and chemical properties of ostrich skins and leathers*, Indian Journal of Chemical Technology 11 (2004) 654–658.
- [4] E. Onem, M. M. Mutlu, S. Gunay, H. Azeri, *Natural dyestuff extraction from onion (Allium Cepa) skin and utilization for leather dyeing*, Journal of Textiles and Engineer 19 (88) (2012) 1–8.
- [5] M. Islam, K. M. F. Hasan, H. Deb, M. F. Ashik, W. Xu, *Improving the fastness properties of cotton fabric through the implementation of different mordanting agents dyed with natural dye extracted from Marigold*, American Journal of Polymer Science and Engineering 4 (1) (2016) 1–17.
- [6] F. Galip, *Obtaining of natural dyestuff and applicability in supercritical extraction of blackberry fruits (Rubus Sp.) with carbon dioxide*, Master's Thesis Gazi University (2007) Ankara.
- [7] O. Genevieve, N. Onyekachi, O. S. Nonso, O. Pascal, *Acid-base indicator properties of dye from local plant: The Rosella Calyces (Hibiscus sabdariffa)*, Journal of Textile Science and Engineering 10 (4) (2020) 1–4.
- [8] Y. Berkli, A. Zencirkıran, F. Yilmaz, *The history of natural dyeing and investigation of the antibacterial activity of Hibiscus sabdariffa L. on woolen fabrics*, Pigment and Resin Technology (accepted/in press).
- [9] J. Arora, P. Agarwal, G. Gupta, *Rainbow of natural dyes on textiles using plants extracts: Sustainable and eco-friendly processes*, Green and Sustainable Chemistry 7 (1) (2017) 35–47.
- [10] Z. Omerogullari Basyigit, C. Eyupoglu, S. Eyupoglu, N. Merdan, *Investigation and feed-forward neural network-based estimation of dyeing properties of air plasma treated wool fabric dyed with natural dye obtained from Hibiscus sabdariffa*, Coloration Technology 139 (4) (2023) 441–453.
- [11] A. C. G. V. Gheller, J. Kerkhoff, G. M. Vieira Júnior, K. E. de Campos, M. M. Sugui, *Antimutagenic effect of Hibiscus sabdariffa L. aqueous extract on rats treated with monosodium glutamate*, The Scientific World Journal 2017 (2017) 9392532 8 pages.
- [12] B. Sankaralingam, L. Balan, S. Chandrasekaran, A. M. Selvam, *Anthocyanin: A natural dye extracted from Hibiscus sabdariffa (L.) for textile and dye industries*, Applied Biochemistry and Biotechnology 195 (2023) 2648–2663.
- [13] P. S. Vankar, D. Shukla, *Natural dyeing with anthocyanins from Hibiscus rosa sinensis flowers*, Journal of Applied Polymer Science, 122 (2011) 3361–3368.

- [14] H. H. Mert, Y. Doğan, S. Başlar, *Some plants used in obtaining natural dyes*, Ecology (5) (1992) 14–17.
- [15] A. Zubairu, Y. M. Mshelia, *Effects of selected mordants on the application of natural dye from onion skin (*Allium cepa*)*, Science and Technology 5 (2) (2015) 26–32.
- [16] F. N. Ölmez, *Colours and fastness degrees obtained from dyeing wool carpet yarns with various mixing methods*, Süleyman Demirel University Journal of Natural and Applied Sciences 8 (3) (2004) 86–94.
- [17] M. Demir, S. Çelik, Ö. F. Noyan, *Production techniques of some important dye plants grown in Türkiye and the fastness degrees of the colors obtained*, III. National Black Sea Forestry Congress, Artvin, 2010, pp. 1187–1196.
- [18] H. Güngörmez, *Natural Dyes and Salt*, Iğdır University Journal of the Institute of Science and Technology 5 (1) (2015) 57–63.
- [19] A. S. Nateri, E. Dehnavi, *The effect of mordanting method on the absorption behavior of natural dyes*, Pigment and Resin Technology 51 (5) (2022) 489–498.
- [20] P. Ganesan, T. Karthik, *Analysis of colour strength, colour fastness and antimicrobial properties of silk fabric dyed with natural dye from red prickly pear fruit*, The Journal of the Textile Institute 108 (7) (2017) 1173–1179.
- [21] P. Sasivatchutikool, M. Nakpathom, *Application of natural dye extracted from Cassia Fistula ripe pods for dyeing of silk fabric*, Fibers and Polymers 20 (9) (2019) 1841–1849.
- [22] Y. Kobayashi, K. Kosaka, T. Nakanishi, *Deodorizing and antibacterial abilities of knitted cotton fabrics mordant dyed with reactive dyes and copper (II) sulfate*, Textile Research Journal 80 (3) (2010) 271–278.
- [23] S. Pervaiz, T. A. Mughal, F. Z. Khan, S. Hayat, A. Aslam, S. F. Shah, *Environmental friendly leather dyeing using Tagetes erecta L. (Marigold) waste flowers*, International Journal of Biosciences 10 (1) (2017) 382–390.
- [24] W. Pancapalaga, Jamroji, T. Sulistyowati, R. Harinni, R. P. Utari, M. K. Fuddin, R. A. R. Fathoni, E. S. Hartati, A. Hidayati, *Eco-printing leather quality in different mordant methods*, 9th International Conference on Advanced Materials and Systems (ICAMS), Bucharest, 2022, pp. 511–516.
- [25] E. Onem, G. Gulumser, B. Ocak, *Evaluation of natural dyeing of leather with Rubia tinctorum extract*, Ekoloji 20 (80) (2011) 81–87.
- [26] J. Sheikh, P. S. Jagtap, M. D. Teli, *Ultrasound assisted extraction of natural dyes and natural mordants vis a vis dyeing*, Fibers and Polymers 17 (2016) 738–743.
- [27] M. Yusuf, M. Shabbir, F. Mohammad, *Natural colorants: Historical, processing and sustainable prospects*, Natural Products and Bioprospecting 7 (2017) 123–145.
- [28] S. Adeel, N. Amin, F. Rehman, T. Ahmed, K. Singha, F. Batool, A. Hassan, *Sustainable isolation of natural dyes from plant wastes for textiles*, in Recycling from Waste in Fashion and Textiles, Scrivener Publishing LLC, 2020, Ch. 17, pp.363–390.
- [29] M. R. Repon, B. Dev, M. A. Rahman, S. Jurkonienė, A. Haji, Md. A. Alim, E. Kumpikaitė, *Textile dyeing using natural mordants and dyes: A review*, Environmental Chemistry Letters 22 (2024) 1473–1520.
- [30] N. Tayyab, A. A. Javeed, R. Y. Sayed, A. Mudassar, R. Faisal, F. Ahmad, W. Wang, A. Muhammad, *Dyeing and colour fastness of natural dye from Citrus aurantium on Lyocell fabric*, Industria Textila 71 (4) (2020) 350–356.
- [31] S. Pervaiz, T. A. Mughal, M. Najeebullah, F. Z. Khan, *Extraction of natural dye from Rosa damascena Miller - a cost-effective approach for leather industry*, International Journal of Biosciences 8 (6) (2016) 83–92.

- [32] L. J. Rather, Q. F. Dar, Q. Zhou, L. Haofan, Q. Li, *Binary mix metal mordant dyeing of merino wool fibers using Cinnamomum camphora waste/fallen leaves extract: a brief statistical analysis of color parameters*, The Journal of the Textile Institute 112 (5) (2021) 742–751.
- [33] T. Bouagga, T. Harizi, F. Sakli, *Effect of mordant bleaching on the optical and mechanical properties of black Tunisian wool and optimization of the bleaching process*, Journal of Natural Fibers 19 (8) (2022) 3015–3027.
- [34] S. Mandal, J. Venkatramani, *A review of plant-based natural dyes in leather application with a special focus on color fastness characteristics*, Environmental Science and Pollution Research 30 (2023) 48769–48777.
- [35] J. Raghava Rao, A. Prakash, E. Thangaraj, K. J. Sreeram, S. Saravanabhavan, B. U. Nair, *Natural dyeing of leathers using natural materials*, Journal of the American Leather Chemists Association 103 (2008) 68–75.
- [36] A. E. Musa, B. Madhan, W. Madhulatha, J. Raghava Rao, G.A. Gasmelseed, S. Sadulla, *Coloring of leather using henna - Natural alternative material for dyeing*, Journal of the American Leather Chemists Association 104 (2009) 183–190.



# Accuracy of the Photometric Redshifts of Brightest Cluster Galaxies Identified in the CFHTLS-W1

Sinan Alis<sup>1</sup> 

<sup>1</sup>Department of Astronomy and Space Sciences, Faculty of Science, İstanbul University, İstanbul, Türkiye

## Article Info

Received: 07 Oct 2024

Accepted: 23 Dec 2024

Published: 31 Dec 2024

Research Article

**Abstract**— We determine the accuracy of photometric redshifts for the brightest cluster galaxies (BCGs) identified in the W1 field of the Canada-France-Hawaii Telescope Legacy Survey (CFHTLS). BCGs were identified from the galaxy cluster sample produced by the Wavelet Z Photometric (WaZP) cluster finding algorithm between  $0.1 < z < 1$ . Provided photometric redshifts with the CFHTLS official galaxy catalogs were compared with spectroscopic redshifts from large surveys. 101713 spectroscopic redshifts have been collected from the databases of major spectroscopic surveys. Cross-matching of 3283 BCGs with this large spectroscopic dataset yielded 1215 BCGs with high-quality spectroscopic redshift. These highly reliable spectroscopic redshifts enabled us to determine the photometric redshift accuracy of BCGs as  $\sigma_{NMAD}=0.020$ . The outlier fraction is obtained as 1.40%. The dispersion obtained in this study is significantly better than typical photometric redshift accuracies provided in the CFHTLS releases when all types of galaxies are included, which suggests the use of BCGs as a control object when determining galaxy cluster redshifts.

**Keywords** — Photometric redshifts, brightest cluster galaxies, redshift surveys, galaxy clusters

**Subject Classification (2020)**

## 1. Introduction

Redshift is an essential tool in extragalactic astronomy as it indicates galaxy distances. When direct distance measurements are not applicable or a large number of galaxy distances are needed, redshift can be used as an alternative measure of distance since the expansion of the Universe is imprinted in the shifts of the spectral lines of galaxy spectra.

Since the first systematic redshift surveys carried out by [1], there have been many spectroscopic redshift surveys such as Two-degree-Field Galaxy Redshift Survey (2dFGRS), Sloan Digital Sky Survey (SDSS), Very Large Telescope Visible Multi-Objects Spectrograph (VIMOS) Public Extragalactic Redshift Survey (VIPERS), Galaxy and Mass Assembly (GAMA), and Extended Baryon Oscillation Spectroscopic Survey (eBOSS). Many galaxy spectra are crucial to characterize the Universe's large-scale structure using galaxy clustering and identification of galaxy clusters. The launching of the SDSS has had an enormous impact on this regard, and thus [2] was the first to show baryonic acoustic oscillations (BAO) imprinted on the galaxy distributions due to the expansion of the Universe. The

<sup>1</sup>salis@istanbul.edu.tr (Corresponding Author)

discovery of the BAO signal from large-scale galaxy distributions triggered many other projects and surveys since the BAO signal is a vital tool to characterize the Universe's expansion history. The Dark Energy Spectroscopic Instrument (DESI) will obtain 35 million galaxy spectra in the next five to ten years [3]. Euclid is a space telescope designed to conduct imaging and spectroscopic surveys to obtain millions of galaxy spectra from space, specifically at the L2 point of the Earth-Sun system [4]. Nevertheless, obtaining spectra of galaxies is quite expensive in terms of telescope time, meaning longer exposure times and more extensive observational programs are required. A new era starts with large-diameter telescopes for extensive spectroscopic surveys, such as the Wide-field Spectroscopic Telescope (WST) and Mauna Kea Spectroscopic Explorer (MSE).

Another approach to overcome the need for spectroscopic redshifts is to utilize photometric redshifts. The concept of photometric redshift is based on the galaxy colors as different galaxy populations have different spectral energy distributions (i.e., SED) [5]. In this case, spectral resolution is not enough to resolve spectral lines but the overall shape of the galaxy SED.

Nowadays, all large-scale imaging surveys incorporate photometric redshift estimation in their pipelines or data products. The essential requirement for a photometric redshift estimation is imaging in multi-bands. As demonstrated in the Cosmic Evolution Survey (COSMOS), the more photometric bands, the better the accuracy of photometric redshifts [6].

In this work, we determine the accuracy of photometric redshifts of the BCGs. BCGs are giant, luminous, and hence massive early-type galaxies in the central parts of galaxy clusters. The enormous potential well at the cluster center makes BCG very special as they grow in mass and size by merging with other member galaxies of the cluster, a process known as cannibalism [7]. Using galaxy clusters detected from SDSS, [8] showed that BCGs constitute a distinct galaxy population compared to similar mass non-BCG galaxies. BCGs have steeper ( $\sim 0.2$  dex) size-luminosity relation than regular early-type galaxy populations [9]. Simulations and observational studies show that most of the stellar mass of BCGs form before  $z \sim 1 - 2$ . Thus, BCGs' recent size growth is primarily due to dry mergers taking place at the cluster centers [10–12].

We compare the photometric redshifts of our BCG sample with their spectroscopic counterparts. Determining the accuracy of photometric redshifts is crucial, as most studies rely on them. Even though accuracy is not required for large-scale studies, most galaxy evolution or galaxy population studies benefit from photometric redshifts. In this work, we aim to demonstrate the accuracy of BCGs and compare them with the ones for normal galaxies from the same survey and similar surveys.

The structure of the paper is as follows: The selection of the BCG sample, details of our photometric redshift catalog, and descriptions of spectroscopic redshift sources are given in Section 2. Section 3 compares spectroscopic redshift catalogs and cross-match photometric and spectroscopic redshifts of BCGs. The accuracy of photometric redshifts is given in Section 3.3. The conclusion of our study is given in Section 4. Throughout this paper, we use  $H_0 = 70 \text{ km s}^{-1} \text{ Mpc}^{-1}$ ,  $\Omega_m = 0.3$  and  $\Omega_\Lambda = 0.7$ .

## 2. Materials and Methods

In this work, we analyze the accuracy of BCG photometric redshifts using spectroscopic redshifts obtained from public surveys and databases. The present study's BCG sample is drawn from the CFHTLS. Among the four wide survey fields, we used W1, which is the largest and the one with the most extensive spectroscopic redshifts. The coordinates of the CFHTLS-W1 field are given in Table 1.

**Table 1.** Coordinates of the CFHTLS-W1 field

RA center	Dec center	RA(min) (deg)	Dec(min) (deg)	RA(max) (deg)	Dec(max) (deg)
02:18:00	-07:00:00	30.17771	-11.22814	38.82230	-3.70517

Center coordinates are given in sexagesimal format, whereas coordinates of the field corners are in degrees. All coordinates in the J2000 epoch.

The data used in this study were taken from the CFHTLS T0007 (final) data release [13]. CFHTLS is an imaging survey that covers about  $155 \text{ deg}^2$  across four-wide fields (W1, W2, W3 and W4) in  $u^*$ ,  $g'$ ,  $r'$ ,  $i'/y'$ ,  $z'$  passbands. Observations were conducted using MegaCam, a mosaic camera of  $36 \times 2048 \times 4612$  pixels CCDs, with a pixel scale of  $0.186''$ . The effective field of view of the MegaCam is  $0.96 \times 0.94 \text{ deg}^2$ . The images in five passbands have been homogeneously processed by Terapix (the former data center at the Institut d’Astrophysique Paris) to construct the final object catalogs.

In the following sections, we describe our BCG sample, the CFHTLS’s photometric redshifts, and various sources of the spectroscopic redshifts.

### 2.1. Sample of Brightest Cluster Galaxies

The BCG sample used in this study was drawn within the framework of a TUBITAK (The Turkish Scientific and Technological Research Council) 1001 project and has been introduced in [14] and [15]. Here, we briefly describe the procedure for selecting BCGs and provide the basic properties of the sample.

Galaxy clusters in the field of CFHTLS-W1 have been identified by the cluster finder algorithm WaZP. The algorithm relies mainly on galaxy positions (RA-Dec) and photometric redshifts ( $z_{\text{phot}}$ ). Firstly, an overdensity of galaxies for a given position in the survey area is determined. The following steps analyze this position in detail by considering the different redshift slices in the line of sight. Thus, the peak of the overdensity in the redshift space is obtained. A list of cluster (overdensity) candidates is provided as an output of the pipeline. Details of the WaZP algorithm can be seen at [16,17]. In this study, we limit ourselves to cluster candidates with a detection signal-to-noise ratio  $\text{SNR} > 3$ . This selection yields 3283 clusters in the CFHTLS-W1.

We define the BCG for each cluster based on the clustercentric distance, redshift, luminosity, and color. For a member galaxy to be defined as BCG,

- i.* distance to the cluster center should be less than 500 kpc,
- ii.* the photometric redshift of the candidate should satisfy  $|z_{\text{gal}} - z_{\text{cl}}| \leq 0.03(1 + z_{\text{cl}})$
- iii.* the (r-i) color of the candidate should be consistent within  $\pm 0.3$  magnitudes with model elliptical galaxy colors

The choice of 500 kpc for the search radius around the cluster center is motivated by the fact that BCGs are located at the centers of galaxy clusters [7]. The cluster core (i.e., central part) is approximately 300-500 kpc around the cluster center. In [18], BCGs are identified at 300 kpc within the peak of the galaxy density distribution, while in [19], BCGs are identified within 400 kpc of the X-ray peak. Thus, we adopt the 500 kpc radius for BCG identification as also used by [20].

The brightest galaxies that satisfy the above conditions are defined as the BCG of their respective clusters. Figure 1 gives an example of a galaxy cluster used in this study and its corresponding BCG.

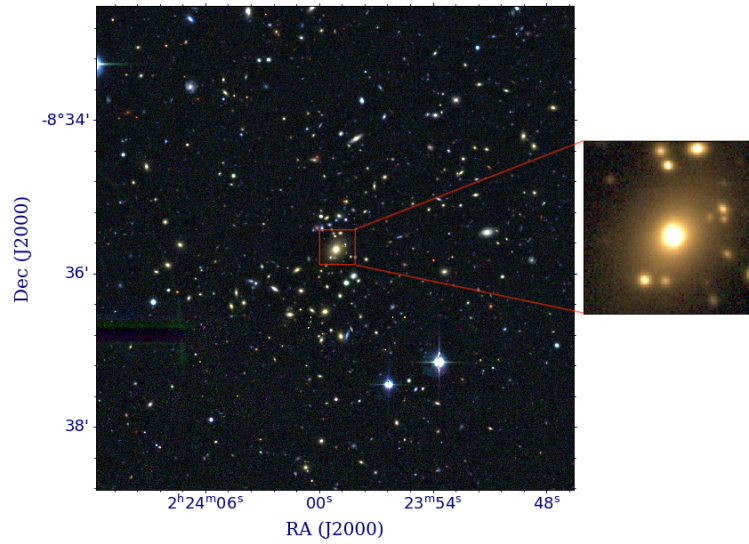


**Figure 1.** An example of a galaxy cluster and its BCG from our sample. The cluster shown in the image is at redshift  $z=0.29$ . The field-of-view of the central image is 1.6 Mpc, whereas the small subset on the right covers a diameter of 100 kpc

Figure 2 shows the final BCG sample’s redshift distribution, and Figure 3 shows the apparent and absolute magnitude distributions.

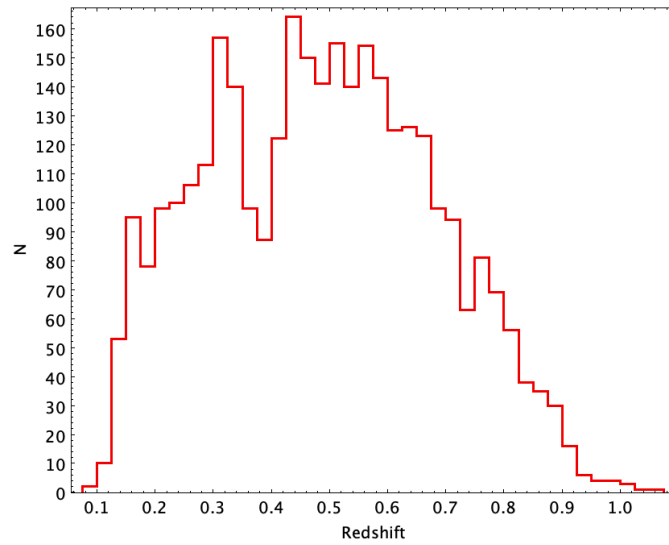


**Figure 2.** The redshift distribution of the BCG sample

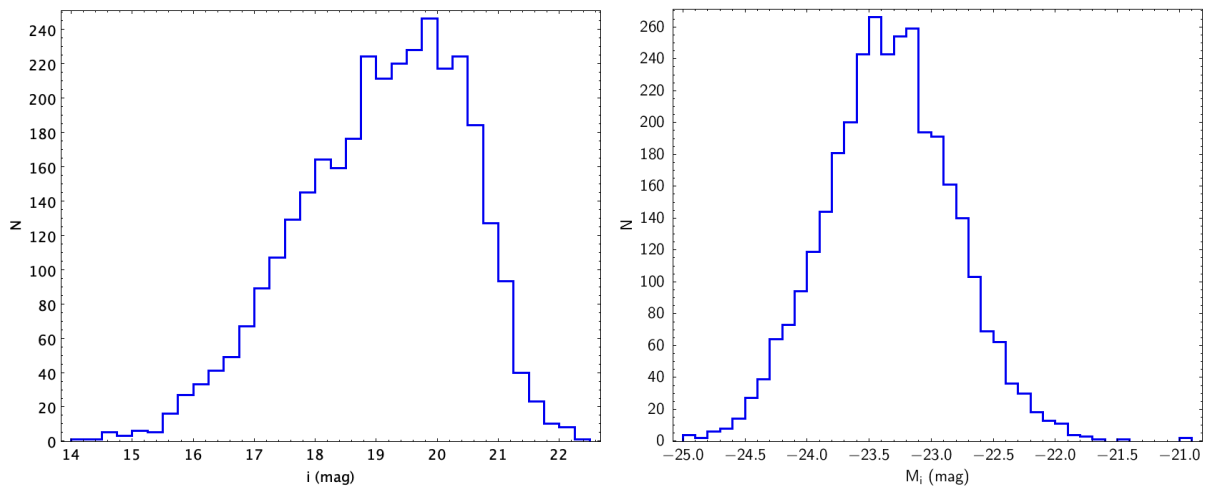


**Figure 3.** The i-band apparent (left) and absolute (right) magnitude distributions of the BCGs

## 2.2. Photometric Redshifts

In addition to object catalogs and images, Terapix also provided photometric redshifts, computed using LePhare software [21, 22]. LePhare computes the photometric redshift by fitting galaxies' spectral energy distributions (SEDs) obtained from the magnitudes in five passbands. While determining redshift, LePhare also provides a spectral type for each galaxy as a by-product. However, several spectral types are kept at a minimum to avoid color-redshift degeneracy.

Five spectral types (E, Sbc, Scd, Irr, SB) are associated with galaxies once the best match is obtained with LePhare during the SED fitting procedure. These spectral types were adopted from the observed galaxy spectra given by [23] and [24] and used similarly to [22]. Four spectra from [23] and two from [24] were extrapolated into 66 spectral templates to represent a wide range of galaxies. Photometric redshifts were computed using these final templates and explicitly optimized for CFHTLS [25] with the help of a sizeable spectroscopic sample obtained from the VIMOS Very Large Telescope Deep Survey (VVDS) [26].

## 2.3. Spectroscopic Redshifts

### 2.3.1. SDSS

SDSS is an imaging sky survey performed since 2000 with a 2.5-meter telescope in New Mexico, USA, funded by the Alfred P. Sloan Foundation. The fifth phase (SDSS-V) in the survey is being carried out. Up to now, via several observing programs, surveys have obtained spectra for more than four million galactic and extragalactic objects. The latest data release of SDSS is DR18. However, in this study, we performed a spectroscopic search within the DR17 spectroscopic catalogs [27]. The main reason is that new galaxy redshifts have not been significantly inhaled into the SDSS database since DR17, especially in the region of CFHTLS-W1. Using the CFHTLS-W1 coordinates, we used a Structured-Query Language (SQL) query and obtained spectroscopic redshifts for 14726 galaxies.

### 2.3.2. GAMA

GAMA survey was mainly an extragalactic survey carried out in five different fields of the celestial sky [28]. The survey was performed with the 3.9 Anglo-Australian Telescope and the AAOmega multi-object spectrograph, which can obtain spectra of nearly 400 objects simultaneously [29]. Among the GAMA observing fields, G02 is the only one overlapping with CFHTLS-W1. GAMA is a flux-limited spectroscopic survey with completeness at  $r < 19.8$  in the G02 field. Similarly to SDSS, we performed a SQL search within the GAMA G02 spectroscopic catalog of the Data Release 4 to obtain spectroscopic redshifts of galaxies. This yields 36970 redshifts from the GAMA Survey.

### 2.3.3. VIPERS

VIPERS was a European Southern Observatory Large Program performed using one of the 8.2 m VLT telescopes and the VIMOS multi-object spectrograph [30]. VIMOS was a very efficient instrument capable of obtaining spectra of nearly 1000 objects simultaneously. VIPERS survey was conducted in the two fields of the CFHTLS, namely in W1 and W4. Since the telescope used for the VIPERS is large, the survey is designed to obtain spectra of galaxies in the redshift range of  $0.5 < z < 1.1$ . This makes the survey the deepest among the other redshift sources used in this study. VIPERS observed galaxies with  $i < 22.5$  and published nearly 90000 spectra for galaxies in CFHTLS W1 and W4. For this study, we used the latest data release of VIPERS (PDR-2), which includes 50017 redshifts for galaxies in the CFHTLS-W1 [31].

### 3. Results and Discussion

#### 3.1. Comparing Spectroscopic Catalogs

Before cross-matching photometric and spectroscopic redshifts for BCGs, we first compared the three spectroscopic redshift sources described in Section 2.3. We then carried out a pairwise comparison of spectroscopic redshifts for all three spectroscopic surveys that overlap with CFHTLS W1. Since the telescope diameters and spectrographic instruments differ, the redshift range and the number of everyday objects vary between the surveys. For this comparison, we did not restrict ourselves to BCGs but used all typical galaxies in three surveys.

Each galaxy redshift catalog is first cross-matched with another catalog, taking into account the galaxies' coordinates (i.e., right ascension and declination). As the astrometry of the respective surveys is very good, we used the matching radius to be 0.5 arcseconds. Once the match has been obtained, the spectroscopic redshift difference ( $\Delta z$ ) is calculated as  $z_{\text{spec1}} - z_{\text{spec2}}$ , where 1 and 2 denote different spectroscopic surveys. Figures 4-6 show the three pairwise spectroscopic redshift comparisons.

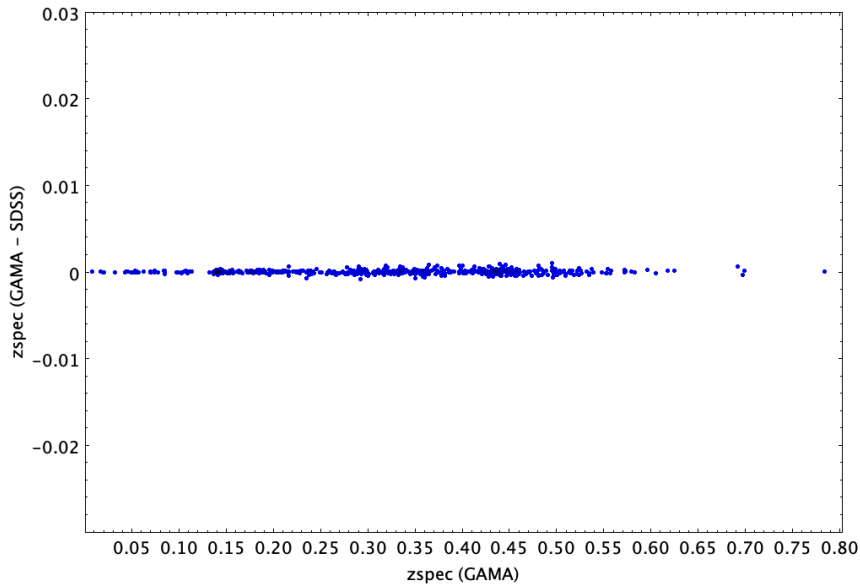


**Figure 4.** Spectroscopic redshift comparison between GAMA and SDSS

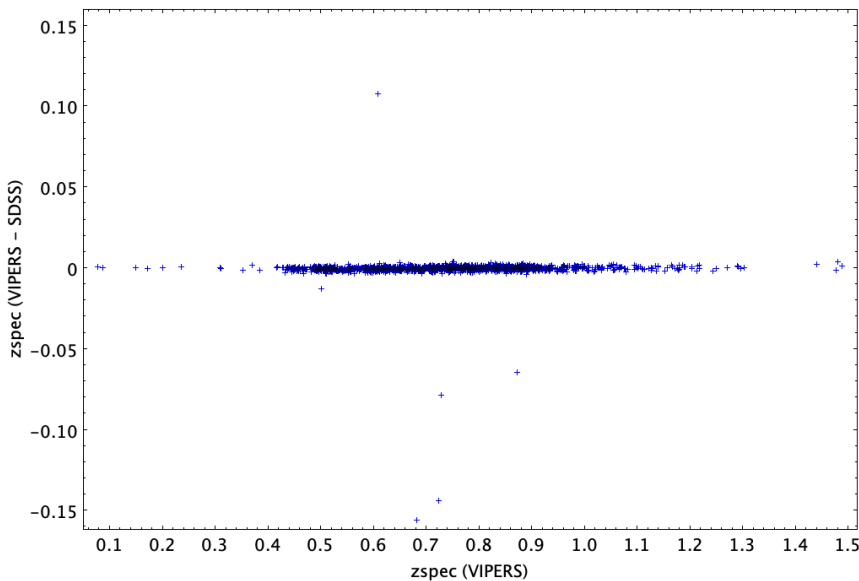


**Figure 5.** Spectroscopic redshift comparison between VIPERS and SDSS

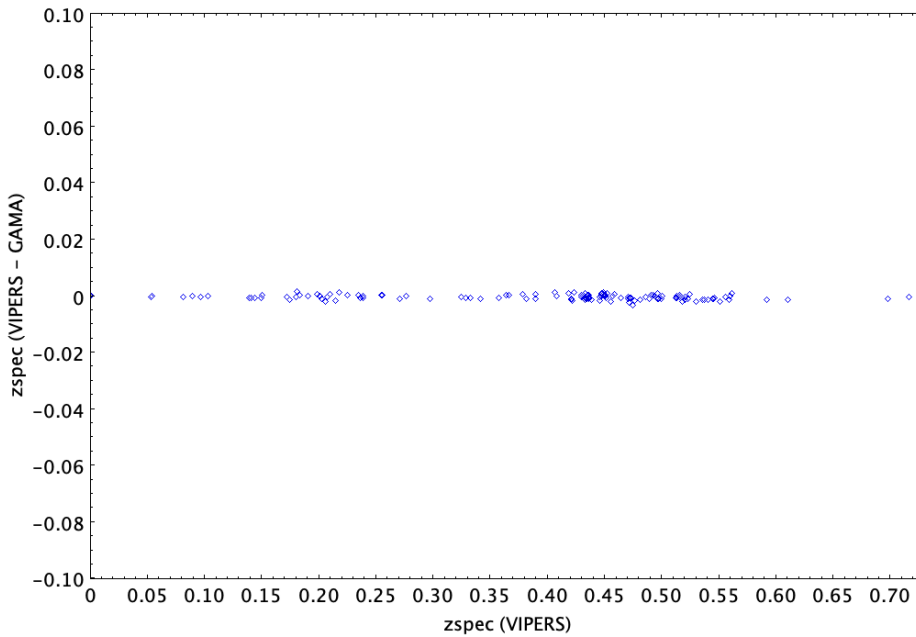


**Figure 6.** Spectroscopic redshift comparison between VIPERS and GAMA

The resulting comparison is summarized in Table 2. We computed the redshift difference’s mean and standard deviation ( $\Delta z$ ). Then, we eliminate galaxies with redshift differences more than three times the standard deviation ( $3\sigma$ ). Table 2 lists the number of galaxies before and after the sigma-clipping and the resulting mean and standard deviation after the clipping has been applied. Due to sigma-clipping, 0.9%, 0.9%, and 6.6% of galaxies are omitted from the comparison for SDSS-GAMA, VIPERS-SDSS, and VIPERS-GAMA, respectively. The relatively large fraction of galaxies omitted in the VIPERS-GAMA comparison comes from the fact that most of the galaxies in this comparison are at higher redshifts; hence, their redshifts can differ in different surveys. It is worth noting that VIPERS was performed with an 8m telescope, whereas GAMA was performed with a 4m telescope.

**Table 2.** Statistics for the pairwise survey comparison

Survey Pair	NGAL	NGAL ( $3\sigma$ )	$\langle \Delta z \rangle$	$\sigma(\Delta z)$
SDSS-GAMA	660	654	0.00002	0.00022
VIPERS-SDSS	1488	1474	-0.00064	0.00683
VIPERS-GAMA	151	141	-0.00054	0.00083

The first column represents survey pairs that are compared, the second column is the number of common galaxies with spectroscopic redshift, the third column is the number after outliers are removed, the fourth and fifth columns are mean difference in  $z_{\text{spec}}$  and its standard deviation, respectively.

In all cases, the mean redshift difference between the survey pairs is much smaller than the typical error of the spectroscopic redshifts (i.e., 0.001). Therefore, all three surveys have reliable and consistent spectroscopic redshifts. Thus, combining spectroscopic redshifts from these surveys would not bring any systematic bias to our study.

### 3.2. Cross-Matching Photometric and Spectroscopic Redshifts

Since we wanted to assess the accuracy of photometric redshifts of BCGs, we decided to keep the most reliable spectroscopic redshifts. Thus, we apply a final filtering based on the spectra quality. Both VIPERS and GAMA surveys provide a redshift quality flag where we only keep redshifts with a confidence level of a minimum 90% for the redshift determination ( $z_{\text{flg}} \geq 2$  for VIPERS and  $nQ \geq$

3 for GAMA). For SDSS, the best approach would be to keep the high signal-to-noise spectra, where we impose a spectral quality with  $\text{snMedian} > 3$ .

A cross-matching between our BCG catalog (i.e., photometric redshifts) and the available high-quality spectroscopic redshifts reveals 94 objects from VIPERS, 447 objects from GAMA, and 682 objects from SDSS. Thus, 1223 BCGs of our sample have spectroscopic redshifts from various redshift databases. However, we did a consistency check for the matched objects and found four BCGs with multiple redshifts from VIPERS, GAMA, and SDSS. We list these BCGs in Table 3 with the corresponding redshift values. Since the listed spectroscopic redshifts in Table 3 are in good agreement and VIPERS have been conducted with an 8m telescope, we keep VIPERS redshifts for these four BCGs.

**Table 3.** Spectroscopic redshifts for four common BCGs from three sources

BCG ID	$z$ (VIPERS)	$z$ (GAMA)	$z$ (SDSS)
5767	0.4967	0.4978	0.4961
6322	0.4553	0.4575	0.4544
7302	0.4708	0.4721	0.4815
7865	0.4299	0.4298	0.4111

After removing multiple occurrences for the BCGs mentioned above, 1215 spectroscopic redshifts are left for 1215 unique BCGs. We perform our analysis for the photometric redshift accuracy with these galaxies.

### 3.3. Photometric Redshift Accuracy of BCGs

The precision of the photometric redshifts is evaluated by the normalized median absolute deviation [32], which is defined as

$$\sigma_{NMAD} = 1.48 \text{ median} \left( \frac{\Delta z}{1 + z_{\text{spec}}} \right)$$

where  $\Delta z = |z_{\text{phot}} - z_{\text{spec}}|$ . This dispersion measure (i.e., NMAD) has been extensively used to determine photometric redshift accuracies in different galaxy surveys [6, 22, 25, 33–35]. Using spectroscopic redshifts that we obtained for 1215 BCGs and their photometric redshifts, the dispersion of the redshift accuracy was obtained as  $\sigma_{NMAD} = 0.020$ . In Figure 7, we compare photometric and spectroscopic redshifts for the BCG sample. The  $1-\sigma$  dispersion lines are plotted around the  $z_{\text{phot}} = z_{\text{spec}}$  line. The scatter that we measure is due to the difference between photometric and spectroscopic redshifts. The less scatter means a better photometric redshift estimation. A better characterization of the spectral energy distribution would yield better estimates. This can be done by increasing the number of bands used to determine photometric redshifts. Table 4 compares our results with relevant imaging surveys with photometric redshift accuracies.

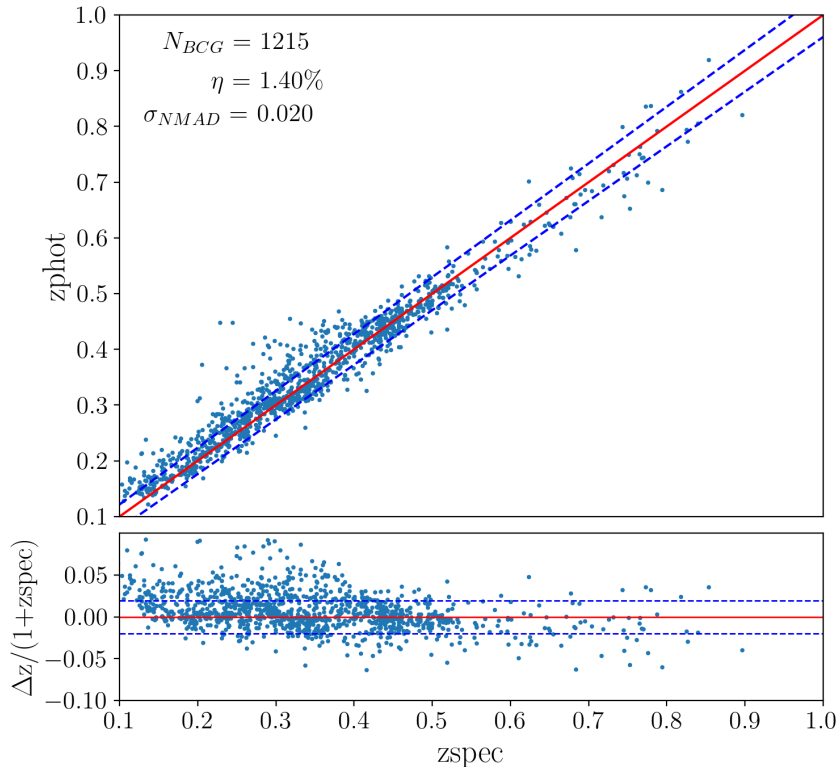


**Figure 7.** Comparison of photometric and spectroscopic redshifts for the 1215 BCGs. The red solid line corresponds to  $z_{\text{phot}}=z_{\text{spec}}$ , and the blue dashed lines show  $\sigma_{NMAD}$  dispersion. The bottom panel shows the  $\frac{\Delta z}{1+z_{\text{spec}}}$  residuals. The outlier fraction ( $\eta$ ) and the 1- $\sigma$  dispersion are given in the top-left side of the plot

In such studies of photometric redshift assessment, the outlier fraction is used to quantify the fraction of galaxies with large photometric and spectroscopic redshift offsets. The outlier fraction,  $\eta$ , (i.e., objects with catastrophic redshift errors) is computed as the fraction of galaxies with  $\frac{|\Delta z|}{1+z_{\text{spec}}} > 0.15$  [22]. There are 17 galaxies in our sample with outlier photometric redshifts according to this definition, which yields an outlier fraction of  $\eta = 1.40\%$ .

**Table 4.** Comparison of photometric redshift accuracies from the literature

Survey	NGAL	$\sigma_{\Delta z/(1+z)}$	$\eta(\%)$	Reference
CFHTLS - Deep	2867	0.029	3.80	[22]
zCOSMOS - bright	4148	0.007	0.70	[36]
CFHTLS - W1	1532	0.037	2.81	[25]
SDSS DR7 - LRG	~ 140000	0.017	0.12	[34]
Subaru HSC-SSP	~ 170000	0.066	1.99	[35]
<b>CFHTLS - BCG</b>	<b>1215</b>	<b>0.020</b>	<b>1.40</b>	<b>This Work</b>

Results given in the last row (i.e., bold-faced) are obtained in this study

Our results are significantly better than those of similar studies for CFHTLS, as shown in Table 4. The results of some other essential surveys are also given in the table. Among these, zCOSMOS has the most negligible dispersion (i.e., better accuracy) because the zCOSMOS survey consists of photometric data for 30 bands [6]. Including several photometric bands ensures a better characterization of the spectral energy distribution of galaxies; however, this is not the case for many imaging surveys, where five bands are used mostly.

This work presents the photometric redshift accuracy of the BCGs for the first time. Thus, it is not easy to compare directly with previous studies. Nevertheless, the survey of luminous red galaxies from the SDSS consists of the most similar galaxy sample to this work. The dispersion for  $\sigma_{\frac{\Delta z}{(1+z)}} = 0.020$  obtained in this study is in good agreement with  $\sigma_{\frac{\Delta z}{(1+z)}} = 0.017$  obtained with the respective SDSS sample (see Table 4). It should be noted that the much smaller outlier fraction of 0.12% obtained from SDSS is mainly the result of good spectroscopic training of the photometric redshift code used in SDSS. Many spectroscopic redshifts available in SDSS enable significantly better training for the photometric redshift code based on neural networks [37, 38].

## 4. Conclusion

We obtained the accuracy of photometric redshifts of the BCGs using available spectroscopic redshifts from major spectroscopic surveys. The photometric redshift accuracy of the BCGs is significantly better  $\sigma_{\frac{\Delta z}{(1+z)}} = 0.020$  than that of normal galaxies in the CFHTLS. The accuracy is better, and the outlier fraction is lower than many similar galaxy samples except the zCOSMOS and the luminous red galaxy sample of SDSS. Our results can represent BCGs or luminous-red galaxies up to redshifts  $z \sim 1$ . Since BCGs are brightest in galaxy clusters, they can easily be detected once a cluster is identified. The present study's results suggest relying on photometric redshifts of BCGs for galaxy cluster detection, especially when spectroscopic redshifts for the other cluster members are unavailable. BCGs were used to constrain cluster detection in a study based on SDSS data [39]. This study's results also suggest investigating the photometric redshift accuracy for different galaxy populations. Current (e.g., DESI, Euclid) and future large imaging surveys, such as the Large Synoptic Survey of Transients with the Rubin Observatory, will provide large galaxy catalogs. Thus, assessing the performance of photometric redshifts will be possible for different subsets of galaxies. Since BCGs are found at the center of galaxy clusters, their properties are unique. This study suggests using BCGs as control objects to constrain redshifts when determining redshifts of galaxy clusters. The photometric redshifts used in this study were obtained with LePhare, one of the most successful codes available in the literature. Incorporating machine learning techniques, especially neural networks, will probably be the primary approach in the future, as it is already being used in many surveys. However, obtaining galaxy SEDs is crucial for galaxy evolution studies; future imaging surveys with multi-bands, including optical and near-infrared, would be beneficial, increasing the photometric redshift accuracies and enabling a better SED characterization.

## Author Contributions

The author read and approved the final version of the paper.

## Conflicts of Interest

The author declares no conflict of interest.

## Ethical Review and Approval

No approval from the Board of Ethics is required.

## Acknowledgement

The brightest cluster galaxy sample of the present study was derived within the framework of the TÜBİTAK project 117F311, supported by the ARDEB-1001 program. The author acknowledges

the support and collaboration of the Extragalactic Astronomy Research Group members at Istanbul University.

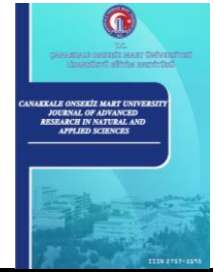
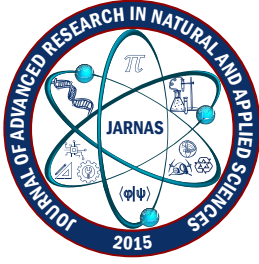
## References

- [1] M. J. Geller, J. P. Huchra, *Mapping the universe*, Science 246 (4932) (2005) 897–903.
- [2] D. J. Eisenstein, I. Zehavi, D. W. Hogg, R. Scoccimarro, M. R. Blanton, R. C. Nichol, R. Scranton, H.-J. Seo, M. Tegmark, Z. Zheng, S. F. Anderson, J. Annis, N. Bahcall, J. Brinkmann, S. Burles, F. J. Castander, A. Connolly, I. Csabai, M. Doi, M. Fukugita, ..., D. G. York, *Detection of the baryon acoustic peak in the large-scale correlation function of SDSS luminous red galaxies*, The Astrophysical Journal 633 (2) (2005) 560–574.
- [3] P. Martini, S. Bailey, R. W. Besuner, D. Brooks, P. Doel, J. Edelman, D. Eisenstein, B. Flaugher, G. Gutierrez, S. E. Harris, K. Honscheid, P. Jelinsky, R. Joyce, S. Kent, M. Levi, F. Prada, C. Poppett, D. Rabinowitz, C. Rockosi, L. C. Sas, ..., R. Wechsler, *Overview of the Dark Energy Spectroscopic Instrument*, in: C. J. Evans, L. Simard, H. Takami (Eds), *Ground-based and air-borne instrumentation for astronomy VII*, Proceedings of the SPIE, Vol. 10702, 2018, Article ID 107021F 11 pages.
- [4] Euclid Collaboration, Y. Mellier, Abdurro'uf, J. A. Acevedo Barroso, A. Achúcarro, J. Adamek, R. Adam, G. E. Addison, N. Aghanim, M. Agüena, V. Ajani, Y. Akrami, A. Al-Bahlawan, A. Alavi, I. S. Albuquerque, G. Alestas, G. Alguero, A. Allaoui, S. W. Allen, V. Allevaro, ..., M. Zumalacarregui, *Euclid. I. Overview of the Euclid mission*, Astronomy and Astrophysics (accepted/in press).
- [5] W. A. Baum, *Photoelectric magnitudes and red-shifts*, in: George Cunliffe McVittie (Ed.), IAU Symposium on Problems of Extragalactic Research, New York, 1962, pp. 390–400.
- [6] O. Ilbert, P. Capak, M. Salvato, H. Aussel, H. J. McCracken, D. B. Sanders, N. Scoville, J. Kartaltepe, S. Arnouts, E. Le Floch, B. Mobasher, Y. Taniguchi, F. Lamareille, A. Leauthaud, S. Sasaki, D. Thompson, M. Zamojski, G. Zamorani, S. Bardelli, M. Bolzonella, ..., E. Zucca, *COSMOS photometric redshifts with 30-Bands for 2-deg<sup>2</sup>*, The Astrophysical Journal 690 (2) (2009) 1236–1249.
- [7] J. Dubinski, *The origin of the brightest cluster galaxies*, The Astrophysical Journal 502 (1998) 141–149.
- [8] A. Linden, P. N. Best, G. Kauffmann, S. D. M. White, *How special are brightest group and cluster galaxies?*, Monthly Notices of the Royal Astronomical Society 379 (2007) 867–893.
- [9] M. Bernardi, J. B. Hyde, R. K. Sheth, C. J. Miller, R. C. Nichol, *The luminosities, sizes, and velocity dispersions of brightest cluster galaxies: Implications for formation history*, The Astronomical Journal 133 (2007) 1741–1755.
- [10] F. S. Liu, Shude Mao, Z. G. Deng, X. Y. Xia, Z. L. Wen, *Major dry mergers in early-type brightest cluster galaxies*, Monthly Notices of the Royal Astronomical Society 396 (2009) 2003–2010.
- [11] C. Lidman, G. Iacobuta, A. E. Bauer, L. F. Barrientos, P. Cerulo, W. J. Couch, L. Delaye, R. Demarco, E. Ellingson, A. J. Faloon, D. Gilbank, M. Huertas-Company, S. Mei, J. Meyers, A. Muzzin, A. Noble, J. Nantais, A. Rettura, P. Rosati, ..., H. K. C. Yee, *The importance of major mergers in the build up of stellar mass in brightest cluster galaxies at  $z = 1$* , Monthly Notices of the Royal Astronomical Society 433 (2013) 825–837.

- [12] S. Lavoie, J. P. Willis, J. Démoclès, D. Eckert, F. Gastaldello, G. P. Smith, C. Lidman, C. Adami, F. Pacaud, M. Pierre, N. Clerc, P. Giles, M. Lieu, L. Chiappetti, B. Altieri, F. Ardila, I. Baldry, A. Bongiorno, S. Desai, A. Elyiv, ..., R. J. Tuffs, *The XXL survey XV: Evidence for dry merger driven BCG growth in XXL-100-GC X-ray clusters*, Monthly Notices of the Royal Astronomical Society 462 (2016) 4141–4156.
- [13] P. Hudelot, J.-Ch. Cuillandre, K. Withington, Y. Goranova, H. McCracken, F. Magnard, Y. Mellier, N. Regnault, M. Betoule, H. Aussel, J. J. Kavelaars, P. Fernique, F. Bonnarel, F. Ochsenbein, O. Ilbert, *The CFHTLS survey (T0007 release)*, 2012, Vizier Online Data Catalog p.II/317, <https://cdsarc.cds.unistra.fr/viz-bin/cat/II/317>.
- [14] E. K. Ulgen, S. Alis, C. Benoist, F. K. Yelkenci, O. Cakir, S. Fisek, Y. Karatas, *Identification and properties of isolated field elliptical galaxies from CFHTLS-W1*, Publications of the Astronomical Society of Australia 39 (2022) Article ID e031 23 pages.
- [15] E. Shaaban, S. Alis, M. Bektasoglu, F. K. Yelkenci, E. K. Ulgen, O. Cakir, S. Fisek, *Structural analysis of brightest cluster galaxies in poor and rich clusters*, New Astronomy 100 (2023) Article ID 101998 13 pages.
- [16] Euclid Collaboration, R. Adam, M. Vannier, S. Maurogordato, A. Biviano, C. Adami, B. Ascaso, F. Bellagamba, C. Benoist, A. Cappi, A. Díaz-Sánchez, F. Durret, S. Farrens, A. H. Gonzalez, A. Iovino, R. Licitra, M. Maturi, S. Mei, A. Merson, E. Munari, ..., G. Zamorani, *Euclid preparation. III. Galaxy cluster detection in the wide photometric survey, performance and algorithm selection*, Astronomy and Astrophysics 627 (2019) Article ID A23 27 pages.
- [17] M. Aguena, C. Benoist, L. N. da Costa, R. L. C. Ogando, J. Gschwend, H. B. Sampaio-Santos, M. Lima, M. A. G. Maia, S. Allam, S. Avila, D. Bacon, E. Bertin, S. Bhargava, D. Brooks, A. Carnero Rosell, M. Carrasco Kind, J. Carretero, M. Costanzi, J. De Vicente, S. Desai, ..., R. D. Wilkinson, *The WaZP galaxy cluster sample of the dark energy survey year 1*, Monthly Notices of the Royal Astronomical Society 502 (3) (2021) 4435–4456.
- [18] M. Oguri, *A cluster finding algorithm based on the multi-band identification of red sequence galaxies*, Monthly Notices of the Royal Astronomical Society 444 (2014) 147–161.
- [19] M. Ricci, C. Benoist, S. Maurogordato, C. Adami, L. Chiappetti, F. Gastaldello, V. Guglielmo, B. Poggianti, M. Sereno, R. Adam, S. Arnouts, A. Cappi, E. Koulouridis, F. Pacaud, M. Pierre, M. E. Ramos-Ceja, *The XXL Survey. XXVIII. Galaxy luminosity functions of the XXL-N clusters*, Astronomy and Astrophysics 620 (2018) Article ID A13 11 pages.
- [20] C. J. Miller, R. C. Nichol, D. Reichart, R. H. Wechsler, A. E. Evrard, J. Annis, T. A. McKay, N. A. Bahcall, M. Bernardi, H. Boehringer, A. J. Connolly, T. Goto, A. Kniazev, D. Lamb, M. Postman, D. P. Schneider, R. K. Sheth, W. Voges, *The C<sub>4</sub> clustering algorithm: Clusters of galaxies in the Sloan digital sky survey*, The Astronomical Journal 130 (2005) 968–1001.
- [21] S. Arnouts, S. Cristiani, L. Moscardini, S. Matarrese, F. Lucchin, A. Fontana, E. Giallongo, *Measuring and modelling the redshift evolution of clustering: The hubble deep field north*, Monthly Notices of the Royal Astronomical Society 310 (2) (1999) 540–556.
- [22] O. Ilbert, S. Arnouts, H. J. McCracken, M. Bolzonella, E. Bertin, O. Le Fèvre, Y. Mellier, G. Zamorani, R. Pellò, A. Iovino, L. Tresse, V. Le Brun, D. Bottini, B. Garilli, D. Maccagni, J. P. Picat, R. Scaramella, M. Scodreggio, G. Vettolani, A. Zanichelli, ..., D. Vergani, *Accurate photometric redshifts for the CFHT legacy survey calibrated using the VIMOS VLT deep survey*, Astronomy and Astrophysics 457 (3) (2006) 841–856.

- [23] G. D. Coleman, C. C. Wu, D. W. Weedman, *Colors and magnitudes predicted for high redshift galaxies*, The Astrophysical Journal Supplement Series 43 (1980) 393–416.
- [24] A. L. Kinney, D. Calzetti, R. C. Bohlin, K. McQuade, T. Storchi-Bergmann, H. R. Schmitt, *Template ultraviolet to near-infrared spectra of star-forming galaxies and their application to K-corrections*, The Astrophysical Journal 467 (1996) 38–60.
- [25] J. Coupon, O. Ilbert, M. Kilbinger, H. J. McCracken, Y. Mellier, S. Arnouts, E. Bertin, P. Hudelot, M. Schultheis, O. Le Fèvre, V. Le Brun, L. Guzzo, S. Bardelli, E. Zucca, M. Bolzonella, B. Garilli, G. Zamorani, A. Zanichelli, L. Tresse, H. Aussel, *Photometric redshifts for the CFHTLS T0004 deep and wide fields*, Astronomy and Astrophysics 500 (3) (2009) 981–998.
- [26] O. Le Fèvre, G. Vettolani, B. Garilli, L. Tresse, D. Bottini, V. Le Brun, D. Maccagni, J. P. Picat, R. Scaramella, M. Scodreggio, A. Zanichelli, C. Adami, M. Arnaboldi, S. Arnouts, S. Bardelli, M. Bolzonella, A. Cappi, S. Charlot, P. Ciliegi, T. Contini,..., D. Rizzo, *The VIMOS VLT deep survey. First epoch VVDS-deep survey: 11 564 spectra with  $17.5 \leq IAB \leq 24$  and the redshift distribution over  $0 \leq z \leq 5$* , Astronomy and Astrophysics 439 (3) (2005) 845–862.
- [27] D. S. Aguado, R. Ahumada, A. Almeida, S. F. Anderson, B. H. Andrews, B. Anguiano, E. A. Ortíz, A. Aragón-Salamanca, M. Argudo-Fernández, M. Aubert, V. Avila-Reese, C. Badenes, S. B. Rembold, K. Barger, J. Barrera-Ballesteros, D. Bates, J. Bautista, R. L. Beaton, T. C. Beers, F. Belfiore,..., H. Zou, *The fifteenth data release of the Sloan digital sky surveys: First release of MaNGA-derived quantities, data visualization tools, and stellar library*, The Astrophysical Journal Supplement Series 240 (2) (2019) Article ID 23.
- [28] S. P. Driver, P. Norberg, I. K. Baldry, S. P. Bamford, A. M. Hopkins, J. Liske, J. Loveday, J. A. Peacock, D. T. Hill, L. S. Kelvin, A. S. G. Robotham, N. J. G. Cross, H. R. Parkinson, M. Prescott, C. J. Conselice, L. Dunne, S. Brough, H. Jones, R. G. Sharp, E. van Kampen,..., S. J. Warren, *GAMA: Towards a physical understanding of galaxy formation*, Astronomy and Geophysics 50 (5) (2009) 12–19.
- [29] I. K. Baldry, M. Alpaslan, A. E. Bauer, J. Bland-Hawthorn, S. Brough, M. E. Cluver, S. M. Croom, L. J. M. Davies, S. P. Driver, M. L. P. Gunawardhana, B. W. Holwerda, A. M. Hopkins, L. S. Kelvin, J. Liske, Á. R. López-Sánchez, J. Loveday, P. Norberg, J. Peacock, A. S. G. Robotham, E. N. Taylor, *Galaxy And Mass Assembly (GAMA): AUTOZ spectral redshift measurements, confidence and errors*, Monthly Notices of the Royal Astronomical Society 441 (3) (2014) 2440–2451.
- [30] L. Guzzo, M. Scodreggio, B. Garilli, B. R. Granett, A. Fritz, U. Abbas, C. Adami, S. Arnouts, J. Bel, M. Bolzonella, D. Bottini, E. Branchini, A. Cappi, J. Coupon, O. Cucciati, I. Davidzon, G. De Lucia, S. de la Torre, P. Franzetti, M. Fumana,..., M. Wolk, *The VIMOS public extragalactic redshift survey (VIPERS). An unprecedented view of galaxies and large-scale structure at  $0.5 < z < 1.2$* , Astronomy and Astrophysics 566 (2014) Article ID A108 20 pages.
- [31] M. Scodreggio, L. Guzzo, B. Garilli, B. R. Granett, M. Bolzonella, S. de la Torre, U. Abbas, C. Adami, S. Arnouts, D. Bottini, A. Cappi, J. Coupon, O. Cucciati, I. Davidzon, P. Franzetti, A. Fritz, A. Iovino, J. Krywult, V. Le Brun, O. Le Fèvre,..., W. J. Percival, *The VIMOS public extragalactic redshift survey (VIPERS). Full spectroscopic data and auxiliary information release (PDR-2)*, Astronomy and Astrophysics 609 (2018) Article ID A84 14 pages.
- [32] D. C. Hoaglin, F. Mosteller, J. W. Tukey, *Understanding robust and exploratory data analysis*, Wiley, New York, 1983.

- [33] T. Dahlen, B. Mobasher, S. M. Faber, H. C. Ferguson, G. Barro, S. L. Finkelstein, K. Finlator, A. Fontana, R. Gruetzbauch, S. Johnson, J. Pforr, M. Salvato, T. Wiklind, S. Wuyts, V. Acquaviva, M. E. Dickinson, Y. Guo, J. Huang, K.-H. Huang, J. A. Newman, ..., G. Wilson, *A critical assessment of photometric redshift methods: A CANDELS investigation*, The Astrophysical Journal 775 (2) (2013) Article ID 93 26 pages.
- [34] N. Greisel, S. Seitz, N. Drory, R. Bender, R. P. Saglia, J. Snigula, *Photometric redshifts and systematic variations in the spectral energy distributions of luminous red galaxies from SDSS DR7*, The Astrophysical Journal, 768 (2) (2013) Article ID 117 21 pages.
- [35] M. Tanaka, J. Coupon, B.-C. Hsieh, S. Mineo, A. J. Nishizawa, J. Speagle, H. Furusawa, S. Miyazaki, H. Murayama, *Photometric redshifts for hyper supprime-cam Subaru strategic program data release 1*, Publications of the Astronomical Society of Japan 70 (SP1) (2018) Article ID S9 30 pages.
- [36] S. J. Lilly, V. Le Brun, C. Maier, V. Mainieri, M. Mignoli, M. Scodreggio, G. Zamorani, M. Carollo, T. Contini, J.-P. Kneib, O. Le Fèvre, A. Renzini, S. Bardelli, M. Bolzonella, A. Bongiorno, K. Caputi, G. Coppa, O. Cucciati, S. de la Torre, L. de Ravel, ..., Y. Taniguchi, *The zCOSMOS 10k-bright spectroscopic sample*, The Astrophysical Journal Supplement 184 (2) (2009) 218–229.
- [37] E. Vanzella, S. Cristiani, A. Fontana, M. Nonino, S. Arnouts, E. Giallongo, A. Grazian, G. Fasano, P. Popesso, P. Saracco, S. Zaggia, *Photometric redshifts with the multilayer perceptron neural network: Application to the HDF-S and SDSS*, Astronomy and Astrophysics 423 (2004) 761–776.
- [38] A. Collister, O. Lahav, C. Blake, R. Cannon, S. Croom, M. Drinkwater, A. Edge, D. Eisenstein, J. Loveday, R. Nichol, K. Pimbblet, R. de Propris, I. Roseboom, N. Ross, D. P. Schneider, T. Shanks, D. Wake, *MegaZ-LRG: A photometric redshift catalogue of one million SDSS luminous red galaxies*, Monthly Notices of the Royal Astronomical Society 375 (1) (2007) 68–76.
- [39] J. Hao, T. A. McKay, B. P. Koester, E. S. Rykoff, E. Rozo, J. Annis, R. H. Wechsler, A. Evrard, S. R. Siegel, M. Becker, M. Busha, D. Gerdes, D. E. Johnston, E. Sheldon, *A GMBCG galaxy cluster catalog of 55,424 rich clusters from SDSS DR7*, The Astrophysical Journal Supplement 191 (2) (2010), 254–274.



# Real-Time Detection of Milk Adulteration with a Portable Multispectral Analysis Device: A Multispectral Sensor and Optimized Logistic Regression Approach

Mahmut Durgun<sup>1</sup> 

<sup>1</sup>Department of Electronic Commerce and Management, Turhal Faculty of Applied Sciences, Tokat Gaziosmanpaşa University, Tokat, Türkiye

## Article Info

Received: 17 Oct 2024

Accepted: 27 Nov 2024

Published: 31 Dec 2024

Research Article

**Abstract** – This study presents the development of a portable, low-cost, and edge computing-based system for real-time milk adulteration detection. Utilizing an AS7265x multispectral sensor and Arduino Nano 33 BLE Sense microcontroller, this system employs an optimized logistic regression model to identify starch adulteration in milk samples with near-perfect accuracy. Unlike complex neural network models, the logistic regression model offers simplicity, low power consumption, and efficient operation on microcontrollers. The collected spectral data is processed in real-time, and results are transmitted via Bluetooth for immediate analysis. The system demonstrates high accuracy, portability, and cost-effectiveness, making it suitable for use in various stages of the milk supply chain, including farms, processing facilities, and retail points. Future work will explore the detection of other adulterants and the integration of cloud-based analytics to enhance monitoring capabilities. This study provides an innovative approach to ensuring milk quality and consumer safety.

**Keywords** – Milk adulteration, portable detection system, multispectral sensor, logistic regression

## 1. Introduction

Milk is a vital source of nutrition and plays a crucial role in human health and dietary needs [1]. However, adulteration carried out for economic gain seriously compromises the quality and safety of milk [2]. Adulterations involving cheaper substances such as water, starch, detergent, urea, and glucose reduce the product's nutritional value and pose health risks, particularly for vulnerable consumer groups [3]. Therefore, it is imperative to subject dairy products to reliable and rapid adulteration detection.

Traditionally, the detection of adulteration in milk has been performed using laboratory analyses that require high technology, such as gas chromatography, mass spectrometry, and liquid chromatography [4]. Although these methods provide highly precise and accurate results, they lack portability. They are costly, complicating real-time quality control, especially in field conditions, on farms, and throughout various stages of the milk supply chain [5]. Consequently, recent years have witnessed significant efforts to develop new technologies for the rapid, portable, and real-time detection of adulterations in dairy products[6].

Numerous portable and rapid detection methods have been developed to identify adulterations in dairy products. For instance, the 3D paper-based microfluidic device developed by Patari et al. [7] can simultaneously detect seven different chemical adulterants in milk and provide results within seconds using

<sup>1</sup>mahmut.durgun@gop.edu.tr (Corresponding Author)

only 1-2 mL of sample. These devices are more user-friendly and economical compared to laboratory-based methods. However, such devices can sometimes have limitations in terms of sensitivity and accuracy.

Biosensors represent another significant technology employed in detecting adulterations in dairy products. Nagraik et al. [8] have reported that biosensors are effective for the rapid and real-time detection of various adulterants in milk. These sensors can identify the presence or concentration of components in milk, thus enabling the evaluation of milk's purity. Biosensors play a pivotal role, particularly in detecting common adulterants such as urea. Poonia et al. [9] have highlighted the portability of biosensors, which facilitates ease of use in the field and proves to be an invaluable tool in applications that require quick results. Spectroscopic techniques are another commonly used method for detecting adulteration in milk [10,11]. Santos et al. have employed near-infrared spectroscopy (NIR) and mid-infrared (MIR) microspectroscopy techniques to detect adulterants in milk, demonstrating that these methods provide both rapid and accurate results [12]. However, spectroscopic methods typically require expensive equipment and complex data analysis techniques. Therefore, research on developing portable spectroscopic devices aims to meet the need for real-time detection [13].

Microwave sensors also play a significant role in detecting milk adulteration. Iram et al. have developed a portable microwave sensor that can detect milk contaminants such as water, urea, and detergent through real-time energy coupling measurements. These types of sensors offer rapid results without the need for complex chemical analyses to determine the composition of dairy products [14]. Microwave sensors' portability and fast response time provide significant advantages for field use. Electrical impedance measurements are also among the methods used to detect milk adulteration. Durante et al. [15] have developed a method using electrical impedance sensors to detect changes in milk composition in real-time. This method is suitable for detecting substances like water, salt, and starch in dairy products. Electrical impedance measurements offer low cost and quick results, but further improvements in sensitivity are needed. IoT-based portable devices have also revolutionized the detection of adulteration in dairy products [16]. An Arduino-based system developed by Aware and Belorkar measures parameters such as the pH and conductivity of milk in real-time, detecting adulteration and transmitting the results to authorities via IoT [17]. These systems provide rapid and effective quality control in the field. Additionally, an IoT-based milk quality monitoring system developed by Pugazhenthil et al. [18] has assessed the purity level of milk using various sensors and enhanced traceability within the supply chain.

Furthermore, automatic freezing point analyzers represent another technology for detecting adulteration in dairy products. Zhang et al. [19] have developed a freezing point-based detector for rapidly and accurately detecting water and other adulterants in milk. This system identifies adulteration by monitoring changes in the freezing point of dairy products and can be implemented outside laboratory settings. Lastly, innovative approaches like the portable Raman spectrometer developed by Nieuwoudt et al. can simultaneously detect various chemical substances in milk and provide results swiftly. Although these portable and user-friendly devices are ideal for real-time analysis, they encounter challenges such as limited sensitivity and accuracy [20].

This study aims to develop a milk adulteration detection system that is portable, economical, real-time, and capable of edge computing, overcoming the limitations of existing methods. The developed system uses an optimized logistic regression model to operate on a microcontroller. This approach offers a solution devoid of the complexity of laboratory-based methods, consumes low power, and can be easily implemented in field conditions. Instantaneous transmission of results to mobile devices via Bluetooth facilitates rapid and effective quality control in field conditions. Consequently, it becomes feasible to maintain the purity of dairy products at every stage of the milk supply chain and ensure consumer safety. This article will comprehensively address the technical details of the developed system, hardware and software components, data collection and analysis processes, and a comparative performance analysis with other existing methods. Our goal is to set a new standard in the field by providing a portable and cost-effective solution for the detection of adulteration in dairy products.

## 2. Materials and Methods

### 2.1. System Design

In this study, hardware architecture has been designed for developing a portable and real-time milk adulteration detection system, consisting of the AS7265x multispectral sensor, Arduino Nano 33 BLE Sense microcontroller, and a Bluetooth module (Figure 1)



**Figure 1.** The mobile spectral setup

**The AS7265x Multispectral Sensor:** This multi-channel multispectral detection solution measures 18 wavelengths ranging from 410 nm to 940 nm. Each sensor communicates via the I2C interface and, thanks to the integrated temperature sensor, can accurately perform spectral analysis of milk samples. The AS7265x is specifically utilized to detect spectral changes in milk samples at various levels of adulteration. These spectral data play a critical role in detecting adulterants such as starch in milk.

**Arduino Nano 33 BLE Sense Microcontroller:** This microcontroller features a 64 MHz ARM Cortex-M4 processor that supports Bluetooth connectivity. It is used for the real-time processing and analysis of spectral data collected from the sensor. The microcontroller's sufficient processing capacity enables the direct execution of machine learning algorithms, such as optimized logistic regression models, on the microcontroller itself. This capability facilitates real-time data analysis and decision-making capabilities in the field.

**Bluetooth Module:** The Bluetooth module, integrated within the microcontroller, facilitates the real-time transmission of analyzed data to mobile devices or computers. This feature allows users to receive instant information in field conditions.

### 2.2. Data Collection

Spectral data collection from milk samples is conducted using the portable Multispectro Optimize Logistic Regression (MSOLR) device. The data collection process proceeds as follows:

**Sample Preparation:** Initially, raw cow's milk (unadulterated) and milk samples adulterated with starch in varying proportions are prepared. This study used milk samples adulterated with starch at volumetric concentrations of 0.01%, 0.02%, 0.04%, 0.06%, and 0.08%. From each prepared sample, 20 ml is taken and placed in a light-proof container. A light-proof box measuring 15 cm<sup>3</sup> is positioned over this container to prevent external light entry. The AS7265x sensor is positioned 1 cm above the sample to capture the spectral data [21].

**Spectral Data Collection:** The AS7265x sensor detects light reflected or transmitted from the milk sample at specific wavelengths (spaced 20 nm apart from 410 nm to 940 nm). The collected spectral data are transmitted to the Arduino Nano 33 BLE Sense microcontroller via the I2C communication protocol. The microcontroller processes the data in an appropriate format and ensures it is free from noise or anomalies.

The data processed by the microcontroller is displayed in real-time on the serial port screen. This lets users instantly observe the spectral data and control the data collection process. The data collection is conducted at specific intervals to ensure continuous and real-time monitoring.

### **2.3. Machine Learning**

The logistic regression model is the machine learning algorithm chosen to detect adulteration. This model is effectively used in classification problems and is known for its high accuracy rate. Logistic regression is commonly employed for binary classification and categorization problems. This study has optimized it to classify milk samples as 'adulterated' or 'unadulterated.' The model is trained using milk samples' spectral data to determine adulteration levels. The model has been optimized for effective training using a comprehensive dataset across various concentration levels. The model is designed to be lightweight and fast, suitable for operation on microcontrollers with limited hardware resources. The logistic regression model has been optimized to run on the microcontroller. It receives the collected spectral data, analyzes the data based on predetermined limiting factors (e.g., wavelength intensity), and predicts the adulteration level of the milk sample. Thanks to the microcontroller's lightweight structure, the model's real-time operation and quick response are facilitated. This enables the model to function independently in the field.

The selection of the logistic regression model was based on several key factors:

**Computational Efficiency:** Logistic regression has low computational requirements, making it suitable for implementation on microcontrollers with limited processing capabilities. This allows for real-time processing without the need for external computational resources.

**Energy Efficiency:** The simplicity of the model results in lower energy consumption, which is essential for portable, battery-powered devices. This ensures longer operational times in field conditions.

**Implementation Simplicity:** Logistic regression is straightforward to implement and requires less memory, aligning well with the constraints of embedded systems used in portable devices.

**Performance:** Despite its simplicity, logistic regression provided high accuracy in detecting starch adulteration, as demonstrated in our results.

To ensure the appropriateness of this model, we compared its performance with other machine learning algorithms, including Support Vector Machines (SVM), Convolutional Neural Networks (CNN), Decision Trees, Random Forests, and Gradient Boosting. The comparison considered factors such as accuracy, precision, processing time, energy consumption, and suitability for portable devices.

### **2.4. Edge Computing and Communication**

One of the primary advantages of this system is the integration of edge computing capabilities.

**Integration of the Model into the Microcontroller:** The logistic regression model has been integrated into the Arduino Nano 33 BLE Sense microcontroller. Consequently, the analysis of spectral data and the detection of adulteration are conducted directly on the microcontroller. This eliminates the need for data processing in the cloud or on a central computer. By running the model on the microcontroller, it processes data and delivers results instantaneously.

**Communication via Bluetooth:** The Bluetooth module on the microcontroller allows for the instant transmission of analysis results to external devices. Once adulteration detection is complete, the results are

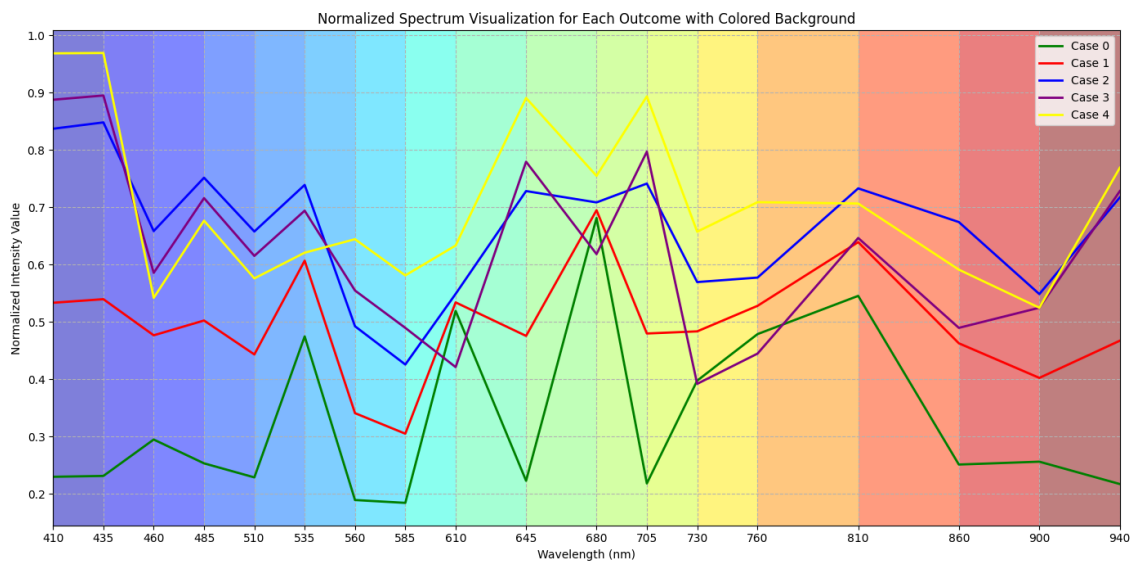
sent to a mobile device or computer via Bluetooth. This enables users in field conditions to monitor the status of milk samples in real time and make quick decisions.

This methodology facilitates the real-time and portable detection of milk adulteration. Equipped with edge computing capabilities, this system can serve as an effective quality control tool in field conditions.

### 3. Results and Discussion

This section should provide/introduce/investigate the findings and discussion/definitions and theorems. Findings/Concepts obtained from the study should be supported in this section by figures and tables/propositions and examples. For “Results and Discussion”, the similarities and differences of the obtained results with other studies should be provided, and the possible reasons for these should be discussed based on the literature. For “Results and Discussion”, the contribution and importance of the results to science should be emphasized. The obtained results should be interpreted, avoiding unnecessary repetitions.

#### 3.1. Model Performance



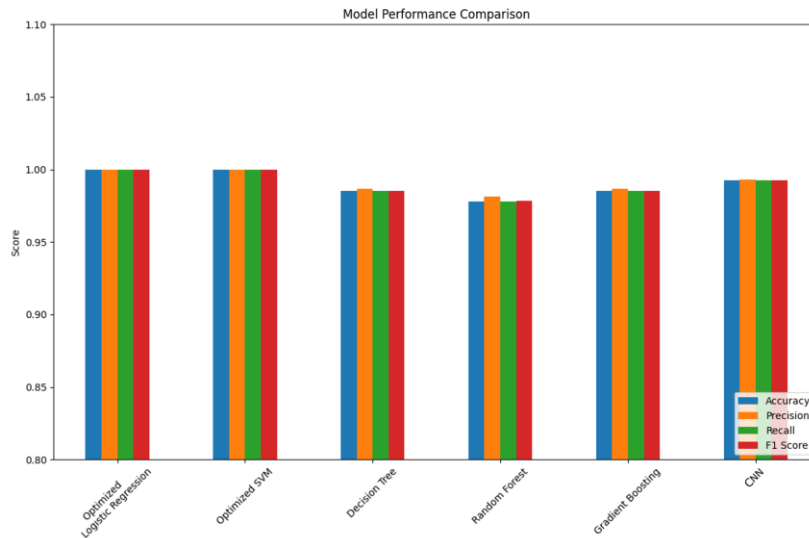
**Figure 2.** Normalized spectrum for different levels of adulteration

Figure 2 [21] displays the average values of normalized spectral data for different adulteration levels (e.g., starch concentrations) in milk samples. The color-coded background according to wavelengths facilitates the visual representation of spectral changes across each wavelength range. As illustrated in the graph, significant changes in spectral intensity occur as the levels of adulteration increase, highlighting the system's efficacy in utilizing spectral data for adulteration detection. In this study, adulteration in milk samples was detected using an optimized logistic regression model along with other machine learning models, such as Optimized Support Vector Machines (SVM), Decision Tree, Random Forest, Gradient Boosting, and Convolutional Neural Network (CNN). Metrics, such as accuracy, precision, recall, and F1 score, have been used to evaluate the performance of these models. The performance results are summarized in Table 1.

**Table 1.** Comparison of machine learning models performance

	Accuracy	Precision	Recall	F1 Score
<b>Decision Tree</b>	0.985185	0.986928	0.985185	0.985409
<b>Random Forest</b>	0.977778	0.981481	0.977778	0.978241
<b>Gradient Boosting</b>	0.985185	0.986928	0.985185	0.985409
<b>CNN</b>	0.992593	0.993056	0.992593	0.992663
<b>Optimized Logistic Regression</b>	1.0	1.0	1.0	1.0
<b>Optimized SVM</b>	1.0	1.0	1.0	1.0

This table shows that the optimized logistic regression model exhibits superior accuracy, precision, recall, and F1 score performance compared to other models. The optimized logistic regression model has achieved near-perfect accuracy rates, surpassing other models. As shown in Table 1, the optimized logistic regression model has achieved near-perfect results across all performance metrics. This model accurately classifies milk samples as 'adulterated' or 'unadulterated.' The simplicity of logistic regression and its efficient operation on a microcontroller make this model ideal for field applications. Models like SVM and CNN have also shown high performance. In particular, the SVM model has provided an accuracy rate similar to logistic regression. However, the complexity of these models and the difficulty of operating them on a microcontroller limit their usability in portable devices.



**Figure 3.** Performance comparison of machine learning models

Figure 3 compares the performance of optimized logistic regression, SVM, Decision Trees, Random Forests, Gradient Boosting, and CNN models. The optimized logistic regression model outperforms the other models across all metrics.

To further understand the model's performance, the confusion matrix of the model is shown in Figure 4. The optimized logistic regression model, in particular, demonstrates excellent alignment between the actual and predicted classes, achieving superior success in accurate classifications. It has been observed that the model's misclassification rate is nearly zero.

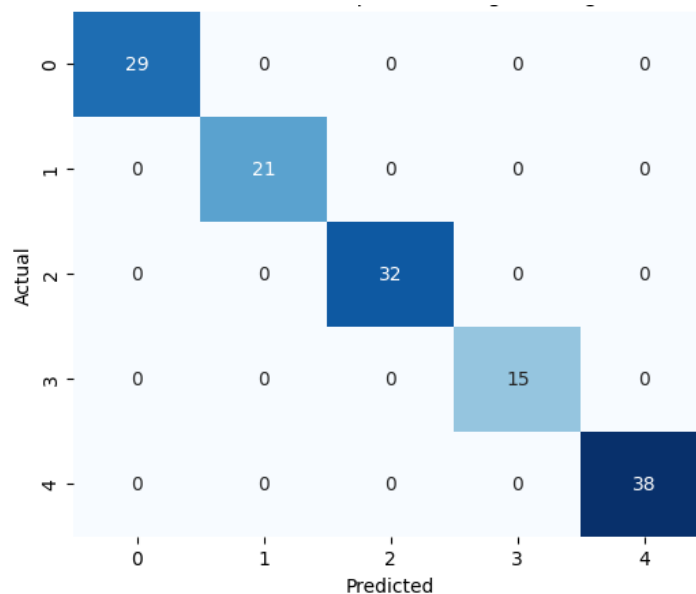


**Figure 4.** Confusion matrix of optimized logistic regression model

**Table 2.** Comparison of model selection criteria for portable applications

Model	Accuracy (%)	Precision (%)	Processing Time (ms)	Energy Consumption (mW)	Suitability for Portable Devices
<b>Optimized Logistic Regression</b>	99.8	99.7	10	50	High
<b>Optimized SVM</b>	99.5	99.4	50	150	Medium
<b>CNN</b>	99.2	99.3	200	500	Low
<b>Decision Trees</b>	98.5	98.7	20	75	High
<b>Gradient Boosting</b>	98.8	98.9	80	300	Medium

The comparison of machine learning models in Table 2 highlights optimized logistic regression's superior suitability for portable applications due to its balance of high accuracy, low energy consumption, and computational efficiency. The metrics in Table 2 are derived from a combination of experimental results and hardware evaluations. While the accuracy and precision values are aligned with machine learning performance shown in Table 1, adjustments were made to reflect real-world conditions, such as field variability and device energy efficiency. The additional characteristics, including processing time and energy consumption, are based on experimental measurements of the system's hardware during operational testing.

Table 2 extends the evaluation beyond machine learning performance by incorporating hardware and system-level characteristics crucial for portable applications. Unlike Table 1, which focuses on controlled experimental conditions, Table 2 highlights practical considerations such as processing time and energy consumption. These additional metrics provide a comprehensive understanding of the system's overall efficiency and suitability for field deployment. For instance, while the accuracy value in Table 2 (99.8%) reflects adjustments for real-time processing scenarios, it remains consistent with the machine learning performance metrics outlined in Table 1. The results from Tables 1 and 2 further validate the practicality of the MSOLR device and the optimized logistic regression model for field applications. However, future advancements could focus on incorporating additional performance metrics to evaluate system-level features comprehensively, such as robustness under varying environmental conditions and scalability for broader use cases. The insights gained from real-world testing reinforce the need to refine the device further, ensuring its adaptability to diverse field scenarios.

### 3.2. Real-World Application and Validation

To validate the effectiveness of the developed system in real-world conditions, on-site testing was conducted at local dairy farms and milk processing facilities.

**Methodology:** The MSOLR device was used to test raw milk samples collected directly from five farms. Each sample was analyzed on-site, and the results were compared with standard laboratory tests conducted later.

**Findings:** The device achieved 99.6% accuracy in detecting starch adulteration in real-world conditions, consistent with laboratory findings. The portable design enabled seamless operation in the field, and the Bluetooth connectivity facilitated immediate data transmission for quality control decisions.

**Implications:** These results demonstrate the system's reliability and practicality for on-site use, highlighting its potential for broader adoption in the dairy industry.

### 3.3. System Assessment

The developed system's portability, ease of use, and efficiency offer an ideal solution for quality control throughout the milk supply chain.

**Portability and Ease of Use:** The portable design of the MSOLR device provides a practical solution that users can easily utilize in the field. Its lightweight and compact design enables instant quality control at various stages of the milk production chain. With real-time data transmission via Bluetooth, users can instantly view analysis results.

Efficiency and Energy Consumption: Using the optimized logistic regression model on the microcontroller ensures rapid and effective analysis with low energy consumption. The device's low power consumption allows for extended operation on battery power, which is a significant advantage in situations requiring continuous monitoring and analysis in the field.

Comparison with Existing Portable Systems: A comparison of the developed system with existing portable systems (e.g., Arrieta et al. [22]) is provided in Table 2. This comparison demonstrates that the MSOLR device excels in portability, speed, accuracy, and energy efficiency. For instance, the voltammetric electronic tongue system developed by Arrleta et al., effective in detecting milk adulteration, is costly and requires more processing power.

**Table 3.** Comparison of the developed system with existing portable systems

Feature	MSOLR Device (Developed System)	Existing Portable Systems (e.g., Voltammetric Electronic Tongue)
Portability	High Lightweight and compact design	Medium: Larger and heavier components
Analysis Speed	High Real-time (<1 sec)	Medium: Moderate speed (1-5 minutes)
Accuracy	High Accuracy close to 100%	Medium-High: 90-95% accuracy
Energy Consumption	Low: Microcontroller-based, long-term use with battery	Medium: Higher power consumption, may require a portable power source
Cost	Low: Economical sensors and microcontroller	Medium-High: Requirement for more expensive equipment
Data Communication	High Real-time data transmission over Bluetooth	Medium Wired or limited wireless communication
Ease of Use	High: Easy installation and use	Medium Requires more complex installation and operation
Application Area	Wide Field and laboratory use	Medium: Mainly laboratory use
Sensitivity	High: Low levels of starch and other additives detected	Medium Detection capacity depends on the type of adulteration
Working Principle	Spectroscopy and Machine Learning	Electrochemical Sensing

Table 3 shows that the MSOLR device outperforms existing systems' portability, analysis speed, accuracy, and energy consumption criteria. In conclusion, the developed optimized logistic regression model and portable MSOLR device offer an effective, economical, and practical solution for detecting milk adulteration in field conditions. These results, supported by graphs and tables, highlight the system's potential to provide rapid and accurate quality control at various stages of the milk supply chain.



**Figure 5.** Measurement visual with MSOLR device

This visual depicts the moment of measurement as the milk sample is analyzed using the MSOLR device. The MSOLR device collects spectral data from the milk sample using the AS7265x multispectral sensor and transmits this data instantly to the Arduino Nano 33 BLE Sense microcontroller via an I2C connection. During the measurement process, as shown in Figure 5, the device performs a spectral scan over the sample in a light-proof environment, analyzing the light reflections and transmittances at specific wavelengths of the milk sample. The obtained data are transferred to a mobile device or computer via Bluetooth. The visual demonstrates the portability and field usability of the MSOLR device during measurement.

The developed MSOLR device and optimized logistic regression model offer several advantages compared to other milk adulteration detection methods in the literature. Specifically, the CNN-based approach introduced by Mhapsekar et al., which utilizes a more complex neural network architecture, has achieved an accuracy rate of 94.87% for detecting milk adulteration [22]. While CNN and other deep learning models stand out for their capacity to handle the complexity of spectral data, running them on microcontrollers presents challenges in processing power and energy consumption. Consequently, such deep learning models often require larger, more power-consuming hardware and are limited in their application in portable systems. The optimized logistic regression model in this study has been highly successful, achieving nearly 100% accuracy. The simplicity of optimized logistic regression, its low data processing requirements, and efficient operation on a microcontroller make it an ideal option for practical and portable applications.

Tables 1 and 2 serve complementary purposes in evaluating the system's capabilities. Table 1 focuses solely on the machine learning performance, providing raw metrics from controlled experiments. In contrast, Table 2 integrates these results with system-level evaluations, emphasizing the balance between computational efficiency, energy consumption, and portability. The slight variations in accuracy and precision between the tables highlight the adjustments made to accommodate practical field scenarios, ensuring a realistic assessment of the system's performance under operational conditions. This offers a more effective solution in field conditions than laboratory-dependent systems such as the spectroscopic analysis methods presented by Santos et al. [12]. Unlike portable systems like the voltammetric electronic tongue developed by Arrleta et al., the MSOLR device provides a real-time and autonomous monitoring system with Bluetooth communication capability and low energy consumption [23]. Additionally, the portable systems based on microwave sensors developed by Iram et al. have effectively detected adulterants such as water and detergent [14]. However, the sensitivity and accuracy of these systems have not been as high as the spectral analysis and optimized logistic regression-based approach of the developed MSOLR device. This demonstrates that the developed system can detect common adulterants in milk products, such as starch, even at low levels.

The developed MSOLR device and optimized logistic regression model offer several advantages for detecting milk adulteration:

The microcontroller-based system's low power consumption enables long battery life, a critical advantage for portable devices and ideal for extended use in the field [24]. Compared to other portable systems like those developed by Mahapatra et al., the energy efficiency of the developed system is higher [7]. The device can analyze spectral data in real-time and provide immediate results. This facilitates quick decision-making and continuous quality control at various stages of the milk supply chain in field conditions. This feature offers the advantages of the IoT-based milk quality monitoring system developed by Pugazhenthii et al. in a portable device [18]. The use of the AS7265x multispectral sensor and Arduino Nano 33 BLE Sense microcontroller makes the system economical and accessible. This provides a cost-effective solution suitable for various applications, unlike expensive laboratory-based spectroscopic methods or complex electronic tongues. The device offers portability with its user-friendly design and lightweight structure, making it ideal for field conditions. Wireless data transmission via Bluetooth facilitates the immediate display of analysis results. Although the developed system offers various advantages, it also has some limitations: The type of adulteration focused on in this study is limited to starch. The model needs to be extended to detect other common adulterants in dairy products (e.g., detergent, water, melamine). Future research may expand the system's capabilities to detect these substances through spectral analysis.

Currently, the system relies entirely on edge computing capabilities. In the future, integrating data with cloud platforms could provide more comprehensive data analytics and monitoring capabilities. The optimized logistic regression model will also be tested for its applicability to detect other common milk adulterants, including water, detergent, and melamine. This will involve training the model on expanded datasets and validating its performance with different adulteration levels. Future efforts should also focus on refining the system's real-world performance under varying environmental conditions, ensuring robustness and scalability for broader use cases. Additionally, integrating sensor and microcontroller components into a more compact structure could improve portability and durability, expanding its usability in diverse operational scenarios. This study confirms the MSOLR device's ability to provide accurate, real-time milk adulteration detection while ensuring portability and low energy consumption. This dual perspective bridges the gap between laboratory-based and portable solutions for milk adulteration detection, providing a comprehensive tool for quality control in the dairy industry. Such advancements aim to extend the model's utility and enhance its adaptability in real-world scenarios.

In this study, the focus was on starch detection; however, expanding the scope of the method is considered essential. In future studies, we plan to optimize our model to detect other common milk adulterants, such as water, detergent, and melamine. This will enhance both the applicability of the method in the field and enable a broader evaluation of milk product purity. This could enable more extensive monitoring and control of the milk supply chain. While the model is effective up to a certain accuracy level, further improvements could be made in detecting adulteration at very low concentrations. This could be enhanced through more sophisticated data processing techniques and the integration of additional sensors. Although the current design is usable in field conditions, the size and durability of the device can be further optimized for future applications. Integrating sensor and microcontroller components into a more compact structure could expand the device's usability.

In conclusion, the developed MSOLR device and optimized logistic regression model offer a low-cost, energy-efficient, and portable solution for detecting milk adulteration. Compared to existing portable systems, it provides a simpler yet effective approach, enabling real-time analysis in the field. By providing a detailed evaluation of both machine learning performance and system-level characteristics, Tables 1 and 2 demonstrate the developed system's superior balance of accuracy, portability, and energy efficiency. This dual perspective ensures the device is not only effective but also practical for real-world use, bridging a critical gap in current quality control technologies for dairy products. Future studies could focus on expanding the functionality and scope of the device, providing more comprehensive solutions for quality control in dairy products.

The results from real-world testing further validate the system's practicality and effectiveness in field conditions. The high accuracy achieved in on-site testing underscores the device's utility for immediate quality control in the dairy industry. The results from Tables 1 and 2 further validate the practicality of the MSOLR device and the optimized logistic regression model for field applications. These results emphasize the device's real-world applicability, demonstrating its potential to meet industry demands for rapid, accurate, and portable quality control tools. By enabling real-time detection of adulteration at various stages of the supply chain, the system addresses a critical gap in current quality assurance practices.

While we highlight the importance of adapting to emerging technologies to enhance the capabilities of our detection system, we must also acknowledge the potential challenges associated with such advancements. Implementing more sophisticated algorithms, for instance, might require more processing power and could increase the system's energy consumption. Furthermore, while integrating advanced sensors can improve detection accuracy, these components may raise the cost and complexity of the device, potentially limiting its accessibility and scalability in low-resource settings. Addressing these challenges requires a balanced approach to system design, ensuring that enhancements in technology do not compromise the practicality and affordability of the solution.

## 4. Conclusion

This study addresses the development of a portable and edge computing-based system for detecting adulteration in dairy products. Utilizing the AS7265x multispectral sensor and Arduino Nano 33 BLE Sense microcontroller, the system, equipped with an optimized logistic regression model, has successfully detected adulteration in milk samples with high accuracy. The main findings can be summarized as follows: The optimized logistic regression model has detected starch adulteration in milk samples with nearly 100% accuracy. Additionally, the model's potential applicability to other common milk adulterants, such as water, detergent, and melamine, offers promising avenues for future research. This result demonstrates that the model can perform highly effectively despite its simple structure. Compared to other complex models, such as CNN and SVM, the optimized logistic regression model offers significant advantages by operating on a microcontroller with lower power consumption while achieving similar accuracy rates. The developed MSOLR device provides a portable solution in the field by enabling real-time spectral analysis of milk samples. Instant data transmission via Bluetooth allows users to make quick decisions, facilitating continuous quality control at various stages of the milk supply chain (farms, milk processing facilities, retail points). The system's hardware components are selected to be low-cost and easily accessible. The low power consumption of the microcontroller-based system enables long battery life, supporting uninterrupted use of portable devices in the field. The developed system has numerous potential applications within the dairy industry:

**Field Detection and Quality Control:** The device can be used on farms and in milk processing facilities to instantly assess the purity of dairy products. This enables early intervention within the supply chain, reducing economic losses due to adulteration.

**Retail and Consumer Safety:** At grocery stores and retail outlets, the device ensures real-time verification of dairy products, which can enhance consumer trust.

**Regulation and Inspection:** Food safety authorities and regulatory agencies can use this portable device for rapid field checks and inspections, thus effectively combating food fraud.

The results of this study demonstrate the effectiveness and practicality of the developed system while also pointing to various aspects of future research:

**Detection of Other Types of Adulteration:** Future studies could expand and optimize the model to detect other common adulterants in milk, such as water, detergent, and melamine, in addition to starch.

**Data Analytics and Cloud Integration:** Integrating the device with cloud platforms could offer new possibilities for more comprehensive data analytics and monitoring of the milk supply chain, enhancing the overall surveillance of dairy product quality.

**Miniaturization and Durability of the Device:** Future work could further reduce the size and enhance its durability, making it more suitable for a wider range of applications in field conditions.

In conclusion, this study significantly contributes by offering a portable, low-cost, and edge computing-based solution for detecting milk adulteration. Equipped with real-time detection capabilities in field conditions, this system is an effective tool for quality control at every stage of the milk supply chain. This is of great importance for both producer and consumer safety and satisfaction.

## Author Contributions

The author read and approved the final version of the paper.

## Conflicts of Interest

The author declares no conflict of interest.

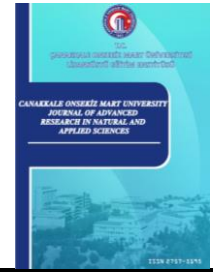
## Ethical Review and Approval

No approval from the Board of Ethics is required.

## References

- [1] F. Cimmino, A. Catapano, L. Petrella, I. Villano, R. Tudisco, G. Cavaliere, *Role of milk micronutrients in human health*, *Frontiers in Bioscience-Landmark* 28 (2) (2023) 41–16 pages.
- [2] S. Das, B. Goswami, K. Biswas, *Milk adulteration and detection: A review*, *Sensor Letters* 14 (1) (2016) 4–18.
- [3] M. Momtaz, S. Y. Bubli, M. S. Khan, *Mechanisms and health aspects of food adulteration: A comprehensive review*, *Foods* 12 (1) (2023) 199–25 pages.
- [4] M. Kamal, R. Karoui, *Analytical methods coupled with chemometric tools for determining the authenticity and detecting the adulteration of dairy products: A review*, *Trends in Food Science and Technology* 46 (1) (2015) 27–48.
- [5] M. M. Ferreira, L. Marins-Gonçalves, D. De Souza, *An integrative review of analytical techniques used in food authentication: A detailed description for milk and dairy products*, *Food Chemistry* 457 (2024) 140206 20 pages.
- [6] O. Boukria, S. Boudalia, Z. F. Bhat, A. Hassoun, A. Aït-Kaddour, *Evaluation of the adulteration of camel milk by non-camel milk using multispectral image, fluorescence and infrared spectroscopy*, *Spectrochimica Acta Part A: Molecular and Biomolecular Spectroscopy* 300 (2023) 122932 10 pages.
- [7] S. Patari, P. Datta, P. S. Mahapatra, *3D Paper-based milk adulteration detection device*, *Scientific Reports* 12 (1) (2022) 13657 14 pages.
- [8] R. Nagraik, A. Sharma, D. Kumar, P. Chawla, A. P. Kumar, *Milk adulterant detection: Conventional and biosensor based approaches: A review*, *Sensing and Bio-Sensing Research* 33 (2021) 100433 9 pages.
- [9] A. Poonia, A. Jha, R. Sharma, H. B. Singh, A. K. Rai, N. Sharma, *Detection of adulteration in milk: A review*, *International Journal of Dairy Technology* 70 (1) (2017) 23–42.
- [10] T. Azad, S. Ahmed, *Common milk adulteration and their detection techniques*, *International Journal of Food Contamination* 3 (1) (2016) 1–9.
- [11] A. Ravindran, F. P. Nesamani, D. Nirmal, *A Study on the use of spectroscopic techniques to identify food adulteration*, *International Conference on Circuits and Systems in Digital Enterprise Technology* (2018) 1–6.
- [12] P. M. Santos, E. R. Pereira-Filho, L. E. Rodriguez-Saona, *Rapid detection and quantification of milk adulteration using infrared microspectroscopy and chemometrics analysis*, *Food Chemistry* 138 (1) (2013) 19–24.
- [13] C. McVey, C. T. Elliott, A. Cannavan, S. D. Kelly, A. Petchkongkaew, S. A. Haughey, *Portable spectroscopy for high throughput food authenticity screening: Advancements in technology and integration into digital traceability systems*, *Trends in Food Science and Technology* 118 (2021) 777–790.
- [14] L. Iram, M. Y. Sandhu, A. K. M. Z. Hossain, S. Khan, *Portable real time microwave milk quality monitoring sensor*, *9th International Conference on Computer and Communication Engineering* (2023) 167–172.
- [15] G. Durante, W. Becari, F. A. S. Lima, H. E. M. Peres, *Electrical impedance sensor for real-time detection of bovine milk adulteration*, *IEEE Sensors Journal* 16 (4) (2016) 861–865.

- [16] R. Kodan, P. Parmar, S. Pathania, *Internet of things for food sector: Status quo and projected potential*, Food Reviews International 36 (6) (2020) 584–600.
- [17] A. M. Aware, U. A. Kshirsagar, *Design of milk analysis system for dairy farmers using embedded system*, International Journal of Innovative Research in Electrical, Electronics, Instrumentation and Control Engineering 5 (5) (2017) 11–16.
- [18] K. Pugazhenthii, A. Sengamalam, B. Ganesan, *Milk quality monitoring system using IoT*, International Conference on Sustainable Computing and Smart Systems (2023) 1096–1098.
- [19] R. C. Zhang, X. Yu, X. J. Liu, J. H. Zhai, Z. W. Ning, *Study on mechanical automation with design of rapid milk detector based on freezing point*, Advanced Materials Research 703 (2013) 282–286.
- [20] M. K. Nieuwoudt, S. E. Holroyd, C. M. McGoverin, M. C. Simpson, D. E. Williams, *Screening for adulterants in liquid milk using a portable Raman miniature spectrometer with immersion probe*, Applied Spectroscopy 71 (2) (2017) 308–312.
- [21] Y. Durgun, M. Durgun, *Cost-Effective Multispectral Sensor and Artificial Neural Networks for the Detection of Starch Adulteration in Raw Milk.*, Applied Sciences 14 (21) (2024), 9800 14 pages.
- [22] R. U. Mhapsekar, L. Abraham, N. O’Shea, S. Davy, *Edge-AI implementation for milk adulteration detection*, IEEE Global Conference on Artificial Intelligence and Internet of Things (2022) 108–113.
- [23] A. A. Arrieta-Almario, M. S. Palencia-Luna, P. L. Arrieta-Torres, *Determination of adulterant in milk through the use of a portable voltammetric electronic tongue*, Revista Mexicana. Ingeniería. Química 17 (2018) 877–884.
- [24] A. S. Sekhon, P. Unger, S. Sharma, B. Singh, X. Chen, G. M Ganjyal, M. Michael, *Hyperspectral imaging of foodborne pathogens at colony and cellular levels for rapid identification in dairy products*, Food Science and Nutrition 12 (1) (2024) 239–254.



# Ecological Footprint Awareness of Generation Z: A Case Study of Selçuk University Faculty of Science

Halil Osman Erbek<sup>1</sup> , Yunus Akdoğan<sup>2</sup> , Tenzile Erbayram<sup>3</sup> 

<sup>1</sup>Department of Management Information Systems, Faculty of Business and Management Sciences, Istanbul Esenyurt University, Istanbul, Türkiye

<sup>2,3</sup>Department of Statistics, Faculty of Science, Selcuk University, Konya, Türkiye

## Article Info

Received: 07 Nov 2024

Accepted: 15 Dec 2024

Published: 31 Dec 2024

Research Article

**Abstract** – Achieving a sustainable ecosystem requires a harmonious relationship between biological capacity and ecological footprint. However, in today's rapidly industrializing world, population growth and lack of awareness about ecological footprints negatively impact biological capacity. Consequently, global ecological limits have been exceeded, straining the planet's carrying capacity. Human dominance over nature drives biodiversity loss and contributes to climate change, disrupting ecosystem balance, overconsuming natural resources, and causing environmental degradation. Industrialization and rapid urbanization have significantly increased resource consumption, leading to a sharp rise in greenhouse gas emissions—central to the carbon footprint and primary causes of climate change—that critically affect air quality, ecosystem stability, and biodiversity protection. Environmental factors directly influence human well-being, economic activities, and the health of all living organisms while reshaping the ecological order. This study aims to provide a fresh perspective on ecological awareness and inspire actionable steps in terms of building a sustainable ecosystem through a survey assessing the ecological literacy of Selcuk University Faculty of Science (SUFS) students. The survey reveals students' environmental awareness levels while examining its impact on their ecological behaviors. The general evaluation shows that SUFS students exhibit high awareness levels in the Ecological Footprint Awareness scale; however, scores related to recycling and transportation are lower than other dimensions. This indicates that targeted training for recycling and transportation is necessary to enhance overall awareness levels regarding ecological footprints. The findings will serve as a valuable resource for identifying strategies to improve environmental consciousness while emphasizing individuals' roles in fostering a sustainable future.

**Keywords** – *Ecological footprint, biological capacity, sustainability in the ecosystem, climate change, ecological awareness*

## 1. Introduction

Human communities are closely intertwined with their environment, forming a unified whole. In creating this whole, natural resources are often used unknowingly, leading to one of today's and the future's greatest challenges: environmental pollution. According to survey results from the United Nations Educational, Scientific, and Cultural Organization (UNESCO), the most significant global issues over the next 10 years will be climate change and biodiversity loss, making their resolution a primary challenge [1]. Ecological footprint studies, introduced by sustainability advocates Mathis Wackernagel and Bill Rees, emerged in the early 1990s during discussions about the Earth's human carrying capacity. These studies have played a vital role in raising awareness of ecological footprints as one of the most pressing global issues identified by UNESCO [2].

<sup>1</sup>halilosmanerbek@esenyurt.edu.tr; <sup>2</sup>yakdogan@selcuk.edu.tr; <sup>3</sup>tenzile.erbayram@selcuk.edu.tr (Corresponding Author)

Research shows that the ecological footprint is essential for maintaining a livable planet and ensuring sustainability [2-5]. The ecological footprint measures how much of the planet's biological capacity we use to counterbalance the effects of our consumption and is expressed in global hectares (gha). Biological capacity refers to the ability of renewable natural resources to sustain life in specific geographical areas and is also expressed in global hectares. The ecological footprint is divided into six main subcategories: carbon footprint, grazing land footprint, fishing ground footprint, forest land footprint, agricultural land footprint, and built-up land footprint [3].

Carbon footprint refers to carbon dioxide emissions from human activities such as transportation (cars, airplanes, etc.) and the burning of fossil fuels. It is the largest contributor to the ecological footprint, accounting for 0.46 of the total [4-5].

Grazing land footprint refers to the land used for livestock-related products, such as meat and dairy, and pastureland for grazing. It contributes 0.03 to the ecological footprint [4-5]. Fishing ground footprint measures the freshwater and saltwater areas required to sustain the seafood we consume, accounting for 0.02 of the total ecological footprints [4-5]. Forest land footprint calculates the forest area needed to produce textiles, cosmetics, paper, and wood materials. It contributes 0.11 to the ecological footprint [4-5]. The agricultural land footprint includes areas used for producing food, animal feed, vegetable oils, rubber, and fiber for the population. It is the second largest contributor, making up 0.35 of the total ecological footprints [4-5].

Built-up land footprint represents the impact of infrastructure such as transportation, housing, industrial buildings, and power plants. It accounts for 0.03 of the ecological footprints [4-5].

The primary goal of the ecological footprint is to quantify humanity's demand for ecological goods and services while preventing the Earth's ecological capacity from being exceeded and ensuring sustainability. Public awareness of the ecological footprint is one of the most critical factors in achieving these goals.

With a growing population and rapid industrial development, ecological challenges in Türkiye have become increasingly pronounced. A literature review reveals that Türkiye's biocapacity reserves have declined from 1961 to 2018, as shown in Table 1 [6]. As the table illustrates, biocapacity reserves have progressively moved into a negative trend, indicating that ecological limits have been exceeded.

**Table 1.** Ecological footprint and biocapacity amounts between 1961-2018

Years	Biological Capacity Per Capita	Ecological Footprint Per Capita	Biocapacity Reserve (+/-)
1961	2.6 gha	1.6 gha	+1.0 gha
1973	2.1 gha	1.8 gha	+0.3 gha
1980	2.1 gha	2.1 gha	0.0 gha
1991	1.9 gha	2.4 gha	-0.5 gha
1998	1.8 gha	2.8 gha	-1.0 gha
2005	1.6 gha	2.8 gha	-1.2 gha
2010	1.5 gha	3.2 gha	-1.7 gha
2018	1.3 gha	3.4 gha	-2.1 gha

As mentioned earlier, the problems highlighted by the UNESCO survey are climate change and biodiversity. For a more sustainable planet, the biological capacity per person must be equal to or greater than the ecological footprint per person, and biocapacity reserves are expected to show a positive trend [6]. In recent years, Ecological Footprint Awareness (EFA) studies have examined the relationship between individuals' consumption habits and environmental impact. The EFA scale consists of the subdimensions Energy, Laws, Recycling, Transportation, Water Consumption, and Food. The Energy subdimension includes 8 items, the Legal Scope subdimension includes 4 items, the Recycling subdimension includes 5 items, the Transportation subdimension includes 5 items, the Water Consumption subdimension includes 4 items, and the Food subdimension includes 4 items, totaling 30 items across 6 subdimension [7].

The conceptual understanding of the ecological footprint is of great importance for significantly contributing to the field. While the ecological footprint is often discussed regarding its environmental impacts and

calculation methods, its theoretical foundations and connections to sustainability concepts need to be explored in greater depth. A comprehensive discussion on the definition, historical development, and ecological footprint measurement across different sectors could provide valuable insights for researchers and policymakers. Furthermore, studies examining how various theoretical approaches to the ecological footprint intersect with environmental awareness and behavior can clarify its role in promoting sustainable practices. Expanding the conceptual boundaries of ecological footprint research will enhance understanding and contribute to developing more effective strategies for implementing environmental policies and raising awareness. This deeper understanding also opens opportunities to explore the relationships between the ecological footprint, consumption habits, and societal attitudes toward sustainability.

For example, the "Ecological Footprint Calculation Survey" is administered to 81 teacher candidates at Aksaray University [8]. Similarly, an individual ecological survey is conducted among 241 students and employees at Akdeniz University [9]. At Mustafa Kemal University Faculty of Agriculture, the ecological footprint of 91 academicians is evaluated using the same survey; despite their footprint being above the global average, it remained below the Turkish average [10]. The EFA scale, developed by Coşkun, is administered to 217 teacher candidates in the 1st and 4th grades of the Science Education and Turkish Language Teaching departments at Akdeniz University [11]. An ecological footprint survey is also applied to 390 engineering students at Sakarya University [12], while the same awareness scale is used with 433 students from Süleyman Demirel University's Faculty of Architecture [13]. The EFA scale developed by Çelik Coşkun and Sarıkaya is used by selecting 194 individuals from the faculty of sports sciences [14]. The scale is also administered to 66 teacher candidates from the Biology Education Department [15].

Additionally, the ecological footprint is calculated regionally in Southern Colorado [16], and the scale is applied to 536 classroom teachers across four districts in the city center of Diyarbakir [17]. The EFA Scale, developed by Coşkun, is administered to 47 science teacher candidates continuing their education in the 3rd and 4th years. The EFA levels of these 47 teacher candidates are examined about various demographic variables. A significant difference is observed between the class levels of the participants [18]. The EFA Scale is administered to students at the Faculty of Health Sciences at Sivas Cumhuriyet University. The students' EFA levels are found to be high [19]. In another study, the EFA Scale is administered to 85 students studying in the Forestry Engineering Department at Karabük University. It was found that the students scored the highest in the Legal Scope and Energy subdimensions, while the Transportation subdimension had the lowest score [20].

According to the 2021 census of the Turkish Statistical Institute, 15.3% of the Turkish population consists of Generation Z [21]. In a society where knowledge is passed down from generation to generation, raising awareness about ecological footprint and biocapacity is critical for individuals to continue their sustainable lives today and in the future. However, despite this important issue, there is no study in the literature focusing on the ecological footprint of Generation Z. This study aims to fill this gap by using the newly developed EFA scale to assess the awareness levels of Generation Z students at Selçuk University Faculty of Science regarding the ecological footprint.

## **2. Materials and Methods**

### **2.1. Research Purpose, Scope, and Limitations**

Human activities have a negative impact on climate change and biodiversity. If we fail to prevent the exceedance of ecological limits, our planet will move toward becoming uninhabitable. The most effective strategy for preventing ecological limit exceedance is to increase awareness among individuals and institutions regarding their ecological footprint. To protect the ecological balance and ensure the sustainability of human societies, it is essential to address the six main factors affecting the ecological footprint to meet the needs of present and future generations. This study aims to assess students' EFA and literacy levels at the Faculty of Science, Selçuk University.

## 2.2. Research Method

This study is conducted at the Faculty of Science, Selçuk University, to examine students' EFA levels. A face-to-face survey is employed to gather the data necessary for the study. The survey consists of two sections: the first section will collect sociodemographic information from the participants (such as age, gender, and expenditure patterns), while the second section will assess the participant's knowledge of the ecological footprint.

## 2.3. Research Group

The study population consists of university students from the Faculty of Science at Selçuk University. The sample size is determined based on the total student population of 1.722, following the principles outlined in the sampling guide [22]. To account for potential invalid responses, 250 questionnaires are planned for distribution, exceeding the 10% sample size. Table 2 presents a detailed account of the sample sizes calculated using the stratified sampling method, along with their distribution across departments and the targeted number of students for each department.

**Table 2.** Number of surveys to be applied by departments

Department	Number of Students Survey to be Conducted	
Actuarial Sciences	106	15
Biochemistry	221	33
Biology	311	45
Biotechnology	242	35
Physics	103	15
Statistics	154	23
Chemistry	165	24
Mathematics	420	60
Total	1722	250

## 2.4. Analysis of Data

The responses collected from the questionnaire are coded and entered into the Statistical Package for Social Sciences (SPSS) Program 22.0 software for analysis. To ensure the data is prepared for analysis, frequency analysis is conducted for each scale item, and the maximum and minimum values, means, and standard deviations are reviewed. Missing data and incorrect entries are identified, and the dataset is cleaned accordingly. Following the data validation process, frequency analysis is performed for categorical (grouped) data, while descriptive statistics are calculated for continuous (ungrouped) data from the final dataset. Descriptive statistics are utilized to report demographic information, and frequency analysis is conducted, including means and standard deviations, as appropriate for the data type.

The data is then transferred into SPSS 22, where relevant definitions and assignments are made to facilitate further analysis. After data entry, the statistical methods used in the study are determined. Given that established scales from the literature are employed, Confirmatory Factor Analysis (CFA) is conducted to validate the scales and their respective dimensions. Cronbach's alpha coefficient is calculated to assess the reliability of each scale. The total scores for each scale are computed after removing invalid items based on the fit values and factor loadings derived from the CFA.

The analysis of the resulting scores involved assessing the normality of the data distribution and the homogeneity of variance, which informed the choice between parametric and nonparametric tests. The Kaiser-Meyer-Olkin (KMO) test and Bartlett's Test of Sphericity are used to evaluate the adequacy of the sample for factor analysis. The study examines the relationships between EFA and demographic and behavioral variables,

and various hypotheses are tested in this direction. These hypotheses and the way they are included in the analysis can be summarized as follows:

One of the main focuses of the study is to examine whether there is a significant difference between the EFA levels of the participants according to their gender. Another critical issue is to evaluate the effect of the place where the participants live on EFA. In addition, the effect of the parents' education level on individuals' EFA is investigated.

In the context of economic factors, the effect of the participants' monthly expenditure levels on EFA levels is analyzed. In terms of behavioral variables, the relationship between cigarette and alcohol use and awareness levels is examined. Finally, the effect of the participants' book reading habits on ecological awareness levels is investigated. Each hypothesis is analyzed using appropriate statistical tests to determine whether there is a significant difference between EFA levels. The Kolmogorov-Smirnov test is applied to evaluate the normality of the data. In cases where normality could not be achieved, the Mann-Whitney U test is used for comparisons between two independent groups, and the Kruskal-Wallis test is used for comparisons between three or more independent groups. With these methods, a comprehensive analysis is carried out to understand the effects of the study on different variables.

### 3. Findings

#### 3.1. Demographic Findings

Table 3 presents the distribution of participants from the Faculty of Science at Selçuk University who completed the survey, organized by department. Of the total respondents, 10.27% (26 students) are from the Statistics Department, 17.78% (45 students) are from the Biology Department, 23.71% (60 students) from the Mathematics department, 5.92% (15 students) from the Physics department, 13.83% (35 students) from the Biotechnology department, 9.48% (24 students) from the Chemistry department, 5.92% (15 students) from the Actuarial Sciences department, and 13.04% (33 students) from the Biochemistry department.

**Table 3.** Distribution of descriptive statistics

		n	%
<b>Department</b>	Statistics	26	10.27
	Biology	45	17.78
	Mathematics	60	23.71
	Physics	15	5.92
	Biotechnology	35	13.83
	Chemistry	24	9.48
	Actuarial Sciences	15	5.92
	Biochemistry	33	13.04
<b>Gender</b>	Female	171	67.6
	Male	82	32.4
<b>Place of residence</b>	City center	182	71.9
	District	61	21.1
	Rural Areas	10	4.0
<b>Mother's Education</b>	Primary School	168	66.4
	High School	62	24.5
	Associate Degree	10	4.0
	Undergraduate and Postgraduate	13	5.1

**Table 3.** (Continued) Distribution of descriptive statistics

		n	%
<b>Mother Occupation Group</b>	Public	13	5.1
	Private	27	10.7
	Housewife	19	77.5
	Other	17	6.7
<b>Father's Education</b>	Primary School	11	44.7
	High School	78	30.8
	Associate degree	28	11.1
	Undergraduate and Postgraduate	34	13.4
<b>Father Occupation Group</b>	Tradesmen	44	17.4
	Public	43	17.0
	Private	67	26.5
	Other	99	39.1
<b>Monthly expenses</b>	Less than 1000₺	35	13.8
	Between 1000₺ and 2000₺	53	20.9
	Between 2000₺ and 3000₺	65	25.7
	Between 3000₺ and 4000₺	48	19.0
	More than 4000₺	52	20.6
<b>Smoking</b>	Yes	45	17.8
	No	20	2.2
<b>Alcohol</b>	Yes	28	28
	No	22	88.9

Table 3 presents the distribution of participants by gender, showing that female participants constitute a higher proportion than male participants, with 67.6% (171 participants) being female and 32.4% (82) male. In terms of residential locations, the majority reside in urban areas, with 71.9% (182 participants) living in city centers, followed by 21.1% (61 participants) in district areas and 4.0% (10 participants) in rural areas. Regarding the educational background of participants' mothers, 24.5% (62) have completed high school, 4.2% (10) hold an associate degree, 5.1% (13) possess an undergraduate degree, and 5.1% (13) have attained a postgraduate degree. Occupational categories show that 77.5% (196) of mothers are housewives, 10.7% (27) are employed in the private sector, 6.7% (17) belong to other occupational groups, and 5.1% (13) work in the public sector. For fathers, 30.8% (78) have completed high school, 11.1% (28) hold an associate degree, 13.4% (34) have obtained an undergraduate degree, and 13.4% (34) possess a postgraduate degree. Additionally, 39.1% (99) of fathers are employed in other occupational groups, 26.5% (67) work in the private sector, 17.4% (44) are tradesmen, and 17.0% (43) are employed in the public sector. The analysis of educational levels reveals that primary school graduates represent the largest group, with 66.4% (168) of mothers and 44.7% (113) of fathers having completed primary school. Monthly spending among the participants varies, with the largest group (25.7%, 65 participants) spending between 2000₺ and 3000₺. Additionally, 20.9% (53) report expenditures of 1000₺ to 2000₺, 20.6% (52) spend more than 4000₺, 19.0% (48) fall within the 3000₺ to 4000₺ range, and 13.8% (35) spend less than 1000₺. In terms of smoking habits, 82.2% (208 participants) are non-smokers, while 17.8% (45) are smokers. Regarding alcohol consumption, 88.9% (225) reported not consuming alcohol, whereas 11.1% (28) indicated that they do consume alcohol. The number of books read by participants each month is also analyzed. The results show that 33.2% (84) of participants read one book per month, 22.9% (58) read two books, and 16.6% (42) did not read any books. Additionally, 13.0% (33) read three books per month, 8.7% (22) read four books, and 5.5% (14) read five books.

### 3.2. Results of Validity and Reliability Analysis of Scales

For a measurement tool to produce accurate results, it is essential to be valid and reliable in scientific research. Accurate results are obtained when both reliability and validity criteria are sufficiently met. To ensure this, the scales' reliability and validity are assessed before analyzing the research data and testing the hypotheses. While there are different reliability analysis methods depending on the measurement tool used, the most commonly used method is internal consistency, which is assessed by calculating Cronbach's alpha coefficient. The alpha value ranges from 0 to 1, with a value of at least 0.70 generally considered acceptable.

Factor analysis is utilized to assess construct validity. CFA, which facilitates the interpretation of multiple variables, is commonly employed to test construct validity, particularly in the social sciences. For this study, Multi-Factor CFA is conducted on the EFA scale using the Analysis of Moment Structures (AMOS) 22 program to evaluate the validity of the scales. CFA examines whether the relationships within the structure defined by the variables align with the collected data. It also assesses the applicability of scales developed by other researchers in the social sciences to the research sample in the present study. Consequently, CFA is initially applied to determine the construct validity of the scales associated with the conceptual model of this research. Table 4 presents the KMO test values, which are used to assess the adequacy of the sample size for factor analysis and the suitability of the scales employed in the study.

**Table 4.** KMO and Bartlett test values of the EFA scale

Scales	KMO	Bartlett Test-Ki-Kare	p
EFA Scale	0.916	3143.670	<0.000

As presented in Table 4, the KMO coefficient for the scale used is 0.916, while Bartlett's Test of Sphericity indicated a significance value of  $p = 0.000$ . These results confirm the suitability of the variables for factor analysis, as both the KMO and Bartlett's test values meet the necessary criteria. Consequently, the data collected from the participants are deemed appropriate for factor analysis, suggesting that meaningful factors can be extracted.

To uncover the factor structure of the scales, both rotated (Component Matrix) and principal axis rotated (Rotated Component Matrix-Varimax) principal component analysis is applied. After conducting the necessary structural validity tests, the factor analysis results employed in this study are presented in the following section. Model fit indices are the primary indicators of whether the data support the tested model. Each fit index has strengths and limitations; therefore, it is advised not to rely solely on one fit index to assess whether the tested model is confirmed.

The Chi-square ( $\chi^2$ ) value, the most widely used and oldest goodness-of-fit index, tests the compatibility between the sample data and the theoretically proposed model by the researcher. The  $\chi^2/df$  ratio offers more precise and reliable results when evaluating the overall model's goodness-of-fit, as it divides the Chi-square value by the degrees of freedom. The Goodness of Fit Index (GFI) assesses the model's fit independent of the sample size. The Comparative Fit Index (CFI) compares the covariance matrices of the theoretical and structural models. Finally, the Root Mean Square Error of Approximation (RMSEA) evaluates the degree of fit between the model and the sample covariance. RMSEA is particularly sensitive to model complexity and measures the discrepancy between the theoretical and model derived from the observed variables.

In cases where the fit indices are not satisfactory following CFA for EFA, adjustments should be made based on the modification indices. The CFA measurement model for this situation is presented below. Figure 1 illustrates the Multi-Factor CFA conducted on the EFA scale.

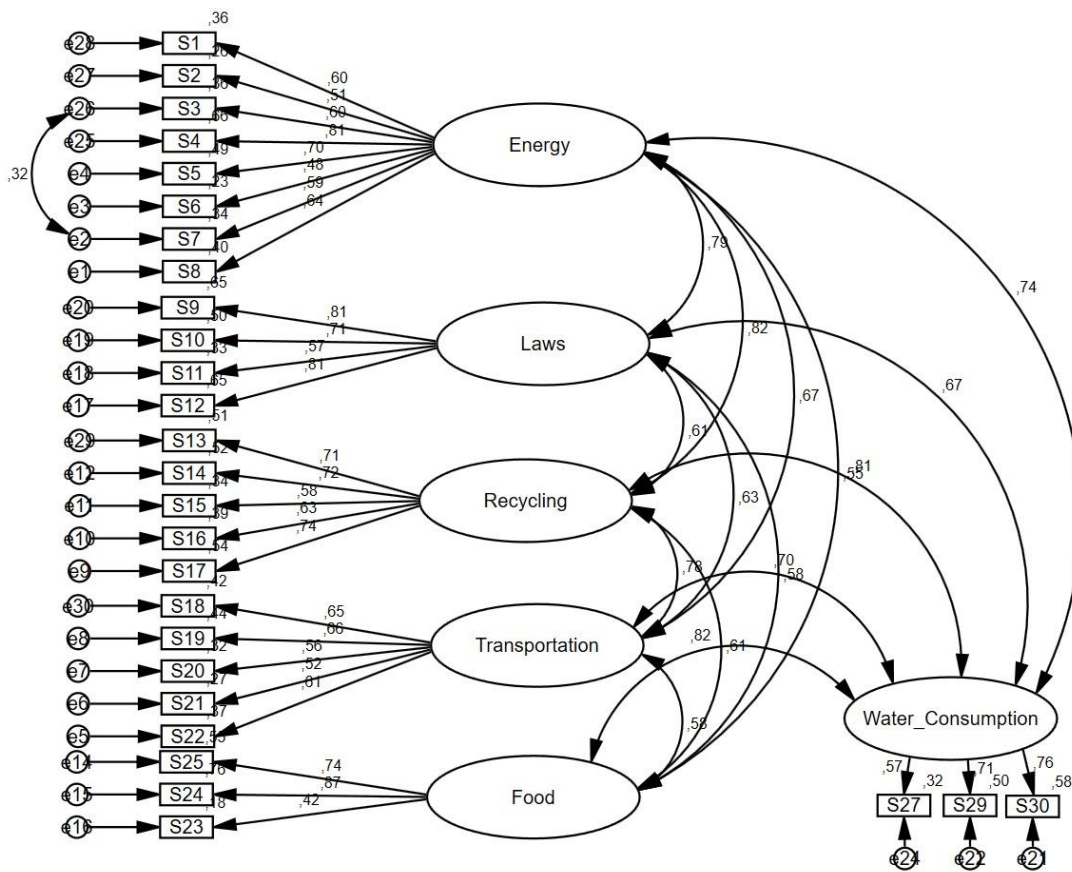


**Figure 1.** Multi-factor CFA on the EFA scale

Table 5 presents the CFA fit indices applied to the EFA scale.

**Table 5.** EFA scale CFA fit values

	$\chi^2$	df	$\chi^2/df$	GFI	CFI	RMSEA
Fit Values	653.477	334	1.957	0.868	0.923	0.062
Good Fit Values *			$\leq 3$	$\geq 0.90$	$\geq 0.95$	$\leq 0.05$
Acceptable Fit Values *			$\leq 3-5$	$0.89-0.85$	$\geq 0.90$	$0.06-0.08$

As a result of the CFA conducted on the EFA scale, it was determined that the fit indices did not meet the acceptable thresholds. Consequently, it is deemed necessary to modify the scale, leading to removing the 26th item from the Food sub-dimension and the 28th item from the Water Consumption sub-dimension. Table 6 presents the percentage of variance explained by the sub-dimensions of the EFA scale, along with the corresponding reliability coefficients.

**Table 6.** EFA scale sub-dimensions variance explanation percentage and reliability results

Scale/Code	Sub-dimension/Code	Variance Explanation Percentage	Cronbach Alpha Coefficient
EFA Scale	Energy	35.171	0.828
	Laws	7.203	0.810
	Recycling	5.439	0.806
	Transportation	4.941	0.738
	Food	3.970	0.705
	Water Consumption	3.453	0.710

Upon examining Table 6, it is evident that the energy dimension accounts for 35.171% of the total variance explained, while the laws dimension contributes 7.203%. The recycling dimension explains 5.439% and 4.941%, respectively. The total variance explained for the scale is 60.178%. Furthermore, the average variance extracted (AVE) value exceeds the accepted threshold of 0.40. The internal consistency coefficient, specifically Cronbach's Alpha, is computed to assess the scale's validity. The resulting Cronbach's Alpha value for the entire scale is found to be 0.926, which is well above the accepted threshold of 0.70. These results affirm that the scale demonstrates high internal consistency, indicating reliability. Table 7 provides the factor loadings for the items of the EFA scale.

**Table 7.** Factor loadings of EFA scale items

Scale	Sub-Dimension	Items/Expressions	Factor
EFA Scale	Energy	Do you prefer using clean and environmentally sustainable energy sources for heating	0.60
		Do you make sure that the windows are closed when the air conditioning is on?	0.51
		Do you make sure not to leave electrical appliances on for long periods of time?	0.60
		Do you prefer energy-efficient lighting and heating products?	0.81
		Do you prefer double-glazed windows because they provide thermal insulation?	0.70
		Do you use LED bulbs instead of old bulbs at home?	0.48
		Do you make sure that devices such as PCs, tablets, and televisions are not left on	0.59
		Do you avoid running washing machines, dishwashers, dryers, etc., without a full load	0.64
	Laws	Do you believe that positioning solar energy in urban structuring where it can be used	0.81
		Do you think that the government should encourage the sale of vehicles with minimal	0.71
		Do you believe that green areas should be preserved and not sacrificed for urbanization and	0.57
		Do you agree that industrial organizations should take measures to protect environmental	0.81
	Recycle	Do you recycle electronic waste?	0.71
		Do you make an effort to recycle household waste?	0.72
		Do you try to repurpose leftover food instead of discarding it?	0.58
		Do you separate household waste based on its type before disposing of it?	0.63
		Do you prefer using recyclable packaging when shopping?	0.74
	Transport	Do you prefer sharing a car with others to minimize environmental impact?	0.65
		Do you prefer using public transportation to reduce environmental harm?	0.66
		Do you prefer vehicles such as Ginger, scooters, and electric skateboards because they	0.56
		Do you prefer riding a bike to driving a car?	0.52
	Food	When the distance is suitable, do you prefer walking over driving?	0.61
		Do you avoid eating foods that are not in season?	0.42
		Do you buy only as much food as you need when shopping?	0.87
	Water Consumption	Do you cook only the amount of food that will be consumed?	0.74
		Do you prefer wiping your car instead of washing it to consume less water?	0.57
		Do you take care not to waste more water than necessary for personal hygiene?	0.71
			Do you prefer to water the plants at home/in the garden using the correct methods?

An item must exhibit a sufficiently high factor loading to be included in a factor. Items with a factor loading below the threshold of 0.50 are recommended for removal, as they do not contribute meaningfully to the factor structure of the measurement instrument [23]. In line with this criterion, the EFA scale, consisting of six dimensions and 28 items, has been confirmed, as shown in the table. A summary of the modifications made to the EFA scale is presented in Table 8.

**Table 8.** Changes made to the EFA scale

	Scales	Number of Statements	Number of Statements Extracted
EFA Scale	Energy	8	-
	Laws	4	-
	Recycling	5	-
	Transportation	5	-
	Food	4	1
	Water Consumption	4	1

### 3.3. Findings Regarding EFA Scores

In statistical analyses, it is considered essential that the data distribution adheres to the normality assumptions. Therefore, normality tests are conducted to assess whether the data obtained from the participants in this study met these assumptions. The Kolmogorov-Smirnov test is utilized to evaluate the conformity of the data to a normal distribution. The results from the Kolmogorov-Smirnov test for the EFA Scale scores reveal that the data do not follow a normal distribution, as the p-value ( $p = 0.000$ ) is less than the 0.05 significance level. Based on these findings, nonparametric tests will be employed in this study: the Mann-Whitney U test will be used to analyze differences in mean values between two independent groups, while the Kruskal-Wallis test will be used to examine differences across three or more groups.

**Table 9.** EFA scale Mann-Whitney U test results

	Energy Mean+SE Mean Rank	Laws Mean+SE Mean Rank	Recycling Mean+SE Mean Rank	Transportation Mean+SE Mean Rank	Food Mean+SE Mean Rank	Water Consumption Mean+SE Mean Rank	EFA Total Score Mean+SE Mean Rank
<b>Gender</b>							
<b>Female (n=171)</b>	33.883+0.384 128.47	17.859+0.212 133.22	18.853+0.332 131.62	18.590+0.340 135.73	11.888+0.173 129.663	11.812+0.196 133.69	112.888+1.330 133.36
<b>Male (n=82)</b>	33.170+0.669 123.93	17.000+0.374 114.03	18.060+0.493 117.37	16.853+0.492 108.80	11.292+0.344 121.51	11.097+0.290 113.05	107.475+2.005 113.73
<b>p-value</b>	0.643	0.043*	0.146	0.006*	0.403	0.034*	0.046*
<b>Smoking of Students</b>							
<b>Yes (n=45)</b>	32.288+0.975 114.90	17.177+0.450 116.58	17.422+0.711 110.74	16.955+0.717 111.77	11.600+0.414 122.69	10.688+0.419 104.74	106.133+2.869 111.53
<b>No (n=208)</b>	33.947+0.351 129.62	17.668+0.208 129.25	18.851+0.296 130.52	18.259+0.307 130.30	11.716+0.176 127.93	11.774+0.174 131.81	112.216+1.201 130.35
<b>p-value</b>	0.220	0.275	0.099	0.122	0.660	0.023*	0.118
<b>Students' Alcohol Use</b>							
<b>Yes (n=28)</b>	32.392+1.150 117.27	17.750+0.495 130.68	17.750+0.965 116.14	17.214+1.018 117.09	11.535+0.510 120.18	10.857+0.574 110.66	107.500+3.699 114.29
<b>No (n=225)</b>	33.808+0.352 128.83	17.560+0.204 126.54	18.702+0.286 128.35	18.128+0.293 128.23	11.715+0.171 127.85	11.671+0.169 129.03	111.587+1.170 128.58
<b>p-value</b>	0.257	0.770	0.403	0.446	0.597	0.206	0.329

Mann-Whitney U test, \*statistical significant ( $p < 0.050$ )

Based on the results presented in Table 9, no significant differences are found in the energy, recycling, and food scores when comparing students' genders. However, the scores for the scope of laws, transportation, water consumption, and EFA are found to be higher for female students than male students. Furthermore, the analysis revealed no significant differences in the energy, scope of laws, recycling, transportation, food scales, or EFA total scores based on students' smoking status. However, it is observed that non-smokers had higher scores on the water consumption scale than smokers (Table 9). Finally, as shown in Table 9, the p-values for the EFA scale and its sub-dimensions are greater than 0.050, indicating no significant differences between students who use alcohol and those who do not.

**Table 10.** EFA scale Kruskal-Wallis test results

Departments	Energy Mean+SE Mean Rank	Laws Mean+SE Mean Rank	Recycling Mean+SE Mean Rank	Transportation Mean+SE Mean Rank	Food Mean+SE Mean Rank	Water Consumption Mean+SE Mean Rank	EFA Total Score Mean+SE Mean Rank
<b>Statistics (n=26)</b>	31.923+1.159 114.26	16.769+0.632 116.24	18.487+0.908 131.36	16.923+0.904 115.37	11.282+0.484 118.90	10.692+0.467 105.58	106.076+4.003 118.24
<b>Biology (n=45)</b>	34.888+0.627 142.28	18.311+0.314 143.41	19.066+0.553 131.80	19.044+0.616 141.53	12.422+0.414 151.03	12.377+0.354 147.62	116.111+2.080 144.10
<b>Mathematics(n=60)</b>	34.011+0.508 128.68	17.595+0.319 127.01	18.505+0.441 123.99	18.359+0.430 129.72	11.404+0.272 116.16	11.674+0.262 128.21	111.550+1.724 124.79
<b>Physics (n=15)</b>	34.777+1.392 137.50	17.444+0.818 115.50	19.222+1.801 137.33	16.777+1.037 100.06	10.888+0.715 104.39	11.000+0.707 104.44	110.111+4.260 118.83
<b>Biotechnology(n=35)</b>	35.105+0.652 139.61	18.210+0.371 132.71	20.000+0.820 148.58	19.000+0.812 139.61	11.947+0.515 134.84	12.000+0.639 142.42	116.263+2.483 145.24
<b>Chemistry (n=24)</b>	33.500+1.784 118.25	16.666+1.145 95.42	19.666+1.605 150.92	17.500+2.045 120.83	11.666+1.085 115.75	10.666+1.358 113.58	109.666+6.264 115.75
<b>Actuarial Science (n=15)</b>	32.307+1.520 104.96	17.461+0.656 113.81	19.153+1.229 137.15	17.538+1.118 119.12	11.923+0.415 127.15	12.307+0.472 144.77	110.692+3.883 123.77
<b>Biochemistry (n=33)</b>	32.454+1.171 116.85	17.393+0.640 128.111	16.939+0.742 99.82	17.121+0.946 117.91	11.969+0.404 136.68	11.090+0.475 113.65	106.969+3.640 115.03
<b>p-value</b>	0.554	0.617	0.346	0.611	0.233	0.142	0.606

Kruskal-Wallis test, \*statistical significant (p<0.050)

As a result of the Kruskal-Wallis tests conducted to examine the differences in the energy, scope of law, recycling, transportation, food, and water consumption scales, as well as the total EFA scores (which represent the sum of these scales), based on students' departments, the p-values for all scales are found to be greater than 0.050, as shown in Table 10. Therefore, no significant differences are observed between the groups. These findings indicate that the scale scores of the students are similar, regardless of their departmental affiliations.

**Table 11.** EFA scale Kruskal-Wallis test results

	Energy Mean+SE Mean Rank	Laws Mean+SE Mean Rank	Recycling Mean+SE Mean Rank	Transportation Mean+SE Mean Rank	Food Mean+SE Mean Rank	Water Consumption Mean+SE Mean Rank	EFA Total Score Mean+SE Mean Rank
<b>Places Where Students Live</b>							
<b>City Center (n=182)</b>	33.428+0.397 123.28	17.494+0.222 124.37	18.329+0.341 122.99	17.939+0.341 124.80	11.708+0.188 125.81	11.521+0.191 125.00	110.423+1.336 123.42
<b>District(n=61)</b>	34.000+0.618 129.19	17.803+0.345 129.88	18.868+0.444 128.64	18.229+0.530 130.42	11.590+0.358 128.95	11.557+0.314 124.80	112.049+1.914 128.38
<b>Village(n=10)</b>	35.600+2.696 181.30	17.800+1.569 157.30	21.800+1.396 189.90	18.400+1.746 146.10	12.100+0.657 136.10	12.800+1.162 176.80	118.500+8.713 183.80
<b>p-value</b>	<b>0.048*</b>	<b>0.033*</b>	<b>0.018*</b>	0.611	0.873	0.085	<b>0.039</b>
<b>Education Status of the Mothers of Students</b>							
<b>Primary Education(n=168)</b>	33.779+0.405 128.03	17.756+0.223 131.04	18.678+0.320 126.32	18.214+0.346 128.57	11.797+0.192 129.31	11.720+0.198 130.43	111.946+1.321 128.18
<b>High School (n=62)</b>	33.661+0.728 129.97	17.322+0.418 122.86	18.435+0.651 129.21	18.145+0.565 130.48	11.693+0.359 130.11	11.354+0.341 121.49	110.612+2.496 131.53
<b>Associate degree (n=10)</b>	30.800+2.085 89.20	15.700+1.212 81.80	18.600+1.194 132.15	17.500+1.654 128.40	10.300+0.882 89.70	11.000+1.085 119.05	103.900+6.893 104.65
<b>Undergraduate and Postgraduate (n=13)</b>	34.153+1.170 128.58	18.000+0.518 129.31	18.307+1.272 121.27	15.461+1.243 88.96	11.461+0.605 111.04	11.307+0.535 115.04	108.692+3.791 107.31
<b>p-value</b>	0.419	0.182	0.977	0.289	0.312	0.751	0.540

**Table 11.** (Continued) EFA scale Kruskal-Wallis test results

	Energy Mean+SE Mean Rank	Laws Mean+SE Mean Rank	Recycling Mean+SE Mean Rank	Transportation Mean+SE Mean Rank	Food Mean+SE Mean Rank	Water Consumption Mean+SE Mean Rank	EFA Total Score Mean+SE Mean Rank
<b>Father's Education Status of the Students</b>							
<b>Primary Education (n=113)</b>	33.238+0.487 118.84	17.539+0.291 126.60	18.433+0.401 122.85	17.761+0.410 121.05	11.610+0.229 122.39	11.628+0.236 126.62	110.212+1.648 120.07
<b>High School (n=78)</b>	34.141+0.704 141.03	17.538+0.367 128.10	18.884+0.535 133.33	18.589+0.524 136.44	11.961+0.324 138.88	11.756+0.306 133.28	112.871+2.252 140.01
<b>Associate degree (n=28)</b>	33.785+0.958 126.25	17.321+0.529 115.38	19.000+0.646 133.13	17.964+0.844 128.77	11.714+0.479 126.29	11.464+0.483 125.32	111.250+2.926 129.48
<b>Undergraduate and Postgraduate (n=34)</b>	33.794+0.717 122.56	18.029+0.401 135.38	18.147+0.827 121.22	17.676+0.840 123.68	11.352+0.417 115.65	11.117+0.471 115.24	110.117+2.681 118.13
<b>p-value</b>	0.219	0.739	0.714	0.543	0.335	0.682	0.260
<b>Students' Mother's Occupation Group</b>							
<b>Public (n=13)</b>	35.000+0.816 138.15	18.153+0.504 133.46	19.615+0.873 141.65	18.538+1.107 136.35	12.307+0.485 139.54	12.230+0.579 142.85	115.846+3.218 141.69
<b>Private (n=27)</b>	32.444+1.089 108.91	16.963+0.701 115.67	17.666+0.930 111.22	15.407+0.967 88.78	10.333+0.541 89.17	11.444+0.460 124.02	104.259+3.682 99.02
<b>Housewife (n=196)</b>	33.693+0.394 128.46	17.581+0.217 127.54	18.683+0.307 128.08	18.352+0.309 131.11	11.846+0.182 131.60	11.515+0.192 125.61	111.673+1.278 129.59
<b>Other (n=17)</b>	34.058+1.158 130.41	18.117+0.520 133.82	18.294+1.330 128.35	18.058+1.246 133.12	11.647+0.605 123.47	12.058+0.558 135.68	112.235+4.069 130.32
<b>p-value</b>	0.556	0.808	0.606	<b>0.039*</b>	<b>0.036*</b>	0.805	0.191
<b>Students' Fathers' Profession Group</b>							
<b>Tradesmen (n=44)</b>	34.340+0.817 138.80	17.431+0.465 121.11	19.136+0.677 134.22	18.113+0.727 128.18	11.681+0.449 130.76	11.454+0.452 126.40	112.159+2.778 129.14
<b>Public (n=43)</b>	34.162+0.624 127.99	18.232+0.301 139.67	19.697+0.571 143.79	18.465+0.613 133.38	11.790+0.330 127.53	11.930+0.341 135.55	114.279+1.799 137.85
<b>Private (n=67)</b>	33.537+0.644 124.06	17.716+0.342 128.78	18.447+0.509 123.52	17.746+0.520 119.90	11.462+0.319 118.44	11.611+0.303 125.92	110.522+2.118 122.46
<b>Other (n=99)</b>	33.202+0.595 123.32	17.272+0.346 122.90	17.979+0.471 118.85	17.989+0.482 128.51	11.818+0.257 130.89	11.464+0.267 124.29	109.727+1.999 123.41
<b>p-value</b>	0.678	0.559	0.251	0.797	0.719	0.860	0.714
<b>Monthly Expenditure Amounts of the Students</b>							
<b>Less than 1000₺ (n=35)</b>	35.285+0.634 146.20	17.457+0.418 117.73	19.314+0.646 134.67	19.228+0.719 143.23	12.171+0.428 142.51	12.514+0.387 152.00	115.971+2.328 140.73
<b>1000-2000₺ (n=53)</b>	33.226+0.804 121.80	17.452+0.470 126.28	19.075+0.535 133.51	18.660+0.529 136.64	12.000+0.323 132.58	11.811+0.341 131.30	112.226+2.536 134.61
<b>2000-3000₺ (n=65)</b>	32.861+0.730 118.06	17.738+0.425 137.50	18.015+0.610 119.62	17.969+0.626 128.64	11.461+0.339 121.70	11.169+0.337 116.68	109.215+2.558 121.77
<b>3000-4000₺ (n=48)</b>	34.687+0.616 138.33	17.458+0.434 122.34	19.020+0.575 132.86	18.291+0.576 128.91	12.062+0.304 135.36	11.541+0.382 126.00	113.062+2.081 132.79
<b>More than 4000₺ (n=52)</b>	33.019+0.811 120.09	17.711+0.329 125.14	17.961+0.673 119.02	16.403+0.663 102.44	11.019+0.406 109.77	11.269+0.363 119.61	107.384+2.500 111.19
<b>p-value</b>	0.258	0.683	0.661	0.071	0.210	0.183	0.301

Kruskal-Wallis test. \*statistical significant (p<0.050)

When examining Table 11, it is observed that no significant differences are found in the transportation, Food, and water consumption scores based on the students' residential areas. However, individuals in rural areas (villages) scored higher on energy, scope of laws, recycling, and total EFA scores than those in urban centers and districts. Regarding the tests conducted based on the occupational groups of the students' mothers, no significant differences are observed in the energy, scope of laws, recycling, water consumption, and total EFA

scores. However, it is found that the transportation and food scale scores of students whose mothers work in the public sector are higher than those of other occupational groups (Table 11). Finally, based on the results presented in Table 11, the analysis of score differences according to the educational background of the student's mothers and fathers, the occupational group of their fathers, and the students' monthly expenditure amounts indicated no significant differences. Specifically, the p-values are greater than 0.050, suggesting that the sub-dimension scores of the EFA scale are similar across these variables.

#### 4. Conclusion

No significant differences are found between the ages of the students about the energy, recycling, transportation, food, water consumption, and EFA scales. The knowledge levels about EFA are nearly identical across all age groups. Similarly, no differences are observed between the genders regarding the energy, recycling, and food scales, with knowledge levels about EFA being almost equal for males and females. However, female students demonstrated higher knowledge levels than male students regarding transportation, water consumption, and EFA scale laws. Furthermore, no significant differences are observed in the transportation, food, and water consumption scales concerning the student's residence, and knowledge levels about EFA remained largely similar across different locations. On the other hand, students residing in urban centers and districts exhibited higher and comparable knowledge levels on the energy, recycling, and EFA scales compared to their peers living in rural areas.

The students' knowledge levels regarding EFA showed no significant differences based on their parents' educational and occupational backgrounds, with the knowledge levels being nearly identical across all groups. Similarly, no differences are observed in the knowledge levels regarding EFA within the context of the laws, recycling, transportation, food, and EFA based on students' smoking status, with the knowledge levels being almost the same for smokers and non-smokers. However, regarding the water consumption scale, students who did not smoke exhibited higher knowledge levels than those who smoked. There are no differences in the knowledge levels regarding EFA across alcohol consumption status, including within the context of the laws, recycling, transportation, food, water consumption, and EFA. Lastly, there is no significant difference in the knowledge levels about EFA based on the number of books students read in a month, with the knowledge levels being similar across different reading habits.

**Table 12.** Averages of EFA scale sub-dimensions

Energy	4.206
Laws	4.395
Recycle	3.719
Transport	3.605
Food	3.898
Water Consumption	3.860
EFA	3.947

Table 12 presents the average values of the EFA scale sub-dimensions and the overall EFA score. The analysis of the EFA scale and its sub-dimensions among students at the Faculty of Science Selçuk University indicated generally high awareness levels. However, lower scores were observed in the Recycling and Transportation sub-dimensions compared to others. To enhance EFA, it is suggested that awareness training be particularly focused on Recycling and Transportation. Various studies in literature address the impact of class level on EFA, but they disagree. For instance, Eraslan and Seçme [13] discovered a significant difference in EFA, specifically in the energy dimension, in favor of first-year students in architecture programs. A different study revealed varied results based on demographic structure. In this study, high-income young individuals living near large shopping malls and far from the airport were found to have a larger "transportation" footprint. Additionally, Akdeniz University Faculty of Economics and Administrative Sciences research revealed that participants' ecological footprints exceeded global and national averages. This study found that ecological footprints increased with higher income and age, while no significant gender differences were observed [9]. In conclusion, the literature shows that the ecological footprint varies across different demographic groups and

geographical regions. These findings emphasize the need for more comprehensive studies on ecological footprints and the importance of raising awareness by collecting additional data across various areas. It is encouraging that generation Z is increasingly aware of these issues, indicating positive prospects for raising ecological awareness.

The findings of this study provide valuable insights into the EFA and environmental awareness of Selçuk University Faculty of Science students. While the overall levels of ecological awareness are high, the relatively low awareness observed in the recycling and transportation sub-dimensions highlights the need for increased educational efforts and awareness campaigns. The findings of this study provide an essential foundation for understanding the relationship between ecological footprint and environmental awareness. Future research can build on these findings using larger, more diverse samples from different universities or individuals from various socio-economic backgrounds. Such studies could offer deeper insights into how environmental awareness levels influence students' environmental behaviors and sustainability practices in their daily lives.

Moreover, there is a need to develop effective and sustainable educational methods to promote environmentally friendly habits among students. Large-scale awareness campaigns utilizing modern digital media and social networks could significantly enhance ecological awareness. Investigating how such campaigns contribute to spreading environmentally friendly habits among students would provide valuable data and insights. Future studies on the effects of ecological awareness education on the environmental attitudes and sustainability consciousness of younger generations, particularly Generation Z, are crucial. These studies can contribute to developing strategies for changing environmental attitudes by understanding generational differences. Finally, developing strategies to improve the effectiveness of environmental sustainability policies and practices across society is essential. Such research could help individuals better understand their environmental responsibilities and contribute meaningfully to the necessary actions for a sustainable future.

## Author Contributions

All the authors equally contributed to this work. They all read and approved the final version of the paper.

## Conflicts of Interest

All the authors declare no conflict of interest.

## Ethical Review and Approval

The research was reviewed and approved by the Board of Ethics of Selçuk University, Approval number: E-16.11.2022-407135.

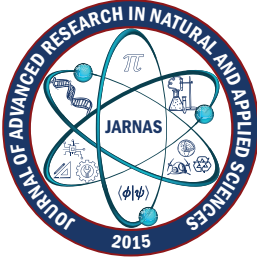
## Acknowledgment

This work was supported by TÜBİTAK 2209-A University Students Research Projects Support Program.

## References

- [1] UNESCO, Biodiversity and Climate Change, <https://www.unesco.org/en/climate-change/biodiversity>, Accessed 27 Oct 2022.
- [2] M. Wackernagel, A. Galli, *An overview on ecological footprint and sustainable development a chat with Mathis Wackernagel*, International Journal of Ecodynamics 2 (1) (2007) 1–9.
- [3] Global Footprint Network, Ecological Footprint Atlas 2010, Accessed 13 Oct 2010.
- [4] J. Kitzes, A. Peller, S. Goldfinger, M. Wackernagel, *Current methods for calculating national ecological footprint accounts*, Science for Environment and Sustainable Society 4 (1) (2007) 1–9.

- [5] D. Öztok, D. Tapan, Turkey's Ecological Footprint Report, Worldwide Fund for Nature-Turkey, (2012), <https://www.wwf.org.tr/?1378/turkiyeninekojikkbilancosu>, Accessed 24 Dec 2023.
- [6] Global Footprint Network, Ecological Footprint and Biocapacity (2022), <https://data.footprintnetwork.org/#/countryTrends?cn=223&type=BCpc,EFCpc>, Accessed 27 Oct 2022.
- [7] M. A. Tekindal, G. Zabzun, Z. Özel, M. Demirsöz, M. Tekindal, *Awareness scale for reducing ecological footprint: A validity and reliability study*, European Journal of Science and Technology (27) (2021) 439–445.
- [8] Ö. Keleş, N. Uzun, S. Özsoy, *Measuring and evaluating preservice teachers' ecological footprints*, Ege Journal of Education 9 (2) (2008) 1–15.
- [9] H. Akıllı, F. Kemahlı, K. Okudan, F. Polat, *The content of ecological footprint concept and calculation of individual ecological footprint in the Akdeniz University Economics and Administrative Sciences Faculty*, Akdeniz University Journal of Economics and Administrative Sciences 15 (2008) 1–25.
- [10] Ö. Eren, O. P. Parlakay, M. Hilal, B. Bozhüyük, *Determination of the ecological footprint of the agricultural faculty academicians: The case of Mustafa Kemal University*, Journal of Agricultural Faculty of Gaziosmanpaşa University 34 (2) (2017) 138–145.
- [11] Ş. Sivrikaya, *Investigation and evaluation of ecological footprint awareness levels of science and Turkish teacher candidates*, Master's Thesis Akdeniz University (2018) Antalya.
- [12] B. Eren, A. Aygün, D. Chabanov, N. Akman, *Ecological footprint score in engineering students*, International Journal of Engineering and Technology Research 1 (1) (2016) 7–12.
- [13] Ş. Eraslan, D. Seçme, *Awareness level of the faculty of architecture students' ecological footprint*, Süleyman Demirel University Journal of Natural and Applied Sciences 25 (3) (2021) 481–491.
- [14] F. K. Duman, E. Atabek-Yiğit, *Ecological footprint awareness of students in faculty of sport sciences*, Gazi Journal of Physical Education and Sports Sciences, 27 (4) (2022) 265–280.
- [15] S. Çıkrık, M. Yel, *Determination of ecological footprint awareness levels of preservice biology teachers*, Social Sciences 14 (6) (2019) 2999–3008.
- [16] M.E. Hopton, D. White, *A simplified ecological footprint at a regional scale*, Journal of Environmental Management 111 (2012) 279–286.
- [17] M. Demirkol, İ. Aslan, *Ecological footprint awareness levels of classroom teachers*, Journal of Computer and Education Research 9 (18) (2021) 904–928.
- [18] T. Karakaş, Ö. Keleş, *Determining the ecological footprint awareness levels of science teacher candidates*, Anatolian Teacher Journal 7 (2) (2023) 116–134.
- [19] T. K. Yıldız, H. Ulusoy, S. Sarıçoban, *Determining the ecological footprint awareness and environmental literacy levels of students in the faculty of health sciences*, Journal of the Institute of Health Sciences Cumhuriyet University 8 (3) (2023) 476–483.
- [20] D. Yıldız, Y. Şenay, *Determining the trends of forestry engineering students in reducing ecological footprint*, Muş Alparslan University Journal of Agriculture and Nature 4 (2) (2024) 63–75.
- [21] Türkiye İstatistik Kurumu Aderese Dayalı Kayıt Sistemi, <https://data.tuik.gov.tr/Bulten/Index?p=Istatistiklerle-Genclik-2021-45634>, Accessed 17 May 2022.
- [22] W. L. Neuman, Social research methods: Qualitative and quantitative approaches, 3rd Edition, Pearson, Boston, 1997.
- [23] N. Shrestha, *Factor analysis as a tool for survey analysis*, American Journal of Applied Mathematics and Statistics 9 (1) (2021) 4–11.



# Classification of Melanoma Cancer Using Deep Convolutional Neural Networks

Ali Güneş<sup>1</sup> , Emrah Dönmez<sup>2</sup> 

<sup>1</sup>Orzax Inc, 901 Mittel Dr Wood Dale, Wood Dale, Chicago, United States

<sup>2</sup>Department of Software Engineering, Faculty of Engineering and Natural Science, Bandırma Onyedi Eylül University, Balıkesir, Türkiye

## Article Info

Received: 27 Jun 2024

Accepted: 16 Oct 2024

Published: 31 Dec 2024

Research Article

**Abstract**— Accurate detection of skin diseases is crucial in healthcare, with early diagnosis being particularly vital for effective treatment. Melanoma, a form of skin cancer with a high potential for metastasis, requires early detection to significantly improve treatment success and prevent further spread across the skin. This study investigates the application of machine learning techniques to diagnose skin lesions, focusing on differentiating between benign moles and malignant melanoma. A Convolutional Neural Network (CNN) model was developed to explore machine learning's efficacy in this context. The initial model featured a primary architecture, progressively refined by adding additional layers and filters to increase its complexity. This iterative enhancement aimed to improve the model's capability to extract and analyze features from skin images. Each model configuration was meticulously evaluated through a series of experiments to determine its diagnostic performance. The results revealed that the proposed CNN model achieved a high accuracy rate of 91%. This significant finding demonstrates the effectiveness of machine learning approaches in the early diagnosis and management of melanoma. The study confirms that advanced CNN architectures can enhance diagnostic precision, thereby contributing to improved patient outcomes in detecting and treating skin diseases.

**Keywords** — CNN, artificial learning, melanoma, mole (nevus), skin cancer

## 1. Introduction

Melanoma is a form of skin cancer that arises when melanocytes, the cells responsible for giving skin its tan or brown hue, start to grow uncontrollably. Cancer begins when cells in the body proliferate without regulation. Virtually any cell in the body has the potential to become cancerous and subsequently spread to other regions. Melanoma is also known as malignant melanoma or cutaneous melanoma. Typically, melanoma cells generate melanin, causing the tumors to appear brown or black. Nonetheless, certain melanomas lack melanin production and may present as pink, tan, or even white. Figure 1 illustrates melanocyte cells. The image credit in Figure 1 is attributed to Designua/Shutterstock.

<sup>1</sup>alisenug@gmail.com (Corresponding Author); <sup>2</sup>emrahdonmez@bandirma.edu.tr

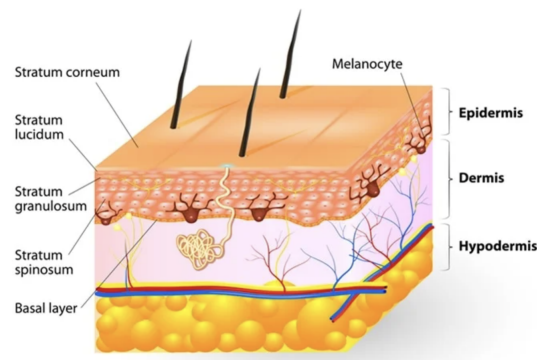


**Figure 1.** Melanocytes located between the upper and lower skin

In 2018, skin cancer emerged as a widespread and perilous condition on a global scale, with 300,000 new diagnoses and over 1 million fatalities occurring each month worldwide [1]. Melanoma is increasingly common worldwide, ranking as the 19th most prevalent disease and exhibiting one of the highest mortality rates [1]. According to the International Agency for Research on Cancer (IARC), approximately 19.3 million new cancer cases were diagnosed in 2020, and about 10 million individuals succumbed to the disease. Furthermore, in the United States, 100,350 new cases were diagnosed in 2020, and about 6,850 people died [2, 3].

Controlling cancer-related mortality is a challenging process; however, recent advances in image processing and artificial intelligence approaches can help in the early detection of melanoma, as early detection and prognosis can improve survival rates. Extensive research solutions and computer vision algorithms have been proposed in the literature to diagnose skin lesions at the earliest stage and overcome the complexities of traditional approaches [4]. Classification methods, such as Decision Trees (DT) [5], Support Vector Machines (SVM) [6], and Artificial Neural Networks (ANN) [7], have been presented in various approaches. Many machine learning techniques face data processing challenges that necessitate high-contrast, noise-free, and clean images, which is often not the case with skin cancer data. Skin classification relies on features like color, texture, and structure. Due to the high inter-class homogeneity and intra-class heterogeneity of skin lesions, using low-quality feature sets can lead to inaccurate classification results [8]. A “low-quality feature” refers to an attribute or variable in the dataset that does not significantly contribute to the model’s predictive power or performance. Such features can impair model performance and result in inaccurate or sub-optimal outcomes. Traditional methods are parametric and often require normally distributed training data; however, skin cancer data is typically unpredictable and may not conform to these assumptions. Each lesion presents a unique pattern, making these methods insufficient. Therefore, deep learning (DL) techniques are more effective for skin classification, enabling dermatologists to diagnose lesions more accurately.

Detecting skin diseases is crucial in healthcare due to its significant impact on patient outcomes. Among various skin conditions, melanoma, a type of skin cancer, is particularly critical because early detection is known to substantially enhance the success of treatment. Identifying melanoma in its initial stages is vital as it prevents the cancer from spreading further across the skin, which can otherwise lead to more severe health issues. This study focuses on diagnosing skin lesions, specifically moles (benign tumors) and melanoma (a malignant skin cancer), through machine learning techniques.

To achieve this, the research involved developing a Convolutional Neural Network (CNN) model, which was initially simple. Gradually, more layers and filters were incorporated into the model, increasing its complexity. The performance of these enhanced CNN models was carefully evaluated and analyzed. The experimental results revealed that the proposed method achieved an impressive success rate of 91%. These results highlight the effectiveness and potential of machine learning approaches in the early

diagnosis and treatment of melanoma, demonstrating their significant role in improving healthcare outcomes.

The remainder of this paper is structured as follows: In the second part, studies on melanoma cancer are presented. The main motivation of the study, the methods, and the dataset are presented in the third and fourth sections, respectively. The results of the experimental studies are presented in the fifth section, while the discussion and conclusions on the results obtained are included in the last section.

## 2. Related Works

DL has achieved great success in medical image classification and many other fields and is gradually replacing other machine-learning methods. Medical images play an essential role in diagnosis and treatment processes. By learning complex relationships in these images, DL models can be effective in many areas, such as disease diagnosis, lesion detection, and drug discovery. Moreover, DL has advantages over other machine learning methods in tasks such as image classification and feature extraction with high accuracy rates.

Promising results have been obtained in studies conducted in the literature. Litjens et al. [9] have shown that DL models can be successfully used in prostate and breast cancer staging. This research reveals that DL methods have significant potential in cancer diagnosis and staging using medical images. Their study shows that DL models can be more frequently used in the early diagnosis and treatment planning of essential diseases, such as prostate and breast cancer. Liu et al. [10] have developed a new deep learning model to detect prodromal and mild cognitive impairment stages of Alzheimer's disease. Their study demonstrates the potential of DL methods for early diagnosis and progression monitoring of Alzheimer's disease. Their research involves the creation of a customized model using deep neural networks on large datasets. The new model has successfully identified markers specific to Alzheimer's disease. A new CNN model proposed by Wang et al. [11] presents an approach that requires less user interaction and can perform medical image segmentation faster than existing methods. Automatic image segmentation refers to the process of identifying and distinguishing specific structures, e.g., organs or lesions, in medical images. Electroencephalography (EEG) signals are data recording electrical activity used to measure brain activity. Analysis of these signals plays a vital role in the diagnosis of epilepsy, sleep disorders, and assessment of neurological and psychiatric conditions such as attention deficit hyperactivity disorder (ADHD). Acharya et al. [12] have used a 13-layer CNN to analyze EEG signals and achieved high accuracy classification.

Esteva et al. [13] have studied skin cancer classification using deep neural networks. They have investigated the feasibility of using deep neural networks to achieve dermatologist-level classification performance. Besides, they have used a large skin cancer dataset containing 129,450 images. The researchers have achieved the accuracy rate  $72.1\% \pm 0.9\%$  when using Google's Inception v3 architecture by scaling the images to  $299 \times 299$ . Harangi [14] has evaluated the effectiveness of deep CNN ensembles in classifying skin lesions. Ensemble methods are a model created by combining several different CNNs.

DL techniques' primary advantage lies in their ability to directly apply to classification tasks without requiring pre-processing steps. In a notable study, Yap et al. [15] have introduced a method that integrates various image modalities and patient metadata. They have employed the Residual Network 50 (ResNet50) [16] network distinctly on both dermoscopic and macroscopic images, subsequently combining their features for the final classification task. This multi-model classifier demonstrated superior performance compared to the baseline model, which utilized only macroscopic images, achieving an Area Under Curve (AUC) value of 0.866. Similarly, Gessert et al. [17] have developed an ensemble model comprising EfficientNets [18], Squeeze-and-Excitation Network (SENet) [19], and Residual

Network Next Generation Weakly Supervised Learning (ResNeXt WSL) [20] to conduct a multi-class classification on the International Skin Imaging Collaboration (ISIC) 2019 dataset. A clipping strategy is applied to the images to cope with multiple model input resolutions. Furthermore, a loss balance approach has been used to deal with imbalanced datasets. Srinivasu et al. [21] have introduced a deep convolutional neural network (DCNN) that integrates MobileNetV2 [22] with Long Short-Term Memory (LSTM) [23] for classifying lesions on the HAM10000 dataset. The MobileNetV2 model demonstrated high efficiency and accuracy, making it suitable for lightweight computational devices. The proposed model excels in maintaining stateful information, leading to more precise predictions. Additionally, a grey-level co-occurrence matrix is employed to evaluate disease progression. The performance of this approach has been compared with other advanced models, including Fine-Tuned Neural Networks (FTNN) [24], CNN, Very deep Convolutional Networks for Large-Scale Image Recognition [25] developed by the Visual Geometry Group (VGG), and a modified convolutional neural network architecture. Utilizing the HAM10000 dataset, the proposed method outperformed these models with over 85% accuracy.

### 3. Materials and Methods

Melanoma skin cancer is one of the most crucial skin disorders. Early diagnosis of melanoma is critical for successful treatment of the disease. Today, melanoma is diagnosed by a specialist physician. Computer-aided systems are also being developed to improve the diagnostic process. Deep learning-based approaches (CNN, etc.) are widely used in these systems. In the CNN model, there are various operations performed in layers. This study evaluates the effects of using different numbers of CNN convolution layers and filters on classification performance.

#### 3.1. Dataset

The dataset used in the study includes a total of 10,605 image data. In the training set, there are a total of 9,605 images, of which 5,000 are labeled as benign tumors and 4,605 as melanoma. The test set includes a total of 1,000 images of which 500 are benign tumor images and 460 melanomas. In experimental studies, 70% of the data for the two classes was utilized for training, while 30% was used for testing. Some sample images of the dataset are shown in Figure 2.

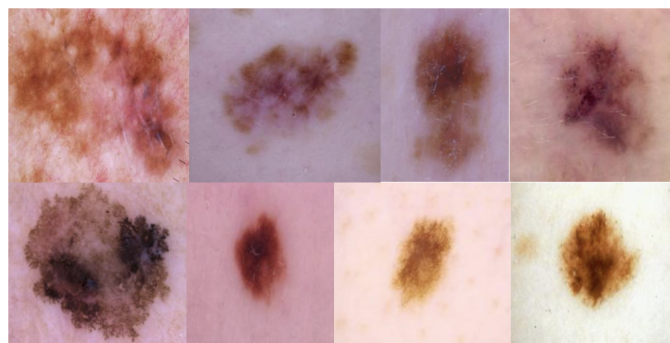


**Figure 2.** First and second rows show malignant and benign samples, respectively

#### 3.2. Deep Features

Extracting relevant attributes is fundamental for predicting patterns and making informed decisions in dataset analysis. Traditionally, feature extraction involved applying mathematical techniques or utilizing third-party methods, such as Speed-Up Robust Features (SURF) [26] and Scale-Invariant Feature Transform (SIFT) [27], designed to detect and describe local features in images. However, the advent of CNNs has revolutionized this process.

CNNs are advanced, multi-layered neural network architectures specifically designed to automatically learn and extract features from raw data. They consist of several types of layers, including convolutional layers that apply various filters to detect features, pooling layers that reduce the dimension while retaining important information, and fully connected layers that integrate these features for final classification or regression tasks.

The features obtained through these CNNs are known as deep features. These features are termed “deep” because they are generated through multiple layers of convolution and pooling, allowing the network to capture increasingly abstract and complex representations of the data. This hierarchical learning process enables CNNs to discern high-level patterns and intricate details within the data, making them highly effective for tasks, such as image recognition and classification.

### 3.3. CNN Model Configuration

CNNs represent a sophisticated class of machine-learning architectures designed for image classification tasks. These networks process images through a series of specialized layers. Initially, the image is fed into the input layer. Subsequently, the convolutional layers apply various filters to extract features, while normalization techniques are employed to standardize the aggregated data across different image channels. The values are then processed through an activation layer in which they are compared against a predefined threshold. Following this, sub-sampling is performed through pooling operations, which reduce the spatial dimensions of the data while preserving essential features. This sequence of convolution, normalization, activation, and pooling layers is iterated multiple times to refine the data representations progressively. Finally, the refined data is forwarded through one or more fully connected layers, which integrate the features for comprehensive analysis. Figure 3 shows the layer structures for a basic CNN model.

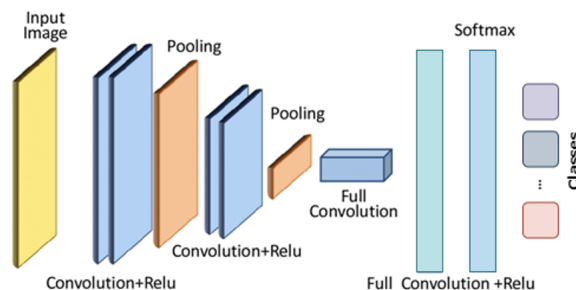


**Figure 3.** Basic CNN structure

We used the algorithm RMSprop (Root Mean Square Propagation) [28] for optimization, a key hyperparameter that adapts the learning rate based on recent gradients. RMSprop stabilizes training and accelerates convergence, essential for training our deep CNN model. The output from the fully connected layers is then classified using a soft-max function, which provides probabilistic predictions for each class. A key characteristic of CNNs is that the features extracted from the data typically improve in quality as the network depth increases. This network deepening enhances its ability to capture complex and hierarchical patterns within the image data, leading to more accurate classification results.

### 3.4. CNN Model with Variable Convolution Layering

This study developed various configurations of CNNs to assess the impact of convolutional layers and the number of filters on model performance. A critical aspect of these configurations is the choice of filter size and the number of filters used in each convolutional layer. Filter size determines the dimensions of the receptive fields that the network uses to extract features from the input data,

influencing the granularity of the detected patterns. Meanwhile, the number of filters controls the number of distinct features that can be learned and captured at each layer, thereby affecting the network’s ability to recognize and represent complex patterns.

Table 1 details the parameters for filter size (FS) and number of filters (NoF) employed across the convolutional layers in these CNN models. By varying these parameters, we aimed to evaluate their effects on the network’s performance and feature extraction capabilities, providing insights into how different configurations impact the overall effectiveness of the CNN in handling and classifying image data.

**Table 1.** Convolution layers’ parameters

Layer	FS	NoF
Conv1	[3 3]	8
Conv2	[3 3]	16
Conv3	[3 3]	32
Conv4	[3 3]	64
Conv5	[3 3]	128

The models created have the convolution layers specified in Table 2. All convolution layers have the same padding ratio.

**Table 2.** CNN models’ convolution layers

Model	Convolution Layers
CNN1	Conv1
CNN2	Conv1, Conv2
CNN3	Conv1, Conv2, Conv3
CNN4	Conv1, Conv2, Conv3, Conv4
CNN5	Conv1, Conv2, Conv3, Conv4, Conv5

The models have a maximum pooling layer after each convolution layer. Maximum pooling computes the average of the elements present in the region of the feature map covered by the filter. In the maximum pooling layer for all models, we used the pool size of [2 2] and the stride value of [2 2]. All models have in common a fully connected layer, a SoftMAX (Soft Maximum) [29] activation layer and a classification layer.

## 4. Experimental Results

Five different CNN models were designed within the experiments’ scope, and experiments were carried out. The CNN model image input size is  $64 \times 64 \times 3$  and in Red-Green-Blue (RGB) space. The hyper-parameter settings are common to all CNN models and are provided in Table 3.

**Table 3.** Common hyper-parameters for CNN models

Training Parameters
Max Epochs = 30
Initial Learn Rate = 0.01
Optimizer = ‘Rmsprop’
Shuffle = ‘every-epoch’
Validation Frequency = 30
Execution Environment = GPU

Figures 4 and 5 show the accuracy versus loss function values of CNN models with one and five convolution layers. While the accuracy value increases slightly in most iterations, the loss function tends to decrease. The decrease in the loss function at each iteration indicates that the model learns the patterns and relationships in the training data better. The parameters were updated to minimize the error. Thus, the improvement of the model is observed.

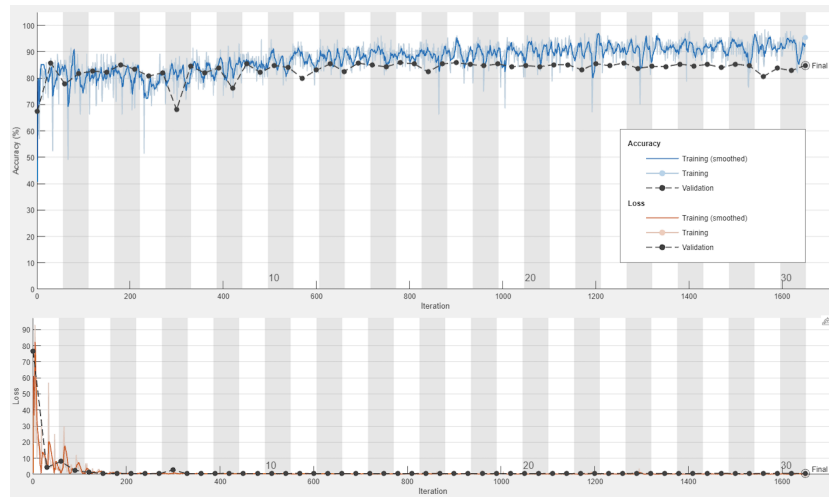


Figure 4. CNN model performance with a single convolution layer

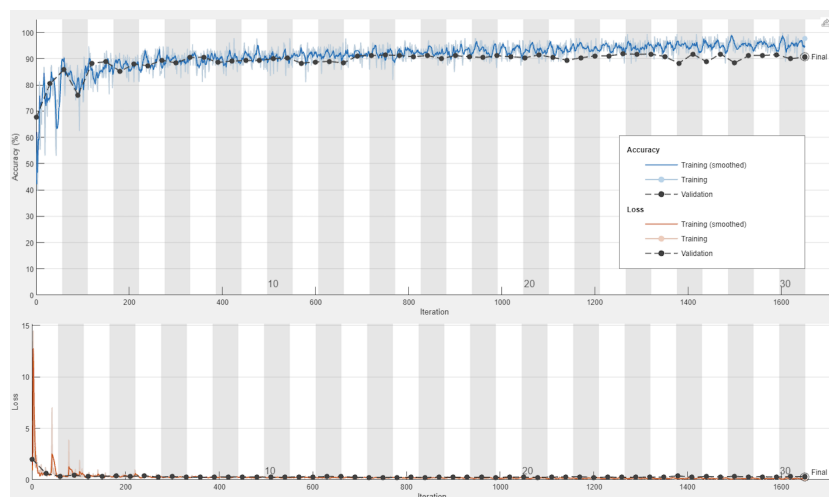


Figure 5. CNN model performance with five convolution layers

It can be observed Figures 4 and 5 that adding more convolution layers and filters improves classification performance. The confusion matrices' values for the CNN models are shown in Table 4. Confusion matrices summarize the performance of a classification model by presenting the counts of true positive (TP), false positive (FP), true negative (TN), and false negative (FN) predictions.

Table 4. Confusion matrices' values for CNN models

Model	TP	FP	TN	FN
CNN1	1693	293	1238	233
CNN2	1707	180	1351	219
CNN3	1719	134	1397	207
CNN4	1770	144	1387	156
CNN5	1757	146	1385	169

The results obtained by the performance metrics Accuracy (Acc), Sensitivity (Sen), Specificity (Spe), and F1-Score (F1) using the confusion matrices of CNN models are provided in Table 5.

**Table 5.** Results obtained by the performance metrics using the confusion matrices of CNN models

Model	Acc	Sen	Spe	F1
CNN1	84,78%	0,879	0,809	0,866
CNN2	88,46%	0,886	0,882	0,895
CNN3	90,14%	0,893	0,912	0,910
CNN4	91,32%	0,919	0,906	0,92
CNN5	90,89%	0,912	0,905	0,918

As can be observed from Table 5, while increasing the number of convolution layers and the number of filters improved the performance up to a certain point, the performance of the final model decreased compared to those of the previous model. Doubling the number of filters in each convolution layer compared to the previous one improved the performance to a certain extent.

## 5. Discussion

Accurate detection of skin diseases is vital in healthcare due to its significant impact on patient outcomes. Among various skin conditions, melanoma—a severe form of skin cancer—is particularly critical. Early detection of melanoma greatly enhances treatment success by preventing further spread and more severe complications. A comparison with similar studies is made in Table 6 below. As can be seen from the table, a significant accuracy value has been obtained with the proposed simple CNN model. It should be stated that the convolution layers and the number of filters in these layers are effective for the final performance, in the proposed model.

**Table 6.** Comparison with featured studies

Study	Method	Data	Performance
[5]	Watershed Segmentation, kNN (k-Nearest Neighbors) [30], RandomForest [31], SVM	1000	89.43% Acc
[6]	ResNet-50, XGBoost (eXtreme Gradient Boosting) [32], Statistical Analysis	11444	89.00% Acc
[7]	Caffe CNN [33], Sparse Coding [34], SVM	2624	73.90% Acc
[14]	Pre-trained CNNs [35], Ensemble [36], Majority Voting [37]	2000	89.10% Acc
This Study	Configurable Simple CNN Model	10605	91.32% Acc

This study used advanced machine learning techniques to diagnose skin lesions, particularly distinguishing between benign moles and malignant melanoma.

We developed a CNN model, which was initially simple but improved by adding more layers and filters. Increasing the number of convolutional layers and filters enhances the model’s ability to learn complex features. Despite these improvements, the increased complexity of the model introduces challenges such as over-fitting and higher computational costs. To address these challenges, future research should explore strategies such as integrating multi-modal data, leveraging transfer learning to reduce training time, and employing advanced regularization techniques. Developing real-time diagnostic tools and mobile applications could also facilitate broader and more accessible melanoma screening. Future studies can enhance the efficacy and practicality of early melanoma detection and improve overall healthcare outcomes.

## 6. Conclusion

Early and precise diagnosis of melanoma is essential for successful treatment and prevention of disease progression. This study explored the application of CNNs to differentiate between benign moles and malignant melanoma, achieving a high accuracy rate of 91%. By systematically enhancing the model architecture with additional layers and filters, we demonstrated the effectiveness of CNN-based approaches in accurately identifying skin lesions. These findings confirm that machine learning models can significantly contribute to the early detection and management of melanoma when properly developed and optimized. Integrating such technology into clinical practice could transform how skin diseases are diagnosed, leading to more efficient and accurate interventions. Future research should aim to further improve model accuracy by expanding the dataset and exploring complementary algorithms to enhance diagnostic reliability and scalability.

## Author Contributions

All the authors equally contributed to this work. They all read and approved the final version of the paper.

## Conflicts of Interest

All the authors declare no conflict of interest.

## Ethical Review and Approval

No approval from the Board of Ethics is required.

## References

- [1] A. Masood, A. Al-Jumaily, *Computer-aided diagnostic support system for skin cancer: A review of techniques and algorithms*, International Journal of Biomedical Imaging 2013 (1) (2013) 323268 22 pages.
- [2] International Agency for Research on Cancer, <https://www.iarc.who.int>, Accessed on 15 May 2024.
- [3] American Cancer Society, Key Statistics for Melanoma Skin Cancer (2024), <https://www.cancer.org/cancer/melanoma-skin-cancer/about/key-statistics.html>, Accessed on 15 May 2024.
- [4] K. Thomsen, L. Iversen, T. L. Titlestad, O. Winther, *Systematic review of machine learning for diagnosis and prognosis in dermatology*, Journal of Dermatological Treatment 31 (5) (2020) 496–510.
- [5] J. R. Quinlan, *Induction of decision trees*, Machine Learning 1 (1986) 81–106.
- [6] C. Cortes, V. Vapnik, *Support-vector networks*, Machine Learning 20 (3) (1995) 273–297.
- [7] F. Rosenblatt. *The perceptron: A probabilistic model for information storage and organization in the brain*, Psychological Review 65 (6) (1958) 386—408.
- [8] N. Codella, J. Cai, M. Abedini, R. Garnavi, A. Halpern, J. R. Smith, *Deep learning, sparse coding, and SVM for melanoma recognition in dermoscopy images*, in L. Zhou, L. Wang, Q. Wang, Y. Shi (Eds.), Machine Learning in Medical Imaging, 2015, pp. 118–126.

- [9] G. Litjens, C. I. Sanchez, N. Timofeeva, M. Hermsen, I. Nagtegaal, I. Kovacs, C. H. van de Kaa, P. Bult, B. van Ginneken, J. van der Laak, *Deep learning as a tool for increased accuracy and efficiency of histopathological diagnosis*, Scientific Reports 6 (2016) Article Number 26286 11 pages.
- [10] S. Liu, W. Cai, S. Pujol, R. Kikinis, D. Feng, *Early diagnosis of Alzheimer's disease with deep learning*, in G. Wang, B. He (Eds.), IEEE 11th International Symposium on Biomedical Imaging, Beijing, 2014, pp. 1015–1018.
- [11] G. Wang, W. Li, M. A. Zuluaga, R. Pratt, P. A. Patel, M. Aertsen, T. Vercauteren, *Interactive medical image segmentation using deep learning with image-specific fine-tuning*, IEEE Transactions on Medical Imaging 37 (7) (2018) 1562–1573.
- [12] U. R. Acharya, S. L. Oh, Y. Hagiwara, J. H. Tan, H. Adeli, *Deep convolutional neural network for the automated detection and diagnosis of seizure using EEG signals*, Computers in Biology and Medicine 100 (2018) 270–278.
- [13] A. Esteva, B. Kuprel, R. A. Novoa, J. Ko, S. M. Swetter, H. M. Blau, S. Thrun, *Dermatologist-level classification of skin cancer with deep neural networks*, Nature 542 (2017) 115–118.
- [14] B. Harangi, *Skin lesion classification with ensembles of deep convolutional neural networks*, Journal of Biomedical Informatics 86 (2018) 25–32.
- [15] J. Yap, W. Yolland, P. Tschandl, *Multimodal skin lesion classification using deep learning*, Experimental Dermatology 27 (11) (2018) 1261–1267.
- [16] K. He, X. Zhang, S. Ren, J. Sun, *Deep residual learning for image recognition*, in T. Tuytelaars, F.-F. Li, R. Bajcsy (Eds.), 29th IEEE Conference on Computer Vision and Pattern Recognition, Las Vegas, 2016, pp. 770–778.
- [17] N. Gessert, M. Nielsen, M. Shaikh, R. Werner, A. Schlaefer, *Skin lesion classification using ensembles of multi-resolution EfficientNets with meta data*, MethodsX 7 (2020) 100864 8 pages.
- [18] M. Tan, Q. V. Le, *EfficientNet: Rethinking model scaling for convolutional neural networks*, in K. Chaudhuri, R. Salakhutdinov (Eds.), 36th International Conference on Machine Learning, California, 2019, pp. 6105–6114.
- [19] J. Hu, L. Shen, G. Sun, *Squeeze-and-excitation networks*, in M. S. Brown, B. Morse, S. Peleg (Eds.), IEEE/CVF Conference on Computer Vision and Pattern Recognition, Salt Lake City, 2018, pp. 7132–7141.
- [20] D. Mahajan, R. Girshick, V. Ramanathan, H. Kaiming, M. Paluri, Y. Li, A. Bharambe, L. V. D. Maaten, *Exploring the limits of weakly supervised pretraining*, in V. Ferrari, M. Hebert, C. Sminchisescu, Y. Weiss (Eds.), 15th European Conference on Computer Vision, Munich, 2018, pp. 181–196.
- [21] P. N. Srinivasu, J. G. SivaSai, M. F. Ijaz, A. K. Bhoi, W. Kim, J. J. Kang, *Classification of skin disease using deep learning neural networks with MobileNet V2 and LSTM*, Sensors 21 (8) (2021) 2852 27 pages.
- [22] M. Sandler, A. Howard, M. Zhu, A. Zhmoginov, L. Chen, *MobileNetV2: Inverted residuals and linear bottlenecks*, in M. S. Brown, B. Morse, S. Peleg (Eds.), IEEE/CVF Conference on Computer Vision and Pattern Recognition, Salt Lake City, 2018, pp. 4510–4520.
- [23] S. Hochreiter, J. Schmidhuber, *Long short-term memory*, Neural Computation 9 (8) (1997) 1735–1780.

- [24] J. Yosinski, J. Clune, Y. Bengio, H. Lipson, *How transferable are features in deep neural networks*, in Z. Ghahramani, M. Welling, C. Cortes, N. D. Lawrence, K. Q. Weinberger (Eds.), 28th International Conference on Neural Information Processing Systems, Cambridge, 2014, pp. 3320–3328.
- [25] K. Simonyan, A. Zisserman, *Very deep convolutional networks for large-scale image recognition*, in Y. Bengio, Y. LeCun (Eds.), International Conference on Learning Representations, San Diego, 2015, pp. 1–14.
- [26] H. Bay, T. Tuytelaars, L. Van Gool, *SURF: Speeded up robust features*, in A. Leonardis, H. Bischof, A. Pinz (Eds.), 9th European Conference on Computer Vision, Graz, 2006, pp. 404–417.
- [27] D. G. Lowe, *Distinctive image features from scale-invariant keypoints*, International Journal of Computer Vision 60 (2) (2004) 91–110.
- [28] M. C. Mukkamala, M. Hein, *Variants of RMSProp and Adagrad with Logarithmic Regret Bounds*, in D. Precup, Y. W. Teh (Eds.), 34th International Conference on Machine Learning, Sydney, 2017, pp. 2545–2553.
- [29] C. M. Bishop, Pattern recognition and machine learning, Springer, New York, 2006.
- [30] E. Fix, J. L. Hodges, *Discriminatory analysis, nonparametric discrimination: Consistency properties*, Technical Report USAF School of Aviation Medicine (1951) Dayton.
- [31] T. K. Ho, *Random decision forests*, in C. Y. Suen (Ed.), 3rd International Conference on Document Analysis and Recognition, Montreal, 1995, pp. 278–282.
- [32] T. Chen, C. Guestrin, *XGBoost: A scalable tree boosting system*, in B. Krishnapuram, M. Shah (Eds.), 22nd ACM SIGKDD International Conference on Knowledge Discovery and Data Mining, San Francisco, 2016, pp. 785–794.
- [33] Y. Jia, E. Shelhamer, J. Donahue, S. Karayev, J. Long, R. Girshick, S. Guadarrama, T. Darrell. *Caffe: Convolutional architecture for fast feature embedding*, in K. A. Hua, Y. Rui, R. Steinmetz (Eds.), 22nd ACM International Conference on Multimedia, Orlando , 2014, 675–678.
- [34] B. A. Olshausen, D. J. Field, *Emergence of simple-cell receptive field properties by learning a sparse code for natural images*, Nature 381 (1996) 607–609.
- [35] A. Krizhevsky, I. Sutskever, G. E. Hinton, *ImageNet classification with deep convolutional neural networks*, in F. Pereira, C. J. Burges, L. Bottou, K. Q. Weinberger (Eds.), Advances in Neural Information Processing Systems 25, Lake Tahoe, 2012, pp. 1097–1105.
- [36] T. G. Dietterich, *Ensemble methods in machine learning*, in J. Kittler, F. Roli (Eds.), Multiple Classifier Systems, Cagliari, 2000, pp. 1–15.
- [37] M. Kearns, Thoughts on Hypothesis Boosting (1988), <https://www.cis.upenn.edu/~mkearns/>, Accessed 10 May 2024.